frontiers | Research Topics

Remote sensing of cloud, aerosols, and radiation from satellites

Edited by
Seiji Kato, Howard Barker, Jens Redemann, Derek Posselt,
Richard Ferrare, Matthew Lebsock and Arlindo Da Silva

Published in
Frontiers in Remote Sensing

ISSN 1664-8714
ISBN 978-2-83250-928-9
DOI 10.3389/978-2-83250-928-9

About Frontiers

Frontiers is more than just an open access publisher of scholarly articles: it is a pioneering approach to the world of academia, radically improving the way scholarly research is managed. The grand vision of Frontiers is a world where all people have an equal opportunity to seek, share and generate knowledge. Frontiers provides immediate and permanent online open access to all its publications, but this alone is not enough to realize our grand goals.

Frontiers journal series

The Frontiers journal series is a multi-tier and interdisciplinary set of open-access, online journals, promising a paradigm shift from the current review, selection and dissemination processes in academic publishing. All Frontiers journals are driven by researchers for researchers; therefore, they constitute a service to the scholarly community. At the same time, the *Frontiers journal series* operates on a revolutionary invention, the tiered publishing system, initially addressing specific communities of scholars, and gradually climbing up to broader public understanding, thus serving the interests of the lay society, too.

Dedication to quality

Each Frontiers article is a landmark of the highest quality, thanks to genuinely collaborative interactions between authors and review editors, who include some of the world's best academicians. Research must be certified by peers before entering a stream of knowledge that may eventually reach the public - and shape society; therefore, Frontiers only applies the most rigorous and unbiased reviews. Frontiers revolutionizes research publishing by freely delivering the most outstanding research, evaluated with no bias from both the academic and social point of view. By applying the most advanced information technologies, Frontiers is catapulting scholarly publishing into a new generation.

What are Frontiers Research Topics?

Frontiers Research Topics are very popular trademarks of the *Frontiers journals series*: they are collections of at least ten articles, all centered on a particular subject. With their unique mix of varied contributions from Original Research to Review Articles, Frontiers Research Topics unify the most influential researchers, the latest key findings and historical advances in a hot research area.

Find out more on how to host your own Frontiers Research Topic or contribute to one as an author by contacting the Frontiers editorial office: frontiersin.org/about/contact

Remote sensing of cloud, aerosols, and radiation from satellites

Topic editors

Seiji Kato — Langley Research Center, National Aeronautics and Space Administration, United States

Howard Barker — Environment and Climate Change Canada (ECCC), Canada

Jens Redemann — University of Oklahoma, United States

Derek Posselt — NASA Jet Propulsion Laboratory (JPL), United States

Richard Ferrare — National Aeronautics and Space Administration (NASA), United States

Matthew Lebsock — NASA Jet Propulsion Laboratory (JPL), United States

Arlindo Da Silva — Goddard Space Flight Center, National Aeronautics and Space Administration, United States

Citation

Kato, S., Barker, H., Redemann, J., Posselt, D., Ferrare, R., Lebsock, M., Da Silva, A., eds. (2022). *Remote sensing of cloud, aerosols, and radiation from satellites*. Lausanne: Frontiers Media SA. doi: 10.3389/978-2-83250-928-9

Table of contents

05 Editorial: Remote sensing of cloud, aerosols, and radiation from satellites
A. M. da Silva, S. Kato, H. Baker, J. Redemann, D. Posselt, R. Ferrare and M. Lebsock

08 The Spectral Nature of Earth's Reflected Radiation: Measurement and Science Applications
Graeme Stephens, Olga Kalashnikova, Jake J. Gristey, Peter Pilewskie, David R. Thompson, Xianglei Huang, Matthew Lebsock and Sebastian Schmidt

26 Improved Lorenz-Mie Look-Up Table for Lidar and Polarimeter Retrievals
Eduard Chemyakin, Snorre Stamnes, Sharon P. Burton, Xu Liu, Chris Hostetler, Richard Ferrare, Brian Cairns and Oleg Dubovik

43 Liquid Phase Cloud Microphysical Property Estimates From CALIPSO Measurements
Yongxiang Hu, Xiaomei Lu, Peng-Wang Zhai, Chris A. Hostetler, Johnathan W. Hair, Brian Cairns, Wenbo Sun, Snorre Stamnes, Ali Omar, Rosemary Baize, Gorden Videen, Jay Mace, Daniel T. McCoy, Isabel L. McCoy and Robert Wood

53 Deep Convection as Inferred From the C2OMODO Concept of a Tandem of Microwave Radiometers
Franck Auguste and Jean-Pierre Chaboureau

67 Mind the Gap - Part 3: Doppler Velocity Measurements From Space
Pavlos Kollias, Alessandro Battaglia, Katia Lamer, Bernat Puigdomenech Treserras and Scott A. Braun

85 Analysis of Scattering Angle Sampling by Multi-Angle Imaging Polarimeters for Different Orbit Geometries
Sabrina N. Thompson, Bastiaan van Diedenhoven, Peter R. Colarco, Patricia Castellanos, Eric Lian and J. Vanderlei Martins

96 Time-Delayed Tandem Microwave Observations of Tropical Deep Convection: Overview of the C^{2}OMODO Mission
Hélène Brogniez, Rémy Roca, Franck Auguste, Jean-Pierre Chaboureau, Ziad Haddad, Stephen J. Munchak, Xiaowen Li, Dominique Bouniol, Alexis Dépée, Thomas Fiolleau and Pavlos Kollias

114 **Polarimeter + Lidar–Derived Aerosol Particle Number Concentration**
Joseph S. Schlosser, Snorre Stamnes, Sharon P. Burton, Brian Cairns, Ewan Crosbie, Bastiaan Van Diedenhoven, Glenn Diskin, Sanja Dmitrovic, Richard Ferrare, Johnathan W. Hair, Chris A. Hostetler, Yongxiang Hu, Xu Liu, Richard H. Moore, Taylor Shingler, Michael A. Shook, Kenneth Lee Thornhill, Edward Winstead, Luke Ziemba and Armin Sorooshian

127 **Polarized Radiative Transfer Simulations: A Tutorial Review and Upgrades of the Vector Discrete Ordinate Radiative Transfer Computational Tool**
Zhenyi Lin, Snorre Stamnes, Wei Li, Yongxiang Hu, Istvan Laszlo, Si-Chee Tsay, Alexander Berk, Jeannette van den Bosch and Knut Stamnes

frontiers | Frontiers in Remote Sensing

TYPE Editorial
PUBLISHED 13 October 2022
DOI 10.3389/frsen.2022.1040835

OPEN ACCESS

EDITED AND REVIEWED BY
Oleg Dubovik,
UMR8518 Laboratoire d'optique
Atmosphèrique (LOA), France

*CORRESPONDENCE
A. M. da Silva,
arlindo.m.dasilva@nasa.gov

SPECIALTY SECTION
This article was submitted to Satellite Missions,
a section of the journal
Frontiers in Remote Sensing

RECEIVED 09 September 2022
ACCEPTED 16 September 2022
PUBLISHED 13 October 2022

CITATION
da Silva AM, Kato S, Baker H, Redemann J, Posselt D, Ferrare R and Lebsock M (2022), Editorial: Remote sensing of cloud, aerosols, and radiation from satellites.
Front. Remote Sens. 3:1040835.
doi: 10.3389/frsen.2022.1040835

Editorial: Remote sensing of cloud, aerosols, and radiation from satellites

A. M. da Silva[1]*, S. Kato[2], H. Baker[3], J. Redemann[4], D. Posselt[5], R. Ferrare[2] and M. Lebsock[5]

[1]Goddard Space Flight Center, National Aeronautics and Space Administration, Greenbelt, MD, United States, [2]Langley Research Center, National Aeronautics and Space Administration, Hampton, VA, United States, [3]Environment and Climate Change Canada, Burlington, ON, Canada, [4]School of Meteorology, University of Oklahoma, Norman, Ok, United States, [5]NASA Jet Propulsion Laboratory (JPL), Pasadena, CA, United States

KEYWORDS

clouds, aerosols, convection, precipitation, radiation, satellite, satellite missions

Editorial on the Research Topic
Remote sensing of cloud, aerosols, and radiation from satellites

Planning a research satellite mission involves a careful study phase in which science objectives are defined and the measurements necessary to achieve these objectives are identified, which then determine instrument and other mission requirements. Obtaining the necessary geophysical variables with the required accuracies necessitates suitable retrieval algorithms and methods to assess how well the objectives can be realized, all within a well-defined budget and schedule. The pre-launch objective assessment phase represents a crucial and invaluable step for defining and justifying a mission. Yet, despite their importance, these algorithms and assessments are generally not readily accessible to researchers who are not involved directly in this mission study phase. This volume aims to add some transparency to this process.

The goal of this research topic is to document some of the pre-launch studies being conducted for NASA's Atmosphere Observing System (AOS, formerly ACCP–Aerosols, Cloud, Convection and Precipitation) and the ESA/JAXA EarthCARE satellite programs. The primary scientific focus of these missions is to elucidate the multifaceted interactions between aerosols, clouds, convection and precipitation at the process level.

Aerosols interact with radiation directly and indirectly *via* perturbations to macro- and micro-physical properties of clouds. The resulting impacts on regional and global weather and climate can perturb radiative forcing induced by changing greenhouse gas concentrations, determine cloud feedback strengths, and their impacts on the dynamics and thermodynamics of the atmosphere. Observing how clouds and aerosols influence atmospheric radiative transfer, thermodynamics and the atmospheric circulation is a key element in understanding how Earth will respond to climate change with far reaching consequences for the hydrosphere, cryosphere and the hydrological cycle of the planet.

In order to infer the vertical properties of aerosol, clouds, precipitation and their impact on the Earth's climate, multiple instruments are required to make simultaneous and synergistic measurements. Specifically, the combination of new active and passive sensors, combined with sensors from the Program of Record (those satellites currently in space or planned for launch in the coming years) can facilitate a paradigm-shift in observing and understanding the roles of clouds and aerosols in weather and climate.

In the first paper in this volume, Stephens et al. introduces the *Atmosphere Observing System* (AOS, formerly known as ACCP, the Aerosols, Cloud, Convection and Precipitation study) being developed by NASA in response to the 2017 Decadal Survey (National Academies of Sciences, Engineering, and Medicine, 2018). With a suite of measurements spanning radars, lidars, polarimeters and microwave radiometers, the AOS mission will provide the next big step in space measurements of aerosol, clouds, convection and precipitation. Stephens et al. describes the science objective of AOS and key science questions it promises to elucidate.

The calculation of aerosol single scattering properties is a computationally challenging task that is at the core of any algorithm that retrieves aerosol microphysical parameters. In *Improved Lorenz-Mie Look-Up Table for Lidar and Polarimeter Retrievals*, Chemyakin et al. explore recent advances in computational resources to develop a novel and improved Lorenz-Mie look-up table of light scattering properties using an ensemble of isotropic spheres at arbitrary wavelengths from ultraviolet to the shortwave infrared part of the spectrum. In addition to the look-up tables proper, the author make freely available all the software used for the calculations.

Machine learning is fast becoming an indispensable tool in many areas of atmospheric remote sensing. In Hu et al., a neural network model informed by CALIOP measurements is developed to retrieve vertically resolved macro and microphysical properties of water clouds. A 14 + yearlong global dataset of cloud properties is developed and validated against airborne measurements and other measurements from the Program of Record.

While great emphasis is placed on measurement accuracy and instrument design when developing a space mission, other mission design aspects such as orbit geometry, solar geometry and swath width can have a profound impact on the resulting datasets. With a focus on polarimetry, in Thompson et al., the authors examine the distribution of scattering angles associated with the inclined and polar orbits being considered for the AOS mission. Their thorough calculations, which explore the sensitivity to elements such as orbit inclination and swath width, provide critical information for the design of the AOS mission.

The concept of delta-t or tendency measurements–measurements provided by a pair of microwave radiometers separated by several tenths of seconds–have received considerable interest as an affordable approach for gaining insights on the dynamics of convective storms. Brogniez et al. provides an overview of the *Convective Core Observations through MicrOwave Derivatives in the TrOpics* (C^2OMODO) concept, and explore the information content provided by such measurements. In *Deep Convection as Inferred From the C^2OMODO Concept of a Tandem of Microwave Radiometers*, Auguste and Chaboureau use numerical simulations of two deep convective events, and an detailed instrument simulator, to derive very useful relationships between the "measured" brightness temperature, its time derivative and key geophysical quantities such as vertical ice momentum, vertical ice velocity and ice water path. Such measurements provide a novel approach to derive geophysical properties that are usually accomplished with active sensors.

Spaceborne measurements of vertical air velocity by Doppler radars is a critical component of emerging satellite missions aiming to elucidate the dynamics of clouds and convective storms. In *Mind the Gap–Part 3: Doppler Velocity Measurements from Space*, Kollias et al. present comprehensive forward simulations for assessing the advantages and drawbacks of six Doppler radars being considered by major space agencies around the world.

Polarized radiative transfer modeling is a foundational tool for the development of cloud and aerosol algorithms based on polarimetric measurements. Lin et al. give us a detailed description of several important upgrades to the Vector Discrete Ordinate Radiative Transfer (VDISORT) model, a polarized (vector) radiative transfer model that can be applied to a range of earth system retrievals. This paper provides very valuable information for developers of retrieval algorithms that seek to understand the internal works of a radiative transfer model.

Finally, the benefits of synergistic lidar-polarimetry measurements is a topic of great relevance to missions such as NASA's Atmosphere Observing System (AOS). In *Polarimeter + Lidar–Derived Aerosol Particle Number Concentration*, Schlosser et al. propose a simple and effective method for deriving vertically-resolved aerosol particle number concentration (N_a) based on active lidar measurements and passive polarimetric measurements. By using airborne observations from the NASA ACTIVATE campaign in the western Atlantic, the authors demonstrate that that the vertically resolved N_a represent a significant improvement over other existing remote sensing estimates.

In summary, the papers presented in this volume provide an excellent overview of some of the upcoming space missions to study aerosols, clouds, convection and precipitation and the candidate measurements that promise to revolutionize the next decade of earth observations.

Author contributions

AS drafted the initial editorial with contributions and review from co-authors.

Conflict of interest

The authors declare that the research was conducted in the absence of any commercial or financial relationships that could be construed as a potential conflict of interest.

Publisher's note

References

National Academies of Sciences, Engineering, and Medicine (2018). *Thriving on our changing planet: A decadal strategy for Earth observation from space*. Washington: DC: The National Academies Press. doi:10.17226/24938

frontiers
in Remote Sensing

REVIEW
published: 26 May 2021
doi: 10.3389/frsen.2021.664291

The Spectral Nature of Earth's Reflected Radiation: Measurement and Science Applications

Graeme Stephens[1]*, Olga Kalashnikova[1], Jake J. Gristey[2,3], Peter Pilewskie[4], David R. Thompson[1], Xianglei Huang[5], Matthew Lebsock[1] and Sebastian Schmidt[4]

[1]Jet Propulsion Laboratory, California Institute of Technology, Pasadena, CA, United States, [2]Cooperative Institute for Research in Environmental Sciences, University of Colorado, Boulder, CO, United States, [3]NOAA Chemical Sciences Laboratory, Boulder, CO, United States, [4]Laboratory for Atmospheric and Space Physics, University of Colorado, Boulder, CO, United States, [5]Department of Climate and Space Sciences and Engineering, The University of Michigan, Ann Arbor, MI, United States

Edited by:
Yongxiang Hu,
National Aeronautics and Space Administration (NASA), United States

Reviewed by:
Norman Loeb,
National Aeronautics and Space Administration (NASA), United States
Zhanqing Li,
University of Maryland, United States
Brian Cairns,
Goddard Institute for Space Studies (NASA), United States

***Correspondence:**
Graeme Stephens
graeme.stephens@jpl.nasa.gov

Specialty section:
This article was submitted to Satellite Missions, a section of the journal Frontiers in Remote Sensing

Received: 04 February 2021
Accepted: 06 May 2021
Published: 26 May 2021

Citation:
Stephens G, Kalashnikova O, Gristey JJ, Pilewskie P, Thompson DR, Huang X, Lebsock M and Schmidt S (2021) The Spectral Nature of Earth's Reflected Radiation: Measurement and Science Applications. Front. Remote Sens. 2:664291. doi: 10.3389/frsen.2021.664291

This paper introduces the aerosol, clouds, convection and precipitation (ACCP) program that is currently in the process of defining a number of measurement objectives for NASA that are to be implemented toward the end of the current decade. Since a (solar) visible-shortwave infrared (VSWIR) spectrometer is being considered as part of the ACCP architecture, illustrations of the different ways these measurements will contribute to this program and how these measurements can be expected to advance the science objectives of ACCP are highlighted. These contributions range from 1) constraining cloud radiative process and related estimates of radiative fluxes, 2) scene discrimination, 3) providing aerosol and cloud optical properties, and 4) providing other enhanced information such as the phase of water in clouds, and total column water vapor. The spectral measurements also offer new capabilities that will further enhance the ACCP science such as the discrimination of dust aerosol and the potential for the vertical profiling cloud droplet size in shallow clouds. The areas where the maturity of approaches is lacking is also highlighted as a way of emphasizing research topics to be a focus in the coming years.

Keywords: solar radiation, spectral solar radiation, cloud properties, aerosol properties, cloud albedo

INTRODUCTION

The reflection of sunlight by Earth to space is a process that exerts a basic control on Earth's climate through the way Earth differentially scatters and absorbs solar energy from place to place which is a basic forcing of the transport of heat poleward. The scattered sunlight also influences Earth's climate through the processes it shapes in the form of feedbacks that principally control the responses to external forcings of the climate system. Insights about these processes are encoded in the spectral nature of the reflected solar radiation to space. On a very gross Earth-system level, the relevance of spectrally resolved measurements of reflected sunlight is underscored in the example of **Figure 1fig1** from Stephens et al. (2015). It offers a commentary on an observational quirk about the broadband albedo of planet Earth in that each hemisphere reflects exactly the same amount of sunlight (von der Haar and Suomi, 1969; Stephens et al., 2015). This curious symmetry is not replicated by current state of the art Earth system models (e.g Haywood et al., 2016; Stephens et al., 2016). While the total energy reflected back to space from each hemisphere of Earth is the same, the details are quite different between hemispheres as revealed in the spectral nature of this reflected energy observed by

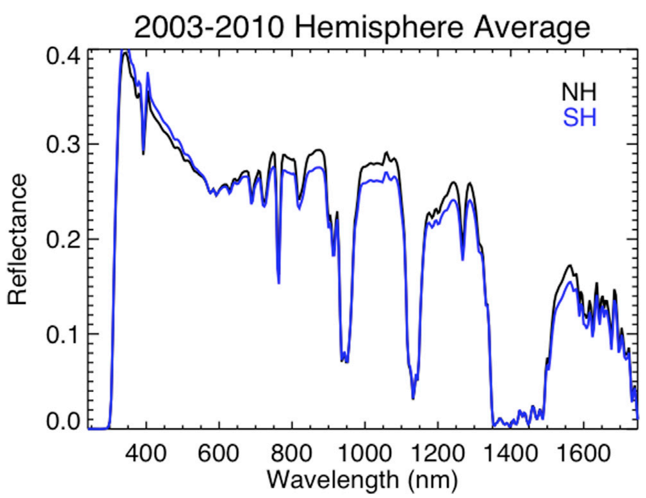

FIGURE 1 | The hemispheric averaged spectral reflection measured by SCIAMACHY that highlighting the nature of the difference in spectral reflection between these two hemispheres (adapted from Stephens et al. (2015)).

SCHIAMACHY shown in **Figure 1**. The Northern Hemisphere has less visible reflection due to a smaller cloud contribution but more SWIR reflection from greater land areas. Conversely the Southern Hemisphere reflects proportionally more at shorter visible wavelengths than in the SWIR do to the larger cloud cover of that hemisphere. These spectral differences hint at how both land and clouds contribute in different ways to the reflection by each hemisphere, hinting at a broad insight on processes that govern the planetary albedo. This is a simple illustration of the way spectral measurements provide a way of deciphering how different reflecting surfaces and scattering media contribute to the total spectrally integrated energy reflected to space.

Also encoded in the spectral properties of reflected sunlight is important information about the scatterers themselves. The retrieval of cloud optical properties using measurements of reflected sunlight, for example, has a relatively long history (e.g. Stephens and Kummerow, 2007 and references therein) with the bi-spectral reflectance method of Twomey and Seton (1980) being mature and now applied to measurements across a number of different satellite sensors. Surface measurements of spectral transmittance have also been used to deduce properties of aerosol for more than a century (e.g. Stephens, 1994; O'Neil et al., 2003) while satellite measurements of spectral reflectance provide the means to deduce properties of aerosol, such as their optical properties classified in terms of fine and coarse mode over ocean (e.g. Kaufman et al., 1997; Levy et al., 2007; Wang et al., 2015) or over land (e.g. Yan et al., 2019; Yan et al., 2021). In addition, UV reflected radiation is sensitive to both aerosol scattering and absorption which makes it possible to deduce both total aerosol optical depth (AOD) and absorption properties expressed as single scattering albedo (Ahn et al., 2014). Still other important information lies in the spectral reflectance as described below.

The purpose of this paper is to expand on the different ways measurements of spectrally resolved VSWIR reflectances serve a number of emerging Earth science objectives in the coming decade. The paper begins with a brief introduction to the Aerosol, clouds, convection and precipitation (ACCP) program that is currently in the process of defining a number of measurement objectives for NASA to be implemented toward the end of the current decade. The full complement of sensor measurements planned for ACCP, and the advantages of combining the different information from these sensors, is not discussed in any detail and is to be a topic of a future paper. This paper focuses specifically on the different ways a VSWIR spectrometer that is being considered as part of the ACCP architecture is expected to contribute to this program and can be expected to advance the science objectives of ACCP. These range from 1) constraining cloud radiative process and related estimates of radiative fluxes described in more detail below in *Top-of-Atmosphere Radiative Effects*, 2) scene discrimination, 3) providing aerosol and cloud optical properties, and 4) providing other enhanced information such as the phase of water in clouds, total column water vapor (TCWV), particle size profiles in shallow clouds among other properties discussed.

THE AEROSOL, CLOUDS, CONVECTION AND PRECIPITATION DESIGNATED OBSERVABLE PROGRAM

The National Academies of Sciences, Engineering, and Medicine conducted the 2017–2027 decadal survey of Earth Science and Applications from Space and produce a series of recommendations in the report (NAS, 2018). This was the second such Earth science survey and it converged to a final, small set of science, applications and observing system priorities starting from a large number of community-provided inputs. Emerging from these were a set of five designated observables (DO's) declared to be of highest priority for the decade and NASA has commenced in developing these observable recommendations into missions.

Observations of aerosol and separately observations of clouds and convection and precipitation were two recommended designated observables. It was recognized from the outset that science of each significantly overlap. Cloud feedback was a preeminent issue considered by the climate panel and convection and precipitation measurements were deemed essential to advance understanding and prediction of moist convection and its influence on weather and extremes. Observations of aerosol were also a high priority to climate science due to their influence on climate forcings as well as on clouds and precipitation. The relation between aerosol and air quality was further considered to be a pressing environmental risk.

The two designated observable recommendations, aerosol (A) and clouds, convection and precipitation (CCP), were subsequently combined into a single study (hereafter ACCP) to define the measurement strategy to advance the observations under these topic areas. ACCP is largely a process focused effort that has a number of integrative elements including, 1) a wider exploitation of the existing and planned instruments and satellites

TABLE 1 | Geophysical variables that are to be derived from solar spectrum and their relation to ACCP objectives.

Geophysical variable	ACCP objectives	Comments/Relationship to other
Cloud droplet effective radius	O1, O6, O7, O8	• mature algorithms provide r_e over the full swath complementing narrow swath polarimeter estimates • spectra offer potential to derive in-cloud r_e profile thereby reducing uncertainty in cloud droplet number concentration and LWP
Cloud optical depth	O1, O2, O6, O7, O8	• high spatial resolution (~0.5 km) improves non-uniformity bias in the larger footprint of the polarimetry
Cloud liquid water path	O1, O8	• derived from the r_e and tau • spectra reduces uncertainty relative to imagery and profiles remove biases inherent to use of cloud top particle sizes
Cloud phase	O4	• cloud phase derived across broad swath compliments narrow swath lidar and polarimeter information
Cloud top pressure	N/A	• needed to derive cloud radiative effects • mature techniques using O2 A-band absorption • swath complements nadir lidar measurements
Areal cloud fraction	O1, O4, O7, O8	• spectra increase accuracy relative to imagery by improved scene discrimination • high spatial resolution provides improved cloud boundaries compared to polarimeter and the imagery of the POR.
Aerosol optical depth	O3, O5, O6, O7, O8	• spectra increase capability of aerosol typing and aerosol property retrievals • swath complements nadir lidar and polarimeter measurements
Aerosol fine mode optical depth	O5, O6, O7, O8	• mature algorithms (e.g. MODIS) use spectral information to partition fine and coarse mode AOD.
Aerosol effective radius	O3, O5, O6, O7, O8	• spectra provide erosol size information
Cloud radiative effects	O2, O4	• provides means to deduce broadband radiative effects by constraining bottom up deductions for broad band fluxes. Also provides much tighter constraints of radiation kernel estimates
Column water vapor	O1	• central to key questions related to convective initiation and aggregation • May help with understanding humidification effects on erosol retrievals near clouds

in the program of record (POR) particularly the spectral imagery from the current ring of geostationary satellites, 2) new spaceborne architectures framed around advanced spaceborne lidar and Doppler radar, 3) an active effort to develop multi-sensor approaches that combine supporting measurements from the active systems with measurements from a polarimeter, the VSWIR spectrometer, and microwave radiometer, 4) an integrated sub-orbital program and 5) a desire to link directly to modeling and analysis systems. The program is defined around eight interconnected science objectives that focus on processes central to low cloud feedbacks (O1), high cloud feedbacks (O2), convective processes (O3), cold cloud and precipitation processes (O4), aerosol property (O5), aerosol process evolution (O6), and aerosol direct (O7) and indirect (O8) forcing.

The measurement approach of ACCP currently under development is formulated around active profiling capabilities provided by a high spectral resolution lidar (HSRL) and multi-frequency Doppler radar. These active sensors will continue the data records started by a number of NASA missions including CloudSat, CALIPSO, TRMM and GPM as well as the ESA mission EarthCARE (e.g. Illingworth et al., 2015).

Table 1 below offers an abbreviated overview of the principal geophysical variables that are to be derived from a VSWIR spectrometer, their relation to ACCP objectives and their relationship to other candidate ACCP instruments. A VSWIR spectrometer contributes to ACCP geophysical measurement capabilities in four distinct ways: 1) the spectra add information content to other observations where they overlap; 2) the spectrometer adds both swath and an imaging capability for both context and cloud property mapping; 3) they offer new potential capabilities highlighted in the examples of particle profiling below and 4) the spectral information offers an important way to constrain estimates of cloud broad band radiation fluxes and radiation kernels at a resolution much finer than that of the current program of record exemplified by CERES (e.g. Wielicki et al., 1996).

VSWIR SPECTROMETRY IN THE ACCP ERA

Two very similar-in-capability spectrometer concepts were offered in response to a request for information that was solicited from the community. The concepts being considered are relatively mature. One has roots in design for a 6U cubesat application while the other is from a provider who has already demonstrated the measurements of spectral solar irradiance on a 6U cubesat (**Figure 2**). Spectral measurements of reflection have also been demonstrated with instruments on micro-satellites. Zhang et al. (2018), for example, describe the vicarious calibration of two spectrometers on two 50 kg microsatellites (SPARK-01 and 02). The credible expectation for ACCP is that a hyperspectral solar measurement implementation ought to be in the form of a small class sensor. In the coming years, the CLARREO pathfinder (CPF; Shea et al., 2020) plans to provide traceable, accurate spectra by direct solar calibration; see Kopp et al., (2017) against which other observing systems would be benchmarked. The characteristics of the proposed ACCP spectrometer is expected to largely duplicate those of the CPF.

Although the spectrometry being discussed in this paper has considerable space heritage, not all applications offer the same degree of ‘science maturity’, a point emphasized below especially in *Top-of-Atmosphere Radiative Effects*. **Table 2** is a summary of like-sensors flown on Earth orbiting satellites, both current and planned. This table is not meant to be a complete review of all such sensors flown, for example its doesn’t include OCO-class

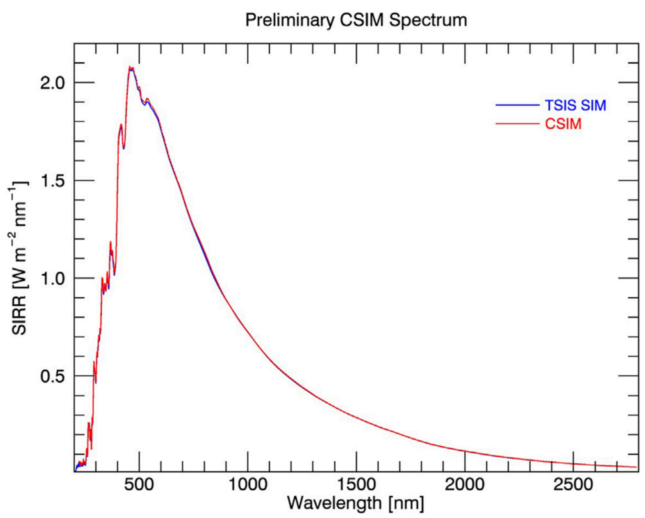

FIGURE 2 | Early results from CSIM-FD comparing the solar spectral irradiance measured by both TSIS-1 and CSIM. Both instruments have their pre-launch spectral irradiance calibrations tied to a cryogenic radiometer. The preliminary agreement is with an absolute SSI differences <1% between 400 – 2,400 nm (from Stephens et al. (2020)).

spectrometry. The characteristics of sensors already flown and expected to be in orbit in the coming ACCP decade are noted. It should be remarked that implementation of the measurement in the form of micro-sat or cube-sat sensors have much less heritage and how these sensors mature in the coming decade remains uncertain.

THE SPECTRAL CHARACTER OF EARTH'S REFLECTED RADIATION

The following discussion provides background to highlight how different components of the Earth system are manifest in solar reflection spectra thereby hinting at how information about these components might be gleaned from measurements of such spectra and exploited in the ACCP era. Extracting this information in many cases is mature, being demonstrated either with observations obtained from sensors on present day orbiting satellites, spectrometers flown on aircraft observations, or both. In some other cases described, the information extraction is less mature, more heuristic in nature and requires further development in the coming years.

Earth's Land Surface as a Source of Atmospheric Aerosols

The VSWIR spectral region carries rich information about surface composition, and airborne hyperspectral reflection measurements have been used in mineralogical exploration for decades (e.g. Kruse et al., 1993; Clark et al., 2003). It is no accident this measurement is a central tool of another recommended DO: the Surface Biology and Geology (SBG) investigation that targets observables spanning snow and glacier albedo, rock and soil properties, vegetation canopy chemistry, and much more (Schimel et al., 2020).

Knowledge of the mineral composition of atmospheric dust exemplifies the direct connection between the land surface and air advanced with hyperspectral reflection measurements. This knowledge is also essential to our understanding of climate forcing, dust downwind impacts on clouds and air-quality, and dust biogeochemical feedbacks and thus relevant to a range of ACCP goals. Dust mineralogical content may also provide clues for understanding the mechanisms behind dust variability and continental provenance (Sokolik et al., 2001). Conventional aerosol retrievals at a few selected wavelengths are designed for retrieving the aerosol optical depth and some information on the particle size (such as fine fraction or Angstrom exponent as noted above; Anderson et al., 2005; Levy et al., 2005; Levy et al., 2007; Chen et al., 2020). Multiangle and polarimetric retrievals add information on dust shape and wavelength-dependent refractive indices (Dubovik et al., 2019), however, the spectral resolution is not sufficient to determine actual dust mineral composition.

To underscore this point and the further potential relevance to ACCP, the spectral properties of different minerals known to represent the composition of dust are shown in **Figure 3A**.

TABLE 2 | VSWIR spectrometer systems either flown on or proposed for Earth orbiting satellites.

Satellite sensor	Spatial res @ nadir (km)	Swath width (km)	Spectral range (nm)	Spectral resolution	Radiometric uncertainty	Availability
GOME	40 × 320	960	240–790	0.2–0.4	2–5%	1996–2011
GOME-2	40 × 80 (Metop-A) 40 × 40 (Metop-B)	960	240–790	0.2–0.4	2–5%	2006-Present 2012-Present
SCIAMACHY	32 × 215	1,000	240–2,380	0.24–1.48	2–4%	2002–2012
Hyperion	0.03 × 0.03	7.75	356–2,577	10	3–5%	2000–2017
CSIM[a]	n/a	n/a	200–2,800	1–35 nm	<0.5%	2019-Present
SPARK	0.05 × 0.05	100	400–1,000	~<5	>~4%	2016–2017
TRUTHS	0.04 × 0.04	40	320–2,450	5–10	0.3%	2026
CLARREO PF	0.5 × 0.5	100	320–2,300	6	0.3%	2022
EMIT	0.06 × 0.06	72	380–2,500	~7	<5%	2021
SBG**	0.03 × 0.03	TBD	380–2,500	10	<5%	Under study

[a] *CSIM is a solar pointed spectrometer measuring spectral solar irradiance. **Values are provisional.*

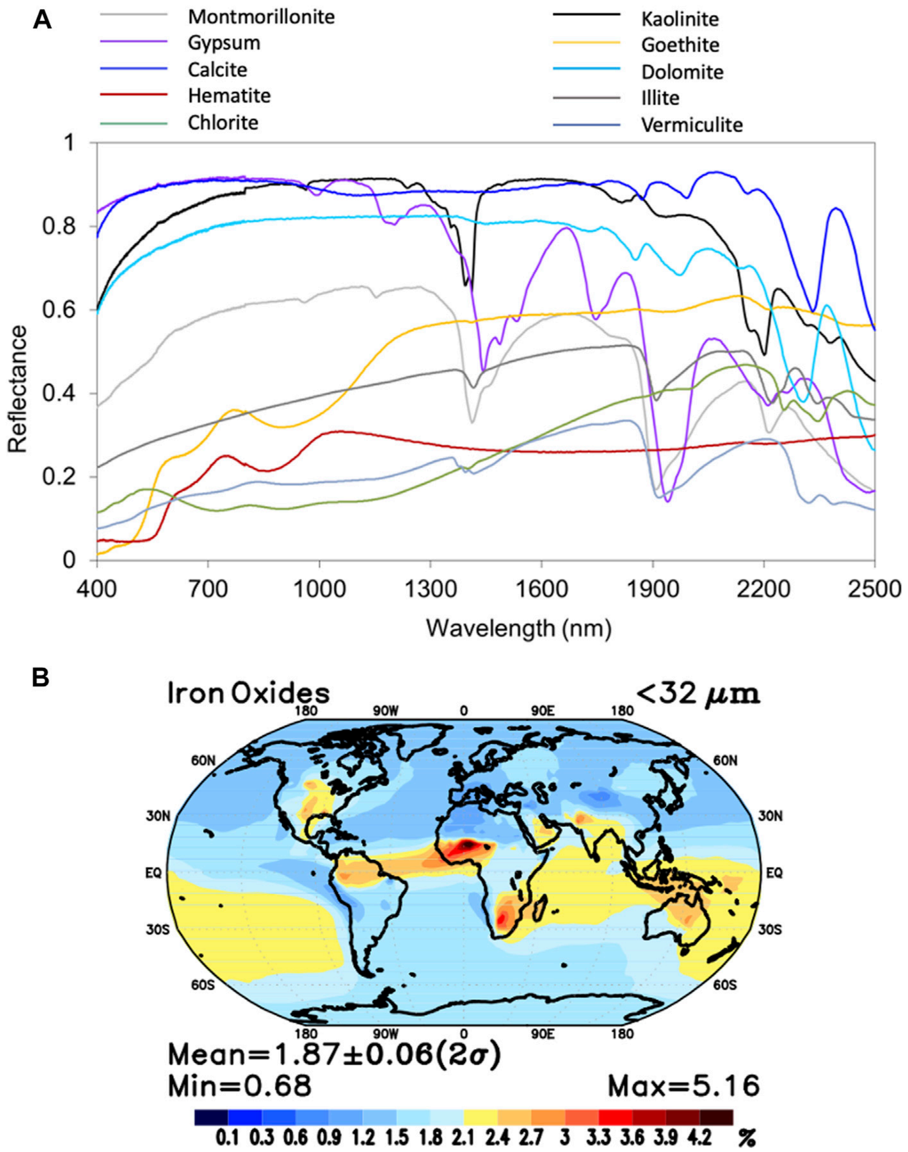

FIGURE 3 | (A) The spectral structure of dust forming minerals. **(B)** The fractional contribution of iron oxides in dust.

The measurement of these spectra is central to the Earth Surface Mineral Dust Source Investigation (EMIT) mission that seeks to quantify dust source emission from the surface (Green et al., 2020). As **Figure 3B** indicates the composition of airborne dust is, however, non-uniform exemplified by the large variability of estimated iron oxide fraction in dust and thus *a priori* not readily approximated with simple composition models as widely used today. Apart from their utility for geology or ecology, the unique spectra of surface materials in the VSWIR range, exploited by EMIT, provide powerful statistical constraints on measured radiance and form a backstop against which one can disambiguate atmospheric effects.

Theoretically, smooth spectral scattering features of the light scattered by aspherical size-distributed atmospheric dust can be separated from the sharp spectral features that characterize the mineral absorption features of **Figure 3A**. The ability to determine the mineralogical composition of airborne dust has been demonstrated with hyperspectral Hyperion satellite observations of a dust storm near the Bodélé Depression in Chad (Chudnovsky et al., 2009; Chudnovsky et al., 2011), which used the longest part of the SWIR (2080–2,380 nm), in particular, where the atmosphere is transparent, optical properties are stable, and absorption features of hydroxyl-bearing minerals, sulfates, and carbonates are most pronounced.

Earth's Atmosphere

Water Vapor

Atmospheric water vapor is of critical importance to most to the ACCP objectives, through its influence on clouds, convection as

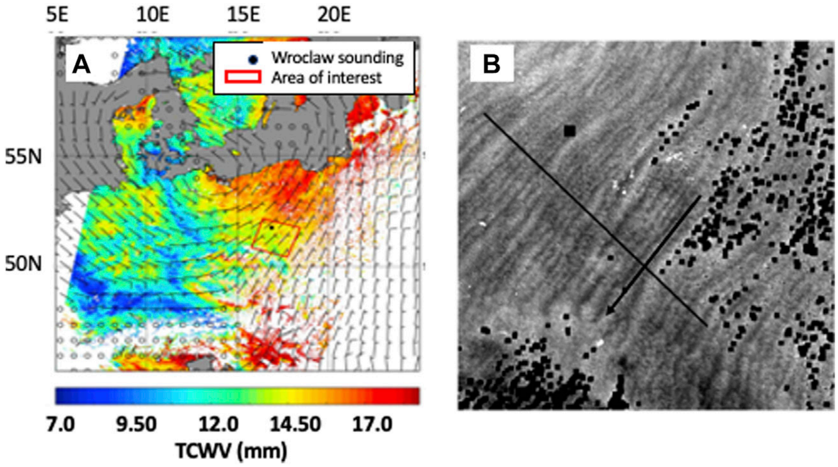

FIGURE 4 | (A),left) MERIS TCWV field overlayed with ERA-Interim wind barbs computed from the mean boundary layer wind field **(B)**, **right)** TCWV field for the area of interest as indicated by the red box in the panel to the **left**. Black areas in the **right** panel indicate cloudy regions for which no TCWV retrievals are performed (adapted from Henken et al. (2015)).

well as in modifying aerosol optical properties (e.g. Wu et al., 2018, Zu et al., 2019). High quality water vapor data products are currently available from many satellite sensors operating in various wavelength regions. Each sensor has its specific advantages and limitations in terms of spatio-temporal resolution, coverage, capability and instrument sensitivity. An extensive overview of satellite measurements of water vapor can be found in Schröder et al. (2018). Multi-band water vapor absorption is a dominant spectral feature of the SWIR spectrum and its presence has significantly shaped many remote sensing methods, either explicitly by using the absorption features, or implicitly by avoiding these features entirely. The retrieval of total column water vapor (TCWV) from SWIR reflectance measurements is one example where the absorption is used directly. The approach to estimate the TCWV can be regarded as mature, exemplified by the column water vapor products of MODIS (e.g. Gao and Kaufman, 2003) MERIS (Diedrich et al., 2015) and GOME (e.g. Grossi et al., 2015). These measurements are especially pertinent over land where microwave measurements fail and the information is also more decisively weighted to the boundary layer (e.g. Christi and Stephens, 2004) than are other column methods of water vapor retrieval. Another important advantage of the VSWIR measurement of TCWV is that very high horizontal resolution which provide mesoscale variability of the water vapor field, an advantage highlighted by the example of **Figure 4**.

In preparing for the MERIS observations, Diedrich et al. (2015) developed a multi-band algorithm that they tested using MODIS data and demonstrated clearly that adding more spectral information from multiple water vapor bands improved known biases in the MODIS product limited only to a pair of channels. Gao and Goetz (1990) and Thompson et al. (2015) further illustrated how a more refined, better constrained and accurate estimate is possible when hyperspectral reflectance measurements of the shape of the H_2O absorption bands are more tightly fitted against forward model calculations.

It is not difficult to appreciate the value of high-spatial-resolution boundary layer water vapor to the science objectives of ACCP as it is central to key questions related to convective initiation and aggregation, to cloud formation and to the definition of aerosol properties. For example, **Figure 4** is a high-resolution MERIS TCWV field that corresponds to a high-pressure event occurring in May 9, 2008 over central Europe (**Figure 4A**) derived on ~250 m spatial scale. Evident is the detection of horizontal convective rolls that appear as quasi-parallel bands of alternating low- and high-TCWV (**Figure 4B**). This distinct PBL moisture structure consists of bands of high humidity that align parallel to the boundary layer winds obtained from a numerical weather prediction model and radiosonde data. Closer examination further reveals that cloud streets observed in the east extend along bands of maximum TCWV.

Aerosol

Methods for retrieving aerosol properties from spectral reflection measurements have a long history (e.g. Kaufman et al., 1997; Remer et al., 2005; Levy et at., 2005). Li et al. (2009) provide a comprehensive review of different methods for estimating aerosol optical depth. Most methods require significant amounts of spectral information beyond that used for aerosol property retrieval alone (e.g. Lyapustin et al., 2018). For example, MODIS aerosol algorithms require inputs from several spectral channels to define the scene. Reflection measurements in the 1.38 μm water band are used to test for the presence of high thin cirrus that, when unaccounted for, contaminates retrievals. Dust is further identified using reflection differences between at 0.47 and 0.66 μm and aerosol properties are then derived by matching reflections in several other spectral channels to model-based look up tables (e.g Remer et al., 2005). Clear sky screening of the observations, critical to any aerosol retrieval method, also relies on spectral analyses as does radiance corrections applied to clear sky radiances, each important components of any surface property retrieval approach to be used in SBG.

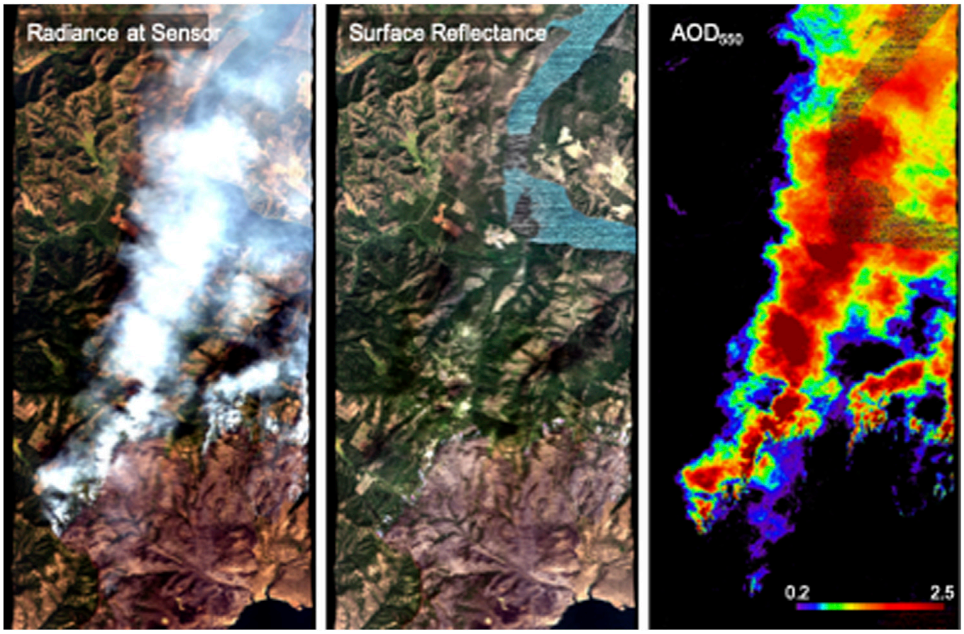

FIGURE 5 | AVIRIS-C data acquired over the Williams Flat Fire, August 2019, demonstrating spectroscopic aerosol measurement at high spatial resolution over heterogeneous terrain. Image courtesy Philip G. Brodrick **(Left)** Visible radiance channels **(Center)** Estimated surface reflectance **(Right)** Estimated aerosol optical depth at 550 nm.

Analysis of data collected from recent airborne field programs like the FIREX-AQ 2019 is ongoing and information content assessments of hyperspectral measurements applied to selected aerosol types, such as dust and smoke, now exist. Furthermore, methods to retrieve AOD of different species within the same airmass have been tested against airborne observations (e.g. Mauceri et al., 2019). Information content analysis of Hou et al. (2017) demonstrates that there are multiple degrees of freedom in the signal for retrieval of aerosol properties, and that this information is improved with observations accumulated over time with repeat observations that further constrain surface reflectance. Three examples are presented to highlight these developments.

1) An example of smoke observed during the recent FIREX-AQ 2019 field campaign by the AVIRIS-C instrument (Green et al., 1998) onboard of the high-altitude ER-2 aircraft is demonstrated in **Figure 5**. A hyperspectral retrieval of aerosol optical depth (AOD) on the right is shown together with RGB imagery of smoke on the left, and simultaneously retrieved surface properties under the smoke in the center of the figure. The solution for AOD and Surface Reflectance is based on a simultaneous model inversion of atmospheric and surface properties (Thomson et al., 2015; Thomson et al., 2019), permitting aerosol retrievals at high spatial resolution (<30 m) over heterogeneous terrain without the need for special scene content such as shadowed or dark vegetation pixels. The uncertainties of simultaneous AOD and surface reflectance retrievals of AVIRIS-C observations collected during the FIREX-AQ have been evaluated and the initial validation shows a good agreement with collocated AERONET observations.
2) An example of the information coded in hyperspectral measurements of African dust is highlighted in **Figure 6** taken from the study of Xu et al. (2017). Shown are spectral Jacobians (the spectral reflection sensitivity) of dust optical depth associated with four different particle size ranges of dust (refer to caption). The reflection spectra exhibit distinct magnitude sensitivities and spectral variability among different size bins. The spectral sensitivities associated with these different size ranges of dust merely underscores the point that information about dust particle size exists in these measurements.
3) Su et al. (2020) demonstrate how spectral information constrains surface albedo and thus enhance retrievals of aerosol optical depth over reflecting surfaces. They apply a machine learning model to estimate surface albedo in a visible region derived from reflection measurements at longer near infrared wavelengths that then results in a significantly improved ability to the retrieve of AOD over land.
4) Mauceri et al. (2019) also demonstrate the utility of hyperspectral imagery applied to a machine learning application of aerosol retrievals and aerosol typing. Eerosol optical thicknesses for brown carbon, dust and sulfate aerosols were shown to be derived from hyperspectral imagery acquired by the AVIRIS-NG instrument. The extraction of aerosol information from these measurements requires no *a priori* information about surface albedo or atmospheric state, in many ways similar to Su et al. (2020). The model, a neural network, was trained on atmospheric radiative transfer

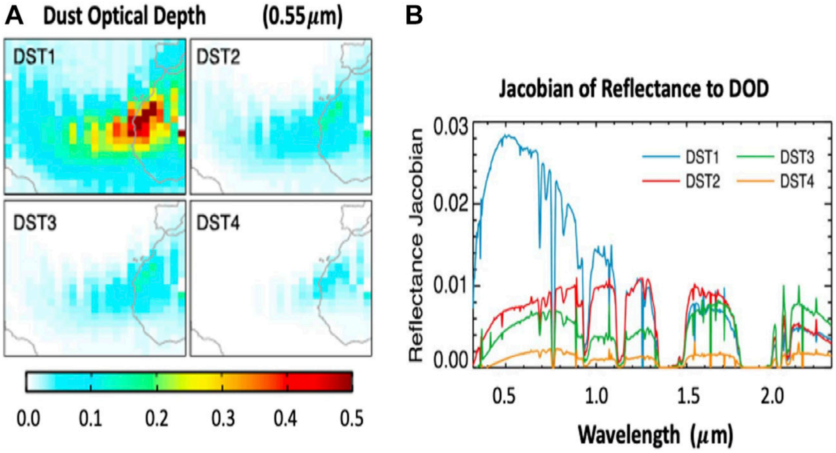

FIGURE 6 | (A) The optical depth of simulated African dust outbreak over the Atlantic in four size bins ranging 0.1–1.0 μm DST1), 1.0–1.8 μm (DST2), 1.8–3.0 μm (DST3), and 3.0–6.0 μm (DST4) **(B)** Averaged Jacobians of reflection spectra associated with the case of **(A)** (after Xu et al., 2017).

simulations with varying aerosol concentration and type, surface albedo, water vapor and viewing geometries. Mauceri et al. were able to distinguish and retrieve AOD of each component with a standard error of better than ±0.05 and used AVIRIS-NG imagery from a recent campaign over India to demonstrate its performance under high and low aerosol loadings and different aerosol types (**Figure 7**). As expected, retrieval performance was degraded when using fewer wavelengths and increased measurement uncertainty. Agreement with independent measurements (MODIS and AERONET) yielded an RMS closer to 0.1, which included errors in these independent datasets as well as discrepancies in spatiotemporal overlap. A related study by Thompson et al. (2019) adopted a similar palette of three aerosol types assumed in retrievals using AVIRIS-NG data also obtained during a campaign in India. Their estimates of total AOT matched *in-situ* and remote observations across a wide range of aerosol loads, confirming the performance of the Mauceri et al. study. Finally, field data from the FireX AQ campaign has confirmed sensitivity to optical properties in scenes where the aerosol compositions were well understood (Brodrick et al., 2021).

Clouds

The spectral reflection by clouds, especially when viewed through the lens of hyperspectral VSWIR measurements, contains a diverse range of information described below. The study of Gristey et al. (2019) who analyzed both global SCIAMACHY observations and SCIAMACHY simulated observations offers a general context for understanding cloud influences on these spectra. **Figure 8** is an example taken from that study and shows spectra clustered according to surface types (**Figure 8A**) and cloud types (**Figure 8B**). Absent broad-band measurements, these cloud spectra hint the value for spectra of this type for defining the broadband reflection from clouds (described below in *Top-of-Atmosphere Radiative Effects*) and, more importantly, how this broadband information changes as cloud properties change. **Figure 8** also hints at the potential wide range of properties that might possibly be gleaned from these spectra. Specifically, the different spectral character between ice and water clouds, evident especially around the 1.6 μm 'window,' discriminates water from ice and is the effective basis for cloud phase detection as described below. Reflection around the oxygen A-band (~0.76 μm) has well understood signatures of cloud top height changes (eg. Fischer and Grassl, 1991). The spectra themselves effectively discriminate clear sky from cloudy sky scenes especially in marginal cases, an observation that has been appreciated for some time and used in modern cloud clearing methods. Water vapor absorption, apparent in these spectra, can also be used to extract total column water vapor over land as described above, and the water vapor absorption around the 1.38 μm water vapor band provides a method not only for detecting high thin clouds but also in deducing profiles of ice cloud properties (Baum et al., 2000, 2005; Meyer and Platnick, 2000; Barnard et al., 2008; Wang et al., 2012). The shape of the spectra, especially the visible portion contrasted against the SWIR portion of the spectra, not only offers bulk information about particle size but also information about the profile of particle size in shallow clouds (eg. King and Vaughan, 2012).

Cloud -Aerosol Radiative Effects

Figure 9 presents spectra of downwelling irradiance measured below a cumulus cloud field adapted from Schmidt et al. (2009). Spectra immediately below cloud and in the gap between clouds are shown respectively as red and blue lines, and respective model simulated spectra are represented by symbols. These spectra are contrasted against a modeled clear sky spectrum without cloud influences (green). This specific contrast, expressed by the spectral difference in black, reveals the influence of neighboring clouds on the spectra measured between them, and on the aerosol radiative effects there. The spectral downwelling irradiance at visible wavelengths, less than about 700 nm, is reduced in the gap regions compared to the purely clear sky spectra. Although the model simulations

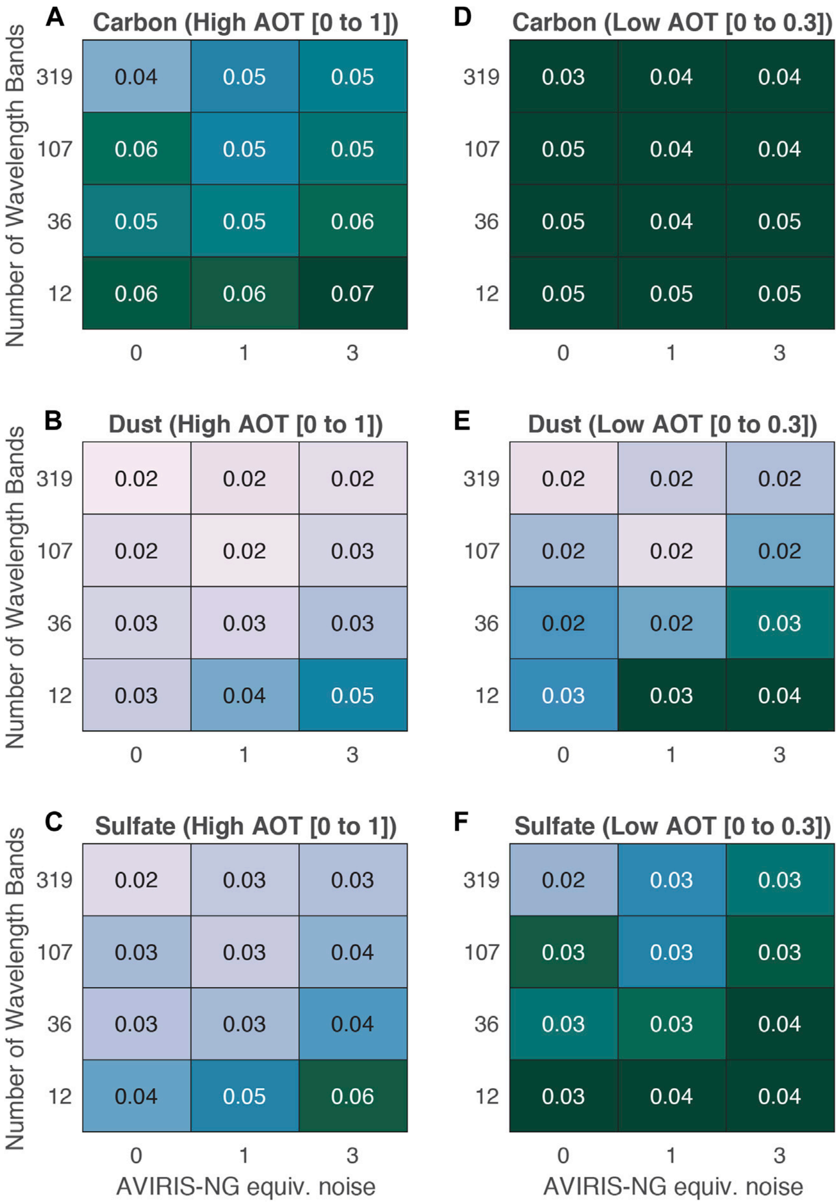

FIGURE 7 | Standard error for retrieved AOT of 12 individually trained neural networks with varying wavelength bands and a varying amount of simulated AVIRIS-NG equivalent noise from the test set. **(A–C)** show the standard error when AOT is varied between 0 and 1. **(D–F)** show the standard error for AOT between 0 and 0.3 (Mauceri et al. (2019).

point to the aerosol as being responsible for this reduction, the reduction is partially compensated by the increased diffuse downward flux from cloud sides. This increase in diffuse flux is evident at longer wavelengths where aerosol effects are small (e.g. wavelengths longer than about 1,000 nm). This set of measurements highlights how 3D cloud effects on radiative transfer confound the estimation of aerosol effects in complex cloudy environments. Although this particular example applies to downwelling fluxes, reciprocal changes to reflected fluxes will also occur. Clearly measurements of spectral transmittance in this example, and by implication spectral reflectance, provide a greater means to constrain estimates of erosol radiative effects in fields of clouds.

Quantitative Cloud Retrieval Examples

Many of the methods for deriving cloud properties from spectral reflectance data, such as the popular bi-spectral methods commonly applied to radiometer measurements like those provided by MODIS, are mature and the limitations on properties derived are, for the most part, well understood, although often difficult to quantify. As hinted at above, a number of different methods have been developed to deduce clouds properties from hyperspectral

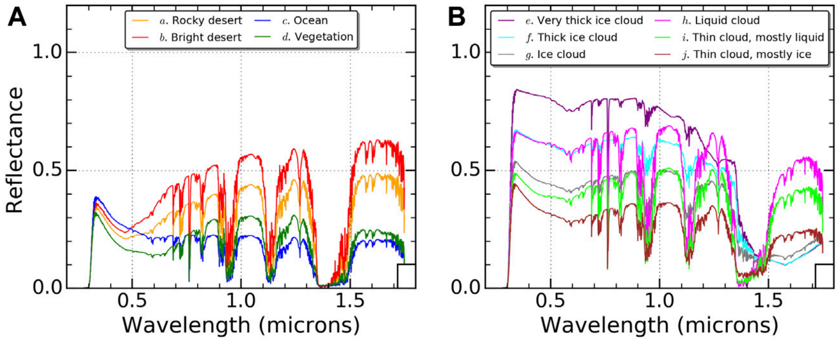

FIGURE 8 | Cluster centroids of top-of-atmosphere reflectance spectra at a spatial scale of 1 km. Ten clusters are shown, separated into **(A)** surface clusters and **(B)** cloud clusters. The cluster centroids are identified from 90,917 computed SCIAMACHY-like reflectance spectra that are re-gridded to a 0.001- micron spectral resolution. Input for the computations is derived from A-Train satellite observations over West Africa in 2010 (Gristey et al., 2019).

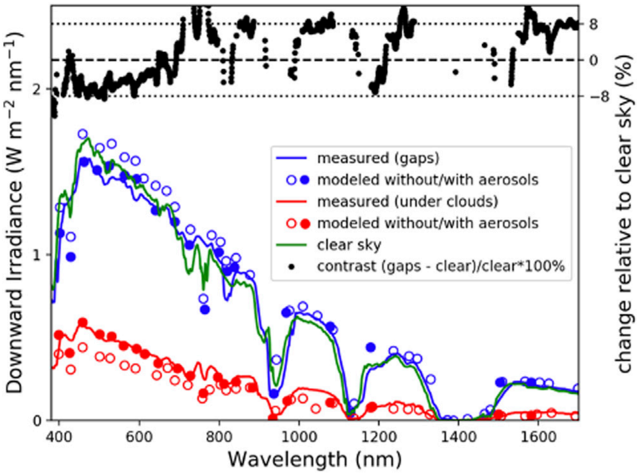

FIGURE 9 | Spectra of measured and modeled downward irradiance (blue: below cloud gaps, red: below clouds). Solid green is the spectrum in clear air, and symbols represent modeled spectra with (solid) and without (open) erosol. The upper spectrum is the difference between the downwelling irradiance in gap regions and the clear sky cloud free spectrum, expressed as a percentage of the latter (modified from Schmidt et al. (2009)).

reflectance observations and some examples are presented below that also include a quantitative assessment of the retrieval performance based on *in situ* observations. The general improvement achieved using hyperspectral measurements for the standard cloud retrieval problem was quantified by Coddington et al. (2012) over the spectral range from 300 to 2,500 nm. The spectrally dependent Shannon information was derived across the spectrum and used to determine the cumulative information content in hyperspectral cloud retrievals for nine different cloud scenes, illustrating the expected improvements by added spectral coverage and improved resolution.

Bulk Cloud properties

Bulk cloud properties here refer to properties averaged or weighted over either an unspecified depth of cloud or over the entire cloud layer. Little vertical profile information is implied and by far the bulk of the cloud information from almost all passive methods fall into this category.

Cloud Phase

Spectral reflection differences between water and ice clouds in the region between 1.4 and 1.8 μm, noted previously (e.g. **Figure 8**), serves as the basis of cloud phase detection. This too is a mature topic dating back to studies in the 1980s (e.g. Pilewskie and Twomey, 1987) and now formerly implemented as a MODIS product (Baum et al., 2012). MODIS phase retrieval using limited near-infrared channels only is, however, limited in its capability (Riedi et al., 2010) and attempts to improve this information include adopting complementary thermal infrared bands. Riedi et al. 2010 developed a joint MODIS -POLDER phase discrimination approach also in an attempt to improve phase discrimination ambiguity and they argue this combination is superior to the discrimination provided by either method separately. Continuous hyperspectral measurements in the near-infrared offers a significant step forward improving on detection making phase discrimination somewhat trivial as the example of **Figure 10** shows. Measurements from an airborne spectrometer, matched to co-located *in situ* microphysics observations (**Figure 10A**), demonstrate the clear relation between spectral indices of ice fraction using spectra between 1.4 and 1.8 μm and the appearance of ice (**Figures 10B,C**, Thompson et al., 2016).

Cloud Optical Properties

Measurements of spectral sunlight reflected by clouds are inputs for deducing cloud 'optical' properties most commonly expressed as the cloud optical depth (τ) and droplet or ice crystal effective radius r_e. This measurement approach has a relatively long history (e.g. refer to the review of Stephens and Kummerow, 2007). These particular properties are minimally required for addressing ACCP O1, O2 and O8 objectives. It was Twomey and Seton (1980) who introduced the present widely used bi-spectral reflectance method to estimate these two cloud variables and Nakajima and King (1990) expanded the method into an operational algorithm that is the basis of the MODIS

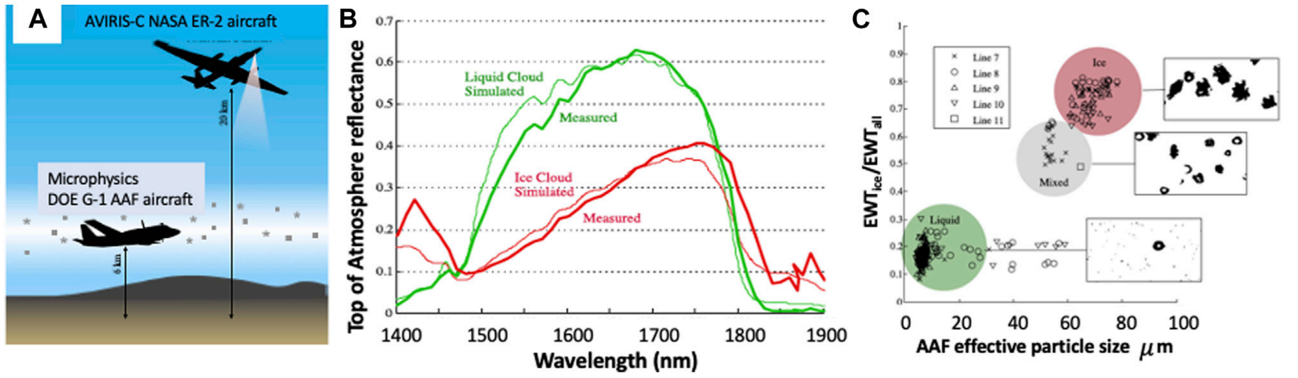

FIGURE 10 | Cloud phase results from airborne measurements with **(A)** cloud particles measured at identical locations, less than 10 min apart by *in situ* high-speed imaging with remote imaging spectroscopy above. **(B)** Red (ice) and green (water) spectra plot of airborne spectrometer measurements of liquid and ice cloud reflectances. Shown are measured and simulated cloud spectra where details of simulations are described in Thompson et al. (2016). The details of the spectral reflectances are accurately reproduced. **(C)** The remotely estimated water fraction of ice (EWTice/EWTall), effectively ice to total water optical depth, derived from spectra of **(B)**. Each point in the plot is a spectrum from one of five flight lines ("lines 7–11"). Image inserts show direct microscopic images of cloud particles obtained *in situ*, confirming the remote classification, adapted from Thompson et al. (2016).

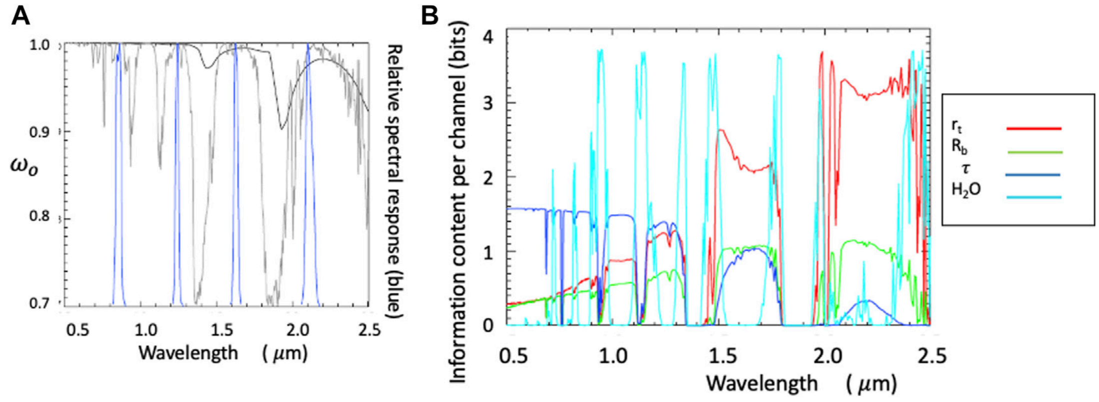

FIGURE 11 | (A) Single scattering albedo of a gamma droplet size distribution with r_e = 10 μm and effective variance = 0.1 (black line). Also plotted are the relative spectral response curves of the MODIS channels centered on 0.8, 1.2, 1.6, 2.1and 3.7 μm (blue lines) and the atmospheric transmission of a standard tropical atmosphere (gray line) **(B)** Shannon information content of hyperspectral reflectances applied to selected cloud properties (cloud top, base particle size optical depth and water vapor) where the information content is a measure of that which lies above *a priori* knowledge (after King and Vaughan, 2012).

cloud products now widely used. This bi-spectral method is based on measurements of narrow-band reflectances in two spectral regions or channels, one at visible wavelengths where reflection varies principally as a function of τ and a second located within the near infrared region in which solar radiation is both absorbed and scattered being influenced by both τ and r_e. The combination of measurements thus yields information on the pair of optical properties, τ and r_e. These essential aspects of the approach are conveyed in **Figure 11** taken from the study of King and Vaughan (2012) showing the spectral distribution of Shannon information content as defined by Rodgers (1998). The **Figure 11B** expresses the initial information content above that of some *a priori* knowledge associated with cloud top effective particle size r_t, cloud base particle size r_b and optical thickness τ_c for a specific cloud state of r_t = 10 μm, r_b = 5 μm, τ_c = 15, a solar zenith angle of 30°, nadir viewing, a standard tropical atmosphere and 2% measurement error. Spectral regions outside the water vapor absorption bands where single scatter albedo ϖ_0 is at a minimum (**Figure 11A**), like the spectral region between 2.1–2.4 μm, offer the most information about r_t whereas the regions where $\varpi_0 \approx 1$ possess most information about τ_c. There are a number of confounding issues inhernet to the bi-spectral approach, such as ambiguities introduced by 3D radiative transfer effects and drizzle (Zhang et al., 2012) and the extent hyperspectal information helps address these issues will be topics of future research.

Droplet Number Concentration N_c

Although a number of studies report on approaches to estimate N_c using spectral reflection measurements (e.g. Grosvernor et al., 2018), the approaches developed for this property have large inherent uncertainties being framed around a simple adiabatic model of cloud properties (e.g. Stephens et al., 2019). It is

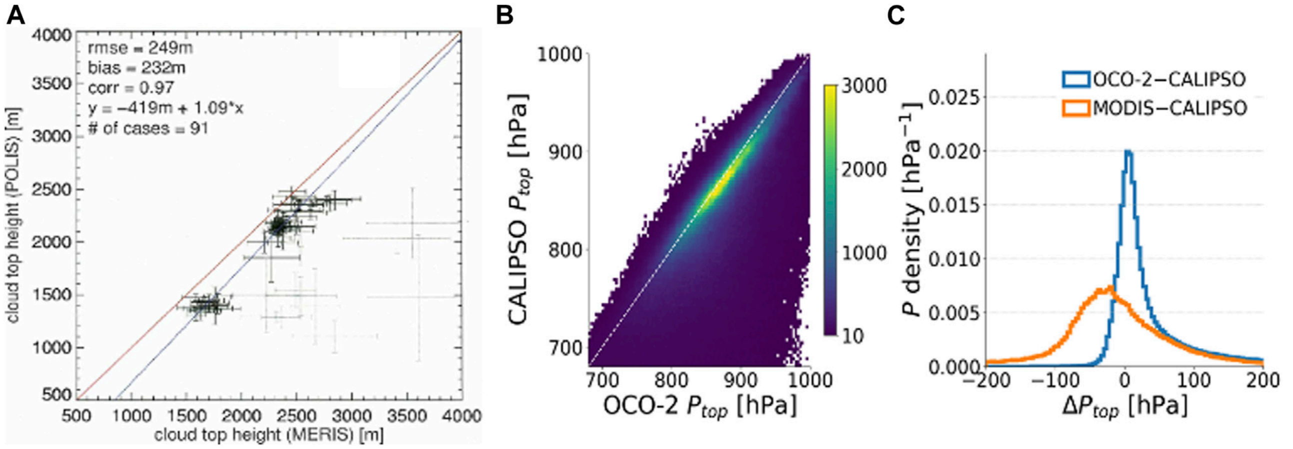

FIGURE 12 | (A), left) Comparison of POLIS (airborne lidar) and MERIS cloud-top heights. Gray crosses mark cases with presence of cirrus clouds. The one-to-one line and the regression line are displayed in red and blue, respectively. Lager studies show the MERIS bias can be removed when other information is added (Henken et al., 2015) **(B), middle and right)** The CTP retrieval of low clouds from OCO verified against CALIPSO CTP and contrasted against the MODIS IR based estimate **(right)**. The interquartile range of the difference is ~30 hPa. The long tail are cases where CALIPSO identified high thin cloud above (Richardson et al., 2019).

expected that the particle size profiling capability described below that is offered by hyperspectral measurements, especially when connected to radar observations that identify drizzle presence (e.g. Wood et al., 2012), would improve on these restrictive and empirical retrieval assumptions and thereby improve our ability to deduce Nc.

Cloud Profile Properties

Cloud Top Pressure (CTP)

Retrieval of cloud top pressure from measurements of sunlight reflected in the oxygen A-Band is mature, being supported by several theoretical studies (e.g. Fischer and Grassl, 1991; Kuze and Chance, 1994), analyses of airborne measurements (Henken et al., 2015), as well as to satellite measurements. MERIS on ENVISAT provided global A-band measurements and a number of validation efforts have been developed to support the MERIS CTP product. With OCO we now have measurements at much finer spectral resolution than available previously and are now able to assess and confirm the benefits of such higher spectral resolution previously posed theoretically.

Understanding the measurement approach and the expected performances of the different satellite systems is now well advanced. **Figure 12** illustrates this point providing two different examples of spaceborne estimates of cloud top height. **Figure 12A** is a MERIS A-Band cloud top pressure retrieval assessed against matched under flights of an airborne lidar. The second example is that using the A-band measurements of OCO showing low cloud top pressure assessed in this case matched against CALIPSO lidar observations. The uncertainty of these CTP estimates is equivalent to about 200 m in both examples.

Low Cloud Particle Size Profiles

A few studies have explored particle-size profile information primarily based on multi-spectral MODIS observations (e.g. Platnick, 2000; Chang and Li, 2002). These studies have explored this capability using the limited spectral capability of MODIS offering some insights on the capabilities. Despite these studies, the actual information about particle sizes within and through the cloud that is contained in spectral data is not well appreciated. The cloud base particle size information is one form of expression of this profile information and the results of **Figure 11** suggest the near infrared spectra contain non-trivial information content relating to r_b, provided the measurements have sufficient absolute accuracy. As Platnick (2000) had shown, this information maximizes in the region around 1.6 µm which is a where a significant proportion of photons penetrate to lower levels provided optical depth are not so large that reflection becomes invariant to changes in drop size (see also Nakajima et al., 2010a; Nakajima et al., 2010b). Since the mean optical depth of oceanic low clouds is less than 15 (e.g. Christensen et al., 2013), hyperspectral measurements potentially offer a significant capability for profiling droplet size in low clouds (see below) of τ_c<15. However, the accuracy needed to profile to cloud base according the King and Vaughn is order 1% and how much of the profile can be retrieved practically with VSWIR measurements from space will require more study.

King and Vaughan (2012) developed a retrieval of the profile of drop sizes and applied the method to airborne spectrometer measurements collected during VOCALS. These retrieved profiles were then evaluated against matched *in situ* profiles of cloud drop radius. **Figure 13A** is an example of two cases showing the capability for extracting information about microphysics profiles of low clouds. The *in situ* profiles each exhibit the typical increase of r_e with height whereas the MODIS like bi-spectral retrieval (indicated as TBLUT) corresponds to the droplet sizes near to cloud top and being a bulk property then applies through the entire layer. The difference between the constant profile vs. a retrieved profile, as highlighted in this figure, profoundly influences our ability to deduce liquid water path (LWP) from solar reflection measurements as highlighted in

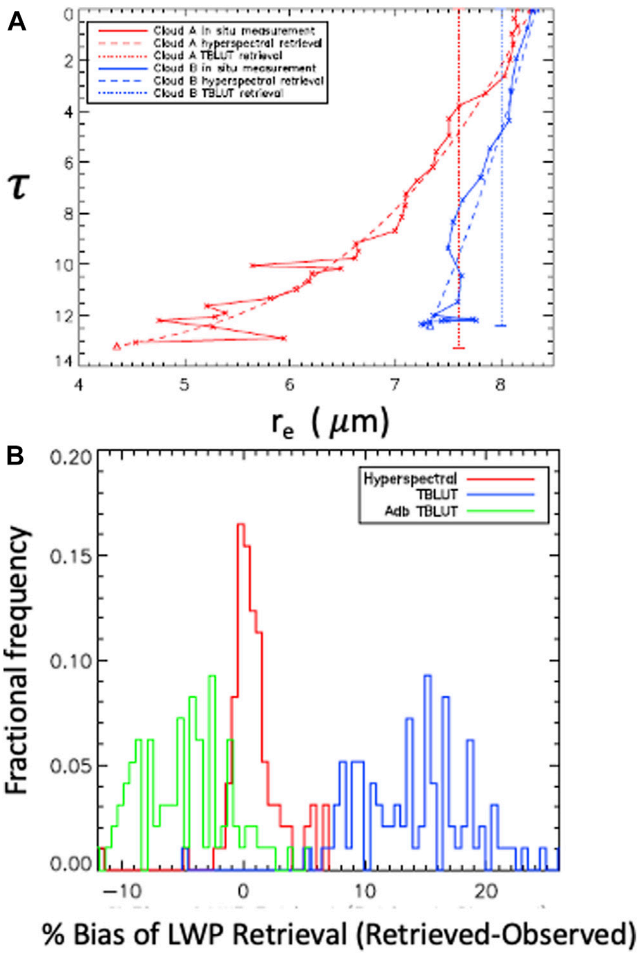

FIGURE 13 | (A) Two examples of *in situ* measurements of cloud droplet radius profiles measured during VOCALS plotted with the corresponding hyperspectral retrieved profile and contrasted against a two channel MODIS-like retrieval (vertical lines). Cloud A has a total optical thickness of 13.3 and LWP of 58.0 gm^{-2}. Cloud B has a total optical thickness of 12.4 and a LWP of 60.8 g m^{-2}. **(B)** Histogram of the difference between retrieved and observed total liquid water path using a hyperspectral retrieval and estimations from a TBLUT retrieval using constant vertical profile (blue line) and adiabatic (green line) assumptions (King and Vaughan, 2012).

Figure 13B. When applied to all VOCALS-Rex clouds sampled by aircraft throughout the entire experiment the histogram of the percentage differences between the retrieved and *in situ* values for MODIS-like LWP retrievals vs. that using the profile-based retrievals made possible with hyperspectral observations reveals a significant LWP overestimate using MODIS. Since the MODIS-like retrieval (TBLUT) corresponds to the larger droplet sizes near cloud top, the total liquid water path is then overestimated by between 5 and 25% whereas the hyperspectral retrieval of liquid water path agreed with *in situ* LWP to within 3% in all but two cases. Because the results reveal that the magnitudes of this LWP biases vary considerably, they cannot be simply be corrected by applying some form of *a priori*, fixed adiabatic correction to MODIS-like retrievals. The improvement to LWP retrievals that profiles of particle size offers was also noted in the studies of Chen et al., 2008; Chen et al., 2011.

TOP-OF-ATMOSPHERE RADIATIVE EFFECTS

The need to relate broad band radiative fluxes to the cloud and aerosol properties obtained from the measurements provided by different sensors being proposed for ACCP is central to a number of ACCP objectives. The desire to examine these relationships on the sub-kilometer to kilometer scale more characteristic of clouds and aerosol plumes and more typical of the cloud information to be provided by ACCP measurements, and also exemplified by the measurements discussed in relation to **Figure 9**, is a challenge given that the spatial coarseness of the available single footprint derived flux data of CERES and proposed for the Libera mission expected in the ACCP time frame is approximately 20 km.

The ACCP approach to address this challenge is not yet mature and advancing the approach will be the focus of much more intense research during the early phases of ACCP. The approach for shortwave fluxes revolves around use of the VSWIR spectral radiance measurements combined with radiative transfer calculations applied to inputs provided by cloud and aerosol profile information measured by the radar and lidar of ACCP on the cloud scale. A parallel approach for LW fluxes, not described here, will also be based on using LW spectral radiance measurements. The strategy will follow that first proposed by Barker et al. (2011) for EarthCARE and is to be tested and evaluated in greater depth using EarthCARE data as it becomes available after the launch planned for 2023. In contrast to the EarthCARE approach, which employs broadband radiances at nadir and two additional angles, the ACCP concept exploits the spectral radiance measurements at nadir as a way of tightly constraining the derived fluxes. In a broad sense, this overall approach that uses atmospheric profile input is analogous to that developed for the CloudSat flux product (Hendersen et al., 2013), although on a different spatial scale, as well as closely following the EarthCARE approach. Both have been shown to perform similarly to CERES observed fluxes at the top of atmosphere while also delivering vertical flux profiles and related radiative heating rates (Barker et al., 2015; Tornow et al., 2018). Construction of broad band shortwave fluxes from spectral radiances has also been demonstrated in a few studies, such as in Doelling et al., 2013 who used geostationary spectral radiances to derive CERES-like time resolved fluxes and Oyola et al., 2019 who provide a case study field experiment example combining airborne HSRL lidar measurements with spectral radiance imagery to quantify radiative properties of aerosol.

A very preliminary, albeit empirical example of how spectral radiances can be expected to constrain broad band flux estimates is provided by **Figure 14A**. This is an example of the construction of broadband fluxes from spectral MODIS data. The figure shows comparison of broadband SW fluxes, globally distributed and deduced using 11 VSWIR channels of MODIS compared to the collocated CERES broadband SSF fluxes. In producing this result,

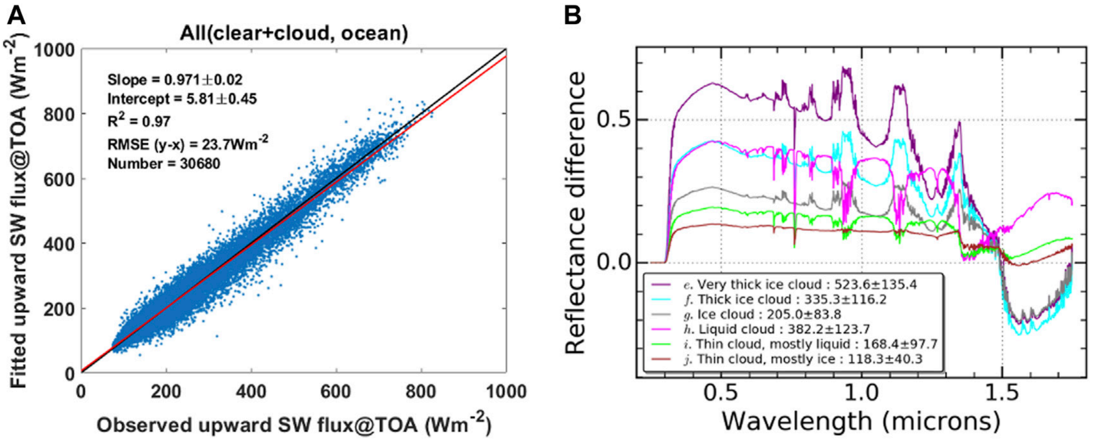

FIGURE 14 | (A) A reconstructed broadband TOA solar flux from 11 MODIS channels (ordinate) compared to the CERES SSF flux (abscissa). The correlation is for one month of global data and applies to all scenes, both cloudy and clear. The fluxes correspond to instantaneous fluxes and the RMSE is similar in magnitude to the projected RMSE of the SSF flux itself. Results shown here is for all observations over oceans with SZA between 22° and 36°, VZA 12° and 19°, and RAA 2° and 6°. **(B)** The mean spectral SWCRE (all sky minus clear) for computed SCIAMACHY- like reflectance spectra belonging to each of the six cloud clusters presented in **Figure 8B**. To the right of the colon in the legend is the mean broadband SWCRE of the given cluster with one standard deviation (Wm^{-2}). Positive SWCRE represents an increase in reflected solar radiation when clouds are present (adapted from Gristey et al. (2019)).

MODIS Aqua Level 1B calibrated radiances, sub-sampled at 5 km, were co-located with CERES SSF 4.0SW fluxes and with associated ancillary scene type information. A simple linear regression of these 11 channels of radiances, binned by fixed solar zenith angles (SZA), viewing zenith angles (VZA), and relative azimuthal angle (RAA), was created by regressing these combined channels against SSF broadband data. The training of this regression was based on one month of data and then applied to data collected for different times. The results of the reconstructed broadband fluxes from the empirical regression are then compared to the matched CERES SSF. These fluxes correspond to instantaneous reflected solar fluxes for the local time of approximately 1,330. The performance of this simple empirical regression, characterized by the RMSE of 23.7 W m^{-2}, is similar to the flux consistency estimated from a MODIS-based narrow-to-broadband flux conversion (Su et al., 2015) and meets the requirements of ACCP attached to instantaneous solar fluxes. These requirements are currently in development and how they are arrived at is a topic of a future paper. The performance from this limited, and by design, simple example is consistent with other analysis developed for EarthCARE (Barker et al., 2011) and suggests spectral radiances will provide broadband fluxes that meet not only EarthCARE requirements but also the ACCP requirements currently under development. Much more work is needed to refine the approach and quantify uncertainties that arise across different spatial scales.

Not only does the integration of spectral data provide a meaningful way of deriving broadband radiances and then fluxes but more importantly spectral measurements offer a more direct way of differentiating responses of these fluxes to changes in aerosol and cloud properties. This is an essential step in providing meaningful observational constraints either on aerosol-radiative effects, as highlighted above in the discussion of **Figure 9**, or on radiative kernels which expresses the sensitivity of the fluxes to changes in given cloud properties and is an important tool in quantitative analyses of cloud feedback (e.g., Colman, 2003; Zelinka et al., 2012). **Figure 14B** underscores this point. It shows the spectral character of the shortwave cloud radiative effect (SWCRE) expressed in the form of both spectral reflectance differences and broadband flux differences both being differences between reflected radiation from cloudy and clear skies. As in the example of **Figure 14A**, the broadband SWCRE values (provided in the legend inset) are instantaneous at the time of satellite overpass based on an equator crossing (1,330 local time). The spectra shown differentiate the clusters of different cloud types identified previously in **Figure 8** and reveal how differences between the clusters emerge more clearly in the spectra. This point is emphasized in a number of ways in **Figure 14B**. For example, the changes to SWCRE spectra at visible wavelengths, such as at 0.5 µm, reflects the sensitivity of the reflected flux to cloud optical depth. The high and low cloud example, labeled spectra f and h, are of clouds of the same optical depth and thus same visible SWCRE yet the broadband SWCRE differ by almost 50 W m^{-2}. This underscores the point that factors other than optical depth obviously contribute to this broadband SWCRE difference. Consequently, the broadband SWCRE, and changes to it, cannot be expected to be reproduced from visible measurements alone. Specifically, the spectral structure of the SWCRE reveals an important sensitivity to height, through influences of water vapor absorption on it. The presence of a swing in reflectance around 1.6 µm between water and ice clouds is indicative of the influence of the thermodynamic phase of water on cloud particle scattering discussed above. These positive and negative SWCRE responses in different parts of the spectrum partly compensate in the broadband obscuring the sensitivities of these cloud properties in broadband fluxes. The broadband

SWCRE from two distinctly different cloud regimes can thus appear similar, such as in the case of spectra g and i, respectively associated with ice cloud and thin liquid cloud, while possessing very different sensitivities to parameters that define them and the environment in which they form.

SUMMARY

This paper discusses the different ways spectrally resolved measurements of reflected sunlight can be expected to serve a number of emerging Earth science objectives in the coming decade. The paper briefly introduced the aerosol, clouds, convection and precipitation (ACCP) program currently in the process of defining a number of measurement objectives for NASA to be implemented toward the end of the current decade. A (solar) VSWIR spectrometer is being considered as part of the ACCP architecture and the different ways these measurements can be expected to advance the science objectives of ACCP were summarized (**Table 1**) and examples of how the spectral measurements might specifically be used were presented. These potential uses range from:

1) *Determining the composition of dust aerosol*: Although multiangle and polarimetric measurements contain information on dust shape and wavelength-dependent refractive indices, the spectral resolution is not sufficient to determine actual dust mineral composition. Smooth spectral scattering features of the light scattered by aspherical, size-distributed atmospheric dust can be separated from the sharp spectral features that characterize the mineral absorption features in hyperspectral measurements which thus offers some capability for determining the mineralogical composition of dust simultaneously with underlying surface properties.
2) *Determining total column water vapor:* Water vapor absorption is a dominant spectral feature of the near infrared reflection spectrum. The retrieval of total column water vapor (TCWV) from reflectance measurements, over land where microwave measurements fail and for which the information is more decisively weighted to the boundary layer, makes spectral SWIR measurements particularly pertinent to ACCP. Studies have clearly demonstrated that fitting of spectral SWIR information from multiple water vapor bands significantly improves on biases in TCWV products derived from a much more limited channel method.
3) *Cloud properties and profiles of cloud microphysics:* Existing methods for deriving cloud properties from spectral reflectance data, such as the popular bi-spectral methods commonly applied to radiometer measurements provided by MODIS, are mature and can be readily adopted to spectral VSWIR measurements of the type being proposed for ACCP. The advantage of more spectrally continuous hyperspectral measurements, however, extends beyond significant improvement on bulk layer information, including improved estimates of cloud phase (*Cloud Phase*) and more advanced information about the profile of cloud properties. This in turn directly improves estimates of cloud water (and ice) content properties (**Figures 13A,B**).
4) *Radiative fluxes and radiative kernels:* Although spectral measurements will provide important constraints to estimates of broadband fluxes reflected by clouds and aerosol on the sub-kilometer scale more typical of clouds, much more work is needed to mature the approach pioneered under EarthCARE and is being adopted for ACCP including research to quantify the expected errors, which will undoubtedly arise not only from 3D effects at such a small scale but also from other effects. The sensitivity of radiative fluxes to changes in cloud and aerosol properties on these same scales, critical in studies of aerosol radiative effects and cloud feedbacks, are also potentially better resolved in spectra of reflectances than in the broadband fluxes (refer to discussions of **Figures 9**, **14**). Quantifying these sensitivities is an essential step in providing meaningful observational constraints either on aerosol-radiative effects, as highlighted above in the discussion of **Figure 9**, or on radiative kernels which expresses the sensitivity of the fluxes to changes in given cloud properties and is a main factor in quantitative analyses of cloud feedback.

AUTHOR CONTRIBUTIONS

The corresponding author wrote the paper, assimilated information provided by co-authors Co-authors provided inputs to different sections of the paper and provided some figures.

ACKNOWLEDGMENTS

Aspects of this work were performed at the Jet Propulsion Laboratory, California Institute of Technology, under a contract 80NM0018D004 with the National Aeronautics and Space Administration.

REFERENCES

Ahn, C., Torres, O., and Jethva, H. (2014). Assessment of OMI Near-UV Aerosol Optical Depth Over Land. *J. Geophys. Res. Atmos.* 119, 2457–2473. doi:10.1002/2013JD020188

Anderson, T. L., Wu, Y., Chu, D. A., Schmid, B., Redemann, J., and Dubovik, O. (2005). Testing the MODIS Satellite Retrieval of Aerosol Fine-Mode Fraction. *J. Geophys. Res.* 110, D18204. doi:10.1029/2005JD005978

Barker, H. W., Jerg, M. P., Wehr, T., Kato, S., Donovan, D. P., and Hogan, R. J. (2011). A 3D Cloud-Construction Algorithm for the EarthCARE Satellite Mission. *Q.J.R. Meteorol. Soc.* 137, 1042–1058. doi:10.1002/qj.824

Barker, H. W., Cole, J. N. S., Domenech, C., Shephard, M. W., Sioris, C. E., Tornow, F., et al. (2015). Assessing the Quality of Active-Passive Satellite Retrievals Using Broad-band Radiances. *Q.J.R. Meteorol. Soc.* 141, 1294–1305. doi:10.1002/qj.2438

Barnard, J., Long, C., Kassianov, E., McFarlane, S., Comstock, J., Freer, M., et al. (2008). Development and Evaluation of a Simple Algorithm to Find

Cloud Optical Depth with Emphasis on Thin Ice Clouds. *Open Atmos. Sci. J.* 2, 46–55. doi:10.2174/1874282300802010046

Baum, B. A., Heymsfield, A. J., Yang, P., and Bedka, S. T. (2005). Bulk Scattering Properties for the Remote Sensing of Ice Clouds. Part I: Microphysical Data and Models. *J. Appl. Meteorol.* 44, 1885–1895. doi:10.1175/jam2308.1

Baum, B. A., Kratz, D. P., Yang, P., Ou, S. C., Hu, Y., Soulen, P. F., et al. (2000). Remote Sensing of Cloud Properties Using MODIS Airborne Simulator Imagery during SUCCESS: 1. Data and Models. *J. Geophys. Res.* 105, 11767–11780. doi:10.1029/1999JD901089

Baum, B. A., Menzel, W. P., Frey, R. A., Tobin, D. C., Holz, R. E., Ackerman, S. A., et al. (2012). MODIS Cloud-Top Property Refinements for Collection 6. *J. Appl. Met. Climatol.* 51, 1145–1163. doi:10.1175/JAMC-D-11-0203.1

Brodrick, P. G., Thompson, D. R., Garay, M., and Kalashnikova, O. V. (2021). Simultaneous Characterization of Wildfire Smoke and Surface Properties with Imaging Spectroscopy during the FIREX-AQ Field Campaign. *J. Geophys. Res. - Atmos*. doi:10.1002/essoar.10506794.1

Chang, F.-L., and Li, Z. (2002). Estimating the Vertical Variation of Cloud Droplet Effective Radius Using Multispectral Near-Infrared Satellite Measurements. *J. Geophys. Res.* 107 (D15), JD000766. doi:10.1029/2001JD000766

Chen, R., Chang, F., Li, Z., Ferraro, R., and Weng, F. (2008). Impact of the Vertical Variation of Cloud Droplet Size on the Estimation of Cloud Liquid Water Path and Rain Detection. *J. Atmos. Sci.* 64, 3843–3853. 10.1175/2007JAS2126.1

Chen, R., Li, Z., Kuligowski, R. J., Ferraro, R., and Weng, F. (2011). A Study of Warm Rain Detection Using A-Train Satellite Data. *Geophys. Res. Lett.* 38, 6217. doi:10.1029/2010GL046217

Chen, X., de Leeuw, G., Arola, A., Liu, S., Liu, Y., Li, Z., et al. (2020). Joint Retrieval of the Aerosol Fine Mode Fraction and Optical Depth Using MODIS Spectral Reflectance over Northern and Eastern China: Artificial Neural Network Method. *Remote Sensing Environ.* 249, 112006. doi:10.1016/j.rse.2020.112006

Christensen, M. W., Stephens, G. L., and Lebsock, M. D. (2013). Exposing Biases in Retrieved Low Cloud Properties from CloudSat: A Guide for Evaluating Observations and Climate Data. *J. Geophys. Res. Atmos.* 118, 120–121. doi:10.1002/2013JD020224

Christi, M. J., and Stephens, G. L. (2004). Retrieving Profiles of Atmospheric CO2 in Clear Sky and in the Presence of Thin Cloud Using Spectroscopy from the Near and Thermal Infrared: A Preliminary Case Study. *J. Geophys. Res.* 109, 58. doi:10.1029/2003JD004058

Chudnovsky, A., Ben-Dor, E., Kostinski, A. B., and Koren, I. (2009). Mineral Content Analysis of Atmospheric Dust Using Hyperspectral Information from Space. *Geophys. Res. Lett.* 36, 22. doi:10.1029/2009GL037922

Chudnovsky, A., Kostinski, A., Herrmann, L., Koren, I., Nutesku, G., and Ben-Dor, E. (2011). Hyperspectral Spaceborne Imaging of Dust-Laden Flows: Anatomy of Saharan Dust Storm from the Bodélé Depression. *Remote Sensing Environ.* 115 (4), 1013–1024. doi:10.1016/j.rse.2010.12.006

Clark, R. N., Swayze, G. A., Eric Livo, K., Kokaly, R. F., Sutley, S. J., Brad Dalton, J., et al. (2003). Imaging Spectroscopy: Earth and Planetary Remote Sensing with the USGS Tetracorder and Expert Systems. *J.-Geophys.-Res.* 108 (E12), 1847. doi:10.1029/2002JE001847

Coddington, O., Pilewskie, P., and Vukicevic, T. (2012). The Shannon Information Content of Hyperspectral Shortwave Cloud Albedo Measurements: Quantification and Practical Applications. *J. Geophys. Res.* 117, 771. doi:10.1029/2011JD016771

Colman, R. (2003). A Comparison of Climate Feedbacks in General Circulation Models. *Clim. Dynam.* 20865, 865–873. doi:10.1007/s00382-003-0310-z

Diedrich, H., Preusker, R., Lindstrot, R., and Fischer, J. (2015). Retrieval of Daytime Total Columnar Water Vapour from MODIS Measurements over Land Surfaces. *Atmos. Meas. Tech.* 8, 823–836. doi:10.5194/amt-8-823-2015

Doelling, D. R., Loeb, N. G., Keyes, D. F., Nordeen, M. L., Morstad, D., Nguyen, C., et al. (2013). Geostationary Enhanced Temporal Interpolation for CERES Flux Products. *J. Atmos. Oceanic Technol.* 30, 1072–1090. doi:10.1175/JTECH-D-12-00136.1

Dubovik, O., Li, Z., Mishchenko, M. I., Tanré, D., Karol, Y., Bojkov, B., et al. (2019). Polarimetric Remote Sensing of Atmospheric Aerosols: Instruments, Methodologies, Results, and Perspectives. *J. Quant. Spectrosc. Radiat. Transfer* 224, 474–511. doi:10.1016/j.jqsrt.2018.11.024

Fischer, J., and Grassl, H. (1991). Detection of Cloud-Top Height from Backscattered Radiances within the Oxygen A Band. Part 1: Theoretical Study. *J. Appl. Meteorol.* 30 (9), 1245–1259. doi:10.1175/1520-0450(1991)030<1245:docthf>2.0.co;2

Gao, B.-C., and Goetz, A. F. H. (1990). Column Atmospheric Water Vapor and Vegetation Liquid Water Retrievals from Airborne Imaging Spectrometer Data. *J. Geophys. Res.* 95 (D4), 3549–3564. doi:10.1029/JD095iD04p03549

Gao, B.-C., and Kaufman, Y. J. (2003). Water Vapor Retrievals Using Moderate Resolution Imaging Spectroradiometer (MODIS) Near-Infrared Channels. *J. Geophys. Res.* 108, JD003023. doi:10.1029/2002JD003023

Gristey, J. J., Chiu, J. C., Gurney, R. J., Shine, K. P., Havemann, S., Thelen, J.-C., et al. (2019). Shortwave Spectral Radiative Signatures and Their Physical Controls. *J. Clim.* 32, 4805–4828. doi:10.1175/JCLI-D-18-0815.1

Grosvenor, D. P., Sourdeval, O., Zuidema, P., Ackerman, A., Alexandrov, M. D., Bennartz, R., et al. (2018). Remote Sensing of Droplet Number Concentration in Warm Clouds: A Review of the Current State of Knowledge and Perspectives. *Rev. Geophys.* 56, 409–453. doi:10.1029/2017RG000593

Green, R. O., Mahowald, N., Ung, C., Thompson, D. R., Bator, L., Bennet, M., et al. (2020). The Earth Surface Mineral Dust Source Investigation: An Earth Science Imaging Spectroscopy Mission. *IEEE Aerospace Conf.* 2020, 1–15. doi:10.1109/AERO47225.2020.9172731

Green, R. O., Eastwood, M. L., Sarture, C. M., Chrien, T. G., Aronsson, M., Chippendale, B. J., et al. (1998). Imaging Spectroscopy and the Airborne Visible/Infrared Imaging Spectrometer (AVIRIS). *Remote Sensing Environ.* 65 (3), 227–248. doi:10.1016/S0034-4257(98)00064-9

Grossi, M., Valks, P., Loyola, D., Aberle, B., Slijkhuis, S., Wagner, T., et al. (2015). Total Column Water Vapour Measurements from GOME-2 MetOp-A and MetOp-B. *Atmos. Meas. Tech.* 8, 1111–1133. doi:10.5194/amt-8-1111-2015

Henderson, D. S., L'Ecuyer, T., Stephens, G., Partain, P., and Sekiguchi, M. (2013). A Multisensor Perspective on the Radiative Impacts of Clouds and Aerosols. *J. Appl. Meteorol. Climatol.* 52, 853–871. doi:10.1175/JAMC-D12-025.110.1175/jamc-d-12-025.1

Haywood, J. M., Jones, A., Dunstone, N., Milton, S., Vellinga, M., Bodas-Salcedo, A., et al. (2016). The Impact of Equilibrating Hemispheric Albedos on Tropical Performance in the HadGEM2-ES Coupled Climate Model. *Geophys. Res. Lett.* 43, 395–403. doi:10.1002/2015GL066903

Henken, C. K., Diedrich, H., Preusker, R., and Fischer, J. (2015). MERIS Full-Resolution Total Column Water Vapor: Observing Horizontal Convective Rolls. *Geophys. Res. Lett.* 42 (10), 81. doi:10.1002/2015GL066650

Hou, W., Wang, J., Xu, X., and Reid, J. S. (2017). An Algorithm for Hyperspectral Remote Sensing of Aerosols: 2. Information Content Analysis for Aerosol Parameters and Principal Components of Surface Spectra. *J. Quant. Spectrosc. Radiat. Transfer* 192, 14–29. doi:10.1016/j.jqsrt.2017.01.041

Illingworth, A. J., Barker, H. W., Beljaars, A., Ceccaldi, M., Chepfer, H., Clerbaux, N., et al. (2015). The EarthCARE Satellite: The Next Step Forward in Global Measurements of Clouds, Aerosols, Precipitation, and Radiation. *Bull. Amer. Meteorol. Soc.* 96, 1311–1332. doi:10.1175/BAMS-D-12-00227.1

Kaufman, Y. J., Tanré, D., Remer, L. A., Vermote, E. F., Chu, A., and Holben, B. N. (1997). Operational Remote Sensing of Tropospheric Aerosol over Land from EOS Moderate Resolution Imaging Spectroradiometer. *J. Geophys. Res.* 102 (D14), 17051–17117. doi:10.1029/96jd03988

King, N. J., and Vaughan, G. (2012). Using Passive Remote Sensing to Retrieve the Vertical Variation of Cloud Droplet Size in Marine Stratocumulus: An Assessment of Information Content and the Potential for Improved Retrievals from Hyperspectral Measurements. *J. Geophys. Res.* 117, 15026. doi:10.1029/2012JD017896

Kopp, G. P., Smith, C., Belting, Z., Castleman, G., Drake, J., Espejo, K., et al. (2017). Radiometric flight results from the HyperSpectral Imager for Climate Science (HySICS). *Geosci. Instrum. Method. Data Syst.* 6, 169–191. doi:10.5194/gi-6-169-2017

Kruse, F. A., Lefkoff, A. B., and Dietz, J. B. (1993). Expert System-Based Mineral Mapping in Northern Death Valley, California/Nevada, Using the Airborne Visible/infrared Imaging Spectrometer (AVIRIS). *Remote Sensing Environ.* 44 (2–3), 309–336. doi:10.1016/0034-4257(93)90024-R

Levy, R. C., Remer, L. A., Martins, J. V., Kaufman, Y. J., Plana-Fattori, A., Redemann, J., et al. (2005). Evaluation of the MODIS Aerosol Retrievals over Ocean and Land during CLAMS. *J. Atmos. Sci.* 62, 974–992. doi:10.1175/jas3391.1

Levy, R. C., Remer, L. A., Mattoo, S., Vermote, E. F., and Kaufman, Y. J. (2007). Second-generation Operational Algorithm: Retrieval of Aerosol Properties over Land from Inversion of Moderate Resolution Imaging Spectroradiometer Spectral Reflectance. *J. Geophys. Res.* 112, D13211. doi:10.1029/2006JD007811

Li, Z., Zhao, X., Kahn, R., Mishchenko, M., Remer, L., Lee, K.-H., et al. (2009). Uncertainties in Satellite Remote Sensing of Aerosols and Impact on Monitoring its Long-Term Trend: a Review and Perspective. *Ann. Geophys.* 27, 2755–2770. doi:10.5194/angeo-27-2755-2009

Mauceri, S., Kindel, B., Massie, S., and Pilewskie, P. (2019). Neural Network for Aerosol Retrieval from Hyperspectral Imagery. *Atmos. Meas. Tech.* 12 (11), 6017–6036. doi:10.5194/amt-12-6017-2019

Meyer, K., and Platnick, S. (2010). Utilizing the MODIS 1.38 μM Channel for Cirrus Cloud Optical Thickness Retrievals: Algorithm and Retrieval Uncertainties. *J. Geophys. Res.* 115, D24209. doi:10.1029/2010JD014872

Lyapustin, A., Wang, Y., Korkin, S., and Huang, D. (2018). MODIS Collection 6 MAIAC Algorithm. *Atmos. Meas. Tech.* 11, 5741–5765. doi:10.5194/amt-11-5741-2018

Nakajima, T., and King, M. D. (1990). Determination of the Optical Thickness and Effective Particle Radius of Clouds from Reflected Solar Radiation Measurements. Part I: Theory. *J. Atmos. Sci.* 47, 1878–1893. 10.1175/1520-0469(1990)047<1878:DOTOTA>2.0.CO;2

Nakajima, T. Y., Suzuki, K., and Stephens, G. L. (2010a). Droplet Growth in Warm Water Clouds Observed by the A-Train. Part I: Sensitivity Analysis of the MODIS-Derived Cloud Droplet Sizes. *J. Atmos. Sci.* 67, 1884–1896. doi:10.1175/2009jas3280.1

Nakajima, T. Y., Suzuki, K., and Stephens, G. L. (2010b). Droplet Growth in Warm Water Clouds Observed by the A-Train. Part II: A Multi-Sensor View. *J. Atmos. Sci.* 67, 1897–1907. doi:10.1175/2010jas3276.1

National Academies of Sciences, Engineering, and Medicine (NAS) (2018). *Thriving on Our Changing Planet: A Decadal Strategy for Earth Observation from Space*. Washington, DC: The National Academies Press. doi:10.17226/24938

O'Neill, N. T., Eck, T. F., Smirnov, A., Holben, B. N., and Thulasiraman, S. (2003). Spectral Discrimination of Coarse and Fine Mode Optical Depth. *J. Geophys. Res.* 108, 4559. doi:10.1029/2002JD002975

Oyola, M. I., Campbell, J. R., Xian, P., Bucholtz, A., Ferrare, R. A., Burton, S. P., et al. (2019). Quantifying the Direct Radiative Effect of Absorbing Aerosols for Numerical Weather Prediction: a Case Study. *Atmos. Chem. Phys.* 19 (1), 205–218. doi:10.5194/acp-19-205-2019

Pilewskie, P., and Twomey, S. (1987). Cloud Phase Discrimination by Reflectance Measurements Near 1.6 and 2.2 μm. *J. Atmos. Sci.* 44, 3419–3420. doi:10.1175/1520-0469(1987)044<3419:cpdbrm>2.0.co;2

Platnick, S. (2000). Vertical Photon Transport in Cloud Remote Sensing Problems. *J. Geophys. Res.* 105 (22), 935. doi:10.1029/2000JD900333

Riedi, J., Marchant, B., Platnick, S., Baum, B. A., Thieuleux, F., Oudard, C., et al. (2010). Cloud Thermodynamic Phase Inferred from Merged POLDER and MODIS Data. *Atmos. Chem. Phys.* 10, 11851–11865. doi:10.5194/acp-10-11851-2010

Remer, L. A., Kaufman, Y. J., Tanré, D., Mattoo, S., Chu, D. A., Martins, J. V., et al. (2005). The MODIS Aerosol Algorithm, Products, and Validation. *J. Atmos. Sci.* 62 (4), 947–973. doi:10.1175/jas3385.1

Richardson, M., Leinonen, J., Cronk, H. Q., McDuffie, J., Lebsock, M. D., and Stephens, G. L. (2019). Marine Liquid Cloud Geometric Thickness Retrieved from OCO-2's Oxygen A-Band Spectrometer. *Atmos. Meas. Tech.Meas. Tech.* 12, 1717–1737. doi:10.5194/amt-12-1717-2019

Rodgers, C. D. (1998). Information Content and Optimisation of High Spectral Resolution Remote Measurements. *Adv. Space Res.* 21, 361–367. doi:10.1016/s0273-1177(97)00915-0

Schimel, D., Nastal, J., and Thompson, D. R. (2020). Science and Applications Traceability Matrix - March 2020 Release. Available at: https://sbg.jpl.nasa.gov/satm/SBG_SATM_Release_20200303.xlsx (Accessed 16 March, 2020).

Schmidt, K. S., Feingold, G., Pilewskie, P., Jiang, H., Coddington, O., and Wendisch, M. (2009). Irradiance in Polluted Cumulus Fields: Measured and Modeled Cloud-Aerosol Effects. *Geophys. Res. Lett.* 36, 848. doi:10.1029/2008GL036848

Schröder, M., Lockhoff, M., Fell, F., Forsythe, J., Trent, T., Bennartz, R., et al. (2018). The GEWEX Water Vapor Assessment Archive of Water Vapour Products from Satellite Observations and Reanalyses. *Earth Syst. Sci. Data* 10, 1093–1117. doi:10.5194/essd-10-1093-2018

Shea, Y., Fleming, G., Kopp, G., Lukashin, C., Pilewskie, P., Smith, P., et al. (2020). IClarreo Pathfinder: Mission Overview and Current Status, IGARSS 2020 - 2020 IEEE International Geoscience and Remote Sensing Symposium, Waikoloa, HI. 3286–3289. doi:10.1109/IGARSS39084.2020.9323176

Sokolik, I. N., Winker, D. M., Bergametti, G., Gillette, D. A., Carmichael, G., Kaufman, Y. J., et al. (2001). Introduction to Special Section: Outstanding Problems in Quantifying the Radiative Impacts of Mineral Dust. *J. Geophys. Res.* 106 (D16), 18015–18027. doi:10.1029/2000JD900498

Stephens, G. L. (1994). *Remote Sensing of the Lower Atmosphere: An Introduction*. Oxford: Oxford University Press.

Stephens, G. L., and Kummerow, C. (2007). The Remote Sensing of Clouds and Precipitation from Space: A Review. *J. Atmos. Sci.* 64, 3742–3765. 10.1175/2006JAS2375.1

Stephens, G. L., O'Brien, D., Webster, P. J., Pilewskie, P., Kato, S., and Li, J.-l. (2015). The Albedo of Earth. *Rev. Geophys* 53, 141–163. doi:10.1002/2014RG000449

Stephens, G., Hakuba, M., Behrangi, A., Haywood, J., Hawcroft, M., Kay, J., et al. (2016). The Curious Nature of the Hemispheric Symmetry of the Earth's Water and Energy Balances. *Curr. Clim. Change Rep.* 2, 9. doi:10.1007/s40641-016-0043-9

Stephens, G. L., Christensen, M., Andrews, T., Haywood, J., Malavelle, F. F., and Suzuki, K. (2019). Cloud Physics from Space. *Quart J. Roy Meteorol. Soc.* 145, 3589. doi:10.1002/qj.3589

Stephens, G. L., Freeman, A., Richard, E., Pilewskie, P., Larkin, P., and Chew, C. (2020). The Emerging Technological Revolution in Earth Observations. *Bull. Amer. Met. Soc.* 101, E274–E285. doi:10.1175/BAMS-D-19-0146.1

Su, W., Corbett, J., Eitzen, Z., and Liang, L. (2015). Next-generation Angular Distribution Models for Top-Of-Atmosphere Radiative Flux Calculation from CERES Instruments: Validation. *Atmos. Meas. Tech.* 8, 3297–3313. doi:10.5194/amt-8-3297-2015

Su, T., Laszlo, I., Li, Z., Wei, J., and Kalluri, S. (2020). Refining Aerosol Optical Depth Retrievals over Land by Constructing the Relationship of Spectral Surface Reflectances through Deep Learning: Application to Himawari-8. *Remote Sens. Environ.* 251, 112093. doi:10.1016/j.rse.2020.112093

Thompson, D. R., Babu, K. N., Braverman, A. J., Eastwood, M. L., Green, R. O., Hobbs, J. M., et al. (2019). Optimal Estimation of Spectral Surface Reflectance in Challenging Atmospheres. *Remote Sensing Environ.* 232, 111258. doi:10.1016/j.rse.2019.111258

Thompson, D. R., Gao, B. C., Green, R. O., Roberts, D. A., Dennison, P. E., and Lundeen, S. R. (2015). Atmospheric Correction for Global Mapping Spectroscopy: ATREM Advances for the HyspIRI Preparatory Campaign. *Remote Sensing Environ.* 167, 64–77. doi:10.1016/j.rse.2015.02.010

Thompson, D. R., McCubbin, L., Gao, B. C., Green, R. O., Matthews, A. A., Mei, F., et al. (2016). Measuring Cloud Thermodynamic Phase with Shortwave Infrared Imaging Spectroscopy. *J. Geophys. Res. Atmos.* 121, 9174–9190. doi:10.1002/2016JD024999

Tornow, F., Barker, H., Blázquez, V., Domenech, C., and Fischer, J. (2018). EarthCARE's Broadband Radiometer: Uncertainties Associated with Cloudy Atmospheres. *J.Atmos. Ocean. Tech.* 35, 2201–2211. doi:10.1175/JTECH-D-18-0083.1

Twomey, S., and Seton, K. J. (1980). Inferences of Gross Microphysical Properties of Clouds from Spectral Reflectance Measurements. *J. Atmos. Sci.* 37, 1065–1069. 10.1175/1520-0469(1980)037<1065:IOGMPO>2.0.CO;2

Vonder Haar, T. H., and Suomi, V. E. (1969). Satellite Observations of the Earth's Radiation Budget: Science. *New Ser.* 163 (3868), 667–669. doi:10.1126/science.163.3868.667

Wang, S., Fang, L., Zhang, X., and Wang, W. (2015). Retrieval of Aerosol Properties for Fine/Coarse Mode Aerosol Mixtures over Beijing from PARASOL Measurements. *Remote Sens* 7, 9311–9324. doi:10.3390/rs70709311

Wang, C., Ding, S., Yang, P., Baum, B., and Dessler, A. E. (2012). A New Approach to Retrieving Cirrus Cloud Height with a Combination of MODIS 1.24- and 1.38-um Channels. *Geophys. Res. Lett.* 39, L24806. doi:10.1029/2012GL053854

Wielicki, B. A., Barkstrom, B. R., Baum, B. A., Charlock, T. P., Green, R. N., and Kratz, D. P. (1996). Clouds and the Earth's Radiant Energy System (CERES): An Earth Observing System. *Bull. Am. Meteorol. Soc.* 72, 853–868. 10.1175/1520-0477(1996)077<0853:CATERE>2.0.CO;2

Wood, R., Leon, D., Lebsock, M., Snider, J., and Clarke, A. D. (2012). Precipitation Driving of Droplet Number Concentration Variability in Marine Low Clouds. *J. Geophys. Res.* 117, D19210. doi:10.1029/2012JD018305

Wu, Z., Chen, J., Wang, Y., Zhu, Y., Liu, Y., Yao, B., et al. (2018). Interactions between Water Vapor and Atmospheric Aerosols Have Key Roles in Air Quality and Climate Change. *Natl. Sci. Rev.* 5 (4), 452–454. doi:10.1093/nsr/nwy063

Xu, X., Wang, J., Wang, Y., Henze, D. K., Zhang, L., Grell, G. A., et al. (2017). Sense Size Dependent Dust Loading and Emission from Space Using Reflected Solar and Infrared Spectral Measurements: An Observation System Simulation Experiment. *J. Geophys. Res. Atmos.* 122, 8233–8254. doi:10.1002/2017JD026677

Yan, X., Li, Z., Luo, N., Shi, W., Zhao, W., Yang, X., et al. (2019). An Improved Algorithm for Retrieving the Fine-Mode Fraction of Aerosol Optical Thickness. Part 2: Application and Validation in Asia. *Remote Sens. Environ.* 222, 90–103. doi:10.1016/j.rse.2018.12.012

Yan, X., Zang, Z., Liang, C., Luo, N., Ren, R., Cribb, M., et al. (2021). New Global Aerosol Fine-Mode Fraction Data over Land Derived from MODIS Satellite Retrievals. *Environ. Pollut.* 276, 116707. doi:10.1016/j.envpol.2021.116707

Zelinka, M., Klein, S., and Hartmann, D. (2012). Computing and Partitioning Cloud Feedbacks Using Cloud Property Histograms. Part I: Cloud Radiative Kernels. *J. Clim.* 25, 3715–3735. doi:10.1175/JCLI-D-11-00248.1

Zhang, Z., Ackerman, A. S., Feingold, G., Platnick, S., Pincus, R., and Xue, H. (2012). Effects of Cloud Horizontal Inhomogeneity and Drizzle on Remote Sensing of Cloud Droplet Effective Radius: Case Studies Based on Large-Eddy Simulations. *J. Geophys. Res.* 117, D19208. doi:10.1029/2012JD017655

Zhang, H., Zhang, B., Chen, Z., and Huang, Z. (2018). Vicarious Radiometric Calibration of the Hyperspectral Imaging Microsatellites SPARK-01 and -02 over Dunhuang, China. *Rem. Sens.* 10, 120. doi:10.3390/rs10010120

Conflict of Interest: The authors declare that the research was conducted in the absence of any commercial or financial relationships that could be construed as a potential conflict of interest.

frontiers
in Remote Sensing

ORIGINAL RESEARCH
published: 06 August 2021
doi: 10.3389/frsen.2021.711106

Improved Lorenz-Mie Look-Up Table for Lidar and Polarimeter Retrievals

Eduard Chemyakin[1,2]*, *Snorre Stamnes*[2], *Sharon P. Burton*[2], *Xu Liu*[2], *Chris Hostetler*[2], *Richard Ferrare*[2], *Brian Cairns*[3] and *Oleg Dubovik*[4]

[1]*Science Systems and Applications, Inc., Hampton, VA, United States,* [2]*NASA Langley Research Center, Hampton, VA, United States,* [3]*NASA Goddard Institute for Space Studies, New York, NY, United States,* [4]*Laboratoire d'Optique Amosphérique, Université des Sciences et Technologies de Lille, Villeneuve d'Ascq, France*

Lidar and polarimeter aerosol microphysical retrievals require calculating single-scattering properties that are computationally expensive. One of the easiest ways to speed up these calculations is to use a look-up table. Two important currently available look-up tables were created about 15 years ago. Advancements in modern computational hardware allows us to create a new look-up table with improved precision over a larger range of aerosol properties. In this new and improved Lorenz-Mie look-up table we tabulate the light scattering by an ensemble of homogeneous isotropic spheres at arbitrary wavelengths starting from $0.355\,\mu$m. The improved look-up table covers spherical atmospheric aerosols with radii in the range of 0.001–$100\,\mu$m, with real parts of the complex refractive index in the range of 1.29–1.65, and with imaginary parts of the complex refractive index in the range of 0–0.05. We test twelve wavelengths from 0.355 to $2.264\,\mu$m and find that the elements of the normalized scattering matrix as well as the asymmetry parameter, the aerosol absorption, backscatter, extinction, and scattering coefficients are precise to within 1% for 99.99% of cases. The look-up table together with C++, Fortran, Matlab, and Python codes are freely available online.

Keywords: lidar, polarimeter, Lorenz-Mie theory, scattering matrix and optical coefficients, look-up table, scale invariance rule

Edited by:
Yingying Ma,
Wuhan University, China

Reviewed by:
Lei Bi,
Zhejiang University, China
Oliver Lux,
Helmholtz Association of German Research Centers (HZ), Germany

***Correspondence:**
Eduard Chemyakin
eduard.v.chemyakin@nasa.gov

Specialty section:
This article was submitted to Satellite Missions, a section of the journal Frontiers in Remote Sensing

Received: *17 May 2021*
Accepted: *23 June 2021*
Published: *06 August 2021*

Citation:
Chemyakin E, Stamnes S, Burton SP, Liu X, Hostetler C, Ferrare R, Cairns B and Dubovik O (2021) Improved Lorenz-Mie Look-Up Table for Lidar and Polarimeter Retrievals. Front. Remote Sens. 2:711106. doi: 10.3389/frsen.2021.711106

1 INTRODUCTION

Recently there is a growing interest in combining simultaneous lidar and polarimeter measurements to perform retrievals of vertically-resolved aerosol properties. For example, it is expected that the combination of lidar and polarimeter observations will significantly reduce uncertainties in aerosol radiative forcing (National Academies of Sci, 2018).

In remote sensing, lidars are active instruments that can contribute a highly accurate assessment of the vertically-resolved distribution of atmospheric aerosols. There are many different types of lidars, but our Lorenz-Mie look-up table (LUT) unit tests focus on the NASA LaRC airborne second-generation high spectral resolution lidar (HSRL-2), which makes three-wavelength lidar measurements of the atmosphere (Burton et al., 2018). HSRL-2 measurements result in the aerosol backscatter and extinction coefficients at wavelengths 0.355 (UV) and $0.532\,\mu$m (VIS) accompanied by the attenuated backscatter coefficient at $1.064\,\mu$m.

Polarimeters are passive sensors that have greater sensitivity to the absorption properties of aerosols, but the sensitivity to vertical distribution is limited. There are many different polarimeters too, but our unit tests focus on the channels provided by the airborne NASA GISS Research Scanning Polarimeter (RSP) (Cairns et al., 1999). The RSP has nine spectral channels that are divided into two groups based on the type of detector used: visible/near infrared bands at 0.41, 0.469, 0.555, 0.67, 0.864, and 0.96 μm, accompanied by shortwave infrared bands at 1.594, 1.88, and 2.264 μm.

Retrievals of aerosol microphysical properties using lidar and polarimeter data separately or combined require significant light single-scattering calculations that can consume a majority of the computational time. In this paper, we describe the improved LUT (which we call: SIR LUT) that uses scale invariance rule (SIR) built on Mishchenko (Mishchenko, 2006) to speed up these calculations with a precision target of 1% for all the optical properties. We also target the accuracy (bias) to be negligible compared to precision. The ± 1% precision was imposed to reduce forward model errors in modeling state-of-the-art airborne lidar and polarimeters, as well as the next generation of satellite polarimetric sensors.

The fundamental design of this Lorenz-Mie LUT for lidar and polarimetric sensors builds on the spherical kernels LUT (SK LUT) (Dubovik and King, 2000; Dubovik et al., 2002a; Dubovik et al., 2006). The SK LUT is already well established and has multiple applications including but not limited to AERONET (Dubovik et al., 2006), GRASP (Dubovik et al., 2011; Dubovik et al., 2014), and many others. The SIR LUT thus represents an improvement of a previously developed approach, but we also describe its methodology in detail to further document this powerful approach and to highlight its beauty, elegance and simplicity. While using the same theoretical underpinnings, we used modern computing resources to calculate a significantly more precise LUT which we share with the community. Simulation tests show that precision of SIR LUT for all optical properties always exceeds that of SK LUT by up to 34%.

Throughout this paper, we will follow the notation used by Dubovik et al. (2006). Our LUT targets spherical aerosols, i.e., Lorenz-Mie scattering theory is applied (Van de Hulst, 1981; Bohren and Huffman, 1983; Mishchenko et al., 2002), but this theoretical approach can also be extended to non-spherical aerosols (Dubovik and King, 2000; Dubovik et al., 2002a; Dubovik et al., 2006; Dubovik et al., 2011; Dubovik et al., 2014).

2 SCATTERING MATRIX AND OPTICAL COEFFICIENTS

A unit test framework was developed to test the following list of aerosol inherent optical properties (IOPs) that we target for fast and precise estimation.

The normalized matrix that relates the incident and the scattered Stokes parameters in the standard Lorenz-Mie theory of light scattering by homogeneous isotropic spheres can be represented as (Van de Hulst, 1981; Bohren and Huffman, 1983; Mishchenko et al., 2002):

$$\mathbf{P}(\Theta, m, \lambda) = \begin{bmatrix} P_{11}(.) & P_{12}(.) & 0 & 0 \\ P_{12}(.) & P_{11}(.) & 0 & 0 \\ 0 & 0 & P_{33}(.) & P_{34}(.) \\ 0 & 0 & -P_{34}(.) & P_{33}(.) \end{bmatrix}, \quad (1)$$

where Θ is the scattering angle in the range from 0° to 180°, λ is the wavelength (μm), and $m = m_R - i{\cdot}m_I$ is the complex refractive index (CRI) consisting of the real part m_R (no unit) and the imaginary part m_I (n.u.).

The four independent elements of the normalized scattering matrix $\mathbf{P}(\Theta, m, \lambda)$ can be computed for each vertically-resolved atmospheric layer as

$$P_{ii'}(\Theta, m, \lambda) = \frac{1}{\mathrm{sca}(m, \lambda)} \int_{r_{\min}}^{r_{\max}} C_{ii'}(\Theta, m, \lambda, r)\; n(r)\,\mathrm{d}r, \quad (2)$$

where r is the particle radius (μm), $n(r) = \mathrm{d}N(r)/\mathrm{d}r$ is the particle size distribution (PSD) function ($\mu\mathrm{m}^{-1}\mathrm{cm}^{-3}$) such that $n(r)\mathrm{d}r$ represents the number of particles with radius between r and $r + \mathrm{d}r$ per cm^3 of air, and $N(r)$ is the number of particles per cm^3 in the size range $[0, r]$, i.e., $N(r) = \int_0^r n(r^*)\mathrm{d}r^*$ (Seinfeld and Pandis, 2006). The terms $C_{ii'}(\Theta, m, \lambda, r) = \pi r^2 Q_{ii'}(\Theta, m, \lambda, r)(\mathrm{m}^2\mathrm{sr}^{-1})$ describe the directional scattering cross sections corresponding to matrix elements $P_{ii'}(\Theta, m, \lambda)$ (sr^{-1}) with subscript $ii' = \{11, 12, 33, 34\}$, whereas $Q_{ii'}(\Theta, m, \lambda, r)$ (sr^{-1}) describe the directional efficiencies, and πr^2 (m^2) is the geometrical cross section (Van de Hulst, 1981; Bohren and Huffman, 1983; Mishchenko et al., 2002). In the ideal case, the integration should be done over the radius range from $r_{\min} = 0$ to $r_{\max} = \infty$, but a non-zero $r_{\min}$ and a finite value of $r_{\max}$ must be chosen for numerical computations.

As a reminder, the aerosol lidar backscatter coefficient $\beta(m, \lambda)$ ($\mathrm{Mm}^{-1}\mathrm{sr}^{-1}$) can be computed as

$$\begin{aligned} \beta(m, \lambda) &= \frac{1}{4\pi} \int_{r_{\min}}^{r_{\max}} C_{11}(180°, \mathrm{m}, \lambda, \mathrm{r})\, n(r)\,\mathrm{d}r \\ &= \frac{\mathrm{sca}(m, \lambda)\, P_{11}(180°, \mathrm{m}, \lambda)}{4\pi}. \end{aligned} \quad (3)$$

The aerosol scattering coefficient $\mathrm{sca}(m, \lambda)$ (Mm^{-1}) that appears in **Eqs. 2**, **3** and the aerosol extinction coefficient $\alpha(m, \lambda)$ (Mm^{-1}) can be computed as

$$\{\mathrm{sca}, \alpha\}(m, \lambda) = \int_{r_{\min}}^{r_{\max}} C_{\mathrm{sca},\alpha}(m, \lambda, r)\, n(r)\,\mathrm{d}r, \quad (4)$$

where $C_{\mathrm{sca},\alpha}(m, \lambda, r) = \pi r^2 Q_{\mathrm{sca},\alpha}(m, \lambda, r)$ (m^2) is a scattering (extinction) cross section and $Q_{\mathrm{sca},\alpha}(m, \lambda, r)$ (n.u.) is a corresponding efficiency (Van de Hulst, 1981; Bohren and Huffman, 1983; Mishchenko et al., 2002).

The aerosol absorption coefficient (Mm^{-1}) is another valuable aerosol IOP to be computed as

$$\mathrm{abs}(m, \lambda) = \alpha(m, \lambda) - \mathrm{sca}(m, \lambda). \quad (5)$$

The ensemble-averaged asymmetry parameter (n.u.) finalizes our list of aerosol optical properties to be tested by our unit test framework:

$$\langle \cos(m, \lambda) \rangle = \frac{1}{2} \int_{0°}^{180°} P_{11}(\Theta, m, \lambda) \sin\Theta \cos\Theta\; \mathrm{d}\Theta, \quad (6)$$

where the $P_{11}(\Theta, m, \lambda)$ element of the normalized scattering matrix $\mathbf{P}$ [see **Eq. 1**] is traditionally referred to as the phase function and the division by $\mathrm{sca}(m, \lambda)$

in **Eq. 2** ensures that the following normalization condition is satisfied:

$$\frac{1}{2}\int_{0^\circ}^{180^\circ} P_{11}(\Theta, m, \lambda)\sin\Theta \; \mathrm{d}\Theta = 1. \tag{7}$$

We already mentioned that precise computation of the elements of the normalized scattering matrix **P** [see **Eq. 1**] and accompanying single-scattering properties [see **Eqs. 3–6**] requires significant amount of time. For the purpose of retrieval of aerosol microphysical properties, it is convenient to find an efficient way to compute all these aerosol IOPs to within ± 1% precision using a precomputed LUT.

3 PRINCIPLES OF LOOK-UP TABLE

In order to reduce the size of the dataset that must be stored in computer memory, the LUT takes advantage of features that are universal and allow us to develop and apply a generalized approach for all the tabulated IOPs.

One can see that **Eqs. 2–4** share some commonality. The core structure of these equations can be generalized as

$$\begin{aligned} p &= \int_{r_{\min}}^{r_{\max}} C_p(.)n(r)\,\mathrm{d}r = \int_{r_{\min}}^{r_{\max}} C_p(.)\frac{\mathrm{d}N(r)}{\mathrm{d}\ln r}\mathrm{d}\ln r \\ &= \int_{r_{\min}}^{r_{\max}} \frac{C_p(.)}{\frac{4}{3}\pi r^3}\frac{\mathrm{d}V(r)}{\mathrm{d}\ln r}\mathrm{d}\ln r, \end{aligned} \tag{8}$$

where $p = \{P_{ii'}(\Theta, m, \lambda), \beta(m, \lambda), \mathrm{sca}(m, \lambda), \alpha(m, \lambda)\}$. The other common feature of **Eqs. 2–4** is that it is optimal to perform the numerical integration on a logarithmic scale because it is often assumed in atmospheric sciences that the PSD $n(r) = \mathrm{d}N(r)/\mathrm{d}r$ has lognormal shape (Seinfeld and Pandis, 2006). The cross sections $C_p(\ldots, r) = \pi r^2 Q_p(\ldots, r)$ are also often plotted and analyzed on a logarithmic scale because they exhibit smoother variability in equal relative steps $\Delta r/r$ (i.e., in equal logarithmic steps, since $\mathrm{d}r/r = \mathrm{d}\ln r$) rather than in equal absolute steps Δr (Dubovik et al., 2006).

In **Eq. 8** we used

$$\frac{\mathrm{d}N(r)}{\mathrm{d}\ln r} = r\frac{\mathrm{d}N(r)}{\mathrm{d}r} = rn(r), \tag{9}$$

$$\frac{\mathrm{d}V(r)}{\mathrm{d}\ln r} = \frac{4}{3}\pi r^3\frac{\mathrm{d}N(r)}{\mathrm{d}\ln r} = v(r)\frac{\mathrm{d}N(r)}{\mathrm{d}\ln r},\ v(r) = \frac{4}{3}\pi r^3, \tag{10}$$

and switched to the volume distribution $\mathrm{d}V(r)/\mathrm{d}\ln r$ because, as a rough approximation of atmospheric conditions, aerosol PSDs are equipartitioned in volume (Thomalla and Quenzel, 1982). In addition, light scattering by an ensemble of small particles depends on the particle surface area or volume rather than on the number concentration (Van de Hulst, 1981; Bohren and Huffman, 1983; Mishchenko et al., 2002).

Let us split the finite range of radii $[r_{\min}, r_{\max}]$ into a set $\{r_j\}$ consisting of $\mathrm{M} \gg 1$ grid bins that are logarithmically equidistant and distributed between $r_1 = r_{\min}$ and $r_\mathrm{M} = r_{\max}$ with a constant step size $\Delta\ln r = (\ln r_\mathrm{M} - \ln r_1)/(\mathrm{M} - 1)$. Now we can reduce the integral of **Eq. 8** to its approximation by a finite sum (Twomey, 1977):

$$p = \int_{r_{\min}}^{r_{\max}} \frac{C_p(.)}{v(r)}\frac{\mathrm{d}V(r)}{\mathrm{d}\ln r}\mathrm{d}\ln r \approx \sum_{j=1}^{\mathrm{M}} C_{p,j,\lambda}\frac{\mathrm{d}V(r_j)}{\mathrm{d}\ln r}. \tag{11}$$

Equation 11 is based on the assumption that the PSD $\mathrm{d}V(r)/\mathrm{d}\ln r$ is a smooth function of $\ln r$ and can be quadratically approximated within the narrow range $r_{j-1} \le r \le r_{j+1}$ of discrete radii on a logarithmic scale. We would like to emphasize that for improved precision we use the quadratic approximation $a_j + b_j\ln r + c_j\ln^2 r$ of the PSD instead of the linear (trapezoidal) approximation that has been used previously (Twomey, 1977; Dubovik et al., 2006). Following the original generalized procedure for the approximation of a PSD (Twomey, 1977), the quadratic coefficients a_j, b_j, and c_j are computed corresponding to the volume distribution function $\mathrm{d}V(r)/\mathrm{d}\ln r$ at three consecutive radii $r_k = r_{j-1}$, r_j, and r_{j+1}:

$$\frac{\mathrm{d}V(r_k)}{\mathrm{d}\ln r} = a_j + b_j\ln r_k + c_j\ln^2 r_k. \tag{12}$$

Equation 12 can be expressed in terms of the quadratic approximation coefficients as

$$\begin{aligned} a_j &= \frac{1}{2(\Delta\ln r)^2}\left[\frac{\mathrm{d}V(r_{j-1})}{\mathrm{d}\ln r}\ln r_j\ln r_{j+1}\right. \\ &\quad \left. - 2\frac{\mathrm{d}V(r_j)}{\mathrm{d}\ln r}\ln r_{j-1}\ln r_{j+1} + \frac{\mathrm{d}V(r_{j+1})}{\mathrm{d}\ln r}\ln r_{j-1}\ln r_j\right], \\ b_j &= \frac{1}{2(\Delta\ln r)^2}\left[-\frac{\mathrm{d}V(r_{j-1})}{\mathrm{d}\ln r}\ln(r_j r_{j+1})\right. \\ &\quad \left. + 2\frac{\mathrm{d}V(r_j)}{\mathrm{d}\ln r}\ln(r_{j-1}r_{j+1}) - \frac{\mathrm{d}V(r_{j+1})}{\mathrm{d}\ln r}\ln(r_{j-1}r_j)\right], \\ c_j &= \frac{1}{2(\Delta\ln r)^2}\left[\frac{\mathrm{d}V(r_{j-1})}{\mathrm{d}\ln r} - 2\frac{\mathrm{d}V(r_j)}{\mathrm{d}\ln r} + \frac{\mathrm{d}V(r_{j+1})}{\mathrm{d}\ln r}\right]. \end{aligned} \tag{13}$$

The range $[r_j, r_{j+1}]$ makes the following contribution to the integral in **Eq. 11**:

$$\int_{r_j}^{r_{j+1}} \frac{C_p(.)}{v(r)}\left(a_j + b_j\ln r + c_j\ln^2 r\right)\mathrm{d}\ln r. \tag{14}$$

Equations 13 and **14** may be grouped by terms that include $\mathrm{d}V(r_{j-1})/\mathrm{d}\ln r$, $\mathrm{d}V(r_j)/\mathrm{d}\ln r$, or $\mathrm{d}V(r_{j+1})/\mathrm{d}\ln r$ (Twomey, 1977). We will focus only on the contribution of $\mathrm{d}V(r_j)/\mathrm{d}\ln r$ to the discretization in **Eq. 11**:

$$\begin{aligned} &\left[\frac{\ln r_{j-1}\ln r_{j+1}}{(\Delta\ln r)^2}\int_{r_j}^{r_{j+1}}\frac{C_p(.)}{v(r)}\mathrm{d}\ln r\right. \\ &- \frac{\ln(r_{j-1}r_{j+1})}{(\Delta\ln r)^2}\int_{r_j}^{r_{j+1}}\ln r\frac{C_p(.)}{v(r)}\mathrm{d}\ln r \\ &\left. + \frac{1}{(\Delta\ln r)^2}\int_{r_j}^{r_{j+1}}\ln^2 r\frac{C_p(.)}{v(r)}\mathrm{d}\ln r\right]\frac{\mathrm{d}V(r_j)}{\mathrm{d}\ln r} + \cdots. \end{aligned} \tag{15}$$

The multiplicative factor $\mathrm{d}V(r_j)/\mathrm{d}\ln r$ also contributes to the ranges $[r_{j-1}, r_j]$ and $[r_{j+1}, r_{j+2}]$. Adding the contributions of the three subranges, we finally can obtain the formula for coefficient $C_{p,j,\lambda}$ of **Eq. 11**:

$$
\begin{aligned}
C_{p,j,\lambda} = & \frac{3\ln r_{j-2}\ln r_{j-1}}{8(\Delta\ln r)^2}\int_{r_{j-1}}^{r_j}\frac{Q_p(.,r,\lambda)}{r}\mathrm{d}\ln r \\
& -\frac{3\ln\left(r_{j-2}r_{j-1}\right)}{8(\Delta\ln r)^2}\int_{r_{j-1}}^{r_j}\ln r\frac{Q_p(.,r,\lambda)}{r}\mathrm{d}\ln r \\
& +\frac{3}{8(\Delta\ln r)^2}\int_{r_{j-1}}^{r_j}\ln^2 r\frac{Q_p(.,r,\lambda)}{r}\mathrm{d}\ln r \\
& -\frac{3\ln r_{j-1}\ln r_{j+1}}{4(\Delta\ln r)^2}\int_{r_j}^{r_{j+1}}\frac{Q_p(.,r,\lambda)}{r}\mathrm{d}\ln r \\
& +\frac{3\ln\left(r_{j-1}r_{j+1}\right)}{4(\Delta\ln r)^2}\int_{r_j}^{r_{j+1}}\ln r\frac{Q_p(.,r,\lambda)}{r}\mathrm{d}\ln r \\
& -\frac{3}{4(\Delta\ln r)^2}\int_{r_j}^{r_{j+1}}\ln^2 r\frac{Q_p(.,r,\lambda)}{r}\mathrm{d}\ln r \\
& +\frac{3\ln r_{j+1}\ln r_{j+2}}{8(\Delta\ln r)^2}\int_{r_{j+1}}^{r_{j+2}}\frac{Q_p(.,r,\lambda)}{r}\mathrm{d}\ln r \\
& -\frac{3\ln\left(r_{j+1}r_{j+2}\right)}{8(\Delta\ln r)^2}\int_{r_{j+1}}^{r_{j+2}}\ln r\frac{Q_p(.,r,\lambda)}{r}\mathrm{d}\ln r \\
& +\frac{3}{8(\Delta\ln r)^2}\int_{r_{j+1}}^{r_{j+2}}\ln^2 r\frac{Q_p(.,r,\lambda)}{r}\mathrm{d}\ln r.
\end{aligned}
\tag{16}
$$

The values of coefficients $C_{p,j,\lambda}$ are independent of the PSD and depend only on the scattering angle Θ (directional scattering), CRI m, and wavelength λ [see **Eq. 16**]. We switched to efficiencies $Q_p(.,r,\lambda)$ instead of cross sections $C_p(.,r,\lambda)$ for convenience in the following discussion.

The sets of coefficients $\{C_p\}$ can be computed once with high precision for the selected scattering angles (directional scattering) and CRIs, and stored as an LUT for each aerosol IOP p. Crucially, we only need to prepare these coefficients at a single "reference" wavelength λ_r which will be chosen to be the shortest wavelength desired (see **Section 4.1**). Aerosol IOPs for longer wavelengths $\lambda \geq \lambda_\mathrm{r}$ can be estimated using the results at the reference wavelength and the scale invariance rule (SIR) of electromagnetic scattering (Dubovik et al., 2006; Mishchenko, 2006).

The discretization in **Eq. 11** requires that the PSDs are smooth and wide enough to cover a significant number of densely distributed radii bins. In the case of narrow, steep PSDs, the discretization becomes less accurate because a strongly oscillating function $\mathrm{d}V(r)/\mathrm{d}\ln r$ can't be accurately approximated by a quadratic function on a sparse grid of radii bins.

Later we will show that **Eq. 16** provides an easy and elegant way to quickly compute all the aerosol IOPs of interest [see **Eqs. 2–6**], for a wide range of wavelengths using an LUT referenced to a single wavelength.

3.1 Lognormal Particle Size Distribution

The following numerical unit tests use a particular type of function as a PSD $n(r)$. An earlier study mathematically proved that the random process of sequential particle crushing naturally leads to a lognormal distribution of particle sizes (Kolmogorov, 1941). The monomodal lognormal PSD is experimentally confirmed to be a good approximation for the shape of naturally occurring aerosol PSDs in the atmosphere (Seinfeld and Pandis, 2006), and can be considered as an example of function $n(r)$ in **Eqs. 2–4**:

$$
n(r) = \frac{\mathrm{d}N(r)}{\mathrm{d}r} = \frac{n_\mathrm{t}}{r\sqrt{2\pi}\ln\sigma}\exp\left[-\frac{(\ln r - \ln r_\mathrm{med})^2}{2\ln^2\sigma}\right], \tag{17}
$$

where r_med describes the count median radius with respect to the number concentration distribution. The count median radius is defined as the radius above which there are as many particles as there are particles with radii below r_med. The term σ is the geometric standard deviation whereas $\ln\sigma$ is commonly referred to as the mode width, and n_t is the total number concentration.

The same PSD on the logarithmic scale can be expressed in terms of volume [see **Eq. 10**] as

$$
\frac{\mathrm{d}V(r)}{\mathrm{d}\ln r} = \frac{4}{3}\pi r^3\frac{n_\mathrm{t}}{\sqrt{2\pi}\ln\sigma}\exp\left[-\frac{(\ln r - \ln r_\mathrm{med})^2}{2\ln^2\sigma}\right]. \tag{18}
$$

In many cases it is more convenient to analyze the monomodal lognormal PSD in terms of effective radius $r_\mathrm{eff} = r_\mathrm{med}\exp(2.5\ln^2\sigma)$ and effective variance $\nu_\mathrm{eff} = \exp(\ln^2\sigma) - 1$. Our analysis of the LUT performance (see **Section 4.5**) includes these two quantities. In our numerical simulations for polarimeter observables (see **Section 4.7**) we also will use a bimodal PSD that is a sum of the fine and coarse mode PSDs [see **Eq. 18**], each defined by its total number concentration, effective radius and effective variance.

However, the LUT can be used with any custom PSD that is smooth and wide enough to cover a significant number of densely distributed radii bins.

4 LOOK-UP TABLE

4.1 Selection of the Reference Wavelength

The fundamental decision in the design of the LUT is the choice of reference wavelength λ_r used to compute the stored coefficients $\{C_p\}$ [see **Eq. 16**]. This choice has a theoretical and practical basis to optimize the application of the LUT.

For the reference wavelength of the LUT we decided to use the shortest wavelength among all remote sensing instruments of interest including the two mentioned in **Section 1**, i.e., $\lambda_\mathrm{r} = 0.355\,\mu$m. Let us justify our choice by noting that the size parameter $x = 2\pi r/\lambda$ is used for all the Lorenz-Mie computations (Van de Hulst, 1981; Bohren and Huffman, 1983; Mishchenko et al., 2002). The size parameter conveniently relates the wavelength and radius such that the Lorenz-Mie scattering properties for a given radius and wavelength are the same as those at another wavelength after adjusting the radius. For example, an aerosol with a radius of $1.4\,\mu$m observed at a wavelength $\lambda = 2.264\,\mu$m will be characterized by the same size parameter and identical

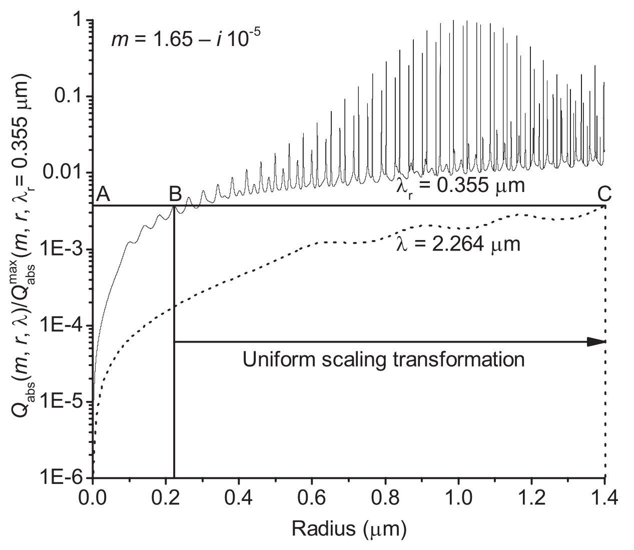

FIGURE 1 | Normalized absorption efficiencies at wavelengths 0.355 and 2.264 μm are related by a uniform scaling transformation which is a type of Euclidean affinity transformation.

Lorenz-Mie scattering properties as an aerosol with radius $\frac{0.355}{2.264} \times 1.4 \approx 0.22\,\mu$m observed at the reference wavelength $\lambda_r = 0.355\,\mu$m:

$$x = 2\pi\frac{1.4}{2.264} = 2\pi\frac{r}{\lambda} = 2\pi\frac{\frac{0.355}{2.264}\cdot 1.4}{0.355} = 2\pi\frac{\frac{\lambda_r}{\lambda}r}{\lambda_r}. \tag{19}$$

As a remark, **Eq. 19** states that a shorter wavelength delivers a greater range of size parameters for a given range of radii.

If the CRI is fixed then **Eq. 19** establishes a direct connection between the efficiencies [see **Eqs. 2–4**] at wavelengths λ and λ_r (for simplicity, we assume $\lambda \geq \lambda_r$) using a simple scaling in the radius domain given by

$$Q_p(.,r,\lambda) = Q_p\left(.,\frac{\lambda_r}{\lambda}r,\lambda_r\right). \tag{20}$$

A direct connection between the efficiencies can also be expressed in terms of integrals using a linear scaling of the integration range as

$$\int_{r_{\min}}^{r_{\max}} Q_p(.,r,\lambda)\mathrm{d}\ln r = \int_{\frac{\lambda_r}{\lambda}r_{\min}}^{\frac{\lambda_r}{\lambda}r_{\max}} Q_p(.,r,\lambda_r)\,\mathrm{d}\ln r. \tag{21}$$

Equations 20 and **21** are the key properties for understanding how this type of LUT works and can be seen as a practical application of the scale invariance rule (Mishchenko, 2006). **Equation 21** can be verified numerically or proved analytically with the assumption that the efficiency $Q_p(.,r,\lambda)$ can be approximated as

$$Q_p(.,r,\lambda) \approx \sum_{j=1}^{\infty} q_{p,j}(.)x^j, \tag{22}$$

where the appropriate coefficients $q_{p,j}(.)$ depend on the scattering angle Θ (directional scattering) and the CRI m.

Let us directly compute and plot (see **Figure 1**) the absorption efficiency $Q_{\text{abs}}(m,\lambda,r) = Q_\alpha(m,\lambda,r) - Q_{\text{sca}}(m,\lambda,r)$ at wavelengths 0.355 and 2.264 μm in order to provide a graphical demonstration of **Eq. 20**. We will use the CRI $m = 1.65 - i\cdot 10^{-5}$ that corresponds to an almost non-absorbing aerosol. **Figure 1** shows that the absorption efficiencies at two selected wavelengths repeat each other with a constant scaling factor in the radius domain. The same conclusion also applies to the other types of efficiencies too [see **Eqs. 2–4**]. **Equation 20** offers a simple way to obtain the efficiencies at longer wavelengths λ if the corresponding efficiency at a shorter reference wavelength λ_r is already known. For example, in order to plot the absorption efficiency at $\lambda = 2.264\,\mu$m from 0^+ to 1.4 μm radius (from point A to point C of dashed line in **Figure 1**), we can substitute 1.4 μm with $\frac{0.355}{2.264}\cdot 1.4 \approx 0.22\,\mu$m radius and perform an affine stretch of the precomputed efficiency at $\lambda_r = 0.355\,\mu$m (from point A to point B of solid line in **Figure 1**).

From **Figure 1** it is reasonable to conclude that the numerical integration over radii in **Eqs. 2–4** for a given precision will require smaller integration steps at shorter wavelengths. The oscillations of the absorption efficiency at the wavelength 2.264 μm (see **Figure 1**, dashed line) are noticeably less pronounced compared to the oscillations seen in the efficiency at 0.355 μm (see **Figure 1**, solid line). The uniform scaling transformation is applied in the radius domain and uses only a partial range of the efficiency precomputed at the shortest wavelength. As the wavelength increases, the oscillations with radius become smoother, corresponding to a stretching of the oscillations at a shorter wavelength (see **Figure 1**). Smoother functions of radius are easier to precisely integrate. Thus, it is easier to numerically compute precise values in **Eqs. 2–6** at a wavelength of 2.264 μm compared to 0.355 μm. With this feature in mind, we can expect that the performance of the SIR LUT in general will also improve as the wavelength λ increases, if we choose the shortest wavelength of interest to be the reference wavelength λ_r.

Figure 1 also helps to graphically illustrate **Eq. 21**. For example, **Eq. 21** demonstrates that integration of the absorption efficiency at a wavelength of 2.264 μm (see **Figure 1**, dashed line) in the radii range from 0.7 to 1.4 μm will result in the same value as integration at 0.355 μm (see **Figure 1**, solid line) in the range from ~ 0.11 to ~ 0.22 μm. Note the logarithmic scale of the vertical axis of **Figure 1** during the visual analysis.

Theoretical reasoning supported by numerical simulations justify choosing the shortest wavelength as the reference wavelength λ_r. To accommodate existing and anticipated future passive and active sensors, we choose $\lambda_r = 0.355\,\mu$m. **Equations 20** and **21** allow us to relate the Lorenz-Mie scattering calculations at this reference wavelength to longer wavelengths for any PSD. In **Section 4.4** we will benefit from using this key property.

4.2 Look-Up Table Parameters

The quadratures that define the precision of the SIR LUT, its speed and number of stored coefficients $\{C_p\}$ [see **Eq. 16**] are now discussed. It is clear that a reduction of stored information can have a negative effect on the precision of the SIR LUT. At the same time, it is inefficient to store redundant information that must be read and kept in RAM. The SIR LUT represents balance between the two conflicting criteria of precision and size.

4.2.1 Quadrature of Radii Grid Bins

Let us start with the quadrature of radii $\{r_j\}$ that was briefly mentioned in **Section 3**. Based on numerical simulations and earlier studies (Dubovik and King, 2000; Dubovik et al., 2002a; Dubovik et al., 2002b; Dubovik et al., 2006), we made a decision to use 650 logarithmically equidistant grid bins to cover a particle size range from $r_{\min} = 10^{-3}$ to $r_{\max} = 100 \mu m$: 10_1^{-3}, $1.018 \times 10_2^{-3}$, $1.036 \times 10_3^{-3}$, $1.055 \times 10_4^{-3}$, $\ldots$, 98.2_{649}, and $100_{650}\,\mu m$. Most of the values are displayed after rounding. The subscripts correspond to the index j in **Eq. 11**, and is provided for reference purposes.

As we discussed in **Section 4.1**, the computation of efficiencies $Q_p(.)$ [see **Eqs. 2–4**] is made using the size parameter. A single size parameter value corresponds to different particle radii and wavelength pairs. If the desired radius r at wavelength $\lambda \geq \lambda_r$ is known then the corresponding radius paired with λ_r in the SIR LUT will be [see also **Eq. 19**]:

$$r_{\lambda_r} = \frac{\lambda_r}{\lambda} r. \tag{23}$$

The exact range of sizes should be used if the optical properties at two different wavelengths are compared. Otherwise, the scattering particle systems are different. Thus, if the integration in **Eqs. 2–4** at an arbitrary wavelength λ is also carried out from 10^{-3} to $100\,\mu m$, then the computations at different wavelengths would require the SIR LUT to cover the different radii range:

- from 10^{-3} to $100\,\mu m$ at $\lambda = \lambda_r = 0.355\,\mu m$;
- from $\frac{0.355}{0.41} \times 10^{-3} \approx 8.7 \times 10^{-4}$ to $\sim 87\,\mu m$ at $\lambda = 0.41\,\mu m$;
- from $\sim 1.6 \times 10^{-4}$ to $\sim 16\,\mu m$ at $\lambda = 2.264\,\mu m$.

One can see that the minimum radius at all wavelengths $\lambda > \lambda_r$ falls below the radii range covered by LUT. In practice, for typical aerosol PSDs, this impact is expected to be small, and as the wavelength increases, the contribution of ultrafine aerosols is reduced. The SIR LUT supports integration over the following radii ranges at different wavelengths:

- from 10^{-3} to $100\,\mu m$ at $\lambda = \lambda_r = 0.355\,\mu m$;
- from $\frac{0.41}{0.355} \times 10^{-3} \approx 1.2 \times 10^{-3}$ to $\sim 120\,\mu m$ at $\lambda = 0.41\,\mu m$;
- from $\sim 6.4 \times 10^{-3}$ to $\sim 640\,\mu m$ at $\lambda = 2.264\,\mu m$.

Thus, increasing the wavelength of interest λ increases the minimum ($r_{\min,\lambda}$) and the maximum ($r_{\max,\lambda}$) radii, resulting in a larger range of covered radii. The increase in $r_{\min,\lambda}$ means that the SIR LUT ignores nanoparticles with radii below $10^{-3}\,\mu m$ at a wavelength of $0.355\,\mu m$ and below $\sim 6.4 \times 10^{-3}\,\mu m$ at $2.264\,\mu m$. As mentioned, the impact of this for aerosol PSDs is negligible. Scattering of light in this regime is best described by the Rayleigh scattering (Van de Hulst, 1981; Bohren and Huffman, 1983; Mishchenko et al., 2002).

The selected reference wavelength λ_r and radii range result in the SIR LUT that covers the range of size parameters x from ~ 0.018 to $\sim 1{,}770$.

4.2.2 Quadrature of Scattering Angles

Another decision that affects the number of stored coefficients $\{C_p\}$ [see **Eq. 16**] is the choice of a finite set of scattering angles Θ (angular quadrature). The SIR LUT includes 123 scattering angles Θ in the range between 0° and 180° (see **Table 1**). One may use an appropriate interpolation scheme to estimate the values of aerosol IOPs of interest for the other scattering angles too.

We would like to emphasize that the use of this angular quadrature helps to reduce the size of the SIR LUT and optimize its information content. The angular quadrature near scattering angles of 0° and 180° has 0.2° spacing because the elements of the normalized scattering matrix **P** [see **Eq. 1**] can rapidly change there (Hansen and Travis, 1974). The rate of change in **P** is relatively small between scattering angles of 10° and 170° that allows a coarser angular quadrature with 2° spacing.

The SK LUT uses an angular quadrature consisting of 181 scattering angles with an equidistant step of 1° (Dubovik and King, 2000; Dubovik et al., 2002a; Dubovik et al., 2006). This step is too coarse to precisely describe the angular change in the elements of matrix **P** [see **Eq. 1**] near scattering angles of 0° and 180° (Hansen and Travis, 1974).

Let us demonstrate the advantage of our angular quadrature with the help of numerical simulations. The asymmetry parameter [see **Eq. 6**] is a good candidate for a quantitative metric because its computation requires integration over the entire range of scattering angles Θ.

As example input parameters, we select the CRI $m = 1.3 - i \cdot 0.05$ and a lognormal PSD with $n_t = 1\,\text{cm}^{-3}$, $r_{\text{med}} = 1.5\,\mu m$ and $\sigma = 2$ [see **Eq. 17**]. These parameters are quite unrealistic for ambient aerosols in the visible spectrum (Dubovik et al., 2002b), but we would like to ensure that our "± 1 %" requirement is fulfilled across a wide range of scenarios. We selected this particular scenario because it is one of the most difficult cases that we managed to find.

We perform the integration in **Eq. 6** using Simpson's rule on an equidistant grid consisting of 10,001 scattering angles Θ. Out of these 10,001 angles total, the values of phase function are calculated precisely only at a subset of scattering angles, and the rest result from quadratic interpolation. For the tests, we use 101,181 (from 0° to 180° with the equidistant step of 1° as in (Dubovik and King, 2000; Dubovik et al., 2002a; Dubovik et al., 2006)), 201, . . ., and 2,001 scattering angles. The most precise calculation of the asymmetry parameter is therefore the one integrated using a grid of 2,001 scattering angles, and we use this as the reference value. In order to compute the values of the phase function $P_{11}(\Theta, m, \lambda)$ at a wavelength $\lambda = 0.355\,\mu m$, the Lorenz-Mie computations are made using the Bohren and Huffman code (Bohren and Huffman, 1983). The integration in **Eq. 2** is performed for the 2×10^7 logarithmically equidistant radii bins in the range from 10^{-3} to $100\,\mu m$ (see **Section 4.5** for more details).

Figure 2 and **Table 2** show the results of the simulations. One can see that the value of the asymmetry parameter computed using 101, 181, and 201 of scattering angles is different by more than 1% of the reference value. The " ± 1%" requirement is fulfilled for the cases of 401 or more scattering angles (see **Figure 2** and **Table 2**). The requirement is also fulfilled by the LUT (see horizontal dashed line at **Figure 2** and **Table 2**). With this we conclude that our quadrature of 123 scattering angles (see **Table 1**) performs about as well as an equidistant grid consisting of 2,001 scattering angles.

TABLE 1 | Scattering angles Θ included into the SIR LUT.

j_Θ	Θ	j_Θ	Θ	j_Θ	Θ	j_Θ	Θ	j_Θ	Θ	j_Θ	Θ	j_Θ	Θ
1	0°	19	7°	37	40°	55	76°	73	112°	91	148°	109	176°
2	0.2°	20	8°	38	42°	56	78°	74	114°	92	150°	110	176.5°
3	0.4°	21	9°	39	44°	57	80°	75	116°	93	152°	111	177°
4	0.6°	22	10°	40	46°	58	82°	76	118°	94	154°	112	177.5°
5	0.8°	23	12°	41	48°	59	84°	77	120°	95	156°	113	178°
6	1°	24	14°	42	50°	60	86°	78	122°	96	158°	114	178.2°
7	1.2°	25	16°	43	52°	61	88°	79	124°	97	160°	115	178.4°
8	1.4°	26	18°	44	54°	62	90°	80	126°	98	162°	116	178.6°
9	1.6°	27	20°	45	56°	63	92°	81	128°	99	164°	117	178.8°
10	1.8°	28	22°	46	58°	64	94°	82	130°	100	166°	118	179°
11	2°	29	24°	47	60°	65	96°	83	132°	101	168°	119	179.2°
12	2.5°	30	26°	48	62°	66	98°	84	134°	102	170°	120	179.4°
13	3°	31	28°	49	64°	67	100°	85	136°	103	171°	121	179.6°
14	3.5°	32	30°	50	66°	68	102°	86	138°	104	172°	122	179.8°
15	4°	33	32°	51	68°	69	104°	87	140°	105	173°	123	180°
16	4.5°	34	34°	52	70°	70	106°	88	142°	106	174°		
17	5°	35	36°	53	72°	71	108°	89	144°	107	175°		
18	6°	36	38°	54	74°	72	110°	90	146°	108	175.5°		

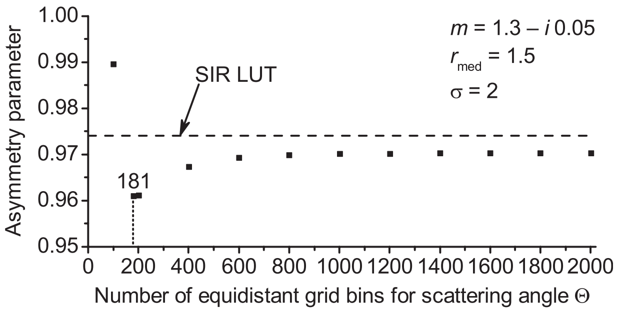

FIGURE 2 | Example asymmetry parameter computation. The vertical dotted line marks the result from the angular quadrature used in the SK LUT.

TABLE 2 | Computed values of the asymmetry parameter.

Number of Θ grid bins	$\langle \cos(m, \lambda) \rangle$	Relative difference (%)
101	0.989622	1.99
181	0.960103	−1.05
201	0.960131	−1.05
401	0.967307	−0.31
601	0.969269	−0.11
801	0.969861	−0.05
…	…	…
2,001. The reference value	0.970321	–
Computed from the SIR LUT	0.974039	0.38

4.2.3 Quadrature of Complex Refractive Indexes

The choice of the CRI quadrature is the last factor which must be chosen to balance the precision of the SIR LUT against the number of stored coefficients $\{C_p\}$ [see **Eq. 16**]. Based on our numerical simulations and earlier studies (Dubovik and King, 2000; Dubovik et al., 2002a; Dubovik et al., 2002b; Dubovik et al., 2006), we decided to use $31 \cdot 75 = 2{,}325$ CRIs:

- 31 real parts (m_{R}) of the CRI in the range between 1.29 and 1.65 with a step 0.012 (see **Table 3**);
- 75 imaginary parts (m_{I}) of the CRI: 0, and 74 logarithmically equidistant values between 10^{-5} and 5×10^{-2} (see **Table 4**, most of the values are shown rounded).

Sequential numbers for the real (j_{R} in **Table 3**) and imaginary (j_{I} in **Table 4**) parts are provided to help navigation inside the SIR LUT file (see **Section 4.3**).

4.3 Structure of Look-Up Table File

In **Section 3** we described the theoretical background of the SIR LUT and in **Section 4.2** provided a justification for the selection of quadratures that formed the actual LUT. Starting from this section, we switch our focus on the matters related to the practical application of the SIR LUT.

We computed the coefficients $\{C_p\}$ [see **Eq. 16**] at a reference wavelength λ_{r} and stored them in a file on the computer's hard drive. The SIR LUT file is binary and consists of a header (3,536 bytes, see **Table 5**) that is followed by $31 \cdot 75 = 2{,}325$ data records (1,284,408 bytes per record, see **Table 6**) for each CRI separately (see **Section 4.2.3**). The total size of the file is equal to $3{,}536 + 2{,}325 \cdot 1{,}284{,}408 = 2{,}986{,}252{,}136$ bytes. We intentionally limited the size of the SIR LUT file to 3 GB because the majority of modern blade servers have at least 4 GB of RAM per core. The SIR LUT file can then be uploaded into the memory of each core of the blade to further speed up the computations. In the future, we plan to refine the quadratures for the radii and CRIs when the progress in computational hardware will allow us to increase the size of LUT file.

The header contains information defining the reference wavelength and the quadratures for the radii, scattering angles, and CRIs (see **Table 5**).

Each data record of the SIR LUT contains the sets of values $\{C_p\}$ that were computed using **Eq. 16** at the reference wavelength $\lambda_{\text{r}} = 0.355\,\mu\text{m}$ (see **Table 6**). For the computations we used a reliable and accurate Lorenz-Mie scattering program (Mishchenko et al., 2002; Mishchenko, 2019). We slightly modified the program to make it

TABLE 3 | Real parts of the CRI covered by the SIR LUT.

j_R	m_R	j_R	m_R	j_R	m_R	j_R	m_R	j_R	m_R	j_R	m_R	j_R	m_R
1	1.29	6	1.35	11	1.41	16	1.47	21	1.53	26	1.59	31	1.65
2	1.302	7	1.362	12	1.422	17	1.482	22	1.542	27	1.602		
3	1.314	8	1.374	13	1.434	18	1.494	23	1.554	28	1.614		
4	1.326	9	1.386	14	1.446	19	1.506	24	1.566	29	1.626		
5	1.338	10	1.398	15	1.458	20	1.518	25	1.578	30	1.638		

TABLE 4 | Imaginary parts of the CRI covered by the SIR LUT.

j_I	m_I	j_I	m_I	j_I	m_I	j_I	m_I	j_I	m_I	j_I	m_I
1	0	14	4.1×10^{-5}	27	1.8×10^{-4}	40	8.4×10^{-4}	53	3.8×10^{-3}	66	1.7×10^{-2}
2	10^{-5}	15	4.6×10^{-5}	28	2.1×10^{-4}	41	9.5×10^{-4}	54	4.3×10^{-3}	67	2×10^{-2}
3	1.1×10^{-5}	16	5.1×10^{-5}	29	2.3×10^{-4}	42	1.1×10^{-3}	55	4.8×10^{-3}	68	2.2×10^{-2}
4	1.3×10^{-5}	17	5.8×10^{-5}	30	2.6×10^{-4}	43	1.2×10^{-3}	56	5.4×10^{-3}	69	2.5×10^{-2}
5	1.4×10^{-5}	18	6.5×10^{-5}	31	2.9×10^{-4}	44	1.3×10^{-3}	57	6.1×10^{-3}	70	2.8×10^{-2}
6	1.6×10^{-5}	19	7.3×10^{-5}	32	3.3×10^{-4}	45	1.5×10^{-3}	58	6.9×10^{-3}	71	3.1×10^{-2}
7	1.8×10^{-5}	20	8.2×10^{-5}	33	3.7×10^{-4}	46	1.7×10^{-3}	59	7.7×10^{-3}	72	3.5×10^{-2}
8	2×10^{-5}	21	9.2×10^{-5}	34	4.2×10^{-4}	47	1.9×10^{-3}	60	8.7×10^{-3}	73	4×10^{-2}
9	2.3×10^{-5}	22	10^{-4}	35	4.7×10^{-4}	48	2.1×10^{-3}	61	9.8×10^{-3}	74	4.4×10^{-2}
10	2.5×10^{-5}	23	1.2×10^{-4}	36	5.3×10^{-4}	49	2.4×10^{-3}	62	1.1×10^{-2}	75	5×10^{-2}
11	2.9×10^{-5}	24	1.3×10^{-4}	37	5.9×10^{-4}	50	2.7×10^{-3}	63	1.2×10^{-2}		
12	3.2×10^{-5}	25	1.5×10^{-4}	38	6.7×10^{-4}	51	3×10^{-3}	64	1.4×10^{-2}		
13	3.6×10^{-5}	26	1.6×10^{-4}	39	7.5×10^{-4}	52	3.4×10^{-3}	65	1.6×10^{-2}		

TABLE 5 | Structure of the SIR LUT header.

Description	Type	Size (bytes)	Content
Reference wavelength (μm)	Float	4	0.355
Number of radii grid bins	Int	4	650
$\{r_j\}$ set of radii bins (μm)	650*float	2,600	See **Section 4.2.1**
Number of scattering angles	Int	4	123
Angular quadrature $\{\Theta\}$	123*float	492	See **Section 4.2.2**
Number of real parts	Int	4	31
$\{m_R\}$ set of real parts	31*float	124	See **Section 4.2.3**
Number of imaginary parts	Int	4	75
$\{m_I\}$ set of imaginary parts	75*float	300	See **Section 4.2.3**
Total		3,536	

TABLE 6 | Structure of the SIR LUT data record.

Description	Type	Size (bytes)	Content
Real part of CRI (m_R)	Float	4	See **Section 4.2.3**
Imaginary part of CRI (m_I)	Float	4	See **Section 4.2.3**
$\{C_\alpha\}$ set	650*float	2,600	See **Eqs. 4**, **16**
$\{C_{sca}\}$ set	650*float	2,600	See **Eqs. 4**, **16**
$\{C_{11}\}$ set	650*123*float	319,800	See **Eqs. 2**, **16**
$\{C_{12}\}$ set	650*123*float	319,800	See **Eqs. 2**, **16**
$\{C_{33}\}$ set	650*123*float	319,800	See **Eqs. 2**, **16**
$\{C_{34}\}$ set	650*123*float	319,800	See **Eqs. 2**, **16**
Total		1,284,408	

suitable for parallel computation of the coefficients C_{p,j,λ_r} [see **Eq. 16**], but the core part of the program remained intact. We used 100,000 points over each integration range of radii $[r_j, r_{j+1}]$ by setting the program input parameters N = 1,000 (number of subintervals within $[r_j, r_{j+1}]$) and NK = 100 (number of Gaussian division points) (Mishchenko et al., 2002; Mishchenko, 2019). All the SIR LUT related computations were performed on blade servers equipped with Intel Xeon "Skylake" processors on the NASA LaRC K-Cluster.

The $\{C_{11}\}$, $\{C_{12}\}$, $\{C_{33}\}$, and $\{C_{34}\}$ sets in **Table 6** are two dimensional arrays that are stored line by line, i.e., 650 lines (corresponding to the radii quadrature, see **Section 4.2.1**) with 123 columns each (corresponding to the scattering angles quadrature, see **Section 4.2.2**).

The beginning position in the SIR LUT file for the data record that corresponds to a certain CRI can be computed using the sequential numbers of the real and imaginary parts (see **Section 4.2.3**) as $3{,}536 + 1{,}284{,}408 \cdot (75 \cdot (j_R - 1) + j_I - 1)$ bytes. For instance, if one needs the data record that corresponds to the CRI with real part $m_R = 1.362$ ($j_R = 7$) and imaginary part $m_I = 2.6 \times 10^{-4}$ ($j_I = 30$) then the pointer inside of the SIR LUT file should be set at the position of 615,234,968 bytes from the beginning of file.

We also share with the community codes written in C++, Fortran, Python and Matlab that can be used to efficiently compute all aerosol IOPs of interest [see **Eqs. 2–6**] from the SIR LUT.

4.4 Usage of Look-Up Table

To make the practical use of the SIR LUT, it is necessary to develop a way of computing the coefficients $C_{p,j,\lambda}$ at longer wavelengths λ using coefficients C_{p,j,λ_r} precomputed at the reference wavelength λ_r. At this point, we have already decided on reference wavelength and quadratures that define the structure of the SIR LUT and highlighted the useful properties of efficiencies by applying the scale invariance rule (Mishchenko, 2006). We return to theoretical derivations one last time to complete the final assembly by collecting these fragments into a working mechanism.

As discussed in **Section 4.1**, since it is the size parameter that drives the single-scattering computations, the integration of efficiencies at longer wavelengths can be directly expressed through the integration of efficiencies calculated at a shorter wavelength. **Equation 21** allows us to apply a linear scaling of the quadratic approximation range [see **Eq. 12**] from $[r_{j-1}, r_{j+1}]$ to $\left[\frac{\lambda_{\mathrm{r}}}{\lambda} r_{j-1}, \frac{\lambda_{\mathrm{r}}}{\lambda} r_{j+1}\right]$ in order to switch in **Eq. 16** from an arbitrary wavelength $\lambda \geq \lambda_{\mathrm{r}}$ to the reference wavelength λ_{r}. After repeating the PSD quadratic approximation procedure [see **Eqs. 12–16**], the coefficient $C_{p,j,\lambda}$ in **Eq. 16** can be computed as

$$
\begin{aligned}
\frac{\lambda_{\mathrm{r}}}{\lambda} \Bigg[& \frac{3 \ln \frac{\lambda_{\mathrm{r}}}{\lambda} r_{j-2} \ln \frac{\lambda_{\mathrm{r}}}{\lambda} r_{j-1}}{8 (\Delta \ln r)^2} \int_{\frac{\lambda_{\mathrm{r}}}{\lambda} r_{j-1}}^{\frac{\lambda_{\mathrm{r}}}{\lambda} r_j} \frac{Q_p(\cdot, r, \lambda_{\mathrm{r}})}{r} \mathrm{d} \ln r \\
& - \frac{3 \ln \frac{\lambda_{\mathrm{r}}^2}{\lambda^2} r_{j-2} r_{j-1}}{8 (\Delta \ln r)^2} \int_{\frac{\lambda_{\mathrm{r}}}{\lambda} r_{j-1}}^{\frac{\lambda_{\mathrm{r}}}{\lambda} r_j} \ln r \frac{Q_p(\cdot, r, \lambda_{\mathrm{r}})}{r} \mathrm{d} \ln r \\
& + \frac{3}{8 (\Delta \ln r)^2} \int_{\frac{\lambda_{\mathrm{r}}}{\lambda} r_{j-1}}^{\frac{\lambda_{\mathrm{r}}}{\lambda} r_j} \ln^2 r \frac{Q_p(\cdot, r, \lambda_{\mathrm{r}})}{r} \mathrm{d} \ln r \\
& - \frac{3 \ln \frac{\lambda_{\mathrm{r}}}{\lambda} r_{j-1} \ln \frac{\lambda_{\mathrm{r}}}{\lambda} r_{j+1}}{4 (\Delta \ln r)^2} \int_{\frac{\lambda_{\mathrm{r}}}{\lambda} r_j}^{\frac{\lambda_{\mathrm{r}}}{\lambda} r_{j+1}} \frac{Q_p(\cdot, r, \lambda_{\mathrm{r}})}{r} \mathrm{d} \ln r \\
& + \frac{3 \ln \frac{\lambda_{\mathrm{r}}^2}{\lambda^2} r_{j-1} r_{j+1}}{4 (\Delta \ln r)^2} \int_{\frac{\lambda_{\mathrm{r}}}{\lambda} r_j}^{\frac{\lambda_{\mathrm{r}}}{\lambda} r_{j+1}} \ln r \frac{Q_p(\cdot, r, \lambda_{\mathrm{r}})}{r} \mathrm{d} \ln r \\
& - \frac{3}{4 (\Delta \ln r)^2} \int_{\frac{\lambda_{\mathrm{r}}}{\lambda} r_j}^{\frac{\lambda_{\mathrm{r}}}{\lambda} r_{j+1}} \ln^2 r \frac{Q_p(\cdot, r, \lambda_{\mathrm{r}})}{r} \mathrm{d} \ln r \\
& + \frac{3 \ln \frac{\lambda_{\mathrm{r}}}{\lambda} r_{j+1} \ln \frac{\lambda_{\mathrm{r}}}{\lambda} r_{j+2}}{8 (\Delta \ln r)^2} \int_{\frac{\lambda_{\mathrm{r}}}{\lambda} r_{j+1}}^{\frac{\lambda_{\mathrm{r}}}{\lambda} r_{j+2}} \frac{Q_p(\cdot, r, \lambda_{\mathrm{r}})}{r} \mathrm{d} \ln r \\
& - \frac{3 \ln \frac{\lambda_{\mathrm{r}}^2}{\lambda^2} r_{j+1} r_{j+2}}{8 (\Delta \ln r)^2} \int_{\frac{\lambda_{\mathrm{r}}}{\lambda} r_{j+1}}^{\frac{\lambda_{\mathrm{r}}}{\lambda} r_{j+2}} \ln r \frac{Q_p(\cdot, r, \lambda_{\mathrm{r}})}{r} \mathrm{d} \ln r \\
& + \frac{3}{8 (\Delta \ln r)^2} \int_{\frac{\lambda_{\mathrm{r}}}{\lambda} r_{j+1}}^{\frac{\lambda_{\mathrm{r}}}{\lambda} r_{j+2}} \ln^2 r \frac{Q_p(\cdot, r, \lambda_{\mathrm{r}})}{r} \mathrm{d} \ln r \Bigg] \cdot
\end{aligned}
\tag{24}
$$

The common multiplier $\frac{\lambda_{\mathrm{r}}}{\lambda}$ in front of the bracket appears in **Eq. 24** to compensate the division by radius r during each integration. If desired, one can verify the equivalence of **Eqs. 16** and **24** numerically or prove it analytically using **Eq. 22**.

In practice, it is necessary to use an interpolation technique to estimate the coefficient $C_{p,j,\lambda}$ because in the general case the scaled radius $\frac{\lambda_{\mathrm{r}}}{\lambda} r_j$ does not coincide with any of the SIR LUT radius quadrature points $\{r_j\}$ (see Sections 3 and 4.2.1). As an option, quadratic interpolation may be used with the known LUT values of coefficient at radius quadrature points r_{k-1}, r_k, and r_{k+1}:

$$
\begin{aligned}
C_{p,j,\lambda} \approx \frac{\lambda_{\mathrm{r}}}{\lambda} \Bigg[& C_{p,k-1,\lambda_{\mathrm{r}}} \frac{\left(\frac{\lambda_{\mathrm{r}}}{\lambda} r_j - r_k\right)\left(\frac{\lambda_{\mathrm{r}}}{\lambda} r_j - r_{k+1}\right)}{(r_{k-1} - r_k)(r_{k-1} - r_{k+1})} \\
& + C_{p,k,\lambda_{\mathrm{r}}} \frac{\left(\frac{\lambda_{\mathrm{r}}}{\lambda} r_j - r_{k-1}\right)\left(\frac{\lambda_{\mathrm{r}}}{\lambda} r_j - r_{k+1}\right)}{(r_k - r_{k-1})(r_k - r_{k+1})} \\
& + C_{p,k+1,\lambda_{\mathrm{r}}} \frac{\left(\frac{\lambda_{\mathrm{r}}}{\lambda} r_j - r_{k-1}\right)\left(\frac{\lambda_{\mathrm{r}}}{\lambda} r_j - r_k\right)}{(r_{k+1} - r_{k-1})(r_{k+1} - r_k)} \Bigg],
\end{aligned}
\tag{25}
$$

where the index k is generally selected to fulfill $r_k \leq \frac{\lambda_{\mathrm{r}}}{\lambda} r_j \leq r_{k+1}$ when the quadrature point r_{k-1} is available for the case $\lambda \geq \lambda_{\mathrm{r}}$ and the quadrature point r_{k+1} can go up to $r_{\max} = 100 \mu\mathrm{m}$. If the index k is found to be equal to unity then the coefficient $C_{p,j,\lambda}$ is computed using **Eq. 25** at the radius quadrature points r_1, r_2, and r_3. If the scaled radius $\frac{\lambda_{\mathrm{r}}}{\lambda} r_j$ is too small and not covered by the SIR LUT at all (see discussion related to the increase of $r_{\min,\lambda}$ in **Section 4.2.1**) then the coefficient $C_{p,j,\lambda}$ vanishes. As the wavelength of interest λ increases, the contribution from the smallest particles is lost with the relatively minor impact.

Different interpolation techniques, instead of quadratic as in **Eq. 25**, also may be applied. One should keep in mind that quadratic interpolation provides reasonable results and requires only nine multiplications and three divisions that can be done quite fast considering that 650 interpolations are needed for each aerosol IOP p [see **Eq. 11**].

Equation 25 offers a simple way to compute the coefficients $C_{p,j,\lambda}$ at longer wavelengths using the precomputed and stored coefficients $C_{p,j,\lambda_{\mathrm{r}}}$. One may skip all the mathematical theory behind **Eq. 25** as it might look complicated. In the end, the elegance of this LUT approach allows us to exchange the integration in **Eqs. 2–4** at longer wavelengths with an integration at a shorter reference wavelength over a range of smaller radii.

4.5 Validation of the Scale Invariance Rule Look-Up Table: Unit Tests

To demonstrate the improved capabilities of the SIR LUT, we will compute the aerosol IOPs of interest [see **Eqs. 2–6**] using the SIR LUT [see **Eqs. 11**, **25**] and compare them to simulated truth values (see **Section 4.5.1**).

At the beginning we set a $\pm 1\%$ relative difference for all single-scattering properties [see **Eqs. 2–6**] as the precision target. The $\pm 1\%$ precision shall be achieved at all the wavelengths of interest, i.e., at $\{\lambda\} = \{0.355, 0.41, 0.469, 0.532, 0.555, 0.67, 0.864, 0.96, 1.064, 1.594, 1.88, 2.264\}\, \mu\mathrm{m}$ (see **Section 1**). In **Section 4.1** we anticipated that the targeted precision would be most difficult to achieve at the shortest wavelength, i.e. at $\lambda = 0.355\, \mu\mathrm{m}$, despite the fact that it is the reference wavelength.

We compute the relative difference for the aerosol IOPs $p = \{\beta(m, \lambda), \mathrm{sca}(m, \lambda), \alpha(m, \lambda), \mathrm{abs}(m, \lambda), \langle\cos(m, \lambda)\rangle\}$ [see **Eqs. 3–6**] as

$$\delta_p = \frac{p - p_t}{p_t} \cdot 100\%, \tag{26}$$

where p_t is the simulated truth value for the aerosol IOP p.

For the elements of the normalized scattering matrix **P** [**see Eq. 2**] the relative difference is computed slightly differently:

$$\delta_{P_{ii'}}(\Theta) = \frac{P_{ii'}(\Theta) - P_{ii',t}(\Theta)}{\max\limits_{\Theta}\left|P_{ii',t}(\Theta)\right|} \cdot 100\%, \tag{27}$$

where $P_{ii',t}(\Theta)$ is the simulated truth of the normalized scattering matrix element $P_{ii'}(\Theta)$. We compare the difference between the SIR LUT and the simulated truth values with the maximum absolute simulated truth value because at some scattering angles Θ the value of $P_{ii',t}(\Theta)$ element may be close to zero or vanish for natural reasons. It is important to reproduce the shape of $P_{ii',t}(\Theta)$ functions around their peaks, which for aerosols mainly occur at scattering angles Θ close to 0° and 180° (see **Section 4.2.2**). By contrast, a 1% disagreement when the absolute value of the element is small tends to be more acceptable for our purposes of modeling lidar and polarimeter observables.

4.5.1 Simulated Truth

It is now time to clarify the aerosol IOPs $\{p_t, P_{ii',t}(\Theta)\}$ that we consider to be the simulated truth for comparisons in the unit tests. To compute the true IOPs $\{p_t, P_{ii',t}(\Theta)\}$, we have to decide which CRIs, PSDs, and scattering angles Θ, as well as the integration range $[r_{\min}, r_{\max}]$ and integration settings to use in **Eqs. 2–6**.

During retrievals of aerosol microphysical properties using real lidar and polarimeter data, the values of the CRIs will not necessarily coincide with the CRI quadrature of the SIR LUT (see **Section 4.2.3**). A two-dimensional interpolation scheme is used to obtain the off-CRI-grid values of aerosol IOPs $\{p, P_{ii'}(\Theta)\}$ using several values of the same IOP estimated using the LUT at CRI grid points. We recommend the use of quadratic interpolation [see **Eq. 25**] in two dimensions since we found it to be fast and reliable.

In the unit tests we shall focus on the off-grid CRIs that are covered but not directly included into the SIR LUT (see **Section 4.2.3**) and that are realistic from the perspective of ambient aerosols (Dubovik et al., 2002b). Keeping this in mind, we selected to use the set consisting of $18 \cdot 101 = 1{,}818$ CRIs: 18 real parts (m_R) of the CRI in the range between 1.31 and 1.65 with a step of 0.02, and 101 imaginary parts (m_I) of the CRI consisting of 0, and 100 equidistant values between 2.5×10^{-4} and 0.04975 with a step of 5×10^{-4}. Among these 1,818 CRIs there are six that form a subset $\{\mathrm{m}\} = \{1.35, 1.41, 1.47, 1.53, 1.59, 1.65\}$ that intersects with the CRI quadrature of the SIR LUT (see **Section 4.2.3**). It is reasonable to expect high precision of the SIR LUT at CRIs $\in \{\mathrm{m}\}$. We will use this property of the $\{\mathrm{m}\}$ subset as an additional benchmark test to help evaluate the quality of our unit tests.

Let us use a monomodal lognormal distribution (see **Section 3.1**) as the function $n(r)$ in **Eqs. 2–6** to simulate an ambient aerosol PSD (Kolmogorov, 1941; Seinfeld and Pandis, 2006). The count median radius r_{med} [see **Eq. 18**] in our unit tests will vary from 0.075 to 1.501 μm with a constant step of 0.002 μm (for a total of 714 values). Twelve geometric standard deviations σ [see **Eq. 18**] in the range from 1.35 to 2.01 with a constant step of 0.06 will accompany each median radius. It is enough to consider a single total number concentration $n_t = 1\,\mathrm{cm}^{-3}$ [see **Eq. 18**] to evaluate relative differences in the single-scattering properties. These $714 \cdot 12 = 8{,}568$ PSDs cover a wide range of aerosol size distributions (Dubovik et al., 2002b).

Thus, the total number of CRI–PSD unit tests is equal to $1{,}818 \cdot 8{,}568 = 15{,}576{,}624$ at each wavelength of interest $\{\lambda\}$.

Recall from **Section 4.2.2**, the SIR LUT uses a quadrature of 123 scattering angles that precisely represents the aerosol asymmetry parameter as well as equidistant quadratures with many more angles. Therefore, we use this scattering angle quadrature in our unit test dataset as well. Let us compute the simulated truth elements $P_{ii',t}(\Theta)$ of normalized scattering matrices [see **Eq. 1**] for the same angular quadrature.

Putting it all together, we track $5 + 4 \cdot 123 = 497$ relative differences [see **Eqs. 26**, **27**] of aerosol IOPs [see **Eqs. 2–6**] with a ± 1% precision target.

For all wavelengths of interest let us compute the simulated truth $\{p_t, P_{ii',t}(\Theta)\}$ by integrating over the radius range $[r_{\min} = 0.001\,\mu\mathrm{m}, r_{\max} = 100\,\mu\mathrm{m}]$ that the SIR LUT uses at a wavelength of 0.355 μm (see **Section 4.2.1**). This radius integration range covers the majority of ambient fine and coarse mode aerosol PSDs (Dubovik et al., 2002b). With nanoparticles included into integration at all wavelengths, we can evaluate the losses of information about nanoparticles by the SIR LUT with the increase of wavelength (see discussion related to the increase of $r_{\min,\lambda}$ in **Section 4.2.1**).

The only remaining decision is how many radius quadrature points are used if Simpson's rule is applied to the numerical integration in **Eqs. 2–6**. The absorption coefficient at $\lambda = 0.355\,\mu\mathrm{m}$ is an IOP that can help us make this decision. In **Section 4.2.1** we selected the CRI $m = 1.65 - i \cdot 10^{-5}$ as an example where the absorption efficiency oscillates with an amplitude exceeding two orders of magnitude (see **Figure 1**, solid curve). Such highly oscillatory functions require a very narrow integration step to produce a precise result. For such cases, if we increase the number of logarithmically equidistant radii bins by factor of ten, we expect the computed absorption coefficient to converge and the relative difference to decrease and approach zero. We set the parameters of the aerosol PSD to $n_t = 1\,\mathrm{cm}^{-3}$, $r_{\mathrm{med}} = 0.7\,\mu\mathrm{m}$ and $\sigma = 1.35$ [see **Eq. 18**].

To compute the simulated truth values, the Lorenz-Mie single-scattering calculations were performed using the well-established Bohren and Huffman program (Bohren and Huffman, 1983). As a reminder, the SIR LUT coefficients (see **Section 4.3**) were computed using the Mishchenko et al. program (Mishchenko et al., 2002; Mishchenko, 2019). By cross-checking the two Lorenz-Mie programs we achieved a high level of confidence in the unit tests.

4.5.2 Results of the Unit Tests

Table 7 lists the results of the numerical integration. As the number of radius quadrature points increases, the value of the absorption coefficient converges, as expected. After the number of points reaches 10^5, the ± 1% precision level is achieved, but even more points are needed to converge to the value that would be considered the simulated truth. The relative difference between the 10^7 and 2×10^7 radius quadrature points is close to numerical zero, which is the best we can expect in terms of convergence.

The absolute value of the absorption coefficient in this test is small because the imaginary part of CRI is very close to zero. We intentionally selected this almost non-absorbing aerosol because during the SIR LUT development stage we experienced the most difficulties in achieving ± 1% precision for the low absorbing particles.

Based on **Table 7**, we made a decision to compute all the simulated truth aerosol IOPs $\{p_t, P_{ii',t}(\Theta)\}$ [see **Eqs. 2–6**] by applying Simpson's rule using 2×10^7 logarithmically equidistant radius quadrature points in the range from 10^{-3} to 100 μm. We may have to use even more quadrature points if, in the future, the SIR LUT is extended to have more imaginary parts of the CRI between 0 and 10^{-5}. One can see that solid curve in **Figure 1** has multiple spikes at least two orders of magnitude from the basic trend. For imaginary parts below 10^{-5} we expect to see efficiencies that are even more oscillatory compared to the solid curve of **Figure 1**.

Moving further, we computed the simulated truth values for all the aerosol IOPs [see **Eqs. 2–6**] at twelve wavelengths $\{\lambda\}$ and compared them [see **Eqs. 26, 27**] to the corresponding LUT values [see **Eqs. 11**, **25**]. The targeted ± 1% precision level was achieved in all cases except for the $P_{12}(\Theta)$ element of the normalized scattering matrix, which turned out to be the most difficult aerosol IOP to tabulate. All the other aerosol IOPs were computed using the SIR LUT within the targeted precision.

Figures 3, **4** and **Table 8** show the details of the CRI–PSD unit tests at two minimum wavelengths of interest that lead to a relative error [see **Eq. 27**] larger than ± 1% for the element $P_{12}(\Theta)$. Panels **(A)** and **(B)** of **Figures 3**, **4** detail the locations of the problematic PSDs in terms of median radius and geometric standard deviation **(A)**, and effective radius and effective variance **(B)**. Panel **(C)** of **Figures 3**, **4** depicts the locations of problematic CRIs, and panel **(D)** provides the histograms of relative differences for only the unit tests that failed to reach the 1% precision.

One can see that the problematic PSDs describe coarse mode aerosols with an effective radius exceeding 3.5 μm and an effective variance exceeding 0.45 (see panel **(B)** of **Figures 3**, **4**). These effective radii and variances correspond to large aerosols with sizes that are sparsely covered by our logarithmically equidistant distributed set $\{r_j\}$ of radius quadrature points (see Sections 3 and 4.2.1). All the problematic CRIs have an imaginary part around zero (see panel **(C)** of **Figures 3**, **4**). We thus expect that the $Q_{12}(\Theta, m, \lambda = 0.355\mu m, r)$ directional scattering efficiency for small imaginary parts oscillates even more vigorously than the absorption efficiency (see solid curve of **Figure 1**). If we find it necessary to improve the precision of $P_{12}(\Theta)$, in the next version of the SIR LUT we will need to have more radius quadrature points M (see **Section 4.2.1**), denser coverage of imaginary parts of CRI around zero (see **Section 4.2.3**), and possibly use additional integration points to compute the values of simulated truth and the SIR LUT coefficients [see **Eq. 16**]. The current version of the SIR LUT allows us to estimate the $P_{12}(\Theta)$ element of the normalized scattering matrix to within ± 2.5% (see panel **(D)** of **Figures 3**, **4** and **Table 8**).

TABLE 7 | Computed values of the aerosol absorption coefficient.

Number of radius quadrature points	Abs (Mm^{-1})	Relative difference (%)
10^3	0.00175102	−5.135
10^4	0.00208741	13.388
10^5	0.00184286	0.104
10^6	0.00184106	0.007
10^7	0.00184094	~0
$2{\times}10^7$. The simulated truth value	0.00184094	–
Computed from the SIR LUT	0.00183823	−0.147

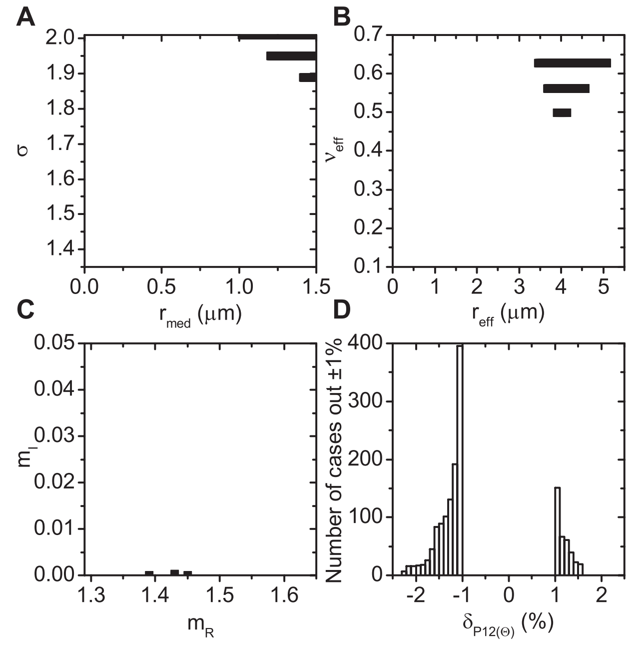

FIGURE 3 | Outliers in $P_{12}(\Theta)$ computations from the SIR LUT at λ = 0.355 μm. Description of labels is given in text.

Let us point out that panel **(C)** of **Figures 3**, **4** is missing the points corresponding to the subset $\{m\}$ mentioned earlier. Interestingly, the CRI point $(1.41, 0) \in \{m\}$ is absent from panel **(C)** but two of its closest neighbors $(1.39, 0) \notin \{m\}$ and $(1.43, 0) \notin \{m\}$ are marked as the problematic CRIs. Intuition suggests that the CRI point between those two also has a potential to be problematic. We expect to have the highest precision of the SIR LUT at the points of the CRI quadrature and one of them is the point $(1.41, 0) \in \{m\}$, which explains its absence from panel **(C)**. We consider this feature to be an additional indicator of proper behavior by the SIR LUT.

Panel **(D)** of **Figures 3**, **4** show the histograms of $P_{12}(\Theta)$ relative differences [see **Eq. 27**] for the problematic CRI–PSD unit tests out

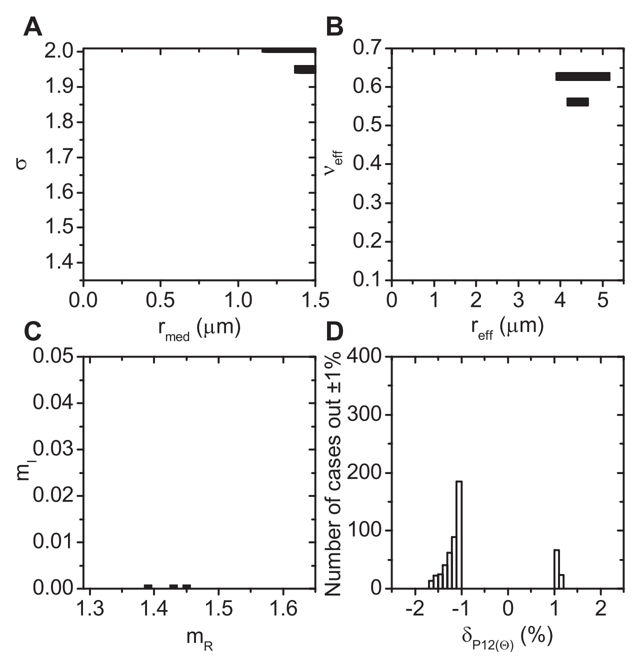

FIGURE 4 | Outliers in $P_{12}(\Theta)$ computations from the SIR LUT at λ = 0.41 μm. Description of labels is given in text.

of 15,576,624 total tests spanning the entire scattering angle quadrature consisting of 123 angles (see **Section 4.2.2**). The ± 1% precision target was not achieved 1,494 times at a wavelength of 0.355 μm (7.8×10^{-5}%; see **Figure 3D** and **Table 8**) and 529 times at 0.41 μm (2.8×10^{-5}%; see **Figure 4D** and **Table 8**). In **Section 4.1** we anticipated improvement in the SIR LUT precision as the wavelength increases and **Figures 3**, **4** together with **Table 8** confirm this behavior. The trend of a reduction in the number of problematic cases continues as the wavelength increases and the number drops to zero at 0.532 μm.

To increase confidence in the precision of the SIR LUT, we conducted an additional test using 1,000,000 random λ–CRI–PSD unit tests. A uniform random number generator provided evenly distributed values of wavelength λ in the range from 0.355 to 2.264 μm, count median radius r_{med} from 0.075 to 1.5 μm, geometric standard deviation σ from 1.35 to 2.01, real part of the CRI m_{R} from 1.31 to 1.65, and imaginary part of the CRI m_{I} from 0 to 0.05. Using these random inputs, we computed the simulated truth values for all the aerosol IOPs [see **Eqs. 2–6**] and compared them to the corresponding SIR LUT values [see **Eqs. 11, 25**]. The ± 1% precision was not achieved in eleven cases for the aerosol absorption coefficient and once for the $P_{12}(\Theta)$ element of the normalized scattering matrix. All these cases have an imaginary part of the CRI between 0 and 10^{-5}. Qualitatively, the assessment is very similar to what is shown in **Figures 3**, **4**.

With the presented results of numerical simulations, we conclude that the performance of the SIR LUT for all the aerosol IOPs of interest is precise to within ± 1% except for a few cases where $P_{12}(\Theta)$ is within ± 2.5%. The impact of the precision of $P_{12}(\Theta)$ on polarimeter observables will be explored in **Section 4.7**.

4.6 Validation of the Spherical Kernels Look-Up Table: Unit Tests

An important topic to consider is the precision of the SK LUT that is currently in use and served as the inspiration for the SIR LUT (Dubovik and King, 2000; Dubovik et al., 2002a; Dubovik et al., 2006). It is first necessary to understand what improvements, if any, are achieved using quadratic approximation of the aerosol PSD [see **Eq. 12**] and by the cost of increasing the number of stored coefficients (see Sections 4.2–4.3). We will also provide more details on the aerosol lidar backscatter and extinction coefficients. For the other aerosol IOPs we provide histograms with relative differences. It is sufficient to explore only the 0.355 and 0.532 μm wavelengths to study if the precision of the SK LUT also improves as the wavelength increases. For brevity, we skip the wavelength of 1.064 μm that is also used by the HSRL-2 instrument. The relative difference comparisons are made using the same simulated truth values for the 15,576,624 unit tests that are described in **Section 4.5**.

Figures 5–10 and **Table 9** show the results of comparisons. Each dot in the panels **(A–C)** of **Figures 5–8** indicates that ± 1% relative difference was not achieved for at least one HSRL-2 UV–VIS observable for a given CRI or PSD. The histograms in panel **(D)** of **Figures 5–8** and all panels of **Figures 9**, **10** plot the distribution of relative differences [see **Eqs. 26, 27**] that are greater than ± 1%.

TABLE 8 | Overview of the SIR LUT performance.

IOP			**$\lambda = 0.355\,\mu$m**				**$\lambda = 0.41\,\mu$m**	
	Min	**Max**	**Accuracy**	**Outliers**	**Min**	**Max**	**Accuracy**	**Outliers**
	(%)	**(%)**	**(%)**	**Number**	**(%)**	**(%)**	**(%)**	**Number**
β	−0.63	0.81	-5×10^{-2}	0	−0.58	0.62	-5×10^{-2}	0
sca	-10^{-2}	5×10^{-3}	-3×10^{-3}	0	-10^{-2}	5×10^{-3}	-3×10^{-3}	0
α	-4×10^{-3}	5×10^{-3}	5×10^{-5}	0	-4×10^{-3}	5×10^{-3}	-7×10^{-5}	0
abs	-5×10^{-2}	10^{-2}	5×10^{-3}	0	-4×10^{-2}	10^{-2}	5×10^{-3}	0
⟨cos⟩	-2×10^{-3}	4×10^{-3}	10^{-3}	0	-2×10^{-3}	4×10^{-3}	10^{-3}	0
P_{11}	-8×10^{-3}	10^{-2}	-2×10^{-4}	0	-8×10^{-3}	10^{-2}	3×10^{-4}	0
P_{12}	−2.24	1.59	3×10^{-4}	1,494	−1.66	1.17	3×10^{-4}	529
P_{33}	-8×10^{-3}	10^{-2}	3×10^{-4}	0	-8×10^{-3}	10^{-2}	3×10^{-4}	0
P_{34}	−0.15	0.09	3×10^{-4}	0	−0.12	0.07	4×10^{-4}	0

In this test of the SK LUT, we found that the backscatter coefficient at 0.355 μm had the worst accuracy and precision (see **Figure 5** and **Table 9**). The ± 1% relative difference was not achieved 13,473,394 times at a wavelength of 0.355 μm (86.5%) and 12,094,591 times at 0.532 μm (77.65%). The relative differences of HSRL-2 UV–VIS observables are within ± 35% at 0.355 μm (see **Figure 5D** and **Table 9**) and ± 31% at 0.532 μm (see **Figure 7D** and **Table 9**). The relative difference also improves as the wavelength increases as we anticipated in **Section 4.1** for this type of LUT, and which we have already seen for the SIR LUT in **Section 4.5**. The improvement is relatively minor and every CRI and PSD was found to result in a computed lidar backscatter coefficient with a relative difference of greater than ± 1% at least once (see panels **(A–C)** of **Figures 5**, **7**).

All four relative difference histograms (see panel **(D)** of **Figures 5–8**) of the HSRL-2 UV–VIS observables are asymmetric, and indicate a tendency of the SK LUT to overestimate the HSRL-2 observables. It is unexpected to see an overestimation here, because of the significant difference in the integration range for radius. We computed the simulated truth values with the integration range up to $r_{\max} = 100\,\mu$m [see **Eqs. 3**, **4**]. By contrast, the SK LUT stops at ~ 33.9 μm in terms of particle radius (Dubovik and King, 2000; Dubovik et al., 2002a; Dubovik et al., 2006). The information between ~ 33.9 and 100 μm is lost, and that naturally should lead to underestimations. The reason for systematic overestimates is unknown but will be investigated separately.

Compared to the lidar backscatter coefficient, the accuracy and precision of the extinction coefficient are noticeably better (see **Figures 6**, **8** and **Table 9**). The ± 1% relative difference was not achieved 1,330,281 times at a wavelength of 0.355 μm (8.54%) and 2,029,788 times at 0.532 μm (13.03%). The relative differences are within ± 3% at both 0.355 (see **Figure 6D** and **Table 9**) and 0.532 μm (see **Figure 8D** and **Table 9**). It is unexpected to see that the SK LUT precision for the extinction coefficient degrades with the increase of wavelength, but the interesting feature is that degradation appears to be approximately proportional to the scaling factor $\frac{0.532}{0.355} \approx 1.5$. The same scaling factor of ~ 1.5 can be noticed in terms of the effective radius too. The estimations with SK LUT show precision issues for PSDs with effective radius up to 1.2 μm at wavelength 0.355 μm and up to 1.8 μm at 0.532 μm (see panel **(B)** of **Figures 6**, **8**). Most probably, this decrease in precision happens because of features specific to the extinction efficiencies that are amplified by the fact that the SK LUT has only 41 radius quadrature points (Dubovik and King, 2000; Dubovik et al., 2002a; Dubovik et al., 2006) compared to 650 for the SIR LUT (see **Section 4.2.1**). It is known that extinction efficiencies are the most oscillatory for the values of the size parameter $x \geq 10$ (Van de Hulst, 1981; Bohren and Huffman, 1983; Mishchenko et al., 2002). As the size parameter increases, the extinction efficiencies asymptotically approach a constant value. As a result, it is sufficient to use fewer radius quadrature points to characterize the extinction efficiency function for PSDs of larger particles; this leads to more precise extinction coefficients for coarse mode aerosols by the SK LUT.

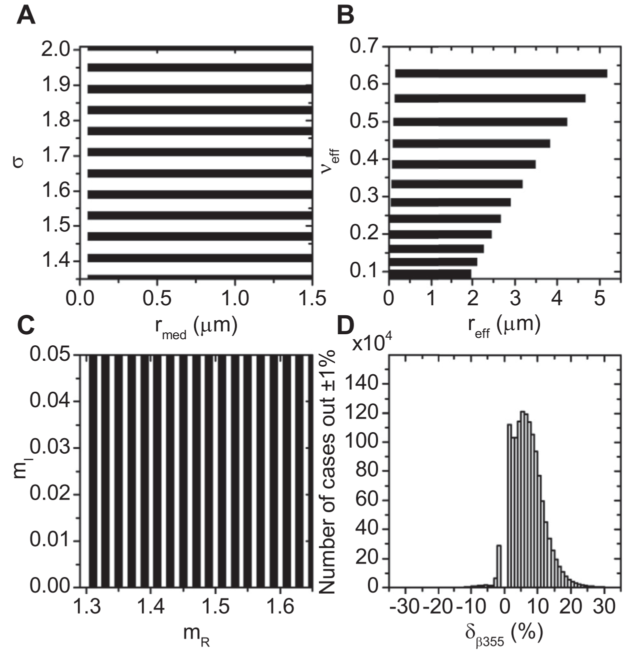

FIGURE 5 | Outliers in β_{355} computations from the SK LUT. Description of labels is given in text.

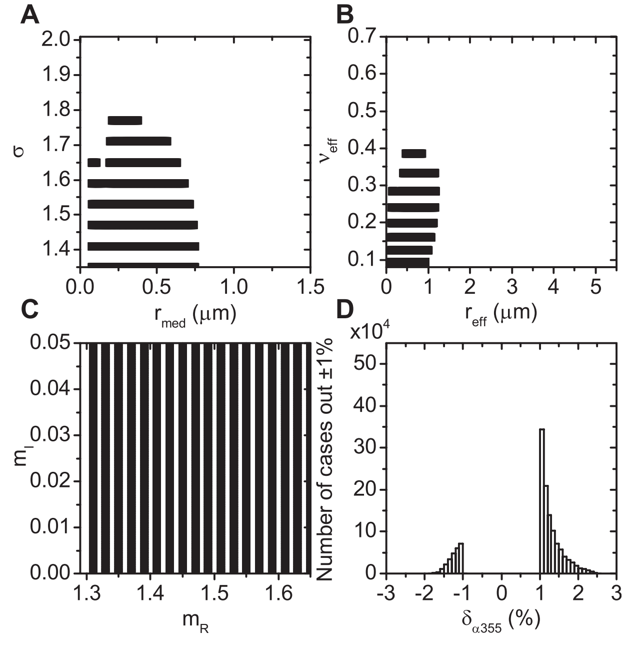

FIGURE 6 | Outliers in α_{355} computations from the SK LUT. Description of labels is given in text.

The accuracy and precision of the SK LUT for the absorption coefficient (see panel **(A)** of **Figures 9**, **10** and **Table 9**) and all the four elements of the normalized scattering matrix (see panels **(C–F)** of **Figures 9**, **10** and

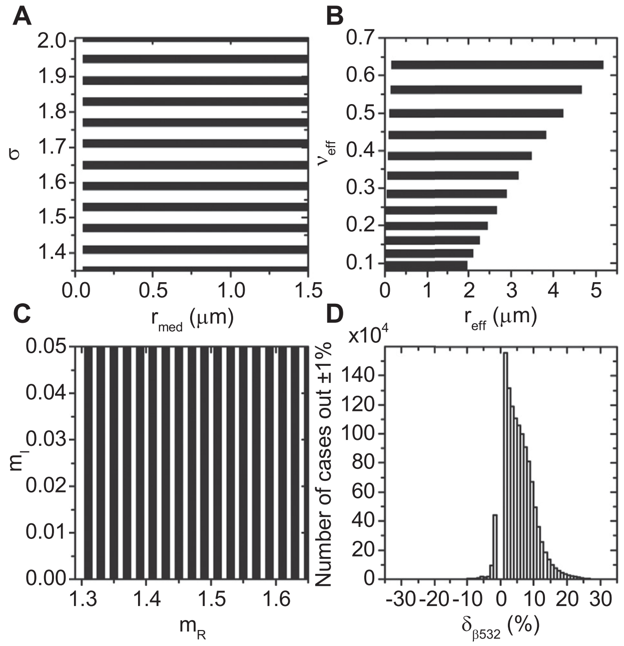

FIGURE 7 | Outliers in β_{532} computations from the SK LUT. Description of labels is given in text.

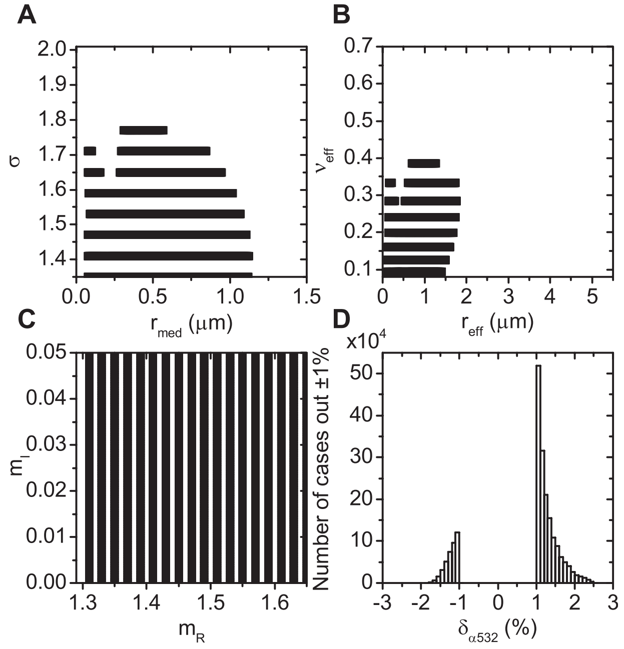

FIGURE 8 | Outliers in α_{532} computations from the SK LUT. Description of labels is given in text.

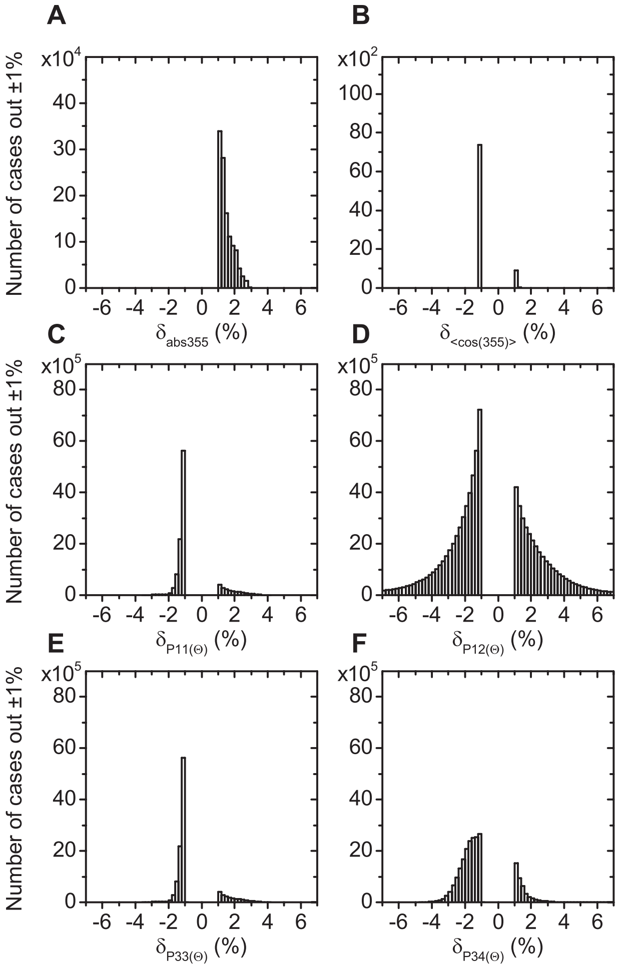

FIGURE 9 | Overview of the SK LUT outliers at $\lambda = 0.355\,\mu m$. Description of labels is given in text.

Table 9) also degrade as the wavelength increases. Only the $P_{12}(\Theta)$ element has a fairly symmetric histogram of relative differences (see panel **(D)** of **Figures 9**, **10**). Panels **(C–F)** of **Figures 9**, **10** and **Table 9** reflect the results of comparisons that were done only at 101 scattering angles which are common between the angular quadratures of the SIR LUT (see **Section 4.2.2**) and the SK LUT (Dubovik and King, 2000; Dubovik et al., 2002a; Dubovik et al., 2006).

One can see that the degradation with increasing wavelength in the relative difference of the aerosol IOPs is a general feature of the SK LUT. We do not plot the results of comparisons for the third HSRL-2 wavelength at 1.064 μm for brevity, but the relative difference further degrades compared to 0.532 μm. We believe that it is related to the use of only 41 radius quadrature points, which is most probably not enough to fulfill the conditions of Nyquist–Shannon–Kotelnikov sampling theorem, which states that twice as many quadrature points are needed compared to the oscillation frequency (Lüke, 1999).

In summary, the new SIR LUT significantly improves upon the precision of the SK LUT at a cost of a factor of ninety in computer RAM. We recommend using the improved SIR LUT to model lidar and polarimeter observables from high precision instruments.

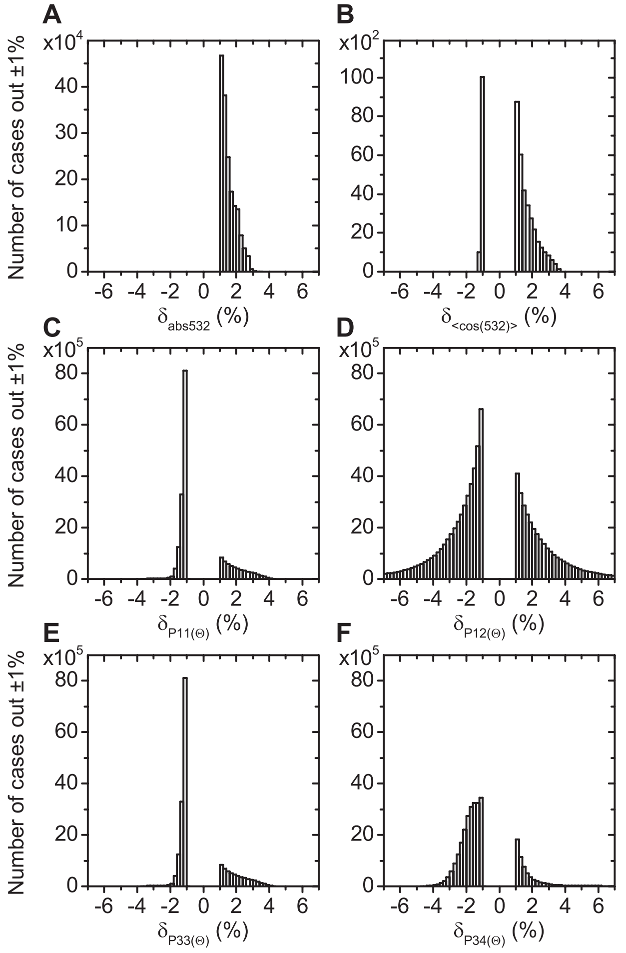

FIGURE 10 | Overview of the SK LUT outliers at $\lambda = 0.532\,\mu$m. Description of labels is given in text.

4.7 Validation of the Scale Invariance Rule and Spherical Kernel Look-Up Tables With Stokes Parameters

As a final test, let us compute and compare the Stokes parameters of scattered light for a selection of simulated cases. We will focus on the Stokes parameters I, Q, U, and the degree of linear polarization DLP $= \sqrt{Q^2 + U^2}/I$ (Van de Hulst, 1981; Bohren and Huffman, 1983; Mishchenko et al., 2002). The Stokes parameters will be computed at the top of the atmosphere using the Advanced Doubling-Adding code for the Earth's atmosphere including molecular scattering (Hansen and Travis, 1974; Stamnes et al., 2018). We will consider 3,024 cases that are formed by seven real parts (from 1.35 to 1.65 with a step 0.05), four imaginary parts (0, 0.001, 0.005, and 0.03) of the CRI, three fine ($r_{\mathrm{eff,f}} = 0.1, 0.2$, and 0.3 μm) and coarse mode ($r_{\mathrm{eff,c}} = 0.9, 1.8$, and 3.6 μm) effective radii coupled with single fine ($\nu_{\mathrm{eff,f}} = 0.3$) and coarse ($\nu_{\mathrm{eff,c}} = 0.6$) mode effective variances [see **Eq. 18**], accompanied by four fine mode (0.04, 0.08, 0.3, and 0.6) and three coarse mode (0.04, 0.08, and 0.16) atmospheric optical depths.

We continue targeting ± 1% precision for all the Stokes parameters and use **Eq. 27** as a measure because I, Q, U, and DLP depend on the scattering angle Θ. Let us use the extreme wavelengths of $\{\lambda\}$, i.e., 0.355 and 2.264 μm, to reveal the λ-dependency in the quality of performance of LUTs.

We computed 160 scattering angles Θ between −65° and 65° for the 3,024 cases, resulting in 483,840 test points, and we compared the simulated truth values of I, Q, U, and DLP for each of them to the corresponding values computed with each of the two LUTs. We found that for all 483,840 test values the SIR LUT reached the ± 1% precision for all the Stokes parameters. The SK LUT demonstrated precision better than ± 1% only at wavelength $\lambda = 0.355\,\mu$m.

Figure 11 shows the results of comparisons for the SK LUT at $\lambda = 2.264\,\mu$m, but again only for the tests that failed to reach the 1% precision. The ± 1% test failed 642 times for I (0.13%; see panel **(A)** of **Figure 11**), 6,663 times for Q (1.38%; see panel **(B)** of **Figure 11**), 7,817 times for U (1.62%; see panel **(C)** of **Figure 11**), and 8,533 times for DLP (1.76%; see panel **(D)** of **Figure 11**). **Figure 11** confirms that degradation with increasing wavelength is a general feature of the SK LUT and the increase of wavelength has negative impact on the precision of estimations.

With these results we conclude that the performance of the SIR LUT for polarimeter observables stays within ± 1% without degrading at increasing wavelength. Also, as another conclusion, it is interesting to see that precise computation of Stokes parameters requires fewer radii grid bins compared to the elements of the normalized scattering matrix and lidar observables.

TABLE 9 | Overview of the SK LUT performance.

IOP			$\lambda = 0.355\,\mu$m				$\lambda = 0.532\,\mu$m	
	Min	Max	Accuracy	Outliers	Min	Max	Accuracy	Outliers
	(%)	(%)	(%)	Number	(%)	(%)	(%)	Number
β	−22.1	34.1	6.05	13,473,394	−16.5	30.6	4.49	12,094,591
sca	−2.5	3.3	0.99	10,018,378	−2.1	3.3	0.93	10,432,117
α	−1.8	2.6	0.67	1,330,281	−1.8	2.6	0.62	2,029,788
abs	−0.7	90.8	1.04	1,303,511	−0.7	91.8	1.09	1,870,540
⟨*cos*⟩	−1.2	1.4	−0.39	8,326	−1.2	3.7	−0.35	44,104
P_{11}	−3.5	4.1	−0.02	10,942,269	−3.7	4.3	−0.03	18,754,373
P_{12}	−75.4	80.2	−0.15	99,240,602	−80.7	79.7	−0.22	133,411,322
P_{33}	−3.5	4.1	−0.02	10,937,936	−3.7	4.3	−0.03	18,744,124
P_{34}	−4.7	8.1	−0.03	21,940,573	−4.7	27.8	−0.04	29,401,117

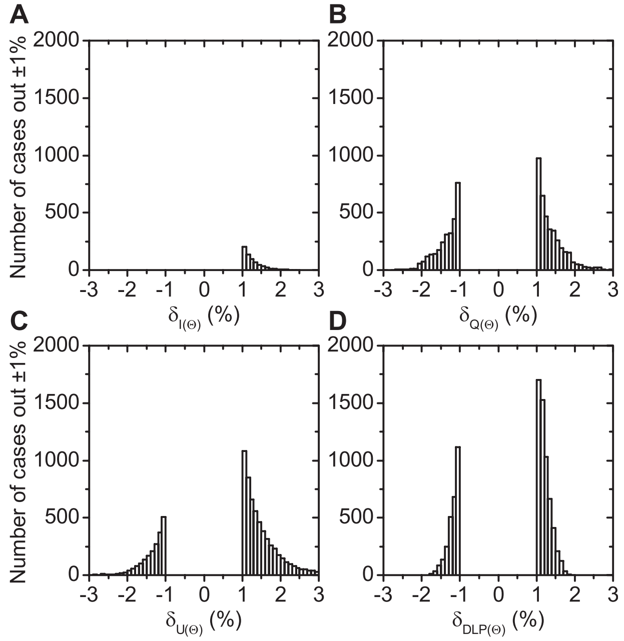

FIGURE 11 | Selected Stokes parameters. Overview of the SK LUT outliers at $\lambda = 2.264\,\mu$m. Description of labels is given in text.

5 CONCLUSION

The SIR LUT provides an improved aerosol inherent optical properties LUT that can be used with advanced lidar and polarimeter aerosol microphysical retrievals as well as other remote sensing and *in situ* applications. Depending on the aerosol IOP, the SIR LUT improves precision by up to 34% compared to the SK LUT. The design of the LUT takes into account mathematical features of Lorenz-Mie scattering theory and can be applied to a range of wavelengths starting at $0.355\,\mu$m and a range of aerosol PSDs. The theoretical background of the LUT design was published as a minor part of earlier studies. In this contribution we attempted to provide a complete and thorough description of the most important mathematical aspects of the SIR LUT.

We introduced several theoretical and practical improvements to the existing LUT approach. We implemented quadratic approximation of the aerosol PSD since we found it improves precision over linear approximation. The new irregular angular quadrature allows us to use fewer scattering angles and improves precision at the same time. The range of size parameters was widened and now covers values from ~ 0.018 to $\sim 1{,}770$. Due to our access to superior computational hardware, we also increased the number of radius quadrature points to the extent that it fulfills the conditions of Nyquist–Shannon–Kotelnikov sampling theorem. The larger number of radius quadrature points solves the SK LUT's issue that causes degraded accuracy and precision of the aerosol IOPs as the wavelength increases.

For verification, we used two reliable Lorenz-Mie single-scattering programs developed by two independent and well established scientific groups in the field of light scattering by small particles. One program was used to compute the coefficients of the SIR LUT itself at the reference wavelength of $0.355\,\mu$m. The other program was used to compute the simulated truth data at twelve wavelengths of interest via direct integration of the aerosol PSD using Simpson's rule. Aerosol IOPs computed from the SIR LUT are precise to within $\pm 1\%$ with the exception that $P_{12}(\Theta)$ is precise to within $\pm 2.5\%$ when the imaginary part of the CRI is below 10^{-5}. As anticipated, the shortest tested wavelength delivers the least precise results in terms of aerosol IOPs and the precision of the SIR LUT improves as the wavelength increases. Further improvements in the precision of IOPs will likely require more radius quadrature points and denser coverage of the CRI that will increase the size of the SIR LUT.

Overall, the precision of aerosol IOPs computed from the SIR LUT is nearly equivalent to direct integration of the PSD using Simpson's rule with 2×10^7 of logarithmically equidistant radius quadrature points from 10^{-3} to $100\,\mu$m, but can be used to make calculations about 1,000 times as quickly. The SIR LUT and examples of its use in several programming languages including C++, Fortran, Matlab, and Python are publicly available for the benefit of community at the web page https://science.larc.nasa.gov/polarimetry.

DATA AVAILABILITY STATEMENT

The datasets presented in this study can be found in online repositories. The names of the repository/repositories and accession number(s) can be found below: https://science.larc.nasa.gov/polarimetry.

AUTHOR CONTRIBUTIONS

Look-up table design and theory development: EC, SS, OD. Look-up table balancing between the size and precision: EC, SS, XL, BC. Quality control: SS, SB, CH, RF. Text: all authors. Grammar and wording improvements: SB, SS.

FUNDING

This research was partially funded by a NASA Remote Sensing Theory award.

ACKNOWLEDGMENTS

The authors acknowledge the support of NASA LaRC K-Cluster staff, and thank Steven H. Carrithers in particular for his expert support in scientific computing. The authors also thank reviewers for their useful feedback leading to improvements of this work.

REFERENCES

Bohren, C. F., and Huffman, D. R. (1983). *Absorption and Scattering of Light by Small Particles*. New York: John Wiley & Sons.

Burton, S. P., Hostetler, C. A., Cook, A. L., Hair, J. W., Seaman, S. T., Scola, S., et al. (2018). Calibration of a High Spectral Resolution Lidar Using a Michelson Interferometer, with Data Examples from ORACLES. *Appl. Opt.* 57, 6061–6075. doi:10.1364/ao.57.006061

Cairns, B., Russell, E. E., and Travis, L. D. (1999). Research Scanning Polarimeter: Calibration and Ground-Based Measurements. *Proc. SPIE* 3754, 186–196.

Dubovik, O., Holben, B. N., Lapyonok, T., Sinyuk, A., Mishchenko, M. I., Yang, P., et al. (2002a). Non-spherical Aerosol Retrieval Method Employing Light Scattering by Spheroids. *Geophys. Res. Lett.* 29 (10). doi:10.1029/2001gl014506

Dubovik, O., Lapyonok, T., Litvinov, P., Herman, M., Fuertes, D., Ducos, F., et al. (2014). *GRASP: A Versatile Algorithm for Characterizing the Atmosphere*. Newsroom: SPIE.

Dubovik, O., Herman, M., Holdak, A., Lapyonok, T., Tanré, D., Deuzé, J. L., et al. (2011). Statistically Optimized Inversion Algorithm for Enhanced Retrieval of Aerosol Properties from Spectral Multi-Angle Polarimetric Satellite Observations. *Atmos. Meas. Tech.* 4, 975–1018. doi:10.5194/amt-4-975-2011

Dubovik, O., Holben, B., Eck, T. F., Smirnov, A., Kaufman, Y. J., King, M. D., et al. (2002b). Variability of Absorption and Optical Properties of Key Aerosol Types Observed in Worldwide Locations. *J. Atmos. Sci.* 59, 590–608. doi:10.1175/1520-0469(2002)059<0590:voaaop>2.0.co;2

Dubovik, O., and King, M. D. (2000). A Flexible Inversion Algorithm for Retrieval of Aerosol Optical Properties from Sun and Sky Radiance Measurements. *J. Geophys. Res.* 105, 20673–20696. doi:10.1029/2000jd900282

Dubovik, O., Sinyuk, A., Lapyonok, T., Holben, B. N., Mishchenko, M., Yang, P., et al. (2006). Application of Spheroid Models to Account for Aerosol Particle Nonsphericity in Remote Sensing of Desert Dust. *J. Geophys. Res.* 111, D11208. doi:10.1029/2005jd006619

Hansen, J. E., and Travis, L. D. (1974). Light Scattering in Planetary Atmospheres. *Space Sci. Rev.* 16, 527–610. doi:10.1007/bf00168069

Kolmogorov, A. N. (1941). About the Logarithmic-normal Law of Particle Size Distribution during Crushing. *Proc. USSR Acad. Sci.* 31 (2), 99–101.

Lüke, H. D. (1999). The Origins of the Sampling Theorem. *IEEE Commun. Mag.* 37 (4), 106–108. doi:10.1109/35.755459

Mishchenko, M. I. (2019). *Double-precision Lorenz-Mie Program for the Case of a Nonabsorbing Host Medium*. Available at http://www.giss.nasa.gov/staff/mmishchenko/Lorenz-Mie.html.

Mishchenko, M. I., Travis, L. D., and Lacis, A. A. (2002). *Scattering, Absorption and Emission of Light by Small Particles*. Cambridge: Cambridge University Press.

Mishchenko, M. I. (2006). Scale Invariance Rule in Electromagnetic Scattering. *J. Quantitative Spectrosc. Radiative Transfer* 101, 411–415. doi:10.1016/j.jqsrt.2006.02.047

National Academies of Sciences, Engineering, and Medicine (2018). *Thriving on Our Changing Planet: A Decadal Strategy for Earth Observation from Space*. Washington, DC: The National Academies Press.

Seinfeld, J. H., and Pandis, S. N. (2006). *Atmospheric Chemistry and Physics. From Air Pollution to Climate Change*. Hoboken: John Wiley & Sons.

Stamnes, S., Hostetler, C., Ferrare, R., Burton, S., Liu, X., Hair, J., et al. (2018). Simultaneous Polarimeter Retrievals of Microphysical Aerosol and Ocean Color Parameters from the "MAPP" Algorithm with Comparison to High-Spectral-Resolution Lidar Aerosol and Ocean Products. *Appl. Opt.* 57, 2394–2413. doi:10.1364/ao.57.002394

Thomalla, E., and Quenzel, H. (1982). Information Content of Aerosol Optical Properties with Respect to Their Size Distribution. *Appl. Opt.* 21, 3170–3177. doi:10.1364/ao.21.003170

Twomey, S. A. (1977). *Introduction to the Mathematics of Inversion in Remote Sensing and Indirect Measurements*. Amsterdam: Elsevier.

Van de Hulst, H. C. (1981). *Light Scattering by Small Particles*. New York: Dover.

Conflict of Interest: Author EC is employed by Science Systems and Applications, Inc.

The remaining authors declare that the research was conducted in the absence of any commercial or financial relationships that could be construed as a potential conflict of interest.

frontiers
in Remote Sensing

METHODS
published: 08 September 2021
doi: 10.3389/frsen.2021.724615

Liquid Phase Cloud Microphysical Property Estimates From CALIPSO Measurements

Yongxiang Hu[1]*, *Xiaomei Lu*[1], *Peng-Wang Zhai*[2], *Chris A. Hostetler*[1], *Johnathan W. Hair*[1], *Brian Cairns*[3], *Wenbo Sun*[1], *Snorre Stamnes*[1], *Ali Omar*[1], *Rosemary Baize*[1], *Gorden Videen*[4,5], *Jay Mace*[6], *Daniel T. McCoy*[7], *Isabel L. McCoy*[8,9,10] and *Robert Wood*[8]

[1]Science Directorate, NASA Langley Research Center, Hampton, VA, United States, [2]Physics Department, University of Maryland, Baltimore County, Baltimore, MD, United States, [3]NASA Goddard Institute for Space Studies, New York, NY, United States, [4]Space Science Institute, Boulder Suite, CO, United States, [5]US Army Research Laboratory, Adelphi, MD, United States, [6]Department of Atmospheric Sciences, University of Utah, Salt Lake City, UT, United States, [7]Department of Atmospheric Science, University of Wyoming, Laramie, WY, United States, [8]Department of Atmospheric Sciences, University of Washington, Seattle, WA, United States, [9]Rosenstiel School of Marine and Atmospheric Sciences, University of Miami, Miami, FL, United States, [10]University Corporation for Atmospheric Research, Boulder, CO, United States

Edited by:
Howard Barker,
Environment and Climate Change,
Canada

Reviewed by:
Husi Letu,
Institute of Remote Sensing and Digital Earth (CAS), China
Weizhen Hou,
Aerospace Information Research Institute, (CAS), China

***Correspondence:**
Yongxiang Hu
yongxiang.hu-1@nasa.gov

Specialty section:
This article was submitted to Satellite Missions, a section of the journal Frontiers in Remote Sensing

Received: *13 June 2021*
Accepted: *18 August 2021*
Published: *08 September 2021*

Citation:
Hu Y, Lu X, Zhai P-W, Hostetler CA, Hair JW, Cairns B, Sun W, Stamnes S, Omar A, Baize R, Videen G, Mace J, McCoy DT, McCoy IL and Wood R (2021) Liquid Phase Cloud Microphysical Property Estimates From CALIPSO Measurements. Front. Remote Sens. 2:724615. doi: 10.3389/frsen.2021.724615

A neural-network algorithm that uses CALIPSO lidar measurements to infer droplet effective radius, extinction coefficient, liquid-water content, and droplet number concentration for water clouds is described and assessed. These results are verified against values inferred from High-Spectral-Resolution Lidar (HSRL) and Research Scanning Polarimeter (RSP) measurements made on an aircraft that flew under CALIPSO. The global cloud microphysical properties are derived from 14+ years of CALIPSO lidar measurements, and the droplet sizes are compared to corresponding values inferred from MODIS passive imagery. This new product will provide constraints to improve modeling of Earth's water cycle and cloud-climate interactions.

Keywords: CALIPSO, water cloud, microphysics, number concentration, water content

INTRODUCTION

CALIPSO Lidar measurements provide the first ever direct measurements of the global distribution of water-cloud extinction coefficients from space. Water-cloud backscattering β decays exponentially with propagation depth z as $\beta = \beta_0 e^{-\lambda z}$, which is demonstrated in CALIPSO lidar measurements. Without multiple scattering, the decay rate λ and extinction coefficient of vertically homogenous water clouds σ are equal. Multiple scattering significantly reduces the decay rate of water-cloud backscattering profiles in the CALIPSO measurements. The decay rate λ of the CALIPSO water-cloud backscattering profile approximately equals the extinction coefficient σ of water clouds multiplied by a multiple-scattering factor η: $\beta = \beta_0 e^{-\eta\sigma z}$. Our previous studies (Hu et al., 2006 and, 2007; Hu, 2007) suggest that the multiple-scattering factor is a function of water-cloud depolarization ratio δ: $\eta = \left(\frac{1-\delta}{1+\delta}\right)$. The depolarization ratio is accurately measured by CALIPSO. To accurately estimate the decay rate of water clouds from CALIPSO measurements and in turn retrieve the water-cloud extinction coefficient, we developed an algorithm that can properly account for the measurement issues that may cause biases, e.g. detector transient response, low-pass filter, discretized range bins, cloud top structure and heterogeneity, as well as uncertainty associated with measurement noise.

It is also possible to estimate the water-cloud lidar ratio *Sc*, i.e. the ratio of the extinction to the backscattering cross section measured at 180° scattering angle obtained from CALIPSO measurements (Hu, 2007). Water-cloud lidar ratios are inversely proportional to cloud droplet sizes (Hu et al., 2006; Mace et al., 2020). Thus, it is theoretically possible to estimate the effective water-cloud droplet size R_e from CALIPSO measurements. There are measurement issues to be resolved in order to derive R_e accurately using CALIPSO observations, e.g., shot noise from sunlight creates difficulty in detecting aerosols and sub-visual clouds above water clouds, and thus causes biases in lidar-ratio estimates. Here we develop a R_e retrieval technique that allows us to avoid such biases.

In this paper we describe the retrieval algorithm for estimating microphysical properties of water clouds (e.g., extinction coefficient, effective drop size, liquid water content, and droplet number concentration) from 14 + years of global lidar measurements acquired by NASA's CALIPSO satellite.

Airborne measurements made by the co-manifested NASA Langley Research Center (LaRC) high spectral resolution lidar (HSRL) and the Goddard Institute of Space Studies (GISS) research scanning polarimeter (RSP) have been used to derive an identical set of water-cloud microphysical properties. The results obtained from these joint HSRL + RSP retrievals agree closely with the coincident *in situ* measurements acquired during multiple field campaigns conducted in various locations around the planet. These retrievals from airborne remote-sensing platforms are used in validating our experimental CALIPSO water-cloud microphysics products.

While space-based passive remote sensors only derive water-cloud microphysical parameters from daytime measurements, our experimental CALIPSO data product provides a full set of water-cloud microphysical information for both daytime and nighttime. In our initial studies of diurnal differences, we have found large day/night contrasts in water-cloud microphysical properties. It turns out that the difference is due to depolarization calibration inconsistency. After the inconsistency is removed, the day-night differences in cloud microphysics are reduced significantly.

The cloud microphysical properties derived from the CALIPSO lidar measurements will enable new and more accurate constraints to be developed and applied to weather and climate models, such as cloud parameterization schemes with their associated simulations of radiation and condensation (e.g., Wilson et al., 2008). This study provides the community with the first long-term, global, nighttime cloud microphysics data products. It also provides an independent, validated daytime water-cloud droplet number concentration data product complementary to those from passive remote sensing (Han et al., 1998; Wood, 2006; Grosvenor et al., 2018).

TECHNICAL APPROACH

In addition to cloud-top height (Mace et al., 2020) and cloud thermodynamic-phase identification (Hu et al., 2007), CALIPSO's lidar measurements can be mined to retrieve many other important water-cloud microphysical properties. For example, lidar ratios derived from the CALIPSO water-cloud measurements have been shown to be well-correlated with effective cloud droplet size (Mace et al., 2020), and CALIPSO's dual polarization backscattering profiles are sensitive to changes in extinction coefficients (Li et al., 2018). Estimation of cloud liquid-water content and droplet number density from CALIPSO observations hinges upon retrievals of cloud droplet effective radius and cloud extinction (Hu et al., 2007).

The retrieval of cloud-droplet effective radius from CALIPSO data is illustrated in **Figure 1**. Lidar ratios S_c of moderately thick water clouds (in this work defined as the effective optical depths at 532 nm larger than 2.5 and two-way transmittances less than 0.0067) can be derived from layer-integrated attenuated-backscattering and depolarization-ratio measurements of water clouds. The layer-integrated attenuated backscattering β of moderately thick water clouds is inversely proportional to S_c and the layer-integrated multiple scattering factor η; i.e., $\beta = 1/[2\eta^* S_c]$ (Platt, 1973). The multiple-scattering factor can be accurately computed from the layer-integrated volume depolarization ratio δ using $\eta=(1-\delta)2/(1+\delta)^2$ (Hu et al., 2006; Hu, 2007; Hu et al., 2007). Lidar ratios of water clouds computed from the Lorenz-Mie theory are inversely correlated with the effective droplet radius (**Figure 1**, left panel) if the effective variance of the size distribution is greater than 0.1 (e.g., green and blue dotted lines). As the relationship between droplet size and lidar ratio varies with effective variance of size distribution, water-cloud droplet size cannot be estimated accurately from lidar ratio alone. To estimate droplet size accurately, we also need another independent measurement that is sensitive to the size distribution, e.g., color-ratio measurements. The right panel of **Figure 1** shows that the color ratio also varies with particle size and effective variance.

It is possible to estimate the effective radius of water clouds relatively accurately from lidar-ratio and color-ratio information derived from lidar measurements. Comparing with 532 nm, theoretical calculations (Hu et al., 2007) suggest that multiple scattering at 1064 nm is roughly 25% higher for CALIPSO, due to the fact that the size parameter at 1064 nm is half of 532 nm and multiple scattering is inversely proportional to the third power of the size parameter (Hu et al., 2007). Thus the effective color ratio from the CALIPSO measurements (right panels of **Figure 2**) is 25% higher compared with the single-scattering color ratio and is consistent with theoretical calculations. Other information, such as cloud temperature, estimated from CALIPSO cloud-height measurements, can also provide extra information about the effective variance of the droplet size distribution.

Collocated MODIS and CALIPSO measurements show that for warm water clouds with cloud-top temperatures higher than 0°C (upper-left panel of **Figure 2**), the lidar ratio increases as the effective radius decreases. The effective variance of the droplet size distribution from both the lidar ratios and color ratios is likely greater than 0.16 when effective radius is less than 10 μm. For warm clouds with effective radius larger than 15 μm, lidar ratios are considerably lower than theoretical Lorenz-Mie calculations. For cold water clouds with cloud-top temperatures colder than −20°C (lower panels of **Figure 2**), both the lidar-ratio and color-ratio measurements suggest that the effective variance of the size distribution is likely smaller than 0.04.

Although there is sufficient information about cloud droplet effective radius in lidar measurements, there are

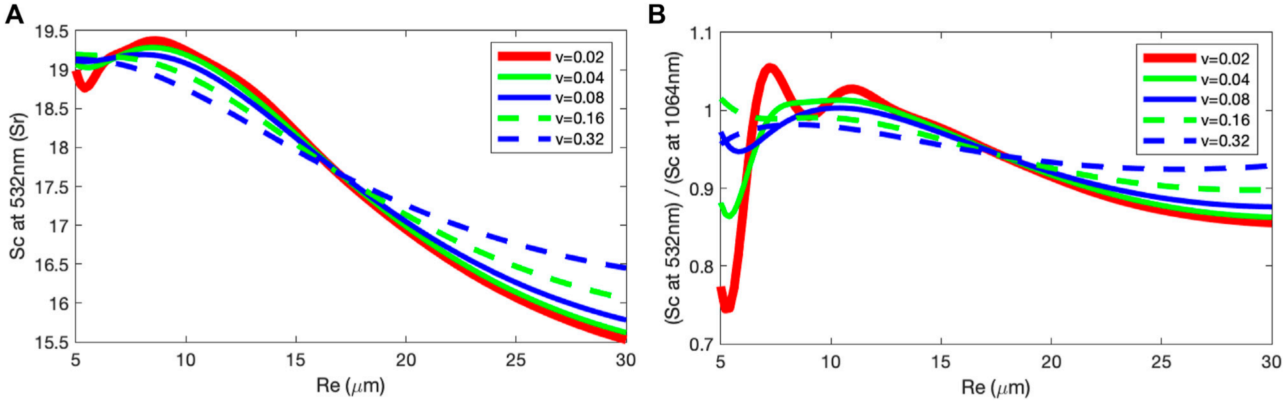

FIGURE 1 | (A): relationship between water-cloud droplet effective radius R_e and water-cloud lidar ratio S_c calculated using the Lorenz-Mie theory. **(B)**: the single-scattering color ratio (1064 nm backscatter cross section/532 nm backscatter cross section) as a function of R_e.

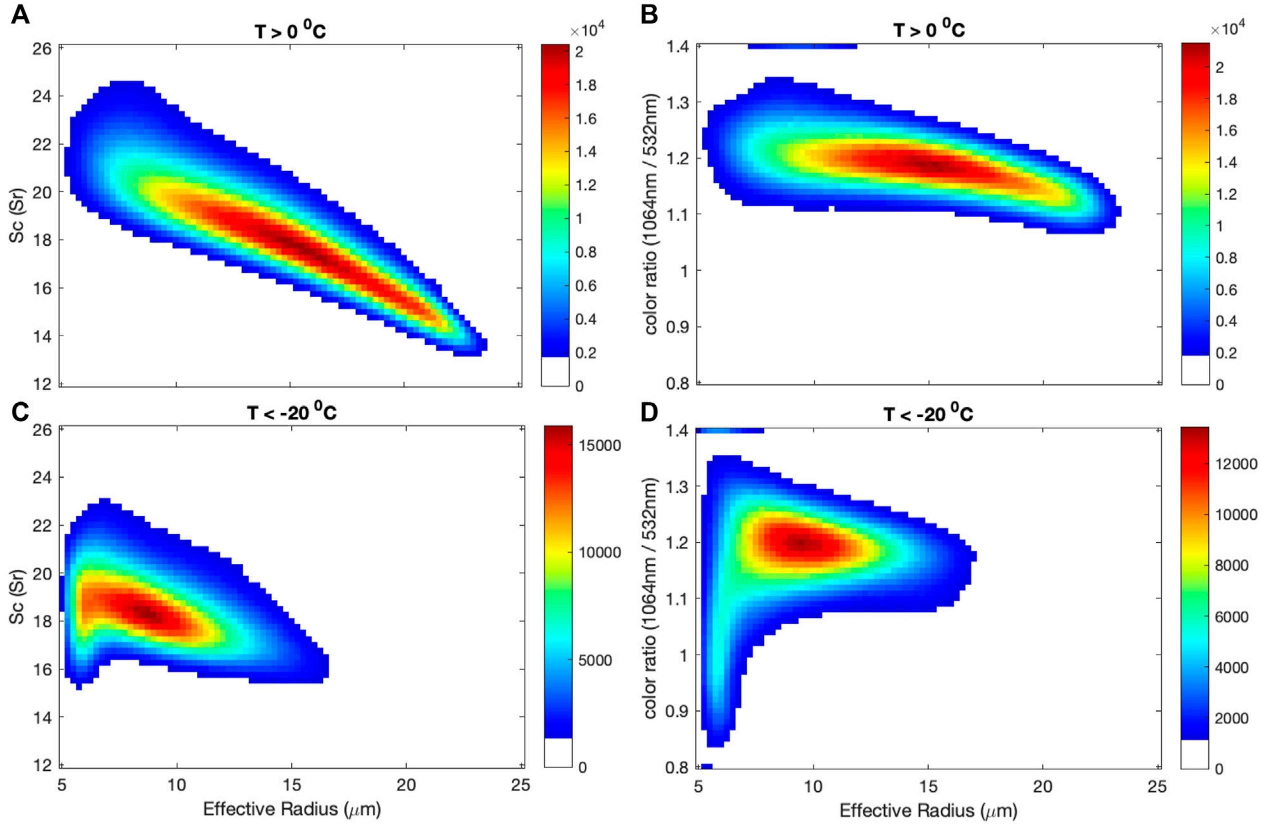

FIGURE 2 | Left panels: relationship between the collocated MODIS water-cloud droplet effective radius R_e and CALIPSO water-cloud lidar ratio *Sc* for warm water clouds **(A)** and supercooled liquid water clouds **(B)**. Right panel: relationship between collocated MODIS Collection 6 water cloud droplet effective radius R_e (Platnick et al., 2017) and CALIPSO water-cloud color ratio for warm water clouds **(C)** and supercooled liquid water clouds **(D)**.

measurement issues that may affect the accuracy of effective-radius estimates from the lidar-ratio and color-ratio measurements. Subvisual cirrus and background aerosols above the clouds may cause over-estimations of the lidar ratio. Fine-mode aerosols above water clouds cause over-estimation of the color ratio. For water clouds having droplets with an effective radius larger than 20 μm, lidar ratios estimated from the CALIPSO measurements are significantly smaller than the ones from Lorenz-Mie calculations.

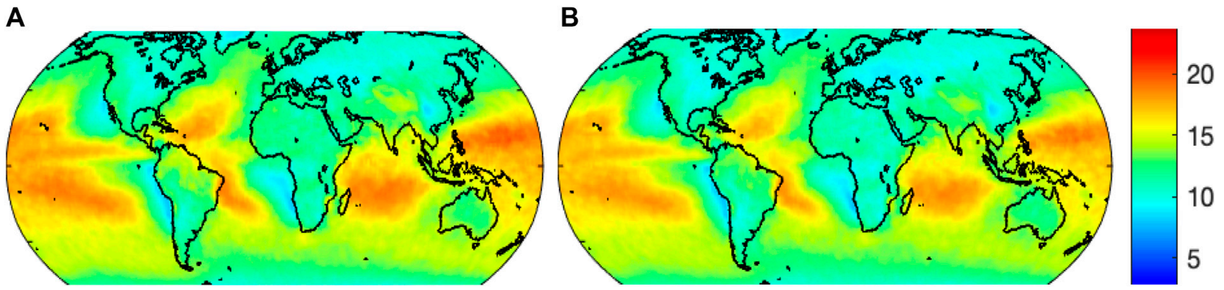

FIGURE 3 | Comparisons of water-cloud-droplet effective radius R_e from 2008 MODIS **(A)** and CALIPSO **(B)** measurements.

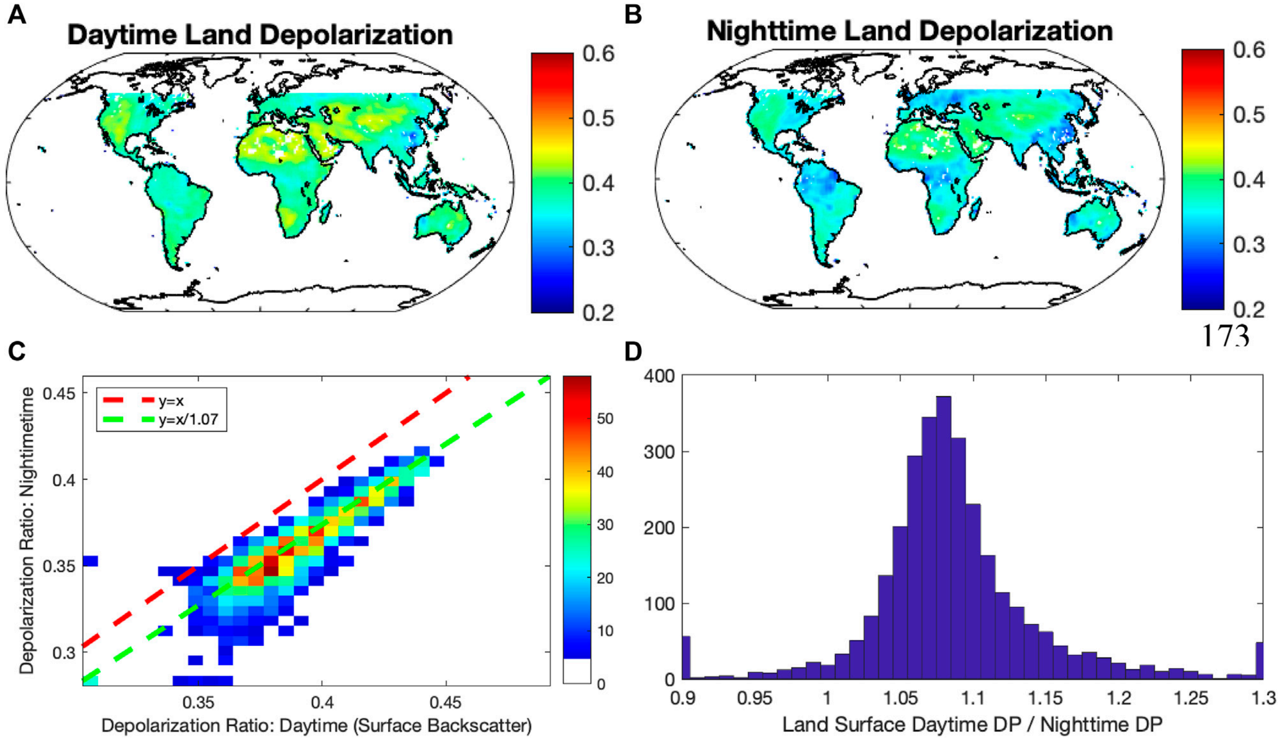

FIGURE 4 | Comparisons of daytime **(A)** and nighttime **(B)** land surface depolarization ratio from CALIPSO measurements, as well as the 3D histogram **(C)** and 2D histogram **(D)** of the day-night land surface difference.

A neural-network-based nonlinear functional approximation (Beal et al., 1992; Beal et al., 2021) that links CALIPSO water-cloud measurements to effective radius derived from collocated MODIS observations is developed in order to overcome these issues effectively. The neural-network algorithm takes in the CALIPSO measurements, such as the layer-integrated attenuated water-cloud backscattering and the vertically integrated, attenuated backscattering of the air above water clouds, as input and the effective radius of collocated MODIS as output for training the neural network. The collocated MODIS effective radius and CALIPSO lidar measurements during January 2008 are used for training the neural-network algorithm and applied to all CALIPSO daytime measurements between 2008 and 2020. The effective radius from CALIPSO (right panel of **Figure 3**) agrees with MODIS (left panel of **Figure 3**) within ± 2 microns.

We also applied the algorithm to the CALIPSO nighttime measurements and found that the droplet sizes are unrealistically large compared with daytime measurements. This is most likely due to differences in the calibration. While daytime and nighttime statistics of all three channels of the lidar measurements suggest good consistency of daytime and nighttime 532 nm parallel and 1064 nm total backscattering measurements, there are significant differences between daytime and nighttime 532 nm perpendicular lidar backscattering statistics. For example, while nighttime 532 nm

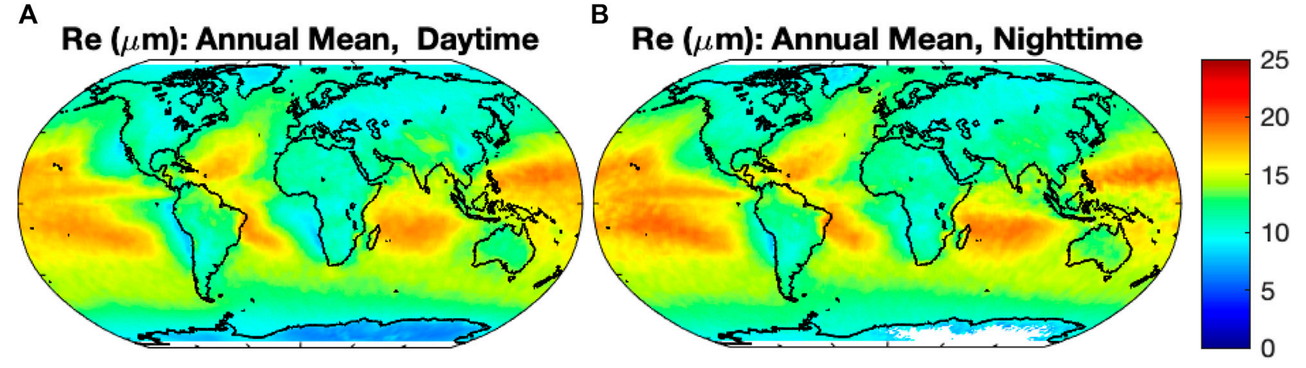

FIGURE 5 | Comparisons of daytime **(A)** and nighttime **(B)** water-cloud droplet effective radius R_e estimated from CALIPSO measurements (2008).

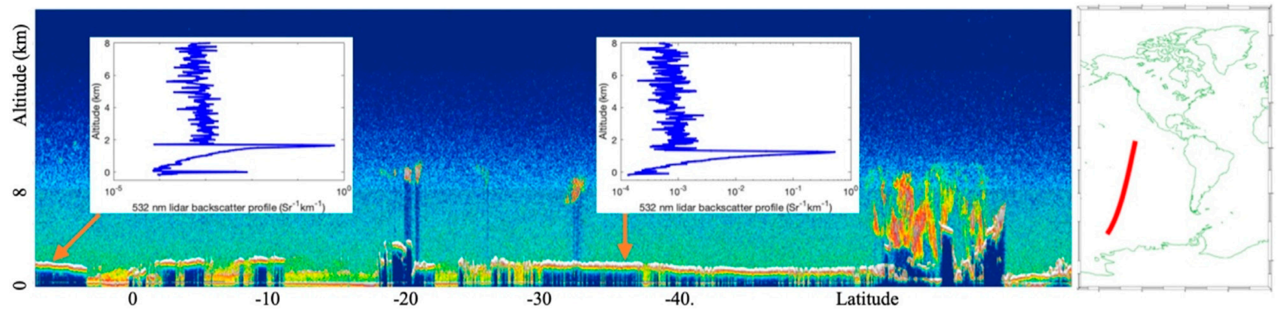

FIGURE 6 | Examples of water-cloud backscattering profiles from CALIPSO measurements.

parallel-polarized backscattering from land surfaces agrees with daytime measurements, nighttime backscattering depolarization ratios of land surfaces (upper right panel of **Figure 4**) are very different from daytime measurements (upper left panel of **Figure 4**), and the nighttime depolarization ratios are roughly 7% lower compared with daytime measurements (lower panels of **Figure 4**). We raised nighttime depolarization ratios by 7% to make it consistent with daytime measurements and thus possible to apply the neural-network algorithm to nighttime CALIPSO measurements for effective radius estimation. With the adjustment of nighttime depolarization ratios, the daytime and nighttime difference in cloud effective radius estimated from the neural-network algorithm is significantly reduced (**Figure 5**).

We also developed a second neural-network algorithm (CALIPSO 2) to reduce potential uncertainties in cloud-droplet radius estimates due to undetected aerosols above water clouds and calibration errors. This method uses depolarization ratios and color ratios as input parameters of the neural-network algorithm to replace the three CALIPSO 1 attenuated-backscattering channels. The effective radii derived from these two algorithms agree with each other in general (lower right panel of **Figure 8** and middle panel of **Figure 11**).

We also developed two different algorithms to determine the water-cloud extinction coefficient from CALIPSO measurements. Method #1 is a profile-shape algorithm in which the water-cloud extinction coefficient σ is determined from the five range bins that measure the largest attenuated-backscattering coefficients (i.e., including one prior and three subsequent to the peak backscattering, β_{-1}, β_0, … , β_3). This technique is based on simulations of the CALIPSO water-cloud measurements for various extinction coefficients that fully account for measurement complexity, such as the non-ideal CALIPSO receiver transient responses (Hu et al., 2007), cloud top bumpiness, and issues associated with averaging over 30 m range bins (**Figures 6** and **7**). Using these simulated lidar measurements, a neural network nonlinear functional approximation, $f(\beta_I) = \sigma$, is trained with attenuated-backscattering coefficients computed for various extinction coefficients as the input and the extinction coefficients as the output (**Figure 7**).

Extinction-coefficient retrieval method #2 derives extinction coefficients σ from depolarization ratios δ and effective radii R_e by applying the theoretical relationship $f(\sigma, R_e, \delta) = 0$ established by extensive Monte Carlo simulations of laser-light propagation in water clouds (Hu et al., 2007; Li et al., 2011; Zeng et al., 2014) while the formula is modified based on the measurements:

$$\sigma\left(\frac{2\pi R_e}{\lambda}\right)^{-0.333} = 216\left(\frac{\delta}{1+\delta}\right)^2$$

Where λ is the lidar wavelength (0.532 μm) and the unit of R_e is μm.

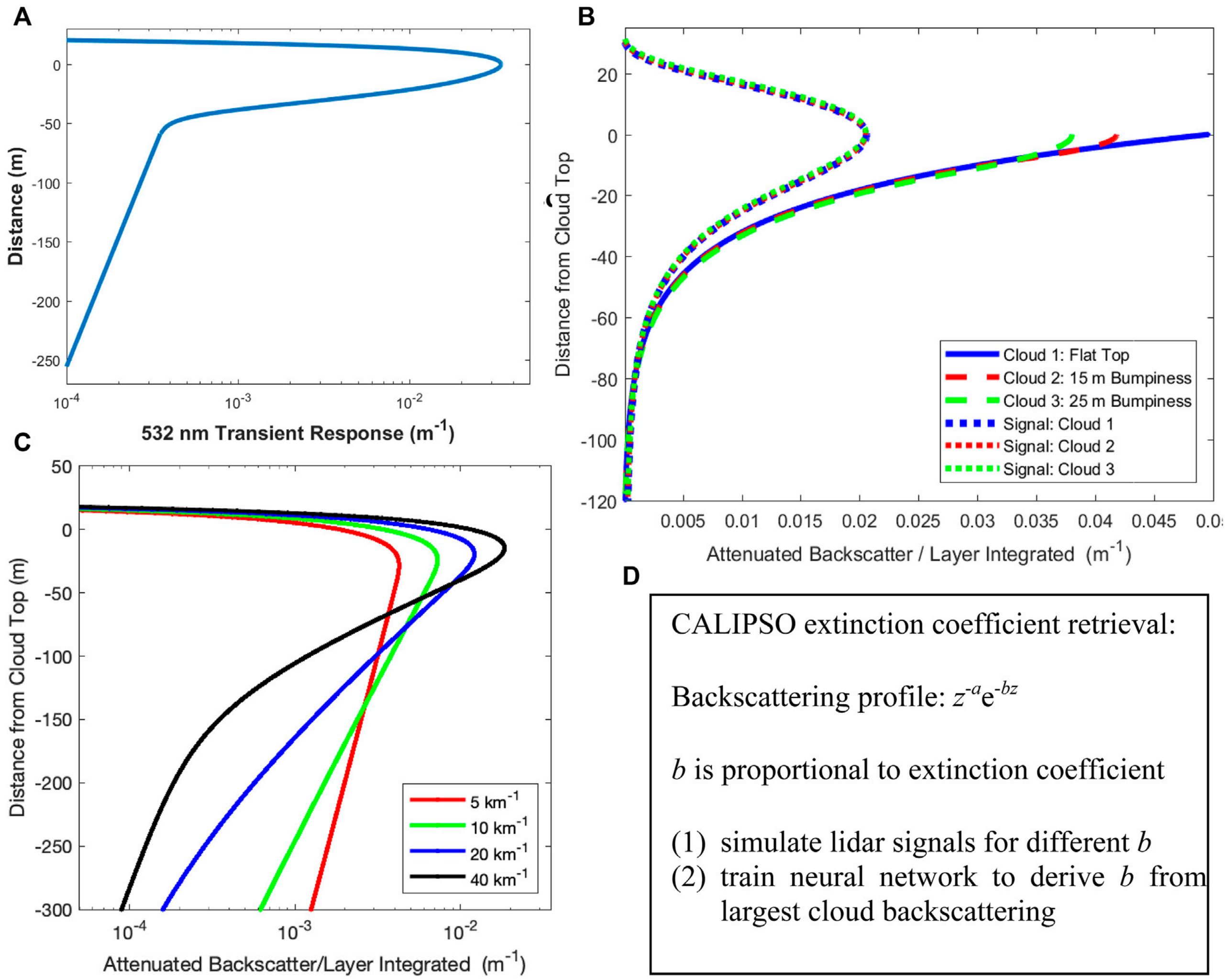

CALIPSO extinction coefficient retrieval:

Backscattering profile: $z^{-a}e^{-bz}$

b is proportional to extinction coefficient

(1) simulate lidar signals for different *b*
(2) train neural network to derive *b* from largest cloud backscattering

FIGURE 7 | Physics behind water-cloud extinction-coefficient retrievals using five largest cloud backscattering range bins. **(A)**: transient response function CALIPSO's 532 nm channel. **(B)**: one silver lining of CALIPSO's transient response and coarse-resolution sampling is that the backscattering profiles are insensitive to cloud-top bumpiness. **(C)**: backscattering profiles before discretized sampling for different effective extinction coefficients. **(D)**: a neural-network algorithm for determining extinction coefficients.

As seen in the lower left panel of **Figure 8**, the extinction coefficients derived using the two different methods agree reasonably well. Similarly, estimates of effective radius also can be derived from depolarization ratios and extinction coefficients. The water-cloud effective radii derived from this method also agree with the effective radii obtained from lidar-ratio measurements (lower right panel of **Figure 8**).

Other physical properties of water clouds, such as liquid-water content w and droplet number concentration N_d, can be derived from the extinction coefficient σ and effective radius R_e (Hu et al., 2007):

$$w = \frac{4_\rho R_e \sigma}{3eQ_c} \approx \frac{2R_e\sigma}{3}$$

$$N_d = \frac{\sigma}{2\pi R_e^2}\,\frac{1}{(1-\nu)(1-2\nu)}$$

Here ρ is the density of water (1 g/cm^3), Q_c is the extinction efficiency of water-cloud droplets, which for droplets large compared with the wavelength $Q_c \approx 2$, and υ is the variance of the droplet size distribution. In this study, we assume υ = 0.13. A study to derive the variances directly from the lidar measurements by training it to the variances derived from collocated POLDER measurements is in progress.

Figure 9 shows the liquid-water content (left panel) and droplet number concentration (right panel) derived from R_e and extinction coefficient for the same section of the orbit as in **Figure 8**. The blue and red lines represent w and N_d derived from R_e and extinction coefficient using Method 1 and Method 2 respectively, which agree with each other reasonably well.

Figure 10 shows the annual mean microphysical properties of water clouds, including R_e (upper left panel), extinction coefficient (upper right panel), liquid-water content (lower left panel) and droplet number concentration (lower right panel).

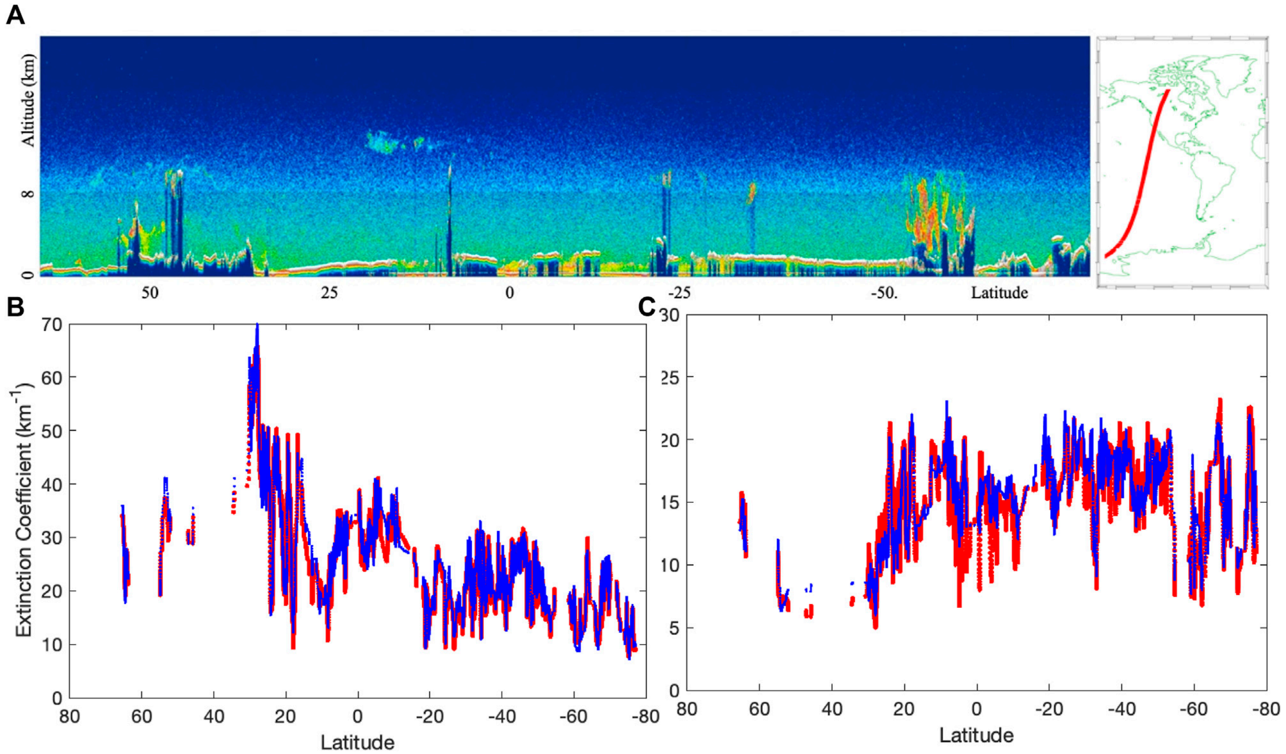

FIGURE 8 | Examples of the extinction coefficient **(A)** and effective radius **(B)** estimates for water-cloud measurements of a nighttime CALIPSO orbit **(C)**. Method 1 (blue lines) and Method 2 (red lines) are two different retrieval algorithms described in the text. The unit of latitudes in all the figures are in degrees.

COMPARISONS OF CALIPSO WATER-CLOUD PROPERTIES WITH CLOUD MICROPHYSICAL PROPERTIES FROM HSRL AND RSP MEASUREMENTS

Over the last several years, the NASA HSRL and RSP teams have invested heavily in both instrument and algorithm development in order to improve the accuracy of their measurements and optimize their retrievals of cloud microphysical properties. The HSRL/RSP water-cloud-microphysical-property product is validated against *in situ* measurements acquired during the North Atlantic Aerosols and Marine Ecosystems Study (NAAMES). The extinction coefficients from the HSRL measurements agree reasonably well with *in situ* measurements (Alexandrov, et al., 2018; Hair et al., 2018). Similarly, the mean droplet extinction cross section areas ($2\pi * R_e^2$) from the RSP measurements (Cairns et al., 2020) also show reasonable agreement with the corresponding *in situ* measurements.

Water-cloud measurements have been made by the HSRL and RSP instruments in many field campaigns that have taken place in different parts of the world over the last few years. Thus, we can use the global data set of HSRL and RSP measurements to assess uncertainties in the CALIPSO water-cloud-microphysical-property data products as discussed below.

Figure 11 shows an example of the HSRL/RSP water-cloud measurements when the aircraft underflew the CALIPSO orbit track (blue line in the upper panel) on May 27, 2016 during the NAAMES mission. The water-cloud effective radii determined from the RSP measurements (blue line in the middle panel of **Figure 11**) agree better with CALIPSO's R_e estimates derived with the lidar ratio method (green and red line) within uniform clouds. For relatively broken clouds, R_e derived from the CALIPSO extinction coefficient and depolarization-ratio method (red line) agrees better with the RSP data (blue). CALIPSO extinction coefficients (green and red lines of lower panel of **Figure 11**) also agree with the ones from HSRL measurements (blue line). Cloud microphysical properties derived from the under-flying aircraft measurements agree similarly well with collocated water-cloud microphysical properties derived from CALIPSO.

SUMMARY

Water-cloud lidar ratios can be derived from water-cloud layer-integrated attenuated-backscattering and depolarization ratios of CALIPSO lidar measurements. Lidar ratios and color ratios of water clouds are both sensitive to changes in effective radius and variance of the water-cloud size distribution. Using the CALIPSO lidar measurements and collocated MODIS effective-size measurements, a neural-network algorithm is developed to retrieve water-cloud effective radius from CALIPSO's water-cloud backscattering measurements.

Vertical profiles of lidar backscattering from water clouds are sensitive to changes in cloud extinction coefficients. It is

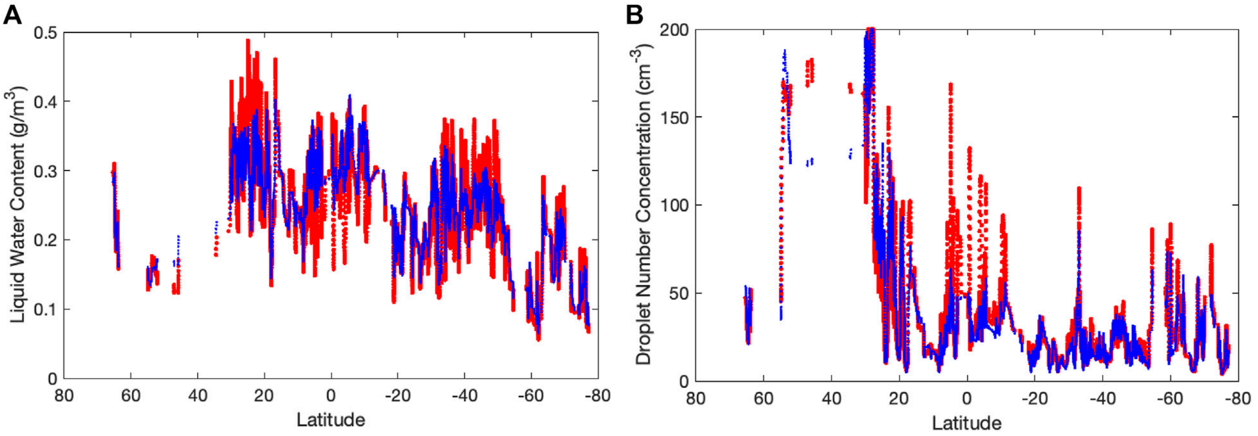

FIGURE 9 | CALIPSO measurements of cloud liquid-water content **(A)** and droplet number concentration **(B)** from the same section of orbit as in as **Figure 8**.

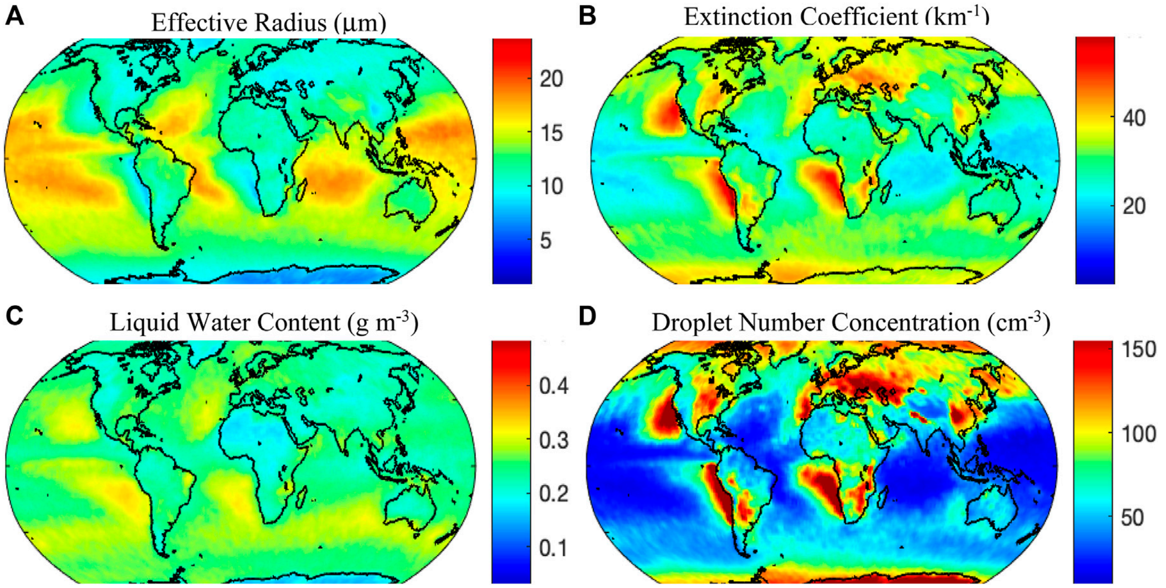

FIGURE 10 | Annual mean effective radius **(A)**, extinction coefficient **(B)**, cloud liquid-water content **(C)** and droplet number concentration **(D)** of CALIPSO water-cloud measurements.

challenging to deriving extinction coefficients from the CALIPSO lidar backscattering profile because of the cloud top heterogeneity and CALIPSO's detector transient response. Based on simulations of the cloud measurements, a neural-network algorithm is developed to determine extinction coefficients accurately from the water-cloud backscattering profile.

Based on daytime and nighttime land surface depolarization statistics, adjustments are made to the nighttime water-cloud depolarization ratios in order to apply an algorithm to determine effective radii from nighttime CALIPSO measurements. This algorithm is trained from daytime MODIS and CALIPSO measurements.

Based on the theoretical analysis, we developed an experimental data product that retrieves microphysical properties of water clouds (e.g., extinction coefficient, effective drop size, liquid-water content, and droplet number concentration) from 14 + years of global lidar measurements acquired by NASA's CALIPSO satellite. This new product will provide constraints to improve modeling of the water cycle and cloud-climate interactions. To realize this potential, the product must be properly validated.

Airborne measurements made by the co-manifested LaRC HSRL and the GISS RSP can be used to derive an identical set of water-cloud microphysical properties. These retrievals from airborne remote-sensing platforms agrees with our experimental CALIPSO water-cloud microphysical product.

For future studies, we plan to improve the algorithm with more sophisticated treatments of droplet variances, vertical changes of cloud droplet sizes, and aerosols/subvisual

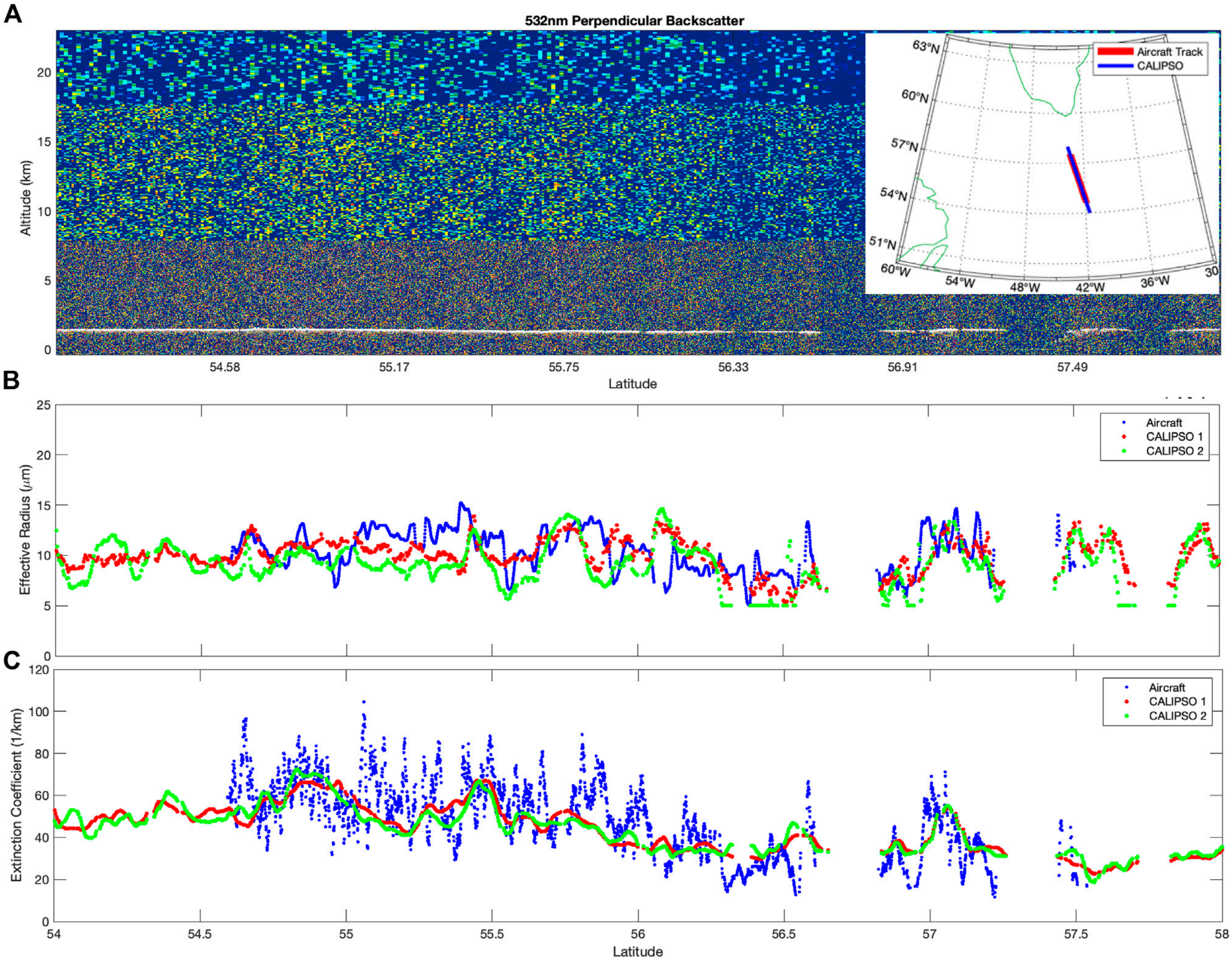

FIGURE 11 | (A): NAAMES May 27, 2016 flight track (red) and CALIPSO overflight (blue). **(B)**: comparisons of CALIPSO measurements of water-cloud effective radius (green and red) with effective-radius measurements from RSP (blue). **(C)**: comparisons of CALIPSO measurements of water-cloud extinction coefficient (green and red) with extinction-coefficient measurements from HSRL (blue).

clouds located above the water cloud. Additional information from aircraft measurements and collocated MODIS, AMSR-E and other A-Train satellite measurements will be analyzed for future algorithm improvements.

DATA AVAILABILITY STATEMENT

The original contributions presented in the study are included in the article/supplementary material, further inquiries can be directed to the corresponding author.

AUTHOR CONTRIBUTIONS

YH developed the algorithm, with considerable guidance and corrections from RW, JM, DM, IM, WS, SS, AO, RB, GV, XL, and PZ provided algorithm support and data analysis. CH, JH, BC provided aircraft measurements and data analysis for validation.

FUNDING

This study is supported by NASA Radiation Science Program and Atmospheric Composition Campaign Data Analysis and Modeling Program, and by NASA CALIPSO project.

ACKNOWLEDGMENTS

We would like to thank Mark Vaughan and CALIPSO team for discussions and the CALIPSO data.

REFERENCES

Alexandrov, M. D., Cairns, B., Sinclair, K., Wasilewski, A. P., Ziemba, L., Crosbie, E., et al. (2018). Retrievals of Cloud Droplet Size from the Research Scanning Polarimeter Data: Validation Using *In Situ* Measurements. *Remote Sensing Environ.* 210, 76–95. doi:10.1016/j.rse.2018.03.005

Beal, M. H., Hagan, M. T., and Demuth, H. B. (2021). Deep Learning Toolbox Reference. Available at: https://www.mathworks.com/help/pdf_doc/deeplearning/nnet_ref.pdf.

Beal, M. H., Hagan, M. T., and Demuth, H. B. (1992). Neural Network Toolbox: User's Guide. Available at: https://citeseerx.ist.psu.edu/viewdoc/download?doi=10.1.1.699.4831.

Grosvenor, D. P., Sourdeval, O., Zuidema, P., Ackerman, A., Alexandrov, M. D., Bennartz, R., et al. (2018). Remote Sensing of Droplet Number Concentration in Warm Clouds: A Review of the Current State of Knowledge and Perspectives. *Rev. Geophys.* 56, 409–453. doi:10.1029/2017rg000593

Hair, J. W., Cairns, B., Alexandrov, M. D., Hostetler, C. A., Hu, Y., Scarino, A. J., et al. (2018). *Lidar and Polarimeter Measurements of Water Clouds during the North Atlantic Marine Aerosols and Ecosystems Study (NAAMES) Campaigns*. American Geophysical Union Fall Meeting 2018, Washington DC.

Han, Q., Rossow, W. B., Chou, J., and Welch, R. M. (1998). Global Variation of Column Droplet Concentration in Low-Level Clouds. *Geophys. Res. Lett.* 25, 1419–1422. doi:10.1029/98gl01095

Hu, Y. (2007). Depolarization Ratio-Effective Lidar Ratio Relation: Theoretical Basis for Space Lidar Cloud Phase Discrimination. *Geophys. Res. Lett.* 34, L11812. doi:10.1029/2007GL029584

Hu, Y., Liu, Z., Winker, D., Vaughan, M., Noel, V., Bissonnette, L., et al. (2006). Simple Relation between Lidar Multiple Scattering and Depolarization for Water Clouds. *Opt. Lett.* 31, 1809–1811. doi:10.1364/ol.31.001809

Hu, Y., Vaughan, M., McClain, C., Behrenfeld, M., Maring, H., Anderson, D., et al. (2007). Global Statistics of Liquid Water Content and Effective Number Concentration of Water Clouds over Ocean Derived from Combined CALIPSO and MODIS Measurements. *Atmos. Chem. Phys.* 7, 3353–3359. doi:10.5194/acp-7-3353-2007

Li, J., Hu, Y., Huang, J., Stamnes, K., Yi, Y., and Stamnes, S. (2011). A New Method for Retrieval of the Extinction Coefficient of Water Clouds by Using the Tail of the CALIOP Signal. *Atmos. Chem. Phys.* 11, 2903–2916. doi:10.5194/acp-11-2903-2011

Li, J., Jian, B., Huang, J., Hu, Y., Zhao, C., Kawamoto, K., et al. (2018). Long-term Variation of Cloud Droplet Number Concentrations from Space-Based Lidar. *Remote Sensing Environ.* 213, 144–161. doi:10.1016/j.rse.2018.05.011

Mace, G. G., Benson, S., and Hu, Y. (2020). On the Frequency of Occurrence of the Ice Phase in Supercooled Southern Ocean Low Clouds Derived from CALIPSO and CloudSat. *Geophys. Res. Lett.* 47, e2020GL087554. doi:10.1029/2020GL087554

Platnick, S., Meyer, K. G., King, M. D., Wind, G., Amarasinghe, N., Marchant, B., et al. (2017). The MODIS Cloud Optical and Microphysical Products: Collection 6 Updates and Examples from Terra and Aqua. *IEEE Trans. Geosci. Remote Sensing* 55 (1), 502–525. doi:10.1109/TGRS.2016.2610522

Wood, R. (2006). Rate of Loss of Cloud Droplets by Coalescence in Warm Clouds. *J. Geophys. Res.* 111, D21205. doi:10.1029/2006JD007553

Zeng, S., Riedi, J., Trepte, C. R., Winker, D. M., and Hu, Y.-X. (2014). Study of Global Cloud Droplet Number Concentration with A-Train Satellites. *Atmos. Chem. Phys.* 14, 7125–7134. doi:10.5194/acp-14-7125-2014

Conflict of Interest: The authors declare that the research was conducted in the absence of any commercial or financial relationships that could be construed as a potential conflict of interest.

frontiers | Frontiers in Remote Sensing

ORIGINAL RESEARCH
published: 06 April 2022
doi: 10.3389/frsen.2022.852610

Deep Convection as Inferred From the C2OMODO Concept of a Tandem of Microwave Radiometers

Franck Auguste and Jean-Pierre Chaboureau *

Laboratoire d'Aérologie (LAERO), Université de Toulouse, CNRS, UPS, Toulouse, France

Probing the atmosphere from space using radiometers is a challenging way to improve our knowledge of deep convection. Exploration of water absorption bands in the 183, 325, and 448 GHz range is promising because of the radiation scattered by icy hydrometeors produced by deep convection. We investigate what properties of deep convection could be inferred from the Convective Core Observations through MicrOwave Derivatives in the trOpics (C2OMODO) concept of a tandem of microwave radiometers separated by several tens of seconds. Two tropical deep convective events (Hector the Convector and a radiative-convective equilibrium case) are simulated with the Meso-NH non-hydrostatic numerical model, the outputs of which are used to compute brightness temperatures (Tbs) using the Radiative Transfer for the Television and Infrared Observation Satellite (TIROS) Operational Vertical Sounder (RTTOV) code. We find different relationships between the ice water path, vertical ice momentum, vertical ice velocity, and the time derivative dTb/dt. They depend on where they are probed after separating the growing convective cores from their surrounding environment with a radiometric point of view. Tb and dTb/dt are highly dependent on the ice water path that depends on horizontal and vertical ice advection and microphysical processes. Looking at deep convection in general, we find that the ice water path increases linearly with decreasing dTb/dt. In the specific case of the core of growing convective cells, the vertical ice momentum and the vertical ice velocity are related to dTb/dt. However, such a relationship breaks down in the anvil because horizontal ice advection can dominate microphysical processes. These results are robust to horizontal resolution and time delay.

Keywords: microwave radiometer, satellite observation, deep convection, icy cloud dynamics, Meso-NH numerical model, RTTOV

Edited by:
Matthew Lebsock,
NASA Jet Propulsion Laboratory (JPL), United States

Reviewed by:
Bing Lin,
National Aeronautics and Space Administration (NASA), United States
David Painemal,
Science Systems and Applications, Inc., United States

***Correspondence:**
Jean-Pierre Chaboureau
jean-pierre.chaboureau@aero.obs-mip.fr

Specialty section:
This article was submitted to Satellite Missions, a section of the journal Frontiers in Remote Sensing

Received: *11 January 2022*
Accepted: *07 March 2022*
Published: *06 April 2022*

Citation:
Auguste F and Chaboureau J-P (2022) Deep Convection as Inferred From the C2OMODO Concept of a Tandem of Microwave Radiometers. Front. Remote Sens. 3:852610. doi: 10.3389/frsen.2022.852610

1 INTRODUCTION

Deep convection is a key driver of weather and climate. In particular, deep convective updrafts transport momentum, mass, water, and other gases from the surface to the upper troposphere and stratosphere and downdrafts from the upper to the lower atmosphere. Our knowledge of vertical convective motions remains partial in part because of the lack of frequent observations at the global scale. Among the wide range of space-based instruments, passive microwave radiometers operating at high microwave (MW) frequencies are particularly interesting for the observation of deep convection because of the high sensitivity of the measured signal due to the scattering by icy hydrometeors (while the absorption by ice is very low). Another advantage is their large swath allowing polar orbiting radiometers to scan almost the whole planet in 12 h. For example, the microwave signal at 183 GHz is used to retrieve the ice water path (IWP) (Gong and Wu, 2014; Rysman et al., 2021) and to assess deep convection predicted by models (Rysman et al., 2016). Measuring a microwave signal above deep convective systems at an interval of several tens of seconds would therefore allow us to retrieve not only IWP but also its time derivative dIWP/dt. It might be also possible to deduce information about the vertical velocity inside deep convective systems.

The Convective Core Observations through MicrOwave Derivatives in the trOpics (C2OMODO) concept (Brogniez et al., 2022) aims at measuring microwave signal at short time intervals (less than 3 min) using a train of passive microwave radiometers aboard low-orbit satellites. Its main objective is to infer the vertical air motion in deep convection. Inferring this information would be very valuable as it would provide an observational constraint that is currently lacking. As shown in an intercomparison study of an intense mesoscale convective system (Varble et al., 2014), vertical velocity is one of the meteorological variables from which cloud-resolving models can strongly diverge. At the time of writing this article, neither radiometers of the C2OMODO concept nor their swathes have yet been designed. However, it is expected that these radiometers will measure several strong water vapor absorbing lines in the MW. The most likely option is to have two bands at 183 and 325 GHz with a pixel resolution of 5 and 3 km at nadir, respectively, while another option would be to add the 448 GHz band to the other two bands.

The objective of this study is to explore the content of information of the C2OMODO concept in order to characterize tropical deep convective cells. The approach consists in using an explicit model of high-resolution atmospheric convection combined with a radiative transfer code in order to simulate, on the one hand, a multispectral high-frequency imaging in the microwaves and, on the other hand, the imaging difference at different time intervals to explore the contribution of the flight in close formation of two radiometers. In the first step, the microwave brightness temperature (Tb) response to deep convection is examined at the simulation scale to describe the relationships of the Tb response with the dynamic and microphysical fields of the model that may exist. In the second step, the sensitivity of the results to temporal and spatial resolutions is examined.

Section 2 describes the model and the data set of two simulations and defines the geophysical and satellite variables. **Section 3** presents the relationships between the ice water path and Tbs for specific frequencies. **Section 4** analyzes the relationships between geophysical and satellite variables for 10 convective cells in the growth phase in an environment free of icy hydrometeors. **Section 5** explores the robustness of these relationships over the full data set. **Section 6** presents the conclusions and gives some perspectives.

2 MODEL AND METHOD

2.1 Meso-NH and Variable Definitions

The simulations are run with the anelastic non-hydrostatic mesoscale model Meso-NH (Lac et al., 2018) developed by Meteo-France and Laboratoire d'Aerologie for research purposes (see http://mesonh.aero.obs-mip.fr/). The model has been widely used to investigate cloud and precipitation properties using satellite observations (e.g., Chaboureau et al., 2000; Wiedner et al., 2004; Meirold-Mautner et al., 2007; Chaboureau et al., 2008; Rysman et al., 2016). Momentum variables are advected with a centered fourth-order scheme, while scalar variables are advected with the piecewise parabolic method advection scheme (Colella and Woodward, 1984). Meso-NH includes the Surface Externalisée (SURFEX) scheme for surface fluxes (Masson et al., 2013), 1.5-order closure scheme for turbulence (Cuxart et al., 2000), parameterization of dry thermals and shallow cumuli (Pergaud et al., 2009), two-stream scheme of Fouquart and Bonnel (1986) for shortwave radiation, and rapid radiative transfer model (Mlawer et al., 1997) for longwave radiation.

Mixed-phase clouds are parameterized using the bulk microphysics scheme of Pinty and Jabouille (1998). It follows the evolution of six water species including vapor, liquid cloud, and rain and three icy species which are cloud ice, snow, and graupel defined by increasing degree of riming. If we consider the total ice content, that is, the sum of cloud ice, snow, and graupel, the local conservation of the ice mixing ratio r_{ice} can be written as follows:

$$\frac{\partial\left(\rho\bar{r}_{\mathrm{ice}}\right)}{\partial t}=-\nabla.\left(\rho\bar{r}_{\mathrm{ice}}\bar{\mathbf{u}}\right)+\rho\bar{\mathbf{F}}_{\mathrm{ice}}-\nabla.\left(\rho\overline{\mathbf{r}'_{\mathrm{ice}}\mathbf{u}'}\right), \qquad (1)$$

where ρ is the air density, $\bar{\mathbf{u}}$ the resolved air velocity field, and $\bar{F}_{\mathrm{ice}}$ the source term containing the phase change and diffusive processes. The variable $\bar{r}_{\mathrm{ice}}$ (resp. r'_{ice}) is the resolved (resp. unresolved) part of r_{ice} due to the large eddy type of the simulations. The turbulent diffusion of cloud ice can be neglected and the $^{-}$ symbol is omitted throughout the study.

The vertical integration of **Eq. 1** allows us to define several column-average variables. The ice water path (IWP) is the vertical integral of ρr_{ice}, the surface horizontal ice momentum (HIM) is that of the horizontal component of $\rho r_{\mathrm{ice}}\mathbf{u}$, and the surface vertical ice momentum (VIM) is that of its vertical component. Since the vertical integration of the vertical flux divergence is zero, it reads as follows:

$$\frac{\partial \mathrm{IWP}}{\partial t}=-\nabla_h.(\mathrm{HIM})+\left.\frac{\partial \mathrm{IWP}}{\partial t}\right|_{\mu\varphi}, \qquad (2)$$

where the subscript μ refers to the microphysical changes (phase transformation and sedimentation) of IWP. The time tendency of IWP due to the microphysical changes is diagnosed as the residual after subtracting the ice advection terms from the time tendency of IWP. Note that, the contribution of ice sedimentation to **Eq. 2** is small in the core of growing convective cells. The anelastic framework operating in Meso-NH states is $\nabla.(\rho\,\mathbf{u})=0$. Consequently, the divergence of the ice flux is approximated as the sum of the horizontal IADV_h and vertical IADV_v ice advections, which are defined as the horizontal and vertical components of the vertical integration of $\mathbf{u}\nabla(\rho r_I)$. In addition, we define w_{ice}, the vertical ice velocity, as VIM divided by IWP.

2.2 Simulations

Two simulations were carried out at the convective scale using Meso-NH. One simulation considers Hector the Convector (HEC) over the Tiwi Islands, while the other is a radiative-convective equilibrium (RCE) ocean case. HEC was run for 6 h over a domain of 256 × 200 km^2 with 1-km horizontal grid spacing. The model top is at 30 km with 146 vertical levels spaced between 60 and 200 m below 22 km. The initial conditions are the same as those defined by Dauhut et al. (2015), which are based on the radiosonde launched from Darwin, Australia, at 0000 UTC 30 November 2005. Because of the relatively high horizontal resolution of 1 km, the parameterization of dry thermals and shallow cumuli was not used. RCE corresponds to four periods of 15 min taken from the configuration with a large domain (*RCE_large*) of the Radiative-Convective Equilibrium Model Intercomparison Project (RCEMIP) (Wing et al., 2020) using a sea surface temperature of 300 K. The domain is a grid of 384 × 6000 km^2 with a horizontal resolution of 3 km. The model top is at 31 km with 76 vertical levels spaced 500 m apart above 3 km.

Brightness temperatures (Tbs) were computed in-line every 30 s using the Radiative Transfer for the Television and Infrared Observation Satellite (TIROS) Operational Vertical Sounder (RTTOV) code, version 12.3 (Saunders et al., 2018). The interface with RTTOV has been written and included in the Meso-NH code itself (Chaboureau et al., 2008). This allows the creation of satellite images during the simulation, at each time step of the model if needed. For microwave instruments at all frequencies below 1000 GHz, the atmospheric gas absorption model of RTTOV derives its spectroscopic parameters from the millimeter wave propagation model of Liebe et al. (1989) updated for the oxygen, ozone, and water vapor lines (see Saunders et al., 2018 for more details). Under clear skies, the accuracy of RTTOV is much better than the noise of current MW radiometer instruments (e.g., the error with a line-by-line reference is 0.04 K at 183 GHz). The Mie tables were created with rttov-scatt from the RTTOV package. Scattering properties are described for rain, cloudy liquid water, and ice using the Mie theory. The permittivity formulation of Rosenkranz (2015) is used for spheres composed of liquid water and that of Matzler and Wegmuller (1987) for cloud ice. The latter is assumed to be composed of a mixture of air and ice making its density equal to 900 kg m^{-3}. Their particle size distribution follows a Marshall–Palmer shape for rain and a modified gamma shape for cloud liquid water and ice. Snow and graupel are represented as snowflake sector [with crystal type 9 in the database of Liu (2008) in which the ice portion of the particle is made of pure ice with a density of 916 kg m^{-3}] using the discrete dipole approximation and the tropical version of size distribution of Field et al. (2007). This led to generate a Tb at nadir sight for three sets of 50 channels of bandwidth b = 200 MHz. From the three frequencies of rotational water vapor lines at f_0 = 183.3, 325.1, and 448.0 GHz, each channel n covers 10 GHz with a flat spectral response between the frequencies $f_0 + (n - 1) \times b$ and $f_0 + n \times b$.

3 RELATIONSHIP BETWEEN IWP AND TB

A first overview of the database is shown with the temperature and water content profiles (**Figure 1**). The temperature decay in the upper troposphere is similar in the two cases with little variation around the median profile. Up to 14-km altitude, the air is a few Kelvin warmer in HEC than in RCE. Thus, the freezing level is 4.5 km for HEC and 4 km for RCE. In the lower and middle troposphere, the water vapor content is higher in HEC than in RCE up to a difference of 5 g kg^{-1} at the surface. The variability around the median profile is lower in HEC than in RCE. This is explained by the configuration of the simulations. HEC simulates a convective system initiated from a single atmospheric profile, while RCE simulates organized thunderstorm systems surrounded by large-scale subsidence zones. Due to more vigorous convection, the hydrometeor profiles have larger median and 90 percentile values for HEC than for RCE, while the icy hydrometeors are at a higher altitude. The lower freezing level elevation in RCE shifts the minimum icy hydrometeor altitude and the maximum rain altitude downward by 0.5 km.

An example of the relationship that can be obtained between IWP and Tbs is shown for the Tb depression due to ice (**Figure 2**). The Tb depression is usually obtained by subtracting the calculated Tb omitting the ice contribution from the full Tb. This would require calculating Tb twice and would generate a very large data set. Instead, we take advantage of the Tbs calculated every 30 s and search for the closest Tb in time and space for which IWP is near zero (less than 10^{-6} kg m^{-2}). More precisely, smoothing is applied on three points in time (1 min 30 s) and space (3 km for HEC and 9 km for RCE) to limit the small-size variations of the atmosphere variability.

As expected for ice scattering, the Tb depression decreases with increasing IWP regardless of frequency and case. The farther the frequency is from the center of the band, the larger the Tb depression. This is due to the low water vapor opacity of the mid-wing and wing channels making them more sensitive to ice content. This results in the Tb-depression minimum to be around −150 K or less. For the channels at band center, the Tb-depression minimum is much smaller, around −80 K for 183.3 GHz, −120 K for 325.1 GHz, and −30 K for 448.0 GHz.

About one per thousand columns has IWP larger than 30 kg m^{-2} in both simulations. The maximum IWP is greater than 50 kg m^{-2} in HEC, while it does not exceed 40 kg m^{-2} in RCE. This is due to more intense deep convection in HEC due to strong forcing by the surface fluxes over land. For IWPs larger than 40 kg m^{-2}, the slope of the Tb depression with increasing IWP is close to zero for the 183 and 325 GHz bands but remains constant for the 448 GHz band. This suggests that only the 448 GHz band could be used to infer the largest IWP values because its greater water vapor opacity reduces the impact of scattering at the lowest altitudes. Between 5 and 40 kg m^{-2}, the slope is steeper for RCE than for HEC. Since the freezing level located at about 4 km for RCE and around 4.5 km for HEC, the ice content is more likely distributed over a wide range of altitudes for RCE than for HEC. This results in a greater sensitivity of the Tb depression to IWP.

Another way to provide a general view of the relation between IWP and Tbs is shown for the Tb difference between the band

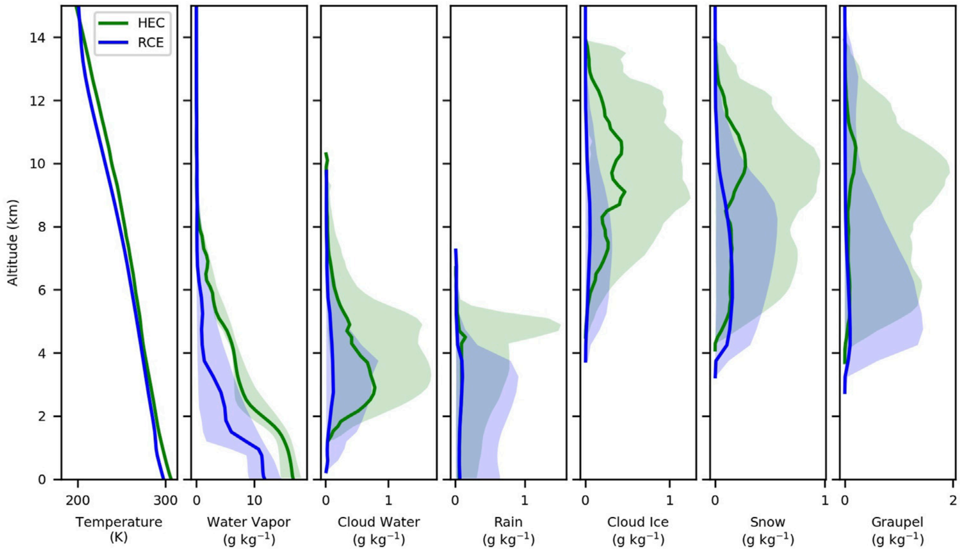

FIGURE 1 | Profiles of (from left to right) temperature, water vapor, cloud water, rain, cloud ice, snow, and graupel mixing ratios. The median (bold lines) and the 10–90 percentile ranges (shadings) are shown for HEC (green) and RCE (blue).

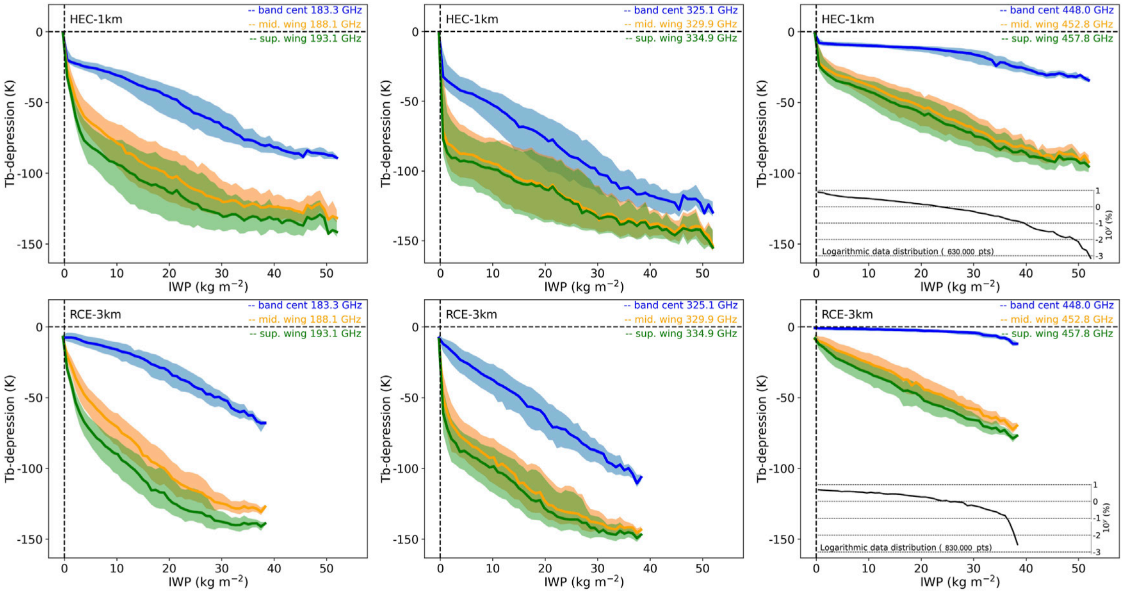

FIGURE 2 | Tb depression as a function of IWP for (top) HEC and (bottom) RCE and for (from left to right) 183.3, 325.1, and 448.0 GHz bands. The median (bold lines) and the interquartile ranges (shadings) are shown for the band center (blue), the mid-wing (+5 GHz, orange), and the wing (+10 GHz, green) of the upper band. In the right column, the insert shows the data distribution in logarithmic scale.

center and the wing of the upper band and the mid-wing and the wing (**Figure 3**). Such Tb differences at 183 GHz have been widely used to detect deep convection (Funatsu et al., 2007; Rysman et al., 2016).

Regardless of the band, the Tb difference between the band center and the wing is the largest (except for the 448 GHz band when IWP is less than 15–20 kg m^{-2}). It increases with IWP, at least for small IWP values. For larger IWP values, this increase is no longer valid. The threshold at which the increase stops differs from the band. It varies between 5 and 20 kg m^{-2} at 183 GHz, around 1–2 kg m^{-2} at 325 GHz, and 30 kg m^{-2} at 448 GHz. While the Tb difference decreases even at 183 and 325 GHz, a monotonic function

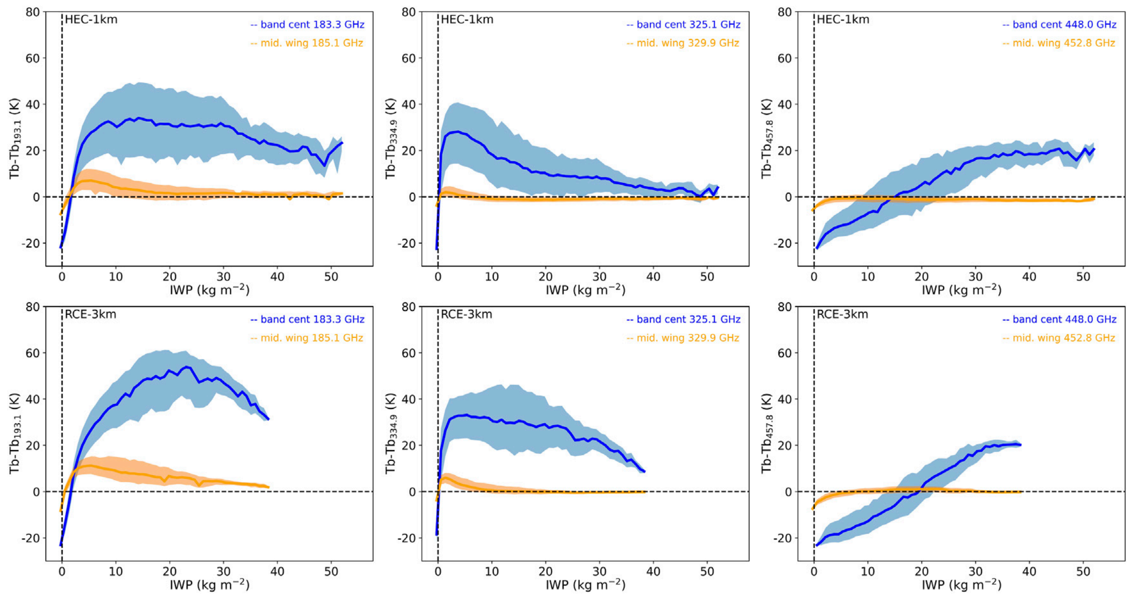

FIGURE 3 | Same as **Figure 2** but for the Tb difference between the band center and the wing (Tb_{center} – Tb_{+10GHz}, blue), the mid-wing and the wing (Tb_{+5GHz} – Tb_{+10GHz}, orange).

between IWP and the Tb difference is found at 448 GHz. This again suggests the usefulness of this band for inferring IWP over a wide range.

For the 325 and 448 GHz bands, the Tb difference between the mid-wing and the wing show too little sensitivity to the change in IWP. This makes this Tb difference irrelevant for detecting deep convection. For the 183 GHz band, it varies from 5 to 10 K as the IWP increases from 0 to about 5 kg m^{-2}. However, it is much smaller than the 40 K increase for the Tb difference between the band center and the wing. As a result, the condition of an IWP larger than 1 kg m^{-2} is satisfied when the Tb difference between the band center and the wing of the upper band is larger than −5 K at 183 GHz, + 5 K at 325 GHz, and −25 K at 448 GHz. In the following, we used these thresholds to detect deep convection for each band (it is expected that each band will have a different pixel size).

4 TB AND DELTA-TB EVOLUTION DUE TO THE GROWTH OF SINGLE CELLS

The relationship between geophysical and satellite variables is studied in the simple framework of convective cells in the growing phase. The selection of these cells is first presented, followed by the Tb response to convective growth for a single cell, and finally the Tb response for all selected cells.

4.1 Selection of Convective Cells in the Growing Phase

Selection of convective cells in the growing phase is made based on three criteria. First, the cell must be single in order to distinguish its core from its anvil environment. Second, the cell must be isolated to avoid any IWP change due to another cell in its vicinity. Third, the cell must be characterized by a monotonic increase of IWP and its cloud top during the selected window time to facilitate the interpretation of the change in Tb with time. In this study, an icy cloud is defined at a r_{ice} threshold value of 10^{-4} kg kg^{-1}. This results in a selection of 10 convective cells (CCs). They are classified and named according to their simulation origin and their increase in cloud tops, that is, from CC-A to CC-D for RCE and from CC-E to CC-J for HEC (**Table 1**). Their duration varies from 7 to 14 min during which their cloud top increases from 6 to 9 km to reach an altitude between 9 and 15 km. Their increase in IWP varies greatly with the convective cell, from 10 kg m^{-2} for CC-E to 30 kg m^{-2} for CC-J. The decrease in Tb is also highly variable with the convective cell and the band center frequency. It presents a maximum of −1 K at 448.0 GHz for CC-A and CC-E and a minimum of −80 K at 325.1 GHz for CC-J.

4.2 Icy Cloud Dynamic and Radiometric Response for a Growing Convective Cell

An example of the growth of a convective cell is analyzed for CC-H. CC-H grows for 10 min to reach an IWP of 22 kg m^{-2} and a cloud top of 13 km (**Table 1**). The cell is shown at four time steps spaced 2 min apart on a horizontal cross section of 6 × 6 km^2 (**Figure 4**). This is a single, isolated cell consisting of a core where the IWP is maximum and an anvil with non-zero IWP values in the dozen, or so, grid points around it.

During this 8-min interval, the convective core is characterized by an increase in IWP from 1 to 22 kg m^{-2} and VIM from 100 to 500 kg m^{-1} s^{-1}. Around the core, IWP also increases with time as the convective core supplies ice to its surrounding environment by

TABLE 1 | Overview of the convective cells in the growing phase selected in RCE and HEC.

CC index	Core location (i,j)	Time (duration) (min)	Cloud top (km)	IWP (kg m^{-2})	Tb$_{183.3}$ (K)	Tb$_{325.1}$ (K)	Tb$_{448.0}$ (K)
RCE (3 km)							
A	(1340,38)	H1412 (2 → 12)	6 → 10	3 → 17	235 → 225	235 → 230	208 → 207
B	(1261,15)	H1414 (2 → 14)	8 → 12	8 → 23	235 → 210	235 → 180	208 → 206
C	(1378,75)	H1412 (2 → 12)	9 → 13	18 → 29	225 → 180	215 → 145	208 → 204
D	(1273,59)	H1414 (1 → 08)	9 → 14	17 → 30	225 → 180	210 → 140	208 → 203
HEC (1 km)							
E	(099,59)	0H (131 → 140)	6 → 9	2 → 12	245 → 235	245 → 230	219 → 218
F	(042,55)	0H (146 → 153)	6 → 10	1 → 12	245 → 230	245 → 225	219 → 217
G	(062,26)	0H (155 → 163)	6 → 11	1 → 19	245 → 220	245 → 200	219 → 216
H	(118,50)	0H (182 → 192)	6 → 13	1 → 22	245 → 200	245 → 165	219 → 214
I	(129,58)	0H (180 → 194)	6 → 14	1 → 24	245 → 215	245 → 190	219 → 211
J	(061,52)	0H (214 → 222)	9 → 15	7 → 37	240 → 185	235 → 155	219 → 204

advection (top detrainment) and, to a lesser extent, by mixing (turbulent processes). When the increase in IWP is combined with positive values of vertical velocity in the surrounding environment of the core, the result is an increase in VIM but with lower values than in the core.

The evolution in IWP is further examined by showing dIWP/dt and the two dominant terms governing its change in **Eq. 2** using a 1-min interval. The growing cell is characterized by a positive dIWP/dt. This is mainly due to the ice production during the first two time steps, as shown in the microphysical term. This corresponds approximately to the location where VIM is positive. At the two last time steps, IADV$_h$ shows positive values at the core and negative around it. In other words, part of IWP is detrained from the core to the anvil. So the surrounding environment of the core is mainly controlled by horizontal advection of ice. As a consequence, inferring VIM or any other variable related to the vertical air velocity from observations sensitive to IWP variation would be very challenging in the surrounding environment of a convective core. It is therefore necessary to distinguish the core from its surroundings.

In the core, IADV$_h$ remains small at 3h08 compared to the microphysical term. The change in dIWP/dt is still controlled by this term, in agreement with the large value of VIM. At 3h10, the detrainment of ice is so strong that it is counterbalanced by the microphysical production of ice, while dIWP/dt takes a smaller value. This suggests that it is possible to infer VIM from measurements sensitive to dIWP/dt in the convective core when it produces more ice than it detrains. This requires characterizing the development of the core.

The radiometric response during the convective growth is shown with the time evolution of Tb$_{183.3}$, Tb$_{325.1}$, and Tb$_{457.8}$ (**Figure 5**). The channels shown here are have the largest sensitivity to IWP, as discussed in **Section 3**. They are in the band center for the 183 and 325 GHz bands and in the wing for the 448 GHz band. In addition, the green solid line shows the area where deep convection is detected using the band-depending criterion defined in **Section 3**, while the green dashed line shows the convective core area detected using another band-depending criterion. The radiometric response during the convective growth is shown at the simulation scale (here, 1 km) to study the Tb response to the change in IWP and dIWP/dt.

Regardless of the band and the time, each Tb image is characterized by minimum and larger values around. As expected from the effect of microwave scattering by ice, the Tb minimum is found at the location of the IWP maximum. Except at 3h04, it is located at the core center. The decrease of Tb with respect to the highest value outside the core is between −50 K and −90 K depending on the band, with the lowest value for the 325.1 GHz channel. Since this decrease is due to the ice scattering effect, the size of the area where Tb changes is similar to that encompassed by the IWP (**Figure 4**).

The area size where Tb changes is larger for the 325.1 GHz channel than for the 183.3 GHz channel. This can be explained by a combination of two effects. First, the scattering of Tb by the small ice is stronger at higher frequencies. Second, the dominant process in horizontal ice advection is detrainment at the top of the cloud where the small ice portion is important in the solid–water composition (anvil formation). This explanation does not apply to the 457.8 GHz channel. Indeed, a wing channel, here for the 448 GHz band, has a low sensitivity for Tb to the change of water vapor, thus ice.

A requirement for inferring VIM from satellite observations is to locate the growing convective core using Tbs. In the geophysical space, the criterion for a growing convective core is the co-location of the largest IWP and the largest dIWP/dt. In the radiometric space, it results in the co-location of the lowest Tb and the lowest dTb/dt (green dashed line in **Figure 5**). The combination of these two conditions leads to a growing convective core correctly found at 3h06 and 3h08 for CC-H in the center of the image. At 3h10, the convective core is no longer growing. Therefore, the location of the lowest Tb differs from the location of the lowest dTb/dt.

The relationship between geophysical and radiometric variables is examined for CC-H during its entire growth from 3h02 to 3h12 using scatter plots for the three selected channels (**Figure 6**). The color code shows the horizontal distance to the core.

In the core, VIM increases with decreasing dTb/dt up to a value close to 500 kg m^{-1} s^{-1} whatever the channel. The same is true for dIWP/dt up to 60 g m^{-2} s^{-1}. This growth phase is characterized by dIWP/dt values higher than that of IADV$_h$. Once VIM reaches 500 kg m^{-1} s^{-1} (at 3h10 as shown in **Figure 5**),

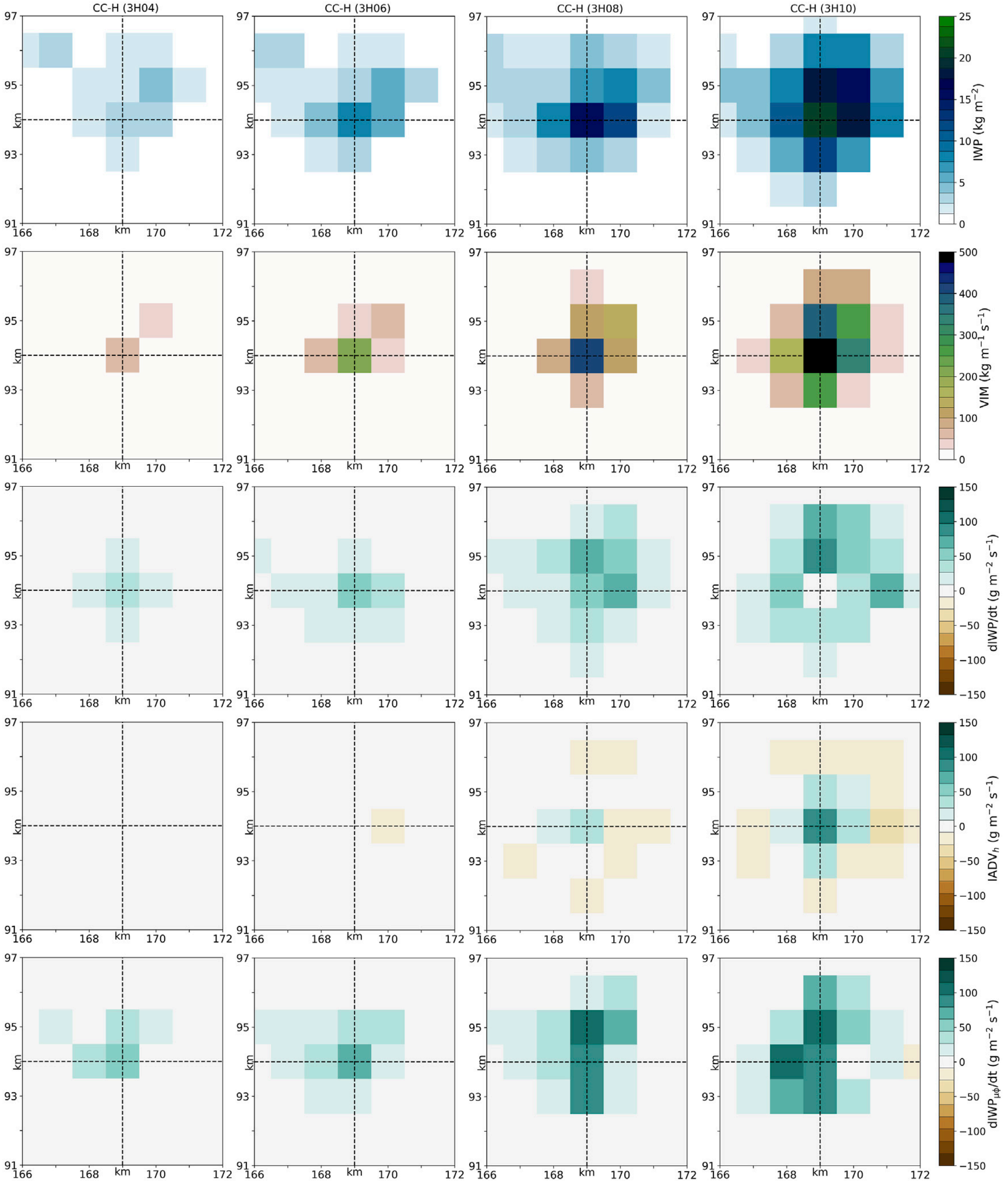

FIGURE 4 | Horizontal cross section of IWP, VIM, dIWP/dt, IADV$_h$, and dIWP$_{\mu\phi}$/dt (from top to bottom) at four times spaced 2-min apart (from left to right) during the growth of CC-H (HEC simulation). The crossing of the dashed lines locates the core of CC-H.

the growth rate of IWP is reduced to values well below IADV$_h$. The relationship between VIM and dTb/dt breaks down: VIM no longer varies with dTb/dt.

In the anvil, the relation between dTb/dt and the geophysical variables depends on the distance to the core. Many grid points closest to the core (in the greenish color) show values of VIM and dIWP/dt as large as in the core. This suggests that the core could be defined in more than one grid point. Further away from the core, VIM remains below 200 kg m^{-1} s^{-1} at two grid points and even close to zero at three grid points. In other words, negative values of dTb/dt can correspond to zero VIM. If dIWP/dt can have high values as in the core, it is partly due to ice advection as shown by the negative values of IADV$_h$. Note that, regardless of the process affecting IWP, the scatter plots show an increase in dIWP/dt with decreasing dTb/dt.

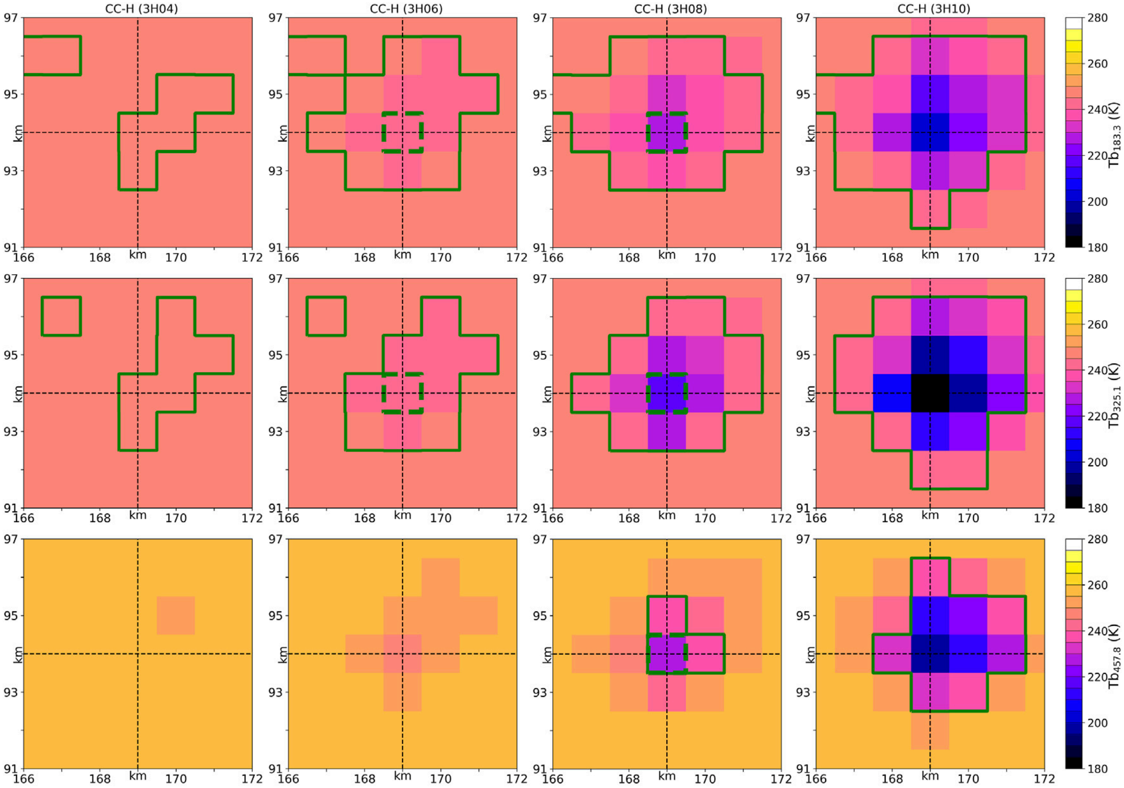

FIGURE 5 | same as in **Figure 4** but for Tb at 183.3, 325.1, and 457.8 GHz. The green solid line shows the boundary where the deep convection criterion is satisfied and the dashed line where the growing convective core criterion is satisfied.

4.3 Tb Response to Ice Change for Convective Cells in the Growing Phase

The Tb response to ice change for the three selected channels is shown for all selected convective cells in HEC and RCE (**Figure 7**). The core and surrounding grid points are examined, that is, a total of 5 × 5 grid points. Because of different grid spacing, the area covers 25 km^2 for HEC and 225 km^2 for RCE. This makes the implicit assumption that the response of Tb to ice change varies independently of resolution. The points are shaded according to their distance to the core, with color when the growing convective core criterion is satisfied, with grey otherwise.

VIM shows a large dispersion of positive values, up to more than 1000 $\mathrm{kg\,m^{-1}\,s^{-1}}$. It is always positive because the convective cells are in their growth phase. No apparent dependence of VIM on dTb/dt can be found, except for growing convective cores. In the latter case, VIM increases quite linearly with decreasing dTb/dt regardless of the channel. As with VIM, dIWP/dt shows a near-linear dependence on dTb/dt for convective cores. But unlike VIM, the smaller dispersion of dIWP/dt with dTb/dt suggests that their relationship may also be valid outside of convective cores.

It is interesting to note that the range of values of IADV_h is similar to that of dIWP/dt. This confirms that the change in IWP can be explained by ice detrainment (or entrainment) alone and not necessarily by ice production in an updraft (or ice loss in a downdraft). The large scatter of the points suggests the difficulty of inferring such quantity using dTb/dt information. However, a near-linear relationship between IADV_h and dTb/dt exists for convective cores. This suggests that inferring IADV_h might be possible for convective cores, as it might be for VIM.

5 STUDY OF THE FULL DATA SET

The relationships between geophysical and satellite variables are now explored over the full data set. The objective is to examine whether these relationships previously found for 10 convective cells in the growth phase in a surrounding environment free of icy hydrometeors are robust regardless of the time in the deep convection life cycle, for the two tropical cases examined here. In order to provide guidance for the design of the satellite tandem, these relationships are examined for time delays ranging from 30 s to 3 min and for two horizontal resolutions, the one of the simulations and the pixel resolution of 6 km. The delay range is in the order of magnitude of what can be expected. The 6-km resolution corresponds to the largest pixel size expected for C2OMODO,

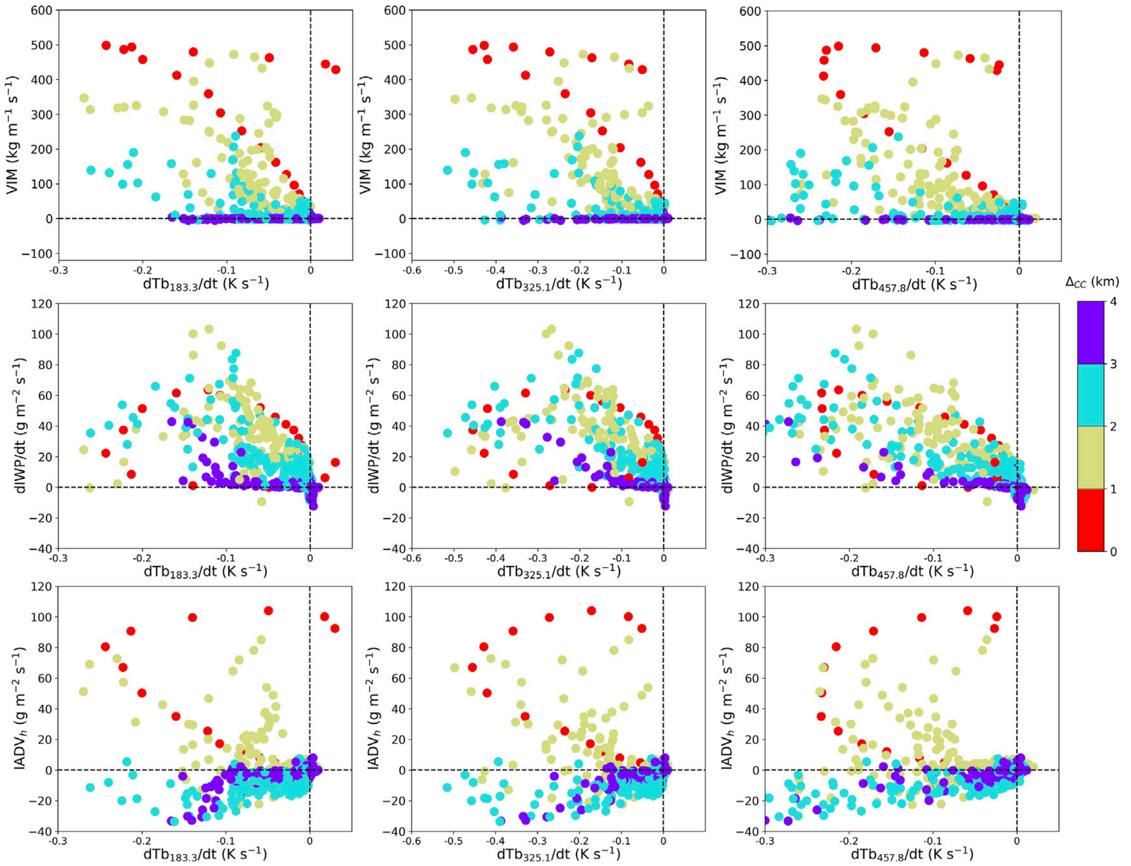

FIGURE 6 | Scatter plot of VIM, dIWP/dt, and IADV$_h$(from top to bottom) vs. dTb/dt using a 1-min interval for the 183.3, 325.1, and 457.8 GHz channels (from left to right) for CC-H (3h02 to 3h12). The color code indicates the horizontal distance to the convective core.

that is, the 183 GHz band, while finer resolution is expected for the higher MW frequency bands. Outputs at 6-km resolution are obtained after linear interpolation of the simulation outputs.

The data set is about 10 million columns for HEC and 30 millions for RCE at the resolution of the simulations. The icy situations defined by IWP > 1 kg m^{-2} represent 8.9 and 6.5% of the HEC and RCE outputs, respectively. A part of these icy situations corresponds to cases for which the associated Tb change is weak. These situations are filtered out considering a radiometric uncertainty in Tb change $|$ dTb/dt $| \leq 0.017$ K s^{-1} whatever the MW frequency. The value of this threshold is arbitrarily fixed at a realistic value equivalent to an uncertainty of 1 K for a delay time of 1 min of the satellite tandem. It can be considered as the best possible scenario because it does not take into account the errors due to intercalibration and geolocation between the two radiometers. It gives an order of magnitude assuming a noise level of 0.707 K on the Tb measurements. A doubling of this noise level would double the value of the threshold, while a doubling of the delay would half it. This leaves the icy situations with $|$ dTb/dt $| > 0.017$ K s^{-1} accounting for 4.4 ± 1.7% and 1.0 ± 0.4% (as a function of the MW frequency) of the HEC and RCE outputs, respectively.

5.1 Relationship Between the Time Derivatives of IWP and Tb

The relationship between the time derivatives of IWP and Tb is examined for all the grid points satisfying the deep convection criterion. The goal is to determine whether the quasi-linear relationship between the time derivatives of IWP and Tb found for convective cells in the growing phase is valid for all these grid points. As defined in **Section 3**, the deep convection criterion is designed for detecting icy situations. It changes with MW frequency, that is, Tb$_{183.3}$-Tb$_{193.1}$ > -5 K, Tb$_{325.1}$-Tb$_{334.9}$ $>$ 5 K, and Tb$_{448.0}$-Tb$_{457.8}$ > -25 K. After filtering out the icy situations with $|$ dTb/dt $| \leq 0.017$ K s^{-1}, the grid points satisfying the deep convection criterion account for 84 ± 4% and 86 ± 9% (as a function of the MW frequency) of the icy situations of the HEC and RCE simulations, respectively. There are between 4×10^4 and 5×10^5 grid points depending on the frequency and case and show a quasi-Gaussian distribution of dIWP/dt as a function of change in Tb.

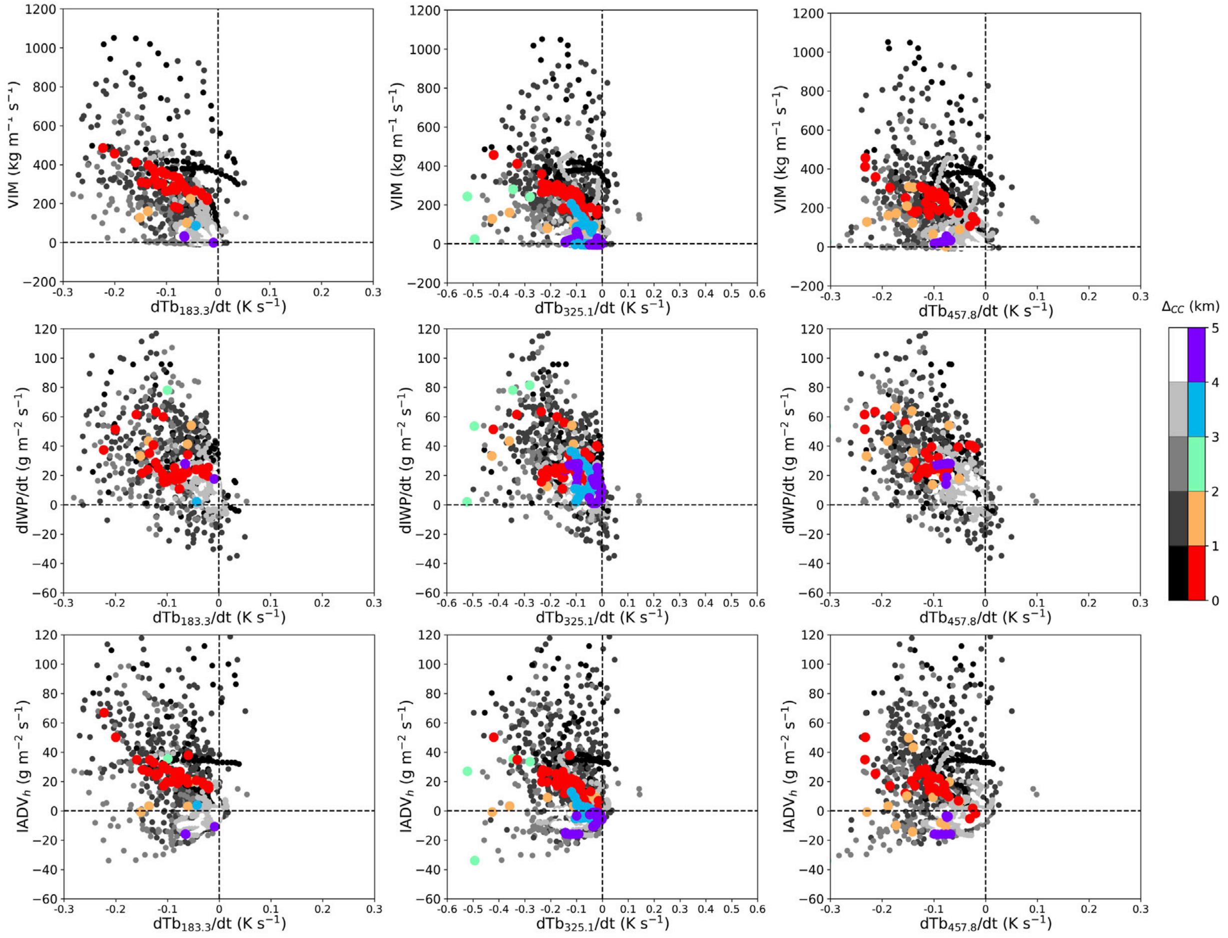

FIGURE 7 | Same as **Figure 6** for the selected convective cells in HEC and RCE.

The distribution of dIWP/dt vs. dTb/dt is examined with a delay time of 1 min for the selected channels (**Figure 8**). For each 0.02 K s^{-1} bin of dTb/dt, the median, the interquartile values of dIWP/dt and the least squares regression (for negative values of dTb/dt) are calculated and shown at both the horizontal resolution of the simulations and at a linearly interpolated 6-km pixel resolution. Overall, dIWP/dt is a monotonically decreasing function of dTb/dt whatever the resolution and the MW frequency. The absolute value of the slope of the regression line is about 100 g m^{-2} K^{-1} for the 325.1 GHz channel and 150–200 g m^{-2} K^{-1} for the 183.3 and 457.8 GHz channels. These differences in slope between the frequencies are mainly explained by differences in atmospheric opacity due to water vapor. At the horizontal resolution of the simulations, the slope differs between the two tropical cases. The agreement in the slope between the cases is better at the 6-km resolution, and the interquartile range is reduced. Note that, regardless of channel and resolution, the range of dTb/dt is much wider than that of the radiometric uncertainty of 0.017 K s^{-1} considered here. These results suggest that dIWP/dt, at least its largest values, can be estimated such as a linear function of dTb/dt using a delay time of 1 min.

The sensitivity of the relationship of dIWP/dt with dTb/dt to delay time is examined at both resolutions. The results are summarized by showing the absolute value of the slope dIWP/dt as a function of dTb/dt for the 183.3, 325.1, and 457.8 GHz channels, at both resolutions (**Figure 9**). At the horizontal resolution of the simulations, the absolute value of the slope is higher for RCE than for HEC regardless of frequency and time delay. It increases with time delay. At the 6-km resolution, except for the 3-min delay, these differences disappear. For each frequency, the absolute value of the slope is similar between the tropical case and the time delay. In other words, these results suggest that the change in IWP can be inferred for tropical conditions at 6-km resolution using the C2OMODO concept.

5.2 Relationship Between the Vertical Ice Velocity and the Time Derivative of Tb

The relationship between w_{ice} and the time derivative of Tb is examined. The dynamical variable w_{ice} defined as VIM divided by IWP is preferred to VIM as its unit in m s^{-1} is the most familiar. Note that, the results shown below for w_{ice} are similar to those obtained for VIM. As with the growing cells in **Section 4.3**, the results are examined for grid points verifying the growing convective core criterion. The latter is defined as the co-location of the lowest Tb

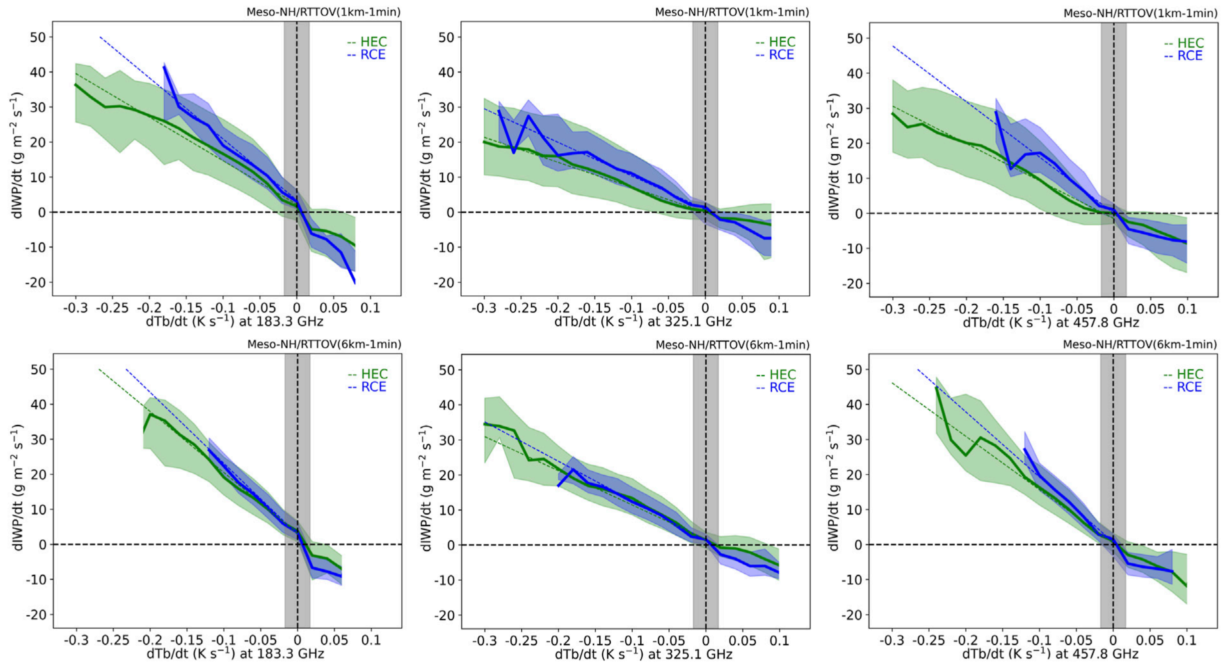

FIGURE 8 | dIWP/dt as a function of dTb/dt for the 183.3, 325.1, and 457.8 GHz channels (from left to right) at the horizontal resolution of the simulations (top) and at a linearly interpolated 6-km pixel resolution (bottom). The time delay of the satellite tandem is 1 min. The bin interval is 0.02 K s^{-1}. The median (bold lines), the interquartile range (shadings), and the least squares regression (dashed lines) are shown for HEC (green) and RCE (blue). The grey band delimits a dTb/dt uncertainty of 0.017 K s^{-1}, corresponding to a 1 K uncertainty in the Tb measurement for a 1-min delay in the satellite tandem. Results are shown for grid points verifying the deep convection criterion.

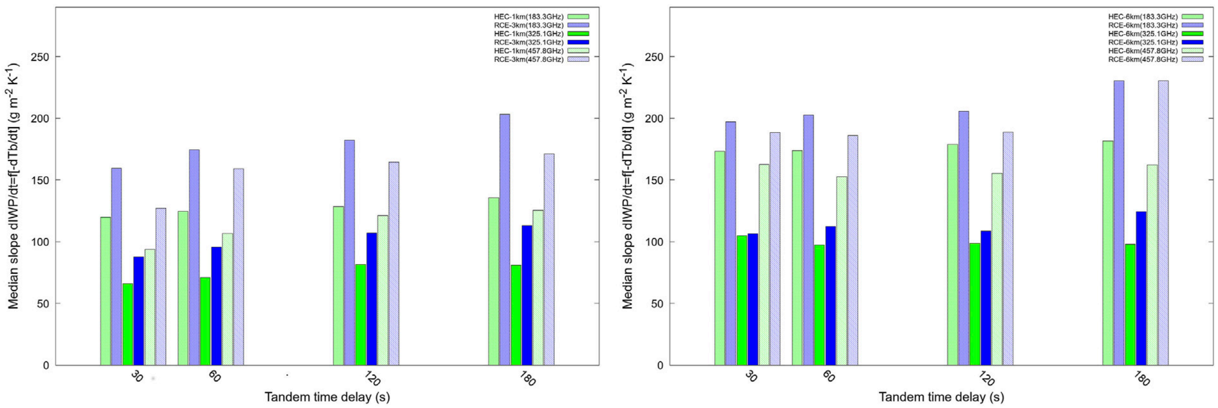

FIGURE 9 | Slope of dIWP/dt as a function of dTb/dt for the 183.3, 325.1, and 457.8 GHz channels at the horizontal resolution of the simulations (left) and at a linearly interpolated 6-km pixel resolution (right). The time delay of the satellite tandem ranges from 30 s to 3 min. Results are shown for grid points verifying the deep convection criterion.

and the lowest dTb/dt. Since the convective core produces most of the ice, the IWP and its variation within a convective core are statically larger than those in its surroundings. The lowest Tb condition looks for convective cores and the lowest dTb/dt condition for the most intense activity of the growing convective cores. The grid points satisfying the growing core criterion represent 1.6 ± 1.0% and 2.1 ± 1.4% (depending on the MW frequency) of the HEC and RCE icy situations with | dTb/dt | > 0.017 K s^{-1}. They are between 10^3 and 10^4 points depending on the frequency and case and show a quasi-Gaussian distribution of w_{ice} as a function of change in Tb.

Figure 10 shows the distribution of w_{ice} versus dTb/dt with a delay time of 1 min for the two resolutions and the three selected channels. The larger and more active the convective core, the more ice it is able to produce and transport vertically. The lowest dTb/dt

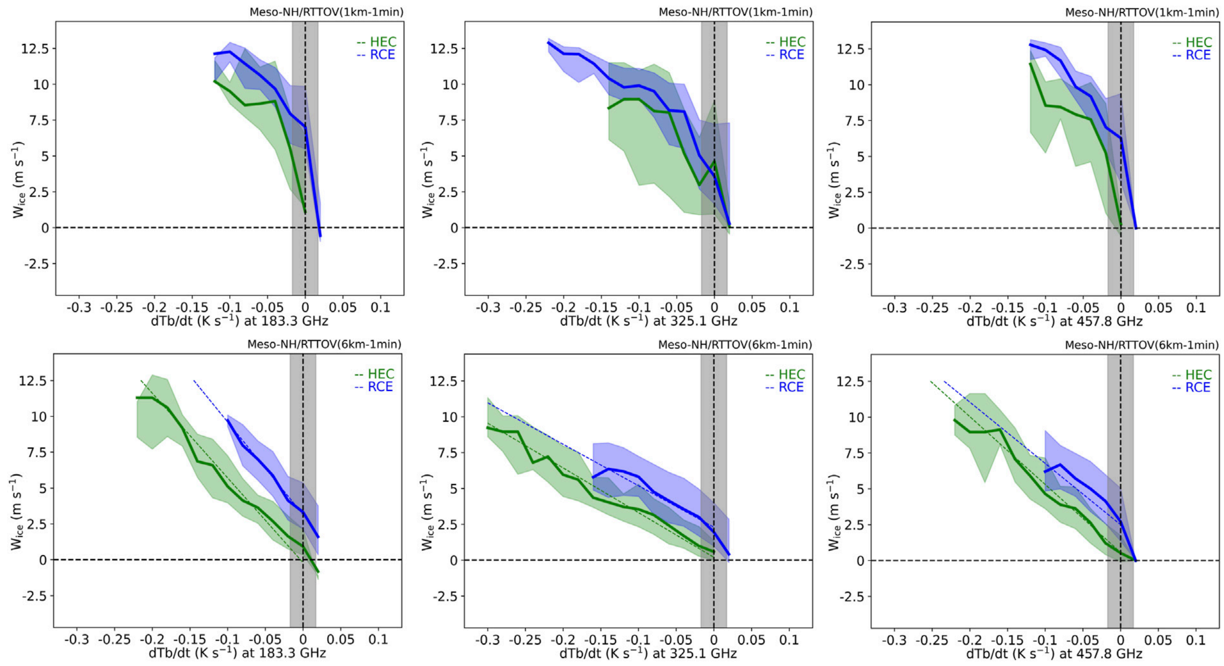

FIGURE 10 | Same as **Figure 8** but for w_{ice}. Results are shown for grid points verifying the growing core criterion. The least squares regressions (dashed lines) are shown for the 6-km resolution only.

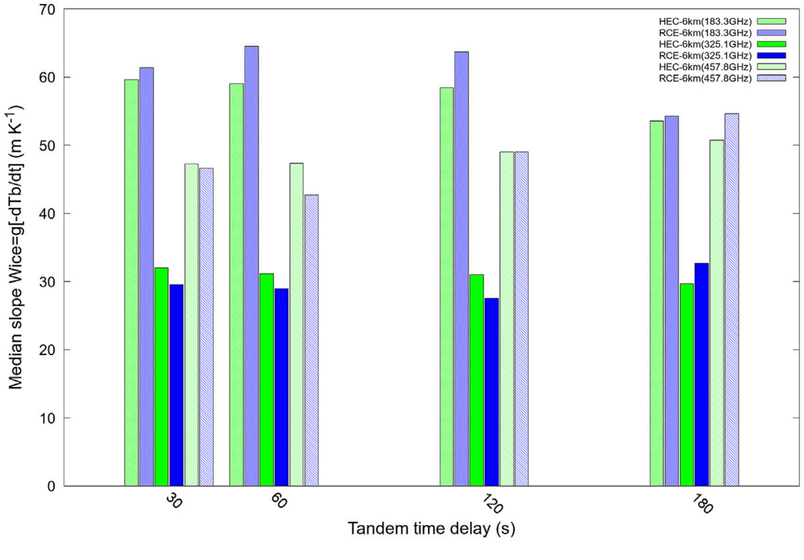

FIGURE 11 | Same as **Figure 9** but for w_{ice} at the 6-km resolution. Results are shown for grid points verifying the growing convective core criterion.

values between −0.2 and −0.1 K s^{-1} correspond to the highest convective velocity (~10 m s^{-1}). For the 183.3 and 457.8 GHz channels, this minimum value is equal to −0.1 K s^{-1}, which is only about five times larger than the radiometric uncertainty of 0.017 K s^{-1}. This highlights the need for a small noise level if one wants to infer w_{ice} with the C2OMODO concept. A weak dependence on the tropical case is found. Only the 6-km resolution suggests a near-linear relation between w_{ice} and dTb/dt.

The sensitivity of the slope to time delay is studied for the range between 30 s and 3 min at the 6-km resolution. **Figure 11** shows the absolute value of the slope as a function of the MW frequency and the tropical case. Its value depends weakly on the delay time but varies a lot with the MW frequency. It is equal to about 30 m K^{-1} for the 325.1 GHz channel and 50–60 m K^{-1} for the 183.3 and 457.8 GHz channels. The variation of the slope with MW frequency is similar to that found for dIWP/dt, suggesting a link between the changes in

IWP and w_{ice}. Overall, these results suggest that w_{ice} could be inferred in the growing convective cores from the C2OMODO concept.

6 CONCLUSION

A data set is built to study the feasibility of the C2OMODO concept. This concept relies on the dependence of some microwave observations of the ice content and on the assumption that a short time delay in the microwave observation of deep convective systems would inform the time derivative of ice content, hence the vertical velocity in the updrafts. The data set is based on the two kilometer-scale simulations of tropical cases, one over land and the other over ocean. The relationship between Tbs at the wing and center of the 183, 325, and 448 GHz bands and some 2D variables characterizing ice content and convective updrafts has been examined as well as their dependence on horizontal resolution and delay. It is shown that IWP and dIWP/dt can be inferred in all deep convective scenes while w_{ice} and VIM in growing convective cores only. It is explained that the relationship w_{ice} and VIM breaks down in the anvil due to the dominance of horizontal ice advection over microphysical processes.

The relationship between geophysical and satellite variables is first studied for deep convective condition. The latter is defined as an atmospheric column in which the IWP exceeds a threshold of 1 kg m^{-2}. In the radiometric space, this criterion translates into the difference in Tb between the wing and the center of the band above a threshold that differs between the three bands considered here. This highlights the difference in sensitivity of the bands to ice change. It can be seen that the 183 and 325 GHz bands are sensitive to IWP up to 40 kg m^{-2}, while the 448 GHz band is sensitive to larger IWP values. Because the time change in IWP may depend more on horizontal advection of ice than on ice production in the updraft, the relationship is then studied for the growing convective cores. The latter is defined as the co-location of the local minimum in Tb and the local minimum in dTb/dt.

The time variation of IWP shows a near-linear relationship with dTb/dt for the center band channels at the 183 and 325 GHz bands and the wing channel of the 448 GHz band. This relationship is valid for both deep convection and growing convective core conditions. It is also robust to grid spacing and time delay, at least those studied here, that is, from 1 to 6 km and from 30 s to 3 min. These results suggest that the time variation of IWP could be easily inferred using the C2OMODO concept.

Two variables related to vertical velocity are examined: the vertical ice momentum VIM and the vertical ice velocity w_{ice}, defined as VIM divided by IWP. Both are found to increase with decreasing dTb/dt. This relationship is obtained for convective growing core condition only. Another limitation is that the relationship is not linear, with a slope that differs between the oceanic and continental cases. This disagreement in slope may be due to the difference in grid resolution between the two simulations. This aspect deserves further investigation.

We conclude that a stand-alone use of microwave observations using the C2OMODO concept to retrieve dIWP/dt, w_{ice} and VIM would be possible. First, we used only pseudo-observations to state the convective development: 1) deep convection scenes detected by the difference in Tb between the wing and the center of the band above a fixed threshold and 2) growing convective cores defined as the co-localization of the local minimum of Tb and the local minimum of dTb/dt. Second, we showed the existence of the relationships between dIWP/dt, w_{ice}, VIM, and dTb/dt.

The conclusions drawn here are based on two tropical cases only. Other cases should be investigated in addition to these two. At the time of writing, the C2OMODO radiometers would also cover mid-latitude areas. Future study will address a larger data set. Also note that the simulations are performed with a particular microphysics scheme of a convection-permitting model combined with a radiative transfer model, here Meso-NH combined with RTTOV. It is of interest to investigate the robustness of the relationships found here, at least for mid-latitude conditions, a different microphysics scheme, and a different radiative transfer model. Future study will be conducted to test the sensitivity of these relationships to the optical properties of frozen hydrometeors using the new capabilities offered by RTTOV (Geer et al., 2021).

Another aspect worth studying is the use of hyper-spectral information. Depending on their sensitivity to water absorption, the 50 channels in a band probe the atmosphere at different altitudes. This information should make it possible to deduce the vertical structure of IWP and, hence, of dIWP/dt. This would be also useful for retrieving VIM or w_{ice} in part of the atmospheric column. As a pure demonstration, Brogniez et al. (2022) showed that the VIM can be retrieved from Tbs. They found that the maximum vertical velocity within a convective column can be estimated with low error, especially for high velocities. More information on the C2OMODO concept and its possibilities, including promising synergies if a Doppler radar is aligned with the microwave radiometer tandem, is given by Brogniez et al. (2022).

DATA AVAILABILITY STATEMENT

The raw data supporting the conclusions of this article will be made available by the authors, without undue reservation.

AUTHOR CONTRIBUTIONS

J-PC conceptualized the study and designed the computational framework. FA analyzed the numerical data. All authors discussed the results and contributed to the final manuscript.

FUNDING

This work was supported under the AOS (Atmosphere Observing System) program and funded by the CNES (Centre National d'Etudes Spatiales, Toulouse, France).

ACKNOWLEDGMENTS

Computer resources were allocated by GENCI through Project 90569. The authors thank the CNES and the C2OMODO working group: H. Brogniez and A. Dépée (LATMOS, Paris, France), R. Roca and T. Fiolleau (LEGOS, Toulouse, France), and D. Bouniol (CNRM, Toulouse, France). We thank the reviewers for their comments, which helped to improve the overall quality of the study.

REFERENCES

Brogniez, H., Roca, R., Auguste, F., Chaboureau, J.-P., Haddad, Z., Munchak, S. J., et al. (2022). Time-delayed Tandem Microwave Observations of Tropical Deep Convection: Overview of the C2OMODO mission. *Front. Remote Sens*. n/a, accepted. doi:10.3389/frsen.2022.854735

Chaboureau, J.-P., Cammas, J.-P., Mascart, P., Pinty, J.-P., Claud, C., Roca, R., et al. (2000). Evaluation of a Cloud System Life-Cycle Simulated by the Meso-NH Model during FASTEX Using METEOSAT Radiances and TOVS-3I Cloud Retrievals. *Q.J.R. Meteorol. Soc.* 126, 1735–1750. doi:10.1002/qj.49712656609

Chaboureau, J.-P., Söhne, N., Pinty, J.-P., Meirold-Mautner, I., Defer, E., Prigent, C., et al. (2008). A Midlatitude Precipitating Cloud Database Validated with Satellite Observations. *J. Appl. Meteorol. Climatol.* 47, 1337–1353. doi:10.1175/2007JAMC1731.1

Colella, P., and Woodward, P. R. (1984). The Piecewise Parabolic Method (PPM) for Gas-Dynamical Simulations. *J. Comput. Phys.* 54, 174–201. doi:10.1016/0021-9991(84)90143-8

Cuxart, J., Bougeault, P., and Redelsperger, J.-L. (2000). A Turbulence Scheme Allowing for Mesoscale and Large-Eddy Simulations. *Q.J R. Met. Soc.* 126, 1–30. doi:10.1002/qj.49712656202

Dauhut, T., Chaboureau, J. P., Escobar, J., and Mascart, P. (2015). Large-eddy Simulations of Hector the Convector Making the Stratosphere Wetter. *Atmos. Sci. Lett.* 16, 135–140. doi:10.1002/asl2.534

Field, P. R., Heymsfield, A. J., and Bansemer, A. (2007). Snow Size Distribution Parameterization for Midlatitude and Tropical Ice Clouds. *J. Atmos. Sci.* 64, 4346–4365. doi:10.1175/2007JAS2344.1

Fouquart, Y., and Bonnel, B. (1986). Computations of Solar Heating of the Earth's Atmosphere: A New Parametrization. *Beitr. Phys. Atmos.* 53, 35–62.

Funatsu, B. M., Claud, C., and Chaboureau, J.-P. (2007). Potential of Advanced Microwave Sounding Unit to Identify Precipitating Systems and Associated Upper-Level Features in the Mediterranean Region: Case Studies. *J. Geophys. Res.* 112, D17113. doi:10.1029/2006JD008297

Geer, A. J., Bauer, P., Lonitz, K., Barlakas, V., Eriksson, P., Mendrok, J., et al. (2021). Bulk Hydrometeor Optical Properties for Microwave and Sub-millimetre Radiative Transfer in RTTOV-SCATT v13.0. *Geosci. Model. Dev.* 14, 7497–7526. doi:10.5194/gmd-14-7497-2021

Gong, J., and Wu, D. L. (2014). CloudSat-constrained Cloud Ice Water Path and Cloud Top Height Retrievals from MHS 157 and 183.3 GHz Radiances. *Atmos. Meas. Tech.* 7, 1873–1890. doi:10.5194/amt-7-1873-2014

Lac, C., Chaboureau, J.-P., Masson, V., Pinty, J.-P., Tulet, P., Escobar, J., et al. (2018). Overview of the Meso-NH Model Version 5.4 and its Applications. *Geosci. Model. Dev.Model Dev.* 11, 1929–1969. doi:10.5194/gmd-11-1929-2018

Liebe, H. J., Manabe, T., and Hufford, G. A. (1989). Millimeter-wave Attenuation and Delay Rates Due to Fog/cloud Conditions. *IEEE Trans. Antennas Propagat.* 37, 1617–1612. doi:10.1109/8.45106

Liu, G. (2008). A Database of Microwave Single-Scattering Properties for Nonspherical Ice Particles. *Bull. Amer. Meteorol. Soc.* 89, 1563–1570. doi:10.1175/2008BAMS2486.1

Masson, V., Le Moigne, P., Martin, E., Faroux, S., Alias, A., Alkama, R., et al. (2013). The surfexv7.2 Land and Ocean Surface Platform for Coupled or Offline Simulation of Earth Surface Variables and Fluxes. *Geosci. Model. Dev.* 6, 929–960. doi:10.5194/gmd-6-929-2013

Matzler, C., and Wegmuller, U. (1987). Dielectric Properties of Freshwater Ice at Microwave Frequencies. *J. Phys. D: Appl. Phys.* 20, 1623–1630. doi:10.1088/0022-3727/20/12/013

Meirold-Mautner, I., Prigent, C., Defer, E., Pardo, J. R., Chaboureau, J.-P., Pinty, J.-P., et al. (2007). Radiative Transfer Simulations Using Mesoscale Cloud Model Outputs: Comparisons with Passive Microwave and Infrared Satellite Observations for Midlatitudes. *J. Atmos. Sci.* 64, 1550–1568. doi:10.1175/jas3896.1

Mlawer, E. J., Taubman, S. J., Brown, P. D., Iacono, M. J., and Clough, S. A. (1997). Radiative Transfer for Inhomogeneous Atmospheres: RRTM, a Validated Correlated-K Model for the Longwave. *J. Geophys. Res.* 102, 16663–16682. doi:10.1029/97JD00237

Pergaud, J., Masson, V., Malardel, S., and Couvreux, F. (2009). A Parameterization of Dry Thermals and Shallow Cumuli for Mesoscale Numerical Weather Prediction. *Boundary-layer Meteorol.* 132, 83–106. doi:10.1007/s10546-009-9388-0

Pinty, J.-P., and Jabouille, P. (1998). "A Mixed-phase Cloud Parameterization for Use in a Mesoscale Non-hydrostatic Model: Simulations of a Squall Line and of Orographic Precipitations," in *Conference on Cloud Physics* (Everett, WA: American Meteorological Society), 217–220.

Rosenkranz, P. W. (2015). A Model for the Complex Dielectric Constant of Supercooled Liquid Water at Microwave Frequencies. *IEEE Trans. Geosci. Remote Sensing* 53, 1387–1393. doi:10.1109/TGRS.2014.2339015

Rysman, J.-F., Claud, C., Chaboureau, J.-P., Delanoë, J., and Funatsu, B. M. (2016). Severe Convection in the Mediterranean from Microwave Observations and a Convection-Permitting Model. *Q.J.R. Meteorol. Soc.* 142, 43–55. doi:10.1002/qj.2611

Rysman, J.-F., Claud, C., and Dafis, S. (2021). Global Monitoring of Deep Convection Using Passive Microwave Observations. *Atmos. Res.* 247, 105244. doi:10.1016/j.atmosres.2020.105244

Saunders, R., Hocking, J., Turner, E., Rayer, P., Rundle, D., Brunel, P., et al. (2018). An Update on the RTTOV Fast Radiative Transfer Model (Currently at Version 12). *Geosci. Model. Dev.* 11, 2717–2737. doi:10.5194/gmd-11-2717-2018

Varble, A., Zipser, E. J., Fridlind, A. M., Zhu, P., Ackerman, A. S., Chaboureau, J.-P., et al. (2014). Evaluation of Cloud-Resolving and Limited Area Model Intercomparison Simulations Using TWP-ICE Observations: 1. Deep Convective Updraft Properties. *J. Geophys. Res. Atmos.* 119, 13,891–13,918. doi:10.1002/2013JD021371

Wiedner, M., Prigent, C., Pardo, J. R., Nuissier, O., Chaboureau, J.-P., Pinty, J.-P., et al. (2004). Modeling of Passive Microwave Responses in Convective Situations Using Output from Mesoscale Models: Comparison with TRMM/TMI Satellite Observations. *J. Geophys. Res.* 109, n/a. doi:10.1029/2003JD004280

Wing, A. A., Stauffer, C. L., Becker, T., Reed, K. A., Ahn, M. S., Arnold, N. P., et al. (2020). Clouds and Convective Self Aggregation in a Multimodel Ensemble of Radiative-Convective Equilibrium Simulations. *J. Adv. Model. Earth Syst.* 12, e2020MS002138. doi:10.1029/2020MS002138

Conflict of Interest: The authors declare that the research was conducted in the absence of any commercial or financial relationships that could be construed as a potential conflict of interest.

frontiers | Frontiers in Remote Sensing

ORIGINAL RESEARCH
published: 08 April 2022
doi: 10.3389/frsen.2022.860284

Mind the Gap - Part 3: Doppler Velocity Measurements From Space

Pavlos Kollias [1,2,3]*, ***Alessandro Battaglia*** [4,5], ***Katia Lamer*** [2], ***Bernat Puigdomenech Treserras*** [3] ***and Scott A. Braun*** [6]

[1]Division of Atmospheric Sciences, Stony Brook University, Stony Brook, NY, United States, [2]Environmental and Climate Sciences Department, Brookhaven National Laboratory, Upton, NY, United States, [3]Department of Atmospheric and Oceanic Sciences, McGill University, Montreal, QC, Canada, [4]Department of Environment, Land and Infrastructure Engineering, Politecnico of Torino, Turin, Italy, [5]Physics and Astronomy Department, University of Leicester, Leicester, United Kingdom, [6]NASA Goddard Space Flight Center, Greenbelt, MD, United States

Convective motions and hydrometeor microphysical properties are highly sought-after parameters for evaluating atmospheric numerical models. With most of Earth's surface covered by water, space-borne Doppler radars are ideal for acquiring such measurements at a global scale. While these systems have proven to be useful tools for retrieving cloud microphysical and dynamical properties from the ground, their adequacy and specific requirements for spaceborne operation still need to be evaluated. Comprehensive forward simulations enable us to assess the advantages and drawbacks of six different Doppler radar architectures currently planned or under consideration by space agencies for the study of cloud dynamics. Radar performance is examined against the state-of-the-art numerical model simulations of well-characterized shallow and deep, continental, and oceanic convective cases. Mean Doppler velocity (MDV) measurements collected at multiple frequencies (13, 35, and 94 GHz) provide complementary information in deep convective cloud systems. The high penetration capability of the 13 GHz radar enables to obtain a complete, albeit horizontally under-sampled, view of deep convective storms. The smaller instantaneous field of view (IFOV) of the 35 GHz radar captures more precise information about the location and size of convective updrafts above 5–8 km height of most systems which were determined in the portion of storms where the mass flux peak is typically located. Finally, the lower mean Doppler velocity uncertainty of displaced phase center antenna (DPCA) radars makes them an ideal system for studying microphysics in shallow convection and frontal systems, as well as ice and mixed-phase clouds. It is demonstrated that a 94 GHz DCPA system can achieve retrieval errors as low as 0.05–0.15 mm for raindrop volume-weighted mean diameter and 25% for rime fraction (for a −10 dBZ echo).

Keywords: radar, convection, satellite, remote sensing, Doppler

Edited by:
Jens Redemann,
University of Oklahoma, United States

Reviewed by:
David Painemal,
Science Systems and Applications, Inc., United States
Federico Fierli,
European Organisation for the Exploitation of Meteorological Satellites, Germany

Correspondence:
Pavlos Kollias
pavlos.kollias@stonybrook.edu

Specialty section:
This article was submitted to Satellite Missions, a section of the journal Frontiers in Remote Sensing

Received: *22 January 2022*
Accepted: *11 March 2022*
Published: *08 April 2022*

Citation:
Kollias P, Battaglia A, Lamer K, Treserras BP and Braun SA (2022) Mind the Gap - Part 3: Doppler Velocity Measurements From Space. Front. Remote Sens. 3:860284. doi: 10.3389/frsen.2022.860284

1 INTRODUCTION

Improvements in weather and forecast models require thorough understanding of processes occurring in cloud and precipitation systems (Zelinka et al., 2017; Satoh et al., 2018). An accurate representation of cloud-scale dynamics and hydrometeor fall velocities is an important step toward understanding these processes. Convective clouds serve as a primary mechanism for the transfer of thermal energy, moisture, and momentum through the troposphere, significantly impacting the large-scale atmospheric circulation and local environment and also affecting the probability of subsequent cloud formation (Hartmann et al., 2018; Gasparini et al., 2021). Furthermore, several different assumptions for hydrometeor terminal fall velocities are used for different processes in models whether in large-scale parameterized clouds and precipitation (vanZanten et al., 2011). Climate models are very sensitive to the specification of fall speeds. For example, Sanderson et al., 2008 found that the ice fall speed was the second most important parameter for determining climate sensitivity. A decrease in the fall velocity of ice crystals can affect upper tropospheric water vapor amounts (Mitchell and Finnegan, 2009) while changes to the fall velocity of raindrops can induce changes in the evaporation rate and hence affect the temperature structure in the lower part of the atmosphere (vanZanten et al., 2011).

Despite their importance, there are considerable measurement gaps in convective updrafts and hydrometeor fall velocities. These gaps limit our ability to constrain these important aspects of model parameterization and verification. Observations of the number and magnitude of updrafts contributing to vertical transport in deep convection are not available over the tropical oceans and are rarely available over land. Measuring convective motions from surface-based observatories remains challenging owing to a shortage of profiling sensors and the shortcoming of multi-Doppler radar retrievals (Oue et al., 2021). On the other hand, surface-based observatories can provide high-quality, long-term records of hydrometeor fall velocities (Kalesse and Kollias, 2013); however, such measurements are sparse in the southern hemisphere and over the oceans.

Spaceborne Doppler radar observations can offer global observations of Doppler velocities, thus providing an unprecedented opportunity to help constrain weather and climate models (Battaglia et al., 2020a). The *Earth Cloud Aerosol and Radiation Explorer* (EarthCARE) satellite is a joint European Space Agency (ESA) and Japanese Aerospace Exploration Agency (JAXA) mission scheduled to launch in 2023. EarthCARE (EC) will host the first 94-GHz Doppler cloud profiling radar (CPR) in space (Illingworth et al., 2018). However, signal attenuation by hydrometeors and the presence of multiple scatters are expected to limit the ability of the EarthCARE CPR to study deep convective clouds (Kollias et al., 2018). Furthermore, the Doppler velocity measurements in large-scale precipitation regimes will be considerably impacted by the platform motion (Kollias et al., 2014).

Post-processing and spatial averaging of the EarthCARE CPR raw Doppler velocity observations are expected to reduce the uncertainty in the Doppler velocity measurements (Kollias et al., 2014). However, a different observing platform is required to address the remaining gap in convective dynamics and to provide even higher quality Doppler velocity measurements in shallow clouds and large-scale cloud and precipitation systems. These critical measurements gaps were acknowledged in the latest NASA Earth Science Decadal Survey Report (National Academies of Sciences, Engineering, and Medicine, 2018). NASA recently completed a study, known as Aerosols, Clouds, Convection, and Precipitation (ACCP), to identify candidate spaceborne architectures to pursue coupled aerosol-cloud-precipitation science in the next decade. The recommended architecture is currently being evaluated as part of NASA's Earth System Observatory (https://science.nasa.gov/earth-science/earth-system-observatory) and is named as the Atmosphere Observing System (AOS). The need for multi-frequency Doppler radar measurements were deemed critical to capturing all types of cloud and precipitation systems. Other space agencies such as JAXA and ESA are looking for future spaceborne Doppler radar missions. JAXA is currently evaluating different options for a follow-up to the NASA/JAXA Global Precipitation Measurement (GPM) Mission Dual-frequency Precipitation Radar (DPR) with a 13-GHz radar with Doppler capability and ESA recently selected *WInd VElocity Radar Nephoscope* (WIVERN, Illingworth et al., 2018), a 94-GHz conically scanning Doppler radar for additional study as part of ESA's Earth Explorer program. Finally, the explosive growth in the use of CubeSats in Earth Sciences offers ample opportunities for creative approaches on how to best monitor and investigate cloud and precipitation processes (Stephens et al., 2020).

Here, the third part of the "Mind the Gap" article series is presented. The Mind the Gap articles highlight existing gaps in satellite-based radar measurements of cloud and precipitation systems and suggest future improvements. The first Mind the Gap study (Lamer et al., 2020) focused on the challenge of detecting hydrometeors in the lowest km of the atmosphere detection due to the Earth's surface return. The Lamer et al. (2020) study highlighted the advantages of a short-pulse radar (Kollias, 2007). The second Mind the Gap study (Battaglia et al., 2020a) focused on the biases in liquid water path (LWP) estimates due to the large radar footprint and the limited sensitivity in small LWP amounts using Path Integrated Attenuation (PIA) techniques. The added value of brightness temperature (T_B) derived by adopting radiometric radar modes was investigated. The third Mind the Gap article focuses on the third large spaceborne radar measurement gap: Doppler velocity. High resolution model output and a comprehensive forward and inverse spaceborne Doppler radar simulator is used to characterize the impact of the sampling volume on the characterization of updraft and downdraft properties. Furthermore, the impact of the uncertainty in the Doppler velocity measurements on the estimation of hydrometeor mean size and density is presented. The performance of different planned spaceborne Doppler radar systems against these requirements is analyzed using state-of-the-art forward and inverse simulations. The spaceborne Doppler radar systems considered in this study operate at three different frequencies: 94, 35, and 13 GHz, thus, covering the frequency range of existing and planned spaceborne radar systems. The radar systems are also separated into two categories based on the technique they used to acquire Doppler velocity measurements from space. Three systems that employ the displaced phase center antenna (DPCA) technique that rely on two antennas strategically deployed such that their combined measurements can effectively remove the satellite motion effects on the Doppler

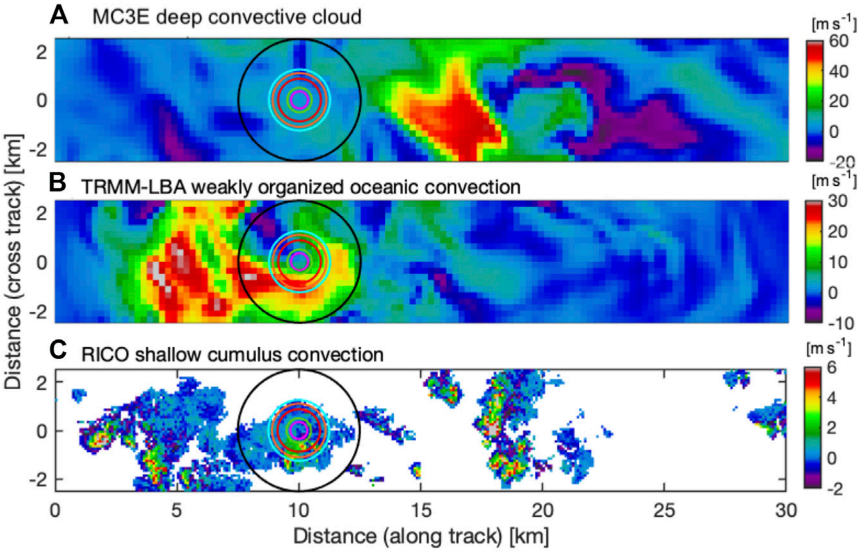

FIGURE 1 | Horizontal cross-section showing vertical air motion (V_{AIR} in ms^{-1}; positive indicates upward motion) from three different model simulations: **(A)** MC3E at 12 km height, **(B)** TRMM-LBA at 10 km height, and **(C)** RICO at 1 km height. Overlaid circles represent the instantaneous field of view (IFOV) of the six radars under consideration (color coded as in **Table 1**).

velocity measurements are evaluated (Tanelli et al., 2002; Durden et al., 2007; Tanelli et al., 2016). These systems resemble those considered during the ACCP study. Three additional radars that utilize a single antenna are also considered. One of them is the EarthCARE CPR and the other two are large antenna 13-GHz radar systems that resemble spaceborne radar concepts considered by space agencies. The trade-offs between the selected radar frequency, footprint, and the technology used for the Doppler velocity estimation are presented

2 DATASETS AND METHODS

2.1 Observations

In this study, a dataset of over 20,000 5 min averaged raindrop spectra from two-dimensional video disdrometers (2DVDs) is used to estimate the impact of mean Doppler velocity accuracy on the characterization of hydrometeor diameter. The 2DVD dataset is described in Williams et al. (2014). For the forward calculations, the raindrops are simulated as oblate spheroids (Brandes et al., 2002), with a terminal velocity described in Lhermitte (2002) and the T-matrix scattering theory (Waterman, 1965) is used for the radar reflectivity estimation.

2.2 Numerical Model Simulations

Numerical simulations obtained from high spatial resolution (<250 m) conducted under the scope of NASA ACCP study complement the sparse observational datasets of convective cloud properties. ACCP relied on an array of models that proved accurate at simulating different cloud systems ranging from shallow to deep convection including warm, mixed-phase, and ice clouds. The following numerical model simulations are analyzed in the current study:

- A Weather Research and Forecasting (WRF, Model V3.8.; Skamarock et al., 2008; Skamarock, 2008; Varble et al., 2020) simulation on the 20 May 2011 squall-line event that took place during the Mid-Latitude Continental Convective Clouds Experiment (MC3E; Jensen et al., 2016) in Oklahoma. A horizontal cross section through the MC3E simulation taken at 12-km height allows us to appreciate the inhomogeneity of this convective storm that presented vigorous updrafts within only a few hundred meters of downdrafts (**Figure 1A**).
- A Regional Atmospheric Modeling System (RAMS, v6.2.05; Cotton et al., 2003; Storer and Posselt, 2019) simulation of the deep convection cases of 11th and 17th August 1999, that took place during the Kwajalein Experiment (KWAJEX, Yuter et al., 2005) and of the weakly organized oceanic convection case of 3 February 1999, that took place during the Tropical Rainfall Measuring Mission—Large Scale Biosphere-Atmosphere Experiment (TRMM-LBA, Silva Dias et al., 2002). A horizontal cross section through the TRMM-LBA simulation taken at 10 km height allows us to appreciate the inhomogeneity of individual coherent updraft structures that formed in this storm (**Figure 1B**).
- A System for Atmospheric Modeling (SAM, V6.11.2; Khairoutdinov and Randall 2003) is simulation of the strong tropical oceanic convection cases that occurred during the Global Atmospheric Research Program's Atlantic Tropical Experiment (GATE, Zipser and Gautier, 1978; Xu and Randall, 2001) and of the shallow convective cumulus case that took place during the Rain in Cumulus

TABLE 1 | Technical specifications for the six spaceborne radar architectures under consideration.

Radar Parameters	Radar 1	Radar 2 (EarthCARE)	Radar 3	Radar 4	Radar 5	Radar 6
Frequency (GHz)	94	94	35	13	13	13
Antenna Size (m)	2.0	2.5	2.0	2.0	4.0	6.0
Beamwidth (º)	0.106	0.095	0.28	0.725	0.35	0.25
Instantaneous field of view (IFOV; km)	1.0	0.75	2.2	5.06	2.44	1.74
Doppler technique	DPCA	-	DPCA	DPCA	-	-
Single shot sensitivity (dBZ)	-15	-22	+5	+20	+10	+5
Pulse repetition frequency (PRF; Hz)	7500	7500	7500	7500	7500	7500
Along track integration (m)	500	500	1000	1000	1000	1000
Satellite orbit height (km)	400	400	400	400	400	400
Pulse length (m)	150	500	150	150	250	250
Doppler Duty cycle (%)	1	1	1	1	0.1	1

over the Ocean experiment (RICO, Rauber et al., 2007). A horizontal cross section through the RICO simulation taken at 1 km height allows us to appreciate the weak (vertical air motion +2–6 m s^{-1}) and sub-kilometer horizontal scale coherent updrafts that are frequent features of this shallow convective cloud regime (**Figure 1C**).

In the current study, these numerical simulation results are directly used to quantify the individual impacts of signal penetration, instantaneous field of view, and platform motion on the characterization of convective updrafts (results in **Section 3**) and are input to a spaceborne radar forward simulator to emulate the performance of six spaceborne Doppler radar systems, whose specifications are listed in **Table 1** (results in **Section 4**).

2.3 Spaceborne Doppler Radar Forward Simulator

The forward simulator used in the current study was designed to forward-simulate attenuated radar reflectivity factor and mean Doppler velocity (MDV, the sum of the vertical air motion and reflectivity-weighted hydrometeor sedimentation velocity) considering known instrument sampling limitations. It uses scattering calculations to estimate the radar reflectivity factor and the gas and liquid attenuation at the model native resolution following T-matrix for cloud, drizzle, and rain hydrometeor species; the Self-Similar Rayleigh-Gans Approximation (SSRGA, Hogan and Westbrook, 2014) for ice and snow particles; and Mie for hail and graupel particles, that are assumed to have a spherical shape with different densities (0.9 and 0.4 g cm^{-3}, respectively). This information is also combined to produce estimates of attenuated radar reflectivity, MDV, and spectrum width. A realistic Earth's surface echo is added to the first model level as in Burns et al. (2016). The addition of a surface echo produces a more realistic radar performance in the lowest 1 km of the atmosphere (see Lamer et al., 2020 for more details). An instrument forward-simulator is then used to emulate effects caused by an array of radar specifications:

- Sampling geometry parameters including antenna beamwidth, pulse length, and satellite orbit as in the work of Kollias et al. (2014)
- Along-track integration as in the work of Kollias et al. (2014)
- Sampling rate (i.e., pulse repetition frequency) as in the work of Kollias et al. (2014)
- Platform motion as in the work of Kollias et al. (2014)
- Radar receiver noise in the raw I/Q radar signals, which dictates the signal-to-noise (SNR) ratio
- Doppler estimation technique including Pulse-pair or Doppler spectra-based moment estimation as in the work of Kollias et al. (2014)
- Off-nadir operation as in the work of Battaglia et al. (2020a)

The forward-simulated radar observables at the radar resolution are finally used as inputs in a retrieval algorithm to produce "best-estimate" radar observables (i.e., data products) for a complete end-to-end process. Those include the following: a feature mask (location of detected meteorological observations), as well as an MDV field corrected for velocity aliasing as in the work of Kollias et al. (2014).

3 RADAR SAMPLING PARAMETERS AND THEIR INDIVIDUAL IMPACT ON RETRIEVED CLOUD PROPERTIES

In this section, we describe key radar sampling parameters and the radar specifications that influence them. Then, through comparison with observed and simulated benchmarks, we estimate their impact on retrieved cloud properties.

3.1 Signal Penetration

Radar signal penetration is affected by attenuation caused by gases and hydrometeors, which is wavelength specific, and has multiple scattering, which depends on the radar IFOV and the type of hydrometeor present in the radar sampling volume (Battaglia et al., 2016).

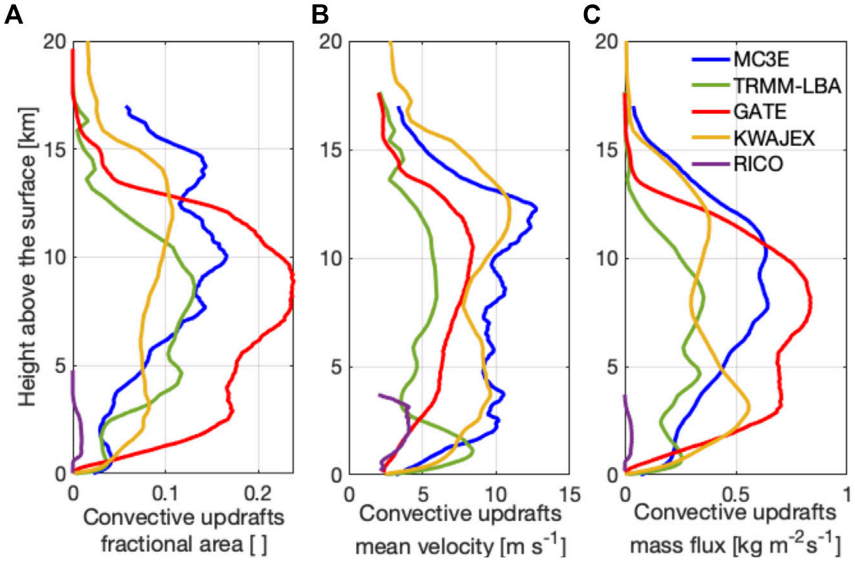

FIGURE 2 | Profiles of storm-averaged convective updraft **(A)** fractional area, **(B)** mean velocity, and **(C)** mass flux estimated directly from the numerical model simulations. Results are shown for the different cloud types under study (MC3E: blue, GATE: red, KWAJEX: yellow, TRMM-LBA: green, RICO: purple).

3.1.1 The Impact of Signal Penetration on Retrieving Convective Updraft Mass Flux

Determining signal penetration depth is important to determine the ability of a spaceborne Doppler radar system to detect the portions of convective storms where most of the convective transport occurs. Here we will focus on quantifying the impact of signal penetration on the characterization of updraft mass flux (M_F), which is central to cumulus parameterization schemes in large-scale models (e.g., Arakawa and Schubert, 1974; Tiedtke, 1989).

The observational record of convective updraft properties is sparse. Under shallow convective cloud conditions, vertically pointing lidar, and radar systems have been used to characterize the sub-cloud and cloud layer dynamics (Lamer et al., 2015; Lamer and Kolias, 2015; Lareau et al., 2018; Endo et al., 2019). Only recently has the information from both these been merged to provide a comprehensive view of the dynamical field in and around shallow convective cloud systems (Zhu et al., 2021). In deep convection, limited aircraft observations and profiling radar techniques are available (e.g., LeMone and Zipser, 1980; Heymsfield et al., 2010; Williams, 2012; Heymsfield et al., 2013; Kumar et al., 2015; Wang et al., 2020). Based on the airborne Doppler radar observations, the peak updraft values are often above 10-km altitude (Heymsfield et al., 2010; Heymsfield et al., 2013). Here, direct sampling of the numerical simulations is used to construct a more comprehensive benchmark of convective updraft properties. A conservative threshold of 2 m s^{-1} is used to identify a model grid point that contains convective updrafts (Houze, 1997). We track information about the fractional area coverage in the entire domain of the simulation (α_U) and the mean air velocity (V_U) of these convective updrafts at each height through the atmospheric column and compute the mass flux (M_F) as

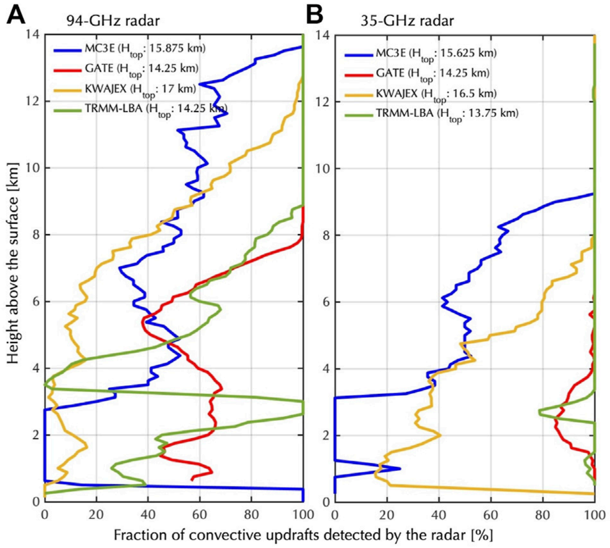

FIGURE 3 | Fraction of convective updraft (V_{AIR} >2 ms^{-1}) detected by the **(A)** 94 GHz and **(B)** 35 GHz radars as a function of height. An estimate of cloud height (H_{top}) for the various cloud types simulated is given in the legend. Results are shown for the different cloud types under study (colors as in **Figure 2**).

$$M_F(Z) = \rho \cdot \alpha_U \cdot V_U \tag{1}$$

where ρ is the air density in kg m^{-3} and Z is the model grid level (i.e., height).

The corresponding profiles for the different convective cases are shown in **Figure 2**. **Figure 2C** indicates that mass flux through the simulated cloud systems generally peaks at or above 6–8 km height except for the RICO shallow convection case which is confined below 4 km, and the KWAJEX case that peaks at 3 km but exhibits a secondary maximum at 11 km. Thus, a spaceborne Doppler radar should be able to penetrate down to ~6 km above the surface to capture most of the shape and the peak of the convective mass flux profile in deep convective systems.

Using the radar forward simulator, we further evaluate the impact of signal penetration on the characterization of convective updraft mass flux. Since the radar simulator used in this study accounts for frequency but lacks representation for multiple scattering effects (Battaglia et al., 2011; Battaglia et al., 2015), a conservative criterion based on signal-to-noise ratio (SNR) is used to estimate the penetration depth of the radar signal under different atmospheric conditions. **Figures 3A,B**, respectively, show the fraction of convective updrafts (V_{AIR} >2 ms^{-1}) with SNR > +5 dB as seen by a 35 and 94 GHz radar as a function of height. Starting at 14 km, both radar systems detect 100% of the scenes for all simulations. Moving downwards to ~12 km, the intense MC3E and KWAJEX deep convective cases produce strong signal attenuation at 94 GHz and, as a result, a decrease in the fraction of updrafts is detected. The 35-GHz system is more resilient and only begins being affected by signal attenuation in these storms at ~9 km. Due to signal attenuation which is generally strongest in the convective core, which is responsible for the bulk of the vertical transport of energy and moisture, even a small loss in the fraction of echoes detected could induce a large underestimation of the mass flux. Assuming that detection of 80% of convective updrafts is sufficient to capture the bulk of the mass flux occurring at each height, we estimate that a 94 GHz radar could be used to characterize the mass flux profile of deep convective systems from cloud top through ~11 km and of weaker convective storms from cloud top through 7 km. Since this height is generally higher than the location of the mass flux peak, we conclude that a 94 GHz radar system alone would not be appropriate to monitor the mass flux of deep convective cloud systems. As for a 35 GHz radar, the intense continental convection (MC3E) case limits its "effective penetration" to 9 km height above the ground. In all other cases, the 35 GHz radar will be able to capture the peak of the convective mass flux and, in the case of weaker convective storms, penetrate much lower. Thus, a 35 GHz radar would be appropriate to monitor the mass flux peak in all, but the strongest deep convective systems.

3.2 Instantaneous Field of View

3.2.1 Factor Impacting Instantaneous Field of View

The IFOV of spaceborne radars is effectively the projection of the radar sampling volume on Earth's surface. IFOV is modulated by four main factors: 1) frequency (*f*), which inversely correlates with IFOV (ceteris paribus), 2) antenna size (D) which directly acts to increase IFOV, 3) number of antennas used for the Doppler velocity estimation, which indirectly acts to increase IFOV by decreasing antenna sizes, and 4) distance from the Earth (H_{SAT}), which directly acts to increase IFOV. A commonly used approximate relationship for the radar IFOV is

$$IFOV \cong 0.369 \frac{H_{SAT}\ [km]}{D\ [m] \cdot f\,[GHz]} \tag{2}$$

The IFOVs for six spaceborne Doppler radar architectures considered in this study are listed in **Table 1**. The average orbit height is the same (H_{SAT} = 400 km) for all the architectures. This results in the 94 GHz radars having an overall smaller IFOV. Number of antennas comes next, with non-DPCA systems having overall smaller IFOV than DPCA systems.

3.2.2 The Impact of Instantaneous Field of View on Retrieving Convective Updraft Mass Flux

The relationship between the updraft chord length (UCL) and the spaceborne radar IFOV is very important to determine the ability of a spaceborne Doppler radar system to resolve, and thus characterize, convective updraft properties. The spaceborne Doppler radar MDV measurements are the result of the convolution of true updraft properties with the IFOV. In the case of under sampling (IFOV > UCL), the estimated MDV is expected to underestimate the updraft magnitude and overestimate the updraft size. In previous studies, the impact of the radar range resolution and IFOV on shallow cloud properties (vertical and horizontal coverage and LWP) was demonstrated (e.g., Battaglia et al., 2020b; Lamer et al., 2020). Here we will assess the impact of sampling geometry on our ability to characterize updraft mass flux (M_F) and its components.

The observational record of convective updraft chord UCLs is sparse and measurements from limited aircraft observations and profiling radar techniques (e.g., LeMone and Zipser, 1980; Williams, 2012; Kumar et al., 2015; Lamer et al., 2015; Wang et al., 2020) are challenging to consolidate due to their limited sampling of individual storms and the strong dependency of their results on the instrument/platform sampling geometry and strategy used. Nevertheless, most reports of deep convective updraft cores document them as being less than 5 km, with their distribution peaking around 2–3 km (Wang et al., 2020) while shallow convective updraft cores were reported to be 100–500 m wide (Lamer et al., 2015).

Once again, direct sampling of the high-resolution model outputs is used to derive additional statistics of the properties of the convective updrafts. Spatially coherent convective updrafts are identified as contiguous updraft regions with air motion larger than 2 m s^{-1}. We track information about the fractional area coverage (α_U) and the mean air velocity (V_U) of convective updrafts of different chord lengths and compute their mass flux (M_F) as

$$M_F\,(UCL) = \rho \cdot \alpha_U \cdot V_U \tag{3}$$

The distribution of α_U, V_U, and M_F as a function of the UCL and the cumulative distribution of the contribution of updrafts with different UCL to the total M_F are shown in **Figure 4**. The UCL bins are 0.25 km wide, with center values from 0.25 to 10 km. Shallow convection is characterized by the narrowest UCL's with only a small fraction of them exceeding 500 m. Deep convection simulations exhibit a broader distribution of UCLs especially for the more intense cases (MC3E, KWAJEX,

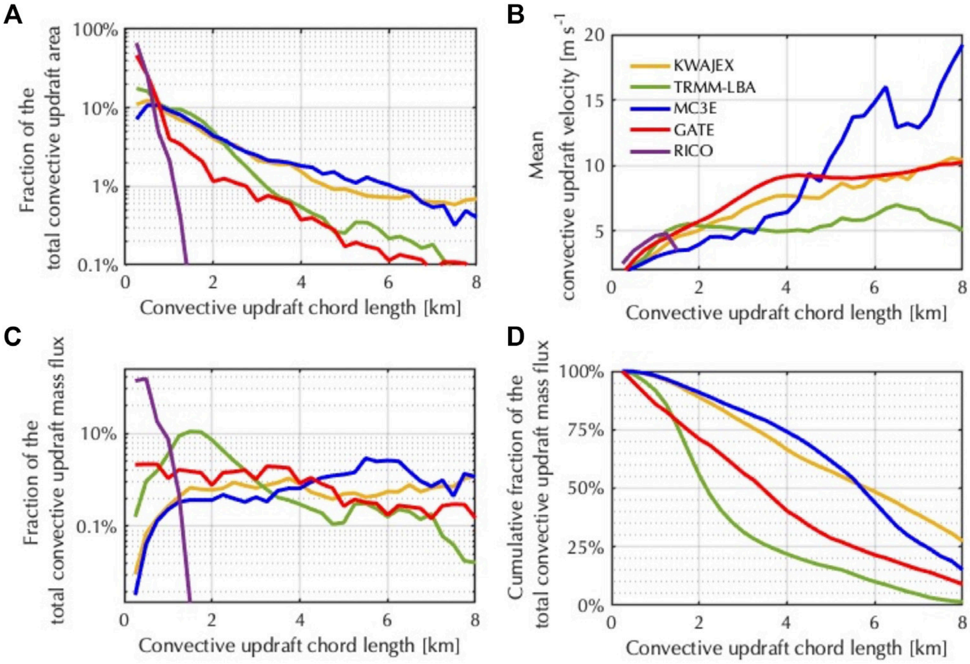

FIGURE 4 | As a function of convective updraft chord length **(A)** fraction area, **(B)** mean updraft velocity, **(C)** contribution to the total convective updraft mass flux, and **(D)** cumulative fraction of the total convective updraft mass flux starting from the largest updrafts. Results are shown for the different cloud types under study (colors as in **Figure 2**). Note that the purple line in "d" is not visible as it runs along the y-axis.

Figure 4A). The mean V_U increases with the UCL, suggesting that broader updrafts are also characterized by stronger updraft magnitudes. This relationship between UCL and V_U can explain the contribution to the total M_F by updrafts with different UCL. Updrafts with UCL larger than 1.5 km equally contribute to the total updraft mass flux occurring in deep convective storms (**Figure 4C**). In weaker convective systems like TRMM-LBA and RICO, smaller convective updrafts (1.8 and 0.5 km UCL, respectively) are seen to be responsible for the bulk of the transport since larger updrafts do not seem to be systematically exhibiting stronger velocities.

The cumulative fraction of $M_F(UCL)$ allows us to determine which updraft sizes together contribute to 50% of the convective updraft mass flux. In the intense deep convective systems, that would be updrafts larger than ~6 km; in weakly organized oceanic deep convective systems, that would be updrafts larger than ~3 km; in shallow convective cloud systems, that would be updrafts <375 m. This behavior drives a need to design radar architectures that have an IFOV $\leq$ 3 km to monitor the bulk of the mass flux in deep convective systems.

Figure 1 allows us to visualize the IFOV achieved by the 6 radar architectures relative to the simulated cloud scenes noting that none of these architectures meet the criteria established for monitoring the mass flux of shallow convective clouds. On the other hand, five of the radar architectures meet the criteria established for monitoring the mass flux of deep convective clouds (radar 1, 2, 3, 5, and 6) except for when significant attenuation occurs.

To further evaluate the impact of IFOV on the characterization of convective updraft mass flux, we perform forward simulations where only the sampling geometry is considered. In effect, we turn on the radar instrument model and estimate the resulting vertical air motion. From those motions, at each radar height, the area fraction, the magnitude of updrafts of velocity $>2\,\mathrm{m\,s^{-1}}$, and their mass flux are computed. Using the same model swaths, the same convective updraft parameters are estimated at each model height using direct sampling at the native model resolution. The differences of these updraft properties as derived by the radar IFOV and the direct model sampling at each height are normalized by the model direct sampling value (i.e., relative errors). The relative errors in the updraft properties from all heights are used to compile the relative error distributions for different convective scenes and radar systems (**Figure 5**). As expected, the 1.0 km IFOV provides the best agreement between the model output and the forward-simulated radar observations for all three convective updraft parameters with most of the relative error values within ±20%. A 2.5-km IFOV results in broader relative error distributions in α_U and V_U (±35%). The M_F relative error distribution is centered around zero; however, in some cases, relative errors up to 50% in the M_F are estimated. The impact of the radar sampling volume on the convective updraft parameters is more drastic at 5 km IFOV with errors up to 100%.

In all cases, non-uniform beam filling (under sampling of the model dynamics) is responsible for the observed errors. Updraft features smaller than the IFOV presenting weak radar reflectivity go undetected (thus causing a negative α_U error) while those

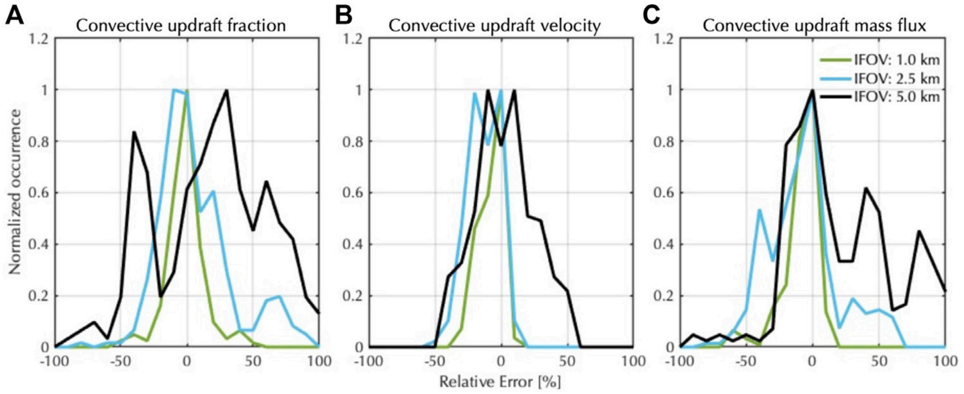

FIGURE 5 | Normalized distribution of the relative error ($\frac{model-radar}{model} \cdot 100\%$) in the **(A)** convective updraft fraction, **(B)** mean convective updraft velocity, and **(C)** convective updraft mass flux. Results are shown for three different instantaneous radar field of views close to that of radar 1 (1.0 km; green), radar 5 (2.5 km; cyan), radar 4 (5.0 km; black).

presenting large radar reflectivity appear horizontally smoothed (thus causing a positive α_U error). Beyond distorting the fractional area of convective updrafts, non-uniform beam filling also tends to cause an underestimation of the velocity of small convective updraft features surrounded by most downdrafts or clear air (thus causing a negative V_U bias). Due to the way we defined convective updrafts (i.e., MDV >2 ms^{-1}) this negative V_U bias may lead to convective updrafts being misclassified as non-convective (weak) updraft, thus taking only the strongest convective updrafts into consideration and yielding an overall positive error in the distribution of V_U and $\mathrm{M_F}$. It is important to note that these results are based only on a small number of simulated cases and that the relative error magnitude depends on the convection type. Exploring these convective type-based errors should be the focus of future studies.

3.3 Platform Motion

Radar mean Doppler velocity (MDV) is the *reflectivity-weighted average* line of sight motion of the targets present within the radar IFOV *relative to the radar frame of reference*. The radar own motion will contribute to the Doppler signal and its effect can be cancelled out by subtracting the contribution due to the projection of the satellite velocity along the antenna boresight. There is, however, an additional effect to be accounted for. Due to the large velocity of LEO satellites, the projection of the velocity along different lines of sight within the IFOV will differ significantly from the boresight projection; correspondingly, the radiation backscattered from the forward/backward (with respect to the satellite motion) part of the IFOV will be phase shifted when backscattered from a target receding/approaching the radar. In perfectly homogeneous atmospheric conditions (i.e., where the reflectivity field is the same throughout the IFOV), the reflectivity contributions of the perceived "away" and "towards" motions are perfectly balanced such that the recorded MDV is solely influenced by hydrometeor sedimentation velocity ($\mathrm{V_{SED}}$) and air motion (V_{AIR}). In inhomogeneous atmospheric conditions, however, the reflectivity contributions of the perceived "away" and "towards" motions are out of balance, thus introducing a bias to the MDV that, to first approximation, is proportional to the radar reflectivity gradient within the IFOV and proportional to IFOV^2 (details are given in the work of Battaglia et al., 2020a).

To alleviate this bias, displaced phase center antenna (DPCA) systems rely on two antennas strategically deployed such that their combined measurements can provide an unbiased MDV estimate (Tanelli et al., 2002; Durden et al., 2007; Sy et al., 2014; Tanelli et al., 2016).

3.3.1 The Impact of Platform Motion on Identifying Convective Updrafts

To quantify the impact of platform motion on the MDV measured by spaceborne radars, we performed forward simulations of the weakly organized convective cloud scene of TRMM-LBA, setting V_{AIR} and $\mathrm{V_{SED}}$ to $0\ \mathrm{m\,s^{-1}}$. **Figure 6** shows results for radar 5, which is a non-DPCA 13-GHz system with a 4 m antenna. Similar results are obtained from forward-simulations of the other two non-DCPA systems (radar 2 and radar 6; not shown). As highlighted by **Figure 6B**, platform motion alone can introduce MDV biases on the order of $30\ \mathrm{m\,s^{-1}}$ in this highly heterogenous cloud scene. The MDV biases due to non-uniform beam filling (NUBF) will occur at the edges of every convective cloud (where large horizontal gradients of radar reflectivity occur) and within the periphery of all convective cores since a vertically oriented area of high radar reflectivity is one of their characteristic radar features. Although the use of the along-track radar reflectivity gradient can be used to correct for most of the NUBF-induced velocity bias, considerable residual errors from the application of an imperfect correction could complicate the detection of convective updrafts and could lead to false detections. Considering that this bias is nearly double the magnitude of the strongest dynamical features simulated by the model and the proximity to the location of the actual convective updrafts,

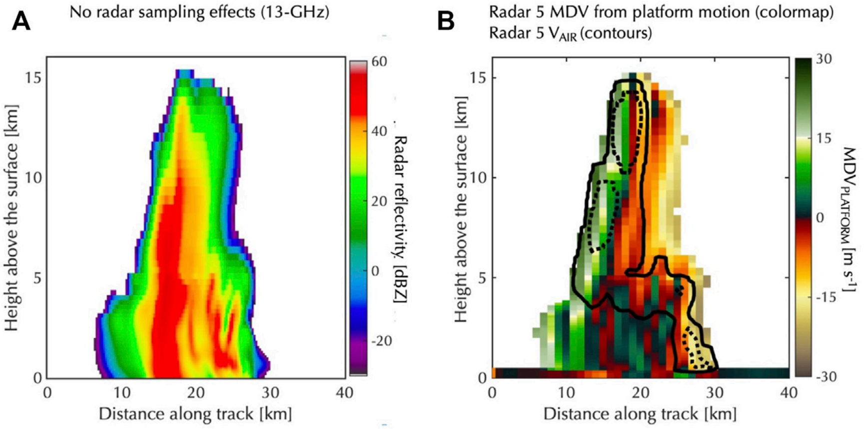

FIGURE 6 | Forward simulation of TRMM-LBA weakly organized convection: **(A)** radar reflectivity at 13 GHz without radar sampling effects and **(B)** apparent MDV induced strictly from platform motion and NUBF conditions for radar 5 (i.e., air motion and particle sedimentation set to 0 m s^{-1}). Overlaid on "b" are V_{AIR} contours drawn from forward-simulations with no platform motion effects (2 m s^{-1}: solid and 8 m s^{-1}: dotted).

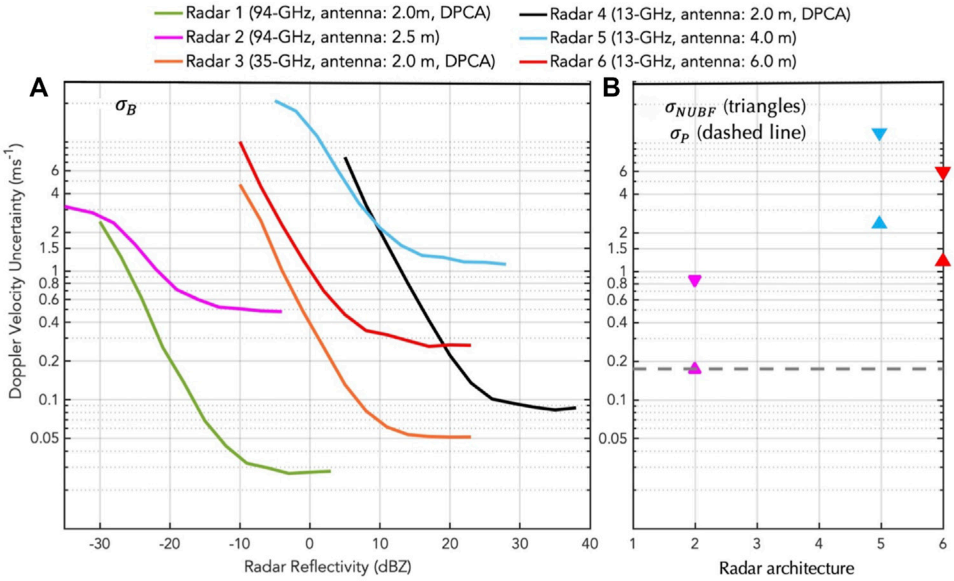

FIGURE 7 | Doppler velocity uncertainty from **(A)** spectral broadening (σ_B) and **(B)** non-uniform beam filling (σ_{NUBF}; triangles), and mis-pointing (σ_P; dashed line). Results are shown for the 6 radars under consideration (color coded as in **Table 1**).

we suggest that a non-DPCA system would be difficult to use for dynamical studies in such complex cloud scenes.

3.4 Mean Doppler Velocity Uncertainty

3.4.1 Factors Impacting Mean Doppler Velocity Uncertainty

The total MDV error budget (σ_{MDV}) for a spaceborne Doppler radar is affected by three main factors 1) intrinsic noise (spectral broadening) introduced by the platform motion (σ_B), 2) outstanding error in correcting MDV biases caused by non-uniform beam filling (σ_{NUBF}), and 3) outstanding error due to uncertainty in the antenna pointing characterization or alternatively error in the estimation of the horizontal wind when off-nadir pointing is needed. The MDV total error budget is given by the following expression:

$$\sigma_{MDV} = \sqrt{\sigma_B^2 + \sigma_{NUBF}^2 + \sigma_P^2} \qquad (4)$$

Figure 7 shows the individual contribution of these factors in the 6 radar architectures under consideration in the current study. The relationship of σ_B with signal-to-noise ratio (SNR) becomes evident (**Figure 7A**); for any of the radar configurations

σ_B is systematically lower for atmospheric features of higher radar reflectivity. The dependency of the MDV uncertainty with SNR is inherent to all the radar architectures; however, the DPCA radar architectures (1, 3, and 4) have negligible σ_B errors, as with any radar on a non-moving platform. On the other hand, the non-DPCA radars (2, 5, and 6) have much higher σ_B errors. This is clearly illustrated in the comparison of the two 94-GHz radar system. Despite its larger antenna and higher sensitivity, the EarthCARE CPR (radar 2) has a much higher σ_B contribution to the overall MDV error budget than the smaller antenna, which is a less sensitive DPCA 94-GHz radar.

In addition to SNR, the σ_B for the non-DPCA radar architectures depends on the normalized spectrum width (Kollias et al., 2014). This explains the difference in their curves. Noticeably, for the same radar frequency, σ_B is lower for the radar with larger antenna. This is illustrated in the case of two of the 13-GHz radars (5 and 6). For a 20 dBZ echo, the σ_B is 1.2 and 0.28 ms^{-1} for radars 5 and 6, respectively. In addition to having a negligible σ_B, the use of a pair of antennas by the DPCA radars allows them to avoid the non-uniform beam filling MDV biases, something that is not the case for the non-DPCA radars. The along-track gradient of the radar reflectivity has been suggested to correct the NUBF velocity bias; however, the correction depends on the detailed distribution of the radar reflectivity within the radar sampling volume that is not known (Sy et al., 2014; Kollias et al., 2018). Thus, there is a residual, unbiased velocity error from the NUBF correction (σ_{NUBF}) that increases the total MDV error budget (σ_{MDV}). The residual error from the NUBF correction is proportional to the square of the radar IFOV ($\sigma_{NUBF} \propto IFOV^2$). In Battaglia et al. (2020b), an estimate for σ_{NUBF} was provided for a gentle along-track radar reflectivity gradients of 3 dBZkm^{-1} (non-convective conditions, Kollias et al., 2014). These estimates should be considered as a lower bound σ_{NUBF} estimate. An along-track radar reflectivity gradient of 15 dBZkm^{-1} (convective conditions) is used to provide an upper bound σ_{NUBF} estimate. The upper and the lower bound σ_{NUBF} estimates are shown in **Figure 7B**. For the EarthCARE CPR, sampling convection is expected to be very challenging, thus, the lower bound σ_{NUBF} estimate is more relevant (Kollias et al., 2018). Due to its very narrow IFOV, the σ_{NUBF} is small compared to the σ_B term. On the other hand, the σ_{NUBF} term dominates the MDV error budget σ_{MDV} for the two non-DPCA 13-GHz radars (5 and 6). The σ_{NUBF} term is the dominant term in the σ_{MDV} budget even for a 6.0-m antenna size.

Finally, the σ_P term represents uncertainty in the MDV introduced by antenna pointing uncertainties related to thermal distortions and vibrations of the antenna structure and/or uncertainty in the estimation of the horizontal wind when off-nadir pointing is needed. An uncertainty of 10–15 μrad in the knowledge of the spaceborne radar antenna pointing at an altitude of 400 km corresponds to an MDV uncertainty of 0.08–0.11 ms^{-1} (Battaglia and Kollias, 2015). For the DPCA radar architectures studied here, a 2 off-nadir forward (along-track) pointing is required to minimize the vertical extend of the surface echo (Beauchamp et al., 2021). In this case, a 5 ms^{-1} uncertainty in the knowledge of the horizontal wind will introduce ~0.2 ms^{-1} uncertainty in the MDV estimate (grey dashed line in **Figure 7**).

Summing these error sources allows us to conclude that DPCA radar configurations are overall more accurate (in terms of MDV) than non-DPCA systems especially in highly heterogenous conditions. It is worth noting that the MDV uncertainty depicted in **Figure 7** estimates for "best-estimate" MDV produced at the highest resolution available. For relatively homogeneous scenes such as stratiform cloud conditions, it may be acceptable to perform additional along-track averaging (Kollias et al., 2014), apply noise-filtering techniques (Sy et al., 2014) or rely on conditional sampling (Protat and Williams, 2011) to produce a coarser but high precision MDV "best-estimate". These techniques have been shown to lead to reduction of the MDV uncertainty by as much as a factor of 2 In forward simulations of the EarthCARE satellite (here radar 2).

3.4.2 The Impact of Mean Doppler Velocity Uncertainty on Retrieving Particle Diameter and Rime Fraction in Weak Air Motion Regimes

The MDV measured by a nadir-looking spaceborne Doppler radar represents the sum of vertical air motion (V_{AIR}) and the reflectivity-weighted hydrometeor sedimentation velocity (V_{SED}):

$$MDV = V_{SED} + V_{AIR} \tag{5}$$

Separating the contributions of these two terms is a necessary step for using MDV for dynamical studies which are associated with V_{AIR} and microphysical studies which are associated with hydrometeor properties that impact V_{SED} (e.g., Kollias et al., 2002; Zhu et al., 2021). The condition $|V_{air}| < 2\ ms^{-1}$ is often used to separate stratiform and convective cloud conditions (Houze, 1997). In stratiform clouds, (e.g., frontal stratiform precipitation, stratiform regions of convective systems, ice clouds), the horizontal microphysical variability is moderate, and the vertical air velocity is much smaller than the hydrometeor sedimentation velocity. When these conditions are satisfied, the MDV can be related to the shape of the particle size distribution (PSD), to relevant moments (e.g., rainfall rate), and, under certain conditions, allow us to study the microphysical processes that influence their evolution (e.g., Protat and Williams, 2011; Kalesse and Kollias, 2013). The extent to which such inferences can be made with reasonable uncertainty, depends on the magnitude of σ_{MDV}.

A combination of experimental and theoretical relationships between MDV and microphysical variables are presented here to illustrate the impact of the MDV uncertainty on microphysical variables in stratiform conditions. The formulation of analytical relationships between radar observables and microphysical variables requires a mathematical representation for the particle size distribution (PSD). The gamma distribution first introduced by Ulbrich (1983) and Willis (1984), and its normalization introduced by Testud et al. (2001) has been widely used to describe the PSD:

$$\mathbf{N}\left(\mathbf{N}_0^*, \mathbf{D_m}, \boldsymbol{\mu}\right) = \mathbf{N}_0^* \mathbf{f}(\boldsymbol{\mu}) \left(\frac{\mathbf{D}}{\mathbf{D_m}}\right)^{\boldsymbol{\mu}} \mathbf{exp}\left(-\left(4+\boldsymbol{\mu}\right)\frac{\mathbf{D}}{\mathbf{D_m}}\right) \tag{6}$$

where

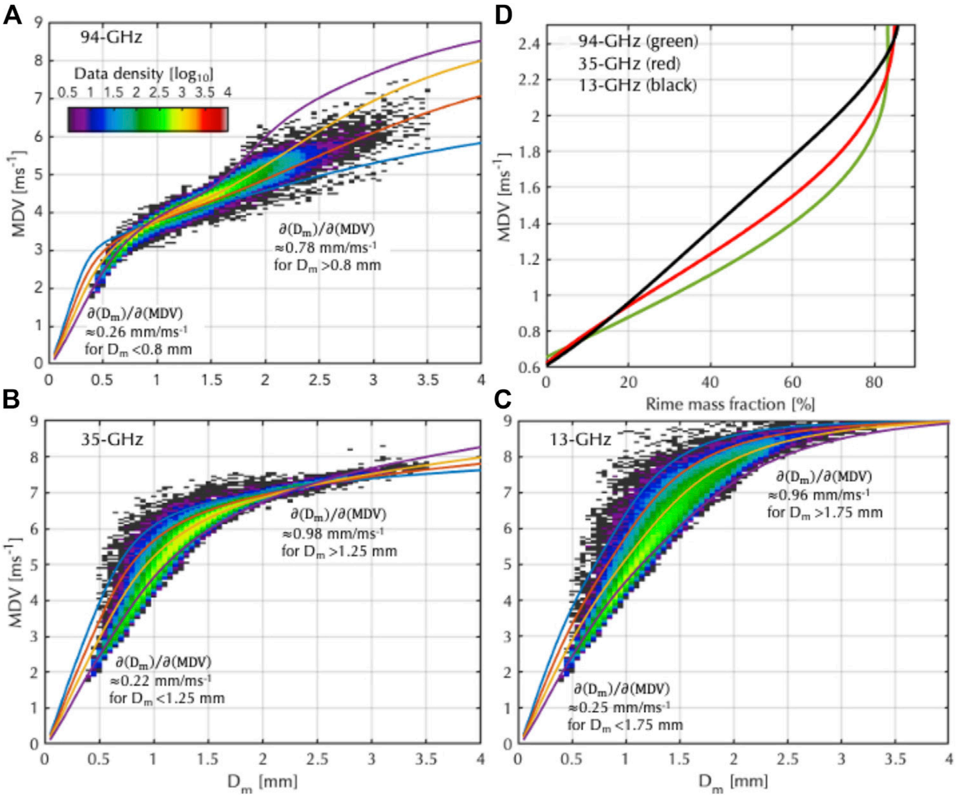

FIGURE 8 | (A) For a 94-GHz radar, relationships between raindrop particle size distribution (PSD's) mean volume-weighted diameter (D$_m$) and mean Doppler velocity (MDV) from ground-based measurements (colormap) and from different MDV-D$_m$ relationships derived for a gamma distribution for different shape parameter (μ) values (colored lines). **(B)** Same as "a" for a 35-GHz radar. **(C)** Same as "a" for a 13-GHz radar. **(D)** relationship between rime mass fraction and mean Doppler velocity (MDV) from literature based on studies performed with a 94 GHz (green), 35 GHz (red) and 13 GHz radar (black).

$$f(\mu) = \frac{\Gamma(4)(4+\mu)^{4+\mu}}{4^4\Gamma(4+\mu)}$$

The three parameters (N_0^*, D_m, μ) have the following meanings: D$_m$ is the volume-weighted mean diameter (defined as the ratio of the 4th to the 3rd moment of the PSD), N_0^* is the intercept parameter of the exponential distribution that has the same water content as D$_m$, and μ describes the PSD shape. The MDV is independent of N_0^* and for liquid phase hydrometeors (drizzle and raindrops), is a function of only D$_m$ and μ In addition, the MDV is the reflectivity-weighted PSD sedimentation velocity; thus, the relationship between MDV and (D$_m$, μ) depends also on the selected radar frequency. The relationship between MDV and D$_m$ is shown in **Figure 8** for four different μ values (−2, 0, 3, and 12) at 94 GHz radar (A), 35 GHz (B), and 13 GHz (C). Plotted under these analytical relationships are MDV and D$_m$ estimates from the two-dimensional video disdrometer (2DVDs) observations (analysis details described in **Section 2.1**). Overall, the experimental data and the theoretical relationships agree and two distinct regimes emerge for each radar frequency.

The D$_m$ estimation is often based on a combination of radar observables, however, here, we assume that MDV is the only available radar measurement. Under this assumption, the error in the D$_m$ estimation is controlled by the rate of change of D$_m$ with MDV and the MDV measurement error:

$$\delta(D_m) \approx \frac{\partial(D_m)}{\partial(MDV)}\delta(MDV) \qquad (7)$$

At W-band, two different $\partial(D_m)/\partial(MDV)$ regimes are present with very different slope values, one for D$_m$ values lower than 0.8 mm where $\partial(D_m)/\partial(MDV) \approx 0.26\, mm/ms^{-1}$ and another one for D$_m$ values higher than 0.8 mm where $\partial(D_m)/\partial(MDV) \approx 0.78\, mm/ms^{-1}$. The lower the $\partial(D_m)/\partial(MDV)$ value, lower the uncertainty in the D$_m$ retrieval for a set MDV uncertainty. For example, an MDV uncertainty of 0.2 ms^{-1} translates to an error of 0.05 and 0.15 mm, respectively, for D$_m$ values less 0.8 than and greater than 0.8 mm. The range of D$_m$ values where the slope $\partial(D_m)/\partial(MDV)$ is low increases at lower radar frequencies, suggesting that lower frequency radars are preferred for retrieving D$_m$ from MDV measurements. On the other hand, at high D$_m$ values (>1.75 mm) the slope $\partial(D_m)/\partial(MDV)$ at 94-GHz smaller thus suggesting that the 94-GHz MDV measurements will exhibit larger dynamic (sensitivity) range to D$_m$ changes in high-D$_m$ regimes. These differences are due to differences in the scattering by raindrops at the different radar frequencies (Kollias et al., 2002; Kollias

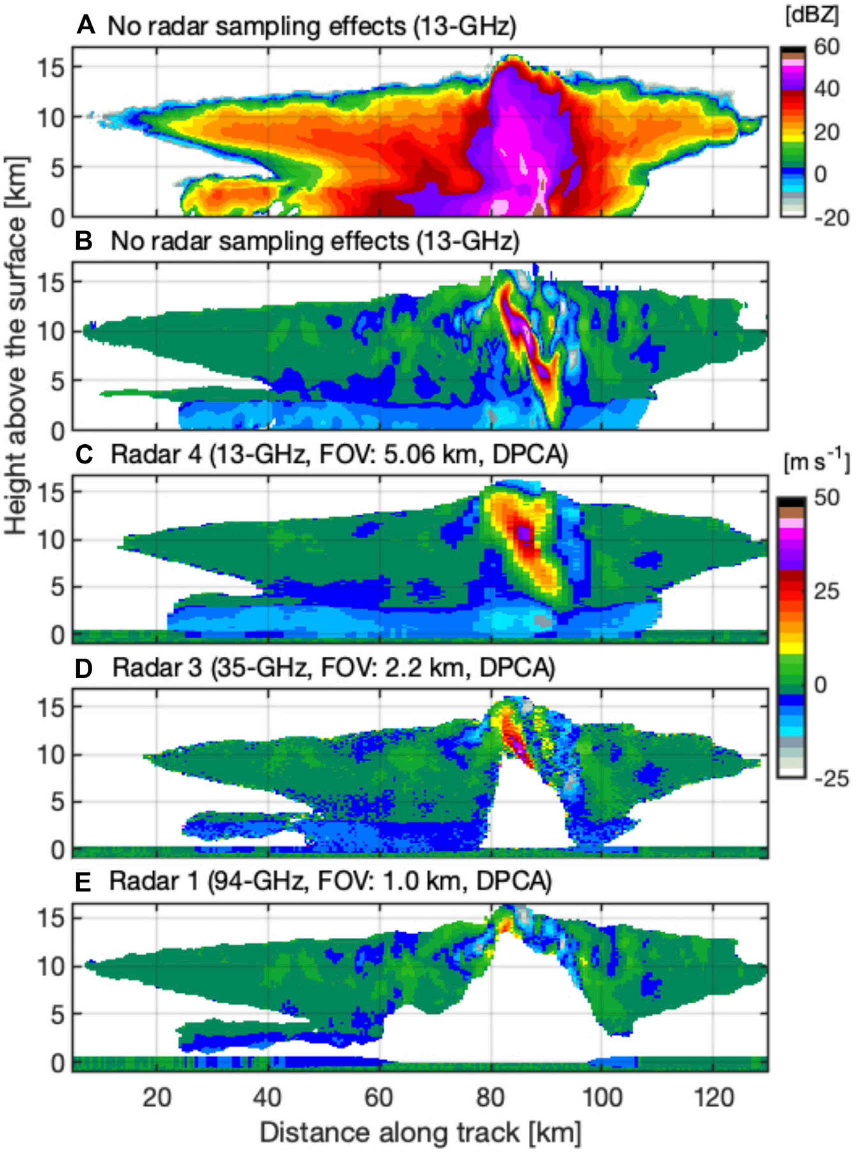

FIGURE 9 | Forward simulation of MC3E deep convection **(A)** radar reflectivity at 13 GHz without radar sampling effects **(B)** mean Doppler velocity at 13 GHz without radar sampling effects (i.e., truth) as well as mean Doppler velocity for **(C)** radar 4, **(D)** radar 3, and **(E)** radar 1.

et al., 2016). The complimentary use of MDV estimates at different radar frequencies can provide a strong constraint for D_m estimation (Giangrande et al., 2012; Matrosov, 2017).

The determination of the rime fraction in ice particles is another example where the use of the MDV can provide a strong constraint (Mason et al., 2018; Oue et al., 2021). In a recent study, Kneifel and Moisseev (2020) analyzed a large dataset of surface-based radar and in-situ observations and derived an experimental relationship between MDV and rime mass fraction (FR). The average relationship between MDV and RF for three radar frequencies (94-GHz, 35-GHz, and 13-GHz) is shown in **Figure 8D**. Although there is a considerable spread, the experimentally derived relationships offer a first order relationship for converting MDV errors to FR errors. If we focus on the FR range of 20–80%, an MDV uncertainty of 0.2 ms^{-1} translates to an error of 14, 12, and 10% in FR at 94-, 35-, and 13 GHz respectively. This assessment ignores the fact that the shape of the particle size distribution (D_m) will also affect the MDV magnitude; thus, here it is assumed that this information is provided by other measurements (e.g., dual-wavelength radar measurements, Pfitzenmaier et al., 2019).

4 SPACEBORNE DOPPLER RADAR PERFORMANCE IN CONVECTION

Six spaceborne Doppler radar systems, whose specifications can be found in **Table 1**, are being forward simulated in this study; these

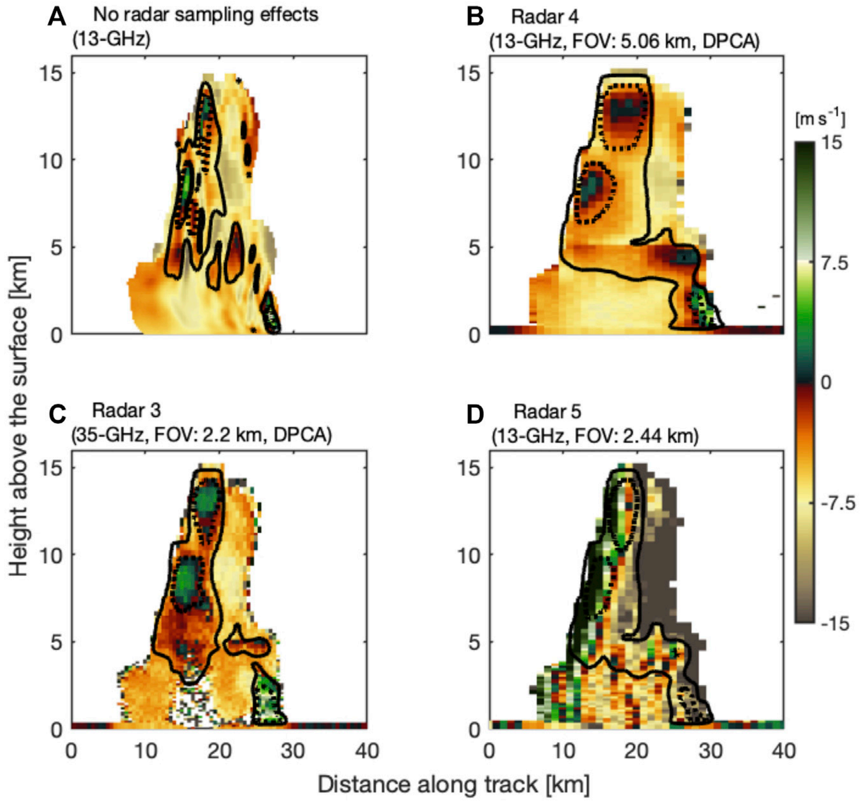

FIGURE 10 | Forward simulation of TRMM-LBA weakly organized convection **(A)** mean Doppler velocity at 13 GHz without radar sampling effects (i.e., truth) as well as mean Doppler velocity for **(B)** radar 4, **(C)** radar 3, and **(D)** radar 5. Overlaid on each plot are air motion contours drawn from forward-simulations with no platform motion effects (2 m s^{-1}: solid and 8 m s^{-1}: dotted). Radar reflectivity was presented in **Figure 6**.

systems resemble those under consideration by NASA's AOS mission, other space agencies, as well as the JAXA/ESA EarthCARE CPR.

4.1 Deep Convective Clouds

A vertical cross section of the 13 GHz radar reflectivity and MDV from the MC3E continental squall line case at the model resolution is shown in **Figure 9** (panels a and b, respectively). The simulation includes a deep convective core with radar reflectivity values between 40 and 55 dBZ and a cloud top above 15 km height trailed by stratiform precipitation. The convective core includes a tilted, coherent updraft structure with V_{AIR} values of more than 30–40 ms^{-1}. In addition, the spaceborne Doppler radar raw, uncorrected MDV simulations of the same event for the 3 DPCA architectures examined here (radars 1, 3, and 4) are shown in **Figure 9**. This comparison highlights tradeoffs between radar frequency, and IFOV choices in observing deep convective cloud dynamics from space.

Of the proposed DPCA radar architectures, radar 4 with its 13 GHz frequency experiences the least amount of attenuation compared to the 35 and 94 GHz radar architectures. Radar 4 can penetrate the entire depth of the convective cloud and its "best-estimate" MDV captures many of the key dynamical features of the squall line. It resolves the main updraft structure, especially above 3–4 km height. A drawback of this system is that its larger IFOV (5.06 km) causes a visible broadening of the high reflectivity updrafts and a misdetection of low reflectivity downdraft structures. The large radar IFOV also modulates the magnitude of the detected updrafts and downdrafts. In addition to the convective core, the 13 GHz MDV can capture well the transition from frozen to melted hydrometeors and some of the broad, weak dynamical structures.

The 35 GHz radar signal experiences considerable attenuation in the convective core, where the radar signal penetrates to an altitude of 9–10 km, thus capturing the upper 5 km of the convective cloud dynamical structure. However, its superior resolution (IFOV 2.44 km) results in an improved representation of the updraft and downdraft coherent structures, both in terms of their true size and true velocity in the upper 5 km of the squall line.

Finally, the 94 GHz radar penetrates only the upper most 2 km from the convective cloud top, thus, providing limited information about the main convective updraft properties. On the other hand, the superior resolution of the 94 GHz radar (IFOV 1 km) allows it to retrieve several weak dynamical structures resolved in the deep convective cloud simulations.

Together, the three simulated MDV fields provide complimentary information. The 13 GHz radar provides a complete view of the

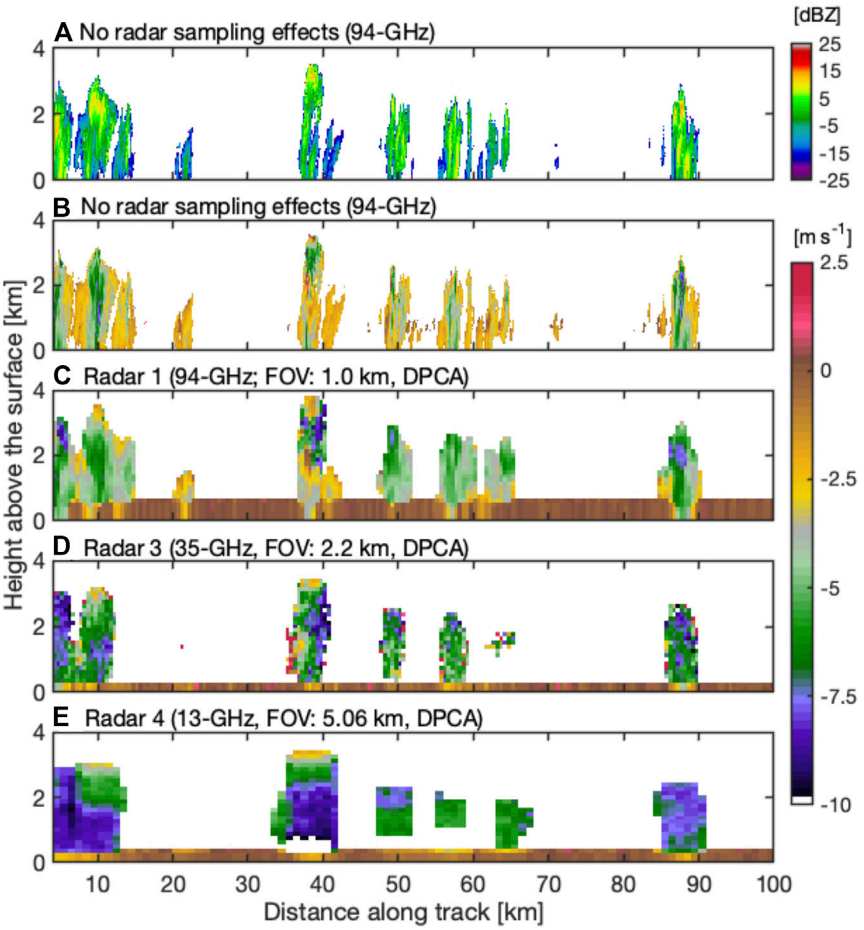

FIGURE 11 | Forward simulation of RICO shallow oceanic convection **(A)** radar reflectivity at 94 GHz without radar sampling effects **(B)** mean Doppler velocity at 94 GHz without radar sampling effects (i.e., truth) as well as mean Doppler velocity for **(C)** radar 1, **(D)** radar 3, and **(E)** radar 4.

storm's main dynamical features from the lower levels to the cloud top. On the other hand, the 35 GHz radar can provide higher resolution V_{AIR} and UCL information in the upper 5 km of the convective core; and the 94 GHz radar can add dynamical information outside of the deep convective core. These confirm previous findings based on airborne observations (Battaglia et al., 2016). Differences in MDVs observed by the different frequency radars resulting from non-Rayleigh scattering can also be exploited (Mroz et al., 2021).

4.2 Weakly Organized Oceanic Convection

A vertical cross section of the 13 GHz radar MDV from the TRMM-LBA weakly organized oceanic convection at the model resolution is shown in **Figure 10A**. In addition, the spaceborne Doppler radar raw uncorrected MDV simulations of the same event for the radar architectures (3, 4, and 5) are shown in **Figure 10**. Note here that "raw" MDV is shown since current techniques to correct for NUBF are too uncertain in this highly heterogeneous case (**Section 3.3**). Comparing the two 13 GHz radar systems highlighting the tradeoff between using 1) a DPCA system that requires two antennas and as such achieves a larger IFOV (radar 4) and 2) one antenna system that can achieve a smaller IFOV (radar 5). For completeness, the performance of the 35-GHz DPCA system (radar 3) is also presented.

Although radar 5 has a smaller IFOV (2.44 km) and is better positioned to resolve narrow dynamical features, this advantage is lessened by the high MDV bias and uncertainty this non-DPCA system experiences. As illustrated in **Figure 10D**, the "raw" MDV from radar 5 looks widely different from the model "truth."

In contrast, it is evident that radar 4 cannot precisely observe the boundaries of the narrow storm and of its narrow updrafts and downdrafts because of its larger IFOV (5.06 km); however, we would argue that it does reasonably well at locating the center location of the strongest dynamical features of the storm (comparing the location of the velocity isocontours in a and b). In addition, the "raw" MDV that this DPCA system measures is undeniably closer in magnitude to the model truth than that measured by the non-DPCA system.

As for the 35-GHz DPCA radar system (radar 3), we see better penetration in this weaker deep convective storm, only missing the lower 3 km of the storm below the updraft core. The small

IFOV of this system (2.2 km) also allows it to better resolve the storm boundaries as well as the boundaries and magnitude of its dynamical features.

This comparison again suggests that 35 GHz and 13 GHz offer complementary information and that the use of DPCA is paramount when it comes to measuring weakly organized convective cloud dynamics.

4.3 Shallow Oceanic Convection

A vertical cross section of the 94 GHz radar reflectivity and MDV from the RICO shallow oceanic convection case at the model resolution is shown in **Figure 11** (panels a and b, respectively). In addition, the spaceborne Doppler radar raw, uncorrected MDV simulations of the same event for the 3 DPCA architectures examined here (radars 1, 3, 4) are shown in **Figure 11**. This comparison highlights the impact of IFOV choice in observing shallow convection from space (Battaglia et al., 2020a; Lamer et al., 2020).

In contrast to the MC3E and TRMM-LBA deep convection cases, the location of the convective updrafts is difficult to determine just from the MDV simulations. The main reason is the weak V_{AIR} magnitude (2–6 ms^{-1}) that is often lower than the sedimentation velocity V_{SED}, thus, resulting in an overall negative MDV value. Due to its narrow IFOV, the 94 GHz DPCA radar is capable of documenting most of the cloud-scale MDV features, especially in the most developed clouds (**Figure 11C**). This is not the case for shallower cloud (**Figure 11C**, 50–70 km along track). These results suggest that the 94 GHz MDV observations will be conditionally useful for documenting the V_{AIR} and V_{SED} using an appropriate inversion technique that will be able to separate their contributions to the observed MDV. At 35 GHz and 13 GHz, the IFOV is 2.5 and 5 km, respectively, and the considerable impact of the radar sampling volume is obvious (**Figures 11D,E**). These findings are in line with those discussed in Lamer et al. (2020) and Battaglia et al. (2013) indicating that this cloud type requires the deployment of spaceborne radar with sub-kilometer IFOV, short pulse and high sensitivity.

5 SUMMARY

The estimation of the Doppler velocity from a spaceborne platform with sufficient accuracy (2–3 ms^{-1}) and resolution in deep convection and 0.2–0.3 ms^{-1} in large particle sedimentation regimes (e.g., weak dynamics regimes such as mid- and high-latitude frontal systems) from low Earth orbiting (~400 km altitude) satellite platforms that move at 7,600 ms^{-1} is a daunting task.

Using an array of numerical simulation examined within the context of the NASA Aerosols, Clouds, Convection, and Precipitation Decadal Survey study and surveying past airborne Doppler radar observations we established that convective updraft mass flux peaks above 6–8 km. This finding drives a need to rely on radar frequencies that can achieve significant penetration to this depth. Using forward simulations, it was determined that both a 35 GHz radar and 13 GHz radar could achieve such penetration in deep convective cloud systems. It was further established that updrafts larger than 3 km are responsible for the bulk of the updraft mass flux through these storms, thus driving a need to deploy radars with IFOV smaller than 3 km.

Platform motion was showed to significantly impact the mean Doppler velocity (MDV) measured by traditional single-antenna radars. Biases on the order of 30 $m\,s^{-1}$ were estimated for the simulated convective clouds. This finding strongly discourages the use of traditional systems for deep convective cloud dynamical studies and favors the use of displaced phase center antenna (DPCA) systems, which are designed to compensate for non-uniform beam filling effects on MDV. A combination of analytical and observed relationships allow us to estimate that outstanding sources of MDV uncertainties would lead to retrieval errors on the order of 0.05–0.15 mm for D_m and 25% for rime fraction (for −10 dBZ echo observed by a 94-GHz DPCA).

Comprehensive forward simulations allow us to appreciate the advantages and drawbacks of each of the six radar architectures currently under consideration by the mission that arose from the ACCP study. We find that the MDV collected by the 94 , 35 , and 13 GHz system provide complementary information. The 13 GHz radar provides a complete view of the storm's main dynamical features from the lower levels to the cloud top. On the other hand, the 35 GHz radar can provide higher spatial resolution air motion and updraft chord length information in the upper 5 km of the convective cores while the 94 GHz radar can provide additional dynamical information outside of the deep convective cores. Furthermore, differences in MDV observed between the different frequency radars results from non-Rayleigh scattering can also be exploited. When it comes to the shallow convective cloud regime, the findings of our analysis are in line with those discussed in the work of Lamer et al. (2020) and Battaglia et al. (2013) indicating that this cloud type requires the deployment of spaceborne radar with sub-kilometer IFOV, short pulse, and high sensitivity.

DATA AVAILABILITY STATEMENT

The original contributions presented in the study are included in the article/Supplementary Material, further inquiries can be directed to the corresponding author.

AUTHOR CONTRIBUTIONS

PK led the analysis and writing of this article. AB and KL contributed to the writing. BT and SB contributed to the analysis and interpretation.

FUNDING

PK's contributions were performed within the ACCP (now AOS) Decadal Survey Study Team supported by NASA (contract no. 80NSSC19K0923). AB and BT's contributions were supported by the European Space Agency under the

“Raincast” activity (contract no. 4000125959/18/NL/NA). KL’s contributions were supported by the US Department of Energy (DOE) Atmospheric System Research Program under contract DE-SC0012704. SB’s contributions were performed within the ACCP (now AOS) Decadal Survey Study Team supported by NASA. SB’s contributions were supported by the ACCP study.

ACKNOWLEDGMENTS

The numerical model simulations used in the current study are freely available online through the links provided in their introductory publications given in **Section 2.2** of this article.

REFERENCES

Arakawa, A., and Schubert, W. H. (1974). Interaction of a Cumulus Cloud Ensemble with the Large-Scale Environment, Part I. *J. Atmos. Sci.* 31, 674–701. doi:10.1175/1520-0469(1974)031<0674:ioacce>2.0.co;2

Battaglia, A., Kollias, P., Dhillon, R., Roy, R., Tanelli, S., Lamer, K., et al. (2020a). Spaceborne Cloud and Precipitation Radars: Status, Challenges, and Ways Forward. *Rev. Geophys.* 58 (No. 3), e2019RG000686–9208. doi:10.1029/2019RG000686

Battaglia, A., Kollias, P., Dhillon, R., Lamer, K., Khairoutdinov, M., and Watters, D. (2020b). Mind the gap - Part 2: Improving Quantitative Estimates of Cloud and Rain Water Path in Oceanic Warm Rain Using Spaceborne Radars. *Atmos. Meas. Tech.* 13, 4865–4883. doi:10.5194/amt-13-4865-2020

Battaglia, A., Augustynek, T., Tanelli, S., and Kollias, P. (2011). Multiple Scattering Identification in Spaceborne W-Band Radar Measurements of Deep Convective Cores. *J. Geophys. Res.* 116, D19201. doi:10.1029/2011JD016142

Battaglia, A., and Kollias, P. (2015). Using Ice Clouds for Mitigating the EarthCARE Doppler Radar Mispointing. *IEEE Trans. Geosci. Remote Sensing* 53 (4), 2079–2085. doi:10.1109/TGRS.2014.2353219

Battaglia, A., Mroz, K., Lang, T., Tridon, F., Tanelli, S., Tian, L., et al. (2016). Using a Multiwavelength Suite of Microwave Instruments to Investigate the Microphysical Structure of Deep Convective Cores. *J. Geophys. Res. Atmos.* 121, 9356–9381. doi:10.1002/2016JD025269

Battaglia, A., Tanelli, S., and Kollias, P. (2013). Polarization Diversity for Millimeter Spaceborne Doppler Radars: An Answer for Observing Deep Convection? *J. Atmos. Oceanic Technology* 30 (12), 2768–2787. doi:10.1175/jtech-d-13-00085.1

Battaglia, A., Tanelli, S., Mroz, K., and Tridon, F. (2015). Multiple Scattering in Observations of the GPM Dual-Frequency Precipitation Radar: Evidence and Impact on Retrievals. *J. Geophys. Res. Atmos.* 120, 4090–4101. doi:10.1002/2014JD022866

Beauchamp, R. M., Tanelli, S., and Sy, O. O. (2021). Observations and Design Considerations for Spaceborne Pulse Compression Weather Radar. *IEEE Trans. Geosci. Remote Sensing* 59 (6), 4535–4546. doi:10.1109/TGRS.2020.3013164

Brandes, E. A., Zhang, G., and Vivekanandan, J. (2002). Experiments in Rainfall Estimation with a Polarimetric Radar in a Subtropical Environment. *J. Appl. Meteorol.* 41, 674–685. doi:10.1175/1520-0450(2002)041<0674:eirewa>2.0.co;2

Burns, D., Kollias, P., Tatarevic, A., Battaglia, A., and Tanelli, S. (2016). The Performance of the EarthCARE Cloud Profiling Radar in marine Stratiform Clouds. *J. Geophys. Res. Atmos.* 121, 525–614. doi:10.1002/2016JD025090

Cotton, W. R., Pielke Sr., R. A., Walko, R. L., Liston, G. E., Tremback, C. J., Jiang, H., et al. (2003). RAMS 2001: Current Status and Future Directions. *Meteorology Atmos. Phys.* 82, 5–29. doi:10.1007/s00703-001-0584-9

Durden, S. L., Siqueira, P. R., and Tanelli, S. (2007). On the Use of Multi-Antenna Radars for Spaceborne Doppler Precipitation Measurements. *Ieee Geosci. Remote Sensing Lett.* 1064, 181. doi:10.1109/lgrs.2006.887136

Endo, S., Zhang, D., Vogelmann, A. M., Kollias, P., Lamer, K., Oue, M., et al. (2019). Reconciling Differences Between Large-Eddy Simulations and Doppler Lidar Observations of Continental Shallow Cumulus Cloud-Base Vertical Velocity. *Geophys. Res. Lett.* 46, 11539–11547. doi:10.1029/2019gl084893

Gasparini, B., Rasch, P. J., Hartmann, D. L., Wall, C. J., and Dütsch, M. (2021). A Lagrangian Perspective on Tropical Anvil Cloud Lifecycle in Present and Future Climate. *J. Geophys. Res. Atmospheres* 126, e2020JD033487. doi:10.1029/2020jd033487

Giangrande, S. E., Luke, E. P., and Kollias, P. (2012). Characterization of Vertical Velocity and Drop Size Distribution Parameters in Widespread Precipitation at ARM Facilities. *J. Appl. Meteorol. Climatol.* 51, 380–391. doi:10.1175/JAMC-D-10-05000.1

Hartmann, D. L., Gasparini, B., Berry, S. E., and Blossey, P. N. (2018). The Life Cycle and Net Radiative Effect of Tropical Anvil Clouds. *J. Adv. Model. Earth Syst.* 10, 3012–3029. doi:10.1029/2018ms001484

Heymsfield, G. M., Tian, L., Heymsfield, A. J., Li, L., and Guimond, S. (2010). Characteristics of Deep Tropical and Subtropical Convection from Nadir-Viewing High-Altitude Airborne Doppler Radar. *J. Atmos. Sci.* 67 (2), 285–308. doi:10.1175/2009jas3132.1

Heymsfield, G. M., Tian, L., Li, L., McLinden, M., and Cervantes, J. I. (2013). Airborne Radar Observations of Severe Hailstorms: Implications for Future Spaceborne Radar. *J. Appl. Meteorology Climatology* 52 (8), 1851–1867. doi:10.1175/jamc-d-12-0144.1

Hogan, R. J., and Westbrook, C. D. (2014). Equation for the Microwave Backscatter Cross Section of Aggregate Snowflakes Using the Self-Similar Rayleigh-Gans Approximation. *J. Atmos. Sci.* 71 (9), 3292–3301. doi:10.1175/jas-d-13-0347.1

Houze, R. A., Jr. (1997). Stratiform Precipitation in Regions of Convection: A Meteorological Paradox? *Bull. Amer. Meteorol. Soc.* 78 (10), 2179–2196. doi:10.1175/1520-0477(1997)078<2179:spiroc>2.0.co;2

Illingworth, A. J., Battaglia, A., Bradford, J., Forsythe, M., Joe, P., Kollias, P., et al. (2018). WIVERN: A New Satellite Concept to Provide Global In-Cloud Winds, Precipitation, and Cloud Properties. *Bull. Am. Meteorol. Soc.* 99 (8), 1669–1687. doi:10.1175/bams-d-16-0047.1

Jensen, M. P., Petersen, W. A., Bansemer, A., Bharadwaj, N., Carey, L. D., Cecil, D. J., et al. (2016). The Midlatitude Continental Convective Clouds Experiment (MC3E). *Bull. Amer. Meteorol. Soc* 97, 1667–1686. doi:10.1175/bams-d-14-00228.1

Kalesse, H., and Kollias, P. (2013). Climatology of High Cloud Dynamics Using Profiling ARM Doppler Radar Observations. *J. Clim.* 26 (17), 6340–6359. doi:10.1175/jcli-d-12-00695.1

Khairoutdinov, M. F., and Randall, D. A. (2003). Cloud Resolving Modeling of the ARM Summer 1997 IOP: Model Formulation, Results, Uncertainties, and Sensitivities. *J. Atmos. Sci.* 60, 607–625. doi:10.1175/1520-0469(2003)060<0607:crmota>2.0.co;2

Kneifel, S., and Moisseev, D. (2020). Long-Term Statistics of Riming in Nonconvective Clouds Derived from Ground-Based Doppler Cloud Radar Observations. *J. Atmos. Sci.* 77, 3495–3508. doi:10.1175/JAS-D-20-0007.1

Kollias, P., Albrecht, B. A., and Marks, F., Jr. (2002). Why Mie? *Bull. Am. Meteorol. Soc.* 83 (10), 1471–1483. doi:10.1175/bams-83-10-1471(2002)083<1471:wm>2.3.co;2

Kollias, P., Battaglia, A., Tatarevic, A., Lamer, K., Tridon, F., and Pfitzenmaier, L. (2018). “The EarthCARE Cloud Profiling Radar (CPR) Doppler Measurements in Deep Convection: Challenges, Post-Processing, and Science Applications,” in Proc. SPIE 10776, Remote Sensing of the Atmosphere, Clouds and Precipitation VIII, Honolulu, HI, October 22, 2018, 107760R. doi:10.1117/12.2324321

Kollias, P., Clothiaux, E. E., Ackerman, T. P., Albrecht, B. A., Widener, K. B., Moran, K. P., et al. (2016). Development and Applications of ARM Millimeter-Wavelength Cloud Radars. *Meteorol. Monogr.* 57 (1), 170065–179401. doi:10.1175/amsmonographs-d-15-0037.1

Kollias, P. (2007). Considerations for Spaceborne 94 GHz Radar Observations of Precipitation. *Geophys. Res. Lett.* doi:10.1029/2007gl031536

Kollias, P., Tanelli, S., Battaglia, A., and Tatarevic, A. (2014). Evaluation of EarthCARE Cloud Profiling Radar Doppler Velocity Measurements in Particle Sedimentation Regimes. *J. Atmos. Oceanic Technol.* 31 (2), 366–386. doi:10.1175/jtech-d-11-00202.1

Kumar, V. V., Jakob, C., Protat, A., Williams, C. R., and May, P. T. (2015). Mass-flux Characteristics of Tropical Cumulus Clouds from Wind Profiler Observations at Darwin, Australia. *J. Atmos. Sci.* 72, 1837–1855. doi:10.1175/jas-d-14-0259.1

Lamer, K., Kollias, P., Battaglia, A., and Preval, S. (2020). Mind the gap - Part 1: Accurately Locating Warm marine Boundary Layer Clouds and Precipitation Using Spaceborne Radars. *Atmos. Meas. Tech.* 13, 2363–2379. doi:10.5194/amt-13-2363-2020

Lamer, K., Kollias, P., and Nuijens, L. (2015). Observations of the Variability of Shallow Trade Wind Cumulus Cloudiness and Mass Flux. *J. Geophys. Res. Atmos.J. Geophys. Res. Atmos.* 120, 6161–6178. doi:10.1002/2014jd022950

Lamer, K., and Kollias, P. (2015). Observations of Fair-Weather Cumuli over Land: Dynamical Factors Controlling Cloud Size and Cover. *Geophys. Res. Lett.* 42, 8693–8701. doi:10.1002/2015gl064534

Lareau, N. P., Zhang, Y., and Klein, S. A. (2018). Observed Boundary Layer Controls on Shallow Cumulus at the ARM Southern Great Plains Site. *J. Atmos. Sci.* 75, 2235–2255. doi:10.1175/jas-d-17-0244.1

LeMone, M. A., and Zipser, E. J. (1980). Cumulonimbus Vertical Velocity Events in GATE. Part I: Diameter, Intensity and Mass Flux. *J. Atmos. Sci.* 37, 2444–2457. doi:10.1175/1520-0469(1980)037<2444:cvveig>2.0.co;2

Lhermitte, R. (2002). *Centimeter & Millimeter Wavelength Radars in Meteorology*. Miami, FL: Lhermitte Publications.

Mason, S. L., Chiu, C. J., Hogan, R. J., Moisseev, D., and Kneifel, S. (2018). Retrievals of Riming and Snow Density from Vertically Pointing Doppler Radars. *J. Geophys. Res. Atmos.* 123, 13807. doi:10.1029/2018jd028603

Matrosov, S. Y. (2017). Characteristic Raindrop Size Retrievals from Measurements of Differences in Vertical Doppler Velocities at Ka- and W-Band Radar Frequencies. *J. Atmos. Oceanic Technology* 34 (1), 65–71. doi:10.1175/jtech-d-16-0181.1

Mitchell, D. L., and Finnegan, W. (2009). Modification of Cirrus Clouds to Reduce Global Warming. *Environ. Res. Lett.* 4, 0445102.

Mroz, K., Battaglia, A., Nguyen, C., Heymsfield, A., Protat, A., and Wolde, M. (2021). Triple-frequency Radar Retrieval of Microphysical Properties of Snow. *Atmos. Meas. Tech.* 14, 7243–7254. doi:10.5194/amt-14-7243-2021

National Academies of Sciences, Engineering, and Medicine (2018). *Thriving on Our Changing Planet: A Decadal Strategy for Earth Observation from Space*. Washington, DC: The National Academies Press. doi:10.17226/24938

Oue, M., Kollias, P., Matrosov, S. Y., Battaglia, A., and Ryzhkov, A. V. (2021). Analysis of the Microphysical Properties of Snowfall Using Scanning Polarimetric and Vertically Pointing Multi-Frequency Doppler Radars. *Atmos. Meas. Tech.* 14, 4893–4913. doi:10.5194/amt-14-4893-2021

Pfitzenmaier, L., Battaglia, A., and Kollias, P. (2019). The Impact of the Radar-Sampling Volume on Multiwavelength Spaceborne Radar Measurements Using Airborne Radar Observations. *Remote Sensing* 11, 2263. doi:10.3390/rs11192263

Protat, A., and Williams, C. R. (2011). The Accuracy of Radar Estimates of Ice Terminal Fall Speed from Vertically Pointing Doppler Radar Measurements. *J. Appl. Meteorology Climatology* 50 (10), 2120–2138. doi:10.1175/jamc-d-10-05031.1

Rauber, R. M., Stevens, B., Ochs, H. T., Knight, C., Albrecht, B. A., Blyth, A. M., et al. (2007). Rain in Shallow Cumulus over the Ocean: The RICO Campaign. *B. Am. Meteorol. Soc.* 88, 1912–1928. doi:10.1175/bams-88-12-1912

Sanderson, B. M., Piani, C., Ingram, W. J., Stone, D. A., and Allen, M. R. (2008). Towards Constraining Climate Sensitivity by Linear Analysis of Feedback Patterns in Thousands of Perturbed-Physics GCM Simulations. *Clim. Dyn.* 30, 175–190. doi:10.1007/s00382-007-0280-7

Satoh, M., Noda, A. T., Seiki, T., Chen, Y.-W., Kodama, C., Yamada, Y., et al. (2018). Toward Reduction of the Uncertainties in Climate Sensitivity Due to Cloud Processes Using a Global Non-hydrostatic Atmospheric Model. *Prog. Earth Planet. Sci.* 5, 67. doi:10.1186/s40645-018-0226-1

Schutgens, N. A. J. (2008). Simulated Doppler Radar Observations of Inhomogeneous Clouds: Application to the EarthCARE Space mission. *J. Atmos. oceanic Technol.* 25 (1), 26–42. doi:10.1175/2007jtecha956.1

Silva Dias, M. A. F., Rutledge, S., Kabat, P., Silva Dias, P. L., Nobre, C., Fisch, G., et al. (2002). Cloud and Rain Processes in a Biosphere-Atmosphere Interaction Context in the Amazon Region. *J. Geophys. Res.* 107 (D20), 8072. doi:10.1029/2001JD000335

Skamarock, W. C., Klemp, J. B., Dudhia, J., Gill, D. O., Barker, D., Duda, M. G., et al. (2008). A Description of the Advanced Research WRF Version 3. Boulder, CO: University Corporation for Atmospheric Research, NCAR/TN-475+STR. doi:10.5065/D68S4MVH

Stephens, G. L., van den Heever, S. C., Haddad, Z. S., Posselt, D. J., Storer, R. L., Grant, L. D., et al. (2020). A Distributed Small Satellite Approach for Measuring Convective Transports in the Earth's Atmosphere. *IEEE Trans. Geosci. Remote Sensing* 58, 4–13. doi:10.1109/TGRS.2019.2918090

Storer, R. L., and Posselt, D. J. (2019). Environmental Impacts on the Flux of Mass through Deep Convection. *Q.J.R. Meteorol. Soc.* 145, 3832–3845. doi:10.1002/qj.3669

Sy, O. O., Tanelli, S., Takahashi, N., Ohno, Y., Horie, H., and Kollias, P. (2014). Simulation of EarthCARE Spaceborne Doppler Radar Products Using Ground-Based and Airborne Data: Effects of Aliasing and Nonuniform Beam-Filling. *IEEE Trans. Geosci. Remote Sensing* 52 (2), 1463–1479. doi:10.1109/TGRS.2013.2251639

Tanelli, S., Durden, S. L., and Johnson, M. P. (2016). Airborne Demonstration of DPCA for Velocity Measurements of Distributed Targets. *IEEE Geosci. Remote Sensing Lett.* 13, 1415–1419. doi:10.1109/lgrs.2016.2581174

Tanelli, S., Im, E., Durden, S. L., Facheris, L., and Giuli, D. (2002). The Effects of Nonuniform Beam Filling on Vertical Rainfall Velocity Measurements with a Spaceborne Doppler Radar. *J. Atmos. Oceanic Technol.* 19 (7), 1019–1034. doi:10.1175/1520-0426(2002)019<1019:teonbf>2.0.co;2

Testud, J., Oury, S., Black, R. A., Amayenc, P., and Dou, X. (2001). The Concept of "Normalized" Distribution to Describe Raindrop Spectra: A Tool for Cloud Physics and Cloud Remote Sensing. *J. Appl. Meteorol.* 40, 1118–1140. doi:10.1175/1520-0450(2001)040<1118:tcondt>2.0.co;2

Tiedtke, M. (1989). A Comprehensive Mass Flux Scheme for Cumulus Parameterization in Large-Scale Models. *Mon. Wea. Rev.* 117, 1779–1800. doi:10.1175/1520-0493(1989)117<1779:acmfsf>2.0.co;2

Ulbrich, C. W. (1983). Natural Variations in the Analytical Form of the Raindrop Size Distribution. *J. Clim. Appl. Meteorol.* 22, 1764–1775. doi:10.1175/1520-0450(1983)022<1764:nvitaf>2.0.co;2

vanZanten, M. C., Stevens, B., Nuijens, L., Siebesma, A. P., Ackerman, A. S., Burnet, F., et al. (2011). Controls on Precipitation and Cloudiness in Simulations of Trade-Wind Cumulus as Observed during RICO. *J. Adv. Model. Earth Syst.* 3, a–n. doi:10.1029/2011MS000056

Varble, A., Morrison, H., and Zipser, E. (2020). Effects of Under-resolved Convective Dynamics on the Evolution of a Squall Line. *Monthly Weather Rev.* 148 (1), 289–311. doi:10.1175/mwr-d-19-0187.1

Wang, D., Giangrande, S. E., Feng, Z., Hardin, J. C., and Prein, A. F. (2020). Updraft and Downdraft Core Size and Intensity as Revealed by Radar Wind Profilers: MCS Observations and Idealized Model Comparisons. *J. Geophys. Res. Atmos.* 125, e2019JD031774. doi:10.1029/2019jd031774

Waterman, P. C. (1965). Matrix Formulation of Electromagnetic Scattering. *Proc. IEEE* 53 (8), 805–812. doi:10.1109/proc.1965.4058

Williams, C. R., Carey, L. D., Chandrasekar, V., Gatlin, P. N., Haddad, Z. S., Meneghini, R., et al. (2014). Describing the Shape of Raindrop Size Distributions Using Uncorrelated Raindrop Mass Spectrum Parameters. *J. Appl. Meteorol. Climatol.* 53, 1282–1296. doi:10.1175/JAMC-D-13-076.1

Williams, C. R. (2012). Vertical Air Motion Retrieved from Dual-Frequency Profiler Observations. *J. Atmos. Ocean. Tech.* 29, 1471–1480. doi:10.1175/JTECH-D-11-00176.1

Willis, P. T. (1984). Functional Fits to Some Observed Drop Size Distributions and Parameterization of Rain. *J. Atmos. Sci.* 41, 1648–1661. doi:10.1175/1520-0469(1984)041<1648:fftsod>2.0.co;2

Xu, K.-M., and Randall, D. A. (2001). Explicit Simulation of Cumulus Ensembles with the GATE Phase III Data: Budgets of a Composite Easterly Wave. *Q.J R. Met. Soc.* 127 (575), 1571–1591. doi:10.1002/qj.49712757506

Yuter, S. E., Houze, R. A., Jr., Smith, E. A., Wilheit, T. T., and Zipser, E. (2005). Physical Characterization of Tropical Oceanic Convection Observed in KWAJEX. *J. Appl. Meteorology* 44, 385–415. doi:10.1175/jam2206.1

Zelinka, M. D., Randall, D. A., Webb, M. J., and Klein, S. A. (2017). Clearing Clouds of Uncertainty. *Nat. Clim Change* 7, 674–678. doi:10.1038/nclimate3402

Zhu, Z., Kollias, P., Yang, F., and Luke, E. (2021). On the Estimation of In-Cloud Vertical Air Motion Using Radar Doppler Spectra. *Geophys. Res. Lett.* 48, e2020GL090682. doi:10.1029/2020gl090682

Zipser, E. J., and Gautier, C. (1978). Mesoscale Events within a GATE Tropical Depression. *Mon. Wea. Rev.* 106, 789–805. doi:10.1175/1520-0493(1978)106<0789:mewagt>2.0.co;2

Conflict of Interest: The authors declare that the research was conducted in the absence of any commercial or financial relationships that could be construed as a potential conflict of interest.

frontiers | Frontiers in Remote Sensing

ORIGINAL RESEARCH
published: 13 April 2022
doi: 10.3389/frsen.2022.836262

Analysis of Scattering Angle Sampling by Multi-Angle Imaging Polarimeters for Different Orbit Geometries

Sabrina N. Thompson[1], *Bastiaan van Diedenhoven*[2]*, *Peter R. Colarco*[1], *Patricia Castellanos*[1], *Eric Lian*[3] and *J. Vanderlei Martins*[4]

[1]NASA Goddard Space Flight Center, Greenbelt, MD, United States, [2]SRON Netherlands Institute for Space Research, Leiden, Netherlands, [3]Computer Science and Engineering Division, University of Michigan, Ann Arbor, MI, United States, [4]Department of Physics University of Maryland Baltimore County, Baltimore, MD, United States

Edited by:
Jens Redemann,
University of Oklahoma, United States

Reviewed by:
Lei Li,
Chinese Academy of Meteorological Sciences, China
Tim Kane,
The Pennsylvania State University (PSU), United States

***Correspondence:**
Bastiaan van Diedenhoven
b.van.diedenhoven@sron.nl

Specialty section:
This article was submitted to Satellite Missions, a section of the journal Frontiers in Remote Sensing

Received: *15 December 2021*
Accepted: *14 March 2022*
Published: *13 April 2022*

Citation:
Thompson SN, van Diedenhoven B, Colarco PR, Castellanos P, Lian E and Martins JV (2022) Analysis of Scattering Angle Sampling by Multi-Angle Imaging Polarimeters for Different Orbit Geometries. Front. Remote Sens. 3:836262. doi: 10.3389/frsen.2022.836262

Per the 2017–2027 Decadal Survey for Earth Science and Applications from Space, many resources are being dedicated to identifying the most cost-effective and appropriate space-based approaches to aid in answering important questions related to the roles of aerosols, clouds, convection, and precipitation within the climate system. This includes developing advanced space-based multi-angle polarimetric imagers for observing aerosols and clouds. The information content with respect to aerosol and cloud properties of such instruments partly depends on the observed range of scattering angles. Factors influencing the sampled scattering angle range include orbit geometry, solar, and viewing angle geometry and swath width. The focus of this research is to gain better insight into how each of these factors influence the scattering angle range sampled by different polarimeter platforms. Based on calculations of example precessing and sun-synchronous orbits, we conclude that the maximum observed scattering angles vary primarily with local equator crossing time (LCT) and location across the swath, while the minimum observed scattering angles vary primarily with LCT and latitude. The altitude and inclination of a precessing orbit determines the length of cycles occurring in LCT and thus in the scattering angle sampling statistics. For a nominal polarimeter with a 57° swath width in an orbit with 65.5° inclination, scattering angle ranges that are suitable for aerosol and cloud remote sensing are sampled somewhere across the swath at most covered latitudes roughly 54% of days throughout the year. Unfavorable scattering angles are observed on days where the orbit is near the terminator and LCT are early in the morning or late in the evening, when solar zenith angles are generally not suited for remote sensing. Decreasing the instrument's swath width to 7° primarily decreases the maximum observed scattering angle, and therefore limits the range of crossing times for which a large range of scattering angles are observed. In addition, the fraction of days throughout the year with favorable scattering angles decreases to roughly 37%. These calculations will aid in the development of next-generation observing systems using combinations of instrument platforms in different orbits, as well for other missions such as those using cubesats.

Keywords: clouds, aerosols, satellite, orbits, polarimetry (1278)

1 INTRODUCTION

Aerosols play a major role in Earth's climate. Depending on their type, they can reflect and absorb solar radiation. Furthermore, they provide the basis for cloud formation (Twomey, 1974). Increased aerosol loading may increase cloud brightness, thus reflecting more solar energy away from Earth to cool the planet. In addition, aerosols can suppress precipitation formation and thereby increase cloud lifetime (Albrecht, 1989). On the other hand, aerosols can also prevent cloud formation by absorbing sunlight and heating the surrounding environment (Ackerman et al., 2000). It is because of this complex mix of indirect and direct effects that quantifying aerosol radiative forcing has been deemed one of the most important, yet challenging, tasks in addressing uncertainty in our understanding of how they affect the climate (IPCC, 2021). Aerosol-cloud interactions contribute the largest uncertainties to estimates and interpretations of the global radiation budget.

The 2017–2027 Decadal Survey for Earth Science and Applications from Space (ESAS 2017) (National Academies of Sciences, Engineering, and Medicine, 2018) generated consensus recommendations from the Earth science community and identified several high priority science objectives, one of which is reducing aerosol radiative forcing uncertainty. Addressing such uncertainty requires improving our understanding of the processes associated with aerosol, clouds, and their interactions. Therefore, in response to NASA's Designated Observables Guidance for Multi-Center Study Plans released in June 2018, six NASA centers partnered with universities, and the private-sector to conduct the Aerosol (A) and Cloud, Convection, and Precipitation (CCP) Pre-formulation Study (A-CCP), which lead to the definition of an Atmosphere Observing System (AOS) to address science objectives related to aerosols, clouds, convection, precipitation and their interactions.

The orbital component of AOS includes instruments in both precessing and sun-synchronous orbits. Precessing orbits (i.e., with a shifting local equator crossing time) offer unique opportunities to observe the diurnal variation in clouds and aerosols at monthly to seasonal temporal scales. Boundary layer height change and convection are examples of processes that change throughout the day and can be captured with such an orbit. However, since such an orbit has a low inclination angle by definition, the latitudinal coverage is limited. The sun-synchronous orbit (also often referred to as "polar orbit") offers coverage at essentially all latitudes and daily sampling at a fixed local time. Such an orbit offers the possibility of extending the record of polar observations, such as those from the Afternoon Constellation or A-train (Stephens et al., 2002).

In 1996, the French space agency (CNES) launched the imaging Polarization and Directionality of the Earth Reflectances (POLDER) instrument on the Advanced Earth Observing Satellite (ADEOS-1). After the premature end of the ADEOS-1 mission in 1997 due to communication failure, POLDER-2 was launched on-board ADEOS-II in 2002 to continue recording the polarimetric observations, although this mission ended prematurely after 10 months as well. In 2009, a third generation POLDER (Polarization and Anisotropy of Reflectances for Atmospheric Sciences coupled with Observations from a Lidar, PARASOL) was launched into the A-train constellation (Fougnie et al., 2007). In 2013, PARASOL was permanently shut down. Since then, other polarimeters in various orbits have been deployed and are planned in the future. Currently, the Hyperangular Rainbow Polarimeter (HARP) instrument is deployed on a 3U CubeSat. It was released in 2020 from the International Space Station (ISS) and is in a precessing orbit with an inclination of about 51.6°. In the near future, the multi-angular, multi-spectral polarimeter, SPEXone, and the 60-view angle, four spectral band, three degree of polarization, Hyperangular Rainbow Polarimeter-2 (HARP-2) will be deployed on the upcoming NASA Plankton, Aerosol, Cloud, and ocean Ecosystem (PACE) mission. These instruments will be launched into a sun synchronous orbit with a local equator crossing time (LCT) near 1:00 p.m (Werdell et al., 2019). Furthermore, the Multi-Viewing-Channel-Polarisation Imager (3MI) will be deployed on the MetOp-Second Generation series, which will have an orbit with an early morning crossing time (Marbach et al., 2015). Together, these polarimeters will be used to advance our understanding of aerosols, clouds and their interactions. For a comprehensive list of past and planned polarimeters we refer to Dubovik et al. (2019).

Multi-angular imaging polarimetric observations provide the angular distribution of scattered atmospheric radiation as well as its polarization state at multiple wavelengths (Dubovik et al., 2019). Polarimetric remote sensing allows to accurately characterize atmospheric aerosols and retrieve microphysical properties of clouds (Mishchenko and Travis, 1997; Mishchenko et al., 2004; Hasekamp and Landgraf, 2007; Alexandrov et al., 2012a,b; van Diedenhoven et al., 2012; Stamnes et al., 2018; Li et al., 2020, 2022). Information content of multi-angle polarimetric measurements for aerosol and cloud remote sensing depends on the minimum, maximum, and range of scattering angles sampled. For instance, with a multi-angle imaging polarimeter, cloud droplet size distribution is determined by observing a rainbow at cloud top, properly called "cloud bow" (Alexandrov et al., 2012a).

Cloud-bow retrievals can be performed when the minimum scattering angles sampled is less than 135° and maximum scattering angles are greater than 155° (Alexandrov et al., 2012a,b). Furthermore, the angular resolution of the observation within that scattering angle region needs to be about 2° or better (Miller et al., 2018). Additionally, for ice-topped clouds, the ice crystal shape and scattering asymmetry parameter can be inferred from polarimetric observation in the scattering angle range between about 120° and 150° (van Diedenhoven et al., 2012; van Diedenhoven et al., 2020). For aerosol retrievals, a recent study by Fougnie et al. (2020) has shown that the scattering angle range distribution has a major impact on retrieval performance. Their results indicate that sampling minimum scattering angles close to 120° and maximum scattering angles greater than 150° allows effective retrieval of fine and coarse mode aerosol properties. Furthermore, five viewing angles are generally sufficient for aerosol polarimetry

TABLE 1 | Main orbital parameters derived from two-line element (TLE) data.

Orbit	Mean altitude	Inclination	Right ascension of ascending node	Eccentricity	Argument of periapsis
SSO	450-km	98.2°	304.5°	0.00026	249.8°
PO	407-km	65.5°	129.5°	0.0015	15.5°

(Wu et al., 2015). In summary, sampling scattering angles that at least includes the 120°–155° range is generally favorable for both aerosol and cloud polarimetric retrievals.

Fougnie et al. (2020) also discussed the general sampling of scattering angles with multi-angle instruments across instrument swath and with latitude, which they represent in so-called Scattering Angle Range Distribution (ScARD) plots. Their study is focused on platforms in a sun-synchronous orbit with a morning LCT. However, a better understanding of variability in scattering angle statistics for multi-angle instruments in different orbits is imperative for mission planning and design, as well as development of retrieval algorithms for cloud and aerosol properties. In this paper we will analyze scattering angle statistics as a function of solar and view geometry, as well as season, latitude, swath width, and LCT. The occurrences of favorable viewing geometries to perform aerosol and cloud retrievals from different orbit configurations using multi-angle imaging polarimeters are investigated.

The remainder of the paper is divided into three sections. In **Section 2**, the calculation methods and geometry definitions are discussed. In **Section 3**, the scattering angle sampling statistics are presented, followed by the conclusions and considerations for mission design, which are summarized in **Section 4**.

2 MATERIALS AND METHODS

As part of this study, a HARP-like polarimeter (Martins et al., 2018) was modeled in a precessing and a sun-synchronous orbit (SSO). The precessing orbit (PO) was modeled based on the Global Precipitation Measurement (GPM) mission (Neeck et al., 2014) with an inclination of 65.5°. The inclination of the SSO was set to 98.2° and the LCT was set to match the LCT of Aqua in the A-train constellation at 1:30 p m (Parkinson, 2003). They were modeled using orbital parameters derived from Two-Line Element (TLE) data as shown in **Table 1**. The TLEs were propagated using an Simplified General Perturbations Theory No.4 (SGP4) orbit propagator during the simulation to model a one-year mission period. The SGP4 orbit propagator is one of five mathematical algorithms used for satellite tracking and orbit prediction. It uses TLE sets produced by North American Aerospace Defense Command (NORAD) and NASA to propagate an orbit over a specified time frame, thus calculating the position and velocity (Vallado et al., 2006; Vallado and Crawford, 2008). It considers effect of perturbations due to Earth oblateness, solar and lunar gravitational effects, and orbital decay using an atmospheric drag model. These orbits are used as examples to study the effects of orbital characteristics such as inclination and LCT on the sampling of scattering angles. These two orbits were considered as they were identified as candidates for meeting A-CCP/AOS science objectives.

The HARP-like multi-angle polarimeter used in this study was modeled with 996 cross-track pixels and 10 along-track viewing angles ranging from 56.5° forward to 56.5° aft. The nominal swath width is 57°, leading to a swath width on the surface of about 500-km for both orbits. In addition, the effect of a decreased swath width of 7° (or about 50-km) was investigated. Although the original HARP-2 design includes 60 viewing angles at one wavelength band and 10 at the other three bands (Werdell et al., 2019), here we consider only ten along-track views per observation. However, the statistics are not substantially affected if more viewing angles are considered. Since we are focused on observations of multi-angle polarimeters, only daytime segments of the orbits are considered. **Figure 1** shows the daytime segments of the ground tracks for a single orbit of each orbit-configuration (PO and SSO) on 1 January 2006. On this day, the LCT of both the precessing and sun-synchronous orbit is 1:30 p.m. The year 2006 is modeled in our instrument simulator for compatibility with the output from the high spatial resolution GEOS-5 Nature Run (G5NR) model output, also being used in the A-CCP study to provide synthetic observations of nature to define retrieval algorithms and uncertainties (Castellanos et al., 2018).

The solar and viewing geometry for the ground pixels within the polarimeter swath were determined. Solar calculations are based on equations from Astronomical Algorithms (Meeus, 1991). The view angles of interest from ground-to-instrument locations are view zenith and azimuth angles. The view zenith angle, θ_v, is defined as the complement of the spacecraft elevation angle β as shown in **Figure 2**. Using the Law of Sines and basic properties of triangles, θ_v was determined for each observation ground-pixel. Once the solar and view angles were determined, they were used to compute the scattering angle γ at each observation ground-pixel (target). **Figure 3** shows the geometrical relationship between the three angles. The Spherical Law of Cosine was used to determine the scattering angle γ using:

$$\gamma = 180° - \arccos\left[\cos(\theta_s)\cos(\theta_v) + \sin(\theta_s)\sin(\theta_v)\cos(\phi)\right], \quad (1)$$

where θ_s and θ_v are the solar zenith and view zenith angles, respectively, and ϕ is the relative view azimuth angle.

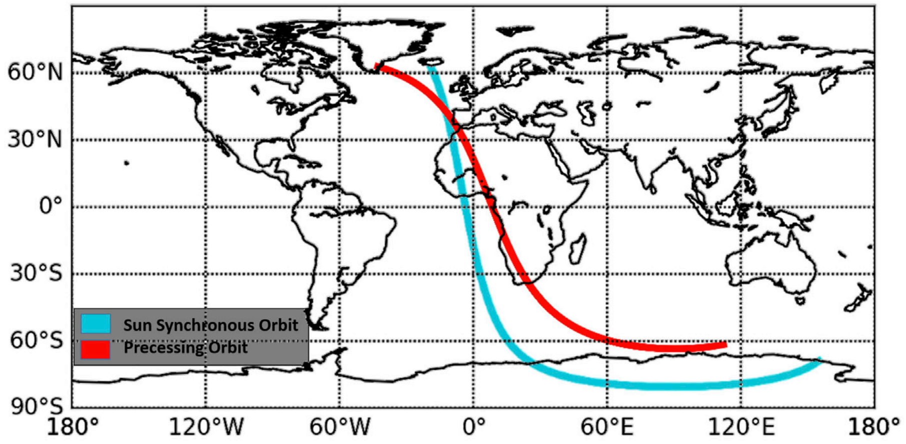

FIGURE 1 | The precessing (red) and sun-synchronous (blue) ground track for a single daytime orbit on 1 January 2006. The orbits are based on GPM and Aqua missions, respectively. The daytime segment of the ground tracks are shown here.

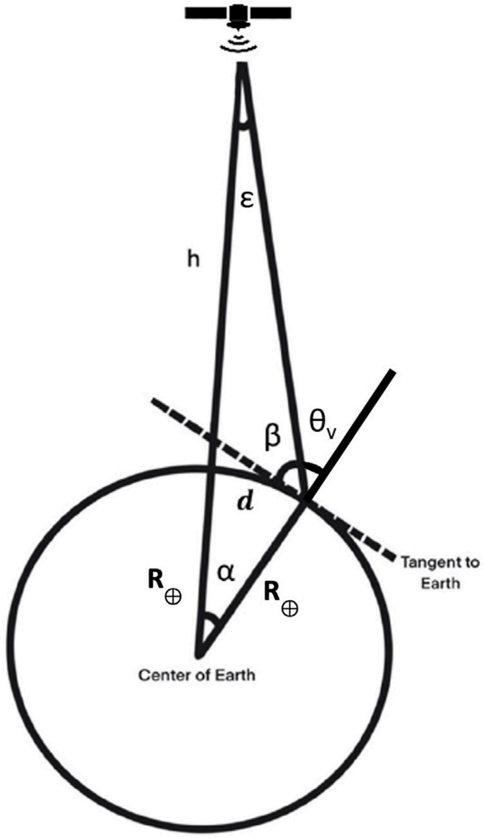

FIGURE 2 | Schematic of viewing geometry relative to Earth. The radius of Earth is represented by $R_{\oplus}$, h is the altitude of the spacecraft/sensor, ϵ is the swath half-angle, β is the spacecraft elevation angle, θ_v is the view zenith angle, α is the angle between the spacecraft position vector and the ground target, and d is the ground coverage of half of the swath [in kilometers].

The output from the simulation are scattering angles, latitudes, longitudes, and time for the multi-angle polarimeter swath at its' various viewing angles. These results are then used to investigate scattering angle statistics for each orbit.

3 ANALYSIS

The inclination of an orbit plays an important role in remote sensing from space. It determines which parts of the Earth the ground track will cover for a given orbit. For instance, the ground track of the precessing orbit (PO) considered in this study is limited to between 65.5° North and 65.5° South in latitude. The sun-synchronous orbit (SSO), on the other hand, covers higher latitudes owing to its high inclination. This is one of the reasons why SSOs are leveraged for most Earth-observing remote sensing applications. In addition to the ground coverage afforded by choice of orbit inclination, there are other factors that come into play for making Earth-observations from these orbits. For instance, the observing platform on the SSO is confined to a single observing time (mean LCT). Since its orbital inclination is retrograde (greater than 90°), the precession of its orbital plane around Earth's axis of rotation (nodal precession) is positive and thus, can be designed to match the precession of the Earth's orbit. This requires specific combinations of the orbital altitude and inclination to reach a desired mean LCT for the SSO. Furthermore, a SSO with a LCT in the afternoon/morning will have its ascending/descending part of the orbit in daytime. In contrast, the PO has an inclination less than 90°, making it a prograde orbit around Earth. The precession is westward and goes against the direction in which the Earth rotates. As a result, the mean LCT of the orbit changes over time. The daylight orbit segment alternates between the descending and ascending parts. This drift in mean LCT may be advantageous for an observing

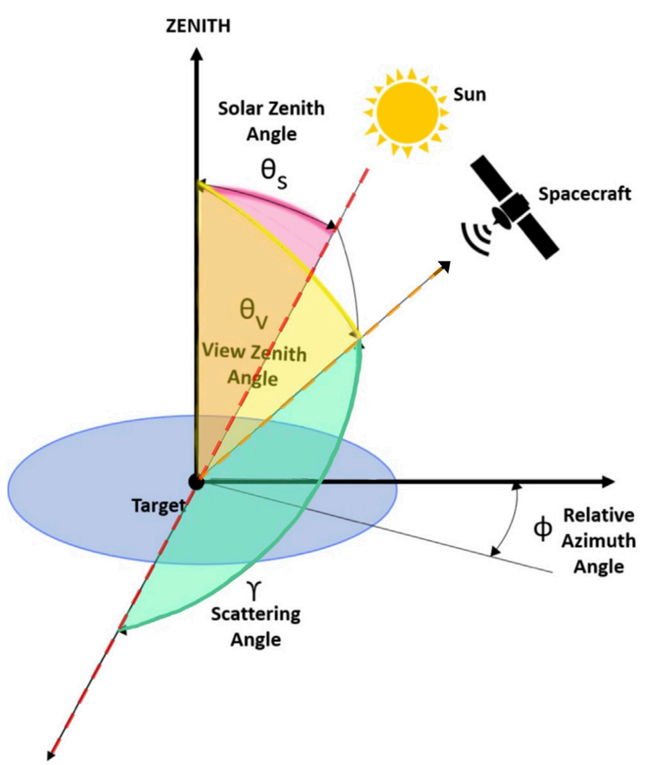

FIGURE 3 | Schematic of a given solar and viewing geometry and corresponding scattering angle, defined as the angle between the solar vector, indicated by the red-dashed line and the viewing vector, indicated by the orange dashed line.

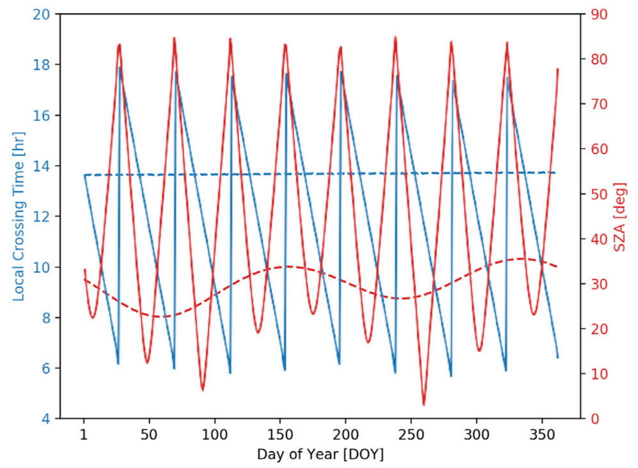

FIGURE 4 | The local equator crossing time (blue) and solar zenith angles at the equator (red) as a function of day of year for the precessing (solid) and sun-synchronous orbits (dashed).

platform on this orbit, as it allows more of the diurnal cycle of atmospheric processes to be captured at seasonal time scales. It is important to note that the rate of precession for an orbit depends not only on inclination, but on the ellipticity of the orbit as well. The two orbits used in this study were circular orbits.

Figure 4 shows LCT and solar zenith angle (SZA) for the PO and SSO for the one-year mission simulation. The data shown in this figure was captured for the day time segment of the orbits. The LCT and SZA for the orbits are depicted in blue and red, respectively. The SSO maintains a constant mean LCT of 1:30 p.m throughout the year, while the SZA varies with season between 20° and 35° when crossing the equator. In contrast to the SSO, both the LCT, and SZA for the PO change in a cyclical pattern throughout the year. For instance, as the orbit moves from south-to-north through the equatorial plane (ascending node) during the day, then shifts to north-to-south (descending node), the LCT changes accordingly. In the beginning of the year, the orbit crosses the descending node during the daytime segment of the orbit. Therefore, on the first day of January, the LCT is roughly 2:00 p.m, then it transitions to an earlier time of roughly 11:00 a.m halfway through the month. By the end of January, the LCT shifts to 6:00 a.m. In the beginning of February, the LCT jumps to 6:00 p.m, as the daytime portion of the orbit switches to the ascending part of the orbit. It then transitions back down to about 6:00 a.m by the end of the month to early March. Then the daytime part of the orbit switches back to descending node and LCT jumps to 6:00 p.m again. This cycle continues throughout the year, with minute-level changes in LCT taking place each day. The SZA changes with the LCT accordingly, while its amplitude varies with season.

The duration of this cycle of LCT (C_{LCT}) for a given orbit around Earth can be approximated based on its orbit characteristics (Capderou, 2014), namely altitude a and inclination i, using:

$$C_{LCT} = \frac{-365.25}{2k\left(\frac{R_{\oplus}}{R_{\oplus}+a}\right)^{\frac{7}{2}} \cos(i) + 2}, \tag{2}$$

where $R_{\oplus}$ is the radius of Earth and k is the constant of Sun synchronicity that takes into account the motion of Earth around the Sun, Earth's mass and so-called J2 perturbations exerted by a non-spherical celestial body on an orbiting spacecraft. For Earth, k is approximately 10.11, meaning at an orbital altitude of 0 km and an inclination of 0°, the nodal precession rate is 10.11 times greater than the angular speed of Earth's axis in its motion around the Sun. For the PO considered in this study, C_{LCT} is approximately -41.7 days. The negative value of C_{LCT} indicates that the line of nodes moves in the opposite direction in which the Earth rotates. Hence, it takes about 41.7 days to return to the same orbital configuration relative to the Sun (taking into account both the ascending and descending segments). This means that about 8 or 9 of such cycles occur in a given year. Furthermore, the orbital configuration relative to the Sun at the start of a year varies per year, with a repeat cycle of about 4 years. The orbit altitude has a relatively small effect on C_{LCT}. For example, increasing the orbit altitude to 700 km leads to a C_{LCT} of 46.7 days. Decreasing (increasing) the inclination angle reduces (increases) the length of time for the platform to return to the same orbital configuration. For the SSO, C_{LCT} is approximately 1,344 days. It is positive because its orbital inclination is retrograde and, hence, the nodal precession is positive. This large number is a clear

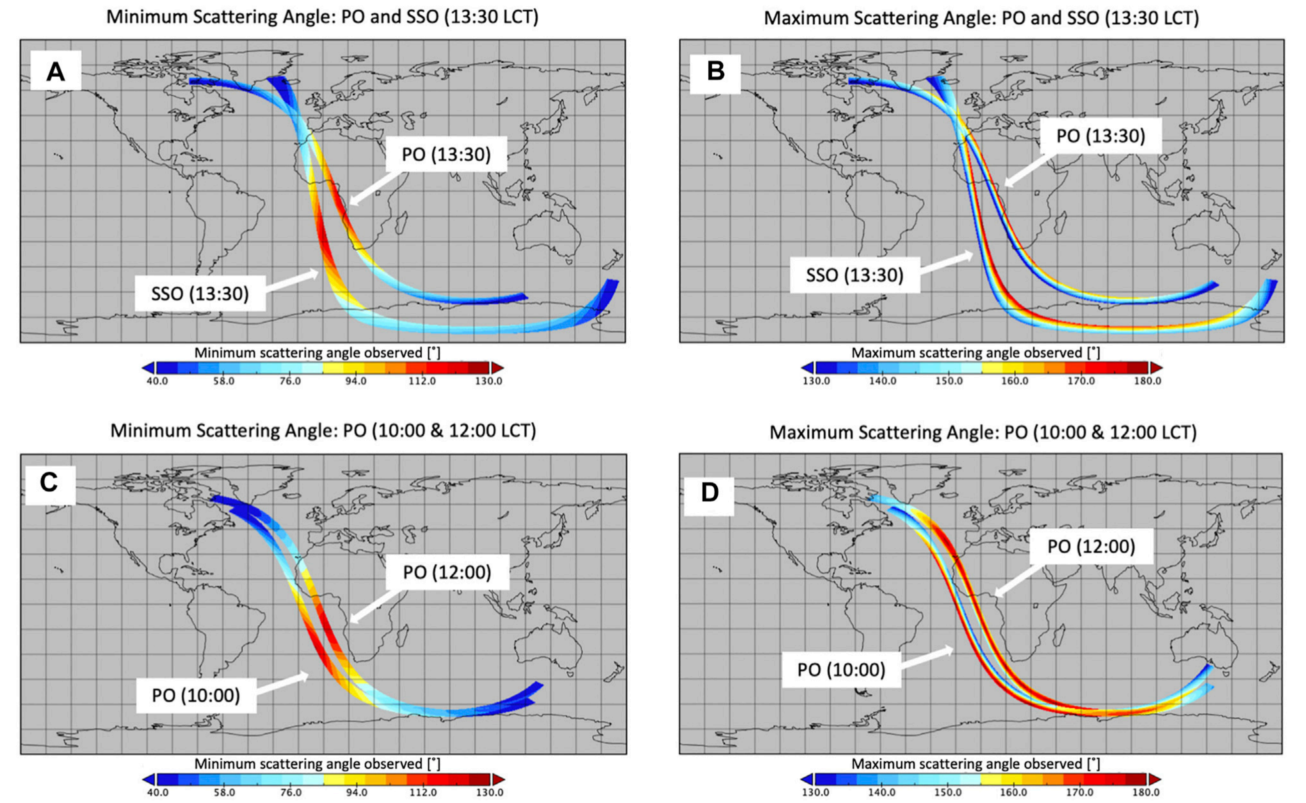

FIGURE 5 | Minimum **(A,C)** and maximum scattering angles **(B,D)** sampled over orbits of the SSO and PO near 13:30 local crossing time **(A,B)** and for the PO near 10:00 and 12:00 noon local crossing time **(C,D)** with the 500-km swath.

indication that the SSO configuration relative to the Sun (and hence, LCT) takes a long time to change. Generally, the slow drift in LCT for polar orbits is compensated via orbital maneuvers so that by design the orbital drift is minimized.

3.1 Scattering Angle Sampling: Variation With Latitude and Across Instrument Swath

Figures 5A,B show the minimum and maximum scattering angles, respectively, observed by the nominal polarimeter over a single SSO and PO orbit on 1 January 2006. On this day, both orbits have a LCT near 1:30 p.m. Generally, the orbits display very similar patterns of minimum and maximum scattering angles, and therefore, range. The minimum scattering angle strongly varies with SZA, and thus latitude, while its variation across the swath is relatively minor. The minimum scattering angle is generally observed by one of the extreme viewing angles (i.e., ±56.5°). In contrast, **Figure 5B** shows that the maximum scattering angle observed is mostly determined by the viewing angle across the swath. The maximum scattering angle is generally observed by the viewing angle observing closest to the anti-solar point. That is, for a SZA of 20°, the viewing angle closest to 20° will observe the maximum scattering angle for a given pixel. The location of the maximum scattering angle across the swath is determined by the relative azimuth angle. Consequently, the scattering angle range for any given pixel will be largely determined by both latitude and place across the swath.

Figures 5C,D show the minimum and maximum scattering angles, respectively, sampled by the PO when LCTs are near 10:00 a.m and noon on 15 and 8 January 2006, respectively. It is apparent that the pattern of minimum scattering angle is more to the south for the earlier LCT, as it is mostly determined by SZA. Furthermore, the variation of maximum scattering angle across the swath is seen to be strongly determined by the LCT as the relative azimuth angle changes. For the noon orbit, highest maximum scattering angles are sampled near the middle of the swath, i.e., by the viewing angle closest to nadir. For the morning orbit, the highest maximum scattering angles are sampled at the west side of the swath, while it was seen on the east side of the swath for the afternoon orbit in **Figure 5B**.

From the results described above, it can be deduced that the minimum scattering angle that can be sampled at a given latitude anywhere within the swath of a multi-angle polarimeter is generally determined by the along-track viewing angle range and not substantially by the swath width. However, the maximum scattering angle that can be sampled anywhere within the swath and is generally determined by the LCT and the swath width. Consequently, the scattering along-track viewing angle range that can be sampled at a given latitude is mostly determined by all three variables, i.e., angular range, LCT

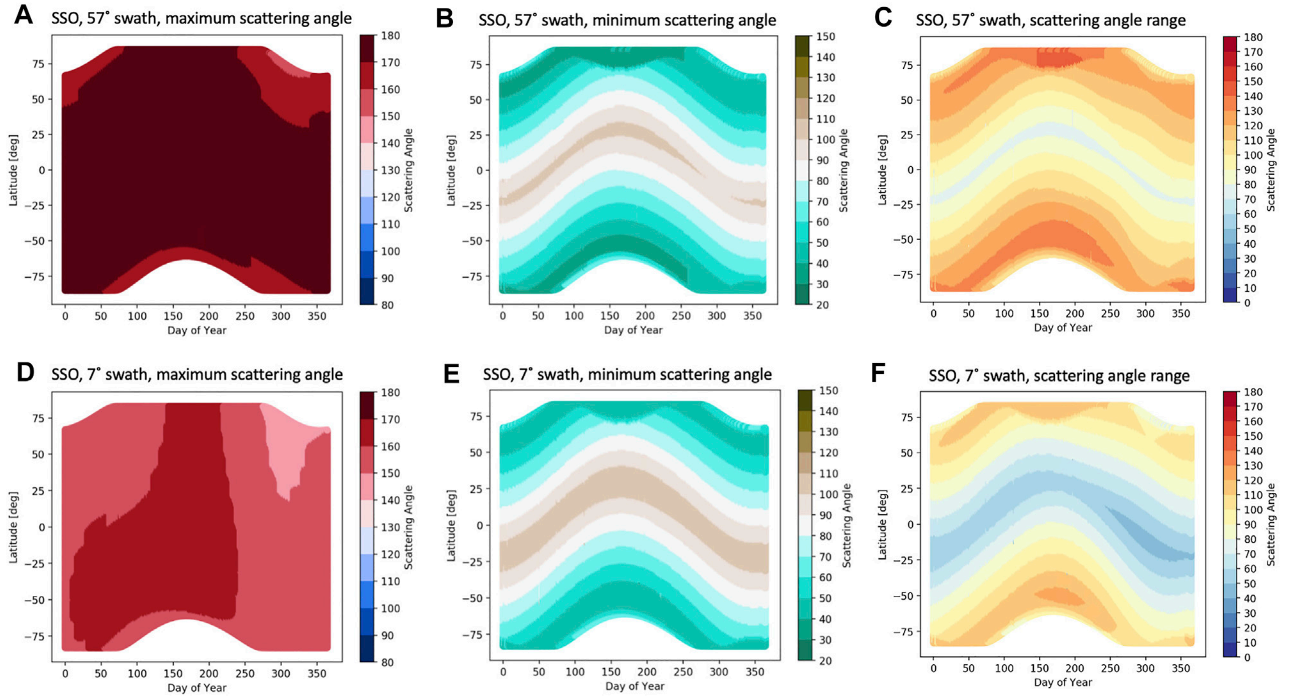

FIGURE 6 | Maximum **(A,D)**, minimum **(B,E)**, and range **(C,F)** of sampled scattering angles for the Sun-Synchronous Orbit (SSO). Results for the 57° (500-km **A–C**) and 7° (50-km **D–F**) swath widths are shown on the top and bottom rows, respectively.

and swath width. These results are consistent with the results presented by Fougnie et al. (2020).

3.2 Scattering Angle Sampling: Variation With Latitude, Day of Year and Swath Width

For both the PO and SSO, the observing platform sensor and solar angles were simulated for an entire year. Since changes in LCT for the PO and SSO are negligibly small during a single day, one orbit was used to represent all orbits that occurred in a day (see **Figure 1**). Only daytime segments of the orbits were analyzed since the sun is the light source for making observations with a passive polarimeter.

As shown in **Figure 4**, for each day of the year, the LCT of the PO changes, while the SSO remains at 1:30 p.m. Scattering angles, γ, at each observation ground-pixel within the instrument swath were computed for each daily-orbit. The maximum and minimum scattering angle observed anywhere within the swath at each latitude was calculated, as well as the scattering angle range.

Figure 6 shows the maximum, minimum, and range of scattering angles, respectively, as a function of latitude and day of year for the SSO. This figure includes the scattering angle statistics for the nominal 57° (500-km) swath width, as well as the narrower, 7° (50-km) swath. There is very little variation in maximum scattering angles throughout the year for the 500-km case. For most latitudes and times, maximum scattering angles greater than 170° are sampled. In the Northern hemisphere during winter, sampled maximum scattering angles are between 160° and 170°.

As expected from the results discussed in **Section 3.1**, the minimum scattering angles mostly vary according to solar zenith angle, and thus with latitude. All minimum scattering angles are smaller than 120° and the sampled scattering angle range is mostly determined by the variation of minimum scattering angle. Note that the minimum scattering angles needed for polarimetric cloud remote sensing are 135° and that availability of smaller scattering angles are not beneficial to the retrieval capabilities (Alexandrov et al., 2012a).

For the case with a 7° (50-km) swath width, the sampled maximum scattering angles are generally a bit lower and there is also more variation in maximum scattering angle throughout the year. In the beginning of the year, the larger maximum scattering angles, between 160° and 170°, can be found in the southern hemisphere. Between early May to early September, these larger maximum scattering angles cover all latitudes in daytime. Then for the remainder of the year, the maximum scattering angles decreases by about 10°, with the exception of areas at latitudes above 25° North, which experience about a 20° decrease. The minimum scattering angles for the two swath widths have a similar magnitude and variability throughout the year, as expected. The ranges sampled for the narrow swath are somewhat smaller, mostly caused by the lower maximum scattering angles that are sampled throughout the swath. Note that these temporal patterns are specifically for afternoon sun-synchronous orbits, which an ascending node in daytime, as used

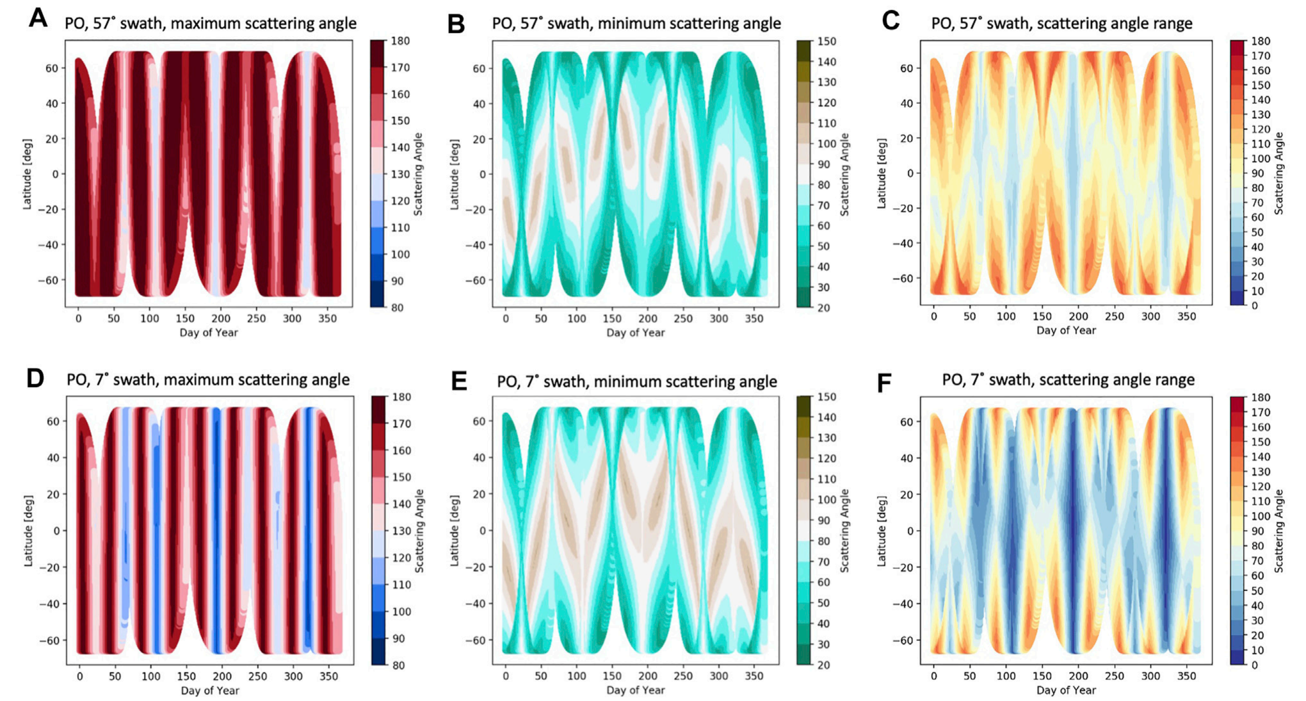

FIGURE 7 | Maximum **(A,D)**, minimum **(B, E)**, and range **(C, F)**, of sampled scattering angles for the Precessing Orbit (PO). Results for the 57° (500-km **A–C**) and 7° (50-km **D–F**) swath widths are shown on the top and bottom plots, respectively.

here. For morning sun-synchronous orbits, which have cross the descending node in daytime, the patterns are inverted in time, i.e., with lowest maximum scattering angles seen in the Northern hemisphere in the beginning of the year (not shown).

For the PO, **Figure 7** shows a very different sampling variation of the maximum, minimum, and range of scattering angles, respectively, as a function of latitude and day of year. As with **Figure 6**, this figure includes the scattering angle statistics for the 57° and 7° (500-km and 50-km) swath widths. Please note that the *y*-axis range is different compared to **Figure 6**, since the PO covers a smaller range of latitudes. Unlike for SSO, in the PO, there is a cyclical variation in minimum and maximum scattering angle and its range throughout the year. This cyclical behavior ties back to the changes in mean LCT and SZAs throughout the year, as shown in **Figure 4**. As discussed in **Section 3**, a full cycle takes about 42 days for this particular precessing orbit leading to about 9 similar periods within a year. For the case with a 57° (500-km) swath width, the maximum scattering angles sampled are above 155° for most of the year. However, on days of the year when the LCT is near 6:00 p.m, or 6:00am, the maximum scattering angles drop to below 130°. Note also that solar zenith angles during these periods are generally also not considered suitable for aerosol and cloud remote sensing (**Figure 4**). Similarly, the minimum scattering angle and the range show a cyclical behavior. Note that the minimum scattering angle is still always smaller than 120°. As a result, favorable viewing conditions for cloud and aerosol remote sensing (with maximum scattering angles greater than or equal to 155° and minimum scattering angles of 120° or lower) occur about 55% of the daytime for the nominal 500-km swath. The frequency of favorable viewing conditions is highest around the equator.

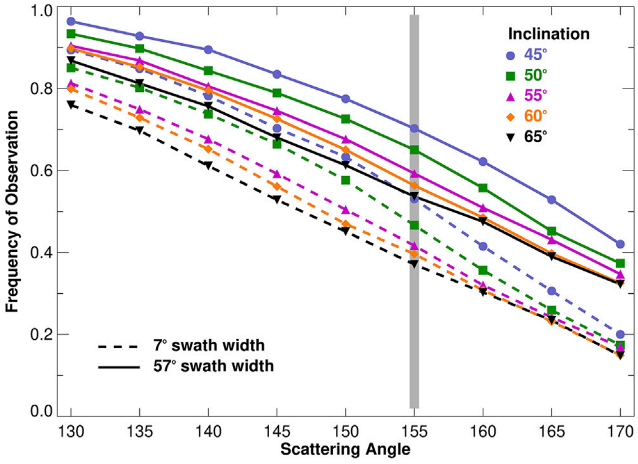

FIGURE 8 | Frequency of sampling maximum scattering angles at the equator greater than the values on the abscissa for precessing orbits with various inclinations (indicated by colors and symbols) and for instruments with a 57° (500-km) or 7° (50-km) swath width, indicated by solid and dotted lines, respectively. The 155° scattering angle is indicated with the grey bar for reference.

For a polarimeter with a narrower swath of 7° (50-km), the periods during which maximum scattering angles above 155° are sampled are substantially shorter, while the periods with low maximum scattering angles (e.g., below 155°) are substantially longer. Furthermore, the minimum scattering angles sampled are slightly increased. Hence, for the narrower 50-km swath, favorable viewing conditions for cloud and aerosol remote sensing occurs less than 40% of the time, thus reducing aerosol and cloud retrieval capabilities compared to the wider-swath instrument.

3.3 Scattering Angle Sampling: Variation With Orbit Inclination

Results shown in **Figure 7** are for a PO with inclination of 65.5°. Lowering the orbit inclination reduces the latitudinal extent of the coverage, while also changing the frequency of the cycles occurring in the scattering angle sampling, according to **Eq. 2**. Furthermore, to investigate how the frequency of scattering angles suitable for aerosol and cloud polarimetry varies with orbital inclination, **Figure 8** shows the frequency of occurrence of observing a maximum scattering angle (X, indicated on the abscissa) as a function of both the instrument swath width and the orbital inclination. This metric is computed as the ratio of, e.g., all points indicated in **Figure 7** with maximum scattering angle greater than or equal to X to the total number of observed points shown. It is thus a relative metric of the frequency of observing at scattering angle $\geq X$ to the total coverage of the platform. Note that the minimal scattering angles are generally below 120° so that the capability for aerosol and cloud polarimetry is mainly determined by the maximum scattering angle sampling only.

The beneficial aspects of the wider swath coverage are apparent in **Figure 8**, where we show at the equator the frequency of days where the maximum scattering angle observed exceeds various thresholds. For the 65° inclination, we find that the instrument observes scattering angles greater 155° for the narrow, 50-km swath, about 37% of the time, increasing to about 54% of the time for the 500 km swath width. The relative frequency of observing higher scattering angles increases as the orbital inclination decreases. For example, at 45° inclination the frequency of observing maximum scattering angle in excess of 155° is about 53% of the time for the 50-km swath and 70% of the time for the 500-km swath. This sensitivity to inclination is because lower inclination orbits are cycling through their precession periods more frequently and so spending a lesser fraction of the time in the unfavorable near-terminator portion of their cycles.

4 CONCLUSION

Based on our analysis, it can be seen that scattering angle statistics observed by a multi-angle instrument for a given orbit are largely determined by LCT, latitude and swath width. For a nominal multi-angle instrument with a ±56.5° viewing angle range and a swath width of 57°, we conclude that:

- the maximum scattering angles sampled varies primarily with LCT and location across the swath;
- the minimum scattering angles sampled varies primarily with SZA and thus with LCT, latitude, and day of year;
- scattering angle ranges suitable for aerosol and cloud remote sensing are sampled at least somewhere across the swath at most covered latitudes throughout the year, except for situations of LCT in the early morning or late evening.

Relative to our nominal HARP-like instrument in the two orbits presented in this study, the following instrument and mission design criteria should be taken into consideration:

- decreasing the instrument’s along-track viewing angle range primarily increases the observed minimum scattering angles;
- decreasing the instrument’s swath width primarily decreases the observed maximum scattering angles and therefore the range of equator crossing times for which scattering angle ranges suitable for aerosol and cloud remote sensing are observed;
- changing the inclination of the precessing orbit will change the latitudinal extent of coverage and the frequency of the cycles occurring in the scattering angle sampling, according to **Eq. 2**. The percentage of viewing conditions favorable for aerosol and cloud polarimetry increases with a decrease of inclination, because of a decreased portion of the overall time spent near the terminator.

In this analysis, we considered the sampling of maximum and minimum scattering angles anywhere in a 57°- or 7°-wide swath. In the case in which the combined observations of a lidar and polarimeter are considered, only a single track within the swath would be taken into account. For example, when considering only the sub-satellite track slightly less favorable results as those seen for the 7°-wide swath are expected. We also note that we assumed the instrument to be pointing straight down. For a sun-synchronous orbit, scattering angle ranges suitable for aerosol and cloud remote sensing are generally sampled in a specific part of the swath depending on LCT. Hence, a narrow-swath instrument could be tilted perpendicular to the flight direction to select the optimal scattering angle sampling. For a precessing orbit, a continuous adjustment of the telescope across-track tilt, e.g., through a gimbal, would be required to select the optimal scattering angle sampling for the varying LCT.

These calculations will aid in decisions for instrument design and choice of orbit for development of next-generation observing systems that include a polarimeter. Furthermore, they may also inform users about the sampling of upcoming multi-angle polarimeters. For example, the SPEXone will be deployed on PACE and, although its swath is relatively narrow at about 8°, it will sample scattering angle ranges suitable for aerosol and cloud remote sensing for most sampled latitudes and days of the year because of PACE’s SSO orbit with a LCT near 1:00 p.m. Furthermore, 3MI will be on the Metop-SG series in a SSO with a LCT near 9:30 a.m, but, as also concluded by Fougnie et al. (2020), will generally sample scattering angle ranges suitable for aerosol and cloud remote sensing because of its relatively wide swath.

DATA AVAILABILITY STATEMENT

The raw data supporting the conclusion of this article will be made available by the authors, without undue reservation.

AUTHOR CONTRIBUTIONS

ST collected the statistical data, performed the comparison and conducted the associated investigations as described in the paper and wrote the initial draft. PC wrote the original code to simulate instrument observations and compute scattering angles for all look angles. EL outfitted the original code to easily manipulate input data and only output data of interest to the study. BvD and PRC provided advisement and contributed to the interpretation of the results in this paper. JVM provided advisement and HARP expertise used for modeling and simulation.

FUNDING

This work was funded through the Internal Research and Development (IRAD) program at NASA Goddard Space Flight Center and by NASA though grant no. 80NSSC20M0224 related to the PACE mission.

ACKNOWLEDGMENTS

The authors would like to thank Dr. Kirk Knobelspiesse, Dr. Robert C. Levy, Dr. Andrew Sayer, Dr. Reed Espinosa, Dr. Edward Nowottnick, Dr. Osku Kemppinen, Dr. Arlindo daSilva, Dr. Xiaoguang Xu, Dr. Lorraine Remer, Dr. Brent McBride, Noah Sienkiewicz, and Dr. Anin Puthukkudy, for insight and constructive feedback throughout the study. Calculations of the orbital viewing geometry were performed at the NASA Center for Climate Science (NCCS) computing center.

REFERENCES

Ackerman, A. S., Toon, O. B., Stevens, D. E., Heymsfield, A. J., Ramanathan, V., and Welton, E. J. (2000). Reduction of Tropical Cloudiness by Soot. *Science* 288, 1042–1047. doi:10.1126/science.288.5468.1042

Albrecht, B. A. (1989). Aerosols, Cloud Microphysics, and Fractional Cloudiness. *Science* 245, 1227–1230. doi:10.1126/science.245.4923.1227

Alexandrov, M. D., Cairns, B., Emde, C., Ackerman, A. S., and van Diedenhoven, B. (2012a). Accuracy Assessments of Cloud Droplet Size Retrievals from Polarized Reflectance Measurements by the Research Scanning Polarimeter. *Remote Sensing Environ.* 125, 92–111. doi:10.1016/j.rse.2012.07.012

Alexandrov, M. D., Cairns, B., and Mishchenko, M. I. (2012b). Rainbow Fourier Transform. *J. Quantitative Spectrosc. Radiative Transfer* 113, 2521–2535. doi:10.1016/j.jqsrt.2012.03.025

Capderou, M. (2014). *Orbit Relative to the Sun: Crossing Times and Eclipse*. Cham: Springer International Publishing, 433–485. doi:10.1007/978-3-319-03416-4_10

Castellanos, P., da Silva, A., Darmenov, A., Buchard, V., Govindaraju, R., Ciren, P., et al. (2018). A Geostationary Instrument Simulator for Aerosol Observing System Simulation Experiments. *Atmosphere* 10, 2. doi:10.3390/atmos10010002

Diedenhoven, B., Ackerman, A. S., Fridlind, A. M., Cairns, B., and Riedi, J. (2020). Global Statistics of Ice Microphysical and Optical Properties at Tops of Optically Thick Ice Clouds. *J. Geophys. Res. Atmos.* 125, e31811. doi:10.1029/2019JD031811

Dubovik, O., Li, Z., Mishchenko, M. I., Tanré, D., Karol, Y., Bojkov, B., et al. (2019). Polarimetric Remote Sensing of Atmospheric Aerosols: Instruments, Methodologies, Results, and Perspectives. *J. Quantitative Spectrosc. Radiative Transfer* 224, 474–511. doi:10.1016/j.jqsrt.2018.11.024

Fougnie, B., Bracco, G., Lafrance, B., Ruffel, C., Hagolle, O., and Tinel, C. (2007). PARASOL In-Flight Calibration and Performance. *Appl. Opt.* 46, 5435–5451. doi:10.1364/AO.46.005435

Fougnie, B., Chimot, J., Vázquez-Navarro, M., Marbach, T., and Bojkov, B. (2020). Aerosol Retrieval from Space - How Does Geometry of Acquisition Impact Our Ability to Characterize Aerosol Properties. *J. Quantitative Spectrosc. Radiative Transfer* 256, 107304. doi:10.1016/j.jqsrt.2020.107304

Hasekamp, O. P., and Landgraf, J. (2007). Retrieval of Aerosol Properties over Land Surfaces: Capabilities of Multiple-Viewing-Angle Intensity and Polarization Measurements. *Appl. Opt.* 46, 3332–3344. doi:10.1364/AO.46.003332

IPCC (2021). *Climate Change 2021: The Physical Science Basis. Contribution of Working Group I to the Sixth Assessment Report of the Intergovernmental Panel on Climate Change*. Cambridge: Cambridge University Press.

Li, L., Che, H., Derimian, Y., Dubovik, O., Luan, Q., Li, Q., et al. (2020). Climatology of fine and Coarse Mode Aerosol Optical Thickness over East and South Asia Derived from Polder/parasol Satellite. *J. Geophys. Res. Atmospheres* 125, e2020JD032665. doi:10.1029/2020JD032665

Li, L., Che, H., Zhang, X., Chen, C., Chen, X., Gui, K., et al. (2022). A Satellite-Measured View of Aerosol Component Content and Optical Property in a Haze-Polluted Case over north china plain. *Atmos. Res.* 266, 105958. doi:10.1016/j.atmosres.2021.105958

Marbach, T., Riedi, J., Lacan, A., and Schlüssel, P. (2015). "The 3MI mission: Multi-Viewing-Channel-Polarisation Imager of the EUMETSAT Polar System: Second Generation (EPS-SG) Dedicated to Aerosol and Cloud Monitoring," in *Polarization Science and Remote Sensing VII. Vol. 9613 of Society of Photo-Optical Instrumentation Engineers (SPIE) Conference Series*. Editors J. A. Shaw and D. A. LeMaster, 961310. doi:10.1117/12.2186978

Martins, J. V., Fernandez-Borda, R., McBride, B., Remer, L., and Barbosa, H. M. J. (2018). "The Harp Hype Ran Gular Imaging Polarimeter and the Need for Small Satellite Payloads with High Science Payoff for Earth Science Remote Sensing," in IGARSS 2018 - 2018 IEEE International Geoscience and Remote Sensing Symposium, 6304–6307. doi:10.1109/IGARSS.2018.8518823

Meeus, J. H. (1991). *Astronomical Algorithms*. Second Edition. Willmann-Bell, Incorporated.

Miller, D. J., Zhang, Z., Platnick, S., Ackerman, A. S., Werner, F., Cornet, C., et al. (2018). Comparisons of Bispectral and Polarimetric Retrievals of marine Boundary Layer Cloud Microphysics: Case Studies Using a LES-Satellite Retrieval Simulator. *Atmos. Meas. Tech.* 11, 3689–3715. doi:10.5194/amt-11-3689-2018

Mishchenko, M. I., Cairns, B., Hansen, J. E., Travis, L. D., Burg, R., Kaufman, Y. J., et al. (2004). Monitoring of Aerosol Forcing of Climate from Space: Analysis of Measurement Requirements. *J. Quantitative Spectrosc. Radiative Transfer* 88, 149–161. doi:10.1016/j.jqsrt.2004.03.030

Mishchenko, M. I., and Travis, L. D. (1997). Satellite Retrieval of Aerosol Properties over the Ocean Using Polarization as Well as Intensity of Reflected Sunlight. *J. Geophys. Res.* 102, 16989–17013. doi:10.1029/96JD02425

National Academies of Sciences, Engineering, and Medicine (2018). *Thriving on Our Changing Planet: A Decadal Strategy for Earth Observation from Space*. Washington, DC: The National Academies Press. doi:10.17226/24938

Neeck, S. P., Kakar, R. K., Azarbarzin, A. A., and Hou, A. Y. (2014). "Global Precipitation Measurement (GPM) Launch, Commissioning, and Early Operations," in *Sensors, Systems, and Next-Generation Satellites XVIII. International Society for Optics and Photonics (SPIE), Vol. 9241*. Editors R. Meynart, S. P. Neeck, and H. Shimoda, 31–44. doi:10.1117/12.2069868

Parkinson, C. L. (2003). Aqua: an Earth-Observing Satellite mission to Examine Water and Other Climate Variables. *IEEE Trans. Geosci. Remote Sensing* 41, 173–183. doi:10.1109/TGRS.2002.808319

Stamnes, S., Hostetler, C., Ferrare, R., Burton, S., Liu, X., Hair, J., et al. (2018). Simultaneous Polarimeter Retrievals of Microphysical Aerosol and Ocean Color Parameters from the "MAPP" Algorithm with Comparison to High-Spectral-Resolution Lidar Aerosol and Ocean Products. *Appl. Opt.* 57, 2394–2413. doi:10.1364/AO.57.002394

Stephens, G. L., Vane, D. G., Boain, R. J., Mace, G. G., Sassen, K., Wang, Z., et al. (2002). The Cloudsat Mission and the A-Train. *Bull. Amer. Meteorol. Soc.* 83, 1771–1790. doi:10.1175/BAMS-83-12-1771

Twomey, S. (1974). Pollution and the Planetary Albedo. *Atmos. Environ. (1967)* 8, 1251–1256. doi:10.1016/0004-6981(74)90004-3

Vallado, D., Crawford, P., Hujsak, R., and Kelso, T. S. (2006). *Revisiting Spacetrack Report #3.* doi:10.2514/6.2006-6753

Vallado, D., and Crawford, P. (2008). *SGP4 Orbit Determination*. doi:10.2514/6.2008-6770

van Diedenhoven, B., Cairns, B., Geogdzhayev, I. V., Fridlind, A. M., Ackerman, A. S., Yang, P., et al. (2012). Remote Sensing of Ice crystal Asymmetry Parameter Using Multi-Directional Polarization Measurements - Part 1: Methodology and Evaluation with Simulated Measurements. *Atmos. Meas. Tech.* 5, 2361–2374. doi:10.5194/amt-5-2361-2012

Werdell, P. J., Behrenfeld, M. J., Bontempi, P. S., Boss, E., Cairns, B., Davis, G. T., et al. (2019). The Plankton, Aerosol, Cloud, Ocean Ecosystem Mission: Status, Science, Advances. *Bull. Am. Meteorol. Soc.* 100, 1775–1794. doi:10.1175/BAMS-D-18-0056.1

Wu, L., Hasekamp, O., van Diedenhoven, B., and Cairns, B. (2015). Aerosol Retrieval from Multiangle, Multispectral Photopolarimetric Measurements: Importance of Spectral Range and Angular Resolution. *Atmos. Meas. Tech.* 8, 2625–2638. doi:10.5194/amt-8-2625-2015

Conflict of Interest: The authors declare that the research was conducted in the absence of any commercial or financial relationships that could be construed as a potential conflict of interest.

frontiers | Frontiers in Remote Sensing

ORIGINAL RESEARCH
published: 27 April 2022
doi: 10.3389/frsen.2022.854735

Time-Delayed Tandem Microwave Observations of Tropical Deep Convection: Overview of the C^{2}OMODO Mission

Hélène Brogniez[1]*, Rémy Roca[2], Franck Auguste[3], Jean-Pierre Chaboureau[3], Ziad Haddad[4], Stephen J. Munchak[5], Xiaowen Li[6], Dominique Bouniol[7], Alexis Dépée[1], Thomas Fiolleau[2] and Pavlos Kollias[8]

[1]Université Paris-Saclay, UVSQ, CNRS, LATMOS/IPSL, Guyancourt, France, [2]LEGOS, CNRS, Toulouse, France, [3]LAERO, Univ Toulouse, CNRS, Toulouse, France, [4]Jet Propulsion Laboratory, Pasadena, CA, United States, [5]NASA GSFC, Greenbelt, MD, United States, [6]GESTARII, Morgan State University, Baltimore, MD, United States, [7]CNRM, Université de Toulouse, Météo-France, CNRS, Toulouse, France, [8]Stony Brook University, Stony Brook, NY, United States

Edited by:
Matthew Lebsock,
NASA Jet Propulsion Laboratory (JPL), United States

Reviewed by:
Rick Schulte,
Colorado State University, United States
Catherine M. Naud,
Columbia University, United States

***Correspondence:**
Hélène Brogniez
helene.brogniez@latmos.ipsl.fr

Specialty section:
This article was submitted to Satellite Missions, a section of the journal Frontiers in Remote Sensing

Received: *14 January 2022*
Accepted: *17 February 2022*
Published: *27 April 2022*

Citation:
Brogniez H, Roca R, Auguste F, Chaboureau J-P, Haddad Z, Munchak SJ, Li X, Bouniol D, Dépée A, Fiolleau T and Kollias P (2022) Time-Delayed Tandem Microwave Observations of Tropical Deep Convection: Overview of the C^{2}OMODO Mission. Front. Remote Sens. 3:854735. doi: 10.3389/frsen.2022.854735

Convective clouds serve as a primary mechanism for the transfer of thermal energy, moisture, and momentum through the troposphere. Arguably, satellite observations are the only viable way to sample the convective updrafts over the oceans. Here, the potential of temporal derivatives of measurements performed in H_2O lines (183GHz and 325 GHz) to infer the deep convective vertical air motions is assessed. High-resolution simulations of tropical convection are combined with radiative transfer models to explore the information content of time-derivative maps (as short as 30 s) of brightness temperatures (dTb/dt). The 183-GHz Tb signal from hydrometeors is used to detect the location of convective cores. The forward simulations suggest that within growing convective cores, the dTb/dt is related to the vertically integrated ice mass flux and that it is sensitive to the temporal evolution of microphysical properties along the life cycle of convection. In addition, the area-integrated dTb/dt, is related to the amount, size, and density of detrained ice, which are controlled by riming and aggregation process rates. These observations, particularly in conjunction with Doppler velocity measurements, can be used to refine these assumptions in ice microphysics parameterizations. Further analyses show that a spectral sampling of the 183 GHz absorbing line can be used to estimate the maximum in-cloud vertical velocity that is reached as well as its altitude with reasonable uncertainties.

Keywords: microwave radiometry, time-derivative, convective mass flux, deep convection, detection of convective updrafts, synergy Doppler radar, passive microwave radiometer

INTRODUCTION

Importance of Convective Transport for Weather and Climate

Tropical convection plays a fundamental role in the climate system by transporting air, water, and momentum from the lower layers of the atmosphere to the free troposphere and has been the subject of numerous field experiments and modeling studies for decades (Houze, 2018). Despite these comprehensive efforts, observations of vertical transport in deep convection over the tropical oceans are simply not available. The lack of understanding of the convective updraft properties and their relationship to environmental factors limits our ability to represent deep convection and its feedbacks in large scale circulation models.

Efficient vertical transport occurs in deep convective cells embedded in organized meso-scale convective cloud structures (Houze and Betts, 1981; Schumacher and Rasmussen, 2020). The two-way relationship between deep convection and its large-scale environment is hence complicated owing to this intermediate agent, that both influences and is influenced by deep convection, and its environment as well. This complexity is perhaps the reason for sustained research despite half a century of dedicated efforts (Tomassini, 2021).

Vertical transport of water permits the formation of large upper level cloud decks that interact with the radiation, the thermodynamics and the dynamics of the large-scale environment in which they form. In return, the cloud mass deposited aloft can feedback onto the initial causes that triggered deep convection in the first place. In the simplest conceptual models, the cloud deck, also known as the stratiform anvil cloud, is associated with a mesoscale circulation that can perturb the surface conditions and help release instability for new deep convective cells to form and contribute to feeding the cloud decks again (Wang et al., 2020). In this simple view, deep convection is a process strongly coupled with its cloud structure. Understanding of this coupling has remained particularly stubborn to unravel despite significant progress over the last decades (Houze, 2018). In particular, the reasons for the observed duration of these convective systems are still debated. From the earlier cold pools-deep convection dynamical coupling theory (Rotunno et al., 1988), the stratiform-cold pools connection (Lafore and Moncrieff, 1989) to the role of radiation in sustaining the system duration (Roca et al., 2020; Gasparini et al., 2021) to the aerosol invigoration process (Seigel and Van Den Heever, 2013), a large suite of candidate lead-processes are at hands. What these considerations all have in common, is the need to couple the deep convection to the cloud deck through, in short, an articulated water budget of the anvil cloud (Redelsperger, 1997). The pathway from deep convection to stratiform anvil mass can be quantified with the convective mass flux. Elsaesser et al. (2021) recently proposed a simple formulation of this relationship. Noting A the surface of the cloud shield of the convective system, A_c the surface of the convective part of cloud shield, M_c the convective mass flux and τ the characteristic decay time, then the growth rate of the surface of the cloud shield of the convective system can be linked to the growth rate of the convective surface A_c and the vertical convergence of the convective mass flux and reads:

$$\frac{dA}{dt} \approx \frac{dA_c}{dt} - \frac{1}{\rho}\frac{dM_c}{dz} - \frac{A}{\tau} \tag{1}$$

with M_c, the convective mass flux over an area that can be spelled out

$$M_c = \rho \sigma w_c \tag{2}$$

where ρ is the air density, σ the surface occupied by deep convective cells and w_c the areal-averaged vertical velocity over the surface σ; the major difficulty is to specify the relative contribution of σ and w_c to M_c (Schubert et al., 2018). This illustrates the importance of both the knowledge of the convective surface and the convective vertical velocity to the cloud budget. While recent investigations seem to favor convective surface variability to explain the variability of cloud mass flux over that of the vertical velocity in the tropics (Feng et al., 2012; Kumar et al., 2015; Giangrande et al., 2016; Masunaga and Luo, 2016; Wang et al., 2020) strong scale dependence is also found and a thorough assessment at the global scale is much needed. Relative humidity in the troposphere also is impacted differently by deep convection with different aggregated states (Bony et al., 2020; Romps, 2021).

Observing the Dynamics of Deep Convection

The role of field campaigns in the investigation of the properties of storm and their control is unquestionable. From the GATE experiment in 1974 that targeted oceanic convection over the tropical Atlantic and its predictability, extensive multi-instrumental campaigns have been conducted. Such campaigns include (cf Houze, 2018): TOGA-COARE in 1992–1993 for the documentation on ocean/atmosphere coupling, AMMA in 2006–2007 for the study of the West African Monsoon, TWPICE in 2006 focusing on the tropical Warm Pool and the Australian Monsoon, DYNAMO in 2011–2012 that deployed over the equatorial Indian Ocean and looked at the Madden-Julian Oscillation. The tremendous deployment of active, passive and *in-situ* instruments during these 2-to-6 months field experiments has been extensively used to develop a better understanding on the micro- and macro-physical properties of convection. Field campaigns are major opportunities to measure vertical motion intensity using airborne instrumentation (Zipser and LeMone 1980; LeMone et al., 1998), in spite of limitations due to aircraft safety.

More recently, using profiling and scanning radars installed on well-instrumented ground-based sites, population of convective updrafts and downdrafts has been statistically characterized at different locations (May and Rajopadhyaya 1999; Ray et al., 2012; Giangrande et al., 2013, 2016; Kumar et al., 2015; North et al., 2017; Kollias et al., 2018; Ovchinnikov et al., 2019; Wang et al., 2020). These studies show that vertical velocity increases with altitude in spite of a competition between entrainment and mixing with the environment and hydrometeor loading that tends to slow the vertical velocity on the one hand and latent heat release on the other (Zipser 2003). They also demonstrate that the vertical mass flux is mainly controlled by the updraft and downdraft core width. These long time series also allow to study the sensitivity of the vertical mass flux to environmental parameters (convective inhibition - CIN, convective available potential energy—CAPE, for instance). Updraft size seems to be strongly related to large scale vertical velocity and to the CIN, whereas higher vertical velocities are observed in relatively dry conditions in the low levels (Kumar et al., 2015; Giangrande et al., 2016).

The quantitative documentation of the properties of embedded deep convection and convective mass flux would help to understand the coupling between deep convection and the associated cloud system. Some works already rely on observations with short revisit time to investigate cloud dynamics. Adler and Fenn (1979) demonstrated the use of infra-red (IR, GOES satellite) imagers and their rapid-scan modes (5min) onboard geostationary platforms to infer the cloud top vertical velocity from the decreasing rate of the IR measurements, assuming a moist adiabatic lapse rate, for a few thunderstorms. This approach was expanded to MTSAT-1R measurements by Hamada and Takayabu (2016) to study cloud top vertical velocity during the growing phase of convection. Low earth orbit (LEO) satellites have also been analyzed in a similar method by Luo et al. (2014) who used the close configuration (1–2min) of the infra-red imagers of the A-Train to study the vertical velocity of convective tops.

As noted, this approach has been applied to IR imagers, which limits the interpretations to cloud tops. In order to reach in-cloud vertical velocities, microwave radiometers and radars in LEO are the instruments to use. However, owing to their long wavelengths (relative to visible light), such instruments must be placed on LEO to achieve the necessary spatial resolution, which makes their temporal sampling quite limited. Indeed, a single LEO instrument will very rarely observe a weather system more than once during the lifetime of the system. On the rare occasion that a single instrument may revisit a storm on two consecutive orbits, the visits are nevertheless separated by the typical amount of time it takes the satellite to complete one orbit, i.e., ~ 90 min. During this re-visit gap, the cloud will typically have undergone dramatic changes, observed only by geostationary satellites orbiting at much higher altitudes.

Recent technological advances have enabled the design of miniaturized microwave instruments that are quite capable and, at the same time, inexpensive enough to consider the formation of a convoy of identical sensors in low-Earth orbit.

Several missions aiming at looking the fast changes of clouds have been proposed in recent years with, for some of them, launch of the demonstrator. For instance, the TEMPEST mission (TEMPoral Experiment for Storms and Tropical systems, JPL/NASA-Colorado State University; Reising et al., 2015; Padmanabhan et al., 2020) proposes to deploy five Smallsats flying 5 min apart to observe the global clouds and their transition to precipitation with microwave sensors. Its demonstrator, TEMPEST-D, successfully deployed from the ISS and operated over 05/2018–07/2021. Rotation maneuvers of the spacecraft allowed to approach the feasibility of the exploitation of measurements of a same scene with a very short revisit time (Schulte et al., 2020). The TROPICS constellation (Time-Resolved Observations of Precipitation structure and storm Intensity with a Constellation of Smallsats, GFSC/NASA-MIT Lincoln Laboratory; Blackwell et al., 2018) will combine six CubeSats distributed into three orbital planes for a 30min revisit time and aims at providing microwave measurements on the lifecycles of extreme meteorological events like storms and cyclones. The test satellite TROPICS-Pathfinder was launched on June 2020 and will be joined in 2022 by the rest of the constellation. One can also mention the C3IEL mission (Cluster for Cloud evolution, ClImatE and Lightning, CNES and ISA; Rosenfeld et al., 2019), that focused on the 3D envelope of clouds from stereocameras onboard two to three nanosats, taking snapshots of the same scene every 20s at two to three different viewing angles. Finally, the 10th Earth Explorer Mission of ESA called Harmony will be a convoy of satellites carrying a multi-beam IR instrument that will measure height-resolved cloud-top movements.

A rather closer formation of satellites, separated in time by Δt ~ 1 min, would reach the temporal scale required to observe the highly nonlinear cloud dynamics present in convective updrafts (Haddad et al., 2017; Sy et al., 2017; Stephens et al., 2019). For instance, Sy et al. (2017) have shown that pairs of Ka-band profiling radars 90s apart would be able to resolve the dry air mass flux and condensed-water flux above the melting level (~5 km in tropical storms). The INCUS mission ("Investigation of Convective UpdraftS") relies on such a constellation of 3 Ka-band radars accompanied by a TEMPEST-D passive radiometer and has been selected recently by NASA as part of its Earth Venture Program.

Inspired by these studies, the proposed C^{2}OMODO mission consists of a tandem of identical passive microwave radiometers separated by less than 3min, that would provide the scientific community with measurements of the convective mass flux M_c and, thanks to the swath of the radiometer, to the surface of the convective cells σ (**Eqs. 1**, **2**).

In **Section 2** we describe further the C^{2}OMODO mission. **Section 3** is dedicated to unravelling the information content of such an observing system thanks to several case studies, idealized (3.1) or nature-like (3.2), to the promising synergies if a Doppler radar is aligned with the tandem (3.3). **Section 4** presents the main lines of retrieval algorithms, from the question of the detection of a convectively active column from d/dt measurements (4.1) to operational "Level-2" products (4.2). **Section 5** draws the main implications of the C^{2}OMODO tandem.

THE C^{2}OMODO "MINI-TRAIN": OVERVIEW OF THE INSTRUMENTS

C^{2}OMODO stands for "Convective Core Observations through MicrOwave Derivatives in the trOpics". This project has been conceptualized in 2018, following a round-table meeting that focused on distributed small instruments (such as radiometers or radars) as an emerging strategy to observe atmospheric dynamics of clouds and storms at very fine temporal scales (Haddad et al., 2017; Sy et al., 2017; Stephens et al., 2019).

The time-delayed observations are conceptually similar to those obtained from ground weather radars, as well as geostationary imagery, which readily show the evolution of precipitation (in the radar case) or cloud tops (in the imagery case) over minutes. The satellite convoys overcome the limitations of geostationary images (sensitive only to the very top of the clouds), and those of ground radar (not available over the tropical oceans). While passive microwave radiometers tend to be more sensitive to the total amount of condensed water in the column (Crewell et al., 2009), multi-channel microwave radiometry, with adequately selected frequencies, may be used

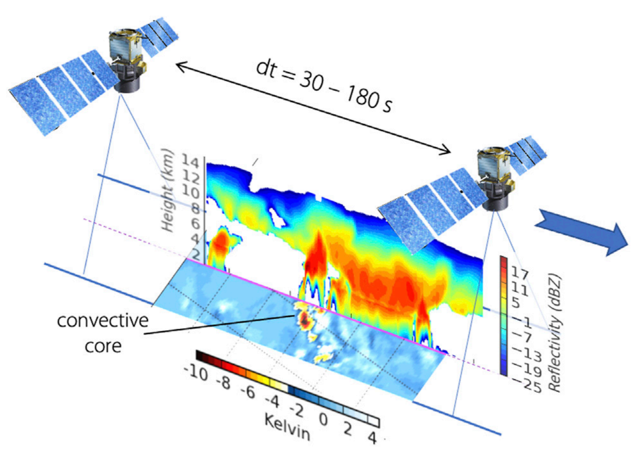

FIGURE 1 | schematic of a convoy of satellites carrying passive microwave instruments providing the horizontal map. The map reveals the intensity of in-cloud upward motion associated to condensed water from time differences of the brightness temperature (in K, over dt = 30s) measured at 183 ± 11 GHz. The vertical cross-section is the vertically-resolved concentration of hydrometeors (reflectivity) as provided by a radar (in the present case, the CloudSat radar at 94 GHz).

to provide vertical information on hydrometeors (Evans et al., 2012; Birman et al., 2017). Then if each satellite instrument is sensitive to the 3-dimensional distribution of condensed water within its field of view, the convoy is sensitive to the change in this condensed water over the minute(s) separating the convoy members.

The C^{2}OMODO mission concept explores this time-difference approach with passive microwave radiometers flying 30–180s apart. The time-lag between the two radiometers is part of ongoing sensitivity studies and is not yet fixed. This is illustrated on **Figure 1** using simulations of the weather forecast model AROME (Application of Research to Operations at MEsoscale) of Météo-France. For this illustration, the two passive radiometers provide the horizontal map of the time difference in brightness temperatures (henceforth Tb and dTb/dt) measured in a 183.31 ± 11 GHz channel, and surround a 94 GHz radar looking at nadir, reflectivity providing vertically resolved distribution of cloud hydrometeors. The convective core sampled for this schematic, associated with the highest values of reflectivities, is clearly visible on the time-difference map and its horizontal structure reveals patterns associated to the convective activity.

The two passive microwave radiometers inherit from the SAPHIR moisture sounder on Megha-Tropiques (Brogniez et al., 2013; Roca et al., 2015), which underwent technical improvements to have a more compact (more receivers for the same volume) and less energy-consuming instrument (Puech et al., 2021), as well as from the ICI sounder onboard the upcoming MetOP-SG (Thomas et al., 2012). This so-called SAPHIR-New Generation (SAPHIR-NG) sounder will observe the 183.31 GHz and 325.15 GHz strong H_2O absorption lines and will be completed by a window channel at 89 GHz (Puech et al., 2021).

At these frequencies, the upwelling radiation from the low troposphere is quite large, and the interaction with the icy hydrometeors that accumulate in the clouds is mostly by scattering. Therefore 183 GHz measurements are generally used very successfully to detect deep convection and overshoots (Burns et al., 1997; Greenwald and Christopher, 2002; Rysman et al., 2016; Chen and Bennartz, 2020; among many others). Since the scattering is strongly dependent to the size of the particle, measurements at 325 GHz will be sensitive to smaller ice particles, thus providing complementary observations to 183 GHz measurements during the formation and dissipation of convection. Hence in presence of hydrometeors the intensity of the depression in the Tb with respect to the Tb of the surrounding clear sky is modulated by the concentration of hydrometeors in the column.

A hyperspectral configuration is also currently considered as an option for the 183 and 325 GHz channels. A reinforced spectral sampling would be valuable for the vertical profiling both for the water vapor estimates in clear sky and the profiling of hydrometeors (Birman et al., 2017). Note that the added-value of this hyperspectral sampling is not considered in the present study.

PRELIMINARY INFORMATION CONTENT STUDIES

This section presents information content studies based on numerical models. An idealized simulation of a single convective cell is first studied and used to test sensitivities to microphysical properties, followed by nature-like simulations covering large domains that convey a wide range of convective activity. The complementarity of the C^{2}OMODO tandem with a Doppler radar is finally addressed with a case study from a large-eddy simulation.

Idealized Study of Individual Convective Cells

The Goddard Cumulus Ensemble (GCE) model was used to conduct two idealized simulations, one with strong and one with weak convection. Warm bubbles are set-up to trigger the convection: a 10-km diameter bubble and peak temperature perturbation of 1K for the strong case and a 3-km diameter bubble and peak temperature perturbation of 3K for the weak case. The characteristics of the GCE model are provided in Appendix A.1. For each of the two idealized situations, four simulations have been conducted: a “control” simulation, a “graupel” simulation that produces less and smaller graupel; a “+cloud ice” simulation that produces more pristine ice particles; and a “graupel and +ice” simulation that combines the changes in “graupel” and “+cloud ice”.

Time series of several parameters from these simulations are shown in **Figure 2**.

Despite the perturbations to the microphysics there are only minor (<10%) differences in the maximum and total condensate at any given time step (**Figure 2** b-c-e-f). This is because the

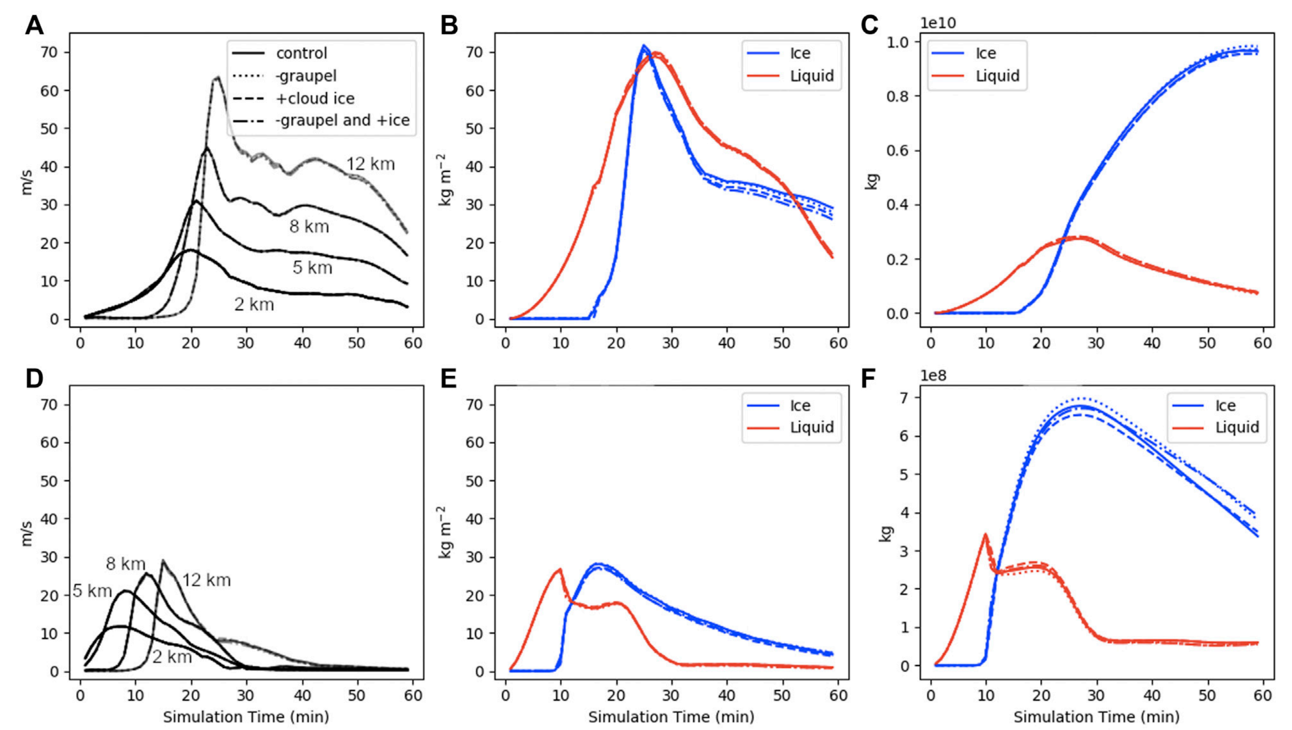

FIGURE 2 | Time series of the maximum updraft speed at four altitudes [in m/s, subplots **(A,C)**], maximum ice and liquid water paths (in kg/m^2, subplots **(B,E)**, and total ice and liquid condensate mass [in kg, subplots **(C,F)**] for the strong (top) and weak (bottom) convection cell simulations and for the four microphysical situations.

instability-driven updraft dominates the condensation process; changes in microphysical process rates affect the partitioning among species, but not the total condensate. There is some separation between experiments after the initial updraft ($t >$ 30 min), where the general effect of the perturbations is to reduce the maximum of ice water path (via reduction of riming, henceforth IWP in kg/m^2), but increase the total ice condensate (by reducing the fall speed as more ice is present in the slower-falling aggregates and cloud ice categories).

The eight GCE simulations were used as input to a radiative transfer model to forward simulate the SAPHIR-NG channels at the radiometer resolution and at 1-min time steps (cf Appendix A.1 for details). Two variables were examined for each channel: the minimum brightness temperature (Tb_{min}, spatial minimum) and the Integrated Scattering Depression (ISD). The ISD (in K.km^2) is defined as the inverse area integral of the Tb at time step t ($Tb_{(t)}$) subtracted from the mean background Tb at the first time step of the simulation, prior to any condensation ($Tb_{(t=0)}$):

$$ISD(t) = \iint \left(Tb_{(t=0)} - Tb_{(t)}\right) dydx \quad (\text{in K.km}^2) \qquad (3)$$

The ISD is computed for each frequency. The time series of Tb_{min} and its derivative dTb_{min}/dt are shown in **Figure 3** for two selected channels in the 183 and 325 GHz bands. These channels were chosen for their similar weighting functions and clear-sky Tb. Differences are therefore due to the frequency dependence of the scattering properties of the various hydrometeor species.

The initial pattern, for both frequencies and convective cell strengths, is a rapid decline of Tb_{min} caused by the formation of large quantities of condensate. Tb_{min} decreases sharply during the initial period when IWP is increasing. There are some differences between the 183 and 325 GHz frequencies: The magnitude of the dTb_{min}/dt is higher and occurs earlier in time at the 325 ± 3.5 GHz channel compared to that of the 183 ± 2.8 GHz channel. This is due to the contribution of supercooled liquid water, which absorbs more strongly at 325 than 183 GHz, which damps the scattering signal more strongly at the higher frequency until the cloud fully glaciates. Thus, dTb_{min}/dt can be used to infer the glaciation state of a convective plume. There is relatively little sensitivity of Tb_{min} or of dTb_{min}/dt to the microphysics perturbations, although the "+cloud ice" experiment did consistently increase Tb_{min} at 325 GHz after the initial updraft stage, due to the change in particle size distribution (smaller cloud ice particles have a lower single scatter albedo than larger aggregate or graupel particles).

The ISD and its time derivative d (ISD)/dt, can also be readily estimated from C^{2}OMODO simulated swath measurements. The time series of these parameters for two selected channels with similar clear-sky weighting functions so the differences can again be attributed to the frequency-dependent scattering properties of the condensed water species that are shown in **Figure 2**.

The ISD is, to the first order, a proxy for the total condensed ice water (**Figure 4**), although some notable differences between

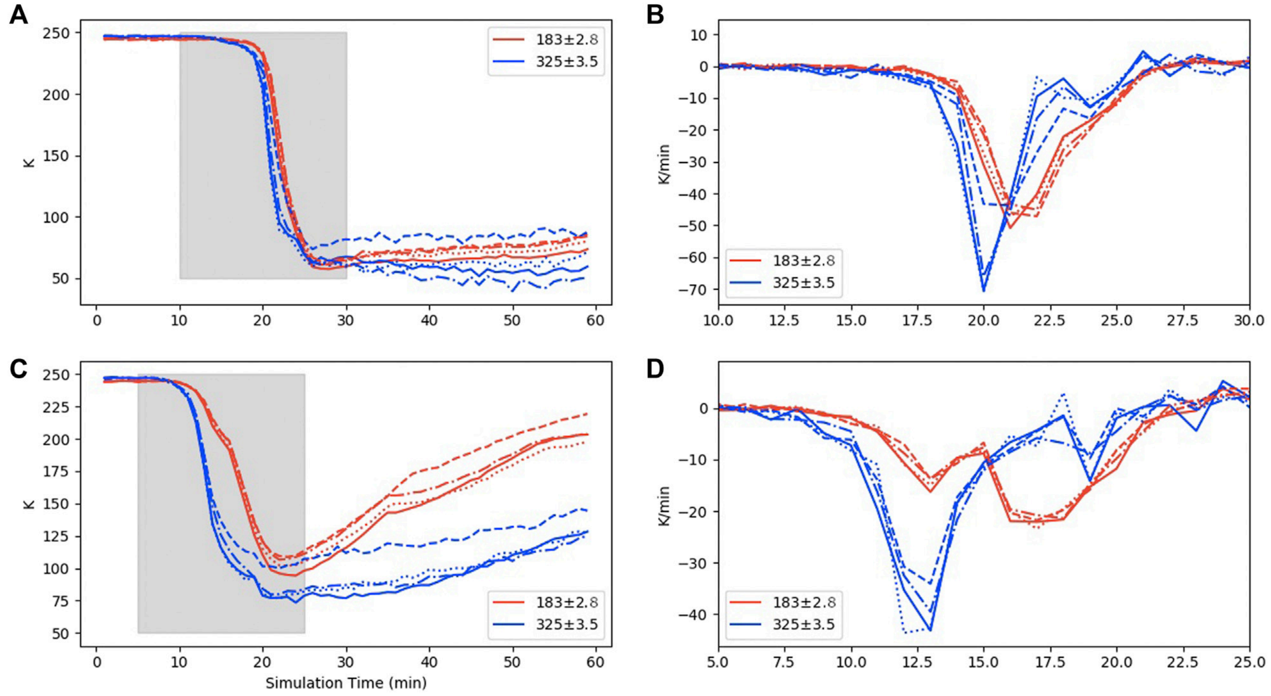

FIGURE 3 | Time series of minimum brightness temperature (Tb_{min} in K, subplots **(A,C)** and its time derivative (dTb_{min}/dt in K/min, subplots **(B,D)**; note the change in time scale) for the C3 (183 ± 2.8 GHz in red) and C8 (325 ± 3.5 GHz in blue) SAPHIR-NG channels. The right panels are temporal zooms of the left panels, covering the period in grey shadings. Top row: strong convection; bottom row: weak convection. The line styles indicate the microphysics perturbation experiments (see **Figure 2**).

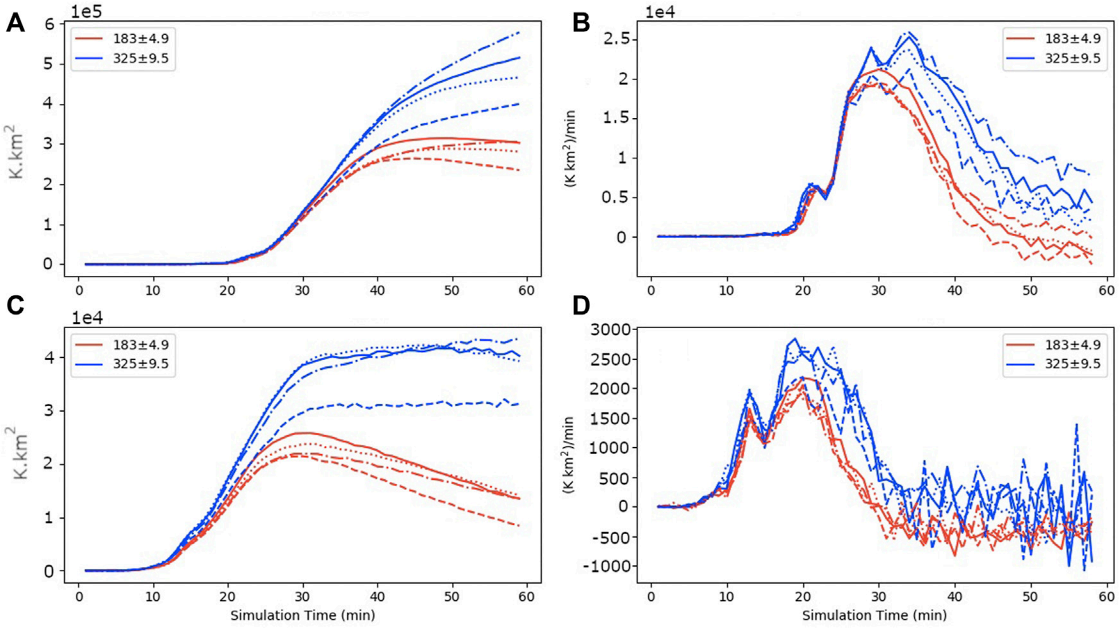

FIGURE 4 | Time series of Integrated Scattering Depression (ISD, in K.km^2, subplots **(A,C)** and its time derivative dISD/dt (in K.km^2/min, subplots **(B,D)** for the C4 (183 ± 4.9 GH, in red) and the C9 (325 ± 9.5 GHz, in blue) SAPHIR-NG channels. Top row: strong convection; bottom row: weak convection. The line styles indicate the microphysics perturbation experiments (see **Figure 2**).

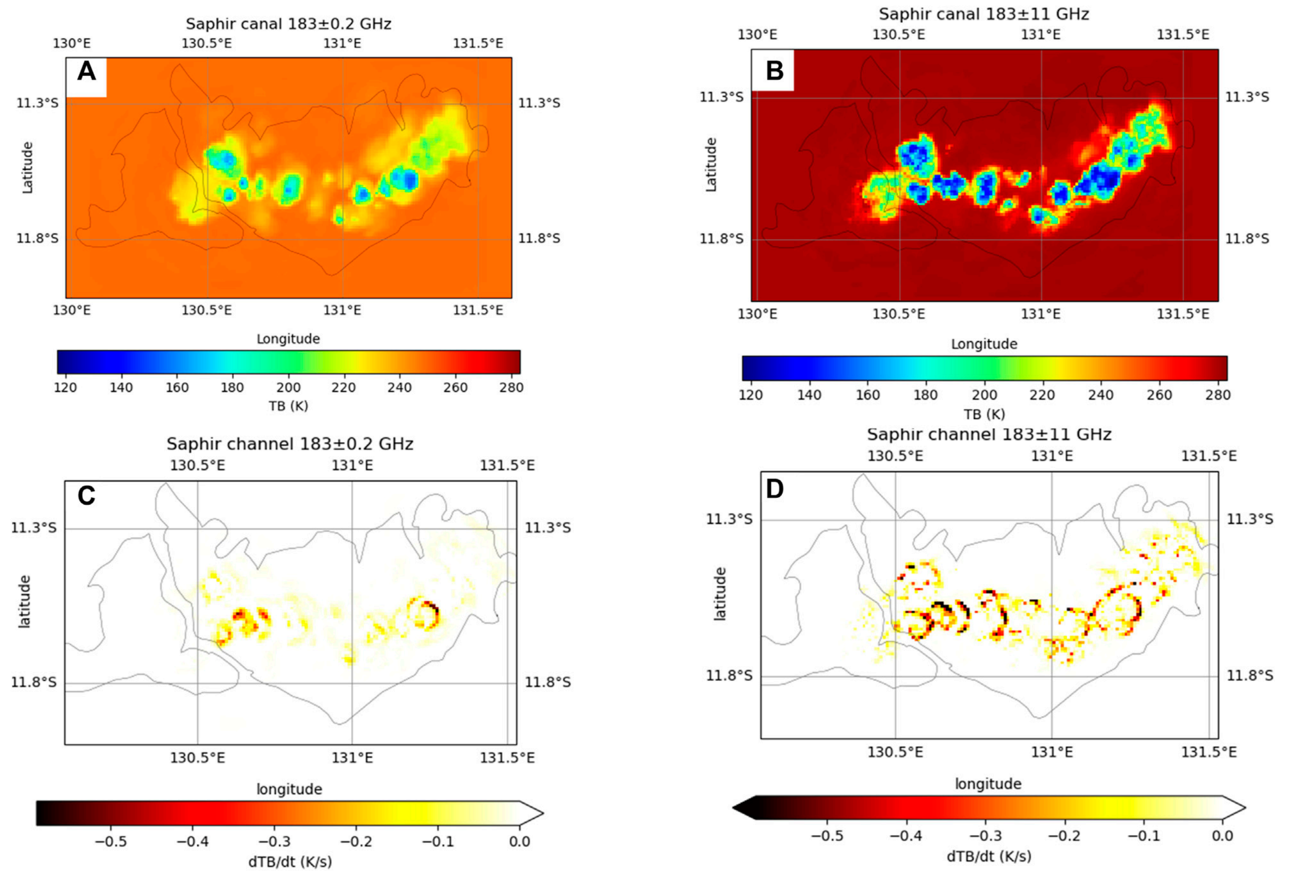

FIGURE 5 | Snapshots from the Meso-NH HEC simulations (model resolution at 1 km). Top panels show the Tb (K) for **(A)** C1 and **(B)** C6 channels, and bottom panels show the dTb/dt for (c) C1 (183.31 ± 0.2 GHz) and (d) C6 (183.31 ± 11 GHz) channels, for a time interval of dt = 1min. On figures **(C)** and **(D)**, the white areas are masked using a deep convection criterion (following **Rysman et al, 2016**) as well as dTb/dt < 0 (see text for details).

frequencies and microphysics experiments can be observed. First, the ISD at 325 GHz exceeds that at 183 GHz, due to the increased scattering optical depth with frequency (Buehler et al., 2007). For the two cases, after the initial updraft (~40min for the strong convective case, ~30min for the weak convective case) the 325 GHz ISD continues to grow or reaches a steady state as the anvil expands, even as the 183 GHz ISD begins to decrease. This is a consequence of the nonlinear dependence of the Tb on IWP. At 325 GHz, the scattering signal saturates at a lower IWP than at 183 GHz and the size of the anvil (not the average IWP) is the dominant factor in determining the ISD.

As with the Tb_{min}, the increase cloud ice experiment ("+cloud ice") had the most consistent effect in reducing the ISD by partitioning the condensed ice into smaller particles with lower single scattering albedos, without a compensating increase in the areal coverage of the anvil. The time derivatives of ISD appear to be more sensitive to the microphysics perturbations at 325 GHz than 183 GHz and are rather noisy on the 1-min scale, especially for the weak convection, suggesting that a longer separation time (~5 min) may be optimal for discerning the microphysical processes that govern anvil evolution than the short (~1 min) timescales that capture the processes in the initial updraft.

Nature-Like Situations Over a Large Domain

In addition to the two idealized simulations described previously, convective-scale simulations from the non-hydrostatic model Meso-NH are used to complete the information content study of the C^2OMODO concept. One situation considers the thunderstorm Hector that develops almost on a daily basis during the period September - April over the Tiwi Islands North of Darwin, Australia (henceforth HEC, initialized by a radiosounding launched on Nov. 30th 2005 at 0000 UTC, Dauhut et al., 2015) while the other situation is a radiative-convective equilibrium ocean case (RCE) from the RCEMIP exercise (Wing et al., 2020). The characteristics of Meso-NH and the details of the simulations are provided in Appendix A.2. Again, the SAPHIR-NG channels are simulated for each set of simulations. **Figure 5** presents a snapshot of the Meso-NH HEC set of simulations in the Tb space for two channels (C1 at 183.31 ± 0.2 GHzand C6 at

TABLE 1 | Main characteristics of the SAPHIR-NG radiometer. DDR: Direct Detection Radiometer. DSB: Double-Sided Band.

Nb of channels	Channels [GHz]	Bandwidth [MHz]	Effective IFOV [km]
1 (DDR)	89 (C0)	4000	≤ 20, 10 km at nadir
6 (DSB)	(rec. SAPHIR/Megha-Tropiques)		≤ 10, 5 km at nadir
	183.31 ± 0.2 (C1)	2 x 200	
	183.31 ± 1.1 (C2)	2 x 350	
	183.31 ± 2.8 (C3)	2 x 500	
	183.31 ± 4.2 (C4)	2 x 700	
	183.31 ± 6.8 (C5)	2 x 1200	
	183.31 ± 11 (C6)	2 x 2000	
3 (DSB)	(rec. ICI/MetOp-SG)		≤ 6, 3 km at nadir
	325.15 ± 1.5 (C7)	2 x 1600	
	325.15 ± 3.5 (C8)	2 x 2400	
	325.15 ± 9.5 (C9)	2 x 3000	

183.31 ± 11 GHz) and the corresponding time derivative dTb/dt, for a 1 min time step (dt = 1 min).

The minimum Tbs for channels C1 (183.31 ± 0.2 GHz, sounding in the upper troposphere) and C6 (183.31 ± 11 GHz, reaching the top of the boundary layer) are colocated as expected, the intensity of the depression with respect to the surrounding clear sky is much stronger for channel C6 than for channel C1. The maps of the corresponding dTb/dt seem to show that the largest temporal variations are on the edges of the minimum of the Tbs, linking to the anvil evolution as mentioned previously (Section 3.1). It should be noted, however, that the true radiometer resolution (5 km at 183 GHz at nadir, see **Table 1**) will reduce the amplitude of the differences.

The relationship between the simulated Tbs and the model variables is examined for both the HEC and RCE simulations. The focus is on the center of two absorption bands defined from the optional hyperspectral configuration at [183.31; 183.31 + 0.2] = 183.41 GHz and [325.15; 325.15 + 0.2] = 325.25 GHz and for a 1-min delay of the satellite tandem.

To match the expected observational pixel resolution (see IFOV on **Table 1**), the simulation outputs were averaged at the 6 km resolution at 183.31 GHz and 3 km at 325.15 GHz. As underlined in the previous section, the Tbs are strongly sensitive to IWP in deep convection. Two model variables for which a relationship with the observations of the C^2OMODO concept is expected are thus examined: the time derivative of IWP (dIWP/dt), and the IWP-weighted vertical velocity (w_{ice}). More precisely, w_{ice} is computed from the vertically integrated momentum of ice (VIM, in kg/m/s) following

$$VIM(x, y, t) = \int_z \rho(z) r_{ice}(z)\, w(z)\, dz \qquad (\text{in kg/m/s}) \tag{4}$$

$$w_{ice}(x, y, t) = VIM/IWP \quad (\text{in m/s}) \tag{5}$$

r_{ice} is the mixing ratio of the total ice (kg/kg), including cloud ice, graupel and snow, ρ is the density of air (kg/m^3), and w is the vertical velocity (m/s). The variable w_{ice} thus characterizes the vertical wind speed within the icy cloud weighted by the ice content and integrated over the atmospheric column.

Results for the 183.41 GHz channel are shown in **Figure 6**. The grey shading delineates the impact of a 1-K uncertainty on the T_b, which can be considered as a best-case scenario. It is indeed expected that the intercalibration and geolocalization between the two radiometers will add noise to the dTb/dt. Only grid points where the criterion $Tb_{183.31}$-$Tb_{193.31}$ > 0 is satisfied are kept, a criterion successfully used by Rysman et al. (2016) among others to detect deep convection. Due to stronger deep convection activity for HEC than for RCE, the dTb/dt reaches larger negative values in the former simulations (-0.2 K/s) than in the later (-0.1 K/s). Consistently, the median value of dIWP/dt extends up to about 40 g/m^2/s (HEC) and 30 g/m^2/s (RCE). For both simulations, a linear relationship between dTb/dt and dIWP/dt is found. The slope of the regression line taken as the median is equal to -200 g/m^2/K and the interquartile range of the distribution remains close to the median. The good agreement between HEC and RCE suggests that this relationship is weakly dependent on meteorological conditions, at least under tropical situations.

The variation of w_{ice} with dTb/dt is analyzed for a subset of situations, keeping only the deep convective cores in growing stage (**Figure 6**, right). For this, we consider only the grid points where deep convection occurs ($Tb_{183.31}$-$Tb_{193.31}$ > 0, as above) and local minima of Tb and dTb/dt in the horizontal space for the 183.41 GHz channel are found. These additional filters are important because the temporal variation in IWP is due to ice transport in both the horizontal and vertical direction and to microphysical changes in the ice. Therefore, a relationship between w_{ice} and dTb/dt is expected only in the deep convective cores where the vertical transport of ice may be the dominant contributor. As previously, a quasi-linear relationship is found between dTb/dt and w_{ice} (**Figure 6**, right). This time, the slope of the linear regression differs between the simulations: 200 m/K for HEC and -100 m/K for RCE. This difference may be due to differences in the characteristics of deep convection (strength, size, lifetime, . . .) over land (HEC) and over ocean (RCE). Further work is needed to evaluate this hypothesis.

Figure 7 presents the evolution of the same variables dIWP/dt and w_{ice} with respect to dTb/dt for the 325.25 GHz channel. The criterion for the detection of deep convection is adapted at this

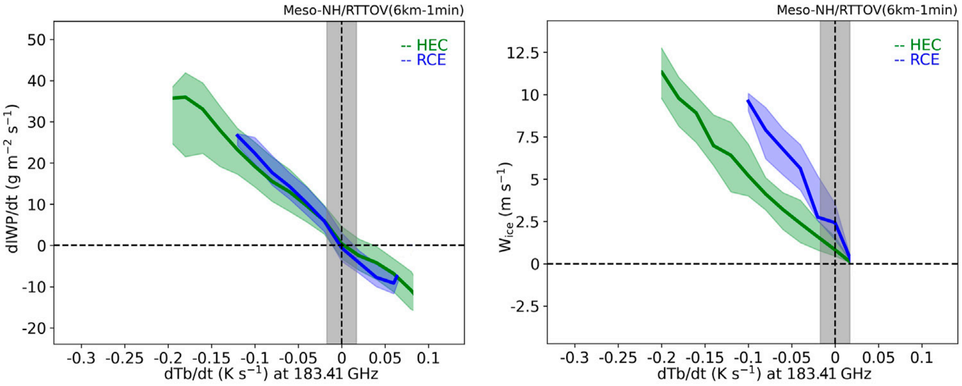

FIGURE 6 | Histogram of dIWP/dt (left, in g/m^2/s) and w_{ice} (right, in m/s) as a function of dTb/dt for the 183.41 GHz channel, at 6 km resolution and with a time delay of the satellite tandem of 1 min. The bin interval is 0.02 K/s. The median (bold lines) and the interquartile ranges (shadings) are shown for HECTOR (HEC/green) and RCE (blue). The grey band delimits a dTb/dt uncertainty of 0.017 K/s, corresponding to a 1 K uncertainty in the Tb measurement for a 1 min time-delay between the satellites. Results are shown for gridpoints verifying the deep convection criterion at 183 GHz (see text), restricted to growing cores for w_{ice} (right).

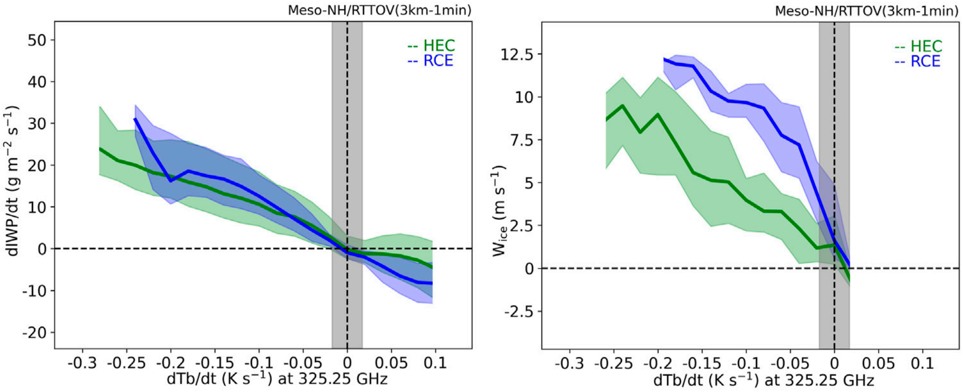

FIGURE 7 | Same as Fig. 6, but for the 325.25 GHz channel and at 3 km resolution.

channel such as only gridpoints where $Tb_{325.15}$-$Tb_{335.15}$ > 0 are kept. The range of dTb/dt goes down to -0.3 K/s. This value is larger than that at 183 GHz because the 3 km resolution at 325 GHz allows to capture more spatial variability in the Tb than the 6-km resolution. The median value of dIWP/dt ranges to about 30 g/m^2/s for both RCE and HEC. This contrasts with the 40 g/m^2/s found for HEC at 183.41 GHz. The stronger absorption of water vapor at 325.25 GHz could explain a lower sensitivity to change in IWP. The time derivative of IWP, dIWP/dt, also varies quasi-linearily with dTb/dt, with an interquartile range closely following the median, but with a slope of the linear regression at median value of about -100 g/m^2/K. This value of the slope is half the value obtained for the 183.41 GHz channel indicating less sensitivity of the 325.25 GHz channel to the amplitude in dIWP/dt. Obtaining information on the time change of the IWP at 3 km resolution is interesting however, to get fine-scale variability.

The variation of w_{ice} with dTb/dt for the 325.25 GHz channel is also shown (**Figure 7**, right). In these cases, a quasi-linear relationship between the two variables can be found with a slope around -40 m/K for HEC and -70 m/K for RCE. Again, the difference in slope for HEC could be due to the contrast of deep convection between land and sea, which requires further study.

Synergy With Doppler Radar

As briefly mentioned previously, the C^{2}OMODO tandem may potentially fly in train with active instruments, in particular a Doppler cloud radar. This section aims at exploring the information content complementarity of both instruments. While the major limitation of a spaceborne Doppler radar is its limited swath, its main strength is its ability to resolve the whole cloud vertical profile. The synergy with the C^{2}OMODO concept and its capability of characterising vertical mass flux at fine resolution over a wide swath is then of particular interest.

This synergy is studied here by simulating a spaceborne 35.5 GHz Doppler radar track. This simulated transect is computed from the Meso-NH RCE runs at 200 m horizontal resolution (large-eddy simulation, see Appendix A.2) The spaceborne Doppler radar simulator (Kollias et al., 2014; Kollias et al., 2018) estimates the total backscatter

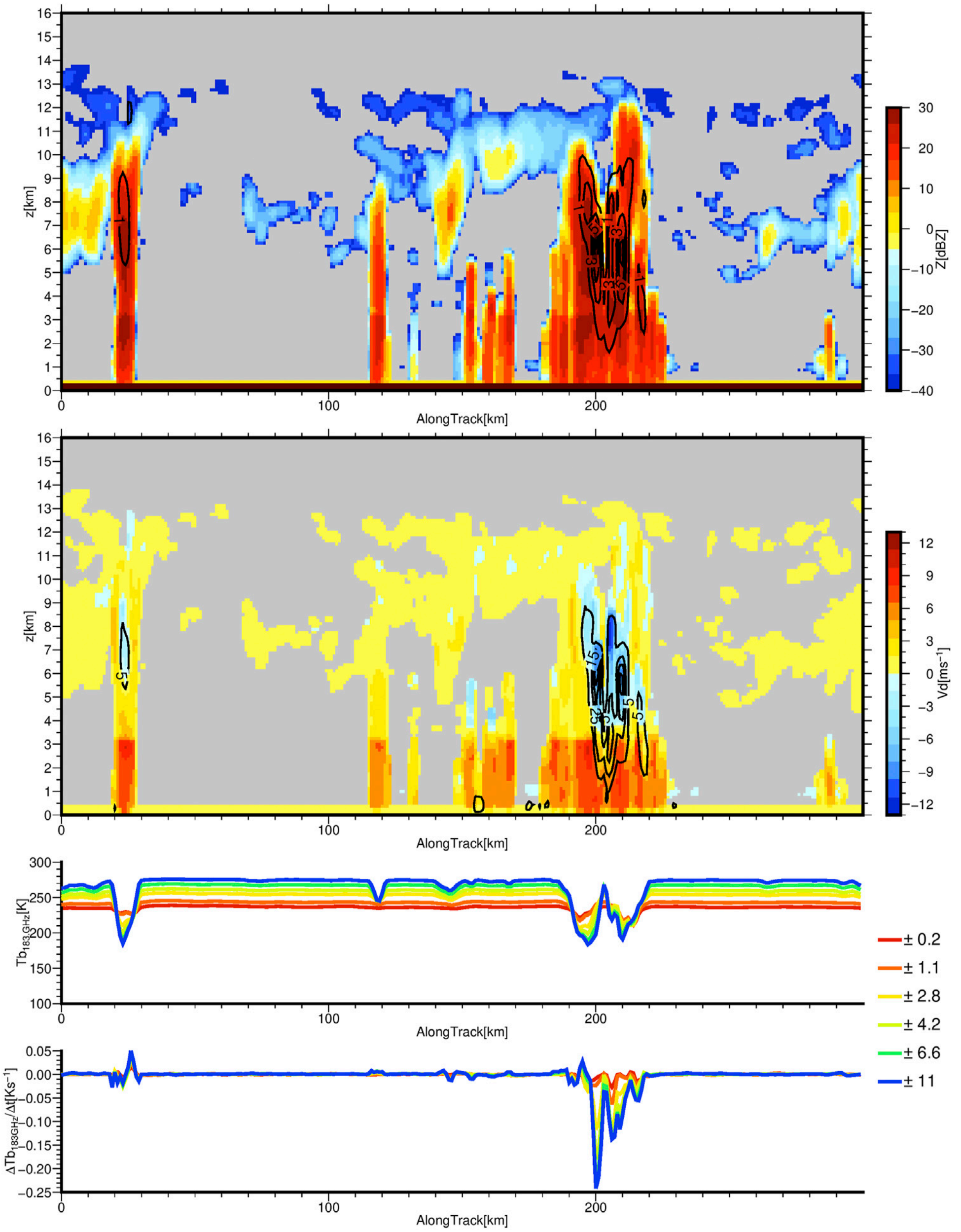

FIGURE 8 | Attenuated radar reflectivity (Z, in dBZ, top panel) and corresponding mean Doppler velocity (V_d in m/s, middle panel) without satellite motion effects at 35.5 GHz emulated from the 200 m resolution RCE simulation. Upward vertical velocity (in m/s) and water mass flux (in g/m^2/s) are respectively superimposed on the two top panels as contour levels. The two lower panels show the Tbs and dTb/dt of the six channels sampling the 183.31 GHz line.

(unattenuated radar reflectivity factor, dBZ), gaseous and hydrometeor signal extinction (dBZ/km) and mean Doppler velocity. T-matrix scattering is used for the cloud, drizzle, and rain hydrometeor species, and the Self-Similar Rayleigh-Gans Approximation (SSRGA, Hogan and Westbrook, 2014) is used for ice and snow particles. Hail and graupel particles are assumed to have spherical shape with different densities (0.9 and 0.4 g/cm^3 respectively). A realistic Earth's surface echo (Lamer et al., 2020; Burns et al., 1997) is introduce to account for missed detections near the Earth's surface and for estimating PIA estimates. These radar observables are used as input to a comprehensive spaceborne Doppler simulator that estimates the raw simulated spaceborne radar signals. The radar simulator accounts for the instrument sampling geometry (antenna and range weighting function, along track integration), receiver noise and platform motion.

Figure 8 shows the simulated 35.5 GHz reflectivity and the corresponding Doppler vertical velocity, as well as the associated 183 GHz Tb and their 1-min temporal derivatives centred over the radar observations. This configuration would correspond to

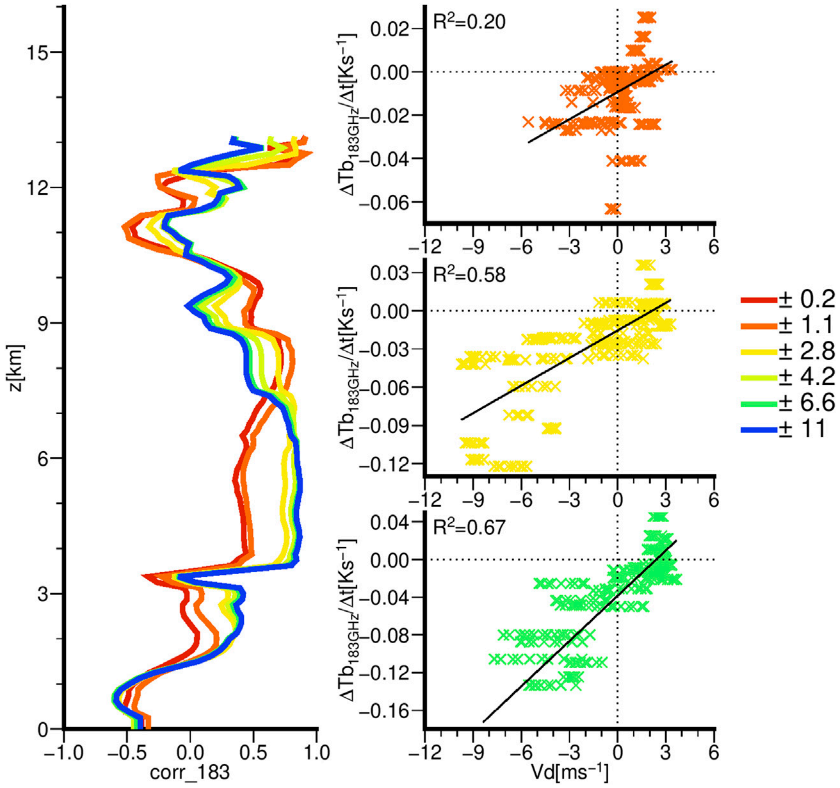

FIGURE 9 | Correlation coefficient computed at each altitude between radar Doppler velocity and temporal derivatives of the six SAPHIR bands sampling the 183 GHz water vapor absorbing band for convective profiles (first vertical panel). Brightness temperature temporal derivatives (dTb/dt in K/s) as a function of Doppler velocity V_d (in m/s) for convective profiles in 1 km-depth altitude layer centered on the peaks of the weighting functions (second vertical panel) for SAPHIR channels C2, C3 and C5. The black lines are linear regressions and the associated R^2 are provided.

two radiometers flying respectively 30s before and after a 35.5 GHz radar. All these simulated instruments have been averaged on a common 2.4 km resolution corresponding to the radar resolution and a sample is provided every kilometre.

This simple version of a C^2OMODO/Doppler radar simulator shows that the depression in the Tb with respect to clear sky is of the same order of magnitude whatever the intensity of convection (compare at x = 20 km and x = 200 km). This saturation effect limits the retrieval of the intense vertical transport of hydrometeors by convective motions. As underlined in the previous sections, the dTb/dt encompasses convective strength, which allows for accurately locating the convective and intensifying cores in a wider swath than what is possible with a radar. Indeed, the lower values in dTb/dt are associated to the atmospheric columns where the more intense vertical motions and condensed mass fluxes are observed. At each altitude, during this short 1-min time interval, hydrometeors are produced through microphysical processes or transported from below (modulus their fall speed) analogous to a Doppler velocity (Stephens et al., 2019).

Figure 9 shows the correlation at each altitude of the radar Doppler velocity V_d with the dTb/dt for the six 183 GHz channels for the situations of deep convection identified using the detection criteria described in Section 3.3. The highest values of correlation (that can be higher than 0.8) are reached at different altitude according to the channel because of their different weighting functions. Under clear sky situations, the peaks of 183 GHz channels are between 7 (183 ± 1 GHz) and 2 km (183 ± 7 GHz) altitude, the actual altitude depending on the water vapor content (Chen and Bennartz, 2020), with upward shifts in cloudy situations. The correlations displayed in **Figure 8** reach the highest values close to the altitude of the peak of the weighting functions. This suggests that the signal that is contained in the Doppler velocity is also contained in the dTb/dt of the passive instruments.

The scatter plots of **Figure 9** show the dTB/dt of the C2 (183 ± 1.1 GHz), the C3 (183 ± 2.8 GHz) and the C5 (183 ± 6.8 GHz) SAPHIR-NG channels as function of the radar Doppler velocity v_d averaged in 1 km-depth layers roughly centered around the peaks of the weighting functions. For these three layers, a linear relationship is found between the dTB/dt and the layer-averaged V_d: a reinforcement of the upward mass flux translates into a higher IWP and thus a larger reduction of the Tb (Chen and Bennartz, 2020).

This is exactly where the synergy between the two sets of observations lies: the vertically-resolved profiles of Doppler

TABLE 2 | Probabilities of detection/false-alarm of non-shallow convective core from measurements of a pair of radiometers, according to different minimum thresholds in condensed water q_{min} and vertical velocities w_{min}.

Minimum Threshold in Condensed Water q_{min}	Minimum Threshold in Vertical Velocity w_{min}	Probability of Detection	Probability of False-Alarm
0.05 g/m^3	1 m/s	0.8522	0.3123
	2 m/s	0.8352	0.2051
	3 m/s	0.838	0.1556
0.2 g/m^3	1 m/s	0.7149	0.3149
	2 m/s	0.7227	0.2259
	3 m/s	0.7255	0.1649

vertical velocity provided by the radar can be extrapolated to the swath of the C^{2}OMODO passive radiometers to obtain layer-averaged upward motion of ice particles as well as their horizontal extent.

TOWARDS A RETRIEVAL ALGORITHM

The previous sections have shown that there is a link between the vertical mass flux in a convective atmosphere and passive microwave observations spaced in time by a short delay dt. Here we draw the main lines of the data processing involving both the observations and their time-derivatives. Such data processing needs to quantify the extent to which the vertical transport in a cloudy column over a discrete time interval dt can be characterized from a set of measurements O = [$Tb_1(t)$,. . ., $Tb_N(t)$, Tb_1 (t + dt), . . ., $Tb_N(t + dt)$] measured in N channels at the initial and final times t and t + dt.

A straightforward approach is to proceed in two steps:

1. Quantify how well the observational setup can detect if the column has any significant vertical transport in the first place—this is the detection step;
2. Then, and only for those columns where vertical transport is detected, quantify how well the coarse vertical characteristics of the transport can be retrieved. The characteristics will necessarily be coarse, because the passive measurements have already been shown to be sensitive to the coarse-scale vertical distribution of condensed water (Jiang et al., 2017; Chen and Bennartz, 2020) without the ability to resolve changes at resolutions on the order of 1,000 m or finer.

Detection of a Convectively Active Column

The first step requires the derivation and evaluation of a detector. Starting with a set of convection-permitting model simulations (CPMs), conducted at horizontal resolution sufficiently fine to represent the vertical transport reasonably accurately (i.e., on the order of 100 m), one can try to derive the joint distribution p_{up} of one's observations O = [$Tb_1(t)$, . . ., $Tb_N(t)$, Tb_1 (t + dt), . . ., $Tb_N(t + dt)$] conditioned on there being a significant vertical transport in the column (subscript "up"), and quantify how different this distribution is from the joint distribution p_{not} when there is no significant vertical transport in the column (subscript "not"). For simplicity, one can define "there is a significant vertical transport in the column" to mean that there is a height h in the column where the vertical velocity w(h) exceeds a threshold w_{min} and where the condensed water content q(h) also exceeds a threshold q_{min}. Each distribution can be approximated by a Gaussian, so that one only needs to compute the two conditional means $O_{m,up} = E\{O \mid \text{updraft}\}$ and $O_{m,not} = E\{O \mid \text{no updraft}\}$, and the two corresponding conditional covariance matrices $C_{up} = Cov\{O \mid \text{updraft}\}$ and $C_{not} = Cov\{O \mid \text{no updraft}\}$.

Here our CPMs is the WRF model which was set-up to simulate Hurricane Isabel at the expected radiometer resolution. The details of the model are provided in Appendix A.3. One half of the simulations obtained during the first 10 min of the run was used as the reference and one half of the simulations in the latter half of the run was used to evaluate the retrieval errors. The columns produced by our CPM have been analyzed for different combinations of w_{min} = 1, two or 3 m/s and q_{min} = 0.05 or 0.2 g/m^3. Only three channels are retained for simplicity: at 166 GHz (a window channel very similar to the C6 channel of SAPHIR-NG), 184 GHz (close to C2), and 190 GHz (close to C5). The results are summarized in **Table 2**.

This observational configuration allows to detect correctly the presence of a significant updraft in the column more than 70% of the time. In the case of the lower detection threshold (q_{min} = 0.05 g/m^3) the probabilities of detection reach higher values (>80%). The false-alarm rates seem to stay the same regardless of what is chosen for q_{min} at a given vertical velocity w_{min}. These results highlight that passive microwave radiometers aligned in a convoy separated by a short time (~1min) can achieve a success rate in excess of 80% for the identification of convective updrafts.

The approach to evaluate the detection can be used to quantify the sensitivity of the observations to the coarse vertical characteristics of the underlying updraft. To the extent that the prototypical updraft, as a function of height, should start with w = 0 at the lowest level (by definition) increasing to a maximum value w_{max} somewhere in the column and then decreasing down to 0 past the top of the cloud, it is not unreasonable to try to determine the value w_{max} along with the height h_{max} at which it is achieved. To determine how sensitive the observation vector O is to the pair (w_{max}, h_{max}), one can start by partitioning the two-dimensional (w_{max}, h_{max})-space into a set of contiguous

TABLE 3 | Root-mean-square errors on w_{max} (in m/s) and h_{max} (in km) for different tiles of the space (w_{max}, h_{max}).

Interval on h_{max}		**<6.35 km**	**6.35–7.75 km**	**7.75–9.25 km**	**9.25–10.5 km**	**>10.5 km**
Interval on w_{max}						
w_{max}	<2 m/s	1.842	2.972	3.872	5.161	4.842
	2–4 m/s	1.461	1.490	2.355	3.396	3.640
	4–6 m/s	1.849	1.593	1.021	1.838	2.374
	6–8 m/s	2.994	3.136	2.099	0.932	1.028
	>8 m/s	4.909	6.930	5.336	3.9566	2.711
h_{max}	<2 m/s	3.233	1.438	2.421	2.574	3.421
	2–4 m/s	2.039	0.831	1.133	2.049	3.459
	4–6 m/s	2.320	0.996	1.038	2.011	3.140
	6–8 m/s	2.670	1.058	0.976	1.469	2.380
	>8 m/s	2.328	1.326	0.742	1.669	1.509

tiles, indexed by a pair of indices (i,j) where i indicates the discrete interval of values of w_{max} and j the discrete interval of values of h_{max}. The CPMs columns that fall in each tile can then be used to approximate the conditional distribution $p_{i,j}$ of O in that tile, namely by considering that $p_{i,j}$ is normal and hence completely determined by the conditional mean $m_{i,j} = E\{O \mid \text{the underlying column is in tile (i,j)}\}$and the conditional covariance $M_{i,j} = Cov\{O \mid \text{the underlying column is in tile (i,j)}\}$, which can be readily computed given the columns in each tile. Armed with these distributions, i.e. the conditional-mean vectors $m_{i,j}$ and conditional-covariance matrices $M_{i,j}$, one can easily determine which tile a given arbitrary observation O "belongs" to: indeed, O is most likely to be from the population (i,j) for which $p_{i,j}(O) > p_{i',j'}(O)$ for all other (i',j'). In other words, for a given observation O one can compute the values of all the conditional distributions $p_{i,j}(O)$ and then choose the one with the largest value as the distribution that O most likely belongs to—and thereby attribute to O the value of (w_{max}, h_{max}) in that maximum-likelihood tile. Rather than stopping at the mean value of

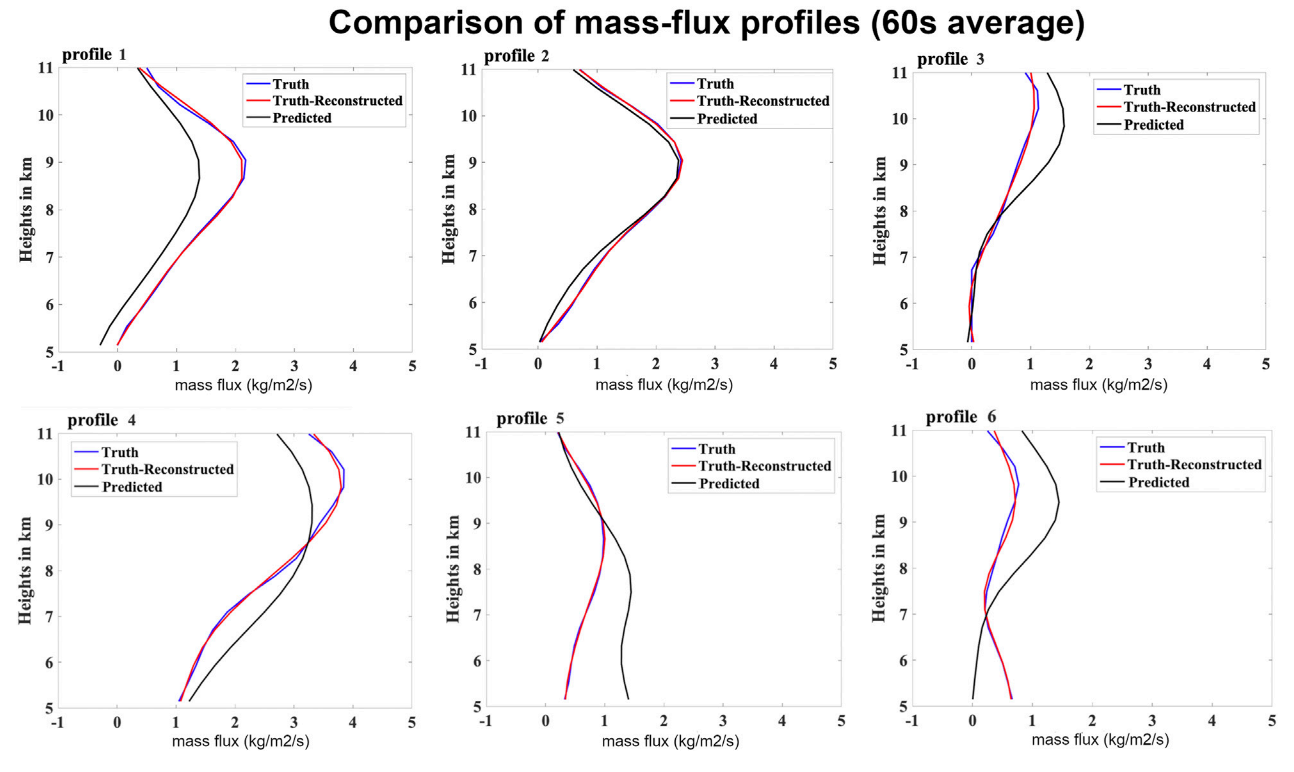

FIGURE 10 | Six examples of profiles of vertical mass flux retrieved the Tbs obtained at t and t + dt: the Tbs are used to estimate w_{max} and h_{max}, which are combined to the cloud top height (CTH) and the top three principal components of each profile obtained from a PCA (see text for details). The blue curve is the original profile, and the red curve is the reconstruction of that profile using only its top three principal components. The black curves are the profiles retrieved from w_{max}, h_{max} and CTH.

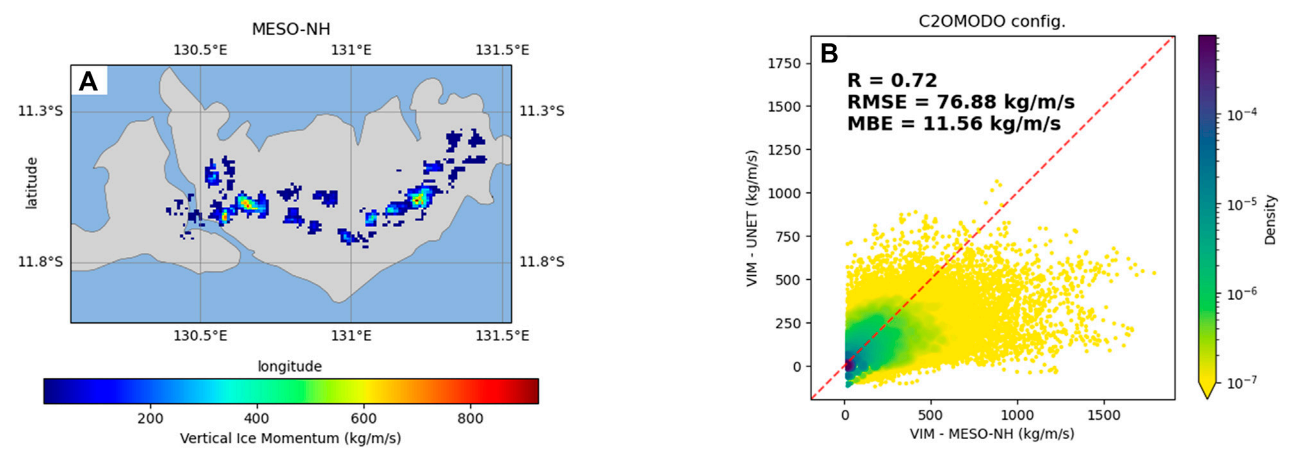

FIGURE 11 | (A) Vertically integrated ice mass flux (VIM, kg/m/s) as simulated by MESO-NH for a snapshot of the HEC set of simulations. **(B)** Meso-NH VIM (*x*-axis) versus predicted VIM (*y*-axis) for the filtered deep convective situations within the entire validation dataset. The Pearson correlation coefficient (R), root-mean-square error (RMSE) and mean bias (MBE) are indicated. The color scale for the scatter plot represents the normalized density of data, in log scale.

(w_{max}, h_{max}) in that tile, we derived a linear regression for (w_{max}, h_{max}) in terms of the entries of O, for each tile. The resulting estimate of $w_{max}(O)$ and $h_{max}(O)$ can then be compared with the true values for the column, to quantify the error in this simple characterization.

In a nutshell, we first compile a reference database D of stormy columns and we partition the database D into tiles $D_{i,j}$ according to the true values of (w_{max}, h_{max}), so that in real time, given an observation vector O, we can calculate the different probabilities $p_{i,j}(O)$ of observing O if the truth was in either one of the tiles and then select the tile for which this probability is the largest: that is the tile to which O most likely "belongs" and therefore the mean of w_{max} and h_{max} in that tile are the values that we associate as the retrieval for the observed O. **Table 3** summarizes the results with root-mean-square errors (rmse).

The values of rmse for w_{max} are highest for the slowest (<2 m/s) and fastest (>8 m/s) updrafts, whatever their altitude in the column. In between, the linear regression established from the observation vector O allows to estimate the maximum vertical velocity w_{max} for each of the pre-defined atmospheric layers with reasonably small uncertainties. In parallel, this detector can also attribute with a good accuracy the altitude h_{max} of w_{max} for each layer, thus enabling to determine vertically the altitude of maximum velocity within the column.

The estimates of w_{max} and h_{max}, together with the estimate of the cloud top height (CTH), defined as the maximum height for which $q > q_{min}$, provide a coarse description of the vertical shape of the vertical transport of mass. Hence, using w_{max}, h_{max} and CTH as well as the top three principal components of the profiles computed from a Principal Component Analysis onto the reference database D (gathering the stormy columns only), one can reconstruct the profile of vertical transport. Examples of reconstructed profiles of mass flux are presented on **Figure 10** and compared with the original ones. As illustrated the retrieved profiles are not perfect replicas of the originals, but the discrepancies follow the errors summarized in **Table 3**.

Development of "Level-2" Geophysical Products

These information content studies make it possible to fully explore the swath of the C^2OMODO concept to infer the upward motion of ice within convection, through the development of a retrieval method. Here we present an insight of such retrieval, as a first stage of future Level-2 products derived from time-differences of microwave Tb.

Both machine learning or deep learning methods are well suited for multi-variate retrievals (Aires et al., 2011; Sivira et al., 2015). For the sake of simplicity in this overview paper on the C^2OMODO mission, we focus on a retrieval based on full convolutional neural networks (also called U-Net, Ronneberger et al., 2015). Such approaches, adapted to image detection and classification, have been recently applied very successfully to highly resolved satellite images and the retrieval of parameters like surface winds (Shen et al., 2019) or rain rates (Veillette et al., 2018; Choi and Kim, 2019; Sadeghi et al., 2020; Duan et al., 2021). Basically, the architecture of U-Net is made of a series of blocks of convolutional functions that detect the spatial structures of the input image and encode them into feature representations at different spatial resolutions. The decoder part of the U-Net projects the features that have been detected into the original image. The advantage of deep learning methods over traditional (e.g. Bayesian) methods lies a lot on the learning of the spatial structures, not just on the signal itself.

The baseline simulation of HEC discussed above underwent slight perturbations to increase the size of available simulations (increases of 10% RH to 40% RH with or without wind, yielding to 10 different versions of HEC). Each one of the simulations underwent a procedure of data augmentation with a random horizontal and vertically flipping to prevent the U-Net from just learning the position of the spatial structures within the maps. The training and prediction stages use these 10 available versions of HEC, through cross-validation procedure: nine out of 10 are used for the training (80%)/validation (20%) steps while the last one is dedicated to test the retrieval. A gradient descent is used to update the weight during the training while the optimization method is ADAM (Kingma and Ba, 2014). The deep convection criteria defined above ($Tb_{183.31}$-$Tb_{193.31}$ > 0, see Sect 3.3.2) is applied to all the simulations, in order to focus on the learning of deep convective structures and not the surrounding clear air.

For the present case, which is purely a demonstration, we make use of the (Tb, d Tb/dt) variables of the six channels at 183 GHz and the three channels at 325 GHz, without the hyperspectral option. A U-Net is thus trained on this subset of 18 variables (dt = 1min) to learn their non-linear relationships with the vertically integrated ice mass flux (VIM, **Eq. (4)**). The results of the VIM retrieved from this U-Net are illustrated in **Figure 11** as a demonstration. The map (**Figure 11A**) shows the structure of the convective systems as defined from the VIM variable for one time step of HEC.

The comparison of the VIM provided by MESO-NH and the predicted VIM from the U-Net for the full set of the validation dataset is presented on **Figure 11B**. The U-Net algorithm performs already really well for the retrieval of the VIM parameter with a good correlation (0.72), a small bias (11.56 kg/m/s) and a quite reasonable RMSE (76.88 kg/m/s). One can also notice a slight tendency to underestimate the large values of VIM. This most certainly comes from the definition of VIM which can lead to values near 0 kg/m/s when there are both downdrafts and updrafts in the column, even if there is a large amount of ice. In such situations the U-Net model learns the relationship between the Tbs and VIM with some complicated situations where the Tb are low (near 130 K), associated to large amount of ice in the column, whereas the VIM is small.

Of course, the retrieval approach can be refined and better tuned to the information content of the C^2OMODO tandem. Several factors can improve the estimations and are currently under study: the use of the hyperspectral option mentioned above; the refinement of the criteria to detect deep convection; an increase of the dataset used for the U-Net training; a more sophisticated architecture than U-Net; the retrieval of the vertical ice mass flux profile instead the integrated column in order to separate downdraft and updraft regions. The retrieval of the pairs (w_{max}; h_{max}) is also under study.

SUMMARY AND WAY FORWARD

Measurement from passive radiometers, organized in a convoy with very short revisit-time Δt ~ 1-min, can be smartly used to look at the fast changes that occur within the updrafts that characterize deep convection.

Within the current trend in miniaturized instruments (active/passive) on Smallsats, the C^2OMODO mission proposes to exploit the information content of microwave measurements at 183 and 325 GHz and their time-derivatives. Numerical models were used to perform idealized simulations of a single convective cell as well as nature-like simulations covering large domains to look at a wide range of convective activity. These simulations were used to infer the information content of the C^2OMODO mission. A third simulation involved a Doppler nadir-viewing radar (35.5 GHz). From these preliminary studies, several aspects can be drawn from the set of observations (Tb, dTB/dt) provided by the C^2OMODO payload:

- the time-derivative dTb/dt at both 183 and 325 GHz can be used to infer the glaciation state of convection via the signature of IWP at these two frequencies that reflects the microphysical changes during the development of convection;
- the relationships between upward ice mass flux and dTb/dt seem weakly dependent on the weather conditions, at least in our set of tropical experiments;
- the maximum vertical velocity reached within a convective atmospheric column, as well as its height can be estimated with a small error, depending on the range of velocity (smaller error for higher speeds) and on the height (more or less close to the ground).
- the vertical information included within the Tb and dTb/dt, via the weighting functions of the channels can be related to the vertically-resolved profiles of vertical velocity from nadir-viewing Doppler radar, thus showing a path of very strong synergy between C^2OMODO and a Doppler radar.

Such new set of observations can be explored to dig further into the physics of deep convection and its place within the energy and water cycle. Emerging global kilometer-scale models are now anticipated for both climate and forecast applications (Neumann et al., 2019; Bauer et al., 2021). The C2OMODO observations together with the various innovative satellite missions under development will bring an invaluable and much needed observational constraint to help improving these models that suffers from long enduring uncertainty on the vertical mass flux and vertical velocity (Varble et al., 2011; Marinescu et al., 2021).

DATA AVAILABILITY STATEMENT

The raw data supporting the conclusions of this article will be made available by the authors, without undue reservation.

AUTHOR CONTRIBUTIONS

HB and RR designed the paper and all authors contributed to the writing of the paper. Authors contributed to writing specific parts: FA and J-PC conducted the Meso-NH simulations and analyzed its results, SM and XL conducted the GCE simulations and analyzed its results, ZH performed the CPM simulations and designed the detection approach, PK ran the radar simulator and DB analyzed the radar/radiometer results, AD developed the U-Net model and HB analyzed the results.

FUNDING

Part of this work was performed thanks to the Megha-Tropiques and C2OMODO projects supported by the CNES French space agency. SM. work was performed within the ACCP (now AOS) Decadal. Survey Study Team supported by NASA HQ under Lead Program Scientist Dr. Hal Maring. XL was supported by PMM funding 80NSSC19K0738 under program manager Gail Skofonick-Jackson. Computer resources for running Meso-NH were allocated by GENCI through Project 90569. The ESPRI-IPSL center is also acknowledged for the computing facilities and data server.

ACKNOWLEDGMENTS

Thanks are also due to James Hocking from the MetOffice for the RTTOV coefficients of the SAPHIR-NG hyperspectral configuration. Finally the two reviewers are thanked for their comments that greatly helped to improve the manuscript.

SUPPLEMENTARY MATERIAL

The Supplementary Material for this article can be found online at: https://www.frontiersin.org/articles/10.3389/frsen.2022.854735/full#supplementary-material

REFERENCES

Adler, R. F., and Fenn, D. D. (1979). Thunderstorm Vertical Velocities Estimated from Satellite Data. *J. Atmos. Sci.* 36, 1747–1754. doi:10.1175/1520-0469(1979)036<1747:tvvefs>2.0.co;2

Bauer, P., Stevens, B., and Hazeleger, W. (2021). A Digital Twin of Earth for the green Transition. *Nat. Clim. Chang.* 11, 80–83. doi:10.1038/s41558-021-00986-y

Birman, C., Mahfouf, J.-F., Milz, M., MendrokBuehler, J. S. A., and Brath, S. A. M. (2017). Information Content on Hydrometeors from Millimeter and Sub-millimeter Wavelengths. *Tellus A: Dynamic Meteorology and Oceanography* 69 (1), 1271562. doi:10.1080/16000870.2016.1271562

Blackwell, W. J., Braun, S., Bennartz, R., Velden, C., DeMaria, M., Atlas, R., et al. (2018). An Overview Of The Tropics Nasa Earth Venture Mission. *Q.J.R. Meteorol. Soc.* 144, 16–26. doi:10.1002/qj.3290

Bony, S., Semie, A., Kramer, R. J., Soden, B., Tompkins, A. M., and Emanuel, K. A. (2020). Observed Modulation of the Tropical Radiation Budget by Deep Convective Organization and Lower-Tropospheric Stability. *AGU Adv.* 1, e2019AV000155. doi:10.1029/2019av000155

Brath, M., Ekelund, R., Eriksson, P., Lemke, O., and Buehler, S. A. (2020). Microwave and Submillimeter Wave Scattering of Oriented Ice Particles. *Atmos. Meas. Tech.* 13, 2309–2333. doi:10.5194/amt-13-2309-2020

Brogniez, H., Kirstetter, P.-E., and Eymard, L. (2013). Expected Improvements in the Atmospheric Humidity Profile Retrieval Using the Megha-Tropiques Microwave Payload. *Q.J.R. Meteorol. Soc.* 139, 842–851. doi:10.1002/qj.1869

Buehler, S. A., Jiménez, C., Evans, K. F., Eriksson, P., Rydberg, B., Heymsfield, A. J., et al. (2007). A Concept for a Satellite mission to Measure Cloud Ice Water Path, Ice Particle Size, and Cloud Altitude. *Q.J.R. Meteorol. Soc.* 133, 109–128. doi:10.1002/qj.143

Buehler, S. A., Mendrok, J., Eriksson, P., Perrin, A., Larsson, R., and Lemke, O. (2018). ARTS, the Atmospheric Radiative Transfer Simulator - Version 2.2, the Planetary Toolbox Edition. *Geosci. Model. Dev.* 11 (4), 1537–1556. doi:10.5194/gmd-11-1537-2018

Burns, B. A., Wu, X., and Diak, G. R. (1997). Effects of Precipitation and Cloud Ice on Brightness Temperatures in AMSU Moisture Channels. *IEEE Trans. Geosci. Remote Sensing* 35, 1429–1437. doi:10.1109/36.649797

Chen, R., and Bennartz, R. (2020). Sensitivity of 89-190-GHz Microwave Observations to Ice Particle Scattering. *J. Clim.* 59, 1195–1215. doi:10.1175/JAMC-D-19-0293.1

Choi, Y., and Kim, S. (2021). Rain-Type Classification from Microwave Satellite Observations Using Deep Neural Network Segmentation. *IEEE Geosci. Remote Sensing Lett.* 18, 2137–2141. doi:10.1109/LGRS.2020.3016001

Crewell, S., Ebell, K., Löhnert, U., and Turner, D. D. (2009). Can Liquid Water Profiles Be Retrieved from Passive Microwave Zenith Observations? *Geophys. Res. Lett.* 36, L06803. doi:10.1029/2008GL036934

Cuxart, J., Bougeault, P., and Redelsperger, J.-L. (2000). A Turbulence Scheme Allowing for Mesoscale and Large-Eddy Simulations. *Q.J R. Met. Soc.* 126, 1–30. doi:10.1002/qj.49712656202

Dauhut, T., Chaboureau, J. P., Escobar, J., and Mascart, P. (2015). Large-eddy Simulations of Hector the Convector Making the Stratosphere Wetter. *Atmos. Sci. Lett.* 16, 135–140. doi:10.1002/asl2.534

Davis, C., Emde, C., and Harwood, R. (2005). A 3-D Polarized Reversed Monte Carlo Radiative Transfer Model for Millimeter and Submillimeter Passive Remote Sensing in Cloudy Atmospheres. *IEEE Trans. Geosci. Remote Sensing* 43 (5), 1096–1101. doi:10.1109/TGRS.2004.837505

Duan, M., Xia, J., Yan, Z., Han, L., Zhang, L., Xia, H., et al. (2021). Reconstruction of the Radar Reflectivity of Convective Storms Based on Deep Learning and Himawari-8 Observations. *Remote Sensing* 13, 3330. doi:10.3390/rs13163330

Elsaesser, G., Roca, R., Fiolleau, T., Del Genio, A. D., and Wu, J. (2021). A Simple Model for Tropical Convective Cloud Shield Area Growth and Decay Rates Informed by Geostationary IR, GPM, and Aqua/AIRS Satellite Data. *Earth Sp. Sci. Open Arch.*, 1–39. doi:10.1002/essoar.10507613.2

Eriksson, P., Ekelund, R., Mendrok, J., Brath, M., Lemke, O., and Buehler, S. A. (2018). A General Database of Hydrometeor Single Scattering Properties at Microwave and Sub-millimetre Wavelengths. *Earth Syst. Sci. Data* 10, 1301–1326. doi:10.5194/essd-10-1301-2018

Evans, K. F., Wang, J. R., O'C Starr, D., Heymsfield, G., Li, L., Tian, L., et al. (2012). Ice Hydrometeor Profile Retrieval Algorithm for High-Frequency Microwave Radiometers: Application to the CoSSIR Instrument during TC4. *Atmos. Meas. Tech.* 5, 2277–2306. doi:10.5194/amt-5-2277-2012

Feng, Z., Dong, X., Xi, B., McFarlane, S. A., Kennedy, A., Lin, B., et al. (2012). Life Cycle of Midlatitude Deep Convective Systems in a Lagrangian Framework. *J. Geophys. Res.* 117, a–n. doi:10.1029/2012JD018362

Fouquart, Y., and Bonnel, B. (1980). Computations of Solar Heating of the Earth's Atmosphere – A New Parameterization. *Beitraege zur Physik der Atmosphaere* 53, 35–62.

Gasparini, B., Rasch, P. J., Hartmann, D. L., Wall, C. J., and Dütsch, M. (2021). A Lagrangian Perspective on Tropical Anvil Cloud Lifecycle in Present and Future Climate. *Geophys. Res. Atmos.* 126, e2020JD033487. doi:10.1029/2020JD033487

Giangrande, S. E., Collis, S., Straka, J., Protat, A., Williams, C., and Krueger, S. (2013). A Summary Of Convective-Core Vertical Velocity Properties Using Arm Uhf Wind Profilers In Oklahoma. *J. Appl. Meteorol. Climat.* 52, 2278–2295. doi:10.1175/Jamc-d-12-0185.1

Giangrande, S. E., Toto, T., Jensen, M. P., Bartholomew, M. J., Feng, Z., Protat, A., et al. (2016). Convective Cloud Vertical Velocity and Mass-flux Characteristics from Radar Wind Profiler Observations during GoAmazon2014/5. *J. Geophys. Res. Atmos.* 121 (12), 12891–12913. doi:10.1002/2016JD025303

Greenwald, T. J., and Christopher, S. (2002). Effect of Cold Clouds on Satellite Measurements Near 183 GHz. *J. Geophys. Res.* 107, 4170. doi:10.1029/2000jd000258

Haddad, Z. S., Sy, O. O., Hristova-Veleva, S., and Stephens, G. L. (20172017). Derived Observations from Frequently Sampled Microwave Measurements of Precipitation-Part I: Relations to Atmospheric Thermodynamics. *IEEE Trans. Geosci. Remote Sensing* 55 (6), 3441–3453. doi:10.1109/TGRS.2017.2671598

Hamada, A., and Takayabu, Y. N. (2016). Convective Cloud Top Vertical Velocity Estimated from Geostationary Satellite Rapid-scan Measurements. *Geophys. Res. Lett.* 43, 5435–5441. doi:10.1002/2016GL068962

Houze, R. A. (2018). 100 Years of Research on Mesoscale Convective Systems. *Meteorol. Monogr.* 59, 1–117. 53. doi:10.1175/AMSMONOGRAPHS-D-18-0001.1

Houze, R. A., and Betts, A. K. (1981). Convection in GATE. *Rev. Geophys.* 19 (4), 541–576. doi:10.1029/rg019i004p00541

Jiang, J. H., Yue, Q., Su, H., Reising, S. C., Kangaslahti, P. P., Deal, W. R., et al. (2017). A Simulation of Ice Cloud Particle Size, Humidity, and Temperature Measurements from the TWICE CubeSat. *Earth Space Sci.* 4, 574–587. doi:10.1002/2017EA000296

Kingma, P. D., and Ba, J. (2014) Adam: A Method for Stochastic Optimization. arXiv preprint arXiv:1412.6980

Kollias, P., Battaglia, A., Tridon, F., Tatarevic, A., Pfitzenmaier, L., and Lamer, K. (2018). The EarthCARE Cloud Profiling Radar (CPR) Doppler Measurements in Deep Convection: Challenges, post-processing, and Science Applications. *Remote Sensing of the Atmosphere, Clouds, and Precipitation VII.* doi:10.1117/12.2324321

Kollias, P., Tanelli, S., Battaglia, A., and Tatarevic, A. (2014). Evaluation of EarthCARE Cloud Profiling Radar Doppler Velocity Measurements in Particle Sedimentation Regimes. *J. Atmos. Oceanic Technol.* 31, 366–386. doi:10.1175/JTECH-D-11-00202.1

Kumar, V. V., Jakob, C., Protat, A., Williams, C. R., and May, P. T. (2015). Mass-flux Characteristics of Tropical Cumulus Clouds from Wind Profiler Observations at Darwin, Australia. *J. Atmos. Sci.* 72 (5), 1837–1855. doi:10.1175/JAS-D-14-0259.1

Lac, C., Chaboureau, J.-P., Masson, V., Pinty, J.-P., Tulet, P., Escobar, J., et al. (2018). Overview of the Meso-NH Model Version 5.4 and its Applications. *Geosci. Model. Dev.* 11, 1929–1969. doi:10.5194/gmd-11-1929-2018

Lafore, J-P., and Moncrief, R. (1989). A Numerical Investigation of the Organization and Interaction of the Convective and Stratiform Regions of Tropical Squall Lines. *J. Atmos. Sci.* 46 (4), 521–544. doi:10.1175/1520-0469(1989)046<0521:anioto>2.0.co;2

LeMone, M. A., Zipser, E. J., and Trier, S. B. (1998). The Role of Environmental Shear and Thermodynamic Conditions in Determining the Structure and Evolution of Mesoscale Convective Systems during TOGA COARE. *J. Atmos. Sci.* 55, 3493–3518. doi:10.1175/1520-0469(1998)055<3493:troesa>2.0.co;2

Luo, Z. J., Jeyaratnam, J., Iwasaki, S., Takahashi, H., and Anderson, R. (2014). Convective Vertical Velocity and Cloud Internal Vertical Structure: An A-Train Perspective. *Geophys. Res. Lett.* 41, 723–729. doi:10.1002/2013GL058922

Marinescu, P. J., Van Den Heever, S. C., Heikenfeld, M., Barrett, A. I., Barthlott, C., Hoose, C., et al. (2021). Impacts of Varying Concentrations of Cloud Condensation Nuclei on Deep Convective Cloud Updrafts-A Multimodel Assessment. *J. Atmos. Sci.* 78 (4), 1147–1172. doi:10.1175/JAS-D-20-0200.1

Masson, V., Le Moigne, P., Martin, E., Faroux, S., Alias, A., Alkama, R., et al. (2013). The SURFEXv7.2 Land and Ocean Surface Platform for Coupled or Offline Simulation of Earth Surface Variables and Fluxes. *Geosci. Model. Dev.* 6, 929–960. doi:10.5194/gmd-6-929-2013

Masunaga, H., and Luo, Z. J. (2016). Convective and Large-scale Mass Flux Profiles over Tropical Oceans Determined from Synergistic Analysis of a Suite of Satellite Observations. *J. Geophys. Res. Atmos.* 121, 7958–7974. doi:10.1002/2016JD024753

May, P. T., and Rajopadhyaya, D. K. (1999). Vertical Velocity Characteristics of Deep Convection over Darwin, Australia. *Mon. Wea. Rev.* 127, 1056–1071. doi:10.1175/1520-0493(1999)127<1056:vvcodc>2.0.co;2

Mlawer, E. J., Taubman, S. J., Brown, P. D., Iacono, M. J., and Clough, S. A. (1997). Radiative Transfer for Inhomogeneous Atmospheres: RRTM, a Validated Correlated-K Model for the Longwave. *J. Geophys. Res.* 102, 16663–16682. doi:10.1029/97jd00237

Morrison, H., Curry, J. A., and Khvorostyanov, V. I. (2005). A New Double-Moment Microphysics Parameterization for Application in Cloud and Climate Models. Part I: Description. *J. Atmos. Sci.* 62 (6), 1665–1677. doi:10.1175/jas3446.1

Neumann, P., Düben, P., Adamidis, P., Bauer, P., Brück, M., KornBlueh, L., et al. (2019). Assessing the Scales in Numerical Weather and Climate Predictions: Will Exascale Be the rescue? *Phil. Trans. R. Soc. A.* 377, 20180148. doi:10.1098/rsta.2018.0148

North, K. W., Oue, M., Kollias, P., Giangrande, S. E., Collis, S. M., and Potvin, C. K. (2017). Vertical Air Motion Retrievals in Deep Convective Clouds Using the ARM Scanning Radar Network in Oklahoma during MC3E. *Atmos. Meas. Tech.* 10, 2785–2806. doi:10.5194/amt-10-2785-2017

Ovchinnikov, M., Giangrande, S., Larson, V. E., Protat, A., and Williams, C. R. (2019). Dependence of Vertical Alignment of Cloud and Precipitation Properties on Their Effective Fall Speeds. *J. Geophys. Res. Atmos.* 124, 2079–2093. doi:10.1029/2018JD029346

Padmanabhan, S., Gaier, T. C., Tanner, A. B., Brown, S. T., Lim, B. H., Reising, S. C., et al. (2021). TEMPEST-D Radiometer: Instrument Description and Prelaunch Calibration. *IEEE Trans. Geosci. Remote Sensing* 59, 10213–10226. doi:10.1109/TGRS.2020.3041455

Pergaud, J., Masson, V., Malardel, S., and Couvreux, F. (2009). A Parameterization of Dry Thermals and Shallow Cumuli for Mesoscale Numerical Weather Prediction. *Boundary-layer Meteorol.* 132, 83–106. doi:10.1007/s10546-009-9388-0

Pinty, J.-P., and Jabouille, P. (1998). "A Mixed-Phased Cloud Parameterization for Use in a Mesoscale Non-hydrostatic Model: Simulations of a Squall Line and of Orographic Precipitation," in *Conf. On Cloud Physics* (WA: Everett), 217–220.

Puech, J., Hermozo, L., Brogniez, H., Chambon, P., Roca, R., Cipolla, V., et al. (2021). SAPHIR-NG High Resolution Microwave Sounder: Towards an Enhanced Observation of the Atmosphere. *IEEE Int. Geosci. Remote Sensing Symp. IGARSS*, 7689–7692. doi:10.1109/IGARSS47720.2021.9554426

Ray, P. S., Ziegler, C. L., Bumgarner, W., and Serafin, R. J. (2012). Multiple-doppler Radar Observations of Tornadic Storms. *Mon. Wea. Rev.* 108 (10), 1607–1625. doi:10.1175/1520-0493

Redelsperger, J.-L. (1997). "The Mesoscale Organization of Deep Convection," in *The Physics and Parameterization of Moist Atmospheric Convection. NATO ASI Series (Series C: Mathematical and Physical Sciences)*. Editor R. K. Smith (Dordrecht: Springer), Vol 505, 59–98. doi:10.1007/978-94-015-8828-7_3

Roca, R., Bouniol, D., and Fiolleau, T. (2020). "On the Duration and Life Cycle of Precipitation Systems in the Tropics," in *Satellite Precipitation Measurement. Advances in Global Change Research*. Editors V. Levizzani, C. Kidd, D. Kirschbaum, C. Kummerow, K. Nakamura, and F. Turk (Cham: Springer), Vol 69, 729–744. doi:10.1007/978-3-030-35798-6_14

Roca, R. m., Brogniez, H. l. n., Chambon, P., Chomette, O., ClochÃ©, S., Gosset, M. E., et al. (2015). The Megha-Tropiques mission: a Review after Three Years in Orbit. *Front. Earth Sci.* 3, 3–17. doi:10.3389/feart.2015.00017

Romps, D. M. (2021). Ascending Columns, WTG, and Convective Aggregation. *J. Atmos. Sci.* 78, 497–508. doi:10.1175/JAS-D-20.0041.110.1175/jas-d-20-0041.1

Ronneberger, O., Fischer, P., and Brox, T. (2015). "U-net: Convolutional Networks for Biomedical Image Segmentation," in *Medical Image Computing and Computer-Assisted Intervention – MICCAI 2015. MICCAI 2015. Lecture Notes in Computer Science*. Editors N. Navab, J. Hornegger, W. Wells, and A. Frangi (Cham: Springer), Vol 9351, 234–241. doi:10.1007/978-3-319-24574-4_28

Rotunno, R., Klemp, J. B., and Weisman, M. L. (1988). A Theory for strong, Long-Lived Squall Lines. *J. Atmos. Sci.* 45 (3), 463–485. doi:10.1175/1520-0469(1988)045<0463:atfsll>2.0.co;2

Sadeghi, M., Nguyen, P., Hsu, K., and Sorooshian, S. (2020). Improving Near Real-Time Precipitation Estimation Using a U-Net Convolutional Neural Network and Geographical Information. *Environ. Model. Softw.* 134, 104856. doi:10.1016/j.envsoft.2020.104856

Saunders, R., Hocking, J., Turner, E., Rayer, P., Rundle, D., Brunel, P., et al. (2018). An Update on the RTTOV Fast Radiative Transfer Model (Currently at Version 12). *Geosci. Model. Dev.* 11, 2717–2737. doi:10.5194/gmd-11-2717-2018

Schubert, W. H., Ciesielski, P. E., and Johnson, R. H. (2018). "Heat and Moisture Budget Analysis with an Improved Form of Moist Thermodynamics," in *Atmospheric and Oceanic Physics*, 1–14. arXiv::1810.11119 [physics].

Schulte, R. M., Kummerow, C. D., Berg, W., Reising, S. C., Brown, S. T., Gaier, T. C., et al. (2020). A Passive Microwave Retrieval Algorithm with Minimal View-Angle Bias: Application to the TEMPEST-D CubeSat

Mission. *J. Atmos. Ocean. Technol.* 37 (2), 197–210. doi:10.1175/JTECH-D-19-0163.1

Schumacher, R. S., and Rasmussen, K. L. (2020). The Formation, Character and Changing Nature of Mesoscale Convective Systems. *Nat. Rev. Earth Environ.* 1 (6), 300–314. doi:10.1038/s43017-020-0057-7

Seigel, R. B., and van den Heever, S. C. (2013). Squall-line Intensification via Hydrometeor Recirculation. *J. Atmos. Sci.* 70 (7), 2012–2031. doi:10.1175/JAS-D-12-0266.1

Shen, D., Liu, B., and Li, X. (2019). Sea Surface Wind Retrieval from Synthetic Aperture Radar Data by Deep Convolutional Neural Networks. *IEEE Int. Geosci. Remote Sensing Symp.*, 8035–8038. doi:10.1109/IGARSS.2019.8898542

Skamarock, W. C., Klemp, J. B., Dudhia, J., Gill, D. O., Liu, Z., Berner, J., et al. (2019) *A Description of the Advanced Research WRF Version 4. NCAR Tech*. Note NCAR/TN-556+STR, 145 pp. doi:10.5065/1dfh-6p97

Stephens, G. L., van den Heever, S. C., Haddad, Z. S., Posselt, D. J., Storer, R. L., Grant, L. D., et al. (2020). A Distributed Small Satellite Approach for Measuring Convective Transports in the Earth's Atmosphere. *IEEE Trans. Geosci. Remote Sensing* 58, 4–13. doi:10.1109/TGRS.2019.2918090

Sy, O. O., Haddad, Z. S., Stephens, G. L., and Hristova-Veleva, S. (2017). Derived Observations from Frequently Sampled Microwave Measurements of Precipitation. Part II: Sensitivity to Atmospheric Variables and Instrument Parameters. *IEEE Trans. Geosci. Remote Sensing* 55 (5), 2898–2912. doi:10.1109/TGRS.2017.2656061

Tao, W.-K., Lang, S., Zeng, X., Li, X., Matsui, T., Mohr, K., et al. (2014). The Goddard Cumulus Ensemble Model (GCE): Improvements and Applications for Studying Precipitation Processes. *Atmos. Res.* 143, 392–424. doi:10.1016/j.atmosres.2014.03.005

Tao, W.-K., and Simpson, J. (1993). Goddard Cumulus Ensemble Model. Part I: Model Description. *Terr. Atmos. Oceanic Sci.* 4, 35–72. doi:10.3319/tao.1993.4.1.35(a)

Thomas, B., Brandt, M., Walber, A., Philipp, M., Gibson, H., Czekala, H., et al. (2012). Submillimetre-wave Receiver Developments for ICI Onboard MetOP-SG and Ice Cloud Remote Sensing Instruments. *IEEE Int. Geosci. Remote Sensing Symp.*, 1278–1281. doi:10.1109/IGARSS.2012.6351306

Tomassini, L. (2020). The Interaction between Moist Convection and the Atmospheric Circulation in the Tropics. *Bull. Am. Meteorol. Soc.* 101 (8), E1378–E1396. doi:10.1175/BAMS-D-19-0180.1

Varble, A., Fridlind, A. M., Zipser, E. J., Ackerman, A. S., Chaboureau, J.-P., Fan, J., et al. (2011). Evaluation of Cloud-Resolving Model Intercomparison Simulations Using TWP-ICE Observations: Precipitation and Cloud Structure. *J. Geophys. Res.* 116 (12), 1–22. doi:10.1029/2010JD015180

Veillette, M. S., Hassey, E. P., Mattioli, C. J., Iskenderian, H., and Lamey, P. M. (2018). Creating Synthetic Radar Imagery Using Convolutional Neural Networks. *J. Atmos. Ocean. Technol.* 35, 2323–2338. doi:10.1175/jtech-d-18-0010.1

Wang, D., Giangrande, S. E., Feng, Z., Hardin, J. C., and Prein, A. F. (2020). Updraft and Downdraft Core Size and Intensity as Revealed by Radar Wind Profilers: MCS Observations and Idealized Model Comparisons. *J. Geophys. Res.* 125 (11). doi:10.1029/2019JD031774

Wing, A. A., Stauffer, C. L., Becker, T., Reed, K. A., Ahn, M. S., Arnold, N. P., et al. (2020). Clouds and Convective Self-Aggregation in a Multimodel Ensemble of Radiative-Convective Equilibrium Simulations. *J. Adv. Model. Earth Syst.* 12, e2020MS002138. doi:10.1029/2020MS002138

Zipser, E. J., and LeMone, M. A. (1980). Cumulonimbus Vertical Velocity Events in GATE. Part II: Synthesis and Model Core Structure. *J. Atmos. Sci.* 37, 2458–2469. doi:10.1175/1520-0469(1980)037<2458:cvveig>2.0.co;2

Zipser, E. J. (2003). Some Views on "Hot Towers" after 50 Years of Tropical Field Programs and Two Years of TRMM Data. *Cloud Systems, Hurricanes, Trmm, Meteorol. Monogr.* 51, 49–58. Amer. Meteor. Soc. doi:10.1007/978-1-878220-63-9_5

Conflict of Interest: The authors declare that the research was conducted in the absence of any commercial or financial relationships that could be construed as a potential conflict of interest.

The handling editor declared a shared affiliation with one of the authors ZH at time of review.

frontiers | Frontiers in Remote Sensing

ORIGINAL RESEARCH
published: 13 May 2022
doi: 10.3389/frsen.2022.885332

Polarimeter + Lidar–Derived Aerosol Particle Number Concentration

Joseph S. Schlosser[1], *Snorre Stamnes*[2]*, *Sharon P. Burton*[2], *Brian Cairns*[3], *Ewan Crosbie*[2,4], *Bastiaan Van Diedenhoven*[5], *Glenn Diskin*[2], *Sanja Dmitrovic*[6], *Richard Ferrare*[2], *Johnathan W. Hair*[2], *Chris A. Hostetler*[2], *Yongxiang Hu*[2], *Xu Liu*[2], *Richard H. Moore*[2], *Taylor Shingler*[2], *Michael A. Shook*[2], *Kenneth Lee Thornhill*[2,4], *Edward Winstead*[2,4], *Luke Ziemba*[2] and *Armin Sorooshian*[1,6,7]*

[1]University of Arizona, Department of Chemical and Environmental Engineering, Tucson, AZ, United States, [2]NASA Langley Research Center, Hampton, VA, United States, [3]NASA Goddard Institute for Space Studies, New York, NY, United States, [4]Science Systems and Applications, Inc., Lanham, MD, United States, [5]Netherlands Institute for Space Research, Utrecht, Netherlands, [6]University of Arizona, James C. Wyant College of Optical Sciences, Tucson, AZ, United States, [7]University of Arizona, Department of Hydrology and Atmospheric Sciences, Tucson, AZ, United States

Edited by:
Qiangqiang Yuan,
Wuhan University, China

Reviewed by:
Weizhen Hou,
Aerospace Information Research Institute (CAS), China
Xiaoguang Xu,
University of Maryland, United States

***Correspondence:**
Snorre Stamnes
snorre.a.stamnes@nasa.gov
Armin Sorooshian
armin@arizona.edu

Specialty section:
This article was submitted to Satellite Missions, a section of the journal Frontiers in Remote Sensing

Received: *28 February 2022*
Accepted: *11 April 2022*
Published: *13 May 2022*

Citation:
Schlosser JS, Stamnes S, Burton SP, Cairns B, Crosbie E, Van Diedenhoven B, Diskin G, Dmitrovic S, Ferrare R, Hair JW, Hostetler CA, Hu Y, Liu X, Moore RH, Shingler T, Shook MA, Thornhill KL, Winstead E, Ziemba L and Sorooshian A (2022) Polarimeter + Lidar–Derived Aerosol Particle Number Concentration. Front. Remote Sens. 3:885332. doi: 10.3389/frsen.2022.885332

In this study, we propose a simple method to derive vertically resolved aerosol particle number concentration (N_a) using combined polarimetric and lidar remote sensing observations. This method relies on accurate polarimeter retrievals of the fine-mode column-averaged aerosol particle extinction cross section and accurate lidar measurements of vertically resolved aerosol particle extinction coefficient such as those provided by multiwavelength high spectral resolution lidar. We compare the resulting lidar + polarimeter vertically resolved N_a product to *in situ* N_a data collected by airborne instruments during the NASA aerosol cloud meteorology interactions over the western Atlantic experiment (ACTIVATE). Based on all 35 joint ACTIVATE flights in 2020, we find a total of 32 collocated *in situ* and remote sensing profiles that occur on 11 separate days, which contain a total of 322 cloud-free vertically resolved altitude bins of 150 m resolution. We demonstrate that the lidar + polarimeter N_a agrees to within 106% for 90% of the 322 vertically resolved points. We also demonstrate similar agreement to within 121% for the polarimeter-derived column-averaged N_a. We find that the range-normalized mean absolute deviation (NMAD) for the polarimeter-derived column-averaged N_a is 21%, and the NMAD for the lidar + polarimeter-derived vertically resolved N_a is 16%. Taken together, these findings suggest that the error in the polarimeter-only column-averaged N_a and the lidar + polarimeter vertically resolved N_a are of similar magnitude and represent a significant improvement upon current remote sensing estimates of N_a.

Keywords: RSP, HSRL-2, column-averaged Na, vertically resolved Na, AOD, ACTIVATE, EVS-3, aerosol

1 INTRODUCTION

Aerosol particle number concentration (N_a) is an important aerosol microphysical property for many applications including air quality and aerosol–cloud interactions. Historically, N_a has been difficult to retrieve from remote sensing measurements that are sensitive to the aerosol scattering cross section, which scales with N_a to the first power and particle diameter (D) to a higher power. Thus, uncertainty in the aerosol size distribution translates directly into a much greater uncertainty in the retrieved N_a than would be the case when trying to retrieve the higher order moments of the aerosol population (e.g., surface area and volume) (Knobelspiesse et al., 2011; Georgoulias et al., 2020). While still limited to optically-active particles (i.e., D $\gtrsim$ 150 nm), the combination of next-generation polarimeter and lidar measurements makes the retrieval of N_a possible. First, multi-angle, multichannel polarimeter observations, such as those from the research scanning polarimeter (RSP), allow for accurate retrieval of column-averaged fine- and coarse-mode aerosol properties (Cairns et al., 1999; Stamnes et al., 2018). Second, multiwavelength high spectral resolution lidar (HSRL-2) measurements provide accurate, vertically resolved measurements of aerosol extinction and depolarization (Hair et al., 2008). The HSRL-2 observations also provide accurate (within ~30 m) retrieval of the mixed layer height (MLH, Scarino et al., 2014).

A previous study demonstrated a median relative bias between HSRL-2 lidar- and in situ–derived N_a of 33% and 47%; the lidar-derived N_a was retrieved by inverting HSRL-2–only aerosol products to produce vertically resolved N_a (Sawamura et al., 2017; Müller et al., 2019). In this study, we demonstrate a simple yet powerful method that uses combined lidar and polarimeter aerosol products to derive vertically resolved N_a in the troposphere that has a median relative bias of 30%. This lidar + polarimeter method has the benefit of being able to rapidly take advantage of column-averaged fine-mode aerosol cross section retrieved by polarimeters such as the RSP and collocated lidar measurements of aerosol extinction coefficient at 532 nm from HSRL lidar such as the HSRL-2 and HSRL-1. However, the two approaches are complementary, particularly since HSRL-2–type lidar with an added 355 nm channel are capable of retrieving the vertically resolved aerosol effective radius, which is one of the main parameters that determines the aerosol extinction cross section, and can be used together with the column-averaged fine- and coarse-mode effective radii retrieved by polarimeters such as RSP to correct the column-averaged aerosol extinction cross section for vertical changes due to changes in aerosol size. Since the lidar + polarimeter method presented in this study requires only profiles of the extinction coefficient at 532 nm, it can be readily applied to lidar + polarimeter data sets that have high spectral resolution capability at 532 nm, such as the NASA airborne HSRL-1 and HSRL-2 lidar, and the HSRL-1–type lidar system that will be onboard the future NASA atmosphere observing system (AOS) mission that is expected to launch by 2030.

Both aerosol index (AI) and aerosol optical depth (AOD) are commonly used as proxies for vertically variable cloud condensation nuclei (CCN) concentrations to quantify aerosol–cloud interactions, but there are limitations to using such proxies. The aerosol index convolves the N_a, size, single-scattering albedo, and complex refractive index into one number, and the accurate retrieval of AI can be subject to accuracy issues depending on which wavelengths are used (Buchard et al., 2015; Hammer et al., 2016). Furthermore, the relationships between AOD (or AI) and cloud drop number concentration (N_d) in pre-industrial and present-day conditions are different, whereas the relationship between CCN and N_d is similar in both of these periods (Gryspeerdt et al., 2017; Grosvenor et al., 2018). It is therefore highly desirable to use observational data to retrieve an aerosol proxy that is as close to CCN as possible since such relationships are expected to be more robust than those using more distant proxies such as AOD and AI (Shinozuka et al., 2015; Hasekamp et al., 2019). A significantly more direct proxy for CCN is the vertically resolved accumulation mode N_a.

There have only been a limited number of aerosol–cloud interaction studies that are historically focused on the western North Atlantic N_a (Sorooshian et al., 2020), but its gradients of low to high aerosol number concentrations provide an excellent environment to demonstrate the capability to remotely sense N_a (Quinn et al., 2019; Dadashazar et al., 2021b,a). For the majority of the year, the western North Atlantic's persistent cloud cover, only temporarily interspersed with clear-sky conditions of broken cloud fields, makes passive remote sensing measurements of aerosol properties in this region very challenging (Feingold, 2003; Braun et al., 2021; Painemal et al., 2021). Methods to process polarimeter and lidar data that perform well across the extreme situations encountered in the western North Atlantic may be expected to work well globally. For this study, we use measurements from the first two deployments of ACTIVATE in 2020.

The first and second ACTIVATE deployments were carried out from 14 February to 12 March 2020 and from 13 August to 30 September 20, respectively. ACTIVATE features a unique data set collected during 35 joint science flights with two aircraft flying in synchronous flight patterns (Sorooshian et al., 2019). One of the two ACTIVATE aircraft, a Beechcraft King Air, was collecting remote sensing data (i.e., lidar and polarimetry) while flying at high altitudes between 8 and 9 km. Simultaneously, the second aircraft, a HU-25 Falcon, was collecting *in situ* data while operating between the ocean surface and the top of the PBL. Throughout ACTIVATE, these two aircraft operated with close spatiotemporal proximity (within 6 min and 15 km) to each other whenever possible.

The experimental design and study region of ACTIVATE offer an ideal opportunity to evaluate the reliability of the novel vertically resolved N_a developed in this work. First, in **Section 2**, we present the instrumentation and corresponding measurements used from the each of the two aircraft to both produce and validate vertically resolved N_a. In **Section 2** we also present the formulation for deriving vertically resolved N_a from 1) column-averaged fine- and coarse-mode aerosol particle extinction cross section (σ_{ext}) from the polarimeter and 2) the total aerosol particle extinction coefficient (α_{ext}) from the lidar. Next, we describe the processing of the *in situ* data that we use to validate the novel N_a product presented in this work. After describing the data processing and collocation methods, we show results of the *in situ* validation of this novel vertically resolved N_a performed using case studies that have acceptable collocation and environmental conditions in **Section 3**. Our conclusions for this method are summarized in **Section 4**.

2 METHODOLOGY

A glossary of all acronyms and symbols used in this study is provided in **Table 1**.

TABLE 1 | Definition of acronyms, variables, and optional subscripts used to mark mode-specific parameters in alphabetical order.

Acronym	Definition
ACTIVATE	Aerosol Cloud meTeorology Interactions oVer the western ATlantic Experiment
AI	Aerosol index
AOD	Aerosol optical depth
AOS	Atmosphere observing system
ATH	Aerosol top height
CCN	Cloud condensation nuclei
CDP	Cloud droplet probe
DLH	Diode laser hygrometer
HSRL-2	Multiwavelength high spectral resolution lidar
LAS	Laser aerosol spectrometer
LDR	Linear depolarization ratio
LWC	Liquid water content
MLH	Mixed layer height
NMAD	Range-normalized mean absolute deviation
NRMSD	Range-normalized root-mean-square deviation
PBL	Planetary boundary layer
RH	Relative humidity
RSP	Research scanning polarimeter
Variable	Definition
α_{ext}	Aerosol particle extinction coefficient
D	Particle diameter
n_p	Number of points used for comparison
N_a	Aerosol particle number concentration
N_{RSP}	Column-averaged aerosol particle number concentration derived from the RSP data
$N_{\mathrm{HSRL+RSP}}$	Vertically resolved aerosol particle number concentration derived from HSRL and RSP data
N_{LAS}	Aerosol particle number concentration of particles with dry optical diameters between 94 and 3,488 nm
N_{CDP}	Number concentration of particles with ambient optical diameters between 2000 and 50,000 nm
N_d	Cloud drop number concentration
p-value	Probability that the two parameters are not correlated (i.e., probability that the null-hypothesis is true)
P_{75}	75th *percentile*
P_{90}	90th *percentile*
r	Correlation coefficient
r_e	Aerosol particle size distribution effective radius
$r_{e,94\text{–}1130}$	Effective radius of the particles that have dry optical diameters between 94 and 1,130 nm
σ_{ext}	Aerosol particle extinction cross section
Subscript	Definition
f	Parameter is specific to the fine mode of aerosol particle size distribution
c	Parameter is specific to the coarse mode of aerosol particle size distribution

2.1 Study Region Description

Figure 1 demonstrates the spatial coverage that was observed during the first two deployments of ACTIVATE. The ACTIVATE study region is characterized as predominately a marine environment impacted by anthropogenic continental outflow (Corral et al., 2021; Painemal et al., 2021). In most marine conditions the coarse-mode aerosol concentrations are composed primarily of sea salt, which accounts for a small percentage of the N_a in the troposphere (Murphy et al., 2019). This is especially true when the marine background is influenced by anthropogenic continental outflow where total N_a can be on the order of 1,000 cm^{-3}.

2.2 Measurement Summary

A list of instruments and corresponding measurements utilized from each of the ACTIVATE aircraft is provided in **Table 2**. The RSP aerosol product is based on an optimal estimate using the research scanning polarimeter–microphysical aerosol properties from polarimetery (RSP-MAPP) algorithm (Stamnes et al., 2018). Fine- and coarse-mode aerosol optical and microphysical properties are directly retrieved using seven channels that measure the total and polarized radiance across the visible–shortwave spectrum (wavelength = 410–2,260 nm) with over 100 viewing angles between ±55°. The RSP has a field of view of 14 mrad, which results in a ~126 m footprint for an aircraft at 9 km altitude. This RSP retrieval uses a coupled atmosphere–ocean radiative transfer model to improve the accuracy of the retrieved aerosol properties.

The RSP-MAPP retrieval algorithm (v1.48) inverts RSP data under the assumption that the aerosols are bimodal, split into a fine-mode and coarse-mode aerosol, with each mode defined by a lognormal size distribution. This version of RSP-MAPP assumes that the aerosol size distribution has one fine-mode and one coarse-mode comprising non-absorbing sea salt particles. Such a

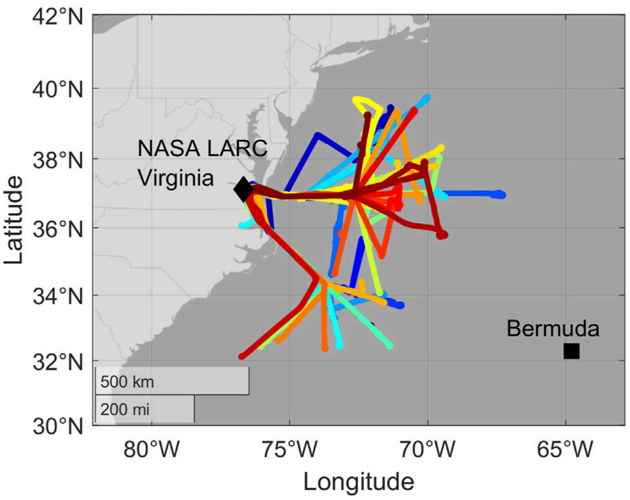

FIGURE 1 | Flight tracks from the 35 two-aircraft research flights that were carried out during the first two deployments of ACTIVATE in the winter and summer of 2020. Each flight track color corresponds to a different ACTIVATE research flight.

bimodal aerosol model works well over the ocean because the RSP visible to shortwave-infrared channels are not sensitive to particles D $\lesssim$ 100 nm. The fine-mode aerosol properties including aerosol absorption are fully retrieved, namely, fine-mode AOD, size distribution parameters of effective radius and effective variance, and complex refractive index. The coarse-mode AOD, effective radius, and effective variance are also retrieved under the assumption that the coarse-mode consists of non-absorbing sea salt particles with a real refractive index close to water. The coarse-mode sea salt aerosol is assumed to be located from the ocean surface to 1 km, while the fine-mode aerosol is assumed to be mixed homogeneously from the ocean surface to the aerosol top height, which is also retrieved. From the aerosol optical and microphysical properties, RSP-MAPP implicitly retrieves the column-averaged fine- and coarse-mode σ_{ext} ($\sigma_{\text{ext},f}$ and $\sigma_{\text{ext},c}$, respectively). The RSP-MAPP algorithm also provides an estimate of fine- and coarse-mode column-averaged N_a ($N_{a,f}$ and $N_{a,c}$, respectively). In cloud-free conditions, RSP and HSRL-2 column AODs have been shown to agree to within 0.02 at 532 nm (Stamnes et al., 2018). The column-averaged aerosol particle number concentration derived from the RSP data (N_{RSP}) is defined as the following:

$$N_{\text{RSP}} = \bar{N}_a = \frac{\text{AOD}}{\bar{\sigma}_{\text{ext}} \times \text{ATH}}, \tag{1}$$

where we explicitly use a bar to represent the *column-averaged* polarimeter-retrieved aerosol cross section and number concentration. The AOD and σ_{ext} are referenced at 532 nm. Both AOD and N_{RSP} are, in part, governed by a retrieval of the aerosol top height (ATH, Wu et al., 2016). RSP-MAPP retrieves the ATH under the assumption that the fine-mode size and composition are uniform throughout the column, and as a result the fine-mode σ_{ext} is implicitly retrieved as a uniform value.

The HSRL-2 products include ambient vertically resolved lidar backscattering and extinction coefficients and ambient linear depolarization ratio (LDR) at wavelengths of 355, 532, and 1,064 nm (Fernald, 1984; Hair et al., 2008; Burton et al., 2018). The HSRL-2 field of view is 1 mrad, which corresponds to a ~9 m footprint for an aircraft at 9 km altitude. Similar to the RSP, the HSRL-2 is not very sensitive to particles that fall in or below the Aitken size range (Burton et al., 2016). The HSRL-2 can also provide AOD by using the difference in the molecular channel signals at the top and bottom of the layer. Finally, the HSRL-2 retrieves the MLH (Scarino et al., 2014). To limit the scope of this analysis to spherical particles, LDR is used to filter out non-spherical from the data set (Burton et al., 2013). A LDR threshold of > 13% was used to filter out non-spherical particles from the analysis. This LDR threshold was chosen because the ACTIVATE study region is characterized as predominately a marine environment impacted by anthropogenic continental outflow (Corral et al., 2021; Painemal et al., 2021).

The measured *in situ* N_a values are used for the validation of the N_a product presented in this work. These data are taken from the laser aerosol spectrometer (LAS, Model 3,340, TSI, Inc.), which measures concentrations of particles with dry D ranging in sizes from 94 to 7,500 nm at a 1 Hz temporal resolution. The N_a measurements provided by the LAS are provided at standard temperature and pressures (273.15 K and 1,013 mb). While the LAS has a measurement range up to 7,500 nm, the maximum cutoff D of the sample inlet prevents the measurement of particles with ambient D greater than 5,000 nm (McNaughton et al., 2007; Chen et al., 2011). To take into account potential hygroscopic effects, we only include particles with dry optical D up to 3,488 nm in this analysis. The total N_a measured by the LAS is referred to from this point forward as N_{LAS}. The lower dry D cutoff of 94 nm is similar to the lower cutoff of the remotely-

TABLE 2 | List of measurement products used in this study, which are grouped by the both the instrument each measurement was derived from and the ACTIVATE aircraft each instrument was mounted on.

Aircraft	Instrument	Aerosol property
King Air	HSRL-2	Vertically resolved α_{ext} at 532 nm, vertically resolved LDR at 532 nm, total AOD at 532 nm, and MLH
King Air	RSP	Fine- and coarse-mode AOD at 532 nm, column-averaged $\sigma_{\text{ext},f}$ at 532 nm, column-averaged $N_{a,f}$, and ATH
Falcon	LAS	N_{LAS} and $r_{e,94-1130}$
Falcon	DLH	RH
Falcon	CDP	LWC and N_d (i.e., N_{CDP})

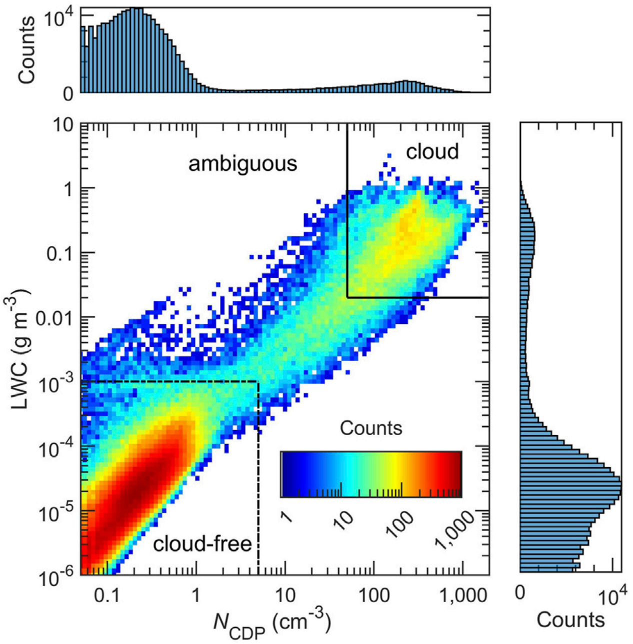

FIGURE 2 | Log-log heat map of liquid water content (LWC) and cloud drop number concentration (N_d) with corresponding marginal semi-log histograms generated using all available 1 *Hz* cloud droplet probe (CDP) data measured during ACTIVATE 2020. The number of points used for comparison (n_p) on each panel is 465, 292. Points on the heat map that are classified as cloud-free have LWC and N_d values that are below horizontal (at 0.001 $g\ m^{-3}$) and vertical (at 5 cm^{-3}) dashed-black lines, respectively. Points on the heat map that are classified as cloud have LWC and N_d values that are above the horizontal (at 0.02 $g\ m^{-3}$) and vertical (at 50 cm^{-3}) solid-black lines, respectively. Points on the heat map that fall outside of the cloud or the cloud-free classifications are classified as ambiguous.

sensed N_a values but the N_{LAS} unavoidably misses some of the coarse-mode N_a due to the aforementioned inlet limitations.

The LAS has a low counting efficiency at three low size bins: 94–106 nm, 106–119 nm, and 119–133 nm, which we compensate for by multiplying the number concentration measured in those size ranges by correction factors of 1.90, 1.45, and 1.20, respectively. Losses for the LAS are calculated at nominal cabin temperature (20 °C) and pressure for low-altitude flight segments (900 mb). These correction factors are calculated using the product of losses by impaction, gravitational settling, and diffusion (Baron and Willeke, 2011). All tubing is conductive silicone and flows are laminar from the inlet manifold to both the LAS optical block. In addition to N_{LAS}, the aerosol particle size distribution effective radius (r_e) of the fine-mode is derived from the corrected LAS and defined as effective radius of the particles that have dry optical diameters between 94 and 1,130 nm ($r_{e,94-1130}$). The $r_{e,94-1130}$ is used primarily to assess the homogeneity of the fine-mode aerosol particles that is assumed to be true for the RSP-MAPP–derived fine-mode σ_{ext}.

Ambient liquid water content (LWC) and N_d are used to classify *in situ* data as cloud-free, ambiguous, or cloud. Ambient LWC and N_d are both derived from ambient particle size distribution measured by using a cloud droplet probe (CDP, Droplet Measurement Technologies, Sinclair et al., 2019). The CDP can measure particles in the ambient D size range of 2,000–50,000 nm, and the N_d-CDP derived by the CDP is noted by N_{CDP}. An important limitation with deriving LWC from the CDP is an integration of the particle size distribution assuming unit density and constrained to the real refractive index of water. If the particles are anything other than spherical, with unit density and with real refractive index of 1.33, this LWC number has no meaning. Previous studies of aerosol–cloud interactions in marine environments have used a LWC threshold of $< 0.02\ \mathrm{g\ m^{-3}}$ to classify data as cloud-free (Wang et al., 2014; Dadashazar et al., 2017; MacDonald et al., 2018). While this LWC threshold generally works well, the LWC of stratiform clouds has been shown to be as low as $0.0012\ \mathrm{g\ m^{-3}}$ (Yin et al., 2014). To ensure the avoidance of cloud edges, measurements where LWC was between 0.001 and $0.02\ \mathrm{g\ m^{-3}}$ and where N_d was between 5 and $50\ \mathrm{cm^{-3}}$ are classified as ambiguous. Only measurements where LWC and N_d were less than $0.001\ \mathrm{g\ m^{-3}}$ and $5\ \mathrm{cm^{-3}}$, respectively, are classified as cloud-free.

To further illustrate the three cloud classifications (cloud-free, ambiguous, and cloud) used in this study, **Figure 2** provides a heat map (with marginal histograms) of all available 1 Hz LWC and N_{CDP} measurements taken during ACTIVATE 2020. In addition to the LWC and N_d thresholds, a sampling inlet flag is used to verify the Falcon aircraft's sampling inlet was sampling air *via* the isokinetic inlet or *via* the counterflow virtual impactor (BMI Inc.; Shingler et al., 2012). The former is used to sample aerosol particles, while the latter is used to sample cloud droplets. Finally, ambient relative humidity (RH) is derived from measurements of the water vapor mixing ratio, which is measured by using a diode laser hygrometer (DLH, Diskin et al., 2002), and of temperature, which is measured by using the turbulent air motion measurement system (TAMMS, Thornhill et al., 2003). Ambient RH is used for an indication of the impacts of water vapor on $r_{e,94-1130}$.

2.3 Deriving Vertically Resolved Aerosol Number Concentration

In this section, we describe the mathematical formulation used to derive N_a from standard HSRL-2 and RSP products. The formulation to derive N_a described in this study has its foundation in the spherical particle Mie theory (Bohren and Huffman, 1983). Using the Mie theory and the environmental setup established in **Section 2.1**, we describe how column-averaged $\sigma_{\mathrm{ext},f}$ (from RSP-MAPP) and vertically resolved α_{ext} (from HSRL-2) can be used to calculate vertically resolved N_a. We limit this analysis to the 532 nm wavelength for simplicity. While the RSP-derived σ_{ext} is a column average and is separated into fine- and coarse-modes, we assume the fine- and coarse-mode aerosols are externally mixed as two distinct aerosol types. This assumption allows us to calculate a mixed σ_{ext} using number concentration weighted averaging as follows:

$$\sigma_{\mathrm{ext}} \equiv \sigma_{\mathrm{ext}}(z) = \frac{N_{a,f}(z) \times \sigma_{\mathrm{ext},f}(z) + N_{a,c}(z) \times \sigma_{\mathrm{ext},c}(z)}{N_{a,f}(z) + N_{a,c}(z)}, \quad (2)$$

where we show explicitly the vertically resolved dependence on altitude z. Aerosol particle extinction cross section is related to N_a at every altitude layer by α_{ext} using the following:

$$N_a \equiv N_a(z) = N_{a,f}(z) + N_{a,c}(z) = \frac{\alpha_{\text{ext}}(z)}{\sigma_{\text{ext}}(z)} \equiv \frac{\alpha_{\text{ext}}}{\sigma_{\text{ext}}}. \tag{3}$$

However, we choose cases based on the HSRL-2 and *in situ* measurements where the coarse-mode α_{ext} has a minimal impact, and accordingly simplify the equation to remove the coarse-mode terms. By setting the $N_{a,c}$ and $\sigma_{\text{ext,c}}$ terms to zero we obtain the following relationship for the aerosol number concentration from **Eqs (2)**, **(3)**, resulting in the method proposed in this study:

$$N_a \equiv N_a(z) = N_{a,f}(z) \approxeq \frac{\alpha_{\text{ext}}(z)}{\bar{\sigma}_{\text{ext},f}} \equiv \frac{\alpha_{\text{ext}}}{\sigma_{\text{ext},f}}, \tag{4}$$

where **Equation (4)** is applied to every altitude bin of the vertically resolved α_{ext} measured by the lidar (HSRL-2), while $\sigma_{\text{ext},f}$ is set equal to the column-averaged value retrieved by the polarimeter (RSP). The $\sigma_{\text{ext},f}$ is dependent on only the fine-mode aerosol size and composition. That the fine-mode aerosol cross section is kept constant is an assumption that the fine-mode aerosol properties do not significantly differ from the column-averaged value in such a way that it significantly biases the retrieval of N_a. Another limitation related to this assumption is that both extinction cross section and extinction coefficient are expected to increase with increasing RH. Using an average cross section could cause $N_{\text{HSRL+RSP}}$ to biased high/low with an increase/decrease of ambient size.

2.4 Data Handling and Analysis

This section describes how remote sensing and *in situ* data are processed to apply the N_a derivation outlined in **Section 2.3**. First, we limit the application of the method to observations of spherical aerosol particles using the LDR threshold of $\leq 13\%$ to filter out non-spherical data points from the smoothed α_{ext} data. Next, the α_{ext} and LDR data are smoothed into temporal-altitude grids of 0.0167 Hz and 150 m. The HSRL-2–derived AOD are also smoothed to a temporal resolution of 0.0167 Hz. Once the HSRL-2–derived α_{ext} and AOD data are smoothed, they are then collocated with the RSP by comparing the timestamps and selecting the nearest HSRL-2 data point (in time) to each of the RSP data points. A total of 7,727 RSP data points are collocated with HSRL-2–derived AOD and vertically resolved profiles of α_{ext}. Once the remote sensing data are placed in the native RSP temporal resolution, any scenes where the HSRL-2- and RSP-derived AOD deviate from each other are discarded. Points are discarded when deviation between the two AOD measurements exceeds whichever is greater 0.05 or 50% of the HSRL-2–derived AOD. As an additional constraint the fine-mode AOD derived from the RSP must be within 0.10 of the HSRL-2 AOD. The HSRL-2- and RSP-derived AOD can deviate from each other when there are cirrus clouds above the King Air, when there is at least one aerosol layer above the King Air, or when there are one or more detached troposphere aerosol layers. As a result of this filtering step, there are 774 collocated data points removed from the total set of 7,727. This empirical method of cloud and multiple aerosol layer influence does not guarantee the removal of all such contamination. In the future, the N_a derivation can be upgraded to be applied to conditions where aerosols are present in one or more detached troposphere layer(s) and in the presence of significant amounts of non-spherical aerosol particles.

After the remote sensing data are aligned and filtered, the aerosol particle number concentration of particles with dry optical diameters between 94 and 3,488 nm (N_{LAS}) data are filtered for clouds and adjusted to ambient temperature and pressure for direct comparison with the remote sensing observations. From the cloud filtered ambient N_{LAS} data, all available *in situ* vertical profiles (e.g., spirals, in-line descents, and in-line ascents) are organized for collocation with the remote sensing data. For this collocation stage the remote sensing profiles are collocated with the *in situ* profiles. The nearest remote sensing profile within 6 min and 15 km to the start or end of the *in situ* profile is selected for comparison. After collocation, N_{LAS} from each *in situ* profile is averaged to the same altitude grid as the HSRL-2 data (i.e., altitude bins that are 150 m in depth and extend from 0 to 9 km).

With collocation performed, the HSRL-2 + RSP-derived N_a (i.e., $N_{\text{HSRL+RSP}}$) can be equivalently compared to the N_{LAS} at each altitude grid point of each collocated vertical profile. In order to validate the column-averaged N_a that is derived from the RSP (i.e., N_{RSP}), the column-averaged N_{LAS} is calculated by taking an arithmetic mean of the entire N_{LAS} profile. With this final step, both $N_{\text{HSRL+RSP}}$ and N_{RSP} can be equivalently quantitatively validated using vertically resolved N_{LAS} or column-averaged N_{LAS}, respectively. This study makes use of correlation coefficient (r), range-normalized root-mean-square deviation (NRMSD), range-normalized mean absolute deviation (NMAD), and relative bias, which have been previously used for quantitative validation of aerosol microphysical properties (Sawamura et al., 2017; Stamnes et al., 2018). Each of these statistical metrics has the following formulations:

$$r = \frac{\sum_{j=1}^{n_p}\left[(X(j) - \bar{X}) \times (Y(j) - \bar{Y})\right]}{\sum_{j=1}^{n_p}[X(j) - \bar{X}]^2 \times \sum_{j=1}^{n_p}[Y(j) - \bar{Y}]^2}, \tag{5}$$

$$\text{NRMSD} = \frac{100\%}{\max(X) - \min(X)} \times \sqrt{\frac{\sum_{j=1}^{n_p}[Y(j) - X(j)]^2}{n_p}}, \tag{6}$$

$$\text{NMAD} = \frac{100\%}{\max(X) - \min(X)} \times \frac{\sum_{j=1}^{n_p}|Y(j) - X(j)|}{n_p}, \tag{7}$$

$$\text{relative bias} = \frac{Y(j) - X(j)}{Y(j) + X(j)} \times 2 \times 100\%, \tag{8}$$

where X and Y are the set of in situ–derived N_a and remote sensing–derived N_a, respectively; n_p is the total number of points for each set; and $\bar{X}$ and $\bar{Y}$ are the mean of sets X and Y, respectively. This study also makes use of the p-value corresponding to each r.

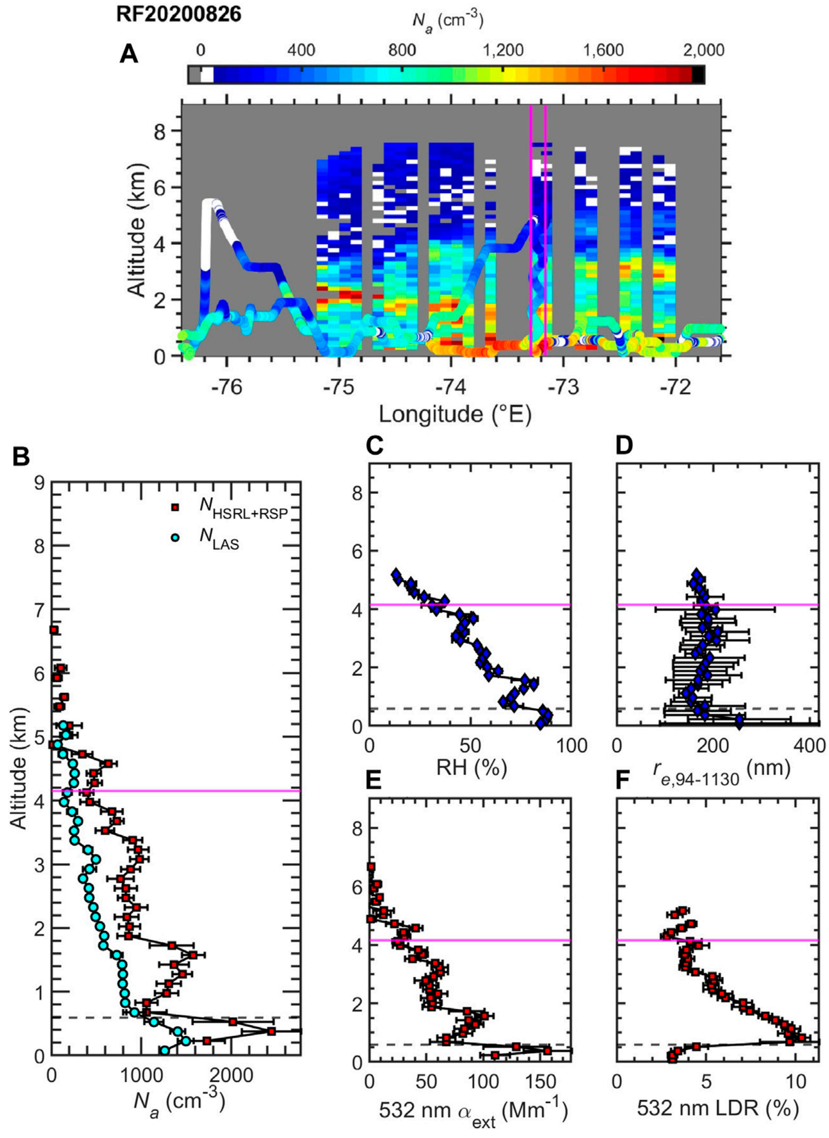

FIGURE 3 | Horizontal curtain **(A)** and vertical profiles **(B–F)** of remote sensing and *in situ* data gathered from the 'optimal' flight that occurred on 26 August 2020. The vertical profiles were taken from the *in situ* profile that occurred between 15:46:25 and 15:58:12 (UTC) on 26 August 2020. Panel **(A)** shows the flight track and surface plot colored by N_{LAS} and $N_{HSRL+RSP}$, respectively, where the magenta vertical lines mark the start and stop locations of the first optimal vertical *in situ* profile. Panel **(B)** show vertical profiles of average aerosol particle number concentration (derived from the various methods), **(C)** RH, **(D)** $r_{e,94\text{–}1130}$, **(E)** 532 nm α_{ext}, and **(F)** 532 nm LDR; where the whiskers mark ± one standard deviation. The horizontal dashed-black and solid-magenta lines mark the MLH and the ATH, respectively.

3 RESULTS

Out of the 35 two-aircraft flights in the first two deployments of ACTIVATE, there are a total of 42 full vertical profiles successfully collocated using the process described in **Section 2.4**. In order to be considered as an *in situ* vertical profile, each of these collocated profiles was required to have measurements across at least four altitude grid points. These 42 profiles are placed into three categories based on whether there are ambiguous- or cloud-flagged *in situ* data in the profile (see **Section 2.2**). The three classifications are described as follows: (1, *cloud-free profile*) vertical profiles where there are no *in situ* data flagged as ambiguous or cloud; (2, *ambiguous profile*) vertical profiles that have one or more *in situ* data point that is flagged as ambiguous but no points flagged as cloud; and (3, *cloud profile*) vertical profiles where at least one data point was classified as cloud. There are 32 profiles classified as cloud-free, two profiles classified as ambiguous, eight profiles classified as cloud of the profiles classified as cloud-free, and two profiles that featured extended spiral vertical profiles, which are fairly unusual for ACTIVATE, and targeted relatively high aerosol loading. These two "optimal" aerosol profiles extended to at least 5 km in altitude; hence, they offer an unprecedented

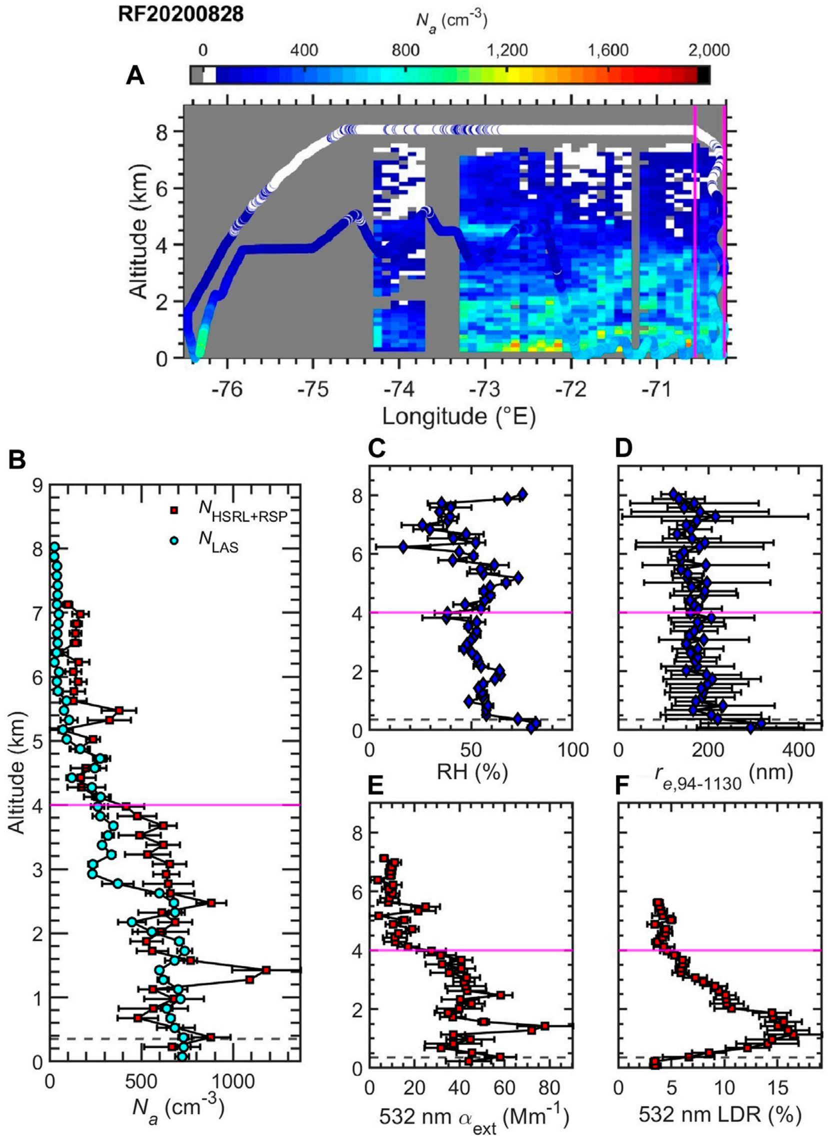

FIGURE 4 | Horizontal curtain **(A)** and vertical profiles **(B–F)** of remote sensing and *in situ* data gathered from the 'optimal' flight that occurred on 28 August 2020. The vertical profiles were taken from the *in situ* profile that occurred between 17:35:18 and 17:54:11 (UTC) on 28 August 2020. Panel **(A)** shows the flight track and surface plot colored by N_{LAS} and $N_{\mathrm{HSRL+RSP}}$, respectively, where the magenta vertical lines mark the start and stop locations of the first optimal vertical *in situ* profile. Panel **(B)** show vertical profiles of average aerosol particle number concentration (derived from the various methods), **(C)** RH, **(D)** $r_{e,94\text{–}1130}$, **(E)** 532 nm α_{ext}, and **(F)** 532 nm LDR, where the whiskers mark ± one standard deviation. The horizontal dashed-black and solid-magenta lines mark the MLH and the ATH, respectively.

opportunity to validate the novel $N_{\mathrm{HSRL+RSP}}$. In **Section 3.1** we analyze these two optimal profiles with more detail and show that the novel $N_{\mathrm{HSRL+RSP}}$ has reasonable closure with N_{LAS}. Following this case study analysis, we analyze the entire *in situ* validation set in **Section 3.2**. These result demonstrated in this analysis warrant further study in future ACTIVATE deployments and other missions with combined lidar-polarimeter aerosol measurements.

3.1 Case Study of Optimal Aerosol Profiles

In this section, we examine the two optimal aerosol profiles from the first deployment of ACTIVATE 2020 (**Figures 3**, **4**). For these two profiles, each corresponding research flight took place in a generally cloud-free conditions (both low level and cirrus), that allow for the use of the novel $N_{\mathrm{HSRL+RSP}}$ product to create altitude vs. longitude color maps of N_a to provide some spatial context to each profile (**Figure 3A**, **Figure 4A**). The $N_{\mathrm{HSRL+RSP}}$ is gridded into 0.01° longitude bins (maintaining the 150 m altitude bins), but the *in situ* sampling flight track is displayed in the native 1 *Hz* resolution for qualitative, observational comparison of N_{LAS} and the $N_{\mathrm{HSRL+RSP}}$. From this qualitative comparison, it is evident that the N_{LAS} and $N_{\mathrm{HSRL+RSP}}$ reasonably agree for these two flights that include the optimal profiles. In addition to the qualitative comparison between N_{LAS} and $N_{\mathrm{HSRL+RSP}}$, these vertically

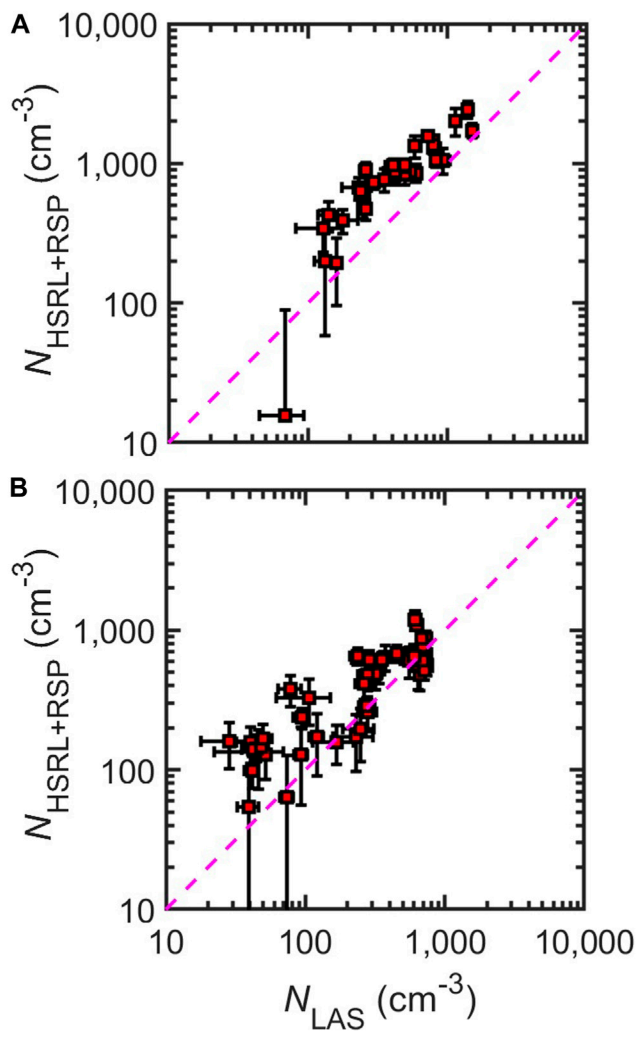

FIGURE 5 | Log-log plots of $N_{\text{HSRL+RSP}}$ versus N_{LAS} from **(A)** optimal *in situ* profile that occurred between 15:46:25 and 15:58:12 (UTC) on 26 August 2020 and **(B)** optimal *in situ* profile that occurred between 17:35:18 and 17:54:11 (UTC) on 28 August 2020. The goodness of fit statistics that correspond to panel **(A)** are r = 0.92, median relative bias = 64%, NMAD = 29%, NRMSD = 33%, and n_p = 34. The goodness of fit statistics for panel **(B)** are r = 0.81, median relative bias = 42%, NMAD = 21%, NRMSD = 28%, and n_p = 47.

resolved profiles illustrate the significant differences in the two profiles.

The first optimal profile's research flight occurred from 13:52:27 to 17:08:12 on 26 August 2020 (**Figure 3**). This first optimal flight appears to have had two aerosol layers, one below 1 km and one between 1 and 2 km (e.g., smoke aerosol), as well as N_{LAS} and $N_{\text{HSRL+RSP}}$ ranges that reached as high as 2,508 and 9,103 cm^{-3}, respectively. The second optimal flight occurred from 16:45:10 to 20:01:40 on 28 August 2020 (**Figure 4**) and had lower maximum N_{LAS} and $N_{\text{HSRL+RSP}}$ (1,031 and 4,209 cm^{-3}, respectively), relative to the first optimal flight. The second optimal profile's research flight had possibly more than one aerosol layer between 1 and 4 km, in addition to a homogeneous aerosol layer up to 1 km. Both of these profiles were observed to have detached aerosol layers above the PBL (e.g., smoke aerosol). Smoke aerosol was found to be present in this region on 26 August (Mardi et al., 2021) and on 28 August (Sorooshian et al., 2021).

Another contrast between the two optimal flight study regions was the MLH, which had the ranges of 0:00–0:88 km and 0:00–0:67 km for the first and second optimal flights, respectively. Both flights had similar RSP-ATH ranges that were 1:14–4:83 km and 1:83–4:85 km for the first and second optimal flights, respectively. In order to better analyze the closure between N_{LAS} and $N_{\text{HSRL+RSP}}$, we examine the closure statistics that result from the optimal profiles (**Figure 3B**, **Figure 4B**) where the aircraft horizontal-temporal separation is constrained (see **Section 2.4**).

The horizontal spatial and temporal aircraft separation of the first and second optimal profiles is 1.94 km–3.79 min and 11.99 km–5.97 min, respectively. The MLH of the first and second optimal profiles are at 0.59 and 0.35 km, respectively. The ATH of the first and second optimal profiles are at 4.15 and 4.00 km, respectively. The median relative bias, NMAD, and NRMSD observed in the first case study were generally worse (median relative bias = 64%, NMAD = 29%, and NRMSD = 33%), relative to the second case study (median relative bias = 42%, NMAD = 21%, and NRMSD = 28%). The r between $N_{\text{HSRL+RSP}}$ and N_{LAS} for the first and second optimal flights are 0.92 and 0.81, respectively, and both profiles are among those that have the most statistically significant correlations in the set of collocated profiles (i.e., r > 0.80 and p-value $\leq 10^{-9}$). In addition to these statistics **Figure 5** also provides a visual illustration of the vertically resolved N_{LAS}-$N_{\text{HSRL+RSP}}$ and column-averaged N_{LAS}-$N_{\text{HSRL+RSP}}$ closure.

To provide insight into the reasons for differences in the N_{LAS}-$N_{\text{HSRL+RSP}}$ closure, we examine the differences in the vertical profiles of RH, $r_{e,94-1130}$, α_{ext}, and LDR that correspond to the optimal profile that occurred on 26 August 2020 (**Figures 3C–F**) and the optimal profile that occurred on 28 August 2020 (**Figures 4C–F**). The RH sampled in the first optimal profile overall decreases with increasing altitude up the ATH at ~ 4 km, while the RH sampled in the second optimal profile remains relatively constant until the ATH, also at ~ 4 km. In both optimal profiles, the RH decreases sharply right above the MLH. Then, in the first optimal profile, both the α_{ext} and RH increase with altitude above the MLH to 1.5 km. In the second optimal profile, α_{ext} and RH and α_{ext} and RH are relatively constant except for a sharp increase about 1.5 km. We found that the RH is negatively correlated with $r_{e,94-1130}$ between 1 and 2 km in the first optimal profile. This behavior is in contrast to the second optimal profile, where the $r_{e,94-1130}$ increases around the spike in RH at 2 km altitude. The increase in α_{ext} might otherwise seem to indicate multiple aerosol layers sampled in both optimal profiles, but the profiles of RH and $r_{e,94-1130}$ suggest that the changes are a result of increases in RH rather than a separate unmixed layer, except in the second optimal profile around 1.5 km. At this location it is observed that LDR is elevated in the second optimal profile, and indicates the presence of non-spherical coarse-mode dust particles in the second optimal profile associated with the sharp increase in α_{ext} at 1.5 km. The dust is likely coarse-mode since there is little change in $r_{e,94-1130}$.

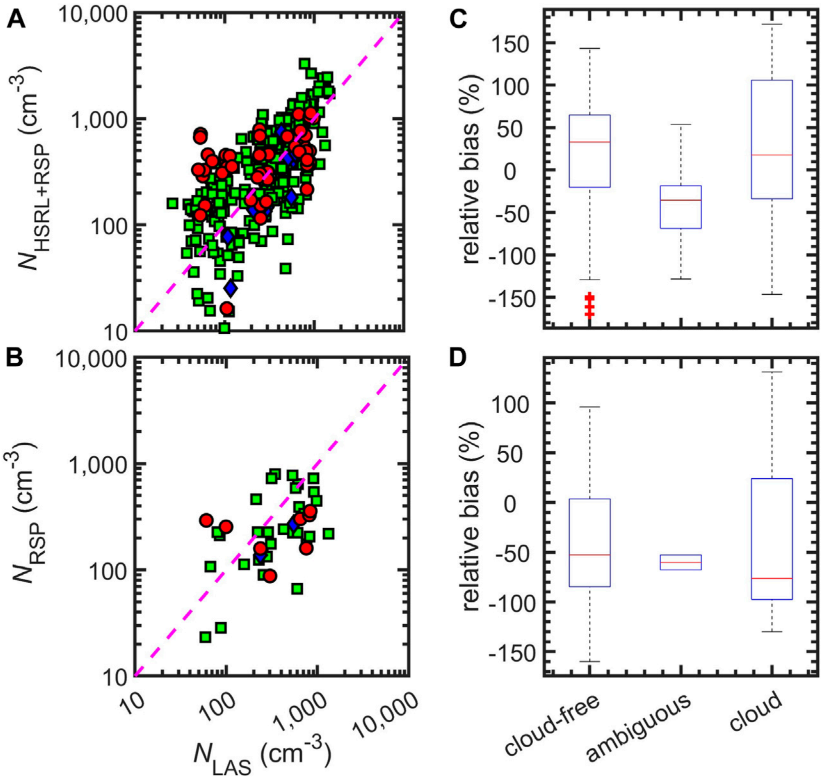

FIGURE 6 | Log-log plots of **(A)** vertically resolved $N_{HSRL+RSP}$ vs. *in situ* N_{LAS} and **(B)** column-averaged N_{RSP} vs. *in situ* N_{LAS}. The collocated vertical profile data come from ACTIVATE 2020. The green squares correspond to data from vertical profiles where all *in situ* data are classified as cloud-free, blue diamonds correspond to the vertical profiles that have one or more *in situ* data point that is classified as ambiguous but no points classified as cloud, and the red circles correspond to data from vertical profiles where at least one data point was classified as cloud. The dashed-magenta line indicates the one-to-one line. Panels **(C)** and **(D)** are box plots illustrating the spread in relative bias of panel **(A)** and panel **(B)**, respectively. Data for these box plots correspond to the same categories as panels **(A)** and **(B)** (i.e., cloud-free, ambiguous, and cloud). Additional goodness of fit statistics for panels **(A)** and **(B)** are shown in Tbl. 3. Red markers on panels **(C)** or **(D)** are points that were flagged as statistical outliers. An outlier is a value that is more than 1.5 times the interquartile range away from the bottom or top of box.

Despite the presence of coarse-mode dust, the retrieval of the vertically resolved $N_{HSRL+RSP}$, which is driven σ_{ext} in addition to α_{ext}, does not seem to be generally impacted except at 1.5 km where the coarse-mode dust loading peaks.

In addition to examining the profiles to identify multiple aerosol layers, the α_{ext} profile, in combination with $r_{e,94-1130}$ and RH profiles, allow us to examine the assumption of using a single fine-mode σ_{ext} to derive vertically resolved $N_{HSRL+RSP}$. The narrow $r_{e,94-1130}$ range observed in the second profile suggests that there is no significant change in the fine-mode aerosol composition and size distribution. Because $r_{e,94-1130}$ can be dependent on N_{LAS}, and RH can indicate the mixing state of the atmosphere, the positive correlation between both N_{LAS} and RH with $r_{e,94-1130}$ near the surface (≤200 km altitude) seen in each profile may indicate that changes in $r_{e,94-1130}$ for near the surface are partly related to atmospheric mixing rather than composition change.

These findings from the analysis of the first optimal profile suggest that method is robust in that the correlation for $N_{HSRL+RSP}$ is high despite a ~60% bias at elevated N_a and despite the separate smoke aerosol observed in the first profile. The analysis of the LDR profile suggests that non-spherical particles are not impacting the retrieval of $N_{HSRL+RSP}$ significantly. In the next section, we combine data from these optimal profiles with the remaining cloud-free collocated profiles of $N_{HSRL+RSP}$ and N_{LAS} to further support these findings and strengthen the validation of the $N_{HSRL+RSP}$ product.

3.2 Statistical Validation

Following the initial validation with the optimal case studies, we use all collocated vertically resolved N_{LAS} data to perform a more statistically weighted validation of $N_{HSRL+RSP}$ product using **Figure 6A**. Furthermore, we show that this error is generally similar to the error observed in the validation of N_{RSP} with column-averaged N_{LAS} (**Figure 6B**). Finally we examine **Figures 6C,D** and **Table 3** to demonstrate the improvements gained in validation of both vertically resolved and column-averaged N_a by removing profiles where cloud presence is detected in the column.

As noted above, there are 32 cloud-free profiles, two ambiguous profiles, and eight cloud profiles, which contain 322, 13, and 47, respectively, vertically resolved points for the comparison validation of $N_{HSRL+RSP}$ and N_{LAS}. The r, median relative bias, NMAD, and NRMSD that result from the comparison of the points

TABLE 3 | Comparison statistics resulting from the comparison of vertically resolved N_{LAS} with $N_{\mathrm{HSRL+RSP}}$ and resulting from the comparison of column-averaged N_{LAS} with N_{RSP} for the *in situ* profiles that were classified as cloud-free, ambiguous, and cloud. The statistics presented for each category are as follows (from left to right): r, *p*-value, P_{75} and P_{90} of the absolute relative bias (i.e., |relative bias|), NMAD, NRMSD, minimum and maximum N_{LAS} (either vertically resolved or column-averaged), and n_p.

	Conditions	r	*p*-value	*|relative bias|* (%)		NMAD	NRMSD	N_{LAS} (cm^{-3})		n_p
				P_{75}	P_{90}	(%)	(%)	min	max	
Vertically resolved	Cloud-free	0.76	$6.1 \cdot 10^{-62}$	81	106	16	24	26	1,495	322
	Ambiguous	0.71	$6.8 \cdot 10^{-3}$	69	107	28	34	109	615	13
	Cloud	0.50	$3.9 \cdot 10^{-4}$	112	145	26	33	51	983	47
Column-averaged	Cloud-free	0.35	$5.3 \cdot 10^{-2}$	90	121	21	28	59	1,327	32
	Cloud	0.36	$3.8 \cdot 10^{-1}$	1.20	131	42	47	61	832	8

contained in the cloud-free profiles are 0.76, 33%, 16%, and 24%, respectively. Additionally, this cloud-free data set resulted in a P_{90} of 106% in absolute relative bias. Data from both the ambiguous profiles and the cloud profiles resulted in worse, i.e., increases in NMAD (28% and 26%, respectively) and NRMSD (34% and 33%, respectively), relative to the NMAD and NMAD that resulted from the data cloud-free profiles. Relative to the cloud-free profile dataset, the r (0.71) and P_{90} in absolute relative bias (107%) did not change much for the ambiguous profile data set but r decreases to 0.50 and P_{90} in absolute relative bias increases to 145% for the cloud profile dataset.

Due to the limited number of column-averaged N_a points (n_p = 2) that are classified as ambiguous, the validation statistics for this set is not meaningful and will be omitted here. The validation statistics resulting from the comparison of the column-averaged N_a points classified as cloud-free and cloud are similar to that resulting from the vertically resolved N_a closure, with the exception of relative bias. The NMAD improves, i.e., decreases, from 42% to 21% and the NRMSD decreases from 47% to 28%. In contrast to the vertically resolved N_a, the median relative bias resulting from the column-averaged N_a comparison of the eight collocated points is −0.76, which improves to −0.53 for the 32 profiles from the column-averaged cloud-free dataset. In addition, the P_{90} in absolute relative bias of the column-averaged cloud data set is larger (131%), relative to the column-averaged cloud-free data set (121%). These findings suggest that the significantly improved performance of one set over the other, which is likely due to the fact that the retrieval of column-averaged N_a is more sensitive to deviations from ideal cloud-free conditions than the vertically resolved N_a. It is also possible that the retrieval of column-averaged N_a is more sensitive to separated aerosol layers that are possibly present. However, due to the relatively limited number of collocated points and profiles, wider application is needed to definitively conclude the main reason for the difference.

4 CONCLUSION

In this study we provide a simple and direct approach to derive vertically resolved aerosol number concentration from collocated polarimeter–lidar measurements. This method has the benefit of rapidly taking advantage of column-averaged polarimeter-derived aerosol cross section from the RSP and collocated lidar measurements of the aerosol extinction coefficient at 532 nm. Since this method only requires profiles of the extinction coefficient at 532 nm, it can be readily applied to lidar + polarimeter datasets provided that the lidar has a 532 nm high spectral resolution channel such as the NASA airborne HSRL-1 and HSRL-2 lidar, and the HSRL-1–type lidar system that will be onboard the future NASA AOS mission. We characterize the retrieval error that is observed from vertically resolved $N_{\mathrm{HSRL+RSP}}$, which is derived from column-averaged σ_{ext} from polarimeter retrievals and vertically resolved α_{ext} from HSRL-2 measurements. We demonstrate that the vertically resolved $N_{\mathrm{HSRL+RSP}}$ product has a median relative bias, P_{90} in absolute relative bias, NMAD, and NRMSD that are 0.33, 106%, 16%, and 24%, respectively. Our results also suggest that the vertically resolved $N_{\mathrm{HSRL+RSP}}$ product has similar NMAD and NRMSD as the column-averaged N_{RSP}. We demonstrate that column-averaged N_{RSP} validation is more sensitive than the vertically resolved $N_{\mathrm{HSRL+RSP}}$ to deviations from ideal conditions (e.g., cloud-free with a single aerosol layer), however elevated LDR $> 10\%$ does not appear to have a significant impact on either vertically resolved or column-averaged N_a.

Although a fully combined polarimeter–lidar retrieval is expected to provide the optimal retrieval of aerosol optical and microphysical properties including aerosol number concentrations, this method provides a simple and direct approach to corroborate the results from such complex retrievals, particularly for simpler cases of single or two-layer aerosol systems. The ACTIVATE field campaign features combined polarimeter (RSP) and lidar (HSRL-2) remote sensing measurements with collocated *in situ* aerosol measurements from a second, low-flying aircraft. The ACTIVATE datasets of simultaneous remote and *in situ* measurements of aerosols in clear-sky conditions will enable us to extensively test the approach outlined here, as well as perform detailed closure studies for relating dry-wet aerosol microphysical and optical properties across passive, active, and *in situ* aerosol measurement techniques. The promise shown by the $N_{\mathrm{HSRL+RSP}}$ method can be further explored by applying the method to the rest of the ACTIVATE datasets (i.e., 2021 and 2022 flights) and to future analyses that can incorporate retrievals of the vertical structure of N_a in the atmosphere to study N_a-N_d relationships for aerosol–cloud interactions. Further application will also allow for in-depth examination of the validity of the assumption of column-averaged extinction cross sections, and the impact of scattering by coarse-mode aerosols such as sea salt aerosol on the retrieved aerosol number concentration. The hope is that the $N_{\mathrm{HSRL+RSP}}$ product can be a robust method to provide required vertical profiles of N_a for many research applications ranging from aerosol–cloud interactions to improving estimates of air quality parameters such as $\mathrm{PM}_{2.5}$.

DATA AVAILABILITY STATEMENT

Publicly available datasets were analyzed in this study. This data can be found at: https://doi.org/10.5067/SUBORBITAL/ACTIVATE/DATA001.

AUTHOR CONTRIBUTIONS

Algorithm development: JS, SS, and BC. Data: RM, LZ, BC, CH, RF, JH, and AS. Text: all authors.

FUNDING

This work was supported through the ACTIVATE Earth Venture Suborbital-3 (EVS-3) investigation, which is funded by NASA's Earth Science Division and managed through the Earth System Science Pathfinder Program Office. Partial support was also provided by ONR grant N00014-21-1-2115.

ACKNOWLEDGMENTS

We wish to thank the pilots and aircraft maintenance personnel of NASA Langley Research Services Directorate for their work in conducting the ACTIVATE flights.

REFERENCES

Baron, P. A., and Willeke, K. (2011). *Aerosol Measurement: Principles, Techniques, and Applications*. Wiley.

Bohren, C. F., and Huffman, D. R. (1983). *Absorption and Scattering of Light by Small Particles*. Wiley.

Braun, R. A., McComiskey, A., Tselioudis, G., Tropf, D., and Sorooshian, A. (2021). Cloud, Aerosol, and Radiative Properties over the Western North Atlantic Ocean. *J. Geophys Res. Atmos.* 126, e2020JD034113. doi:10.1029/2020JD034113

Buchard, V., da Silva, A. M., Colarco, P. R., Darmenov, A., Randles, C. A., Govindaraju, R., et al. (2015). Using the Omi Aerosol Index and Absorption Aerosol Optical Depth to Evaluate the Nasa Merra Aerosol Reanalysis. *Atmos. Chem. Phys.* 15, 5743–5760. doi:10.5194/acp-15-5743-2015

Burton, S. P., Chemyakin, E., Liu, X., Knobelspiesse, K., Stamnes, S., Sawamura, P., et al. (2016). Information Content and Sensitivity of the 3<i>β</i> + 2<i>α</i> Lidar Measurement System for Aerosol Microphysical Retrievals. *Atmos. Meas. Tech.* 9, 5555–5574. doi:10.5194/amt-9-5555-2016

Burton, S. P., Ferrare, R. A., Vaughan, M. A., Omar, A. H., Rogers, R. R., Hostetler, C. A., et al. (2013). Aerosol Classification from Airborne Hsrl and Comparisons with the Calipso Vertical Feature Mask. *Atmos. Meas. Tech.* 6, 1397–1412. doi:10.5194/amt-6-1397-2013

Burton, S. P., Hostetler, C. A., Cook, A. L., Hair, J. W., Seaman, S. T., Scola, S., et al. (2018). Calibration of a High Spectral Resolution Lidar Using a Michelson Interferometer, with Data Examples from Oracles. *Appl. Opt.* 57, 6061–6075. doi:10.1364/AO.57.006061

Cairns, B., Russell, E. E., and Travis, L. D. (1999). "Research Scanning Polarimeter: Calibration and Ground-Based Measurements," in *SPIE's International Symposium on Optical Science, Engineering, and Instrumentation* (Denver, Colorado: International Society for Optics and Photonics), 186–196.

Chen, G., Ziemba, L. D., Chu, D. A., Thornhill, K. L., Schuster, G. L., Winstead, E. L., et al. (2011). Observations of Saharan Dust Microphysical and Optical Properties from the Eastern Atlantic during Namma Airborne Field Campaign. *Atmos. Chem. Phys.* 11, 723–740. doi:10.5194/acp-11-723-2011

Corral, A. F., Braun, R. A., Cairns, B., Gorooh, V. A., Liu, H., Ma, L., et al. (2021). An Overview of Atmospheric Features over the Western North Atlantic Ocean and North American East Coast - Part 1: Analysis of Aerosols, Gases, and Wet Deposition Chemistry. *J. Geophys Res. Atmos.* 126. doi:10.1029/2020JD032592

Dadashazar, H., Alipanah, M., Hilario, M. R. A., Crosbie, E., Kirschler, S., Liu, H., et al. (2021a). Aerosol Responses to Precipitation along North American Air Trajectories Arriving at bermuda. *Atmos. Chem. Phys.* 21, 16121–16141. doi:10.5194/acp-21-16121-2021

Dadashazar, H., Painemal, D., Alipanah, M., Brunke, M., Chellappan, S., Corral, A. F., et al. (2021b). Cloud Drop Number Concentrations over the Western North Atlantic Ocean: Seasonal Cycle, Aerosol Interrelationships, and Other Influential Factors. *Atmos. Chem. Phys.* 21, 10499–10526. doi:10.5194/acp-21-10499-2021

Dadashazar, H., Wang, Z., Crosbie, E., Brunke, M., Zeng, X., Jonsson, H., et al. (2017). Relationships between Giant Sea Salt Particles and Clouds Inferred from Aircraft Physicochemical Data. *J. Geophys. Res. Atmos.* 122, 3421–3434. doi:10.1002/2016JD026019

Diskin, G. S., Podolske, J. R., Sachse, G. W., and Slate, T. A. (2002). "Open-path Airborne Tunable Diode Laser Hygrometer," in *Diode Lasers and Applications in Atmospheric Sensing*. Editor A. Fried (Seattle, Washington D.C.: International Society for Optics and Photonics), 4817, 196–204. doi:10.1117/12.453736

Feingold, G. (2003). Modeling of the First Indirect Effect: Analysis of Measurement Requirements. *Geophys. Res. Lett.* 30. doi:10.1029/2003GL017967

Fernald, F. G. (1984). Analysis of Atmospheric Lidar Observations: Some Comments. *Appl. Opt.* 23, 652–653. doi:10.1364/ao.23.000652

Georgoulias, A. K., Marinou, E., Tsekeri, A., Proestakis, E., Akritidis, D., Alexandri, G., et al. (2020). A First Case Study of Ccn Concentrations from Spaceborne Lidar Observations. *Remote Sens.* 12, 1557. doi:10.3390/rs12101557

Grosvenor, D. P., Sourdeval, O., Zuidema, P., Ackerman, A., Alexandrov, M. D., Bennartz, R., et al. (2018). Remote Sensing of Droplet Number Concentration in Warm Clouds: A Review of the Current State of Knowledge and Perspectives. *Rev. Geophys.* 56, 409–453. doi:10.1029/2017RG000593

Gryspeerdt, E., Quaas, J., Ferrachat, S., Gettelman, A., Ghan, S., Lohmann, U., et al. (2017). Constraining the Instantaneous Aerosol Influence on Cloud Albedo. *Proc. Natl. Acad. Sci. U.S.A.* 114, 4899–4904. doi:10.1073/pnas.1617765114

Hair, J. W., Hostetler, C. A., Cook, A. L., Harper, D. B., Ferrare, R. A., Mack, T. L., et al. (2008). Airborne High Spectral Resolution Lidar for Profiling Aerosol Optical Properties. *Appl. Opt.* 47, 6734–6752. doi:10.1364/ao.47.006734

Hammer, M. S., Martin, R. V., van Donkelaar, A., Buchard, V., Torres, O., Ridley, D. A., et al. (2016). Interpreting the Ultraviolet Aerosol Index Observed with the Omi Satellite Instrument to Understand Absorption by Organic Aerosols: Implications for Atmospheric Oxidation and Direct Radiative Effects. *Atmos. Chem. Phys.* 16, 2507–2523. doi:10.5194/acp-16-2507-2016

Hasekamp, O. P., Gryspeerdt, E., and Quaas, J. (2019). Analysis of Polarimetric Satellite Measurements Suggests Stronger Cooling Due to Aerosol-Cloud Interactions. *Nat. Commun.* 10, 5405. doi:10.1038/s41467-019-13372-2

Knobelspiesse, K., Cairns, B., Ottaviani, M., Ferrare, R., Hair, J., Hostetler, C., et al. (2011). Combined Retrievals of Boreal Forest Fire Aerosol Properties with a

Polarimeter and Lidar. *Atmos. Chem. Phys.* 11, 7045–7067. doi:10.5194/acp-11-7045-2011

MacDonald, A. B., Dadashazar, H., Chuang, P. Y., Crosbie, E., Wang, H., Wang, Z., et al. (2018). Characteristic Vertical Profiles of Cloud Water Composition in Marine Stratocumulus Clouds and Relationships with Precipitation. *J. Geophys. Res. Atmos.* 123, 3704–3723. doi:10.1002/2017JD027900

Mardi, A. H., Dadashazar, H., Painemal, D., Shingler, T., Seaman, S. T., Fenn, M. A., et al. (2021). Biomass Burning over the united states East Coast and Western North Atlantic Ocean: Implications for Clouds and Air Quality. *JGR Atmos.* 126, e2021JD034916. doi:10.1029/2021JD034916

McNaughton, C. S., Clarke, A. D., Howell, S. G., Pinkerton, M., Anderson, B., Thornhill, L., et al. (2007). Results from the Dc-8 Inlet Characterization Experiment (Dice): Airborne versus Surface Sampling of Mineral Dust and Sea Salt Aerosols. *Aerosol Sci. Technol.* 41, 136–159. doi:10.1080/02786820601118406

Müller, D., Chemyakin, E., Kolgotin, A., Ferrare, R. A., Hostetler, C. A., and Romanov, A. (2019). Automated, Unsupervised Inversion of Multiwavelength Lidar Data with Tiara: Assessment of Retrieval Performance of Microphysical Parameters Using Simulated Data. *Appl. Opt.* 58, 4981–5008. doi:10.1364/AO.58.004981

Murphy, D. M., Froyd, K. D., Bian, H., Brock, C. A., Dibb, J. E., DiGangi, J. P., et al. (2019). The Distribution of Sea-Salt Aerosol in the Global Troposphere. *Atmos. Chem. Phys.* 19, 4093–4104. doi:10.5194/acp-19-4093-2019

Painemal, D., Corral, A. F., Sorooshian, A., Brunke, M. A., Chellappan, S., Afzali Gorooh, V., et al. (2021). An Overview of Atmospheric Features over the Western North Atlantic Ocean and North American East Coast-Part 2: Circulation, Boundary Layer, and Clouds. *Geophys Res. Atmos.* 126. doi:10.1029/2020JD033423

Quinn, P. K., Bates, T. S., Coffman, D. J., Upchurch, L., Johnson, J. E., Moore, R., et al. (2019). Seasonal Variations in Western North Atlantic Remote Marine Aerosol Properties. *J. Geophys. Res. Atmos.* 124, 14240–14261. doi:10.1029/2019JD031740

Sawamura, P., Moore, R. H., Burton, S. P., Chemyakin, E., Müller, D., Kolgotin, A., et al. (2017). Hsrl-2 Aerosol Optical Measurements and Microphysical Retrievals vs. Airborne *In Situ* Measurements during Discover-Aq 2013: an Intercomparison Study. *Atmos. Chem. Phys.* 17, 7229–7243. doi:10.5194/acp-17-7229-2017

Scarino, A. J., Obland, M. D., Fast, J. D., Burton, S. P., Ferrare, R. A., Hostetler, C. A., et al. (2014). Comparison of Mixed Layer Heights from Airborne High Spectral Resolution Lidar, Ground-Based Measurements, and the Wrf-Chem Model during Calnex and Cares. *Atmos. Chem. Phys.* 14, 5547–5560. doi:10.5194/acp-14-5547-2014

Shingler, T., Dey, S., Sorooshian, A., Brechtel, F. J., Wang, Z., Metcalf, A., et al. (2012). Characterisation and Airborne Deployment of a New Counterflow Virtual Impactor Inlet. *Atmos. Meas. Tech.* 5, 1259–1269. doi:10.5194/amt-5-1259-2012

Shinozuka, Y., Clarke, A. D., Nenes, A., Jefferson, A., Wood, R., McNaughton, C. S., et al. (2015). The Relationship between Cloud Condensation Nuclei (Ccn) Concentration and Light Extinction of Dried Particles: Indications of Underlying Aerosol Processes and Implications for Satellite-Based Ccn Estimates. *Atmos. Chem. Phys.* 15, 7585–7604. doi:10.5194/acp-15-7585-2015

Sinclair, K., van Diedenhoven, B., Cairns, B., Alexandrov, M., Moore, R., Crosbie, E., et al. (2019). Polarimetric Retrievals of Cloud Droplet Number Concentrations. *Remote Sens. Environ.* 228, 227–240. doi:10.1016/j.rse.2019.04.008

Sorooshian, A., Corral, A. F., Braun, R. A., Cairns, B., Crosbie, E., Ferrare, R., et al. (2020). Atmospheric Research over the Western North Atlantic Ocean Region and North American East Coast: A Review of Past Work and Challenges Ahead. *J. Geophys Res. Atmos.* 125, e2019JD031626. doi:10.1029/2019JD031626

Sorooshian, A., Anderson, B., Bauer, S. E., Braun, R. A., Cairns, B., Crosbie, E., et al. (2019). Aerosol-Cloud-Meteorology Interaction Airborne Field Investigations: Using Lessons Learned from the U.S. West Coast in the Design of ACTIVATE off the U.S. East Coast. *Bull. Am. Meteorological Soc.* 100, 1511–1528. doi:10.1175/BAMS-D-18-0100.1

Sorooshian, A., Atkinson, J., Ferrare, R., Hair, J., and Ziemba, L. (2021). Taking Flight to Study Clouds and Climate. *EOS* 102. doi:10.1029/2021EO158570

Stamnes, S., Hostetler, C., Ferrare, R., Burton, S., Liu, X., Hair, J., et al. (2018). Simultaneous Polarimeter Retrievals of Microphysical Aerosol and Ocean Color Parameters from the "MAPP" Algorithm with Comparison to High-Spectral-Resolution Lidar Aerosol and Ocean Products. *Appl. Opt.* 57, 2394–2413. doi:10.1364/ao.57.002394

Thornhill, K. L., Anderson, B. E., Barrick, J. D. W., Bagwell, D. R., Friesen, R., and Lenschow, D. H. (2003). Air Motion Intercomparison Flights during Transport and Chemical Evolution in the Pacific (Trace-p)/ace-asia. *J. Geophys. Res.* 108. doi:10.1029/2002JD003108

Wang, Z., Sorooshian, A., Prabhakar, G., Coggon, M. M., and Jonsson, H. H. (2014). Impact of Emissions from Shipping, Land, and the Ocean on Stratocumulus Cloud Water Elemental Composition during the 2011 E-Peace Field Campaign. *Atmos. Environ.* 89, 570–580. doi:10.1016/j.atmosenv.2014.01.020

Wu, L., Hasekamp, O., van Diedenhoven, B., Cairns, B., Yorks, J. E., and Chowdhary, J. (2016). Passive Remote Sensing of Aerosol Layer Height Using Near-Uv Multiangle Polarization Measurements. *Geophys. Res. Lett.* 43, 8783–8790. doi:10.1002/2016GL069848

Yin, J.-F., Wang, D.-H., Zhai, G.-Q., and Xu, H.-B. (2014). An Investigation into the Relationship between Liquid Water Content and Cloud Number Concentration in the Stratiform Clouds over North china. *Atmos. Res.* 139, 137–143. doi:10.1016/j.atmosres.2013.12.004

Conflict of Interest: Author EC is employed by Science Systems and Applications, Inc.

The remaining authors declare that the research was conducted in the absence of any commercial or financial relationships that could be construed as a potential conflict of interest.

frontiers | Frontiers in Remote Sensing

ORIGINAL RESEARCH
published: 22 July 2022
doi: 10.3389/frsen.2022.880768

Polarized Radiative Transfer Simulations: A Tutorial Review and Upgrades of the Vector Discrete Ordinate Radiative Transfer Computational Tool

Zhenyi Lin[1], Snorre Stamnes[2], Wei Li[1], Yongxiang Hu[2], Istvan Laszlo[3], Si-Chee Tsay[4], Alexander Berk[5], Jeannette van den Bosch[6] and Knut Stamnes[1]*

[1]Department of Physics, Stevens Institute of Technology, Hoboken, NJ, United States, [2]NASA Langley Research Center, Hampton, VA, United States, [3]NOAA, Center for Satellite Applications and Research, College Park, MD, United States, [4]NASA Goddard Space Flight Center, Greenbelt, MD, United States, [5]Spectral Sciences, Burlington, MA, United States, [6]Air Force Research Laboratory, Albuquerque, NM, United States

We present an overview and several important upgrades to the Vector Discrete Ordinate Radiative Transfer (VDISORT) code. VDISORT is a polarized (vector) radiative transfer code that can be applied to a wide range of research problems including the Earth's atmosphere and ocean system. First, a solution is developed to the complex algebraic eigenvalue problem resulting when the b_2 component of the Stokes scattering matrix is non-zero. This solution is needed to compute the V component of the Stokes vector $\mathbf{I} = [I_{\parallel}, I_{\perp}, U, V]^T$. Second, a significant improvement in computational efficiency is obtained by reducing the dimension of the algebraic eigenvalue by a factor of 2 resulting in a speed increase of about $2^3 = 8$. Third, an important upgrade of the VDISORT code is obtained by developing and implementing a method to enable output at arbitrary polar angles by the integration of the source function (ISF) method for partially reflecting Lambertian as well as general non-Lambertian surfaces. Fourth, a pseudo-spherical treatment has been implemented to provide important corrections for Earth curvature effects at near horizontal solar zenith and observation (viewing) polar angles. Fifth, a post-processing single-scattering correction procedure has been developed to enhance the accuracy and speed for strongly forward-peaked scattering. With these significant improvements the results from the upgraded version of the VDISORT code match published benchmark results for Rayleigh scattering, Mie scattering, and scattering by non-spherical cirrus particles. The performance of VDISORT for a polarized incident beam source is equally satisfactory. The VDISORT vector radiative transfer code is made public and freely available for use by the growing polarimetric research community including the space-borne polarimeters on the future NASA PACE and AOS missions.

Keywords: radiative transfer, multiple scattering, polarization, passive remote sensing, ellipsometry and polarimetry, lidar, aerosol detection, oceanic optics

Edited by:
Oleg Dubovik,
UMR8518 Laboratoire d'optique Atmosphèrique (LOA), France

Reviewed by:
Weizhen Hou,
Aerospace Information Research Institute (CAS), China
Chao Liu,
Nanjing University of Information Science and Technology, China

Correspondence:
Knut Stamnes
kstamnes@stevens.edu

Specialty section:
This article was submitted to Satellite Missions, a section of the journal Frontiers in Remote Sensing

Received: *21 February 2022*
Accepted: *07 June 2022*
Published: *22 July 2022*

Citation:
Lin Z, Stamnes S, Li W, Hu Y, Laszlo I, Tsay S-C, Berk A, van den Bosch J and Stamnes K (2022) Polarized Radiative Transfer Simulations: A Tutorial Review and Upgrades of the Vector Discrete Ordinate Radiative Transfer Computational Tool. Front. Remote Sens. 3:880768. doi: 10.3389/frsen.2022.880768

1 INTRODUCTION

This paper documents a state-of-the-art numerical code called VDISORT for monochromatic polarized radiative transfer in non-isothermal, vertically inhomogeneous, but horizontally homogeneous media. The physical processes included are Planckian thermal emission, scattering with a general phase matrix, absorption, and surface reflection. The system may be driven by parallel or isotropic unpolarized or polarized radiation incident at the boundaries, as well as by internal thermal sources and thermal emission from the boundaries. The Stokes vector is returned at user-specified angles and levels. The azimuthally-averaged Stokes components are also available. Irradiances and mean radiances can be generated from the azimuthally-averaged radiance, i.e., the first component of the Stokes vector $[I,Q,U,V]^T$.

VDISORT is based on articles published in the open literature, but its theoretical background and algorithmic developments have not been systematically described in one single document. This paper provides an up-to-date complete description of VDISORT including a self-contained account of its theoretical basis and a discussion of the numerical implementation of the theory.

Like DISORT, the scalar version, VDISORT has been designed to be a good scientific software package and a numerical code of general utility. The VDISORT package takes advantage of robust existing software tools to make it numerically well-conditioned, and user-friendly. A set of test cases have been adopted to verify the numerical code against published results.

1.1 Outline of Paper

This paper is organized as follows. **Section 1** provides the motivation for and a brief history of VDISORT, while **Section 2** provides theoretical background, introduces the radiative transfer equation for unpolarized and polarized radiation, and discusses the inherent optical properties including the phase matrix. The solution of the vector radiative transfer equation (VRTE) is discussed in **Section 3** including the discrete ordinate method, important upgrades of the vector discrete ordinate code (VDISORT), the ISF method, and treatment of polarized reflectance from the lower boundary. **Section 4** discusses the merits of the 4 × 4 solution versus the 3 × 3 approximation, while **Section 5** is devoted to the single-scattering approximation, which is used in a post-processing step to enhance the accuracy of the computed results for a given number of discrete ordinate streams. Test results are presented in **Section 6** including comparisons with published benchmarks. Finally, in **Section 7** a brief summary and concluding remarks are provided.

1.2 Brief History

The discrete ordinate radiative transfer algorithm (DISORT) has proven to be an accurate, versatile and reliable method for the solution of the scalar radiative transfer problem in plane-parallel, vertically inhomogeneous media (Stamnes et al., 1988; Lin et al., 2015; Laszlo et al., 2016; Stamnes K. et al., 2017). An extension of the scalar discrete ordinate theory to solve for the complete Stokes vector $\mathbf{I} = [I,Q,U,V]^T$ was reported by Weng (1992), who adopted an approach to the solution of the vector problem completely analogous to the scalar case. Hence, the computer code for the vector problem, VDISORT, could rely on the same well-tested routine to obtain the eigenvalues and eigenvectors as the one used in the scalar version (DISORT). Also, the same scaling transformation (Stamnes and Conklin, 1984) could be applied to circumvent the notorious ill-conditioning that occurs when applying boundary and layer interface continuity conditions.

The first version of the FORTRAN code developed by Weng (1992) had a few shortcomings related to the fact that it had been applied exclusively in the microwave region, and thus had not been tested for beam source applications. In addition, the procedure employed to compute the Fourier components of the phase matrix turned out to be both inaccurate and inefficient. To correct these shortcomings an improved version of the code was developed by Schulz et al. (1999). In this new version of the code 1) errors in the numerical implementation were corrected, 2) the procedure used to compute the Fourier components of the phase matrix was replaced by a more accurate and efficient method, 3) the basic performance of the code was tested against benchmark results. However, although the code seemed to have the potential to become an accurate and reliable tool for a variety of applications, no attempt was made to test it in a systematic and comprehensive manner. Also, no attempt was made to document the code thoroughly and extensively, and it was assumed that the homogeneous solution involved only real eigenvalues/eigenvectors, which are sufficient to solve for the *I*, *Q*, and *U* Stokes parameters, but the *V* component requires complex arithmetic.

The original code provided solutions for the *I*, *Q*, and *U* Stokes parameters at the discrete ordinates (i.e. at the quadrature polar angles). Since the computing time required for the discrete ordinate method increases cubically with the number of quadrature angles, it becomes cost-effective to obtain the solution at a limited number of quadrature angles and then generate the solution at additional angles by using an efficient interpolation scheme. To this end analytic expressions were developed that were shown to be accurate for the *I*, *Q*, and *U* components, but not for the *V* component, at arbitrary angles and optical depths (Schulz and Stamnes, 2000) in much the same way they were developed for the scalar version (Stamnes, 1982). These analytic expressions obtained by the ISF method (Stamnes, 1982) satisfy not only the radiative transfer equation, but also the boundary and layer-interface continuity conditions at arbitrary polar angles, and they have proven to be superior to standard interpolation schemes such as cubic splines (Stamnes, 1982; Schulz and Stamnes, 2000). To complete this development, an extension of this ISF method to include accurate computation of the *V* Stokes parameter, which requires complex arithmetic, is described **Section 3.5**.

2 THEORETICAL BASIS

2.1 Unpolarized Radiation

We consider an inhomogeneous horizontal slab of scattering/absorbing material with inherent optical properties that vary only in the vertical direction z, where z increases upward. The corresponding vertical optical depth is defined by

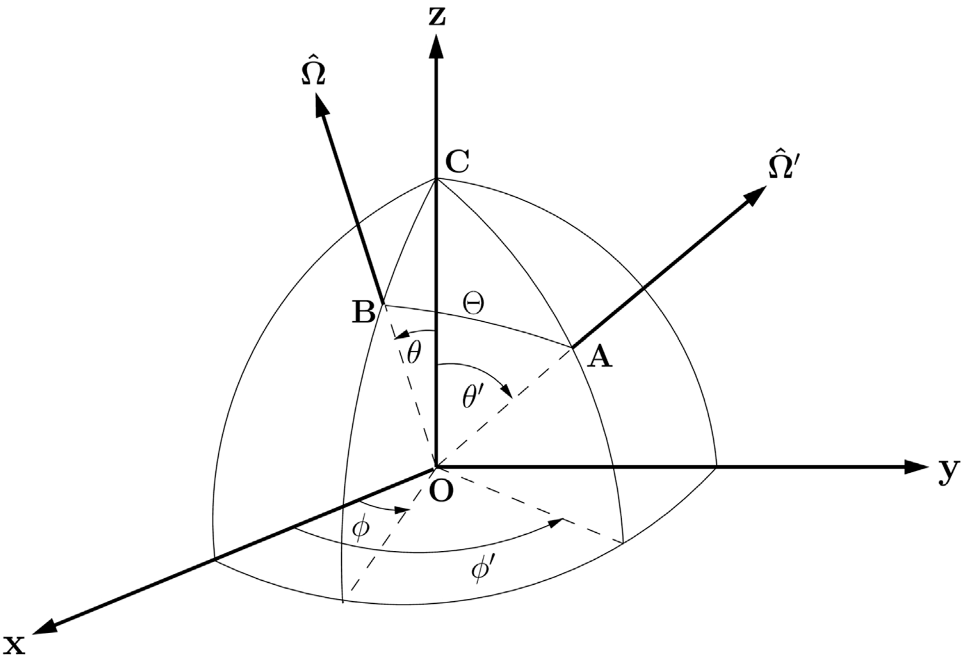

FIGURE 1 | Coordinate system for scattering by a volume element at **O**. The points **C**, **A** and **B** are located on the unit sphere. The incident light beam with Stokes vector $\mathbf{I}_S^{\text{inc}}$ is in direction **OA** (θ', ϕ') with unit vector $\hat{\mathbf{\Omega}}'$, the scattered beam with Stokes vector $\mathbf{I}_S^{\text{sca}}$ is in direction **OB**(θ, ϕ) with unit vector $\hat{\mathbf{\Omega}}$ (Hovenier et al., 2004).

$$\tau(z) = \int_z^\infty [\alpha(z') + \beta(z')]dz' \tag{1}$$

where α and β are the absorption and scattering coefficients in units of reciprocal length, respectively, and the vertical optical depth is defined to increase downward from $\tau(z = \infty) = 0$ at the top of the slab. The slab is assumed to be in local thermodynamic equilibrium so that it emits radiation according to the local temperature T ($\tau(z)$). The diffuse radiance distribution I (τ, u, ϕ) can be described by the scalar radiative transfer equation (RTE)

$$u\frac{dI(\tau,u,\phi)}{d\tau} = I(\tau,u,\phi) - S(\tau,u,\phi) \tag{2}$$

where the source function is given by

$$S(\tau,u,\phi) = S^*(\tau,u,\phi) + [1 - \varpi(+)]B(\tau) + \frac{\varpi(\tau)}{4\pi}\int_0^{2\pi} d\phi' \int_{-1}^1 p(\tau,u',\phi';u,\phi)I(\tau,u',\phi')du'. \tag{3}$$

Here u is the cosine of the polar angle θ, ϕ is the azimuth angle, $\varpi(\tau) = \beta(\tau)/[\alpha(\tau) + \beta(\tau)]$ is the single-scattering albedo, p (τ, u', ϕ'; u, ϕ) is the scattering phase function, and $B(\tau)$ is the thermal radiation field given by the Planck function. The single-scattering source term is given by

$$S^*(\tau,u,\phi) = \frac{\varpi(\tau)}{4\pi}\, p(\tau,-\mu_0,\phi_0;u,\phi)S_b e^{-\tau/\mu_0} \tag{4}$$

where S_b is the incident (solar) irradiance and μ_0 is the cosine of the solar zenith angle. The differential vertical optical depth is [see **Eq. 1**]

$$d\tau(z) = -[\alpha(\tau) + \beta(\tau)]dz \tag{5}$$

where the minus sign indicates that τ increases in the downward direction, whereas z increases in the upward direction, as noted above. The scattering angle Θ and the polar and azimuth angles are related by (see **Figure 1**)

$$\hat{\mathbf{\Omega}}' \cdot \hat{\mathbf{\Omega}} = \cos\Theta = \cos\theta\,\cos\theta' + \sin\theta'\,\sin\theta\,\cos(\phi' - \phi).$$

Here $\hat{\Omega}'$ is the unit vector of the incident beam direction and $\hat{\Omega}$ is the unit vector of the scattered direction. By definition, $\theta = 180^\circ$ is directed toward nadir (straight down) and $\theta = 0^\circ$ toward zenith (straight up). Thus, $u = \cos\theta$ varies in the range $[-1, 1]$ (from nadir to zenith). For oblique illumination of the slab, $\phi_0 = 180^\circ$ is defined to be the azimuth angle of the incident light.

2.2 Polarized Radiation

To generalize **Eq. 2** to apply to polarized radiation, the scalar source function must be replaced by the appropriate vector version. Hence, the multiple-scattering term $S^{\text{ms}}(\tau,u,\phi) = \frac{\varpi(\tau)}{4\pi}\int_0^{2\pi} d\phi' \int_{-1}^1 du' p(\tau,u',\phi';u,\phi)I(\tau,u',\phi')$ in **Eq. 3** must be replaced by

$$\mathbf{S}^{\text{ms}}(\tau,u,\phi) = \frac{\varpi(\tau)}{4\pi}\int_0^{2\pi} d\phi' \int_{-1}^{1} du' \mathbf{P}(\tau,u',\phi';u,\phi)\mathbf{I}(\tau,u',\phi') \tag{6}$$

where $\mathbf{I}\ (\tau, u', \phi')$ is the Stokes vector, and $\mathbf{P}\ (\tau, u', \phi'; u, \phi)$ is the scattering phase matrix. The first element of the vector $\mathbf{S}^{\mathrm{ms}}(\tau, u, \phi)$ represents the energy per unit solid angle, per unit frequency interval, and per unit time that is scattered by a unit volume in the direction $(u = \cos\theta, \phi)$. Hence, in a plane-parallel (slab) geometry, the integro-differential vector radiative transfer equation (VRTE) for polarized radiation is expressed in terms of a Stokes vector $\mathbf{I}\ (\tau, u, \phi)$ as

$$u\frac{d\,\mathbf{I}(\tau,u,\phi)}{d\tau} = \mathbf{I}(\tau,u,\phi) - \mathbf{S}(\tau,u,\phi) \tag{7}$$

where the vector source function is

$$\mathbf{S}(\tau,u,\phi) = \mathbf{S}^{\mathrm{ms}}(\tau,u,\phi) + \mathbf{Q}(\tau,u,\phi). \tag{8}$$

Here $\mathbf{S}^{\mathrm{ms}}(\tau, u, \phi)$ is given by **Eq. 6** and the source term $\mathbf{Q}\ (\tau, u, \phi)$, due to beam and thermal sources, is given by:

$$\mathbf{Q}(\tau,u,\phi) = \frac{\varpi(\tau)}{4\pi}\,\mathbf{P}(\tau,-\mu_0,\phi_0;u,\phi)\mathbf{S}_b e^{-\tau/\mu_0} + \left[1-\varpi(\tau)\right]\mathbf{S}_t(\tau). \tag{9}$$

The first term on the right hand side of **Eq. 9** describes the incident beam $\mathbf{S}_b$ in direction $(-\mu_0, \phi_0)$, which is attenuated at depth τ by a factor $e^{-\tau/\mu_0}$ and undergoes single scattering into the direction (u, ϕ). For an unpolarized incident beam $\mathbf{S}_b$ has the form

$$\mathbf{S}_b = \left[I_0/2, I_0/2, 0, 0\right]^T \text{ or } \left[I_0, 0, 0, 0\right]^T \tag{10}$$

where the superscript ^{T} denotes the transpose, and where the first or second expression corresponds to the choice of Stokes vector representation, $[I_\parallel, I_\perp, U, V]^T$ or $[I,Q,U,V]^T$. The second term on the right hand side of **Eq. 9** is due to thermal emission, which is unpolarized, and $\mathbf{S}_t(\tau)$ is given by

$$\mathbf{S}_t(\tau) = \left[B(T(\tau))/2, B(T(\tau))/2, 0, 0\right]^T \quad \text{or} \quad \left[B(T(\tau)), 0, 0, 0\right]^T \tag{11}$$

where B is the Planck function, and where the first or second expression corresponds to the choice of Stokes vector representation. We have set $\mu_0 \equiv |u_0| \equiv |\cos\theta_0|$, where θ_0 is the polar angle of the incident light beam.

2.3 Effects of Earth Curvature–The Pseudo-Spherical Approximation

For many applications plane-parallel geometry is adequate. For large solar zenith angles ($\theta_0 \geq 70^\circ$ and for near horizontal polar viewing angles θ), however, the plane-parallel approximation (PPA) provides inaccurate results. Then the Earth curvature must be considered. Large solar zenith angles occur around the times of sunrise and sunset at any location on a planet. Such large solar zenith angles are present, for example, in observations made by instruments onboard geostationary satellites that observe a large part of Earth's disk throughout the day. Sensors deployed on polar-orbiting satellite platforms also observe at large solar zenith angles at high latitudes.

As discussed by several investigators (see He et al. (2018) and references therein), the so-called pseudo-spherical approximation (PSA) (Dahlback and Stamnes, 1991) represents a very useful correction to the plane-parallel approximation. In the PSA the direct beam single-scattering term, also called the solar pseudo-source term, is treated in spherical geometry while the multiple-scattering term is treated using the PPA. Hence, in the PSA the exponential attenuation in **Eqs. 4** and **9** is replaced by the Chapman function, that is, $\exp\ (-\tau/\mu_0) \rightarrow \exp\ (-\tau\mathrm{Ch}(\mu_0))$, where the Chapman function $\mathrm{Ch}(\mu_0)$ takes Earth curvature into account, but ignores refraction. As shown by He et al. (2018) the influence of Earth curvature increases rapidly with solar zenith angle, being up to 1, 3, and 12% for solar zenith angles of 75°, 80°, and 85°, respectively.

2.4 Scattering Phase Matrix

The development of vector radiative transfer theory may start with the Stokes vector representation $\mathbf{I} = [I_\parallel, I_\perp, U, V]^T$. In terms of the complex transverse electric field components of the radiation field $E_\parallel = |E_\parallel| \mathrm{e}^{-i\delta_\parallel}$ and $E_\perp = |E_\perp| \mathrm{e}^{-i\delta_\perp}$, these Stokes vector components are given by:

$$\begin{aligned} I_\parallel &= E_\parallel E_\parallel^* \\ I_\perp &= E_\perp E_\perp^* \\ U &= 2|E_\parallel||E_\perp|\cos\delta \\ V &= 2|E_\parallel||E_\perp|\sin\delta \end{aligned} \tag{12}$$

where the phase difference δ is $\delta_\parallel - \delta_\perp$. The connection between the $\mathbf{I} = [I_\parallel, I_\perp, U, V]^T$ Stokes vector representation and the more commonly used $\mathbf{I}_S = [I,Q,U,V]^T$ representation, where $I = I_\parallel + I_\perp$ and $Q = I_\parallel - I_\perp$, is given by:

$$\mathbf{I}_S = \mathbf{D}\mathbf{I} \tag{13}$$

where

$$\mathbf{D} = \begin{pmatrix} 1 & 1 & 0 & 0 \\ 1 & -1 & 0 & 0 \\ 0 & 0 & 1 & 0 \\ 0 & 0 & 0 & 1 \end{pmatrix}, \qquad \mathbf{D}^{-1} = \frac{1}{2}\begin{pmatrix} 1 & 1 & 0 & 0 \\ 1 & -1 & 0 & 0 \\ 0 & 0 & 2 & 0 \\ 0 & 0 & 0 & 2 \end{pmatrix}. \tag{14}$$

The degree of polarization is defined as

$$p = \left[Q^2 + U^2 + V^2\right]^{1/2} / I \tag{15}$$

so that $0 \leq p \leq 1$, where $p = 1$ corresponds to completely polarized light and $p = 0$ to natural (unpolarized) light. The degree of circular polarization is defined as

$$p_c = V/I, \tag{16}$$

the degree of linear polarization as

$$p_l = \left[Q^2 + U^2\right]^{1/2} / I, \tag{17}$$

and alternatively, when $U = 0$ as

$$p_l(U = 0) = -\frac{Q}{I} = \frac{I_\perp - I_\parallel}{I_\perp + I_\parallel}. \tag{18}$$

The transverse electric field vector $[E_\parallel, E_\perp]^T$ of the scattered field can be obtained in terms of the transverse field vector $[E_{\parallel 0}, E_{\perp 0}]^T$ of the incident field by a linear transformation:

$$\begin{pmatrix} E_{\parallel} \\ E_{\perp} \end{pmatrix} = \mathbf{A}\begin{pmatrix} E_{\parallel 0} \\ E_{\perp 0} \end{pmatrix} \tag{19}$$

where **A** is a 2 × 2 matrix, referred to as the amplitude scattering matrix. The corresponding linear transformation connecting the Stokes vectors of the incident and scattered fields in the scattering plane is called the Mueller matrix (in the case of a single scattering event). For scattering by a small volume containing an ensemble of particles, the ensemble-averaged Mueller matrix is referred to as the Stokes scattering matrix **F**. Finally, when transforming from the scattering plane to a fixed laboratory frame, the corresponding matrix is referred to as the scattering phase matrix **P**.

2.4.1 Stokes Vector Representation $\mathbf{I}_S = [I,Q,U,V]^T$

The scattering geometry is illustrated in **Figure 1**. The plane **AOB**, defined as the scattering plane, is spanned by the directions of propagation of the incident parallel beam with Stokes vector $\mathbf{I}_S^{\text{inc}}$ and the scattered parallel beam with Stokes vector $\mathbf{I}_S^{\text{sca}}$. Here the subscript S pertains to the Stokes vector representation $\mathbf{I}_S = [I,Q,U,V]^T$. The scattered radiation, represented by the Stokes vector $\mathbf{I}_S^{\text{sca}}$, is related to the incident radiation, represented by the Stokes vector $\mathbf{I}_S^{\text{inc}}$, by a 4 × 4 scattering matrix [see **Eqs. 20** and **21** below].

If in a small volume of particles any of the following conditions are met (Hovenier and van der Mee, 1983) 1) each particle in the volume element has a plane of symmetry, and the particles are randomly oriented, 2) each volume element contains an equal number of particles and their mirror particles in random orientation, 3) the particles are much smaller than the wavelength of the incident light, then the Stokes scattering matrix in the $\mathbf{I}_S = [I,Q,U,V]^T$ representation has the following form

$$\mathbf{F}_S(\Theta) = \begin{bmatrix} a_1(\Theta) & b_1(\Theta) & 0 & 0 \\ b_1(\Theta) & a_2(\Theta) & 0 & 0 \\ 0 & 0 & a_3(\Theta) & b_2(\Theta) \\ 0 & 0 & -b_2(\Theta) & a_4(\Theta) \end{bmatrix}. \tag{20}$$

Each of the six independent matrix elements in **Eq. 20** depends on the scattering angle Θ, and will in general also depend on the position in the medium. For spherical particles, the matrix in **Eq. 20** simplifies, since $a_1 = a_2$ and $a_3 = a_4$, so that only four independent elements remain.

Two rotations are required to connect the Stokes vector of the scattered radiation to that of the incident radiation. As illustrated in **Figure 1**, the first rotation is from the meridian plane **OAC**, associated with the Stokes vector $\mathbf{I}_S^{\text{inc}}$, into the scattering plane **OAB**, whereas the second rotation is from the scattering plane **OAB** into the meridian plane **OBC**, associated with the Stokes vector $\mathbf{I}_S^{\text{sca}}$. Hence, the Stokes vector for the scattered radiation is given by (Chandrasekhar, 1960)

$$\mathbf{I}_S^{\text{sca}} = \mathbf{R}_S(\pi - i_2)\mathbf{F}_S(\Theta)\mathbf{R}_S(-i_1)\mathbf{I}_S^{\text{inc}} \equiv \mathbf{P}_S(\Theta)\mathbf{I}_S^{\text{inc}}. \tag{21}$$

Here i_1 and i_2 are the angles between the meridian planes of the incident and the scattered radiation, respectively, and the scattering plane (**Figure 1**).The Stokes rotation matrix $\mathbf{R}_S$ represents a rotation in the clockwise direction with respect to an observer looking into the direction of propagation (Chandrasekhar, 1960). For rotation by an arbitrary angle of ω ($0 \le \omega \le 2\pi$) it can be written as

$$\mathbf{R}_S(\omega) = \begin{bmatrix} 1 & 0 & 0 & 0 \\ 0 & \cos(2\omega) & -\sin(2\omega) & 0 \\ 0 & \sin(2\omega) & \cos(2\omega) & 0 \\ 0 & 0 & 0 & 1 \end{bmatrix}. \tag{22}$$

Hence, according to **Eq. 21**, the scattering phase matrix, which connects the Stokes vector of the scattered radiation to that of the incident radiation, is obtained from the Stokes scattering matrix $\mathbf{F}_S(\Theta)$ in **Eq. 20** by

$$\begin{aligned} \mathbf{P}_S(\theta', \phi'; \theta, \phi) &= \mathbf{R}_S(\pi - i_2)\mathbf{F}_S(\Theta)\mathbf{R}_S(-i_1) \\ &= \mathbf{R}_S(-i_2)\mathbf{F}_S(\Theta)\mathbf{R}_S(-i_1) \end{aligned} \tag{23}$$

where $\mathbf{R}_S(\pi - i_2) = \mathbf{R}_S(-i_2)$ since the rotation matrix is periodic with a period π.

According to **Eq. 21** (see also **Figure 1**), the Stokes vector $\mathbf{I}_S^{\text{inc}}$ of the incident parallel beam must be multiplied by the rotation matrix $\mathbf{R}_S(-i_1)$ before it is multiplied by the Stokes scattering matrix $\mathbf{F}_S(\Theta)$, whereafter it must be multiplied by the rotation matrix $\mathbf{R}_S(\pi - i_2)$. In some radiative transfer (RT) models including Monte Carlo simulations these matrix multiplications are carried out explicitly. In other types of RT models such as the adding-doubling method (De Haan et al., 1987) and the discrete ordinate method (Siewert, 2000; Sommersten et al., 2010; Cohen et al., 2013) they are taken care of implicitly through the expansion of the scattering phase matrix in generalized spherical functions (Siewert, 1981, 1982) as discussed in **Section 2.4.3**.

Carrying out the matrix multiplications in **Eq. 23** one finds:

$$\mathbf{P}_S(\Theta) = \begin{bmatrix} a_1 & b_1 C_1 & -b_1 S_1 & 0 \\ b_1 C_2 & C_2 a_2 C_1 - S_2 a_3 S_1 & -C_2 a_2 S_1 - S_2 a_3 C_1 & -b_2 S_2 \\ b_1 S_2 & S_2 a_2 C_1 + C_2 a_3 S_1 & -S_2 a_2 S_1 + C_2 a_3 C_1 & -b_2 C_2 \\ 0 & -b_2 S_1 & -b_2 C_1 & a_4 \end{bmatrix} \tag{24}$$

where $a_j = a_j(\Theta)$, $j = 1, \ldots, 4$, $b_j = b_j(\Theta)$, $j = 1, 2$, and

$$C_1 = \cos 2i_1, \qquad C_2 = \cos 2i_2 \tag{25}$$

$$S_1 = \sin 2i_1, \qquad S_2 = \sin 2i_2. \tag{26}$$

A comparison of **Eqs. 20** and **24** shows that only the corner elements of $\mathbf{F}_S(\Theta)$ remain unchanged by the rotations of the reference planes. The (1.1)-element of both the scattering phase matrix $\mathbf{P}_S(\Theta)$ and the Stokes scattering matrix $\mathbf{F}_S(\Theta)$ is the scattering phase function. Also, since the (4.4)-element of the scattering phase matrix remains unchanged by the rotations, the state of circular polarization of the incident light does not affect the intensity of the scattered radiation after one scattering event.

To compute $\mathbf{P}_S(\theta', \phi'; \theta, \phi)$ given by **Eq. 23** we must relate the angles θ', ϕ', θ, and ϕ on the left side with the angles i_1, i_2, and Θ on the right side. Using spherical geometry, we may apply the cosine rule for Θ, θ, and θ' successively, in **Figure 1**, to obtain ($u = \cos\theta$, $u' = \cos\theta'$) (Hovenier et al., 2004)

$$\cos\Theta = uu' + \left(1-u^2\right)^{1/2}\left(1-u'^2\right)^{1/2}\cos\left(\phi'-\phi\right) \tag{27}$$

$$\cos i_1 = \frac{-u + u'\cos\Theta}{\left(1-u'^2\right)^{1/2}\left(1-\cos^2\Theta\right)^{1/2}} \tag{28}$$

$$\cos i_2 = \frac{-u' + u\cos\Theta}{\left(1-u^2\right)^{1/2}\left(1-\cos^2\Theta\right)^{1/2}}. \tag{29}$$

The trigonometric functions for the double angles can be obtained by using

$$\cos 2\,i = 2\cos^2 i - 1 \tag{30}$$

and

$$\sin 2\,i = 2\sin i\cos i \tag{31}$$

or

$$\sin 2\,i = \begin{cases} 2\left(1-\cos^2 i\right)^{1/2}\cos i & \text{if} \quad 0<\phi'-\phi<\pi \\ -2\left(1-\cos^2 i\right)^{1/2}\cos i & \text{if} \quad \pi<\phi'- \end{cases} \tag{32}$$

where i is i_1 or i_2.

Equations 25–32 describe the conventional way to determine the variables C_1, S_1, C_2, and S_2.

A better approach to compute the variables C_1, S_1, C_2, and S_2 appearing in $\mathbf{P}_S(\theta', \phi'; \theta, \phi)$ given by **Eq. 24** is described in a recent publication (Berk, 2022). This new approach can be described as follows. Defining

$$\Delta\theta = \theta' - \theta \quad \text{and} \quad \Delta\phi = \phi' - \phi, \tag{33}$$

we have

$$\begin{aligned} \sin^2\Theta = {} & \sin^2\Delta\theta + 4\cos\Delta\theta\sin\theta\sin\theta'\sin^2\left(\Delta\phi/2\right) \\ & - 4\sin^2\theta\sin^2\theta'\sin^4\left(\Delta\phi/2\right), \end{aligned} \tag{34}$$

and it can be shown that the variables C_1, S_1, C_2, and S_2 are given by

$$C_1 = \begin{cases} 1 & if \quad \sin\Theta = 0 \\ \dfrac{\left[2\sin\theta\cos\theta'\sin^2\left(\Delta\phi/2\right) + \sin\Delta\theta\right]^2 - \sin^2\theta\sin^2\Delta\phi}{\sin^2\Theta} & otherwise \end{cases} \tag{35}$$

$$S_1 = \begin{cases} 0 & if \quad \sin\Theta = 0 \\ \dfrac{\left[-2\sin\theta\sin\Delta\phi\left[2\sin\theta\cos\theta'\sin^2\left(\Delta\phi/2\right) + \sin\Delta\theta\right]\right.}{\sin^2\Theta} & otherwise \end{cases} \tag{36}$$

$$C_2 = \begin{cases} 1 & if \quad \sin\Theta = 0 \\ \dfrac{\left[2\sin\theta'\cos\theta\sin^2\left(\Delta\phi/2\right) - \sin\Delta\theta\right]^2 - \sin^2\theta'\sin^2\Delta\phi}{\sin^2\Theta} & otherwise \end{cases} \tag{37}$$

$$S_2 = \begin{cases} 0 & if \quad \sin\Theta = 0 \\ \dfrac{\left[-2\sin\theta'\sin\Delta\phi\left[2\sin\theta'\cos\theta\sin^2\left(\Delta\phi/2\right) - \sin\Delta\theta\right]\right.}{\sin^2\Theta} & otherwise. \end{cases} \tag{38}$$

The advantage of using **Eqs. 33–38** instead of **Eqs. 25–32** is that they eliminate numerical instability issues and the need to treat positive and negative relative azimuth angles as separate cases (Berk, 2022).

We now have all the information needed to compute the scattering phase matrix [see **Eq. 24**] as a function of the three variables $u = \cos\theta$, $u' = \cos\theta'$, and $\Delta\phi = \phi' - \phi$. If there is no difference in azimuth (i.e. $\phi' - \phi = 0$), then the meridian planes of the incident and scattered beams in **Fig. 1** coincide with the scattering plane. Hence, there is no need to rotate the reference planes ($\mathbf{R}(-i_2)$ and $\mathbf{R}(-i_1)$ both reduce to the identity matrix), so that

$$\mathbf{P}_S\left(u', u, 0\right) = \mathbf{P}_S\left(u', u, \pi\right) = \mathbf{F}_S(\Theta). \tag{39}$$

It follows from the cosine law of spherical geometry

$$\cos\Theta = uu' + \left(1-u^2\right)^{1/2} 1 - u'^2\Big)^{1/2}\cos\left(\phi'-\phi\right) \tag{40}$$

that the phase matrix is invariant to three basic changes in the polar angles u' and u and azimuthal angles ϕ' and ϕ which leave the scattering angle unaltered: 1) changing the signs of u and u' simultaneously: $\mathbf{P}_S(-u', -u, \phi'-\phi) = \mathbf{P}_S(u', u, \phi'-\phi)$, 2) interchange of u and u': $\mathbf{P}_S(u', u, \phi'-\phi) = \mathbf{P}_S(u, u', \phi'-\phi)$ 3) interchange of ϕ and ϕ': $\mathbf{P}_S(u', u, \phi'-\phi) = \mathbf{P}_S(u', u, \phi-\phi')$. Also, if the b_2-element in **Eq. 24** is zero, then the Stokes parameter V is scattered independently of the others, according to the phase function $a_4(\Theta)$, and the remaining part of the scattering phase matrix referring to I, Q, and U becomes a 3×3 matrix:

$$\mathbf{P}_S(\Theta) = \begin{bmatrix} a_1 & b_1C_1 & -b_1S_1 \\ b_1C_2 & C_2a_2C_1 - S_2a_3S_1 & -C_2a_2S_1 - S_2a_3C_1 \\ b_1S_2 & S_2a_2C_1 + C_2a_3S_1 & -S_2a_2S_1 + C_2a_3C_1 \end{bmatrix}. \tag{41}$$

Finally, in a plane-parallel or slab geometry, there is no azimuth-dependence for light beams traveling in directions perpendicular to the slab (either up or down). Thus, if either the incident or the scattered beam travels in a perpendicular direction, we may use the meridian plane of the other beam as a reference plane for both beams. Since this plane coincides with the scattering plane, **Eq. 39** applies in this situation too.

For Rayleigh scattering with parameter $f = \frac{1-\rho}{1+\rho}$, where ρ is the depolarization factor defined in **Eq. 53**, the Stokes scattering matrix in the Stokes vector representation $\mathbf{I}_S = [I,Q,U,V]^T$ is given by (Chandrasekhar, 1960; Sommersten et al., 2010)

$$\mathbf{F}_S(\Theta) = \frac{3}{3+f}\begin{bmatrix} 1 + f\cos^2\Theta & -f\sin^2\Theta & 0 & 0 \\ -f\sin^2\Theta & f\left(1+\cos^2\Theta\right) & 0 & 0 \\ 0 & 0 & 2f\cos\Theta & 0 \\ 0 & 0 & 0 & (3f-1)\cos\Theta \end{bmatrix}. \tag{42}$$

For the first scattering event of the scalar RTE, only the (1.1)-element of **Eq. 42** matters, and leads to the scattering phase function given by

$$p_{\text{Ray}}(\Theta) = \frac{3}{3+f}\left(1 + f\cos^2\Theta\right). \tag{43}$$

2.4.2 Stokes Vector Representation $\mathbf{I} = [I_\parallel, I_\perp, U, V]^T$

The Stokes vector $\mathbf{I} = [I_\parallel, I_\perp, U, V]^T$ is related to $\mathbf{I}_S = [I,Q,U,V]^T$ by

$$\mathbf{I}_S = \mathbf{DI} \tag{44}$$

where **D** is given by **Eq. 14**, so that $I = I_\parallel + I_\perp$, and $Q = I_\parallel - I_\perp$. Denoting the Stokes vector obtained after a rotation by

$$\mathbf{I}'_S = \mathbf{R}_S(\omega)\mathbf{I}_S \tag{45}$$

we find

$$\mathbf{I}' = \mathbf{D}^{-1}\mathbf{I}'_S = \mathbf{D}^{-1}\mathbf{R}_S(\omega)\mathbf{I}_S = \mathbf{D}^{-1}\mathbf{R}_S(\omega)\mathbf{D}\,\mathbf{I} = \mathbf{R}(\omega)\mathbf{I}. \tag{46}$$

Hence, the rotation matrix for the Stokes vector in the representation $\mathbf{I} = [I_\parallel, I_\perp, U, V]^T$ becomes:

$$\mathbf{R}(\omega) = \mathbf{D}^{-1}\mathbf{R}_S(\omega)\mathbf{D} = \begin{bmatrix} \cos^2\omega & \sin^2\omega & -\frac{1}{2}\sin(2\omega) & 0 \\ \sin^2\omega & \cos^2\omega & \frac{1}{2}\sin(2\omega) & 0 \\ \sin(2\omega) & -\sin(2\omega) & \cos(2\omega) & 0 \\ 0 & 0 & 0 & 1 \end{bmatrix}. \tag{47}$$

The scattering phase matrix $\mathbf{P}(\Theta)$ in the Stokes vector representation $\mathbf{I} = [I_\parallel, I_\perp, U, V]^T$ is related to the scattering phase matrix $\mathbf{P}_S(\Theta)$ in the Stokes vector representation $\mathbf{I}_S = [I,Q,U,V]^T$ by

$$\mathbf{P}(\Theta) = \mathbf{D}^{-1}\mathbf{P}_S(\Theta)\mathbf{D}. \tag{48}$$

Similarly, the Stokes scattering matrix $\mathbf{F}(\Theta)$ associated with the Stokes vector representation $\mathbf{I} = [I_\parallel, I_\perp, U, V]^T$ is related to the Stokes scattering matrix $\mathbf{F}_S(\Theta)$ in **Eq. 20** by

$$\begin{aligned}\mathbf{F}(\Theta) &= \mathbf{D}^{-1}\mathbf{F}_S(\Theta)\mathbf{D} \\ &= \begin{pmatrix} \frac{1}{2}(a_1 + a_2 + 2b_1) & \frac{1}{2}(a_1 - a_2) & 0 & 0 \\ \frac{1}{2}(a_1 - a_2) & \frac{1}{2}(a_1 + a_2 - 2b_1) & 0 & 0 \\ 0 & 0 & a_3 & b_2 \\ 0 & 0 & -b_2 & a_4 \end{pmatrix}.\end{aligned} \tag{49}$$

In the Stokes vector representation $\mathbf{I} = [I_\parallel, I_\perp, U, V]^T$, the Stokes scattering matrix for Rayleigh scattering becomes (using **Eqs. 42** and **49** (Chandrasekhar, 1960)):

$$\mathbf{F}(\Theta) = \frac{3}{2(1+2\zeta)} \begin{pmatrix} \cos^2\Theta + \zeta\sin^2\Theta & \zeta & 0 & 0 \\ \zeta & 1 & 0 & 0 \\ 0 & 0 & (1-\zeta)\cos\Theta & 0 \\ 0 & 0 & 0 & (1-3\zeta)\cos\Theta \end{pmatrix} \tag{50}$$

where $\zeta = \rho/(2-\rho) = \frac{1-f}{1+3f}$.

From **Eq. 50** we see that for an incident beam of natural unpolarized light given by $\mathbf{I}^{\text{inc}} = [I_\parallel^{\text{inc}}, I_\perp^{\text{inc}}, U^{\text{inc}}, V^{\text{inc}}]^T = [\frac{1}{2}I^{\text{inc}}, \frac{1}{2}I^{\text{inc}}, 0, 0]^T$, the scattered intensities in the plane parallel and perpendicular to the scattering plane are obtained by carrying out the multiplication $\mathbf{I}^{\text{sca}} = \mathbf{F}(\Theta)\mathbf{I}^{\text{inc}}$:

$$I_\parallel^{\text{sca}} \propto \frac{3}{4(1+2\zeta)}\left[2\zeta + (1-\zeta)\cos^2\Theta\right]I^{\text{inc}} \tag{51}$$

$$I_\perp^{\text{sca}} \propto \frac{3}{4(1+2\zeta)}\left[(1+\zeta)\right]I^{\text{inc}}. \tag{52}$$

Thus, for unpolarized incident light, the scattered light at right angles ($\Theta = 90°$) to the direction of incidence defines the depolarization ratio:

$$\rho \equiv \left(\frac{I_\parallel^{\text{sca}}}{I_\perp^{\text{sca}}}\right)_{\Theta=90°} = \frac{2\zeta}{1+\zeta} \tag{53}$$

whereas the degree of linear polarization becomes [**Eq. 18**]:

$$\begin{aligned} p_l &= \frac{I_\perp - I_\parallel}{I_\perp + I_\parallel} = \frac{(1-\zeta)(1-\cos^2\Theta)}{1+3\zeta+(1-\zeta)\cos^2\Theta} \to \frac{1-\zeta}{1+3\zeta} = \frac{1-\rho}{1+\rho} \\ &= f \quad \text{as} \quad \Theta \to 90°. \end{aligned} \tag{54}$$

2.4.3 Generalized Spherical Functions–The Greek Constants

For the scalar RTE, only the $a_1(\Theta)$ element of the Stokes scattering matrix **Eq. 20** is relevant, and this element is the scattering phase function given by **Eq. 69** in general, and by **Eq. 43** for Rayleigh scattering. The scattering phase function can be expanded in Legendre polynomials [see **Eq. 69**], which enables expression as a Fourier cosine series.

In a similar manner, the scattering phase matrix can be expanded in generalized spherical functions. In the Stokes vector representation $\mathbf{I}_S = [I,Q,U,V]^T$, the scattering phase matrix is $\mathbf{P}_S(\Theta) = \mathbf{P}_S(u', u; \phi' - \phi)$ with $u = \cos\theta$, θ being the polar angle after scattering, and $u' = \cos\theta'$, θ' being the polar angle prior to scattering. Similarly, ϕ and ϕ' are the azimuth angles after and prior to scattering, respectively. To expand in generalized spherical functions, the scattering phase matrix is first expanded in a $(M+1)$-term Fourier series in the azimuth angle difference ($\Delta\phi' = \phi' - \phi$):

$$\mathbf{P}_S(u', u; \Delta\phi) = \sum_{m=0}^{M}\left\{\mathbf{P}_c^m(u', u)\cos\, m(\Delta\phi') + \mathbf{P}_s^m(u', u)\sin\, m(\Delta\phi')\right\} \tag{55}$$

where $\mathbf{P}_c^m(u', u)$ and $\mathbf{P}_s^m(u', u)$ are the coefficient matrices of the cosine and sine terms, respectively, of the Fourier series.

We use an addition theorem for the generalized spherical functions to express the Fourier expansion coefficient matrices directly in terms of the expansion coefficients of the Stokes scattering matrix $\mathbf{F}_S(\Theta)$ [see **Eq. 20**] as follows (Siewert, 1981; Siewert, 1982; Mishchenko, 1991):

$$\mathbf{P}_c^m(u', u) = \mathbf{A}^m(u', u) + \mathbf{\Delta}_{3,4}\mathbf{A}^m(u', u)\mathbf{\Delta}_{3,4} \tag{56}$$

$$\mathbf{P}_s^m(u', u) = \mathbf{A}^m(u', u)\mathbf{\Delta}_{3,4} - \mathbf{\Delta}_{3,4}\mathbf{A}^m(u', u) \tag{57}$$

where $\mathbf{\Delta}_{3,4}$ = diag (1, 1, −1, 1). The matrix $\mathbf{A}^m(u', u)$ is given by:

$$\mathbf{A}^m(u', u) = \sum_{\ell=m}^{M}\mathbf{P}_\ell^m(u)\mathbf{\Lambda}_\ell\mathbf{P}_\ell^m(u'). \tag{58}$$

The matrix $\mathbf{P}_\ell^m(u)$ is given by:

TABLE 1 | Expansion coefficients for Rayleigh scattering.

ℓ	$\alpha_{1,\ell}$	$\alpha_{2,\ell}$	$\alpha_{3,\ell}$	$\alpha_{4,\ell}$	$\beta_{1,\ell}$	$\beta_{2,\ell}$
0	1	0	0	0	0	0
1	0	0	0	$3d/2$	0	0
2	$c/2$	$3c$	0	0	$\sqrt{3/2}c$	0

$$\mathbf{P}_\ell^m(u) = \begin{pmatrix} P_\ell^{m,0}(u) & 0 & 0 & 0 \\ 0 & P_\ell^{m,+}(u) & P_\ell^{m,-}(u) & 0 \\ 0 & P_\ell^{m,-}(u) & P_\ell^{m,+}(u) & 0 \\ 0 & 0 & 0 & P_\ell^{m,0}(u) \end{pmatrix} \tag{59}$$

where

$$P_\ell^{m,\pm}(u) = \frac{1}{2}\left[P_\ell^{m,-2}(u) \pm P_\ell^{m,2}(u)\right] \tag{60}$$

and the functions $P_\ell^{m,0}(u)$ and $P_\ell^{m,\pm 2}(u)$ are the generalized spherical functions (Hovenier et al., 2004). The matrix $\mathbf{\Lambda}_\ell$ in **Eq. 58** is

$$\mathbf{\Lambda}_\ell = \begin{pmatrix} \alpha_{1,\ell} & \beta_{1,\ell} & 0 & 0 \\ \beta_{1,\ell} & \alpha_{2,\ell} & 0 & 0 \\ 0 & 0 & \alpha_{3,\ell} & \beta_{2,\ell} \\ 0 & 0 & -\beta_{2,\ell} & \alpha_{4,\ell} \end{pmatrix} \tag{61}$$

and

$$a_1(\Theta) = \sum_{\ell=0}^{M} \alpha_{1,\ell} P_\ell^{0,0}(\cos\Theta) \tag{62}$$

$$a_2(\Theta) + a_3(\Theta) = \sum_{\ell=2}^{M} \left(\alpha_{2,\ell} + \alpha_{3,\ell}\right) P_\ell^{2,2}(\cos\Theta) \tag{63}$$

$$a_2(\Theta) - a_3(\Theta) = \sum_{\ell=2}^{M} \left(\alpha_{2,\ell} - \alpha_{3,\ell}\right) P_\ell^{2,-2}(\cos\Theta) \tag{64}$$

$$a_4(\Theta) = \sum_{\ell=0}^{M} \alpha_{4,\ell} P_\ell^{0,0}(\cos\Theta) \tag{65}$$

$$b_1(\Theta) = \sum_{\ell=2}^{M} \beta_{1,\ell} P_\ell^{0,2}(\cos\Theta) \tag{66}$$

$$b_2(\Theta) = \sum_{\ell=2}^{M} \beta_{2,\ell} P_\ell^{0,2}(\cos\Theta). \tag{67}$$

Here the Greek constants $\alpha_{j,\ell}$ and $\beta_{j,\ell}$ are expansion coefficients, and $a_j(\Theta)$ and $b_j(\Theta)$ are the elements of the Stokes scattering matrix $\mathbf{F}_S(\Theta)$ in **Eq. 20**. An example of Greek constants for Rayleigh scattering is provided in **Table 1** (see Mishchenko and Travis (1997)) where

$$c = \frac{2(1-\rho)}{2+\rho} \qquad d = \frac{2(1-2\rho)}{2+\rho} \tag{68}$$

and ρ is the depolarization ratio given by **Eq. 53**.

We note that in the scalar (unpolarized) case all components of the Stokes scattering matrix $\mathbf{F}_S(\Theta)$ [see **Eq. 20**] are zero except for $a_1(\Theta)$, and:

$$a_1(\Theta) = \sum_{\ell=0}^{M} \alpha_{1,\ell}(\tau) P_\ell^{0,0}(\cos\Theta) \equiv p(\tau, \cos\Theta) \approx \sum_{\ell=0}^{M} (2\ell+1)\chi_\ell(\tau) P_\ell(\cos\Theta) \tag{69}$$

since $P_\ell^{0,0}(\cos\Theta) \equiv P_\ell(\cos\Theta)$, where $P_\ell(\cos\Theta)$ is the Legendre polynomial of order ℓ, and $\alpha_{1,\ell}(\tau) \equiv (2\ell+1)\chi_\ell(\tau)$. Here the coefficients $\chi_\ell(\tau)$ are the moments of the phase function expanded in Legendre polynomials. Note also that the expansion coefficients given above [**Eq. 61**] are for the scattering phase matrix $\mathbf{P}_S(\Theta)$, which relates the incident and scattered Stokes vectors in the representation $\mathbf{I}_S = [I,Q,U,V]^T$.

3 SOLUTION OF THE VECTOR RADIATIVE TRANSFER EQUATION

3.1 Isolation of Azimuth Dependence

We start from the scattering phase matrix expanded in a Fourier series (see **Eq. 55**) ($\Delta\phi' = \phi' - \phi$):

$$\mathbf{P}(u', u; \Delta\phi') = \sum_{m=0}^{M} \left\{\mathbf{P}_\mathrm{c}^m(u', u)\cos m\Delta\phi' + \mathbf{P}_\mathrm{s}^m(u', u)\sin m\Delta\phi'\right\}. \tag{70}$$

To isolate the azimuth dependence of the radiation field we expand the Stokes vector $\mathbf{I}(\tau, u, \phi)$ in the VRTE [**Eq. 7**] and the source term $\mathbf{Q}(\tau, u, \phi)$ in **Eq. 9** in a Fourier series in a manner similar to the expansion of the scattering phase matrix in **Eq. 70** ($\Delta\phi_0 = \phi_0 - \phi$):

$$\mathbf{I}(\tau, u, \phi) = \sum_{m=0}^{M} \left\{\mathbf{I}_\mathrm{c}^m(\tau, u)\cos m\Delta\phi_0 + \mathbf{I}_\mathrm{s}^m(\tau, u)\sin m\Delta\phi_0\right\} \tag{71}$$

$$\mathbf{Q}(\tau, u, \phi) = \sum_{m=0}^{M} \left\{\mathbf{Q}_\mathrm{c}^m(\tau, u)\cos m\Delta\phi_0 + \mathbf{Q}_\mathrm{s}^m(\tau, u)\sin m\Delta\phi_0\right\} \tag{72}$$

where the subscript s or c denotes sine or cosine mode. Using these expansions, we obtain the following equations for the Fourier components of the VRTE (see Stamnes and Stamnes (2015) for details)

$$u\frac{d\mathbf{I}_\mathrm{c}^m(\tau, u)}{d\tau} = \mathbf{I}_\mathrm{c}^m(\tau, u) - \frac{\varpi(\tau)}{4}\int_{-1}^{1} du' \left\{\mathbf{P}_\mathrm{c}^m(\tau, u', u)\,\mathbf{I}_\mathrm{c}^m(\tau, u')\,(1+\delta_{0m}) - \mathbf{P}_\mathrm{s}^m(\tau, u', u)\,\mathbf{I}_\mathrm{s}^m(\tau, u')\right\} - \mathbf{Q}_\mathrm{c}^m(\tau, u) \tag{73}$$

$$u\frac{d\mathbf{I}_\mathrm{s}^m(\tau, u)}{d\tau} = \mathbf{I}_\mathrm{s}^m(\tau, u) - \frac{\varpi(\tau)}{4}\int_{-1}^{1} du' \left\{\mathbf{P}_\mathrm{c}^m(\tau, u', u)\,\mathbf{I}_\mathrm{s}^m(\tau, u') + \mathbf{P}_\mathrm{s}^m(\tau, u', u)\,\mathbf{I}_\mathrm{c}^m(\tau, u')\right\} - \mathbf{Q}_\mathrm{s}^m(\tau, u). \tag{74}$$

For scattering by randomly oriented particles, the Fourier coefficient matrix $\mathbf{P}_\mathrm{c}^m(u, u')$ has two (2 × 2) zero submatrices, one in the upper right corner and one in the lower left corner, and the matrix $\mathbf{P}_\mathrm{s}^m(u, u')$ has a (2 × 2) zero submatrix in the upper left corner and one in the lower right corner (Hovenier and van der Mee, 1983). Hence

$$\mathbf{P}_{\mathrm{c}}^{m}(u,u') = \begin{pmatrix} C_{11}^{m} & C_{12}^{m} & 0 & 0 \\ C_{21}^{m} & C_{22}^{m} & 0 & 0 \\ 0 & 0 & C_{33}^{m} & C_{34}^{m} \\ 0 & 0 & C_{43}^{m} & C_{44}^{m} \end{pmatrix}$$

$$\mathbf{P}_{\mathrm{s}}^{m}(u,u') = \begin{pmatrix} 0 & 0 & S_{13}^{m} & S_{14}^{m} \\ 0 & 0 & S_{23}^{m} & S_{24}^{m} \\ S_{31}^{m} & S_{32}^{m} & 0 & 0 \\ S_{41}^{m} & S_{42}^{m} & 0 & 0 \end{pmatrix} \tag{75}$$

where we have defined $\mathbf{P}_{\mathrm{c}}^{m}(u,u')_{i,j} \equiv \mathbf{C}^{m}(u,u')_{i,j}$ and $\mathbf{P}_{\mathrm{s}}^{m}(u,u')_{i,j} \equiv \mathbf{S}^{m}(u,u')_{i,j}$ to simplify the notation. Therefore, the homogeneous VRTE [$Q = 0$ in **Eqs. 73** and **74**] may be rewritten as ($m \in [0, 1, 2, \ldots, 2N]$)

$$u\frac{d\mathbf{I}_{\mathrm{c}}^{m}(\tau,u)}{d\tau} = \mathbf{I}_{\mathrm{c}}^{m}(\tau,u) - \frac{\varpi(\tau)}{4}\int_{-1}^{1}[\mathbf{C}^{m}(u,u')\mathbf{I}_{\mathrm{c}}^{m}(\tau,u') - (1-\delta_{0m})\mathbf{S}^{m}(u,u')\mathbf{I}_{\mathrm{s}}^{m}(\tau,u')]du' \tag{76}$$

$$u\frac{d\mathbf{I}_{\mathrm{s}}^{m}(\tau,u)}{d\tau} = \mathbf{I}_{\mathrm{s}}^{m}(\tau,u) - \frac{\varpi(\tau)}{4}(1-\delta_{0m}) \int_{-1}^{1}[\mathbf{C}^{m}(u,u')\mathbf{I}_{\mathrm{s}}^{m}(\tau,u') + \mathbf{S}^{m}(u,u')\mathbf{I}_{\mathrm{c}}^{m}(\tau,u')]du'. \tag{77}$$

3.1.1 Vector Radiative Transfer Equation for the Combined Mode

We note that the $\mathbf{I}_{\mathrm{c}}^{m}(\tau,u)$ and $\mathbf{I}_{\mathrm{s}}^{m}(\tau,u)$ components in **Eqs. 76** and **77** are still coupled. To produce a pair of independent differential equations, we define combined cosine and sine modes as

$$\tilde{\mathbf{I}}_{\mathrm{c}}^{m}(\tau,u) \equiv \begin{pmatrix} I_{\parallel c}^{m}(\tau,u) \\ I_{\perp c}^{m}(\tau,u) \\ U_{s}^{m}(\tau,u) \\ V_{s}^{m}(\tau,u) \end{pmatrix} \quad \tilde{\mathbf{I}}_{s}^{m}(\tau,u) \equiv \begin{pmatrix} I_{\parallel s}^{m}(\tau,u) \\ I_{\perp s}^{m}(\tau,u) \\ U_{c}^{m}(\tau,u) \\ V_{c}^{m}(\tau,u) \end{pmatrix}. \tag{78}$$

After substantial manipulations, one can show that the *mth* term of the homogeneous VRTE of the combined modes can now be written as ($m \in [0, 1, 2, \ldots, 2N]$):

$$u\frac{d\tilde{\mathbf{I}}_{c}^{m}(\tau,u)}{d\tau} = \tilde{\mathbf{I}}_{c}^{m}(\tau,u) - \frac{\varpi(\tau)}{2}\int_{-1}^{1}\tilde{\mathbf{P}}_{c}^{m}(u,u')\tilde{\mathbf{I}}_{c}^{m}(\tau,u')du' \tag{79}$$

$$u\frac{d\tilde{\mathbf{I}}_{s}^{m}(\tau,u)}{d\tau} = \tilde{\mathbf{I}}_{s}^{m}(\tau,u) - \frac{\varpi(\tau)}{2}\int_{-1}^{1}\tilde{\mathbf{P}}_{s}^{m}(u,u')\mathbf{I}_{s}^{m}(\tau,u')du' \tag{80}$$

where the combined scattering phase matrices are defined as:

$$\tilde{\mathbf{P}}_{c}^{m}(u,u') = \begin{pmatrix} C_{11}^{m} & C_{12}^{m} & -S_{13}^{m} & -S_{14}^{m} \\ C_{21}^{m} & C_{22}^{m} & -S_{23}^{m} & -S_{24}^{m} \\ S_{31}^{m} & S_{32}^{m} & C_{33}^{m} & C_{34}^{m} \\ S_{41}^{m} & S_{42}^{m} & C_{43}^{m} & C_{44}^{m} \end{pmatrix}$$

$$\tilde{\mathbf{P}}_{s}^{m}(u,u') = \begin{pmatrix} C_{11}^{m} & C_{12}^{m} & S_{13}^{m} & S_{14}^{m} \\ C_{21}^{m} & C_{22}^{m} & S_{23}^{m} & S_{24}^{m} \\ -S_{31}^{m} & -S_{32}^{m} & C_{33}^{m} & C_{34}^{m} \\ -S_{41}^{m} & -S_{42}^{m} & C_{43}^{m} & C_{44}^{m} \end{pmatrix}. \tag{81}$$

For the special $m = 0$ case, we have

$$\tilde{\mathbf{P}}_{c}^{0}(u,u') = \begin{pmatrix} C_{11}^{0} & C_{12}^{0} & 0 & 0 \\ C_{21}^{0} & C_{22}^{0} & 0 & 0 \\ 0 & 0 & 0 & 0 \\ 0 & 0 & 0 & 0 \end{pmatrix} \quad \tilde{\mathbf{P}}_{s}^{0}(u,u') = \begin{pmatrix} 0 & 0 & 0 & 0 \\ 0 & 0 & 0 & 0 \\ 0 & 0 & C_{33}^{0} & C_{34}^{0} \\ 0 & 0 & C_{43}^{0} & C_{44}^{0} \end{pmatrix}. \tag{82}$$

Equations 79 and **80** are two independent differential equations to be solved.

3.2 The Discrete Ordinate Method

The discrete ordinate method consists of replacing the integration over u' in **Eqs. 79** and **80** by a discrete sum by introducing the Gaussian quadrature points u_j (the discrete ordinates) and corresponding weights w_j. For each Fourier component one obtains ($i = \pm 1, \pm 2, \ldots, \pm 2N$):

$$u_i\frac{d\tilde{\mathbf{I}}_{\mathrm{c}}^{m}(\tau,u_i)}{d\tau} = \tilde{\mathbf{I}}_{\mathrm{c}}^{m}(\tau,u_i) - \frac{\varpi(\tau)}{2}\sum_{\substack{j=-N\\ j\neq 0}}^{N}\omega_j\tilde{\mathbf{P}}_{\mathrm{c}}^{m}(u_i,u_j)\tilde{\mathbf{I}}_{\mathrm{c}}^{m}(\tau,u_j) \tag{83}$$

$$u_i\frac{d\tilde{\mathbf{I}}_{\mathrm{s}}^{m}(\tau,u_i)}{d\tau} = \tilde{\mathbf{I}}_{\mathrm{s}}^{m}(\tau,u_i) - \frac{\varpi(\tau)}{2}\sum_{\substack{j=-N\\ j\neq 0}}^{N}\omega_j\tilde{\mathbf{P}}_{\mathrm{s}}^{m}(u_i,u_j)\mathbf{I}_{\mathrm{s}}^{m}(\tau,u_j) \tag{84}$$

The convention for the indices of the quadrature points is such that $u_j < 0$ for $j < 0$, and $u_j > 0$ for $j > 0$. These points are distributed symmetrically about zero, i.e., $u_{-j} = -u_j$, and the corresponding weights are equal, i.e. $w_{-j} = w_j$.

The solution of the discrete ordinate approximation to the VRTE **Eqs. 83** and **84** is analogous to that of the scalar RTE. Detailed derivations, including the removal of the notorious ill-conditioning problem, can be found elsewhere (Schulz et al., 1999; Siewert, 2000; Stamnes and Stamnes, 2015), and will not be repeated here.

3.3 Discrete Ordinate Radiative Transfer Upgrades

Below we describe some new important upgrades of VDISORT:

- First, a new algorithm to handle the complex eigenvalue/eigenvector problem is developed and implemented in VDISORT to give an accurate computation of the *V* component of the Stokes vector.
- Second, a reduction of the dimension of the complex eigenvalue problem is developed to reduce the computational burden, and the boundary condition for the complex eigenvalue/vector case is discussed.
- Third, to obtain solutions at arbitrary polar angles, we have developed and implemented an accurate ISF approach that works for both real and complex eigensolutions and an arbitrary bidirectional reflectance distribution matrix is added to compute the polarized reflectance at the lower boundary.

- Fourth, a pseudo-spherical treatment has been implemented to provide important corrections for Earth curvature effects at large (near horizontal) solar zenith and observation polar angles.
- Finally, a single-scattering solution is developed and used to enhance the accuracy and speed for strongly forward-peaked scattering, such as by large water droplets or ice particles.

3.3.1 Complex Eigenvalues/Eigenvectors

The appearance of complex eigenvalues/eigenvectors in the vector radiative transfer problem stems from the asymmetric structure of the Stokes scattering matrix [$\pm b_2(\Theta)$ in **Eq. 20**], or equivalently, from the Greek constant matrix [$\pm \beta_2$ in **Eq. 61**]. In the scalar DISORT model, this 4 × 4 scattering matrix degenerates into the scalar scattering phase function **Eq. 69** and the complex eigenvalue problem does not occur.

3.3.2 The Complex Homogeneous Solution

By seeking exponential solutions to the homogeneous VRTE's, **Eqs. 83** and **84**, one obtains a standard algebraic eigenvalue problem. Writing the VRTE separately for the upward ($u > 0$) and downward ($u < 0$) hemispheres, and defining $\mu = |u|$ and $\alpha = c, s$, the homogeneous version of the Fourier components of the VRTE becomes ($i = 1, 2, \ldots, 2N$):

$$+\mu_i \frac{d\tilde{\mathbf{I}}_\alpha^m(\tau, +\mu_i)}{d\tau} = \tilde{\mathbf{I}}_\alpha^m(\tau, +\mu_i) - \frac{\varpi(\tau)}{2} \sum_{j=1}^{N} w_j \tilde{\mathbf{P}}_\alpha^m(+\mu_i, -\mu_j) \tilde{\mathbf{I}}_\alpha^m(\tau, -\mu_j) - \frac{\varpi(\tau)}{2} \sum_{j=1}^{N} w_j \tilde{\mathbf{P}}_\alpha^m(+\mu_i, +\mu_j) \tilde{\mathbf{I}}_\alpha^m(\tau, +\mu_j) \tag{85}$$

$$-\mu_i \frac{d\tilde{\mathbf{I}}_\alpha^m(\tau, -\mu_i)}{dd\tau} = \tilde{\mathbf{I}}_\alpha^m(\tau, -\mu_i) - \frac{\varpi(\tau)}{2} \sum_{j=1}^{N} w_j \tilde{\mathbf{P}}_\alpha^m(-\mu_i, -\mu_j) \tilde{\mathbf{I}}_\alpha^m(\tau, -\mu_j) - \frac{\varpi(\tau)}{2} \sum_{j=1}^{N} w_j \tilde{\mathbf{P}}_\alpha^m(-\mu_i, +\mu_j) \tilde{\mathbf{I}}_\alpha^m(\tau, +\mu_j). \tag{86}$$

Seeking solutions to **Eqs. 85** and **86** of the form $\tilde{\mathbf{I}}_\alpha^m(\tau, +\mu_i) = \mathbf{g}(\mu_i) \exp(-k\tau)$, we obtain an algebraic eigenvalue problem: $\mathbf{Ag} = k\mathbf{g}$, where the $8N \times 8N$ eigenmatrix $\mathbf{A}$ can be written as (here the *italic* ***I*** is the identity matrix):

$$\begin{pmatrix} \frac{-\varpi(\tau) w_1 \tilde{\mathbf{P}}^m(\mu_1, \mu_1)}{2\mu_1} + \frac{I}{\mu_1} & \cdots & \frac{-\varpi(\tau) w_N \tilde{\mathbf{P}}^m(\mu_1, \mu_N)}{2\mu_1} & \frac{-\varpi(\tau) w_1 \tilde{\mathbf{P}}^m(\mu_1, -\mu_1)}{2\mu_1} & \cdots & \frac{-\varpi(\tau) w_N \tilde{\mathbf{P}}^m(\mu_1, -\mu_N)}{2\mu_1} \\ \vdots & \ddots & \vdots & \vdots & \ddots & \vdots \\ \frac{-\varpi(\tau) w_1 \tilde{\mathbf{P}}^m(\mu_N, \mu_1)}{2\mu_N} & \cdots & \frac{-\varpi(\tau) w_N \tilde{\mathbf{P}}^m(\mu_N, \mu_N)}{2\mu_N} + \frac{I}{\mu_N} & \frac{-\varpi(\tau) w_1 \tilde{\mathbf{P}}^m(\mu_N, -\mu_1)}{2\mu_N} & \cdots & \frac{-\varpi(\tau) w_N \tilde{\mathbf{P}}^m(\mu_N, -\mu_N)}{2\mu_N} \\ \frac{-\varpi(\tau) w_1 \tilde{\mathbf{P}}^m(-\mu_1, \mu_1)}{-2\mu_1} & \cdots & \frac{-\varpi(\tau) w_N \tilde{\mathbf{P}}^m(-\mu_1, \mu_N)}{-2\mu_1} & \frac{-\varpi(\tau) w_1 \tilde{\mathbf{P}}^m(-\mu_1, -\mu_1)}{-2\mu_1} + \frac{I}{-\mu_1} & \cdots & \frac{-\varpi(\tau) w_N \tilde{\mathbf{P}}^m(-\mu_1, -\mu_N)}{-2\mu_1} \\ \vdots & \ddots & \vdots & \vdots & \ddots & \vdots \\ \frac{-\varpi(\tau) w_1 \tilde{\mathbf{P}}^m(-\mu_N, \mu_1)}{-2\mu_N} & \cdots & \frac{-\varpi(\tau) w_N \tilde{\mathbf{P}}^m(-\mu_N, \mu_N)}{-2\mu_N} & \frac{-\varpi(\tau) w_1 \tilde{\mathbf{P}}^m(-\mu_N, -\mu_1)}{-2\mu_N} & \cdots & \frac{-\varpi(\tau) w_N \tilde{\mathbf{P}}^m(-\mu_N, -\mu_N)}{-2\mu_N} + \frac{I}{-\mu_N} \end{pmatrix} \tag{87}$$

In the scalar DISORT case real eigenvalues $\pm k_j$ and eigenvectors $g_{\pm j}$ ($\pm\mu_j$) are obtained, so that the homogeneous solution can be written as a linear combination of the eigensolutions:

$$I_{\text{homogenous}}(\tau, \pm \mu_i) = \sum_{j=1}^{N} C_{-j} g_{-j}(\pm \mu_i) e^{k_j \tau} + \sum_{j=1}^{N} C_j g_j(\pm \mu_i) e^{-k_j \tau}. \tag{88}$$

For the 4 × 4 VDISORT problem the $g_{\pm j}$ ($\pm\mu_i$) eigenvector in the scalar case must be replaced by a 4 × 1 eigenvector $\mathbf{g}_{\pm j}$ ($\pm\mu_i$) for $[I_\parallel, I_\perp, U, V]^T$. Since we have $2N$ quadrature angles $\pm\mu_1, \pm\mu_2, \ldots, \pm\mu_N$, the dimension of the full eigenvector $\mathbf{g}_{\pm j}$ is $8N \times 1$. A matrix with real elements has eigenvalue/eigenvector solutions that either are real or occur in complex conjugate pairs. Therefore, defining k_c, k_c^* as a complex conjugate pair of eigenvalues, $\mathbf{g}_c, \mathbf{g}_c^*$ as a complex conjugate pair of eigenvectors, and $C_{\pm 1}$, $C_{\pm 2}$ as arbitrary coefficients, we may, in analogy with the scalar case with only real solutions, write the complex solution to the homogeneous VRTE as:

$$\mathbf{I}_{\text{homo}}(\tau, \pm \mu_i) = \underbrace{\sum_{j=1}^{N_r} C_j \mathbf{g}_j(\pm \mu_i) e^{-k_j \tau} + \sum_{j=1}^{N_r} C_{-j} \mathbf{g}_{-j}(\pm \mu_i) e^{k_j \tau}}_{\mathbf{I}_{\text{REAL}}} + \underbrace{\sum_{j=1}^{N_i} \left[C_{1j}\, \mathbf{g}_{cj}(\pm \mu_i) e^{-k_{cj}\tau} + C_{2j}\, \mathbf{g}_{cj}^*(\pm \mu_i) e^{-k_{cj}^*\tau}\right] + \sum_{j=1}^{N_i} \left[C_{-1j}\, \mathbf{g}_{-cj}(\pm \mu_i) e^{k_{cj}^*\tau} + C_{-2j}\, \mathbf{g}_{-cj}^*(\pm \mu_i) e^{k_{cj}\tau}\right]}_{\mathbf{I}_{\text{COMPLEX}}} \tag{89}$$

where N_r is the number of real solutions, N_i is the number of complex conjugate pair solutions, and $N = N_r + 2N_i$ is the number of streams in each hemisphere.

The homogeneous solution in **Eq. 89** contains complex numbers that must be converted into real values before solving for the coefficients. Since linear combinations of $\mathbf{g}_{\pm c} e^{\pm k_c \tau}$ and $\mathbf{g}_{\perp c}^{\star} e^{\pm k_c^{\star} \tau}$ are also a solution of **Eqs. 85** and **86**, we can separate the real and imaginary parts. As shown in **Section 8** (**Supplementary Appendix A1**) the complex homogeneous solutions may be converted into the following real solutions:

$$\mathbf{I}_{\text{homo}}(\tau, \pm \mu_i) = \underbrace{\sum_{j=1}^{N_r} C_j \mathbf{g}_j(\pm \mu_i) e^{-k_j \tau} + \sum_{j=1}^{N_r} C_{-j} \mathbf{g}_{-j}(\pm \mu_i) e^{k_j \tau}}_{\mathbf{I}_{\text{REAL}}} + \underbrace{\sum_{j=1}^{N_i} \left[C_{1j}\, \hat{\mathbf{g}}_{1j}(\tau, \pm \mu_i) + C_{2j}\, \hat{\mathbf{g}}_{2j}(\tau, \pm \mu_i)\right] e^{-k_{rj}\tau} + \sum_{j=1}^{N_i} \left[C_{-1j}\, \hat{\mathbf{g}}_{-1j}(\tau, \pm \mu_i) + C_{-2j}\, \hat{\mathbf{g}}_{-2j}(\tau, \pm \mu_i)\right] e^{k_{rj}\tau}.}_{\mathbf{I}_{\text{COMPLEX}}} \tag{90}$$

The new eigenvalue/vector pairs are real numbers, and the coefficients $C_{\pm 1j}$, $C_{\pm 2j}$ will be determined by the top/lower boundary as well as the layer continuity conditions. The beauty of **Eq. 90** is that (after the conversion) it has the same form as that of the scalar homogeneous solution, with all of the differences incorporated in the new (4 × 1) eigenvectors $\hat{\mathbf{g}}_{\pm 1}(\tau, \pm \mu_i)$ and $\hat{\mathbf{g}}_{\pm 2}(\tau, \pm \mu_i)$.

3.3.3 Reduction of the Dimension of the Algebraic Eigenvalue Problem

A reduction of the dimension of the eigenmatrix by a factor of 2 saves a significant amount of computing time. In the scalar DISORT code, this reduction is based on the symmetry $p^m(\mu_i, \mu_j) = p^m(-\mu_i, -\mu_j)$ of the phase function as explained in detail elsewhere (Stamnes K. et al., 2017).

However, in the vector case, the phase matrix $\mathbf{p}_\alpha^m(\mu_i, \mu_j) \neq \mathbf{p}_\alpha^m(-\mu_i, -\mu_j)$, implying that the reduction of dimension can not be applied directly, and that a transformation must be done first as follows:

$$\mathbf{P}_\alpha^m(-\mu, -\mu') = \mathbf{D}\mathbf{P}_\alpha^m(+\mu, +\mu')\mathbf{D} \tag{91}$$

where the matrix $\mathbf{D} = \text{diag}(1, 1, -1, -1)$.

This result just tells us that we need to introduce a new phase matrix $\mathbf{D}\mathbf{P}_\alpha^m(\mu_i, \mu_j)\mathbf{D}$ in the VRTE to restore the special symmetry structure of the eigenmatrix. For the downward VRTE in **Eq. 86**, we multiply it by **D** on both sides, and then add $\mathbf{D} \cdot \mathbf{D} = \boldsymbol{I}$ on the RHS, so that **Eq. 86** becomes:

$$\begin{aligned}-\mu_i\frac{d\tilde{\mathbf{I}}_\alpha^m(\tau, -\mu_j)}{d\tau}\mathbf{D} &= \mathbf{D}\tilde{\mathbf{I}}_\alpha^m(\tau, -\mu_j) - \frac{\varpi(\tau)}{2}\sum_{j=1}^N w_j\mathbf{D}\cdot\tilde{\mathbf{P}}_\alpha^m(-\mu_i, -\mu_j)\mathbf{D}\cdot\mathbf{D}\tilde{\mathbf{I}}_\alpha^m(\tau, -\mu_j)\\ &\quad -\frac{\varpi(\tau)}{2}\sum_{j=1}^N w_j\mathbf{D}\cdot\tilde{\mathbf{P}}_\alpha^m(-\mu_i, +\mu_j)\mathbf{D}\cdot\mathbf{D}\tilde{\mathbf{I}}_\alpha^m(\tau, +\mu_j)\\ &= \mathbf{D}\tilde{\mathbf{I}}_\alpha^m(\tau, -\mu_j) - \frac{\varpi(\tau)}{2}\sum_{j=1}^N w_j\tilde{\mathbf{P}}_\alpha^m(+\mu_i, +\mu_j)\mathbf{D}\tilde{\mathbf{I}}_\alpha^m(\tau, -\mu_j)\\ &\quad -\frac{\varpi(\tau)}{2}\sum_{j=1}^N w_j\tilde{\mathbf{P}}_\alpha^m(+\mu_i, -\mu_j)\mathbf{D}\tilde{\mathbf{I}}_\alpha^m(\tau, +\mu_j).\end{aligned} \tag{92}$$

In **Eq. 85**, we simply just multiply by $\mathbf{D} \cdot \mathbf{D} = \boldsymbol{I}$ in front of the term $\tilde{\mathbf{I}}_\alpha^m(\tau, -\mu_j)$ on the RHS, so that it becomes

$$\begin{aligned}+\mu_i\frac{d\tilde{\mathbf{I}}_\alpha^m(\tau, +\mu_i)}{d\tau} &= \tilde{\mathbf{I}}_\alpha^m(\tau, +\mu_i) - \frac{\varpi(\tau)}{2}\sum_{j=1}^N w_j\tilde{\mathbf{P}}_\alpha^m(+\mu_i, -\mu_j)\mathbf{D}\cdot\mathbf{D}\tilde{\mathbf{I}}_\alpha^m(\tau, -\mu_j)\\ &\quad -\frac{\varpi(\tau)}{2}\sum_{j=1}^N w_j\tilde{\mathbf{P}}_\alpha^m(+\mu_i, +\mu_j)\tilde{\mathbf{I}}_\alpha^m(\tau, +\mu_j).\end{aligned} \tag{93}$$

Now we may rewrite the VRTE with the proper symmetry structure, which is suitable for the reduction of dimension.

$$\begin{aligned}+\mu_i\frac{d\,\tilde{\mathbf{I}}_\alpha^m(\tau, +\mu_i)}{d\tau} &= \tilde{\mathbf{I}}_\alpha^m(\tau, +\mu_i) - \frac{\varpi(\tau)}{2}\sum_{j=1}^N w_j\tilde{\mathbf{P}}_\alpha^m(+\mu_i, -\mu_j)\mathbf{D}\cdot\mathbf{D}\tilde{\mathbf{I}}_\alpha^m(\tau, -\mu_j)\\ &\quad -\frac{\varpi(\tau)}{2}\sum_{j=1}^N w_j\tilde{\mathbf{P}}_\alpha^m(+\mu_i, +\mu_j)\tilde{\mathbf{I}}_\alpha^m(\tau, +\mu_j)\end{aligned} \tag{94}$$

$$\begin{aligned}-\mu_i\frac{d\,\mathbf{D}\tilde{\mathbf{I}}_\alpha^m(\tau, -\mu_j)}{d\tau} &= \mathbf{D}\tilde{\mathbf{I}}_\alpha^m(\tau, -\mu_j) - \frac{\varpi(\tau)}{2}\sum_{j=1}^N w_j\tilde{\mathbf{P}}^m(+\mu_i, +\mu_j)\mathbf{D}\tilde{\mathbf{I}}_\alpha^m(\tau, -\mu_j)\\ &\quad -\frac{\varpi(\tau)}{2}\sum_{j=1}^N w_j\tilde{\mathbf{P}}^m(+\mu_i, -\mu_j)\mathbf{D}\tilde{\mathbf{I}}_\alpha^m(\tau, +\mu_j).\end{aligned} \tag{95}$$

Equations 94 and **95** are identical with **Eqs. 85** and **86** if we make the following connections:

$$\begin{aligned}\tilde{\mathbf{I}}_\alpha^m(\tau, +\mu_i) &\rightarrow \tilde{\mathbf{I}}_\alpha^m(\tau, +\mu_i)\,(\text{unchanged})\\ \tilde{\mathbf{I}}_\alpha^m(\tau, -\mu_j) &\rightarrow \left[\mathbf{D}\tilde{\mathbf{I}}_\alpha^m(\tau, -\mu_j)\right]\\ \tilde{\mathbf{P}}_\alpha^m(+\mu_i, +\mu_j) &\rightarrow \tilde{\mathbf{P}}_\alpha^m(+\mu_i, +\mu_j)\,(\text{unchanged})\\ \tilde{\mathbf{P}}_\alpha^m(+\mu_i, -\mu_j) &\rightarrow \left[\tilde{\mathbf{P}}_\alpha^m(+\mu_i, -\mu_j)\mathbf{D}\right].\end{aligned}$$

To accomplish the reduction of dimension, we define eigenvectors

$$\tilde{\mathbf{g}}_{\alpha,+} = \mathbf{g}_{\alpha,+} = \begin{pmatrix}\mathbf{g}_{\alpha,+1}\\ \vdots\\ \mathbf{g}_{\alpha,+N}\end{pmatrix}(\text{unchanged}) \qquad \tilde{\mathbf{g}}_{\alpha,-} = \begin{pmatrix}\mathbf{D}\mathbf{g}_{\alpha,-1}\\ \vdots\\ \mathbf{D}\mathbf{g}_{\alpha,-N}\end{pmatrix}$$

as well as two $4N \times 4N$ matrices as we did in the scalar case (Lin et al., 2015):

$$\mathbf{E}_\alpha = \begin{pmatrix}\frac{\varpi(\tau)w_1\tilde{\mathbf{P}}_\alpha^m(\mu_1, \mu_1)}{2\mu_1} - \frac{\boldsymbol{I}}{\mu_1} & \cdots & \frac{\varpi(\tau)w_N\tilde{\mathbf{P}}_\alpha^m(\mu_1, \mu_N)}{2\mu_1}\\ \vdots & \ddots & \vdots\\ \frac{\varpi(\tau)w_1\tilde{\mathbf{P}}_\alpha^m(\mu_N, \mu_1)}{2\mu_N} & \cdots & \frac{\varpi(\tau)w_N\tilde{\mathbf{P}}_\alpha^m(\mu_N, \mu_N)}{2\mu_N} - \frac{\boldsymbol{I}}{\mu_N}\end{pmatrix}$$

$$\mathbf{F}_\alpha = \begin{pmatrix}\frac{\varpi(\tau)w_1\tilde{\mathbf{P}}_\alpha^m(\mu_1, -\mu_1)\mathbf{D}}{2\mu_1} & \cdots & \frac{\varpi(\tau)w_N\tilde{\mathbf{P}}_\alpha^m(\mu_1, -\mu_N)\boldsymbol{D}}{2\mu_1}\\ \vdots & \ddots & \vdots\\ \frac{\varpi(\tau)w_1\tilde{\mathbf{P}}_\alpha^m(\mu_N, -\mu_1)\boldsymbol{D}}{2\mu_N} & \cdots & \frac{\varpi(\tau)w_N\tilde{\mathbf{P}}_\alpha^m(\mu_N, -\mu_N)\mathbf{D}}{2\mu_N}\end{pmatrix}$$

to obtain

$$(\mathbf{E}_\alpha + \mathbf{F}_\alpha)(\mathbf{E}_\alpha - \mathbf{F}_\alpha) = k_\alpha^2\left(\tilde{\mathbf{g}}_{\alpha,+} + \tilde{\mathbf{g}}_{\alpha,-}\right). \tag{96}$$

Equation 96 is similar to the one obtained in the scalar case, so we may proceed exactly as in that case (Lin et al., 2015).

3.4 Discrete-Ordinate Approximation of the Vector Source Function

In VDISORT, the source function is a 4 × 1 vector, and the discrete-ordinate approximation of the *mth* Fourier component of the vector source function may be written as

$$\begin{aligned}\mathbf{S}_\alpha^m(\tau, \pm\mu) = {}&\frac{\varpi}{2}\sum_{i=1}^N \omega_i\tilde{\mathbf{P}}_\alpha^m(-\mu_i, \pm\mu)\mathbf{I}_\alpha^m(\tau, -\mu_i)\\ &+ \frac{\varpi}{2}\sum_{i=1}^N \omega_i\tilde{\mathbf{P}}_\alpha^m(+\mu_i, \pm\mu)\mathbf{I}_\alpha^m(\tau, +\mu_i)\\ &+ \mathbf{X}_0^m(\pm\mu)e^{-\tau/\mu_0}\end{aligned} \tag{97}$$

$$\mathbf{X}_0^m(\pm\mu) = (2 - \delta_{0m})\frac{\varpi}{4\pi}\tilde{\mathbf{P}}_\alpha^m(-\mu_0, \pm\mu)\mathbf{S}_\mathbf{b}. \tag{98}$$

In **Eq. 97**, the Stokes vector $\mathbf{I}_\alpha^m(\tau, -\mu_i)$ is given at the quadrature angles where $i = 1, 2, \ldots, 2N$. For the complex eigenvalue/vector case, according to Eq. 168, the general solution can be written as (ignoring the thermal source, which can be treated in a similar manner):

$$\tilde{\mathbf{I}}_{\alpha}^{m}(\tau,\pm\mu_i) = \underbrace{\sum_{j=1}^{N_r} C_j \mathbf{g}_j(\pm\mu_i)e^{-k_j\tau} + \sum_{j=1}^{N_r} C_{-j}\mathbf{g}_{-j}(\pm\mu_i)e^{k_j\tau}}_{\mathbf{I}_{\text{REAL}}} + \underbrace{\mathbf{Z_0}(\pm\mu_i)e^{-\tau/\mu_0}}_{\mathbf{I}_{\text{PARTICULAR}}}$$
$$\underbrace{+ \sum_{j=1}^{N_i}\left[C_{1j}\,\hat{\mathbf{g}}_{1j}(\tau,\pm\mu_i) + C_{2j}\,\hat{\mathbf{g}}_{2j}(\tau,\pm\mu_i)\right]e^{-k_{rj}\tau} + \sum_{j=1}^{N_i}\left[C_{-1j}\,\hat{\mathbf{g}}_{-1j}(\tau,\pm\mu_i) + C_{-2j}\,\hat{\mathbf{g}}_{-2j}(\tau,\pm\mu_i)\right]e^{k_{rj}\tau}}_{\mathbf{I}_{\text{COMPLEX}}} \tag{99}$$

where the first two summation terms on the right hand side are the homogeneous solution for real eigenvalues/vectors, the following term is the particular solution, and the last two summation terms are the homogeneous solution for complex conjugate eigenvalues/vectors. The real vectors $\hat{\mathbf{g}}_{1j}(\tau,\pm\mu_i)$ and $\hat{\mathbf{g}}_{2j}(\tau,\pm\mu_i)$ are defined in Eqs. 163–167.

Substituting **Eq. 99** into the vector source function given by **Eq. 97**, we may write the vector source function [**Eq. 97**] in a compact form similar to the general solutions [**Eq. 99**]:

$$\begin{aligned}\mathbf{S}_{\alpha}^{m}(\tau,\pm\mu) &= \sum_{j=1}^{N_r} C_j\tilde{\mathbf{g}}_j(\pm\mu)e^{-k_j\tau} + \sum_{j=1}^{N_r} C_{-j}\tilde{\mathbf{g}}_{-j}(\pm\mu)e^{k_j\tau} + \tilde{\mathbf{Z}}_0(\pm\mu)e^{-\tau/\mu_0}\\ &+ \sum_{j=1}^{N_i}\left[C_{1j}\,\tilde{\hat{\mathbf{g}}}_{1j}(\tau,\pm\mu) + C_{2j}\,\tilde{\hat{\mathbf{g}}}_{2j}(\tau,\pm\mu)\right]e^{-k_{rj}\tau}\\ &+ \sum_{j=1}^{N_i}\left[C_{-1j}\,\tilde{\hat{\mathbf{g}}}_{-1j}(\tau,\pm\mu) + C_{-2j}\,\tilde{\hat{\mathbf{g}}}_{-2j}(\tau,\pm\mu)\right]e^{k_{rj}\tau}.\end{aligned} \tag{100}$$

In **Eq. 100** the following expressions.

$$\tilde{\mathbf{g}}_{\pm j}(\pm\mu) = \frac{\varpi}{2}\sum_{i=1}^{N_r}\left\{\omega_i\mathbf{P}_{\alpha}^{m}(-\mu_i,\pm\mu)\mathbf{g}_{\pm j}(-\mu_i) + \omega_i\mathbf{P}_{\alpha}^{m}(\mu_i,\pm\mu)\mathbf{g}_{\pm j}(+\mu_i)\right\} \tag{101}$$

$$\tilde{\hat{\mathbf{g}}}_{\pm 1j}(\tau,\pm\mu) = \frac{\varpi}{2}\sum_{i=1}^{N_i}\left\{\omega_i\mathbf{P}_{\alpha}^{m}(-\mu_i,\pm\mu)\hat{\mathbf{g}}_{\pm 1j}(\tau,-\mu_i) + \omega_i\mathbf{P}_{\alpha}^{m}(\mu_i,\pm\mu)\hat{\mathbf{g}}_{\pm 1j}(\tau,\mu_i)\right\} \tag{102}$$

$$\tilde{\hat{\mathbf{g}}}_{\pm 2j}(\tau,\pm\mu) = \frac{\varpi}{2}\sum_{i=1}^{N_i}\left\{\omega_i\mathbf{P}_{\alpha}^{m}(-\mu_i,\pm\mu)\hat{\mathbf{g}}_{\pm 2j}(\tau,-\mu_i) + \omega_i\mathbf{P}_{\alpha}^{m}(\mu_i,\pm\mu)\hat{\mathbf{g}}_{\pm 2j}(\tau,\mu_i)\right\} \tag{103}$$

$$\begin{aligned}\tilde{\mathbf{Z}}_0(\pm\mu) = \frac{\varpi}{2}\sum_{i=1}^{N}\{&\omega_i\mathbf{P}_{\alpha}^{m}(-\mu_i,\pm\mu)\mathbf{Z}_0(-\mu_i)\\ &+\omega_i\mathbf{P}_{\alpha}^{m}(\mu_i,\pm\mu)\mathbf{Z}_0(\mu_i) + \mathbf{X}_0(\pm\mu)\}\end{aligned} \tag{104}$$

are simply convenient analytic interpolation formulas of $\mathbf{g}$, $\hat{\mathbf{g}}_1$, $\hat{\mathbf{g}}_2$, and $\mathbf{Z}_0$. They clearly reveal the interpolatory nature of **Eq. 100** for the vector source function. The fact that they are derived from the basic VRTE to which we seek solutions indicates that these expressions, like the analogous expressions in the scalar case, will be superior to any other interpolation scheme (Stamnes et al., 1988; Schulz and Stamnes, 2000; Lin et al., 2015; Stamnes K. et al., 2017).

3.5 Integration of the Source Function Method–Solutions at User-Desired Polar Angles

The discrete ordinate solutions for the Stokes vector are computed at the quadrature angles as discussed in the previous section. To obtain values at arbitrary angles as desired by the user, an interpolation algorithm has to be implemented. In previous versions of VDISORT, a standard spline interpolation scheme, shown to work well for Rayleigh scattering (Schulz et al., 1999), was used to obtain output at arbitrary polar angles. However, the spline interpolation generally requires a large number of quadrature angles (number of streams), and it may fail when the particles have sharp forward scattering peaks, such as for large cloud droplets or ice crystals, when the Stokes components may change rapidly with polar angle.

A better approach to interpolation is to use the discrete-ordinate solution to derive explicit expressions for the source function that can be integrated analytically. This ISF method is implemented in DISORT (Stamnes et al., 1988; Lin et al., 2015; Stamnes K. et al., 2017) and also in a previous version of VDISORT (Schulz and Stamnes, 2000), but that solution is not valid for the V component of the Stokes vector because the eigenvalues/vectors were assumed to be real. Therefore, the solution must be extended to apply to the general case for which some of the eigenvalues/eigenvectors may be complex. By doing so, we obtain results at arbitrary polar angles for any given number of streams, and we may save computing time by getting accurate results at arbitrary polar angles for a relatively small number of streams. Below we will use the ISF method to derive a new interpolation algorithm that works well also for the complex eigensolutions.

3.5.1 Single-Layer (Homogeneous) Medium

For a slab of thickness $\tau^\star$, we may solve **Eqs. 83 and 84** to obtain.

$$\tilde{\mathbf{I}}_{\alpha}^{m}(\tau,+\mu) = \tilde{\mathbf{I}}_{\alpha}^{m}(\tau^*,+\mu)e^{-(\tau^*-\tau)/\mu} + \int_{\tau}^{\tau^*}\frac{dt}{\mu}\mathbf{S}_{\alpha}^{m}(t,+\mu)e^{-(t-\tau)/\mu} \tag{105}$$

$$\tilde{\mathbf{I}}_{\alpha}^{m}(\tau,-\mu) = \tilde{\mathbf{I}}_{\alpha}^{m}(0,-\mu)e^{-\tau/\mu} + \int_{0}^{\tau}\frac{dt}{\mu}\mathbf{S}_{\alpha}^{m}(t,-\mu)e^{-(\tau-t)/\mu}. \tag{106}$$

Using **Eq. 100** in **Eqs. 105** and **106**, we find that for a slab of thickness $\tau^\star$, the Stokes vectors become

$$\begin{aligned}\tilde{\mathbf{I}}(\tau,+\mu) = {}& \tilde{\mathbf{I}}(\tau^\star,+\mu)e^{-\frac{\tau^\star-\tau}{\mu}} + \sum_{\substack{j=-N_r\\ j\neq 0}}^{N_r} C_j\frac{\tilde{\mathbf{g}}_j(+\mu)}{1+k_j\mu}\left\{e^{-k_j\tau} - e^{-\left[k_j\tau^\star+(\tau^\star-\tau)/\mu\right]}\right\}\\ &+ \sum_{\substack{j=-N_i\\ j\neq 0}}^{N_i}\left\{\mathbf{G}_j(\tau,+\mu)e^{-k_{rj}\tau} - \mathbf{G}_j(\tau^\star,+\mu)e^{-\left[k_{rj}\tau^\star+(\tau^\star-\tau)/\mu\right]}\right\}\\ &+\frac{\tilde{\mathbf{Z}}_0(+\mu)}{1+\mu/\mu_0}\left\{e^{-\tau/\mu_0} - e^{-\left[\tau^\star/\mu_0+(\tau^\star-\tau)/\mu\right]}\right\}\end{aligned} \tag{107}$$

$$
\begin{aligned}
\tilde{\mathbf{I}}(\tau,-\mu) = {} & \tilde{\mathbf{I}}(0,-\mu)e^{-\frac{\tau}{\mu}} + \sum_{\substack{j=-N_r \\ j\neq 0}}^{N_r} C_j \frac{\tilde{\mathbf{g}}_j(-\mu)}{1-k_j\mu}\left\{e^{-k_j\tau} - e^{-\tau/\mu}\right\} \\
& + \sum_{\substack{j=-N_i \\ j\neq 0}}^{N_i} \left\{\mathbf{G}_j(\tau,-\mu)e^{-k_{rj}\tau} - \mathbf{G}_j(0,-\mu)e^{-\tau/\mu}\right\} \\
& + \frac{\tilde{\mathbf{Z}}_0(-\mu)}{1-\mu/\mu_0}\left\{e^{-\tau/\mu_0} - e^{-\tau/\mu}\right\}
\end{aligned} \tag{108}
$$

where

$$
\begin{aligned}
\mathbf{G}_j(\tau,\pm\mu) = {} & \frac{1}{\left(\mu k_{ij}\right)^2 + \left(1 \pm \mu k_{rj}\right)^2} \\
& \times \left\{\left(1 \pm \mu k_{rj}\right)\left[C_{1j}\tilde{\tilde{\mathbf{g}}}_{1j}(\tau,\pm\mu) + C_{2j}\tilde{\tilde{\mathbf{g}}}_{2j}(\tau,\pm\mu)\right]\right. \\
& \left. \pm \mu k_{ij}\left[C_{1j}\tilde{\tilde{\mathbf{g}}}_{2j}(\tau,\pm\mu) - C_{2j}\tilde{\tilde{\mathbf{g}}}_{1j}(\tau,\pm\mu)\right]\right\}.
\end{aligned} \tag{109}
$$

Here we assumed $k_{-j} = -k_j$, $k_{-rj} = -k_{rj}$ and $k_{-ij} = -k_{ij}$ and thus $k_{-cj} = -k_{cj} = -k_{rj} - \mathbf{i}k_{ij}$.

In **Eqs. 107** and **108**, the first term on the RHS is due to beam attenuation of the Stokes vector. The first of the following summation terms stems from the integration of the homogeneous solution with real eigensolutions in the vector source function [**Eq. 100**], whereas the second summation is a new term needed for the complex eigensolutions in the vector source function [**Eq. 100**]. Because $\tilde{\tilde{\mathbf{g}}}_{1j}(\tau,+\mu)$ and $\tilde{\tilde{\mathbf{g}}}_{2j}(\tau,+\mu)$ are functions of $\hat{g}_{1j}(\tau,+\mu)$ and $\hat{g}_{2j}(\tau,+\mu)$ that depend on cos $(k_i\tau)$ and sin $(k_i\tau)$, we used the following equations to handle the integration of the complex eigenvector/vectors:

$$
\int \cos ax\, e^{bx}\, dx = \frac{1}{a^2+b^2}e^{bx}\left(a\sin ax + b\cos ax\right) \tag{110}
$$

$$
\int \sin ax\, e^{bx} dx = \frac{1}{a^2+b^2}e^{bx}\left(b\sin ax - a\cos ax\right). \tag{111}
$$

3.5.2 Multi-Layer (Inhomogenous) Medium

The single-layer case can be extended into a multi-layer medium, for which we need to evaluate the integral by integrating layer-by-layer as follows.

$$
\begin{aligned}
\tilde{\mathbf{I}}_\alpha^m(\tau,+\mu) = {} & \tilde{\mathbf{I}}_\alpha^m(\tau_L,+\mu)e^{-(\tau_L-\tau)/\mu} + \int_\tau^{\tau_p}\frac{dt}{\mu}\mathbf{S}_{\alpha,p}^m(t,+\mu)e^{-(t-\tau)/\mu} \\
& + \sum_{n=p+1}^{L}\int_{\tau_{n-1}}^{\tau_n}\frac{dt}{\mu}\mathbf{S}_{\alpha,n}^m(t,+\mu)e^{-(t-\tau)/\mu}
\end{aligned} \tag{112}
$$

$$
\begin{aligned}
\tilde{\mathbf{I}}_\alpha^m(\tau,-\mu) = {} & \tilde{\mathbf{I}}_\alpha^m(0,-\mu)e^{-\tau/\mu} + \int_{\tau_{p-1}}^{\tau}\frac{dt}{\mu}\mathbf{S}_{\alpha,p}^m(t,-\mu)e^{-(\tau-t)/\mu} \\
& + \sum_{n=1}^{p-1}\int_{\tau_{n-1}}^{\tau_n}\frac{dt}{\mu}\mathbf{S}_{\alpha,n}^m(t,-\mu)e^{-(\tau-t)/\mu}
\end{aligned} \tag{113}
$$

Using **Eq. 100** for $\mathbf{S}_{\alpha,n}^m(t,-\mu)$ in the *nth* layer, **Eqs. 112** and **113** become:

$$
\begin{aligned}
\tilde{\mathbf{I}}_\alpha^m(\tau,+\mu) = {} & \tilde{\mathbf{I}}_\alpha^m(\tau_L,+\mu)e^{-\frac{\tau_L-\tau}{\mu}} \\
& + \sum_{n=p}^{L}\sum_{\substack{j=-N \\ j\neq 0}}^{N} C_{jn}\frac{\tilde{\mathbf{g}}_{jn}(+\mu)}{1+k_{jn}\mu}\left\{e^{-k_{jn}\tau_{n-1}+(\tau_{n-1}-\tau)/\mu} - e^{-\left[k_{jn}\tau_n+(\tau_n-\tau)/\mu\right]}\right\} \\
& + \sum_{n=p}^{L}\sum_{\substack{j=-N \\ j\neq 0}}^{N}\left\{\mathbf{G}_{jn}(\tau_{n-1},+\mu)e^{-k_{rjn}\tau_{n-1}+(\tau_{n-1}-\tau)/\mu} - \mathbf{G}_{jn}(\tau_n,+\mu)e^{-\left[k_{jn}\tau_n+(\tau_n-\tau)/\mu\right]}\right\} \\
& + \sum_{n=p}^{L}\frac{\tilde{\mathbf{Z}}_{0n}(+\mu)}{1+\mu/\mu_0}\left\{e^{-\left[\tau_{n-1}/\mu_0+(\tau_{n-1}-\tau)/\mu\right]} - e^{-\left[\tau_n/\mu_0+(\tau_n-\tau)/\mu\right]}\right\}
\end{aligned} \tag{114}
$$

with τ_{n-1} replaced by τ for $n = p$, and

$$
\begin{aligned}
\tilde{\mathbf{I}}_\alpha^m(\tau,-\mu) = {} & \tilde{\mathbf{I}}_\alpha^m(0,-\mu)e^{-\frac{\tau}{\mu}} \\
& + \sum_{n=1}^{p}\sum_{\substack{j=-N \\ j\neq 0}}^{N} C_{jn}\frac{\tilde{\mathbf{g}}_{jn}(-\mu)}{1-k_{jn}\mu}\left\{e^{-\left[k_{jn}\tau_n+(\tau-\tau_n)/\mu\right]} - e^{-\left[k_{jn}\tau_{n-1}+(\tau-\tau_{n-1})/\mu\right]}\right\} \\
& + \sum_{n=1}^{p}\sum_{\substack{j=-N \\ j\neq 0}}^{N}\left\{\mathbf{G}_{jn}(\tau_n,-\mu)e^{-\left[k_{rjn}\tau_n+(\tau-\tau_n)/\mu\right]} - \mathbf{G}_{jn}(\tau_{n-1},-\mu)e^{-\left[k_{rjn}\tau_{n-1}+(\tau-\tau_{n-1})/\mu\right]}\right\} \\
& + \sum_{n=1}^{p}\frac{\tilde{\mathbf{Z}}_{0n}(-\mu)}{1-\mu/\mu_0}\left\{e^{-\left[\tau_n/\mu_0+(\tau-\tau_n)/\mu\right]} - e^{-\left[\tau_{n-1}/mu_0+(\tau-\tau_{n-1})/\mu\right]}\right\}
\end{aligned} \tag{115}
$$

with τ_n replaced by τ for $n = p$, and where

$$
\begin{aligned}
\mathbf{G}_{jn}(\tau,\pm\mu) = {} & \frac{1}{\left(\mu k_{ijn}\right)^2 + \left(1 \pm \mu k_{rjn}\right)^2} \\
& \times \left\{\left(1 \pm \mu k_{rjn}\right)\left[C_{1jn}\tilde{\tilde{\mathbf{g}}}_{1jn}(\tau,\pm\mu) + C_{2jn}\tilde{\tilde{\mathbf{g}}}_{2jn}(\tau,\pm\mu)\right]\right. \\
& \left. \pm \mu k_{ijn}\left[C_{1jn}\tilde{\tilde{\mathbf{g}}}_{2jn}(\tau,\pm\mu) - C_{2jn}\tilde{\tilde{\mathbf{g}}}_{1jn}(\tau,\pm\mu)\right]\right\}.
\end{aligned} \tag{116}
$$

It can be verified that for a single layer $\tau_{n-1} = \tau$, $\tau_n = \tau_L = \tau^*$ in **Eq. 114**; $\tau_n = \tau$, $\tau_{n-1} = 0$ in **Eq. 115**, they are reduced to **Eqs. 107** and **108**, as they should.

3.5.3 Numerical Example

Many practical problems including remote sensing applications require Stokes vector components at sensor observing angles. Even though one could envision generating results at sensor observing angles by interpolating or extrapolating the quadrature values to such angles, accurate interpolation of these values is difficult, particularly for optical depths close to zero (upper boundary) and for extrapolation to angles close to $\mu = 0$ and $\mu = 1.0$. For example, **Figure 2** shows an example of inaccurate spline interpolation for a benchmark case (Garcia and Siewert, 1989) that has been reproduced by VDISORT.We note that the spline interpolation produces large oscillations, whereas the ISF method, see **Eqs. 105** and **106** yields accurate analytic results that agree with the benchmark values at the quadrature angles.

We emphasize that the ISF method allows one to compute analytically the radiation field at arbitrary angles and optical depths from the discrete ordinate solutions, both for the scalar radiative transfer problem (Lin et al., 2015; Stamnes K. et al., 2017) and, as shown here, for the vector problem including the complete Stokes vector $\mathbf{I}_S = [I, Q, U, V]^T$. This capability is one of the unique advantages of the discrete ordinate method. Also, the ISF solutions satisfy the boundary and continuity conditions not

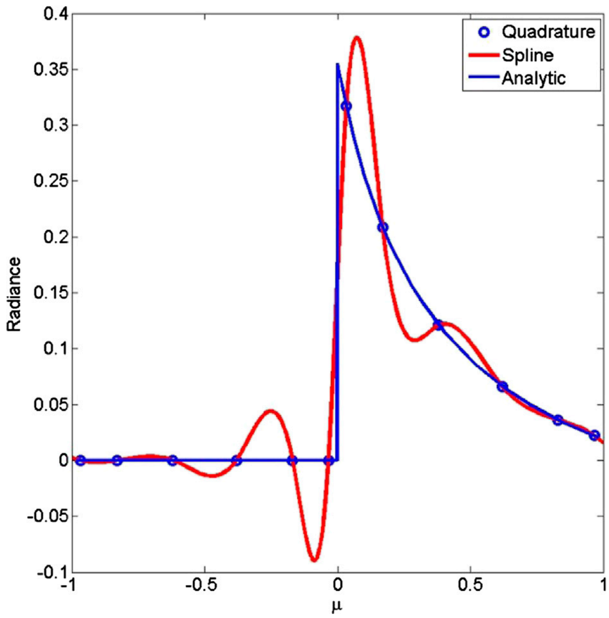

FIGURE 2 | Comparison of output for (i) quadrature angles ($\mu = \cos\theta$, where θ is the polar angle); (ii) spline interpolation; and (iii) analytic results at arbitrary output angles.

only at the discrete set of quadrature angles, but at arbitrary angles μ. In fact, we have found that the ISF method improves the accuracy of the discrete ordinate solution (Schulz and Stamnes, 2000).

3.6 Polarized Reflectance at the Lower Boundary

In **Eq. 99** the homogeneous solution contains unknown constants $C_{\pm j}$, $C_{\pm 1j}$, and $C_{\pm 2j}$, which are to be determined by the boundary conditions at the top and bottom of the medium and continuity conditions at layer interfaces.

3.6.1 Top Boundary

In VDISORT, we assume that the light at the top of the atmosphere is a direct beam such that the diffuse light contribution is zero:

$$\tilde{\mathbf{I}}_{\alpha}^{m}(0,-\mu) = [0,0,0,0]^{T} \tag{117}$$

for $m = 0, \ldots, 2N-1$.

3.6.2 Layer Interfaces

At layer interfaces the Stokes vector must satisfy continuity conditions, because by assumption there is no change in the refractive index between layers. Assuming that $\tau_{n,\mathrm{bottom}}$ is the optical depth at the bottom of the *nth* layer, and that $\tau_{n+1,\mathrm{top}}$ is the optical depth at the top of the $(n+1)^{th}$ layer, we have.

$$\tau_{n,\mathrm{bottom}} = \tau_{n+1,\mathrm{top}} \tag{118}$$

$$\tilde{\mathbf{I}}_{\alpha}^{m}(\tau_{n,\mathrm{bottom}}, \pm\mu) = \tilde{\mathbf{I}}_{\alpha}^{m}(\tau_{n+1,\mathrm{top}}, \pm\mu) \tag{119}$$

where the Stokes vector $\tilde{\mathbf{I}}_{\alpha}(\tau, \pm\mu)$ is given by the sum of homogeneous and particular solutions in **Eq. 99**.The continuity conditions are applied layer by layer for $n = 1, \ldots, L-1$. One important difference from the scalar DISORT model is that the new real eigenvectors associated with the complex solutions depend on the optical depth τ in each layer [**Eq. 90**]. Therefore, for *jth* eigenvector in the *nth* layer, we have.

$$\hat{\mathbf{g}}_{1j}(\tau_{n,\mathrm{top}}, \pm\mu_i) \neq \hat{\mathbf{g}}_{1j}(\tau_{n,\mathrm{bottom}}, \pm\mu_i) \tag{120}$$

$$\hat{\mathbf{g}}_{2j}(\tau_{n,\mathrm{top}}, \pm\mu_i) \neq \hat{\mathbf{g}}_{2j}(\tau_{n,\mathrm{bottom}}, \pm\mu_i). \tag{121}$$

3.6.3 Lower Boundary

For the RTE, the lower boundary is determined by the bidirectional reflectance distribution function/matrix (BRDF). We introduce the matrix or polarized BRDF as the 4 × 4 reflection matrix **R** by writing:

$$\begin{aligned}\mathbf{I}(\mu,\phi,\tau_L) = &\int_0^{2\pi} d\phi' \int_0^1 d\mu' \mathbf{R}(-\mu',\mu,\phi-\phi')\mathbf{I}(-\mu',\phi',\tau_L)\\ &+\mathbf{R}(-\mu_0,\mu,\phi-\phi_0)\mathbf{S}_{\mathbf{b}}e^{-\tau_L/\mu_0}.\end{aligned} \tag{122}$$

The reflection matrix $\mathbf{R}(-\mu',\mu,\phi-\phi')$ is then expanded in a Fourier series:

$$\begin{aligned}\mathbf{R}(-\mu',\mu,\phi-\phi') = &\sum_{m=1}^{L} \mathbf{R}_c^m(-\mu',\mu)\cos m(\phi-\phi')\\ &+\sum_{m=1}^{L} \mathbf{R}_s^m(-\mu',\mu)\sin m(\phi-\phi').\end{aligned} \tag{123}$$

The Fourier mode $\tilde{\mathbf{I}}_{\alpha}^{m}(\tau_L,\mu)$ of the Stokes vector at the polar angle μ just above the lower boundary can then be expressed in terms of $\tilde{\mathbf{R}}(\mu,\mu')$ by (detailed derivation omitted for brevity):

$$\begin{aligned}\tilde{\mathbf{I}}_{\alpha}^{m}(\tau_L,\mu) = &\tilde{\mathbf{R}}_{\alpha,\mathrm{beam}}^{m}(-\mu_0,\mu)\mathbf{S}_{\mathbf{b}}e^{-\tau_L/\mu_0}\\ &+\pi\sum_{j=1}^{N}\omega_j\tilde{\mathbf{R}}_{\alpha}^{m}(-\mu_j,\mu)\tilde{\mathbf{I}}_{\alpha}^{m}(\tau_L,-\mu_j)\end{aligned} \tag{124}$$

where.

$$\tilde{\mathbf{R}}_{c,\mathrm{beam}}^{m}(-\mu_0,\mu) = \begin{pmatrix} R_{c11}^{m} & R_{c12}^{m} & 0 & 0\\ R_{c21}^{m} & R_{c22}^{m} & 0 & 0\\ R_{s31}^{m} & R_{s32}^{m} & 0 & 0\\ R_{s41}^{m} & R_{s42}^{m} & 0 & 0 \end{pmatrix} \tag{125}$$

$$\tilde{\mathbf{R}}_{s,\mathrm{beam}}^{m}(-\mu_0,\mu) = \begin{pmatrix} 0 & 0 & R_{s11}^{m} & R_{s12}^{m}\\ 0 & 0 & R_{s21}^{m} & R_{s22}^{m}\\ 0 & 0 & R_{c31}^{m} & R_{c32}^{m}\\ 0 & 0 & R_{c41}^{m} & R_{c42}^{m} \end{pmatrix} \tag{126}$$

$$\tilde{\mathbf{R}}_{c}^{m}(-\mu_j,\mu) = \begin{pmatrix} \Delta_{0m}^{+}R_{c11} & \Delta_{0m}^{+}R_{c12} & -\Delta_{0m}^{-}R_{s13} & -\Delta_{0m}^{-}R_{s14}\\ \Delta_{0m}^{+}R_{c21} & \Delta_{0m}^{+}R_{c22} & -\Delta_{0m}^{-}R_{s23} & -\Delta_{0m}^{-}R_{s24}\\ \Delta_{0m}^{-}R_{s31} & \Delta_{0m}^{-}R_{s32} & \Delta_{0m}^{-}R_{c33} & \Delta_{0m}^{-}R_{c34}\\ \Delta_{0m}^{-}R_{s41} & \Delta_{0m}^{-}R_{s42} & \Delta_{0m}^{-}R_{c43} & \Delta_{0m}^{-}R_{c44} \end{pmatrix} \tag{127}$$

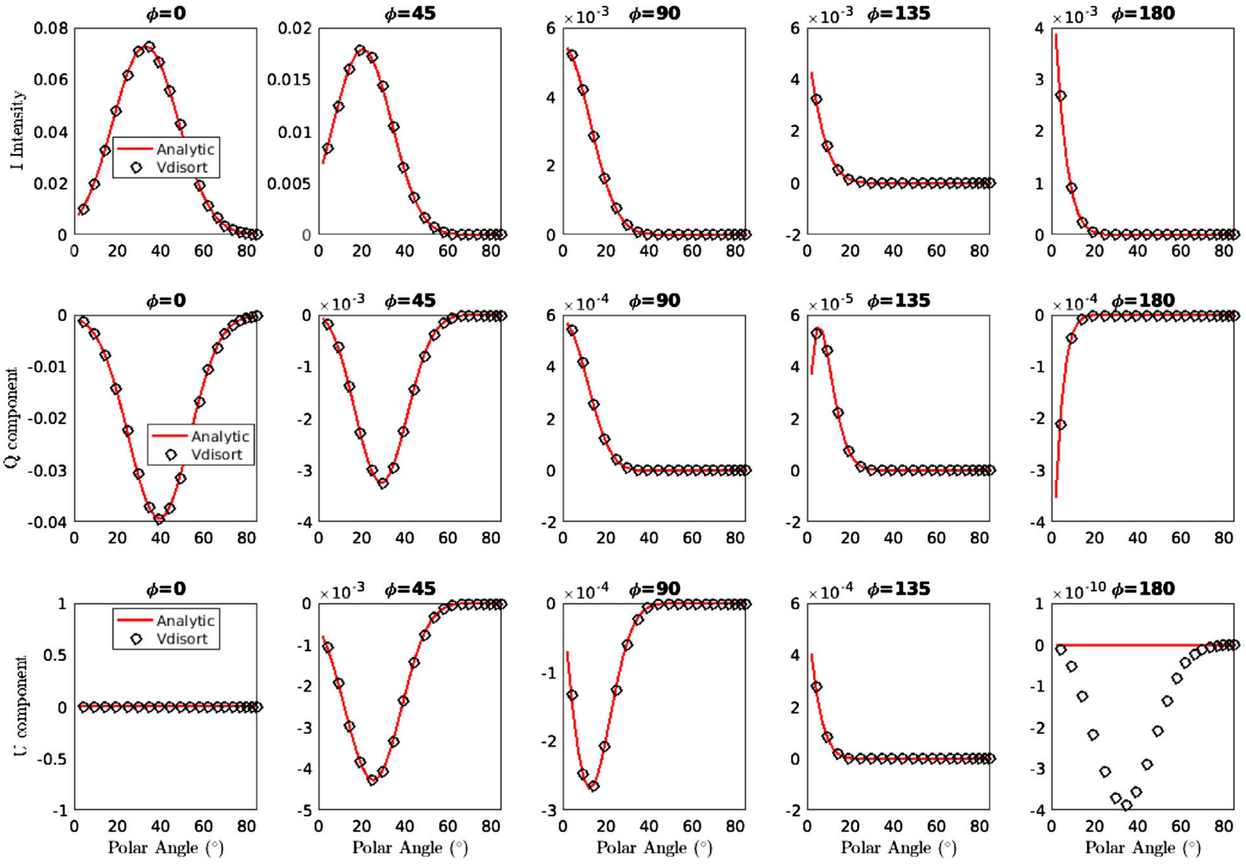

FIGURE 3 | Upper panel: The upward reflection of Stokes parameter *I* (μ, τ_L, ϕ) just above the lower boundary for a 1-D Gaussian surface with a 'Cox-Munk' slope variance distribution for a wind speed of 5 m/s. Middle panel: Same as upper panel except for the Stokes parameter *Q* (μ, τ_L, ϕ). Lower panel: Same as upper panel except for the Stokes parameter *U* (μ, τ_L, ϕ).

$$\tilde{\mathbf{R}}_s^m\left(-\mu_j,\mu\right)=\begin{pmatrix} \Delta^-_{0m}R_{c11} & \Delta^-_{0m}R_{c12} & \Delta^-_{0m}R_{s13} & \Delta^-_{0m}R_{s14} \\ \Delta^-_{0m}R_{c21} & \Delta^-_{0m}R_{c22} & \Delta^-_{0m}R_{s23} & \Delta^-_{0m}R_{s24} \\ -\Delta^-_{0m}R_{s31} & -\Delta^-_{0m}R_{s32} & \Delta^+_{0m}R_{c33} & \Delta^+_{0m}R_{c34} \\ -\Delta^-_{0m}R_{s41} & -\Delta^-_{0m}R_{s42} & \Delta^+_{0m}R_{c43} & \Delta^+_{0m}R_{c44} \end{pmatrix} \quad (128)$$

where $\Delta^{\pm}_{0m}\equiv 1\pm\delta_{0m}$.

In VDISORT, the implementation of the polarized BRDF has been tested by assuming a vacuum layer above a rough ocean surface (Tsang et al., 1985) and by matching the values of the Stokes vector just above the surface (in the upward direction) with analytic values of the BRDF computed without the Fourier expansion. **Figure 3** shows an example of a comparison between VDISORT upward reflected Stokes parameters and analytic Cox-Munk BRDF results for a 1-D Gaussian surface with a wind speed of 5 m/s. The *V* component vanishes because the reflection from an unpolarized direct beam does not produce circular polarization. The results show that VDISORT reproduced the analytic results except for backscattering (ϕ = 180°) of the *U* component where the value of zero is given as numerical noise (~ 10^{-10}) by VDISORT.

4 THE 4 × 4 SOLUTION VERSUS THE 3 × 3 APPROXIMATION

In the discrete ordinate method of radiative transfer, we need to determine homogenous and particular solutions to arrive at the general solution. The particular solution is formulated as a set of linear equations $\mathbf{Ax}=\mathbf{b}$ that can quickly be solved using standard techniques of linear algebra, for example Gaussian elimination. The most time-consuming step is solving the homogenous problem, which is formulated as a standard algebraic eigenvalue problem $(\mathbf{A}-\lambda)\mathbf{x}=\mathbf{0}$. In the case of the 4 × 4 solution, this eigenvalue problem involves matrices of size $4N\times 4N$, where N is the number of quadrature points or "streams" in the upper and lower hemispheres, since a reduction of dimension step (**Section 3.3.3**) is used to reduce the matrix dimension from $8N\times 8N$–$4N\times 4N$. This step is completely analogous to that used in DISORT (Stamnes et al., 1988) to reduce a matrix of dimension $2N\times 2N$ to $N\times N$. Since the presence of the sign on b_2 in **Eq. 20** leads to a matrix **A** in the algebraic eigenvalue problem that cannot be made symmetric, the eigenvalues and corresponding eigenvectors in the 4 × 4

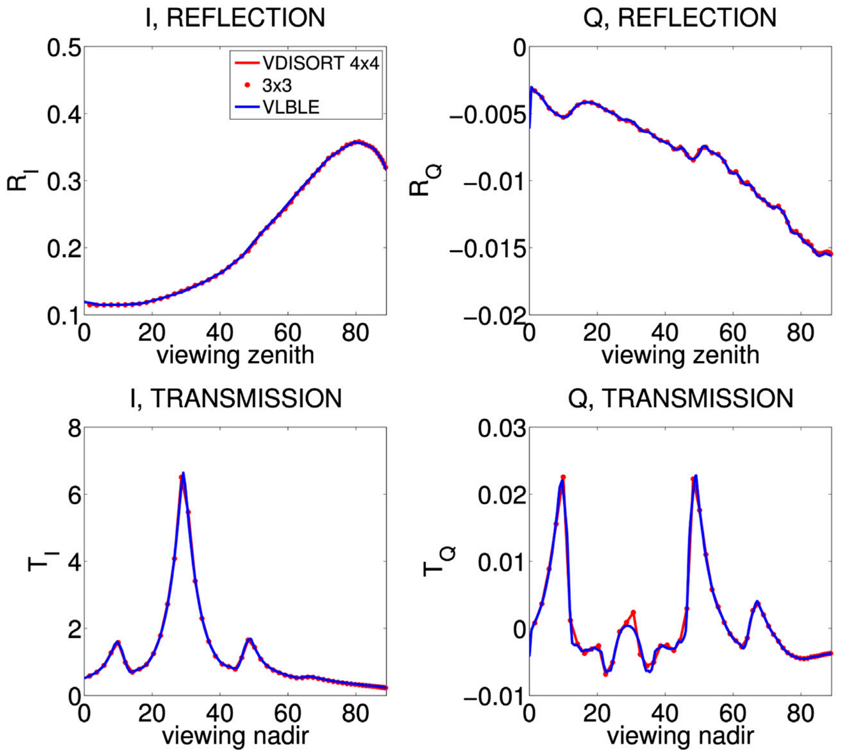

FIGURE 4 | Top panels: reflected *I* and *Q* components at polar angles θ_R; bottom panels: transmitted *I* and *Q* components at polar angles θ_T. The incident Stokes vector is $\mathbf{I}_S$ =[1,0,0,0]. The actual reflection and transmission for *I* and *Q* are scaled by a factor $\frac{\pi}{\mu_0 F_0}$ where F_0=1 and μ_0 is the cosine of the solar zenith angle θ_0. NSTR = 120. The input parameters (phase matrix) for this ice (cirrus) cloud consisting on non-spherical ice crystals are described elsewhere (Stamnes S. et al., 2017).

representation occur in complex conjugate pairs. In the 3 × 3 approximation, the 4th row and column in **Eq. 20** are simply omitted, and the resulting impact on the scattering phase matrix is obtained by setting $b_2 = 0$ in **Eq. 24** which results in **Eq. 41**. Then the matrix **A** is symmetric implying that the resulting eigenvalues and eigenvectors are real. Note that setting $b_2 = 0$ in the 4 × 4 representation leads to *I*, *Q*, and *U* parameters identical to those obtained in the 3 × 3 approximation.

Since setting $b_2 = 0$ decouples the *V* component from *I*, *Q*, and *U*, the eigenvalue problem required to solve the homogeneous system in *N* discrete ordinates is reduced from solving a $4N \times 4N$ system to solving a $3N \times 3N$ system. The computational burden of solving an eigenvalue problem scales like n^3 where *n* is the dimension of the matrix. Therefore, the 3 × 3 approximation reduces the computational burden by a theoretical factor of $4^3/3^3 \approx 2.37$. Since the resulting eigenvectors and eigenvalues for the $3N \times 3N$ system are real, significant further computational savings are obtained by using an eigensolver, such as ASYMTX available in the DISORT package (Stamnes et al., 1988) that avoids unnecessary complex arithmetic. In the 4 × 4 case some of the eigenvectors and eigenvalues occur in complex conjugate pairs implying that complex arithmetic must be considered to obtain accurate solutions when $b_2 \neq 0$.

A comparison of results produced by VDISORT and by a doubling-adding method (VLBLE) is provided in **Figure 4** (Stamnes S. et al., 2017), where the reflected components are plotted against the polar angle θ_R, where $\theta_R = 0^\circ$ is the zenith direction, and $\theta_R = 90^\circ$ is the horizon. The transmitted components are plotted against the polar angle θ_T, where $\theta_T = 0^\circ$ is the nadir direction, and $\theta_T = 90^\circ$ is the horizon. We note that the results for *I* and *Q* produced by the 3 × 3 approximation are essentially identical to the more computationally demanding 4 × 4 results.

The results shown in **Figure 4** pertain to a cirrus cloud consisting of non-spherical ice crystals. The adequacy of the 3 × 3 approximation was investigated for spherical particles by Hansen (1971) who concluded that it is usually adequate to work with 3 × 3 matrices to compute multiple-scattering polarization properties. Hansen (1971) investigated errors only of the reflected radiance and the degree of polarization; errors for the individual Stokes components *Q* and *U*, and transmittances were not considered. The results shown in **Figure 4** suggest that the 3 × 3 approximation holds not only for water clouds, but also for non-spherical ice crystals, and that it applies not just to the reflected radiation, but also to the transmitted radiation and to the Stokes parameters *Q* and *U* (not shown) (Stamnes S. et al., 2017).

5 SINGLE-SCATTERING SOLUTION

Introducing the half-range Stokes vectors (the $^\pm$ signs denote the upper ($^+$) and the lower ($^-$) hemispheres, respectively).

$$\mathbf{I}^+(\tau,\theta,\phi) \equiv \mathbf{I}^+(\tau,\theta \le \pi/2,\phi) = \mathbf{I}^+(\tau,\mu,\phi) \tag{129}$$

$$\mathbf{I}^-(\tau,\theta,\phi) \equiv \mathbf{I}^-(\tau,\theta > \pi/2,\phi) = \mathbf{I}^-(\tau,\mu,\phi) \tag{130}$$

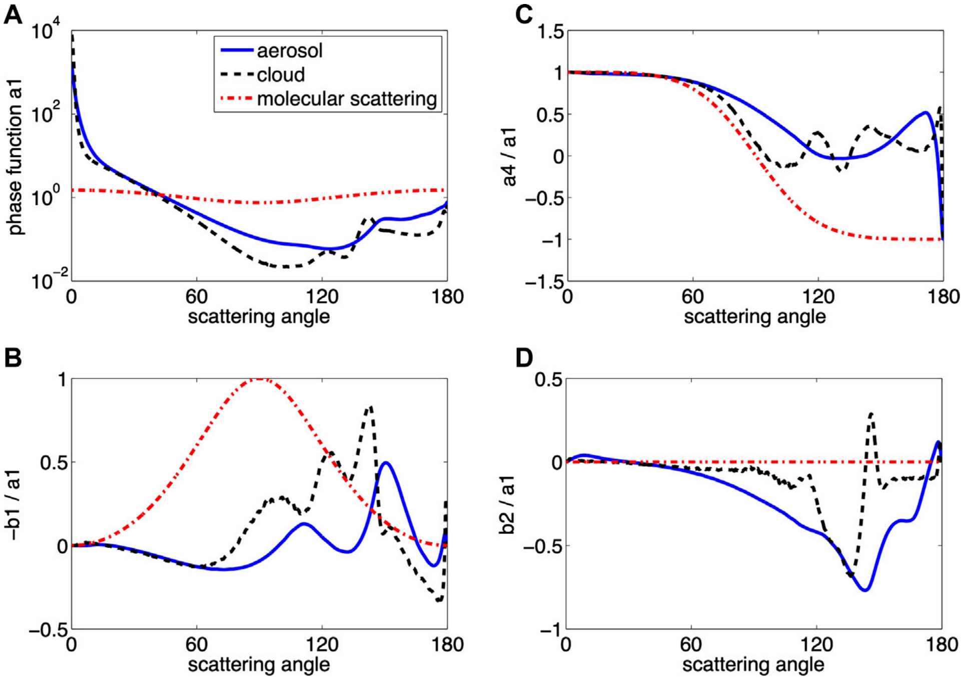

FIGURE 5 | (A) Normalized phase function a_1; **(B)** – b_1/a_1; **(C)** a_4/a_1; **(D)** b_2/a_1 (Kokhanovsky et al., 2010).

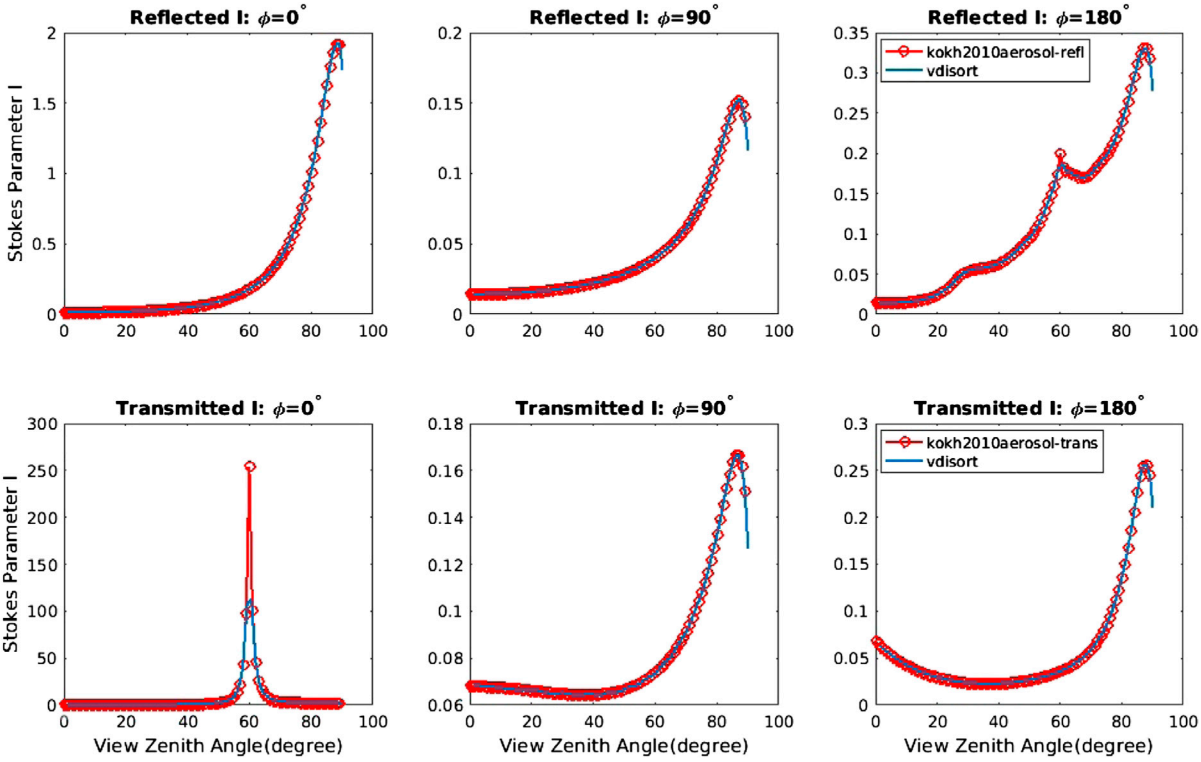

FIGURE 6 | The Stokes parameter I (τ, μ, ϕ) for the aerosol scattering case for reflected (top) and transmitted (bottom) light. Number of discrete ordinate streams, NSTR = 148.

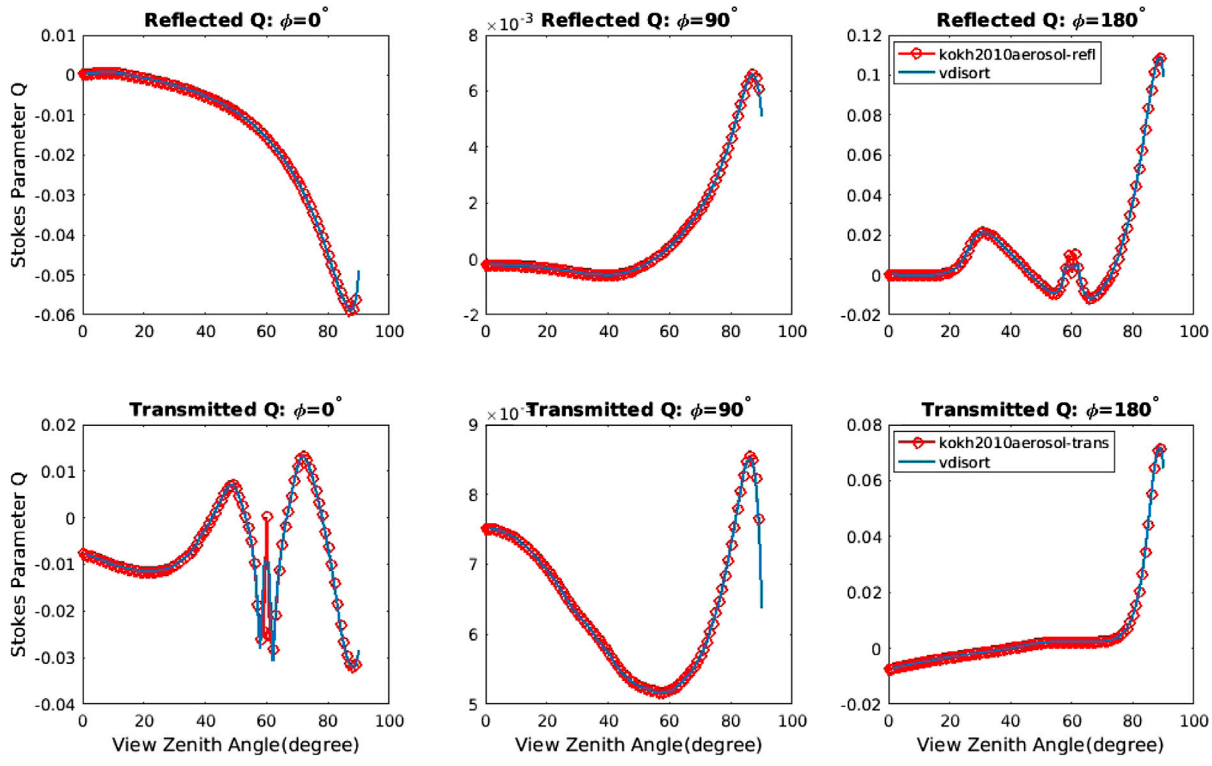

FIGURE 7 | The Stokes parameter Q (τ, μ, ϕ) for the aerosol scattering case for reflected (top) and transmitted (bottom) light. NSTR = 148.

and similar definitions for $\mathbf{S}^{\pm}(\tau, \mu, \phi)$, **Eq. 7** may be re-written as ($\mu \equiv |u|$).

$$\mu \frac{d\mathbf{I}^{+}(\tau,\mu,\phi)}{d\tau} = \mathbf{I}^{+}(\tau,\mu,\phi) - \mathbf{S}^{+}(\tau,\mu,\phi) \tag{131}$$

$$-\mu \frac{d\mathbf{I}^{-}(\tau,\mu,\phi)}{d\tau} = \mathbf{I}^{-}(\tau,\mu,\phi) - \mathbf{S}^{-}(\tau,\mu,\phi). \tag{132}$$

5.1 Single-Layer (Homogeneous) Medium

For a homogeneous slab, we adopt the following notation:

1) τ_0 is the optical depth at the upper boundary (top of the slab);
2) τ_b is the optical depth at the lower boundary (bottom of the slab).

Integrating **Eq. 131** from τ_b to τ and **Eq. 132** from τ_0 to τ ($\tau_0 \le \tau \le \tau_b$), and solving for $\mathbf{I}^{\pm}(\tau, \mu, \phi)$ we obtain.

$$\mathbf{I}^{+}(\tau,\mu,\phi) = \mathbf{I}^{+}(\tau_b,\mu,\phi)e^{-(\tau_b-\tau)/\mu} + \int_{\tau}^{\tau_b} \frac{dt}{\mu}\mathbf{S}^{+}(t,\mu,\phi)e^{-\frac{(t-\tau)}{\mu}} \tag{133}$$

$$\mathbf{I}^{-}(\tau,\mu,\phi) = \mathbf{I}^{-}(\tau_0,\mu,\phi)e^{-(\tau-\tau_0)/\mu} + \int_{\tau_0}^{\tau} \frac{dt}{\mu}\mathbf{S}^{-}(t,\mu,\phi)e^{-\frac{(\tau-t)}{\mu}}. \tag{134}$$

Equations 133 and **134** show that if the source functions $\mathbf{S}^{\pm}(t, \mu, \phi)$ are known, we can obtain a solution to the radiative transfer problem by integration (numerically or analytically).

In the single-scattering approximation, we omit the multiple-scattering term in **Eq. 8**, so that the source function $\mathbf{S}^{\pm}(\tau, \mu, \phi)$ in **Eq. 9** simply becomes:

$$\mathbf{S}^{\pm}(\tau,\mu,\phi) \equiv \mathbf{Q}^{\pm}(\tau,\mu,\phi) = \frac{\varpi(\tau)}{4\pi}\mathbf{P}(\tau,-\mu_0,\phi_0;u,\phi)\mathbf{S}_b e^{-\tau/\mu_0} + [1-\varpi(\tau)]\,\mathbf{S}_t(\tau). \tag{135}$$

The first term on the RHS of **Eq. 135** is proportional to the incident beam $\mathbf{S}_b$ which for an unpolarized incident beam is given by **Eq. 10**, while the second term is due to thermal emission, which is unpolarized, and $\mathbf{S}_t(\tau)$ and is given by **Eq. 11**.

5.2 Multi-Layer (Inhomogeneous) Medium

The vertical variation of the inherent optical properties (IOPs) in a slab may be dealt with by dividing it into a number of adjacent, horizontal layers in which the IOPs are taken to be constant within each layer, but allowed to vary from layer to layer. The number of layers should be large enough to resolve the vertical variation in the IOPs. In such a multi-layered medium, consisting of a total of L layers, we may evaluate the integrals in **Eqs. 133** and **134** by integrating layer by layer as follows ($\tau_{p-1} \le \tau \le \tau_p$ and $\mu > 0$, $\tau_b = \tau_L$, $\tau_0 = 0$) ignoring the boundary terms (setting $\mathbf{I}^{+}(\tau_b, \mu, \phi) = 0$ and $\mathbf{I}^{-}(\tau_0, \mu, \phi) = 0$):

$$\mathbf{I}^{+}(\tau,\mu,\phi) = \int_{\tau}^{\tau_p} \frac{dt}{\mu}\mathbf{S}_p^{+}(t,\mu,\phi)e^{-(t-\tau)/\mu} + \sum_{n=p+1}^{L} \int_{\tau_{n-1}}^{\tau_n} \frac{dt}{\mu}\mathbf{S}_n^{+}(t,\mu,\phi)e^{-(t-\tau)/\mu} \tag{136}$$

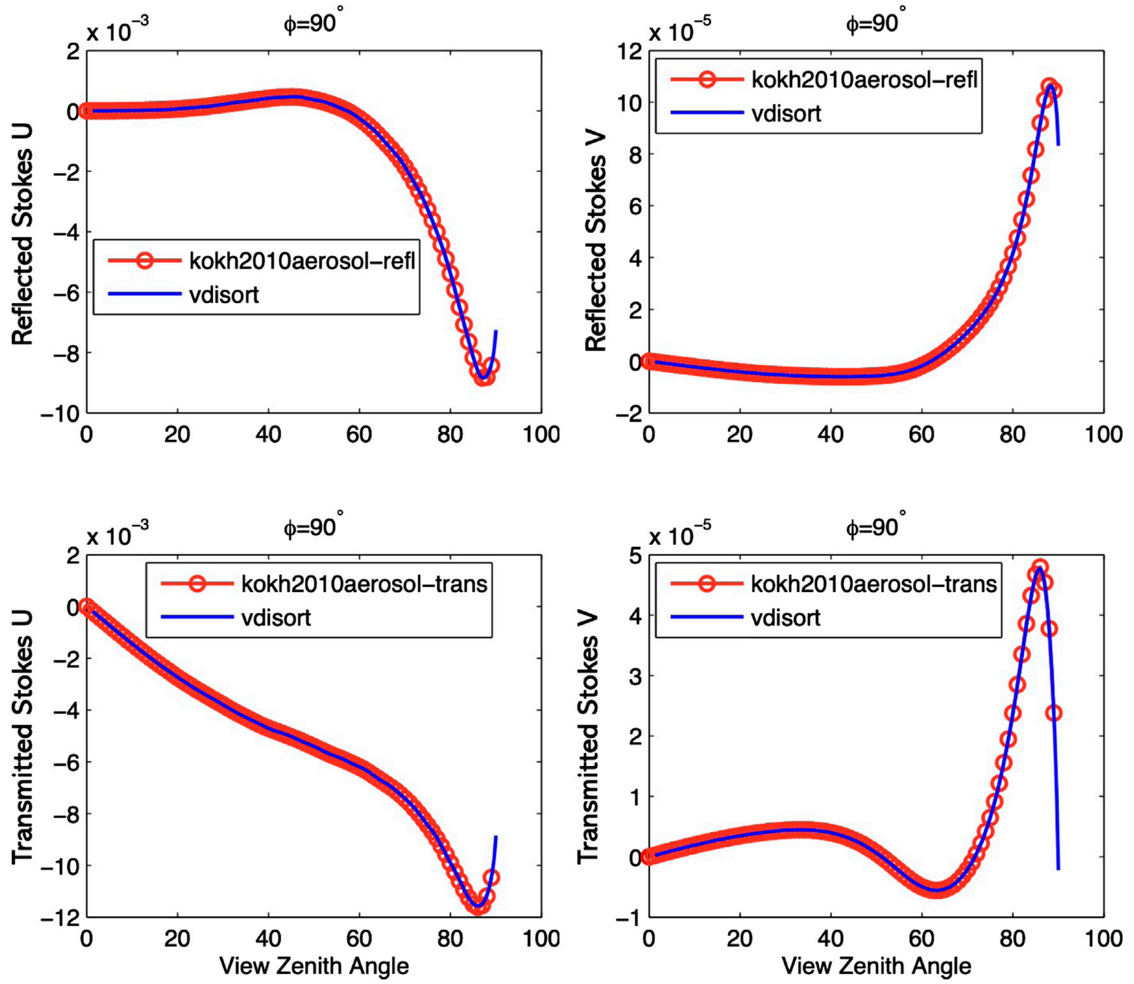

FIGURE 8 | The Stokes parameter *U* (τ, μ, ϕ) (left) and *V* (τ, μ, ϕ) (right) for the aerosol scattering case for reflected (top) and transmitted (bottom) light. The *U* and *V* components vanish for ϕ =0° and ϕ =180°. NSTR = 148.

$$\mathbf{I}^-(\tau,\mu,\phi) = \sum_{n=1}^{p-1}\int_{\tau_{n-1}}^{\tau_n}\frac{dt}{\mu}\mathbf{S}_n^-(t,\mu,\phi)e^{-(\tau-t)/\mu} + \int_{\tau_{p-1}}^{\tau}\frac{dt}{\mu}\mathbf{S}_p^-(t,\mu,\phi)e^{-(\tau-t)/\mu}. \tag{137}$$

We can evaluate the integrals in **Eqs. 136** and **137** either numerically or analytically if the source function $\mathbf{S}_i^{\pm}(t,\mu,\phi)$ in a layer denoted by subscript $i = n$, or p is known. Explicit solutions obtained in the single-scattering approximation are provided in **Section 9** (**Supplementary Appendix A2**).

5.3 Alternative Single Scattering Solution

Another way to understand the one-layer single-scattering solution is to consider the output $I^{\pm}(\tau,\mu,\phi)$ as coming from two sources: 1) the attenuated incident radiation from the layer boundary and in the same direction ($\mu^{\pm}$, ϕ), and 2) the source term contribution from the direct beam scattering. As seen in **Section 5.1** [**Eqs. 133** and **134**], the attenuated boundary contribution is the first term on the right, while the source term is the second term on the right.

Next, we consider the single-scattering solution at layer boundaries τ_n with $n \in [0, 1, 2, \cdots L]$ for a multi-layer medium. Since there is no diffuse radiation at the following two boundaries: 1) TOA (Top-Of-Atmosphere) downward τ_0; 2) BOA (Bottom-Of-Atmosphere) upward τ_L, we have1:

$$\mathbf{I}^-(\tau_0,\mu,\phi) = 0 \tag{138}$$

$$\mathbf{I}^+(\tau_L,\mu,\phi) = 0. \tag{139}$$

Once we have specified the boundary conditions, the one-layer solution can be called consecutively to create the layer boundary radiation of the next layer. Hence, for $n = 1, 2, \ldots, L$, we may recursively compute the downward radiation as:

$$\mathbf{I}^-(\tau_n,\mu,\phi) = \mathbf{I}^-(\tau_{n-1},\mu,\phi)e^{-(\tau_n-\tau_{n-1})/\mu} + \int_{\tau_{n-1}}^{\tau_n}\frac{dt}{\mu}\mathbf{S}_n^-(t,\mu,\phi)e^{-\frac{\tau_n-t}{\mu}}. \tag{140}$$

Similarly, for $n = L, \ldots, 2, 1$, we may recursively compute the upward radiation as:

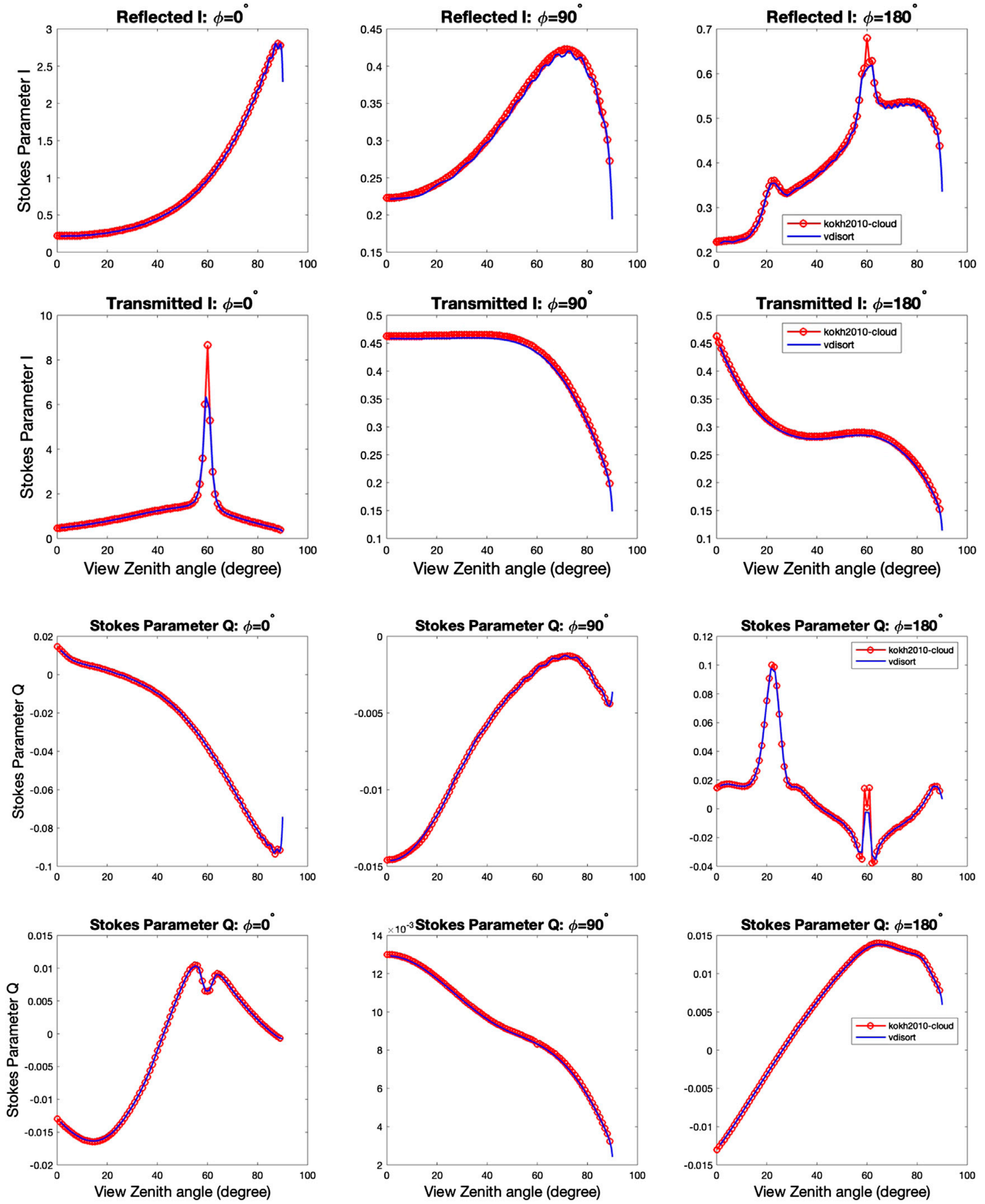

FIGURE 9 | Upper panel: The Stokes parameter $I(\tau, \mu, \phi)$ for the cloud scattering case for reflected (top) and transmitted (bottom) light. NSTR = 148. Lower panel: Same as the upper panel except for the Stokes parameter $Q(\tau, \mu, \phi)$.

$$\mathbf{I}^{+}(\tau_{n-1}, \mu, \phi) = \mathbf{I}^{+}(\tau_n, \mu, \phi) e^{-(\tau_n - \tau_{n-1})/\mu} + \int_{\tau_n}^{\tau_{n-1}} \frac{dt}{\mu} \mathbf{S}_n^{+}(t, \mu, \phi) e^{-\frac{t-\tau_{n-1}}{\mu}}. \tag{141}$$

Having obtained all layer boundary contributions in this manner, we may simply apply the single-layer solution again to get the $\mathbf{I}^{\pm}(\tau, \mu, \phi)$ at arbitrary optical depth τ.

5.4 Single Scattering Correction

The single-scattering correction is a post-processing step that further improves the accuracy of radiance output by correcting the single-scattering term. It was developed by Nakajima and Tanaka Nakajima and Tanaka (1988) and can be used together with several phase matrix truncation methods (Wiscombe, 1977; Hu et al., 2000; Lin et al., 2018).

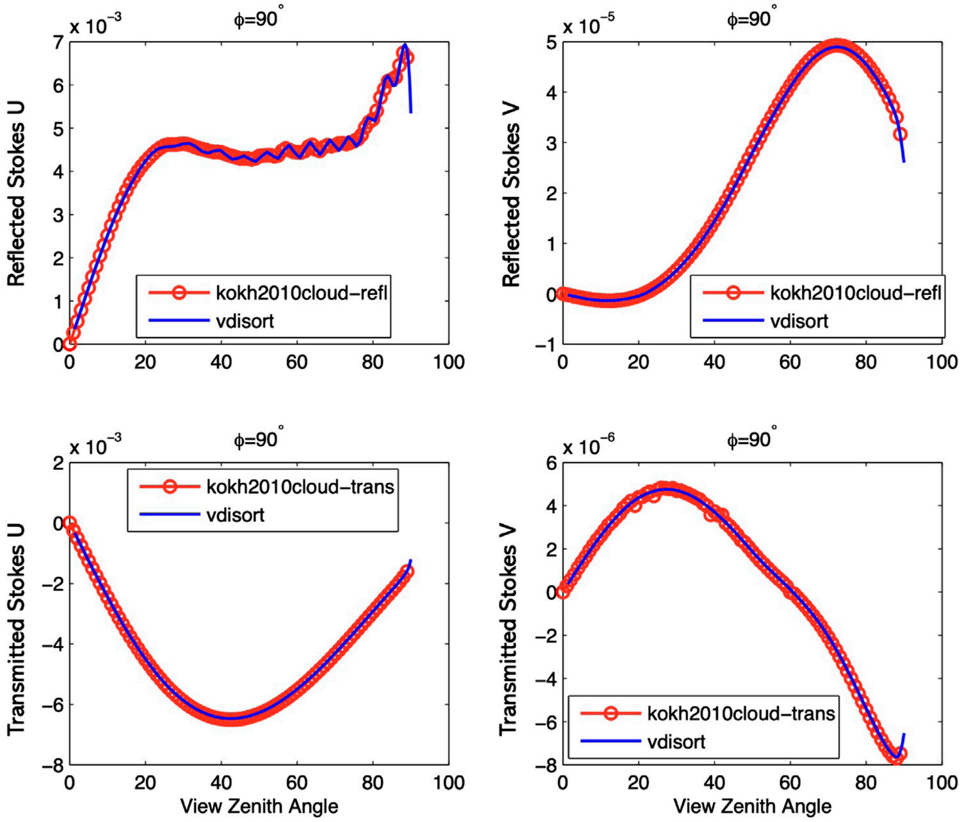

FIGURE 10 | The Stokes parameter $U(\tau, \mu, \phi)$ (left) and $V(\tau, \mu, \phi)$ (right) for the cloud scattering case for reflected (top) and transmitted (bottom) light. The U and V components vanish for $\phi = 0^\circ$ and $\phi = 180^\circ$. NSTR = 148.

In many radiative transfer models, the phase function/matrix is expanded in generalized spherical functions (see **Section 2.4.3**). However, for strongly forward-peaked scattering a large number of phase element expansion coefficients are needed for accurate representation of the phase function/matrix. Due to the computational burden incurred by use of such a large number expansion coefficients, a truncation method is commonly applied so that only the first $2N$ elements are used, where $2N$ is set to be equal to the number of streams. This method greatly improves the computational efficiency, but also introduces radiance errors due to the approximate phase matrix representation. Since the truncation reduces the scattering cross-section and thereby enhances the direct beam contribution, the differential optical depth $d\tau$ and the single-scattering albedo ϖ are both being scaled as follows.

$$\widehat{d\tau} = (1 - f\varpi)d\tau \tag{142}$$

$$\hat{\varpi} = \frac{(1-f)\varpi}{1 - f\varpi} \tag{143}$$

where the factor f depends on the particular truncation method used (Wiscombe, 1977; Hu et al., 2000; Lin et al., 2018).

The single-scattering correction method (Nakajima and Tanaka, 1988) was designed to decrease the error incurred by the truncation. To this end we replace the approximate single-scattering solution obtained by use of the truncated phase matrix by the correct single-scattering solution obtained from the accurate phase matrix as described in **Section 5.3**. Denoting P and $P^\star$ as the original and truncated phase matrix, and $\mathbf{I}^\star$ as the singly-scattered radiance, we may write the single-scattering correction algorithm as follows (Nakajima and Tanaka, 1988):

$$\mathbf{I}_{\text{corrected}}(\hat{\tau}, \hat{\varpi}, P^\star) = \mathbf{I}(\hat{\tau}, \hat{\varpi}, P^\star) - \mathbf{I}^\star(\hat{\tau}, \hat{\varpi}, P^\star) + \mathbf{I}^\star\left(\hat{\tau}, \varpi \Big/ (1 - f\varpi), P\right). \tag{144}$$

On the right hand side of **Eq. 144**, the first term $\mathbf{I}(\hat{\tau}, \hat{\varpi}, P^*)$ is the uncorrected radiance computed with the truncated phase matrix $P^\star$, the scaled optical depth $\hat{\tau}$ and the scaled single-scattering albedo $\hat{\varpi}$. The second (subtracted) term $\mathbf{I}^*(\hat{\tau}, \hat{\varpi}, P^*)$ is the uncorrected singly-scattered radiance obtained by use of the truncated phase matrix P^*, the scaled single-scattering albedo $\hat{\varpi}$ and the scaled optical depth $\hat{\tau}$ (as in the first term). The (added) third term $\mathbf{I}^*(\hat{\tau}, \varpi/(1 - f\varpi), P)$ is the accurate singly-scattered radiance obtained by use of the accurate

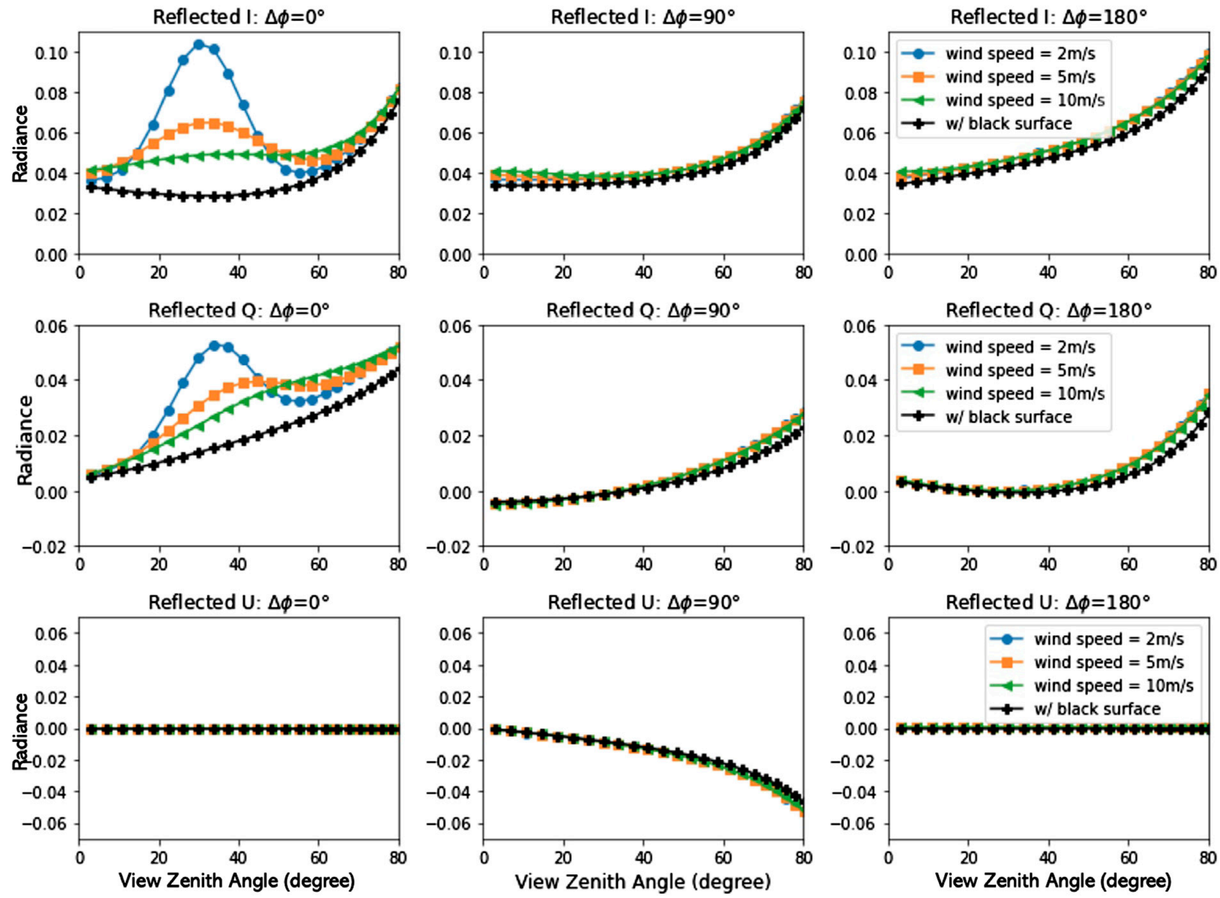

FIGURE 11 | TOA polarization components of sunlight reflected from a molecular atmosphere overlying a wind-roughened water surface for three different wind speeds.

phase matrix P, the scaled $\hat{\tau}$, and another scaled single-scattering albedo $\varpi/(1-f\varpi)$.

6 DISCRETE ORDINATE RADIATIVE TRANSFER TEST RESULTS

Schulz et al. (1999) tested a previous of VDISORT against benchmark results provided by Garcia and Siewert (1989). The result of the first three Stokes components were reproduced, but the V component was not considered. In our new version, this issue is fixed by implementing the complex eigensolutions as already discussed. The current version of VDISORT has been tested against benchmark results provided by (Garcia and Siewert, 1989) and Siewert (2000), and excellent agreement was found (Lin, 2016). Here we provide comparisons with benchmark results provided Kokhanovsky et al. (2010) for more challenging phase matrices that require more than 100 terms in the phase matrix expansion.

6.1 Comparison With Benchmark Results

The Kokhanovsky et al. (2010) benchmark results were provided for the Stokes parameters of both reflected and transmitted light in the case of molecular, aerosol, and cloudy multiple-scattering media at the wavelength $\lambda = 412$ nm. A black underlying surface for three values of the relative azimuth angles $\phi - \phi_0 = 0, 90, 180^\circ$ were considered and the solar zenith angle was set to 60°. The optical thickness was set to 0.3262 for all three single layer cases. Since the Rayleigh test is simple and has been well tested in previous versions of VDISORT, we will focus on the more challenging aerosol and cloud cases.

The phase matrix elements for all three cases are shown in **Figure 5**. Because aerosol and cloud particles are much larger than molecules, their phase matrices were calculated using Mie theory (Kokhanovsky et al., 2010). In contrast to Rayleigh scattering, aerosol and cloud particles both have a strong forward-scattering peak. There are also two peaks around 137° in scattering angle that correspond to the primary and secondary rainbows.

The sharp forward-peaked scattering of aerosol and cloud particles shown in **Figure 5** implies that a large number of terms in the Fourier expansion is required for accurate representation of the phase matrix. In fact, Kokhanovsky et al. (2010) provide about 1,000 terms of Greek constants, and below we use the first 148 terms for both the aerosol and cloud cases in VDISORT in an attempt to match the benchmark results.

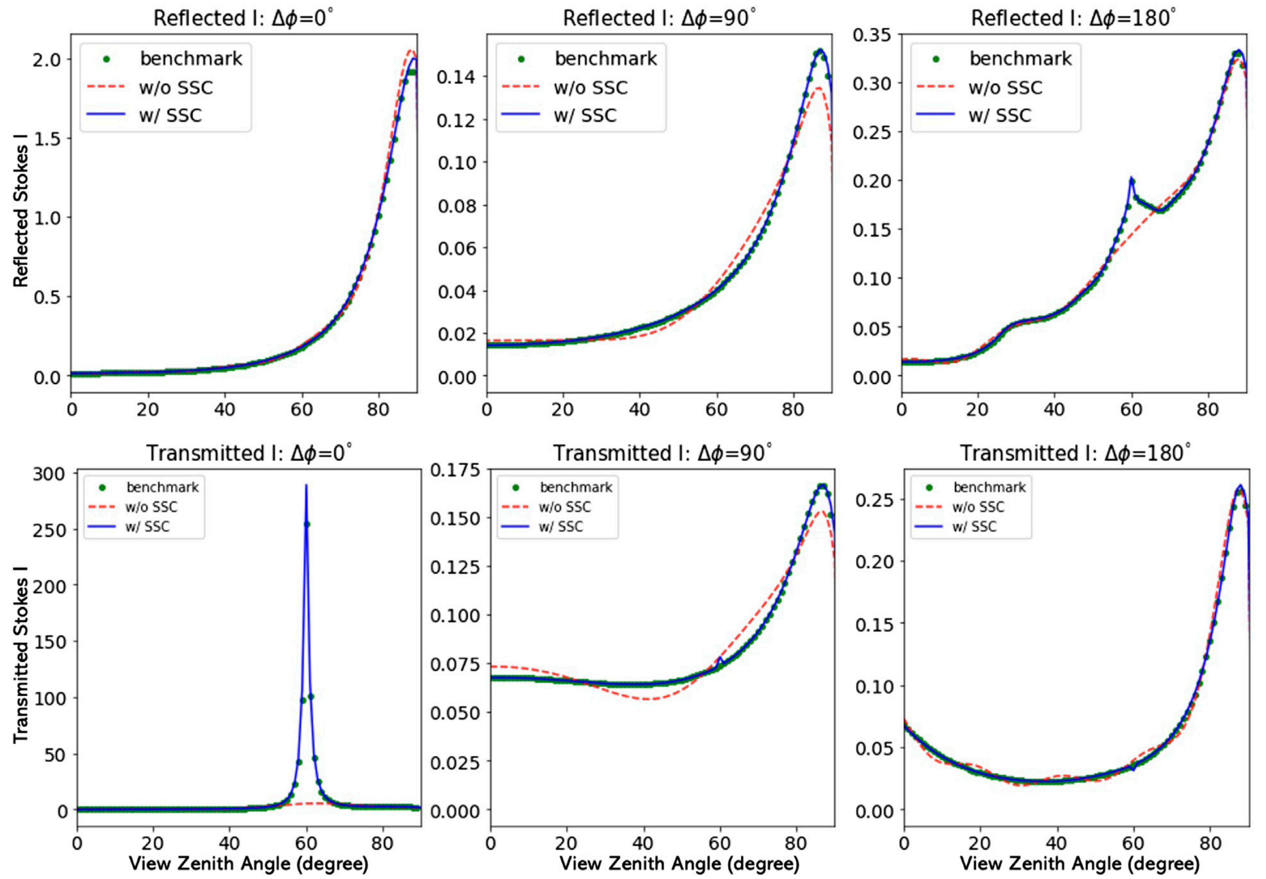

FIGURE 12 | The Stokes parameter I (τ, μ, ϕ) for the aerosol scattering case. Top row: Reflected light. Same as top row of **Figure 6**, but using NSTR = 16 (NSTR = 148 in **Figure 6**) and *with* and *without* SSC. Bottom row: Transmitted light; same as bottom row of **Figure 6**, but using NSTR = 16 (NSTR = 148 in **Figure 6**) and *with* and *without* SSC.

6.1.1 Aerosol Case

The normalized log-normal density distribution of aerosol particles considered in the benchmark computations of Kokhanovsky et al. (2010) had mode radius r_g = 0.3 μm corresponding to a mode size parameter of ~ 2.3 at 412 nm, and a standard deviation σ_g = 0.92. The size distribution was integrated from r_1 = 0.005 μm to r_2 = 30 μm. The refractive index of the aerosol particles was set to m = 1.385, which yields a single-scattering albedo of 1.0, and an asymmetry factor g = 0.79275. **Figure 6** shows reflected (top) and transmitted (bottom) results for the Stokes parameter I (τ, μ, ϕ) for solar beam incidence at 60° solar zenith angle on a homogeneous slab of optical thickness 0.3262 overlying a black surface. Similar results for the Stokes parameter Q (τ, μ, ϕ) are shown in **Figure 7** and for the Stokes parameters U (τ, μ, ϕ) and V (τ, μ, ϕ) in **Figure 8**.

6.1.2 Cloud Case

Benchmark results for a homogeneous slab of optical thickness 5 consisting of a log-normal distribution of cloud particles with r_g = 5 μm (mode size parameter of ~ 38 at 412 nm), and σ_g = 0.4 were also provided by Kokhanovsky et al. (2010). The smallest and largest particle radii were selected to be r_1 = 0.005 μm and r_2 = 100 μm, and the refractive index was set to m = 1.339. These choices yield a single-scattering albedo of 1.0, and an asymmetry factor g = 0.86114 for this ensemble of cloud particles. **Figures 9**, **10** show that VDISORT simulations with NSTR = 148 yield good agreement with the benchmark results for all four Stokes parameters.

6.2 The Bidirectional Polarized Reflectance Distribution Function (BP$_r$DF)

The BP$_r$DF is the vector equivalent that corresponds to the Bidirectional Reflectance Distribution Function (BRDF) in scalar radiative problems for which only the first component of the Stokes vector, the radiance I, is considered. In this version of VDISORT, BP$_r$DFs for two surface types were implemented: a Lambertian surface and a rough surface with a Gaussian distribution of surface slopes, which is frequently used to model scattering from wind-roughened water surfaces.

In general, both the diffuse light and the direct beam are reflected by BP$_r$DF shown as below:

$$\mathbf{I}_{\text{refl}}(\tau^*,\mu,\phi) = \int_0^1 d\mu' \int_0^{2\pi} d\phi' \, \mu' \tilde{\mathbf{R}}(\mu',\mu,\phi-\phi')\mathbf{I}_{\text{inc}}(\tau^*,\mu',\phi') + \frac{\mu_0}{4\pi}\tilde{\mathbf{R}}(\mu_0,\mu,\phi-\phi_0)\mathbf{S}_b e^{-\tau^*/\mu_0} \tag{145}$$

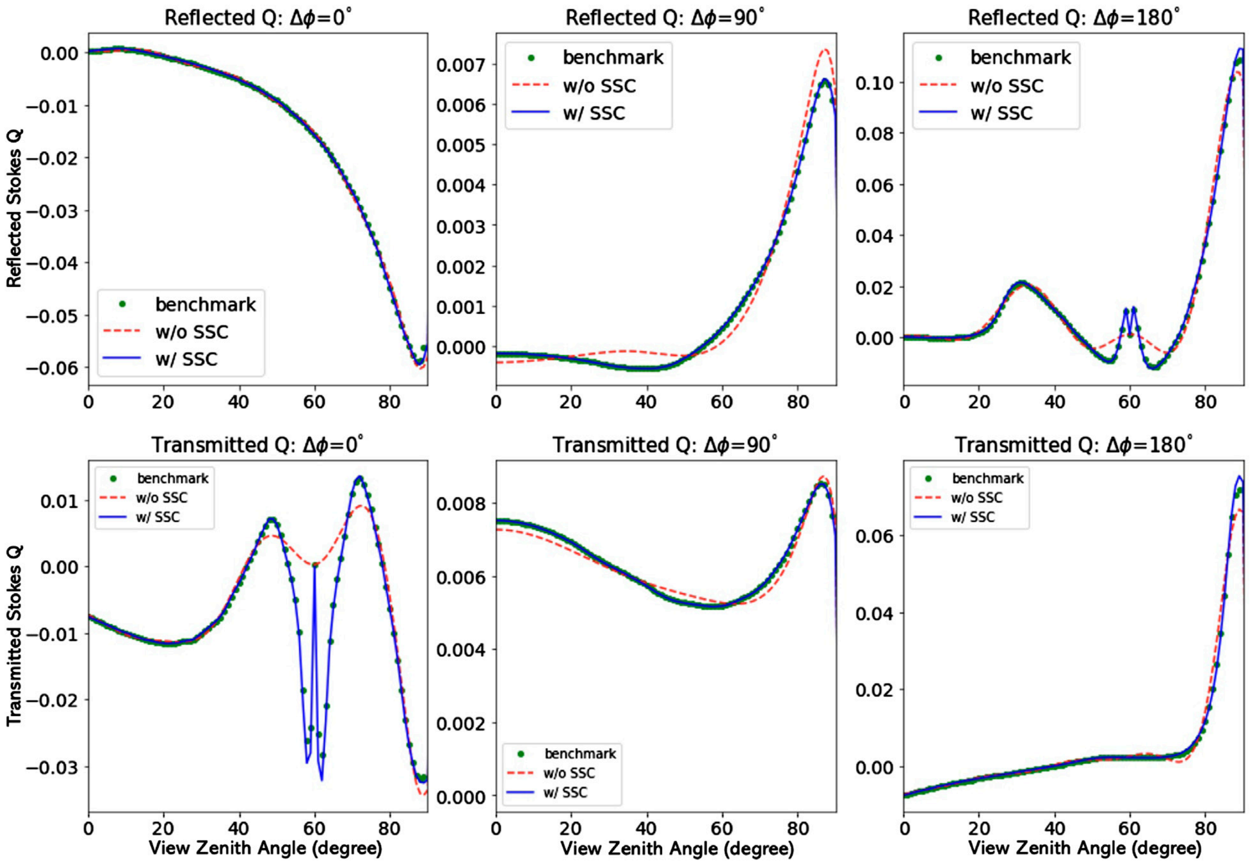

FIGURE 13 | The Stokes parameter $Q\,(\tau, \mu, \phi)$ for the aerosol scattering case. Top row: Reflected light. Same as top row of **Figure 7**, but using NSTR = 16 (NSTR = 148 in **Figure 7**) and *with* and *without* SSC. Bottom row: Transmitted light; same as bottom row of **Figure 7**, but using NSTR = 16 (NSTR = 148 in **Figure 7**) and *with* and *without* SSC.

where μ and μ' are cosines of the polar angles θ and θ' and ϕ' and ϕ are the corresponding azimuth angles. The downward Stokes vector at the surface is denoted $\mathbf{I}_{\mathrm{inc}}\,(\tau^*, \mu', \phi')$, and $\mathbf{S}_b = [I_0/2, I_0/2, 0, 0]^T$ is the TOA direct beam illumination assumed to consist of unpolarized light of irradiance I_0. The 4 × 4 reflection matrix $\tilde{\mathbf{R}}$ depends on the surface properties. It is expanded into a Fourier series to isolate the azimuth dependence and that expansion is consistent with the expansion of the phase matrix.

A Lambertian surface is a special surface that, regardless of the state of polarization of the incident radiation, gives rise to reflected radiation that is uniform, i.e. isotropic over the upward hemisphere, and unpolarized. Therefore, only the first ($m = 0$) term in the Fourier expansion contributes. The reflection matrix is given by

$$\tilde{\mathbf{R}}^{m=0} = \rho_{\mathrm{L}} \begin{pmatrix} 0.5 & 0.5 & 0 & 0 \\ 0.5 & 0.5 & 0 & 0 \\ 0 & 0 & 0 & 0 \\ 0 & 0 & 0 & 0 \end{pmatrix} \tag{146}$$

where ρ_{L} is the surface albedo.

For a wind-roughened water surface, an explicit expression for the reflectance matrix $\tilde{\mathbf{R}}$ is given by

$$\tilde{\mathbf{R}}\,(\mu', \mu, \phi - \phi') = \frac{1}{4\mu'\,\mu\,\mu_n^4}\; p\,(\mu_n) \cdot \mathbf{C}^r_{\mathrm{rs}}\,(\mu', \mu; \phi', \phi) \cdot \mathbf{S}\,(\mu', \mu, \sigma). \tag{147}$$

In **Eq. 147**, the matrix $\mathbf{C}^r_{\mathrm{rs}}$ is determined by the relative refractive index m and is derived from the Fresnel reflectance, with details described in **Supplementary Appendix A3** of Stamnes and Stamnes (2015). $p\,(\mu_n)$ is the rough surface slope probability approximated by a one-dimensional Gaussian distribution (Cox and Munk, 1954).

$$p\,(\mu_n) = \frac{1}{\pi\sigma^2}\exp\left(-\frac{1-\mu_n^2}{\sigma^2\mu_n^2}\right) \tag{148}$$

$$\mu_n = \frac{\mu + \mu'}{\sqrt{2\,(1-\cos\Theta)}} \tag{149}$$

$$\cos\Theta = -\mu'\mu + \sqrt{1-\mu'^2}\sqrt{1-\mu^2}\cos\,(\phi' - \phi) \tag{150}$$

$$\sigma^2 = 0.003 + 0.00512 \cdot w. \tag{151}$$

σ^2 is the mean square *surface slope* determined by the water surface wind speed w in m s^{-1}. $\mathbf{S}\,(\mu, \mu', \sigma)$ is the shadow term

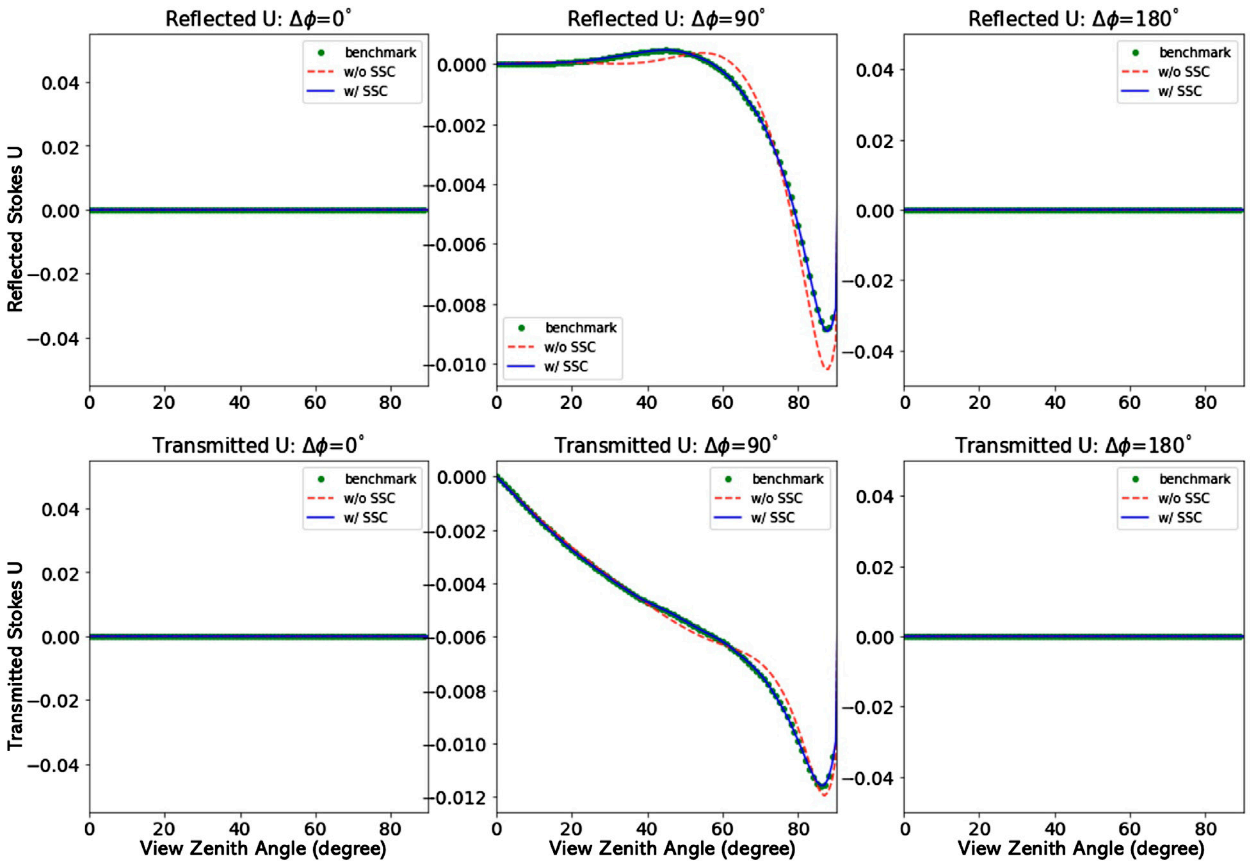

FIGURE 14 | The Stokes parameter $U(\tau, \mu, \phi)$ for the aerosol scattering case. Top row: Reflected light. Same as top row of **Figure 8**, but using NSTR = 16 (NSTR = 148 in **Figure 8**) and *with* and *without* SSC. Bottom row: Transmitted light; same as bottom row of **Figure 8**, but using NSTR = 16 (NSTR = 148 in **Figure 8**) and *with* and *without* SSC.

that is only important for the conditions of large wind speeds and large viewing zenith angles (Tsang et al., 1985). To demonstrate how the surface reflectance is applied, a simple example of an atmospheric simulation is considered with a layer of non-absorbing molecules of scattering optical thickness 0.32 and a depolarization factor of 0.04 at 412 nm (Bodhaine et al., 1999) overlying wind-roughened water surfaces with different wind speeds (2, 5, 10 m s^{-1}). The solar zenith angle is set to 30°. **Figure 11** shows the upward *I*, *Q*, and *U* components at the top of atmosphere. A glint pattern is clearly evident in the principal plane ($\Delta\phi = (\phi' - \phi) = 0^\circ$) for all wind speeds.

6.3 The Single-Scattering Correction

To demonstrate the efficiency and accuracy gained by use of the single-scattering correction (SSC), we provide some examples in this Section. For strongly forward-peaked scattering occurring for particles that are large compared to the light wavelength, use of the delta-M scaling transformation is very useful. Also, use of the ISF method discussed in **Section 3.5** helps producing accurate results at polar angles other than the quadrature angles. **Figure 12** shows that accurate results for the total polarized radiance (the *I* Stokes parameter) can be obtained with as little as 16 streams when the SSC is applied in addition to the delta-M and ISF methods. Similar results for the *Q* and *U* Stokes parameters are shown in **Figures 13, 14**.

6.4 Polarized Beam Incidence

So far we have assumed that the incident beam consisted of natural (unpolarized) light (like sunlight). For some applications, like laser (lidar) or lunar beam illumination, the source would be a polarized beam. VDISORT is capable of handling also the general case of an arbitrarily polarized incident beam source. To test the performance of VDISORT for polarized beam incidence, a polarized beam source term $\mathbf{I}_{\mathrm{inc}} = [I,Q,U,V]^T = \pi[1.0,–0.4.0.2.0.05]^T$ (corresponding to $\mathbf{I}_{\mathrm{inc}} = [I_{\parallel}, I_{\perp}, U, V]^T = \pi[0.3, 0.7, 0.2, 0.05]^T$) was chosen as input for the so-called $L = 13$ case reported by Garcia and Siewert (1989). In this test case the optical thickness of the slab was assumed to be 1.0, the single-scattering albedo was taken to be 0.99, and the surface was assumed to be a Lambertian reflector with albedo 0.1. We calculated the Stokes parameters *I*, *Q*, and *U* and the degree of polarization (DOP) for this test case and reproduced **Figure 5** of Schulz et al. (1999) as shown in **Figure 15.** Schulz

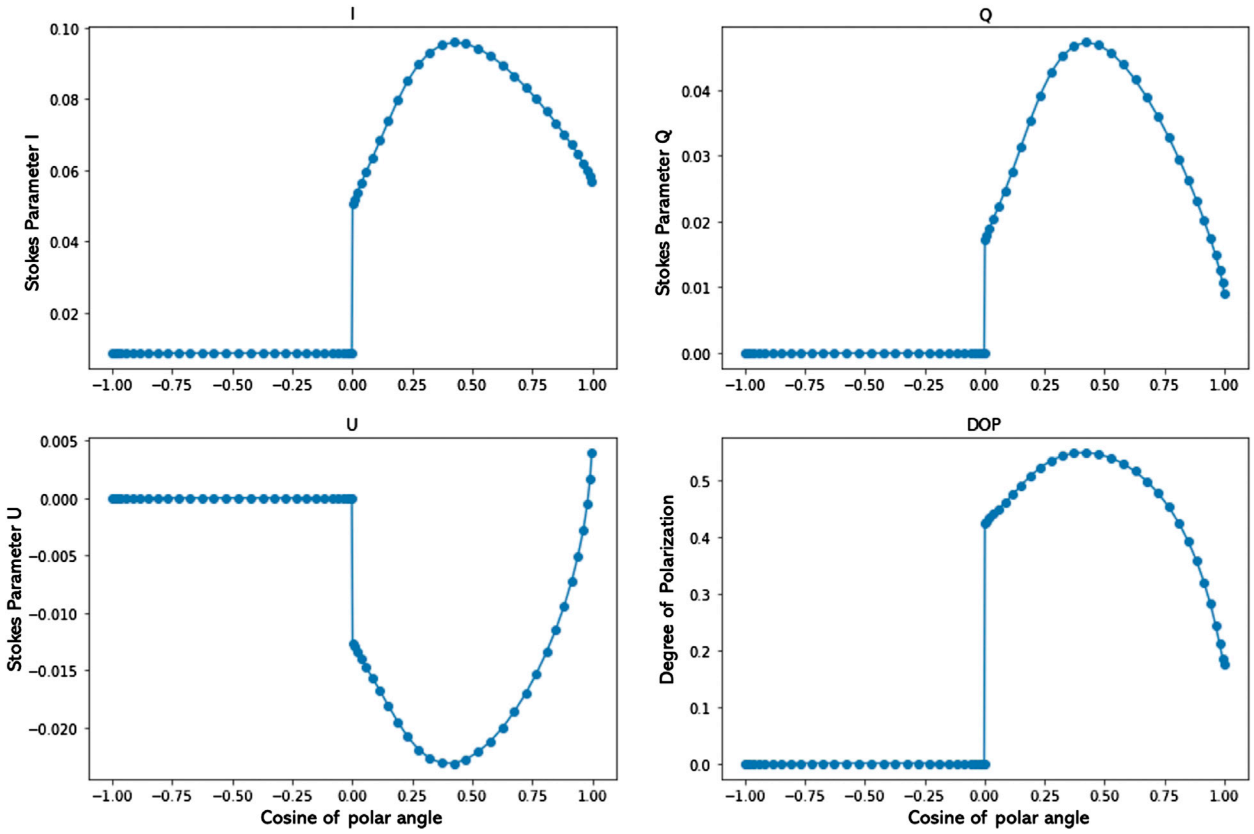

FIGURE 15 | The Stokes parameters for polarized beam incidence with $\mathbf{I}_{\text{inc}} = [I_{\parallel}, I_{\perp}, U, V]^T = \pi[0.3, 0.7, 0.2, 0.05]^T$. Same as **Figure 5** of Schulz et al. (1999).

et al. (1999) verified their results by comparing with output produced by the accurate General Adding Program (GAP) described by De Haan et al. (1987).

7 CONCLUDING REMARKS

A review is provided of the vector discrete ordinate (VDISORT) method of solution to the radiative transfer equation pertinent for polarized transfer of radiation in a vertically stratified medium. Several new features are described and discussed including how to 1) deal with the complex solutions required to compute the V component of the Stokes vector $\mathbf{I} = [I\ Q\ U\ V]^T$, 2) obtain accurate radiances at any desired polar observation angles by use of the ISF method, 3) deal with polarized beam incidence at the top of the atmosphere as well as polarized reflectance by the lower boundary, 4) use a pseudo-spherical treatment to correct for Earth curvature effects, and 5) use the single-scattering correction to enhance the efficiency of the method without sacrificing accuracy. Comparisons with benchmark results are provided to demonstrate the versatility of the VDISORT computer code to provide reliable solutions for aerosol and cloud cases including non-spherical ice cloud phase matrices. In particular, it has been shown that as few as $2N = 16$ discrete-ordinate streams are sufficient to compute accurate polarized radiances for phase matrices appropriate for ensembles of aerosol particles. We encourage future users to help us improve this freely available tool by 1) reporting on bugs found and how they were fixed, 2) making suggestions for how this tool can be improved, and 3) help make it known to friends and co-workers in need of such a resource that this tool is available.

DATA AVAILABILITY STATEMENT

The raw data supporting the conclusions of this article will be made available by the authors, without undue reservation.

AUTHOR CONTRIBUTIONS

KS wrote the first draft of the paper based on notes and material provided by ZL. AB helped with the formulation of the equations in **Section 2.4.1**. All authors provided feedback on the draft including corrections and constructive suggestions. The numerical coding was done primarily by ZL with significant input from SS. Inspection/testing of the numerical VDISORT code was done by WL and IL, who provided substantial suggestions for improvement.

FUNDING

Partial support for the work described in this paper was provided by grants to Stevens Institute of Technology from the Air Force Research Laboratory as well as NASA's Remote Sensing Theory Program.

SUPPLEMENTARY MATERIAL

The Supplementary Material for this article can be found online at: https://www.frontiersin.org/articles/10.3389/frsen.2022.880768/full#supplementary-material

REFERENCES

Berk, A. (2022). A Note on Computing Stokes Phase Matrices for Macroscopically Isotropic Mirror Symmetric Scattering Medium Stokes Scattering Matrices. *J. Quantitative Spectrosc. Radiat. Transf.* 286, 108220. doi:10.1016/j.jqsrt.2022.108220

Bodhaine, B. A., Wood, N. B., Dutton, E. G., and Slusser, J. R. (1999). On Rayleigh Optical Depth Calculations. *J. Atmos. Ocean. Technol.* 16, 1854–1861. doi:10.1175/1520-0426(1999)016<1854:orodc>2.0.co;2

Chandrasekhar, S. (1960). *Radiative Transfer*. New York: Dover Publications.

Cohen, D., Stamnes, S., Tanikawa, T., Sommersten, E. R., Stamnes, J. J., Lotsberg, J. K., et al. (2013). Comparison of Discrete Ordinate and Monte Carlo Simulations of Polarized Radiative Transfer in Two Coupled Slabs with Different Refractive Indices. *Opt. Expr.* 21, 9592–9614. doi:10.1364/oe.21.009592

Cox, C., and Munk, W. (1954). Measurement of the Roughness of the Sea Surface from Photographs of the Sun's Glitter. *Josa* 44, 838–850. doi:10.1364/josa.44.000838

Dahlback, A., and Stamnes, K. (1991). A New Spherical Model for Computing the Radiation Field Available for Photolysis and Heating at Twilight. *Planet. Space Sci.* 39, 671–683. doi:10.1016/0032-0633(91)90061-e

De Haan, J., Bosma, P., and Hovenier, J. (1987). The Adding Method for Multiple Scattering Calculations of Polarized Light. *Astronomy Astrophysics* 183, 371–391.

Garcia, R., and Siewert, C. (1989). The Fn Method for Radiative Transfer Models that Include Polarization Effects. *J. Quantitative Spectrosc. Radiat. Transf.* 41, 117–145. doi:10.1016/0022-4073(89)90133-7

Hansen, J. E. (1971). Multiple Scattering of Polarized Light in Planetary Atmospheres Part Ii. Sunlight Reflected by Terrestrial Water Clouds. *J. Atmos. Sci.* 28, 1400–1426. doi:10.1175/1520-0469(1971)028<1400:msopli>2.0.co;2

He, X., Stamnes, K., Bai, Y., Li, W., and Wang, D. (2018). Effects of Earth Curvature on Atmospheric Correction for Ocean Color Remote Sensing. *Remote Sens. Environ.* 209, 118–133. doi:10.1016/j.rse.2018.02.042

Hovenier, J. W., der Mee, C. D. V., and Domke, H. (2004). *Transfer of Polarized Light in Planetary Atmospheres*. Dordrecht, Netherlands: Kluwer Academic Publsihers.

Hovenier, J. W., and van der Mee, C. V. M. (1983). Fundamental Relationships Relevant to the Transfer of Polarized Light in a Scattering Atmosphere. *Astron. Astrophys.* 128, 1–16.

Hu, Y.-X., Wielicki, B., Lin, B., Gibson, G., Tsay, S.-C., Stamnes, K., et al. (2000). δ-Fit: A Fast and Accurate Treatment of Particle Scattering Phase Functions with Weighted Singular-Value Decomposition Least-Squares Fitting. *J. Quantitative Spectrosc. Radiat. Transf.* 65, 681–690. doi:10.1016/s0022-4073(99)00147-8

Kokhanovsky, A. A., Budak, V. P., Cornet, C., Duan, M., Emde, C., Katsev, I. L., et al. (2010). Benchmark Results in Vector Atmospheric Radiative Transfer. *J. Quantitative Spectrosc. Radiat. Transf.* 111, 1931–1946. doi:10.1016/j.jqsrt.2010.03.005

Laszlo, I., Stamnes, K., Wiscombe, W. J., and Tsay, S.-C. (2016). "The Discrete Ordinate Algorithm, Disort for Radiative Transfer," in *Light Scattering Reviews* (Berlin Heidelberg: Springer), Vol. 11, 3–65. doi:10.1007/978-3-662-49538-4_1

Lin, Z., Chen, N., Fan, Y., Li, W., Stamnes, K., and Stamnes, S. (2018). New Treatment of Strongly Anisotropic Scattering Phase Functions: the Delta-M+ Method. *J. Atmos. Sci.* 75, 327–336. doi:10.1175/jas-d-17-0233.1

Lin, Z. (2016). *Development and Applications of Radiative Transfer Models for Unpolarized and Polarized Light* (Hoboken, NJ: Stevens Institute of Technology). PhD Thesis.

Lin, Z., Stamnes, S., Jin, Z., Laszlo, I., Tsay, S.-C., Wiscombe, W., et al. (2015). Improved Discrete Ordinate Solutions in the Presence of an Anisotropically Reflecting Lower Boundary: Upgrades of the Disort Computational Tool. *J. Quantitative Spectrosc. Radiat. Transf.* 157, 119–134. doi:10.1016/j.jqsrt.2015.02.014

Mishchenko, M. I. (1991). Light Scattering by Randomly Oriented Rotationally Symmetric Particles. *J. Opt. Soc. Am. A* 8, 871–882. doi:10.1364/josaa.8.000871

Mishchenko, M. I., and Travis, L. D. (1997). Satellite Retrieval of Aerosol Properties over the Ocean Using Polarization as Well as Intensity of Reflected Sunlight. *J. Geophys. Res.* 102, 16989–17013. doi:10.1029/96jd02425

Nakajima, T., and Tanaka, M. (1988). Algorithms for Radiative Intensity Calculations in Moderately Thick Atmospheres Using a Truncation Approximation. *J. Quantitative Spectrosc. Radiat. Transf.* 40, 51–69. doi:10.1016/0022-4073(88)90031-3

Schulz, F., and Stamnes, K. (2000). Angular Distribution of the Stokes Vector in a Plane-Parallel, Vertically Inhomogeneous Medium in the Vector Discrete Ordinate Radiative Transfer (Vdisort) Model. *J. Quantitative Spectrosc. Radiat. Transf.* 65, 609–620. doi:10.1016/s0022-4073(99)00115-6

Schulz, F., Stamnes, K., and Weng, F. (1999). Vdisort: an Improved and Generalized Discrete Ordinate Method for Polarized (Vector) Radiative Transfer. *J. quantitative Spectrosc. Radiat. Transf.* 61, 105–122. doi:10.1016/s0022-4073(97)00215-x

Siewert, C. (2000). A Discrete-Ordinates Solution for Radiative-Transfer Models that Include Polarization Effects. *J. Quantitative Spectrosc. Radiat. Transf.* 64, 227–254. doi:10.1016/s0022-4073(99)00006-0

Siewert, C. E. (1981). On the Equation of Transfer Relevant to the Scattering of Polarized Light. *Astrophys. J.* 245, 1080–1086. doi:10.1086/158884

Siewert, C. E. (1982). On the Phase Matrix Basic to the Scattering of Polarized Light. *Astron. Astrophys.* 109, 195–200.

Sommersten, E. R., Lotsberg, J. K., Stamnes, K., and Stamnes, J. J. (2010). Discrete Ordinate and Monte Carlo Simulations for Polarized Radiative Transfer in a Coupled System Consisting of Two Media with Different Refractive Indices. *J. Quant. Spectrosc. Radiat. Transf.* 111, 616–633. doi:10.1016/j.jqsrt.2009.10.021

Stamnes, K., and Conklin, P. (1984). A New Multi-Layer Discrete Ordinate Approach to Radiative Transfer in Vertically Inhomogeneous Atmospheres. *J. Quantitative Spectrosc. Radiat. Transf.* 31, 273–282. doi:10.1016/0022-4073(84)90031-1

Stamnes, K. (1982). On the Computation of Angular Distributions of Radiation in Planetary Atmospheres. *J. Quantitative Spectrosc. Radiat. Transf.* 28, 47–51. doi:10.1016/0022-4073(82)90096-6

Stamnes, K., and Stamnes, J. J. (2015). *Radiative Transfer in Coupled Environmental Systems*. Hoboken, NJ: Wiley VCH.

Stamnes, K., Thomas, G. E., and Stamnes, J. J. (2017a). *Radiative Transfer in the Atmosphere and Ocean*. 2 edn. New York, NY: Cambridge University Press.

Stamnes, K., Tsay, S.-C., Wiscombe, W., and Jayaweera, K. (1988). Numerically Stable Algorithm for Discrete-Ordinate-Method Radiative Transfer in Multiple Scattering and Emitting Layered Media. *Appl. Opt.* 27, 2502–2509. doi:10.1364/ao.27.002502

Stamnes, S., Ou, S., Lin, Z., Takano, Y., Tsay, S., Liou, K., et al. (2017b). Polarized Radiative Transfer of a Cirrus Cloud Consisting of Randomly Oriented Hexagonal Ice Crystals: The 3× 3 Approximation for Non-spherical Particles. *J. Quantitative Spectrosc. Radiat. Transf.* 193, 57–68. doi:10.1016/j.jqsrt.2016.07.001

Tsang, L., Kong, J. A., and Shin, R. T. (1985). *Theory of Microwave Remote Sensing*. Hoboken, NJ: A Wiley-Interscience Publication.

Weng, F. (1992). A Multi-Layer Discrete-Ordinate Method for Vector Radiative Transfer in a Vertically-Inhomogeneous, Emitting and Scattering Atmosphere – I. Theory. *J. Quantitative Spectrosc. Radiat. Transf.* 47, 19–33. doi:10.1016/0022-4073(92)90076-g

Wiscombe, W. (1977). The Delta–M Method: Rapid yet Accurate Radiative Flux Calculations for Strongly Asymmetric Phase Functions. *J. Atmos. Sci.* 34, 1408–1422. doi:10.1175/1520-0469(1977)034<1408:tdmrya>2.0.co;2

Conflict of Interest: AB is employed by Spectral Sciences.

The remaining authors declare that the research was conducted in the absence of any commercial or financial relationships that could be construed as a potential conflict of interest.

Frontiers in
Remote Sensing

Highlights innovation in remote sensing science and its applications

An exciting journal which focuses on physical and quantitative approaches to remote sensing of the land, oceans, biosphere, atmosphere and space at local and global levels.

Discover the latest Research Topics

See more →

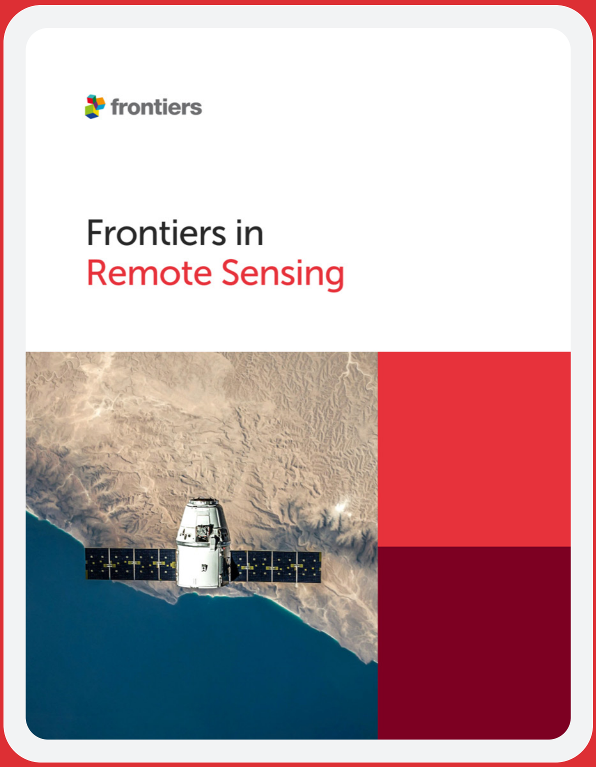

frontiers

Frontiers in
Remote Sensing

Frontiers

Avenue du Tribunal-Fédéral 34
1005 Lausanne, Switzerland
frontiersin.org

Contact us

+41 (0)21 510 17 00
frontiersin.org/about/contact